AN ALTERNATING CURRENT POTENTIAL DIFFERENCE CALIBRATION STUDY AND FATIGUE CRACK GROWTH IN STEEL

A Thesis Submitted for the Degree

of

Doctor of Philosophy

by

LEON GRABOWSKI, B.Sc. (Hons)

Department of Metallurgy and Materials,

University of Birmingham.

July, 1983

UNIVERSITY OF
BIRMINGHAM

University of Birmingham Research Archive

e-theses repository

This unpublished thesis/dissertation is copyright of the author and/or third parties. The intellectual property rights of the author or third parties in respect of this work are as defined by The Copyright Designs and Patents Act 1988 or as modified by any successor legislation.

Any use made of information contained in this thesis/dissertation must be in accordance with that legislation and must be properly acknowledged. Further distribution or reproduction in any format is prohibited without the permission of the copyright holder.

SYNOPSIS

Alternating current potential difference calibration data has been generated for the 'growth' of reference flaws and fatigue cracks upto depths of 24.58 mm in EN3B steel. The response between alternating current potential difference and flaw/crack depth was found to satisfy a degree 2 polynomial relationship which could be approximated to degree 1 over small changes in flaw/crack depth. Traditional methods of rationalising the data failed, and so an empirical normalising technique was developed which normalised all calibration data irrespective of calibration regime.

Fatigue studies of EN19 steel conducted at R = 0.1 in the a/w regime 0.09 to 0.39 revealed that thresholds were independent of crack length. Near threshold crack growth exhibited threshold hysteresis, which was attributed to oxide induced crack closure. Measurement of crack closure during threshold testing at R = 0.1 and 0.7 revealed that near threshold crack growth was closure dominated, and the R effect could be rationalised by adopting a ΔK_{eff} approach.

Fatigue threshold behaviour of EN3B steel of ferrite grain size 10 and 53 μm exhibited similar trends to EN19. At R = 0.1 thresholds were greater and exhibited a grain size effect. Tentative arguments describing this trend are forwarded based on crack closure arising from microstructural crack growth and fretting fatigue.

DEDICATED TO

Jude Fawley

ACKNOWLEDGEMENTS

The author wishes to thank Professor R.E. Smallman for the provision of laboratory facilities and the members of the Department of Metallurgy and Materials for their help with experimental problems.

The author would also like to thank Dr. C.J. Beevers, Dr. P. Irving and Mrs. M. Starkey for their help and encouragement.

The financial support of the Science Research Council and GKN Group Technology Centre is gratefully acknowledged.

Finally, I wish to thank Mary, for putting up with it.

TABLE OF CONTENTS

		Page No.
CHAPTER ONE	INTRODUCTION	1
CHAPTER TWO	STRESS ANALYSIS OF CRACKED BODIES AND CRACK TIP PLASTICITY	2
2.0	Nomenclature	2
2.1	Introduction	4
2.2	Elastic Stress Distribution Around a Statically Loaded Crack	4
2.3	Elastic-Plastic Analysis of a Statically Loaded Crack	7
2.4	Elastic-Plastic Analysis of a Cyclically Loaded Crack	8
2.5	Plasticity and the 'Composite Plastic Zone'	8
2.6	Developments leading to the Generalised Paris 'Law' Describing Crack Growth based on LEFM Parameters	9
2.7	References	13
CHAPTER THREE	MICROCRACK FORMATION AND STAGE I FATIGUE CRACK GROWTH	16
3.0	Introduction	16
3.1	Micro Crack Formation	16
3.2	Stage I Fatigue Crack Growth	18
3.3	References	24
CHAPTER FOUR	MECHANISMS OF STAGE II FATIGUE CRACK GROWTH	26
4.0	Introduction	26
4.1	Stage I to Stage II Transformation	26
4.2	Fracture Surface Observations and Suggested Mechanisms of Stage II Growth	27
4.3	References	31

		Page No.
CHAPTER FIVE	FATIGUE CRACK PROPAGATION AT LOW GROWTH RATES AND THRESHOLD	33
5.0	Nomenclature	33
5.1	Introduction	34
5.2	Stress Effects on Growth Rate	34
5.2.1	Stress Ratio	34
5.2.2	Stress History	36
5.3	Stress Effects on Threshold Stress Intensity Range	36
5.4	Effect of Metallurgical Variables	39
5.4.1	Mechanical Properties	39
5.4.2	Grain Size	41
5.4.3	Microstructure	42
5.5	Environmental Effects	44
5.6	Fatigue Crack Closure	48
5.7	Threshold Hysteresis	53
5.8	Fracture Surface Observations	54
5.9	References	56
CHAPTER SIX	FATIGUE CRACK GROWTH AT SHORT CRACK LENGTHS	61
6.0	Nomenclature	61
6.1	Introduction	61
6.2	Experimental Observations and Theories of Short Crack Behaviour	62
6.3	References	68
CHAPTER SEVEN	FATIGUE CRACK PROPAGATION AT INTERMEDIATE GROWTH RATES	70
7.0	Introduction	70
7.1	Experimental Evidence in Support of a Power Law Relationship	70

Page No.

7.2 Stress Effects on Growth Rate 71

7.2.1 Stress Ratio 71

7.2.2 Stress History 71

7.3 Effect of Metallurgical Variables 73

7.3.1 Microstructure 73

7.3.2 Mechanical Properties 74

7.4 Fracture Surface Observations 75

7.5 References 76

CHAPTER EIGHT ALTERNATING CURRENT FIELD THEORY AND CRACK LENGTH MEASUREMENT 79

8.0 Nomenclature 79

8.1 Introduction 80

8.2 One Dimensional Alternating Current Field Theory 80

8.3 Alternating Current versus Flaw Depth Calibration Studies 82

8.3.1 State of the Art 82

8.3.2 Summary of Observations 86

8.4 References 88

CHAPTER NINE MATERIALS 89

9.0 Introduction 89

9.1 Stock Materials and Composition 89

9.2 Experimental Materials 89

9.2.1 Ferritic Steels EN3BN and EN3BA 89

9.2.2 Tempered Martensitic Steel EN19QH 90

9.3 Quantitative Metallography 91

9.4 Mechanical Properties 91

9.5 References 92

Page No.

CHAPTER TEN AN ALTERNATING CURRENT POTENTIAL DIFFERENCE CALIBRATION STUDY OF EN3BN STEEL 93

10.0 Nomenclature 93

10.1 Introduction 95

10.2 Experimental Equipment and Procedures 95

10.2.1 Specimen Details and Preparation 95

10.2.2 Potential Difference Measurement 96

10.2.3 Groove Cutting using a Spark Erosion Technique 97

10.2.4 Fatigue Crack Growth in SEN and Precracked Specimens 98

10.3 Accuracy of Results 99

10.3.1 Flaw Depth 99

10.3.2 Potential Difference Measurement 99

10.4 Treatment of Results 100

10.5 Results and Discussion 101

10.5.1 Introduction 101

10.5.2 EDM fcg-analogue and SEN-fcg Calibration Studies 102

10.5.2.1 A Comparison of Results 102

10.5.5.2 Potential Difference versus Flaw Depth Relationship 102

10.5.2.3 Conventional Approach to Normalising Data 104

10.5.3 Geometrical Effects on Calibration Response 105

10.5.3.1 Fatigue Crack Growth in a Plane Specimen 105

10.5.3.2 Specimen Thickness Effects 105

10.5.4 Empirical Normalisation of Calibration Data 105

10.5.5 Crack Depth Prediction based on Empirical Normalisation 108

		Page No.
10.5.6	Sensitivity and Resolution	109
10.5.7	Concluding Remarks	109
10.6	Conclusions	111
10.7	Recommendations for Further Work	112
10.8	References	113
CHAPTER ELEVEN	FATIGUE CRACK GROWTH IN STEEL	114
11.0	Nomenclature	114
11.1	Introduction	115
11.2	Experimental Techniques	115
11.2.1	Fatigue Testing	115
11.2.1.1	Introduction	115
11.2.1.2	Specimen Details and Precracking	116
11.2.1.3	Fatigue Crack Growth and Threshold Testing	116
11.2.2	Crack Length Measurement and Accuracy	117
11.2.3	Evaluation of Growth Rate Results	118
11.2.4	Accuracy of Growth Rate Results	119
11.2.5	Crack Closure Measurement	120
11.2.5.1	Measurement of Crack Tip Opening Load	120
11.2.5.2	Treatment of Results	120
11.2.6	Crack Profile Replication and Examination	121
11.2.7	Fractography	122
11.3	Experimental Program	122
11.4	Results	123
11.4.1	Fatigue of Quenched and Hardened Martensitic Steel EN19QH	123
11.4.1.1	Crack Length Effects on Near Threshold Fatigue Crack Growth (R = 0.1)	123
11.4.1.1a	Growth Rate Results	123

Page No.

11.4.1.1b Crack Tip Opening Loads,Stress Intensities and ΔK_{eff} Analysis of Results 124

11.4.1.2 Stress Ratio Effect on Near Threshold Fatigue Crack Growth (R = 0.7) 124

11.4.1.2a Growth Rate Results 124

11.4.1.2b Threshold and Post Threshold Crack Tip Stress Intensities 125

11.4.1.3 A Comparison of Stress Ratio Effects on Near Threshold Fatigue Crack Growth 125

11.4.1.4 A Closure Study of Threshold Testing 125

11.4.1.4a Growth Rate Results 125

11.4.1.4b Crack Tip Opening Loads,Stress Intensities and ΔK_{eff} Analysis of Results 126

11.4.1.5 Fractography 127

11.4.1.5a Macroscopic Fracture Surface Appearance 127

11.4.1.5b Microscopic Fracture Surface Appearance 127

11.4.1.6 Crack Profile Appearance 128

11.4.2 Fatigue of Ferritic Steels EN3BN and EN3BA 129

11.4.2.1 Near Threshold Fatigue Crack Growth 129

11.4.2.1a Growth Rate Results 129

11.4.2.1b Crack Tip Opening Loads,Stress Intensities and ΔK_{eff} Analysis of Results 130

11.4.2.2 Fractography 132

11.4.2.2a Macrosopic Fracture Surface Appearance 132

11.4.2.2b Microsopic Fracture Surface Appearance 132

11.4.2.3 Crack Profile Appearance 133

Page No.

11.5 Discussion 134

11.5.1 Introduction 134

11.5.2 Threshold Fatigue Crack Growth, its Measurement and Crack Closure 135

11.5.3 Near Threshold Fatigue Crack Growth in EN19QH 138

11.5.3.1 Crack Length Effect on Threshold 138

11.5.3.2 A Crack Closure Explanation of Stress Ratio Effects on Threshold 139

11.5.3.3 Crack Closure and Threshold Testing 140

11.5.4 Near Threshold Fatigue Crack Growth and Crack Closure in EN3BN and EN3BA 144

11.5.5 Threshold Hysteresis 147

11.5.6 Fretting Fatigue and Oxide Induced Crack Closure 150

11.5.7 Concluding Remarks 152

11.6 Conclusions 154

11.7 Recommendations for Further Work 155

11.8 References 157

APPENDIX A1 CURRENT AND SENSING LEAD ARRANGEMENT 161

A1.0 Nomenclature 161

A1.1 Introduction 161

A1.2 Current Lead Arrangement and Connection 161

A1.3 Sensing Lead Arrangement and Connection to Plane and SEN Specimens 162

A1.4 References 164

Page No.

APPENDIX A2 ALTERNATING CURRENT POTENTIAL DIFFERENCE VERSUS DETECTOR INTERNAL CALIBRATION 165

A2.0 Introduction 165

A2.1 Experimental Procedure 165

A2.2 Treatment of Results 165

APPENDIX A3 ALTERNATING CURRENT POTENTIAL DIFFERENCE VERSUS PARAFFIN BATH TEMPERATURE 167

A3.0 Experimental Procedure 167

A3.1 Potential Difference versus Paraffin Bath Temperature 167

APPENDIX A4 FATIGUE CRACK GROWTH AND FRACTURE SURFACE WAVE PATTERN ANALYSIS 168

A4.0 Nomenclature 168

A4.1 Introduction 168

A4.2 Techniques of Fracture Surface Crack Wavefront Marking 169

A4.2.1 Alternating Stress Ratio at Constant K_{max} 169

A4.2.2 Overload Marking 169

A4.2.3 Alternating Stress Ratio at Constant Mean Load 169

A4.3 Production of Fracture Surface Wave Patterns 170

A4.4 PD-Wave Pattern Analysis 171

APPENDIX A5 CRACK LENGTH ERROR ANALYSIS BASED ON CRACKED AREA 172

A5.0 Nomenclature 172

A5.1 Introduction 172

A5.2 Determination of Theoretical Cracked Area Representative of a_{ci} 173

Page No.

A5.3 Determination of Actual Cracked Area 173

A5.4 Determination of Percentage Error in Cracked Area 174

A5.5 Determination of Percentage Error in Cracked Depth 174

A5.6 References 174

APPENDIX A6 COMPUTOR PROGRAMME TIDY 175

A6.0 Introduction 175

A6.1 Specific Details 175

A6.2 Running the Progamme 175

APPENDIX A7 ANALYSIS OF LINEAR REGRESSION, CORRELATION AND STANDARD RESIDUAL ERROR 176

A7.0 Nomenclature 176

A7.1 Regression Analysis 177

A7.2 Correlation Coefficient 177

A7.3 Standard Residual Error 178

A7.4 Determination of b, c, R_c and σ_e 178

A7.5 References 179

APPENDIX A8 CURVE FITTING 180

A8.0 Nomenclature 180

A8.1 Introduction 180

A8.2 Approach 180

A8.3 Chebyshev Polynomials 181

A8.4 References 182

APPENDIX A9 AN EMPIRICAL NORMALISING TECHNIQUE 183

A9.0 Nomenclature 183

A9.1 Introduction 183

		Page No.
A9.2	Basic Concept	184
A9.3	Empirical Normalisation	184
A9.4	References	185
APPENDIX A10	DETERMINATION OF COMPLIANCE FUNCTION, STRESS INTENSITY AND GROWTH RATE	186
A10.0	Introduction	186
A10.1	Compliance Function	186
A10.2	Stress Intensity K	186
A10.3	Growth Rate Determination	187
A10.4	References	187

CHAPTER ONE

INTRODUCTION

The experimental investigations of this thesis, which appear in Chapters 10 and 11, were conducted in two areas of research.

A detailed study of the alternating current potential difference response of the 'growth' of mechanical flaws and fatigue cracks was conducted using normalised EN3B steel (EN3BN) in the a/w regime 0.01 and 0.49. The major aim was to evaluate the performance of a Testwell ACPD2 Crack Detector and establish whether its calibration response could be rationalised by a standard normalising technique.

In the second investigation near threshold fatigue crack growth was evaluated in quenched and hardened EN19 (EN19QH), annealed EN3B (EN3BA) and EN3BN steels. In EN19QH a series of tests were conducted at R = 0.1 to establish if there existed a crack length effect on threshold. The R effect on threshold was also evaluated, and similtaneous crack closure measurement facilitated a ΔK_{eff} analysis of growth rates. A more detailed study of crack closure versus threshold testing was also conducted at R = 0.1 to evaluate closure trend at low growth rates. Fatigue tests of EN3BN and EN3BA of ferrite grain sizes 10 and 53 μm respectively, facilitated a comparison of threshold behaviour with that of EN19QH.

In the three materials an attempt is made to relate the occurrance of threshold and associated hysteresis to crack closure, and tentative arguments are presented to describe near threshold closure trend.

CHAPTER TWO

STRESS ANALYSIS OF CRACKED BODIES AND CRACK TIP PLASTICITY

2.0 Nomenclature

σ_a	=	remote applied stress.
τ	=	shear stress.
G	=	shear modulus.
a	=	crack length measured in the specimen width direction.
γ	=	surface workhardening component.
Y	=	compliance function.
ΔK	=	stress intensity range.
r	=	a linear measurement from the crack tip.
σ_{UTS}	=	ultimate tensile stress.
x,y,z	=	co-ordinates in three dimensional space.
K_{IC}	=	static fracture toughness.
E	=	Youngs modulus
n	=	cyclic strain hardening exponent.
δ	=	elastic crack tip opening.
δ_{pe}	=	plane strain elastic crack tip opening.
ΔK_T	=	threshold stress intensity range.
K	=	crack tip stress intensity factor.
m	=	power exponent of fatigue crack growth.

ν	=	poissons ratio.
σ_{ys}	=	monotonic yield stress.
LEFM	=	linear elastic fracture mechanics.
ω_{pe}	=	plane strain plastic zone size.
ω_{ps}	=	plane stress plastic zone size.
L	=	load.
σ_{l}	=	frictional resistance.
E_{μ}	=	strain for necking.
σ_{cys}	=	cyclic yield stress.
I,II,III	=	stress mode.
ΔD	=	displacement per cycle.
$\Delta\sigma$	=	applied stress range.

2.1 Introduction

In this Chapter the theory of continum mechanics is reviewed with respect to the stress distribution in close proximity to a crack tip contained in purely elastic material subject to monotonic loading conditions. Small scale yielding is introduced at the crack tip and its effect on stress distribution is discussed for the plane strain condition. Plastic zone sizes of the monotonic plane stress and plane strain conditions are reviewed and the formation of the plane stress plastic zone resulting from cyclic loading is described. The effect of stress state versus plasticity in a 'composite plastic zone' is also discussed with respect to material displacement at the crack tip. Finally, a brief review is made of the developments leading to the accepted generalised power law relationship describing fatigue crack growth in terms of traditional linear elastic fracture mechanics parameters.

2.2 Elastic Stress Distribution Around a Statically Loaded Crack

The elastic stress distribution in a body containing an infinitely sharp crack can be described using the theory of elasticity if it is assumed that the body undergoing the action of external forces is perfectly elastic, homogeneous and isotropic [2.01]. Although this is not true of structural materials, the theory of elasticity is still applicable because the macroscopic geometrical dimensions of the analysis are more important than the anisotropic properties of the material acting on a microscopic scale. This has been confirmed by many investigators for both isotropic [2.02, 2.04] and orthotropic [2.05, 2.06] materials.

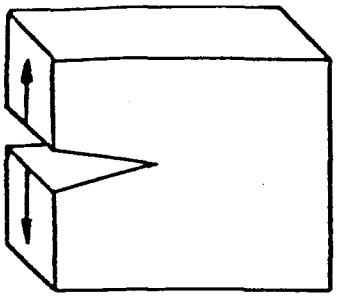
In practical situations the stress field at a crack tip is the result of a complex loading condition which can be resolved into three principle directions. These are associated with three local modes of deformation as shown in Fig. 2.01. For the right handed cartesian co-ordinate system shown in Fig. 2.02 Irwin [2.02, 2.03] determined expressions, Eqs. 2.01, for the state of stress at a crack tip subject to mode I loading using an analysis based on the method of Westergaard [2.07].

$$\left.\begin{aligned}
\sigma_{xx} &= \frac{K_I}{\sqrt{2\pi r}} \cos\frac{\theta}{2}\left[1 - \frac{\sin\theta}{2}\sin\frac{3\theta}{2}\right] \\
\sigma_{yy} &= \frac{K_I}{\sqrt{2\pi r}} \cos\frac{\theta}{2}\left[1 + \frac{\sin\theta}{2}\sin\frac{3\theta}{2}\right] \\
\sigma_{xy} &= \frac{K_I}{\sqrt{2\pi r}} \cos\frac{\theta}{2}\left[\sin\frac{\theta}{2}\cos\frac{3\theta}{2}\right] \\
\sigma_{yz} &= \tau_{xy} = 0, \sigma_{zz} = 0 \quad \ldots \text{(plane stress)} \\
\sigma_{zz} &= \nu(\sigma_{xx} + \sigma_{yy}) \quad \ldots \text{(plane strain)}
\end{aligned}\right\} \quad \ldots(2.01)$$

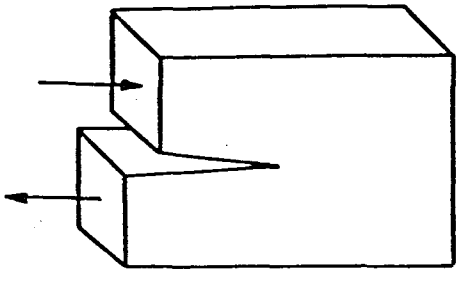
Similar elastic solutions can also be written for in-plane shear (Mode II) and anti plane shear (Mode III) [2.08]; and the stress state around any crack tip can be fully described by superimposing the three elastic modes [2.09] to give a generalised relationship of the form

$$\sigma_{ij} = r^{-\frac{1}{2}}\left(K_I F_{ij}^{I}\theta + K_{II} F_{ij}^{II}\theta + K_{III} F_{ij}^{III}\theta\right) \quad \ldots(2.02)$$

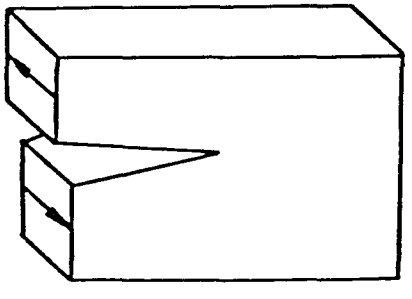
where K_I, K_{II} and K_{III} are the elastic stress intensity factors of the three modes of deformation, and $F_{ij}^{I}\theta$, $F_{ij}^{II}\theta$ and $F_{ij}^{III}\theta$



I TENSILE



II SHEAR
(IN PLANE)



III SHEAR
(ANTI-PLANE)

Fig. 2.01 Basic modes of crack or notch tip deformation.

(After Rice [2.08])

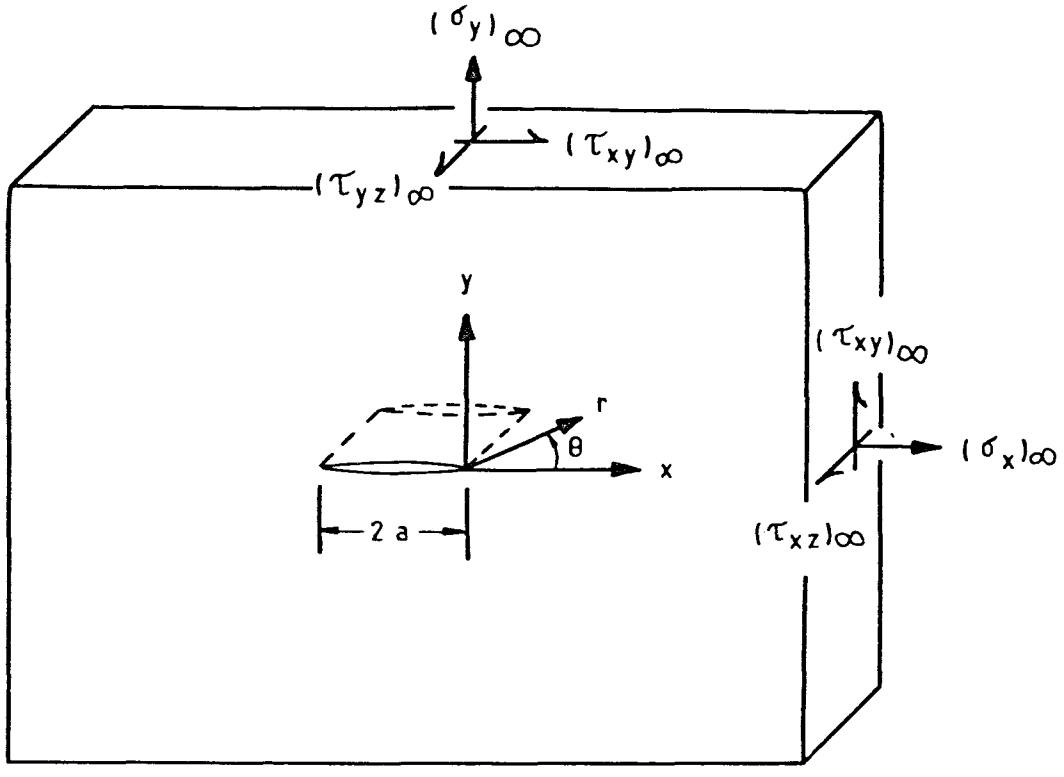


Fig. 2.02 The co-ordinate system used to evaluate the state of stress in an infinite plate containing a crack of length 2a which is subject to a uniform stress at infinity. (After Rice [2.08])

are the radius dependence functions of the stress field.

From Eqs. 2.01 it can be seen that when r is small only the first term of each stress series is significant, hence the crack tip stresses are characterised by the single stress parameter K_I. For the testing geometry of Fig. 2.02 K_I was found [2.08] to be directly related to the applied stress times the square root of the crack length, i.e.

$$K_I = \left[\sigma_y\right]_\infty \sqrt{\pi a} \qquad \ldots(2.03)$$

and similarly

$$K_{II} = \left[\tau_{xy}\right]_\infty \sqrt{\pi a}$$

$$K_{III} = \left[\tau_{zy}\right]_\infty \sqrt{\pi a}$$

In a finite cracked body K_I has been reported [2.09 - 2.11] to be dependent on specimen compliance (Y_I), which is a function of specimen shape and loading geometry and is incorporated into the stress formula as follows:

$$K_I = Y_I \sigma_y \sqrt{a} \qquad \ldots(2.04)$$

Whilst it is mathematically acceptable that linear elastic theory is applicable to all values or r it is physically unreasonable to apply it to a small region at a crack tip because as $r \to 0$ so $\sigma_{xx} \to \infty$, $\sigma_{yy} \to \infty$ and in plane strain $\sigma_{zz} \to \infty$. This is obviously unrealistic because the principle stresses in a cracked elastic body are finite. To explain the discrepency Knott [2.12] and Westergaard [2.07] reasoned that a crack tip subject to a tensile stress in a continuum medium will have a small but finite tip radius produced by elastic opening (δ) of the crack tip where

$$\delta_{pe} = \frac{4(1 - \nu^2)}{\pi E} K\sqrt{2\pi r} \qquad \ldots(2.05)$$

This produces a redistribution of the principle stresses to give the configuration shown in Fig. 2.03.

2.3 Elastic-Plastic Analysis of a Statically Loaded Crack

Knott [2.12] reasoned that in structural materials plastic flow occurs at a crack tip when the maximum difference in principle stress satisfies the Tresca Yield Criteria. He then argued that in a cracked body subject to plane strain mode I loading this results in a stress redistribution as shown in Fig. 2.04, by the formation of a plastic zone in the x ($\theta = 0$) direction which extends to a point at which the yield criteria is just satisfied.

In a cracked body subject to plane stress Rice [2.08] established that yielding in the $\theta = 0$ direction extends to a distance $2r_{ys}$ where r_{ys} corresponds to the distance r at $\theta = 90^{o}$ and $\sigma_{yy} = \sigma_{ys}$. He then argued that provided conditions of linear elastic fracture mechanics were satisfied the mode I plane stress plastic zone size could be expressed in terms of stress intensity and yield stress as follows

$$\omega_{ps} = \frac{1}{\pi} \left[\frac{K_I}{\sigma_{ys}}\right]^2 \qquad \ldots(2.06)$$

Using a similar approach Knott [2.12] found that the Mode I plane strain plastic zone size was one third that of plane stress, i.e.

$$\omega_{pe} = \frac{1}{3} \left[\frac{K_I}{\sigma_{ys}}\right]^2 \qquad \ldots(2.07)$$

π missed out?

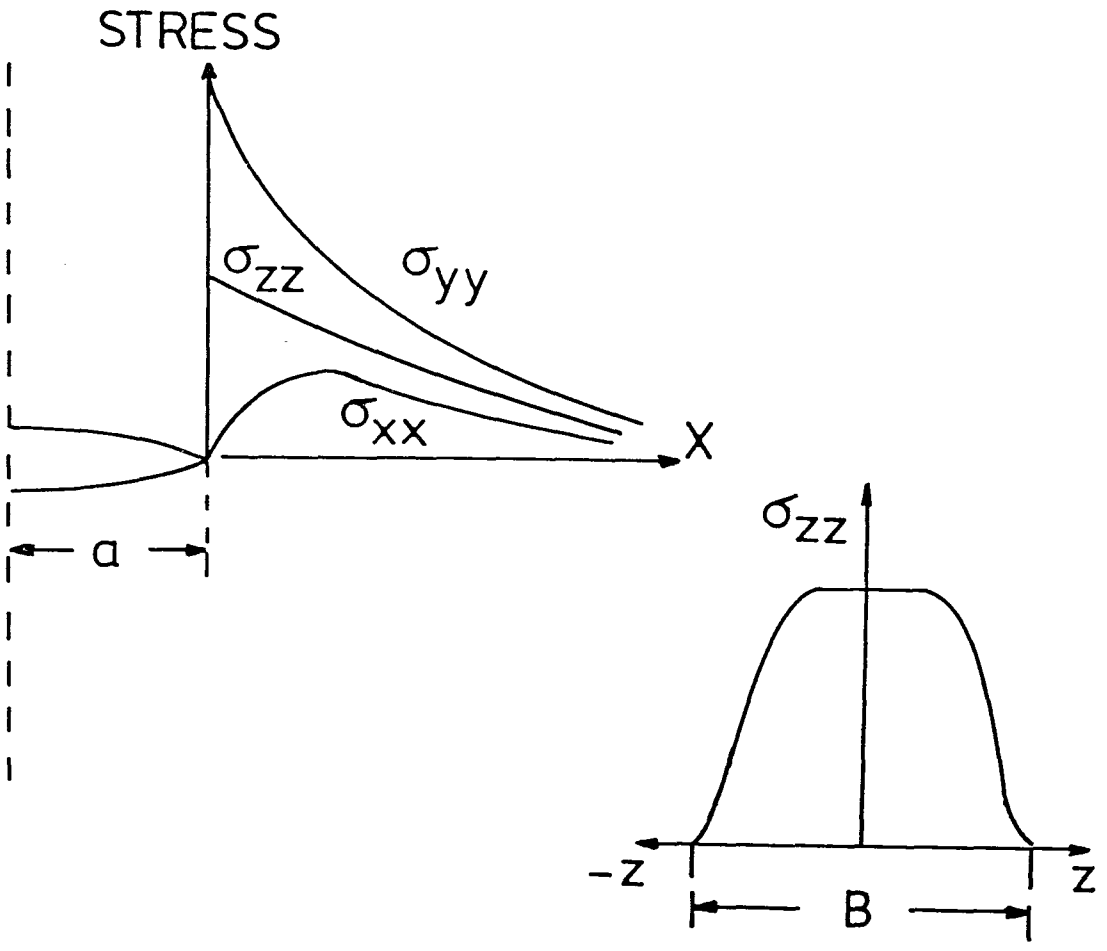


Fig. 2.03 Distribution of principle stresses at a crack tip.
(After Knott [2.12])

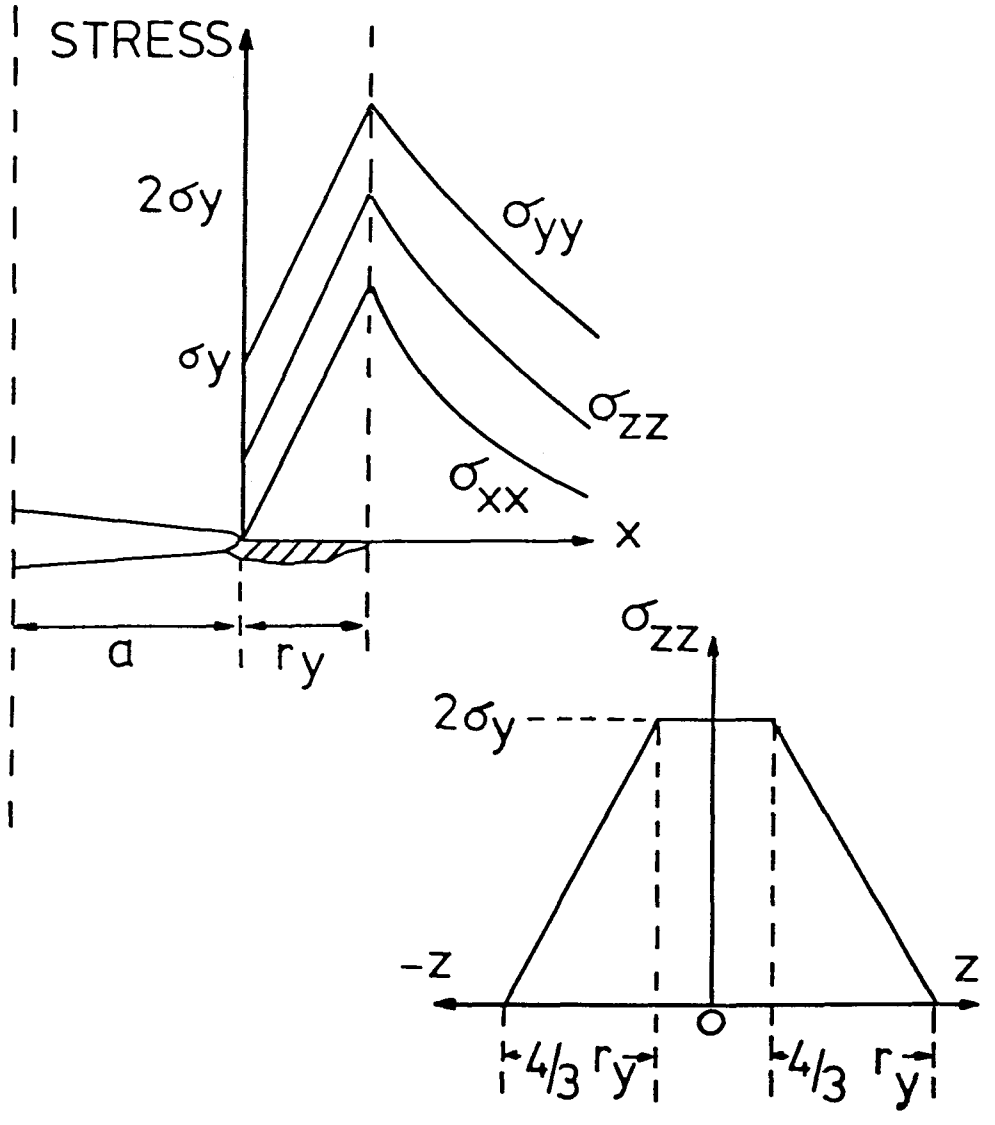


Fig. 2.04 Variation of maximum local tensile stress at the plastic/elastic interface with applied stress.
(After Knott [2.12])

2.4 Elastic-Plastic Analysis of a Cyclically Loaded Crack

Rice [2.08] reasoned that in cracked components subject to cyclic stressing a reversed plastic zone is formed whose size is dependent on stress intensity range ΔK. Using the model of Fig. 2.05 he proposed that the application of an initial tensile load produces a plastic zone whose size is maximum at K_{max}. Reversing the load from L to L-ΔL then results in the formation of a reversed plastic zone embedded in the original whose size is a maximum at K_{min}. Assuming plane strain conditions exist and that the change in stress, strain and displacement due to load reduction are given by a solution identical to the monotonic case, the maximum reversed plastic zone size is given by.

$$\omega_{pe\ (reversed)} = \frac{1}{3\pi} \left[\frac{\Delta K}{2\sigma_{ys}}\right]^2 \qquad \ldots(2.08)$$

In support of this Yokobori et al [2.13, 2.14] have identified "microscopic" and "macroscopic" plastic zones in mild steel which were a function of crack length and ΔK. Hahn et al [2.15] have also reported that the plastic zone sizes in a Fe-Si alloy were comparible with those predicted by Rice.

2.5 Plasticity and the 'Composite Plastic Zone'

In reality a crack in a structural member of finite thickness will experience at its tip both plane stress and plane strain conditions, and a composite zone will be formed as showed in Fig. 2.06. In this case no absolute value of K will accurately describe crack tip plasticity. To overcome this problem the normal practice is to predominantly ensure conditions of plane stress, by reducing specimen thickness to

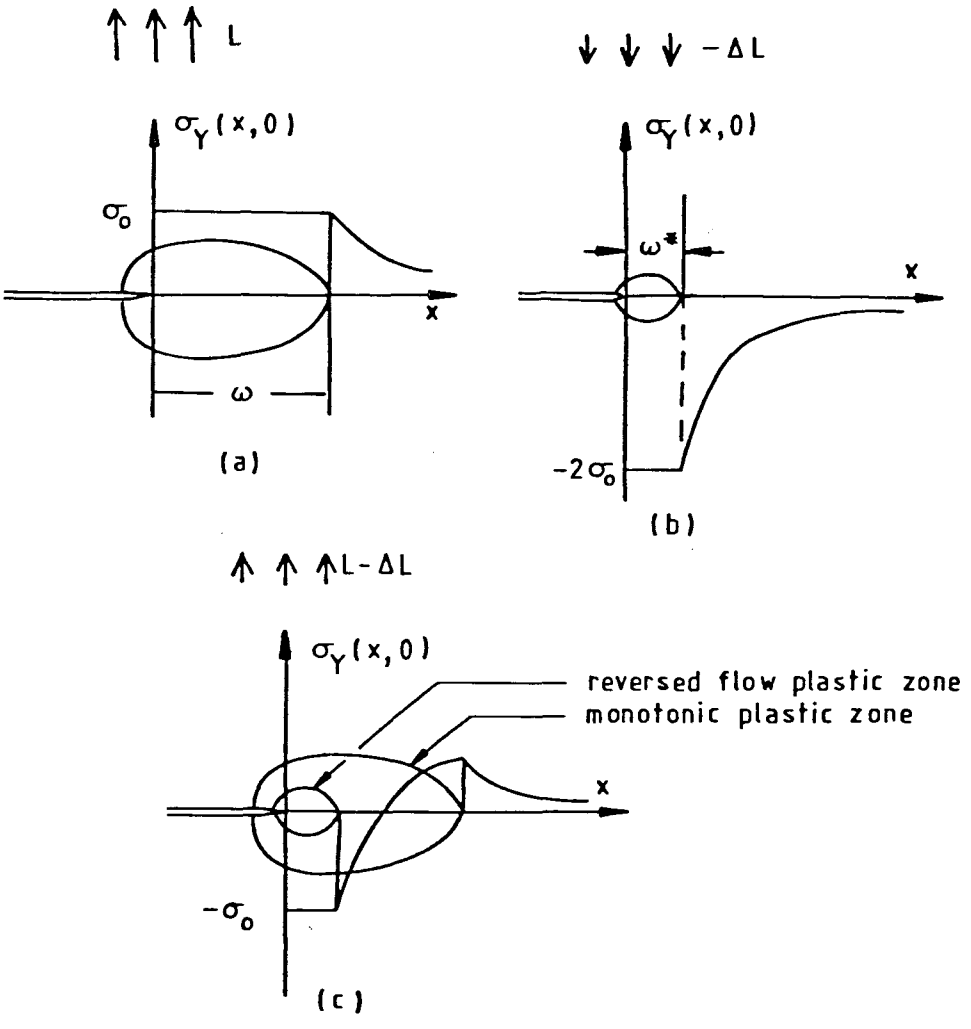


Fig. 2.05 Creation of a reversed plastic zone at the tip of a crack.
(After Rice [2.08])

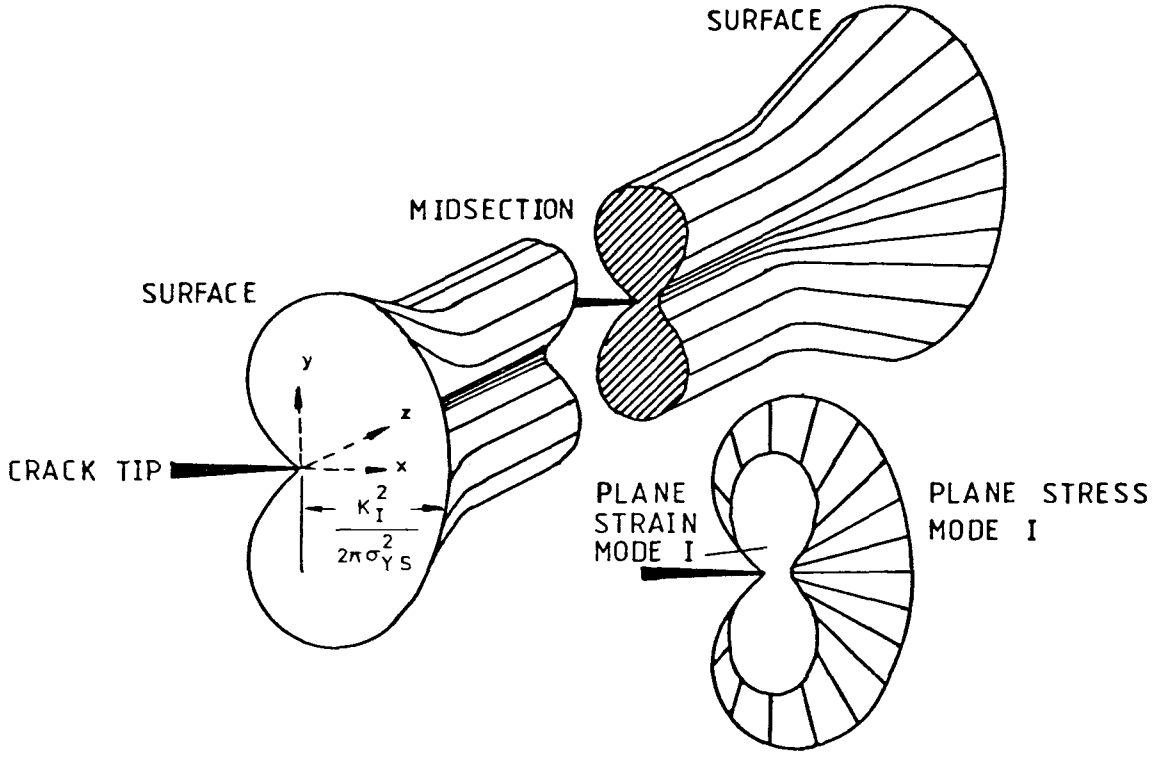


Fig. 2.06 The "composite plastic zone" formed at the front of a through thickness crack in a plate.
(After Brown and Strawley [2.10])

promote through section yielding, or predominantly ensure conditions of plane strain, by increasing specimen thickness to $\geqslant 2.7\ \omega_{ps}$ [2.12].

Movement of material in the composite plastic zone is controlled by stress conditions and can be described with respect to Fig. 2.07. In regions of plane stress the largest imbalance of principle stress exists between σ_{yy} and σ_{zz}. This results in shear on planes lying 45^{o} to the maximum stress in the y - z direction, producing slant fracture in thin sheets and shear lip formation in thicker sheets. In regions of plane strain (where $\sigma_{yy} > \sigma_{zz} > \sigma_{xx}$) movement of material occurs in the x - y direction on planes predominantly orientated at 45^{o} to the maximum stress direction. This is made difficult by the presence of the σ_{zz} hydrostatic component of stress and is constrained by the surrounding elastic body. Eventually separation occurs as the result of cleavage and/or ductile fracture in the plane of crack growth to give a macroscopic flat fracture surface.

2.6 Developments Leading to the Generalised Paris 'Law' Describing Crack Growth Based on LEFM Parameters.

Many attempts have been made to model fatigue crack propagation rate from a continuum mechanics point of view to produce the fatigue crack growth "laws" by relating the growth characteristics of many alloys to the mechanics of fracture, dislocation theories and empirical studies. So extensive has been the work reported in this field that it was deemed necessary only to include here the notable contributions to give sufficient insight into how the growth "laws" were established.

The first law of any significance was proposed by Head [2.17] who assumed that the material ahead of a crack in an infinitely wide

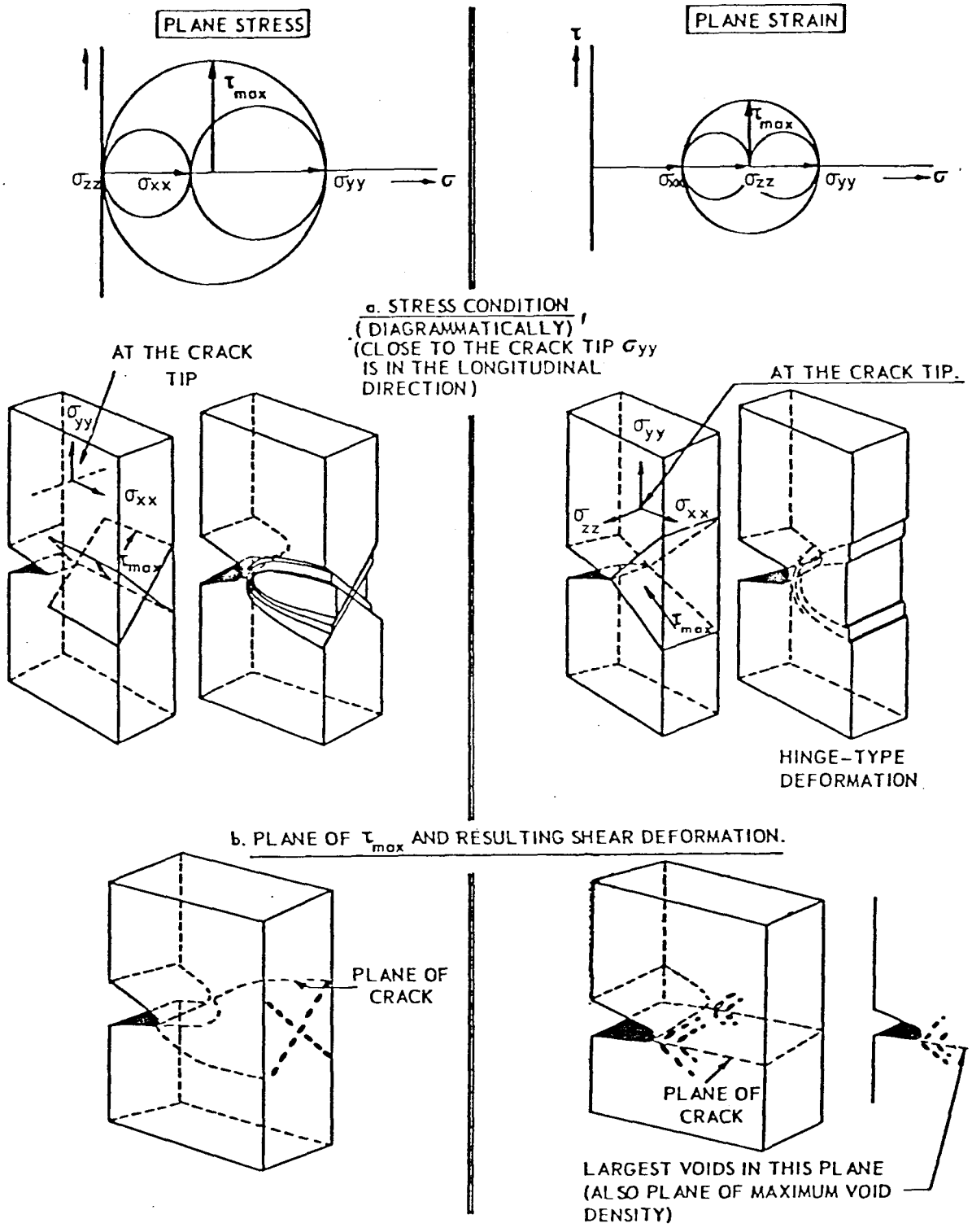


Fig. 2.07 Slant and square fractures produced as the result of stress state.

(After Broek [2.16])

sheet progressively work-hardened until the stress in an element of material immediately ahead of the crack tip reached its fracture stress. By considering the material to be composed of elastic and plastic elements he developed a growth relationship of the form

$$\frac{da}{dN} = \frac{C\ (\Delta\sigma)^3\ a^{\frac{1}{2}}}{(\sigma_{ys} - \Delta\sigma)\ \omega_{pe\ (max)}} \qquad \ldots(2.09)$$

Frost and Dugdale [2.18] claimed this was in error because Head assumed that the maximum plastic zone size remained constant irrespective of crack length. They argued that provided the stress range remained constant, all other continuum variables were controlled by crack length, and proposed the relationship

$$\frac{da}{dN} = C\ (\Delta\sigma)^3\ a \qquad \ldots(2.10)$$

Developing this further Paris et al [2.19] reasoned that growth rate was directly related to the maximum stress intensity factor and stress ratio, i.e.

$$\frac{da}{dN} = F\ (K_{max},\ R) \qquad \ldots(2.11)$$

where $R = K_{min}/K_{max}$.

Paris and Erdogan [2.20] suggested that the stress intensity range provided a single parameter which more accurately described the stress dependence of crack growth. From an extensive review they concluded that a generalised relationship describing most of the available data was

$$\frac{da}{dN} = C\ (\Delta K)^4 \qquad \ldots(2.12)$$

In a later review Johnston and Paris [2.21] illustrated that ΔK^4 was proportional to the plastic zone volume for a unit length of crack front.

Weertman [2.22] proposed a dislocation model based on the crack tip plasticity relationship of Bilby et al [2.23] in which he assumed that the cyclic plastic displacement represented accumulative damage and that failure occurred when a critical value of displacement was exeeded. This led to the expression

$$da \cong \frac{0.4\ a\ \sigma_{ys}}{\gamma\ G\ \tau^2} \qquad \ldots(2.13)$$

which reduces to

$$\frac{da}{dN} \propto \frac{\Delta K^4}{\gamma\ G\ \sigma_{ys}} \qquad \ldots(2.14)$$

Lardner [2.24] on the same theme proposed that

$$\Delta D \approx \frac{\pi\ (1 - \nu)}{4\ G\ \sigma_1}\ \sigma_a^2\ a\ \left(1 + \frac{\pi^3\ \sigma_a^2}{96\ \sigma_1^2}\right) \qquad \ldots(2.15)$$

where ΔD is the displacement per cycle or growth rate. In the high cycle fatigue regime Lardner found that $\sigma_a << \sigma_1$ and simplified Eq. 2.15 to give

$$\frac{da}{dN} = C\ (\Delta K)^2 \qquad \ldots(2.16)$$

McEvily and Johnston [2.25] suggested that a normalised growth rate relationship for many alloys can be obtained by relating da/dN to simple mechanical properties through the constant term (C) of Eq. 2.12. They modified Eq. 2.14 to give the generalised relationship

$$\frac{da}{dN} = \frac{\Delta K^4}{\left[(\sigma_{ys} + \sigma_{UTS})/2\right] E (\sigma_{UTS})^2 E_\mu} \quad \ldots(2.17)$$

Other investigations [2.26, 2.27] have normalised the data of a large range of steels, aluminium and titanium alloys in terms of $\Delta K/E$.

In opposition to this approach Hickerson and Hertzberg [2.28] argued that the cyclic rather than the monotonic mechanical properties should be considered and arrived at an equation of the form

$$\frac{da}{dN} = \frac{1}{En} \quad \Delta K \ (1/En \quad \sigma_{cys}) \quad \ldots(2.18)$$

Forman et al [2.29], who made a comprehensive study of the growth behaviour of aluminium alloys 2024-T3 and 7075-T6 within the high growth rate regime, concluded that as K_{max} approaches the static fracture toughness (K_{IC}) high growth rate behaviour satisfied the relationship

$$\frac{da}{dN} = \frac{C \ \Delta K^m}{(1 - R) \ K_{IC} - \Delta K} \quad \ldots(2.19)$$

Conversely Klesnil and Lukas [2.30], who studied the behaviour of mild steel at low growth rates, reported that decreasing the stress intensity range produced a decrease in growth rate to a level which could not be detected (threshold level). Within the low growth rate regime they arrived at the expression

$$\frac{da}{dN} = C \ (\ \Delta K^m - \Delta K_T^m) \quad \ldots(2.20)$$

From the evidence of a vast number of sources it is generally accepted that the growth rate of many alloys in the medium crack growth regime (approx 10^{-3} - 10^{-5} mm/cycle) can be adequately described

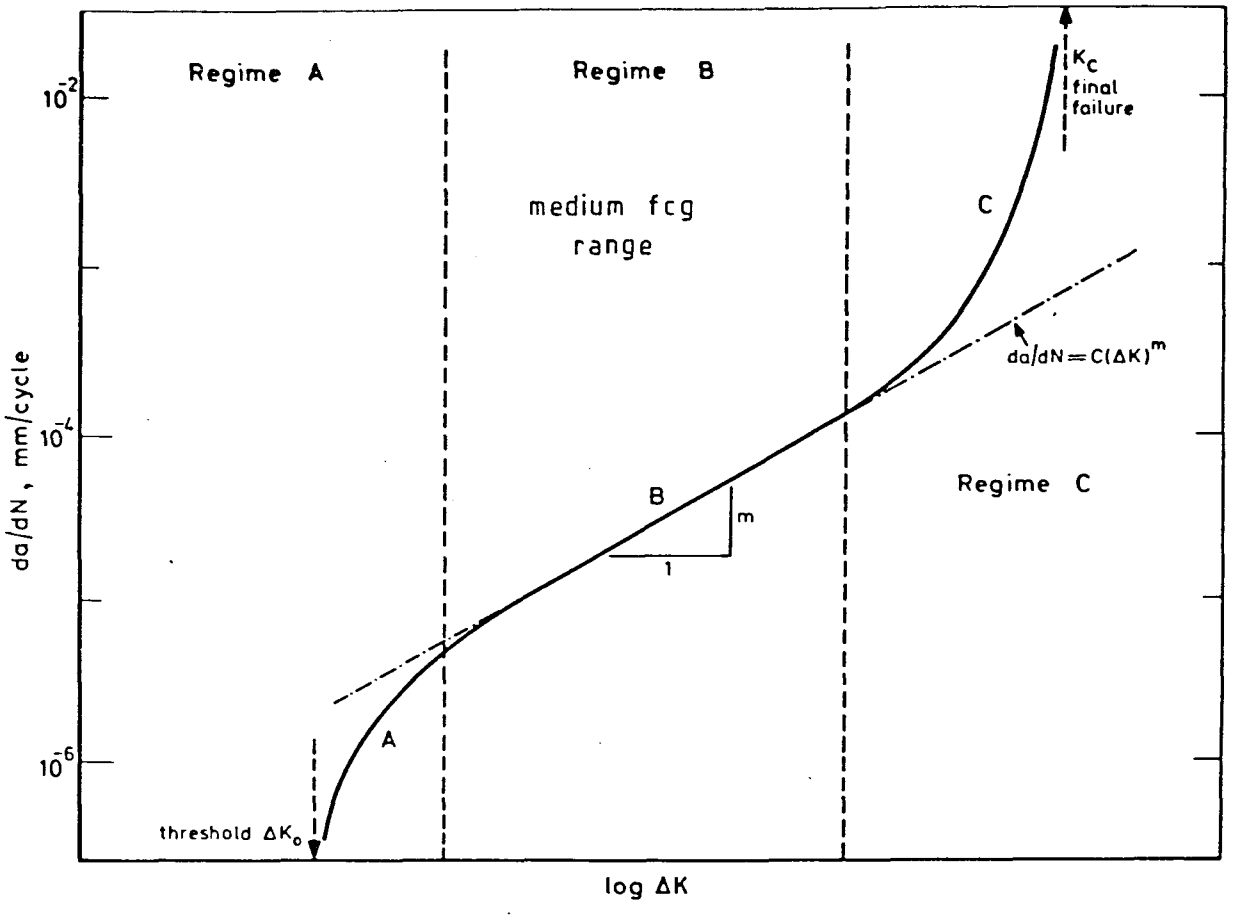


Fig. 2.08 A double logarithm plot of da/dN versus ΔK which is representative of a large amount of published data.

by a generalised version of the original Paris "Law", i.e.

$$\frac{da}{dN} = C\ \Delta K^m \qquad \ldots(2.21)$$

where m is a material property that can take any value between 2 and 10. Normally this is expressed in a logarithmic form (Eq. 2.22) which reduces the data to a linear response as shown in Fig. 2.08.

$$\log\ (da/dN) = m \log\ (\Delta K) + \log C \qquad \ldots(2.22)$$

Examination of this plot, which is representative of a large amount of published data, reveals that in Regions A and C there is a departure from the basic Paris "Law". Many [2.31 - 2.36] have shown that this is the result of numerous factors, i.e. material properties, stress history, stress ratio, grain size, crack length, and environmental effects.

2.7 References

[2.01] Timoshenko, S., and Goodier, J.N., "Theory of Elasticity", McGraw Hill, New York, 1951.

[2.02] Irwin, G.R., "Fracture Mechanics, Structural Materials", Pergammon Press, New York, 1960.

[2.03] Irwin, G.R., Trans. Am. Soc. Mech. Engrs. J. of Applied Mechanics, 1957, 24, pp 361.

[2.04] Sneddon I.N., "The Distribution of Stress in the Neighbourhood of a Crack in an Elastic Body", Proc. R. Soc., 1946, A187, pp 229.

[2.05] Williams, M.L., Trans. Am. Soc. Mech. Engrs. J. of Applied Mechanics, 1957, 24, pp 109.

[2.06] Shi, G.C., Paris, P.C., and Irwin, G.R., Int. J. of Frac. Mech., 1965, 1, pp 189.

[2.07] Westergaard, H.M.,
Trans. Am. Soc. Mech. Engrs. J. of Applied Mechanics, 1939, pp A49.

[2.08] Rice, J.L.,
A.S.T.M., STP 415, 1967, pp 247.

[2.09] Paris, P.C., and Shi, G.C.,
A.S.T.M., STP 381, 1965, pp 30.

[2.10] Brown, W.F., and Strawley, J.E.,
A.S.T.M., STP 410, 1966.

[2.11] Walker, E.F. and May, M.J.,
B.I.S.R.A. Report, MG/E/307/67, 1967.

[2.12] Knott, J.F.,
Material, Sc. Eng., 1971, 7, pp 1.

[2.13] Yokobori, T., Tachikawa, K., and Kamei, A.,
Rep. Res. Inst. Stgth. Frac. of Mats. Tohku Univ., 1970, 6, pp 1.

[2.14] Yokobori, T., Sato, K., and Yamaguchi, Y.,
Rep. Res. Inst. Stgth. Frac. of Mats., Tohku Univ., 1970, 6, pp 49.

[2.15] Hahn, G.T., Hoagland, R.J., and Rosenfield, A.R.,
Met. Trans., 1972, 3, pp 1189.

[2.16] Broek, D.,
Int. J. Frac. Mech. 1968, 4, pp 19.

[2.17] Head, A.K.,
Phil. Mag., 1953, 44, pp 925.

[2.18] Frost, N.E., and Dugdale, D.S.,
J. Mech. Phys. Solids, 1958, 6, pp 92.

[2.19] Paris, P.C., Gomez, M.P. and Anderson, W.E.,
The Trend in Engineering, 1961, 13, pp 9.

[2.20] Paris, P.C. and Erdogan, F.,
J. Basic Engng, 1963, 85, pp 528.

[2.21] Johnston, H.H., and Paris, P.C.,
E.F.M., 1969, 1, pp 3.

[2.22] Weertman, J.,
Int. J. Frac. Mech., 1966, 2, pp 460.

[2.23] Bilby, B.A., Cottrell, A.H., and Swindon, K.H.,
Proc. Royal Soc., 1963, A272, pp 304.

[2.24] Lardner, R.W.,
Phil. Mag., 1968, 17, pp 71.

[2.25] McEvily, A.J., and Johnston, T.L.,
Proc. 1st Int. Conf. on Fracture, 11, pp 515,
Japan 1965.

[2.26] Pearson, S.,
Nature, 1966, 211, pp 1077.

[2.27] Bates, R.C., and Clark, W.G.,
Trans. A.S.M., 1969, 62, pp 179.

[2.28] Hickerson, J.P. and Hertzberg, R.W.,
Met. Trans., 1972, 3, pp 179.

[2.29] Forman, R.G., Kearney, V.E., and Engle, R.H.,
J. Basic Eng., 1967, 89, pp 459.

[2.30] Klesnil, M., and Lukas, P.,
E.F.M., 1972, 4, pp 77.

[2.31] Ritchie, R.O., and Knott, J.E.,
Acta. Met., 1973, 21, pp 639.

[2.32] Richards, C.E., and Lindley, T.C.,
E.F.M., 1972, 4, pp 951.

[2.33] Evans, P.R.V., Owen, N.B., and Hopkins, B.E.,
E.F.M., 1971, 3, pp 463.

[2.34] Beevers, C.J., Cooke, R.J., Knott, J.F., and Ritchie, R.O.,
Met. Sc., 1975, 9, pp 119.

[2.35] Chauhan, P., and Roberts, B.W.,
Metallurgist and Mat. Technologist, 1977, 3, pp 131.

[2.36] Suresh, S., Zamiski, G.F., and Ritchie, R.O.,
American Soc. for Metals.
Metall. Trans. A., 1981, 12A, pp 1435.

CHAPTER THREE

MICROCRACK FORMATION AND STAGE I FATIGUE CRACK GROWTH

3.0 Introduction

The fatigue life of many components can be conveniently subdivided into three parts: (i) microcrack formation (initiation), (ii) the growth of very short cracks in the order of a few microns by a shear mode process (Stage I), and (iii) the subsequent growth of short cracks by a tensile mode process (Stage II). The latter two divisions, originally defined by Forsyth [3.01], are characterised by a generalised orientation as shown in Fig. 3.01.

In this Chapter a review is made of the experimental observations and proposed mechanisms of microcrack initiation and Stage I growth of very short cracks. The mechanisms involved in Stage II growth are described in Chapter 4.

3.1 Micro Crack Formation

Most metals subject to an alternating stress containing a tensile cycle will fail by the process of fatigue at a remote applied stress level below that required for gross plastic instability as the result of crack growth due to a localised high stress concentration associated with a stress raiser. Many commerical materials contain inherent stress raisers produced during primary and secondary processing routes. For example: a cast alloy may contain gas and shrinkage porosity; mechanical working produces fragmentation of inclusions, carbides, precipitates and decohesion of weak

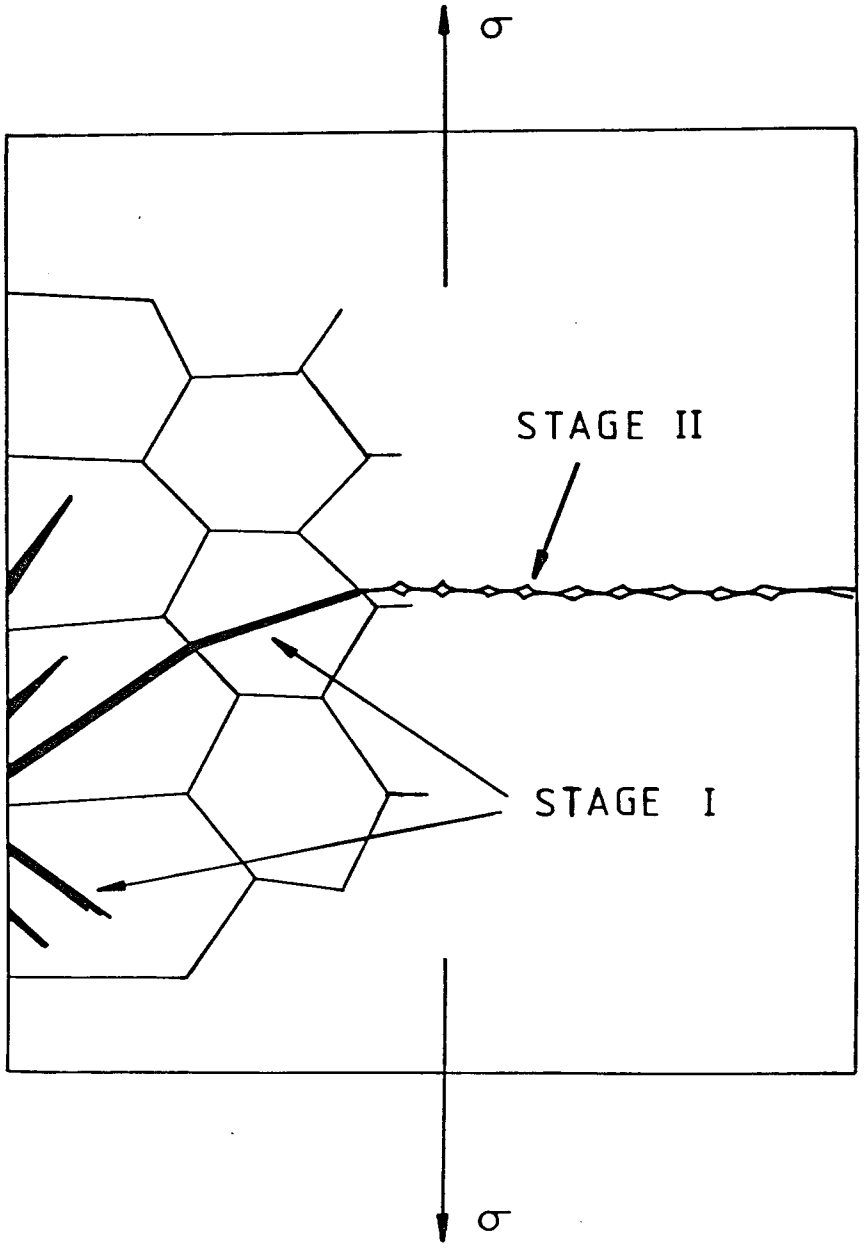


Fig. 3.01 Schematic representation of the two stages of crack propagation.
(After Laird [3.02])

interfaces;dislocation glide leads to microcrack formation at the junction of intersecting slip planes [3.03, 3.04]; overaging of precipitational hardenable alloys produces incoherent precipitates and weak precipitate-matrix interfaces; and simple machining processes introduce stress raisers on a micro and macro scale. Microcracks are also formed as a result of environmental effects [3.05]. Components subject to a liquid corrosive environment undergo preferential dissolution at high energy sites to produce the etch pit microcrack.

During cyclic stressing intergranular cracking normally occurs if the grain boundaries are weakened relative to the grains by either raising the temperature or by alloying, and may also result from the inability of surrounding grains to accommodate a grain which is deforming plastically during a surface rumpling process. Conversely when the grain boundaries are relatively strong in comparison to the grains microcracks form in transgranular positions. Weakening of the grains with respect to the grain boundaries may in some cases be controlled by metallurgical structure. For instance,in high strength solution treated and precipitational hardened aluminium alloys cyclic stressing produces overaging and softening of the solute depleted areas thereby forming preferential sites for microcrack formation by the intrusion-extrusion process [3.06].

The microcrack (i.e. the intrusion) of the intrusion-extrusion phenomena is formed by a process of irreversible slip during cyclic stressing. Initially slip occurs on planes suitably orientated to the maximum tensile stress at an applied remote stress level below the nominal-proof stress. Eventually persistant slip bands are formed and large amounts of irreversible slip arising

from dislocation interaction and surface adsorption effects produces surface roughening, Fig. 3.02. Continued cyclic stressing then leads to the formation of optically visible intrusions and extrusions whose morphology is dependent on material, stress and environment, Fig. 3.03.

In unidirectionally work hardened materials cyclic stressing produces work softened slip band material which promotes the formation of intrusion and extrusion pairs. This is achieved in planar slip materials by a process of dislocation annihilation at low energy sites, and in duplex slip materials by dislocation rearrangement from cell to dipole structure [3.08, 3.09].

To explain the occurrance of microcracks initiating within persistant slip bands which contain work hardened material Brown [3.10] reasoned that during cyclic stressing a macroscopic tensile stress is produced within the slip band which induces a tensile strain (ε) that contributes to the stored elastic energy per unit area of the band (γ_E), i.e.

$$\gamma_E = \frac{1}{2} E \quad \varepsilon^2 \, h \qquad \ldots(3.01)$$

where h is the band width. When γ_E exceeds the persistant slip band-matrix interfacial energy new surface is produced and a microcrack is formed by slip band decohesion.

3.2 Stage I Fatigue Crack Growth

When a material containing surface microcracks is subject to cyclic stressing crack propagation proceeds by Stage I growth

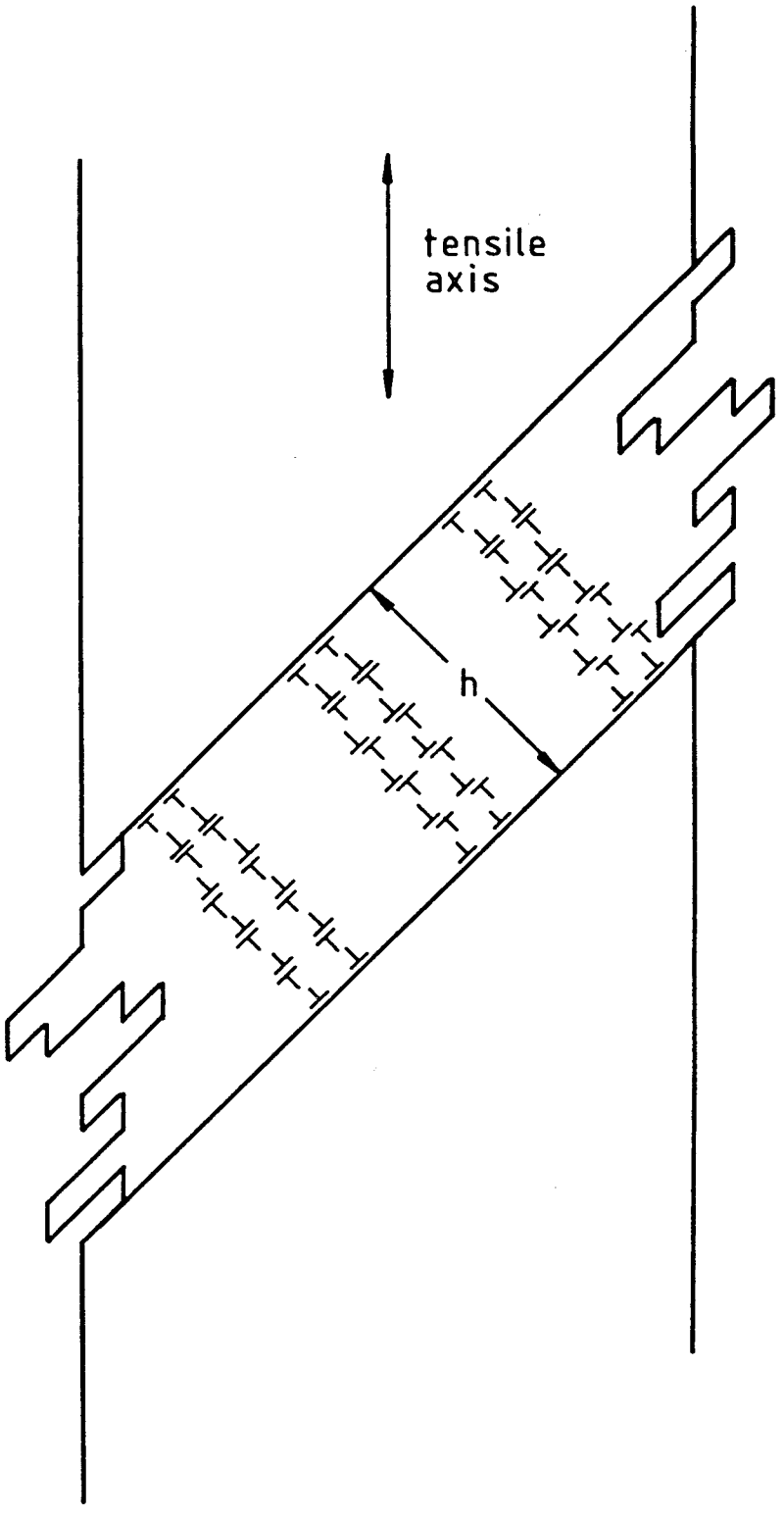


Fig. 3.02 A schematic illustration of vacancy dipole formation and surface roughening in a single crystal.
(After Brown [3.10])

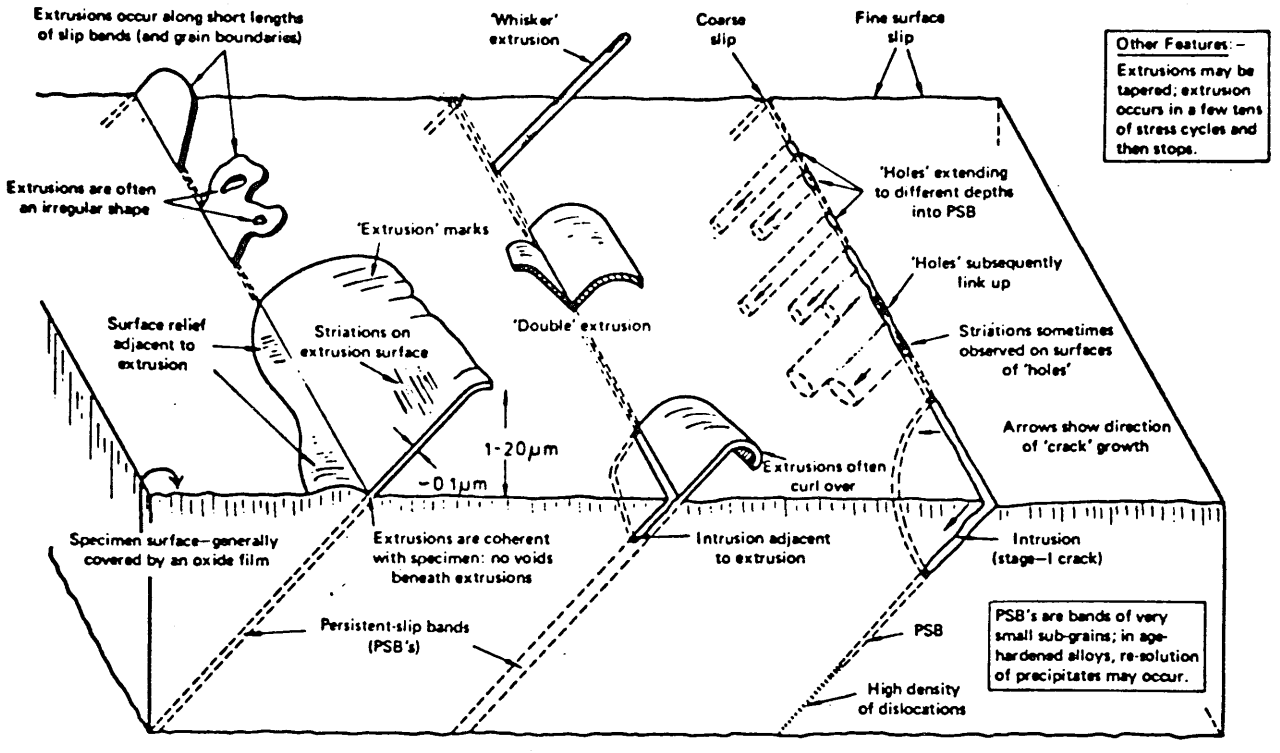


Fig. 3.03 Diagramatic summary of important features of slip-band extrusion and intrusion. Specific details depend on material, stress, environment, etc.
(After Lynch [3.07])

on active slip planes suitably orientated to the maximum tensile axis. The characteristics of this type of growth have been evaluated in many alloys and several possible growth mechanisms have been suggested. A brief review of the notable contributions in this field is given in the following text.

Stubbington [3.11] studied the effect of environment (air and aqueous NaCl) on the fatigue crack growth of an AlZnMg alloy and reported that cracks characteristic of Stage I growth were observed in transgranular positions with an angular dependence from the maximum tensile axis which was a function of suitably orientated slip planes and depth. The morphology of the Stage I cracks in both environments was found to be similar with the fracture surface comprising of faceted lamella orientated approximately 45^{o} to the maximum tensile axis. On a macroscopic scale this was represented by a well defined river pattern. Crack growth was assumed to be an extension of the unslipping intrusion-extrusion process occurring on {110} slip planes which were suggested to operate alternatively connected by short lengths of tensile fracture. Similar studies by Forsyth [3.06] on the same alloy revealed that the faceted texture resulted from shear occurring by a process of irreversible slip on {111}, {110} and {100} planes.

Williams and Smith [3.12] proceeded further and studied the effect of temperature and environment on fatigue crack growth in single crystals of β brass. Similar results were obtained to those of Stubbington, i.e. lamellae transcrystalline fracture occurred along {110} planes whose normals were orientated not more than 20^{o} to the maximum tensile axis. Close fracture surface

examination revealed that towards the end of Stage I very many striations existed across the lamellae in a direction normal to crack growth. Unfortunately this phenomena received very little attention and no explanation.

McEvily and Boettner [3.13] found in single crystals of aluminium that the characteristic lamellae fracture surface of Stage I growth resulted from alternating shear mode fracture occurring on two {111} planes. From surface wave markings they reasoned this was achieved by a sequential process of cross slip operating between the two fracture planes. Fatigue studies were also conducted in aluminium and copper alloys to evaluate the effect of cross slip on crack propagation indirectly through stacking fault energy (an increase in stacking fault energy produces an increase in the ease of cross slip). It was generally observed that a reduction in stacking fault energy produced a reversion in Stage I growth from transgranular to intergranular positions, and an overall decrease in crack propagation rate. This led to the conclusion that cross slip was an important factor involved in the mechanism of Stage I growth.

As a sequel to earlier work Stubbington and Forsyth [3.14] reported that Stage I growth in an AlCuMg alloy was typified by a lamellae appearance with fracture occurring on {111} planes in a <110> direction as illustrated in Fig. 3.04. Close examination of the planar facets, which revealed fretting, suggested that rubbing together of the new surfaces had occurred. When rubbing did not occur similar striations were observed to Williams and Smith. From their observations they concluded that during crack growth permanent microscopic damage (striation formation) resulted from dislocation movement associated with the shearing component of the applied stress.

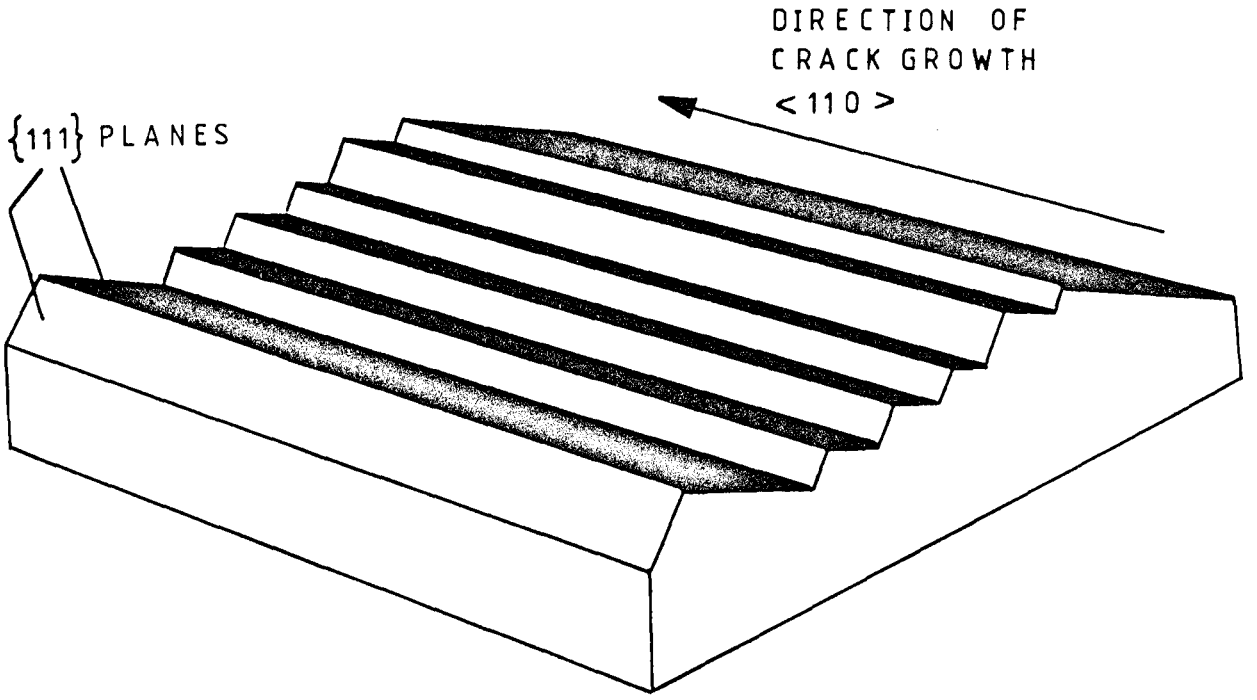


Fig. 3.04 Schematic illustration of the Stage I shear mode fracture surface of an AlZnMg alloy exhibiting parallel lamellae.
(After Stubbington and Forsyth [3.14])

Cleavage fracture, they claim, was controlled by the magnitude of the tensile component across the slip plane.

From crack growth studies in single copper crystals Kaplan and Laird [3.15] suggested two mechanisms of Stage I growth. In planar slip materials crack growth was favoured by an unslipping process, but in materials which readily cross slip, this was achieved by plastic blunting. In the unslipping process, Fig. 3.05, a tensile stress produces crack displacement by shear, Fig. 3.05(b), during compression the original crack-specimen surface geometry is recovered and an increase in crack length results from irreversible slip, Fig. 3.05(c). In the plastic blunting process, Fig. 3.06, new surface is created during tensile loading by flow of material away from the crack tip, Fig. 3.06(b), resharpening then occurs during the following compression stroke to produce an increase in crack length, Fig. 3.06(c).

Gell and Leverant [3.16] studied the effect of high and low cycle fatigue on Stage I growth in a high strength nickel alloy Mar M200 and obtained two different types of fracture surface. On a macroscopic scale fracture morphology was similar to that observed by Stubbington and Forsyth [3.14], but on a microscopic scale low cycle fatigue specimens exhibited a faceted fracture surface which contained small equiaxed dimples similar to those associated with ductile tensile failure. This type of fracture could not be explained by the Stage I growth models proposed by Kaplan and Laird, so they proposed a growth model which involved the normal and shear stresses acting on the crack tip. In this model, which is presented in Fig. 3.07, reverse slip motion is restricted on a limited number of planes ahead

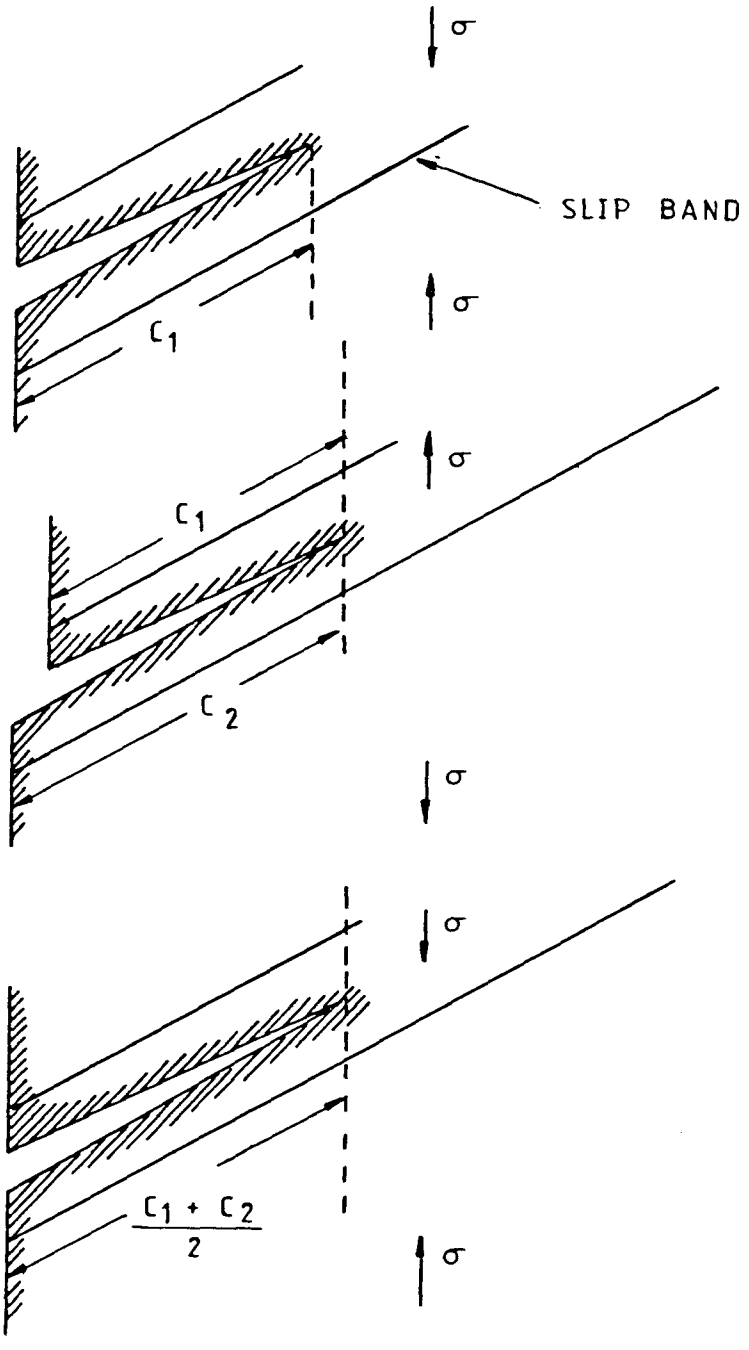


Fig. 3.05 State I crack growth by an unslipping process: (a) compression, (b) tension, (c) compression. (After Kaplan and Laird [3.15])

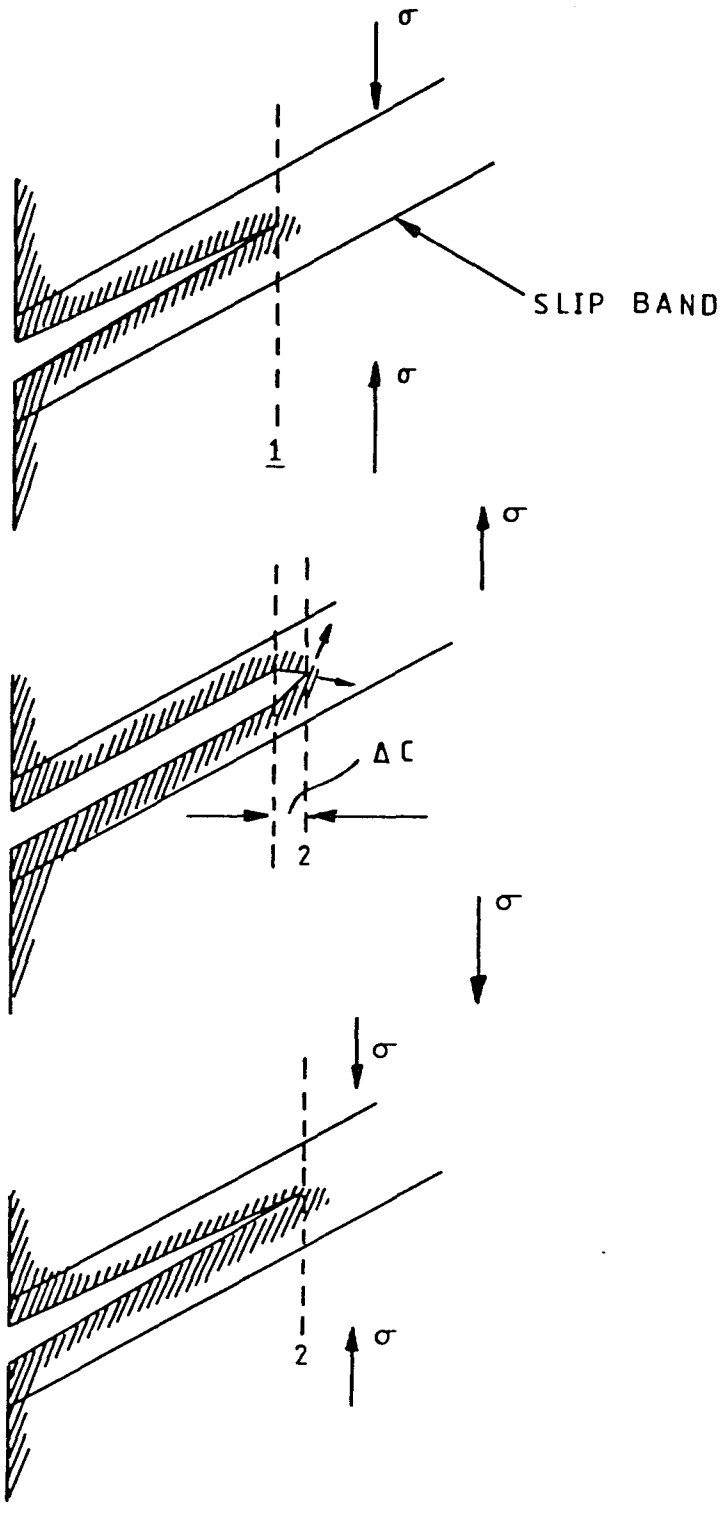


Fig. 3.06 Stage I crack growth by the plastic blunting process: (a) compression, (b) tension, (c) compression.
(After Kaplan and Laird [3.15])

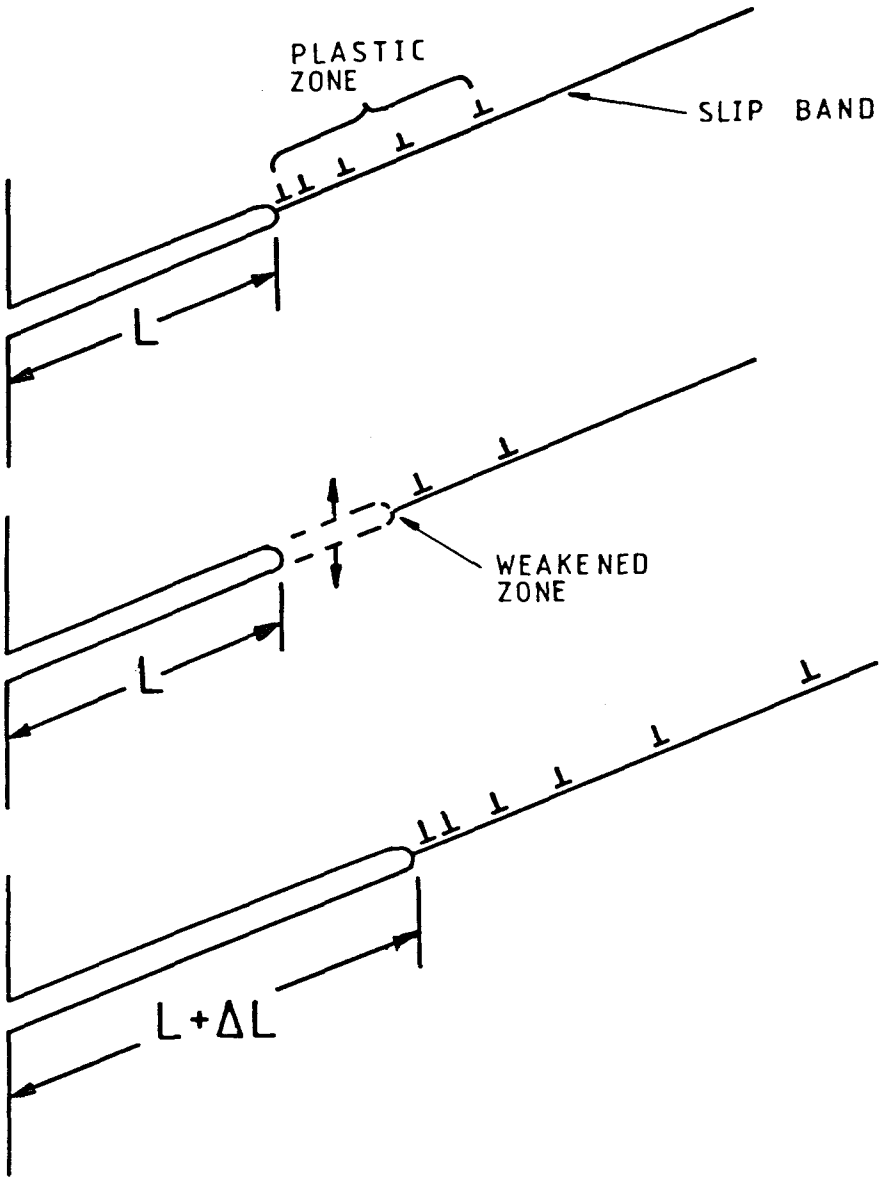


Fig. 3.07 A model of Stage I crack propagation involving both the local normal and shear stresses at the crack tip.
(After Gell and Leverant [3.16])

of the crack, Fig. 3.07(a), this produces weakening in a local area at the crack tip, Fig. 3.07(b), which eventually undergoes a cleavage type tensile fracture to give an increase in crack length, Fig. 3.07(c).

In a later paper [3.17] published on the same work, Gell and Leverant observed that the faceted lamellae of specimens subject to high cycle fatigue contained slip traces and striations during the beginning and latter part of Stage I growth respectively. From fracture surface measurements striation spacing was found to be directly related to crack growth and length, which further supported their Stage I growth model.

Developing this theme further Duquette and Gell [3.18] studied the effect of stress range and environment on the fatigue characteristics of the same alloy and found that Stage I fracture surface topography was a function of stress range and environment. Specimens subject to high stress range fatigue in vacuum and air exhibited a planar fracture surface covered with equiaxed dimples similar to those observed previously in specimens subject to low cycle fatigue. In contrast to this, fracture surface topography of specimens subject to low stress range fatigue in air exhibited a lamella structure comprised of cleavage facets. They suggested two prime factors were responsible for the difference:(a) the magnitude of the applied and localised slip band tensile stress (the latter arising from dislocation dipole formation); and (b) absorption effects. Since Stage I fracture in nickel-base superalloys and other alloy systems involves localised cleavage, Duquette and Gell modified the Griffith-Orowan equation (Eq. 3.02) dealing with cleavage under conditions of

limited plastic deformation to incorporate the applied stress (σ_a), local tensile stress (σ_p), and the lowering of the surface energy term due to gas absorption ($-\gamma_{ads}$) to give Eq. 3.03. In this equation γ_p = energy expanded in plastic deformation during the formation of new crack surface, γ_s = reversible surface energy, E = Youngs Modulus, L = crack length and ν = poissons ratio

Conditions Satisfying Cleavage Fracture

$$\sigma_f > C \sqrt{\frac{E \gamma_s + \gamma_p}{(1 - \nu) \pi L}} \qquad \ldots(3.02)$$

$$(\sigma_a + \sigma_p) > C \frac{E (\gamma_s - \gamma_{ads} - \gamma_p)}{(1 - \nu^2) \pi L} \qquad \ldots(3.03)$$

They then argued that the proportion of cleavage-ductile fracture was directly related to the degree of imbalance of Eq. 3.03 as follows. At low growth rates, were γ_{ads} is significant, the difference in magnitude between the left-right hand side of Eq. 3.03 will be greater in air than in vacuum. At high growth rates however, where σ_a is high, the imbalance in air approaches that in vacuum.

Probably the most generally accepted mechanisms of Stage I growth is that of plastic blunting first proposed by Laird and Smith [3.19] to describe Stage II fracture surface striation formation, and latter extended by Laird [3.02] to describe the observations of Williams [3.20] of Stage I striation formation in β brass. In the later paper Laird suggested that in ductile materials Stage I and II crack growth were essentially the same but the mechanisms differed as the result of two types of dislocation movement. During Stage I growth it was proposed that an increase in crack length per cycle was accomplished by the crack tip spreading to the width of the slip band by a process of duplex slip, whereas Stage II crack growth

resulted from dislocation movement at the crack tip on two active slip planes suitably orientated to the maximum tensile stress axis. Laird also suggested that the effect of microstructure on Stage I growth controls only the extent of plastic deformation and therefore the kinetics rather than the mechanics of propagation.

Implicit in Lairds argument is that the demarkation from Stage I and Stage II growth can be considered to be dependent on stress concentration and available slip systems. In many practical situations a very small crack will experience at its tip a stress concentration which is only sufficient to operate slip within the slip band in which it is contained. But as the crack grows and its length increases the situation develops into one in which the localised crack tip stress concentration becomes sufficiently large to initiate dislocation movement in other slip bands. When this occurs Stage I crack propagation progressively enters into Stage II.

3.3 References

[3.01] Forsyth, P.J.E.,
Proc. Crack. Prop. Symp. 1, pp 76, College of Aeronautics, Cranfield, Beds., England, 1972

[3.02] Laird, C.,
A.S.T.M. STP 415, 1967, pp 131.

[3.03] Cottrell, A.H.,
Trans. Am. Inst. Mech. Engrs., 1958, pp 192.

[3.04] Stroh, A.N.,
Advances in Physics, 6, 1957, pp 418.

[3.05] Evans, U.R.,
'The Corrosion and Oxidation of Metals'
Edward Ardald Ltd., London.

[3.06] Forsyth, P.J.E.,
Acta. Met., 1963, 11, pp 703.

[3.07] Lynch, S.P.,
Met. Sc., 1975, 9, pp 401.

[3.08] Feltner, C.E., and Laird, C.,
Acta. Met., 1967, 15, pp 1633.

[3.09] Feltner, C.E. and Laird, C.,
Acta. Met., 1967, 15, pp 1621

[3.10] Brown, L.M.,
Met. Sc., 1977, 11, pp 315.

[3.11] Stubbington, C.A.,
Metallurgica, 1963, 68, pp 109.

[3.12] Williams, H.D., and Smith G.C.,
Phil. Mag., 1966, 13, pp 835.

[3.13] McEvily, A.J., and Boettner, R.C.,
Acta. Met. 1963, 11, pp 725.

[3.14] Stubbington, C.A., and Forsyth, P.J.E.,
Metallurgica, 1966, 74, pp 15.

[3.15] Kaplan, H.L., and Laird, C.,
Trans of the Met. Soc. A.I.M.E., 1967, 239, pp 1017.

[3.16] Gell, M., and Leverant, G.R.,
Trans. of the Met. Soc. A.I.M.E., 1968, 242, pp 1869.

[3.17] Gell, M., and Leverant, G.R.,
Acta. Met., 1968, 16, pp 553.

[3.18] Dunquette, D.J., and Gell, M.,
Met. Trans., 1971, 2, pp 1325

[3.19] Laird, C., and Smith, G.C.,
Phil. Mag., 1963, 8, pp 145.

[3.20] Williams, H.D.,
'The Fatigue of β-Brass', Ph.D. Thesis, Cambridge University, 1961.

CHAPTER FOUR

MECHANISMS OF STAGE II FATIGUE CRACK GROWTH

4.0 Introduction

In this Chapter a review is made of the mechanisms of Stage II crack growth based on observations of fracture surface morphology using transmission electron microscopy or scanning electron microscopy. The discussion is restricted to observations based on crack growth at intermediate growth rates (10^{-2} to 10^{-5} mm/cycle) subject to Mode I loading conditions.

4.1 Stage I to Stage II Transformation

The departure from Stage I to Stage II crack growth has been associated with a critical ratio of shear to tensile stresses acting on the crack tip and the avaliability of suitably orientated slip systems [4.01 - 4.03]. During the initial stages of Stage I growth, crack propagation is dominated by the critically resolved shear stress and proceeds along planes on which this is a maximum. As the crack grows into more highly constrained material the ratio of shear/tensile stress decreases [4.01], and eventually, when conditions are favourable, shear mode Stage I cracking changes to tensile mode Stage II growth on non-crystallographic planes lying perpendicular to the maximum tensile axis.

The transition from Stage I to Stage II may be gradual or distinct depending upon crack position and material properties. In planar slip materials it normally occurs when a grain boundary is encountered, but in materials which exhibit duplex slip the change in growth direction may occur within a grain, Fig. 4.01. Stage I cracks growing along grain boundaries normally transform into Stage II

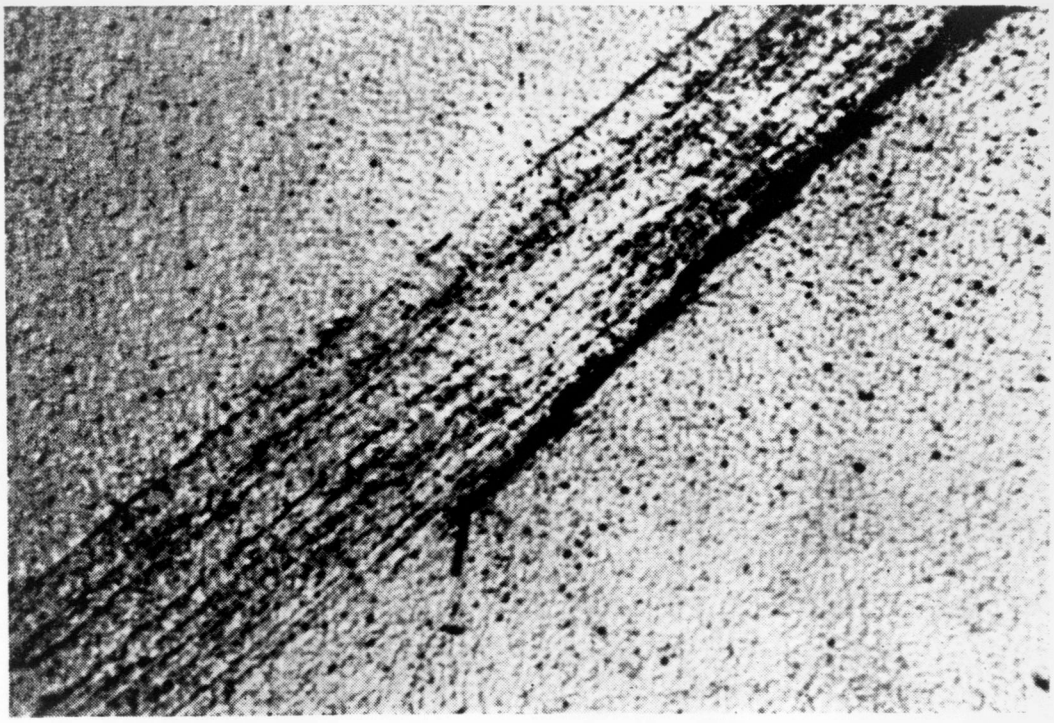


Fig. 4.01 Transition from Stage I to Stage II fatigue crack growth in the middle of a grain (after Stubbington [4.04])

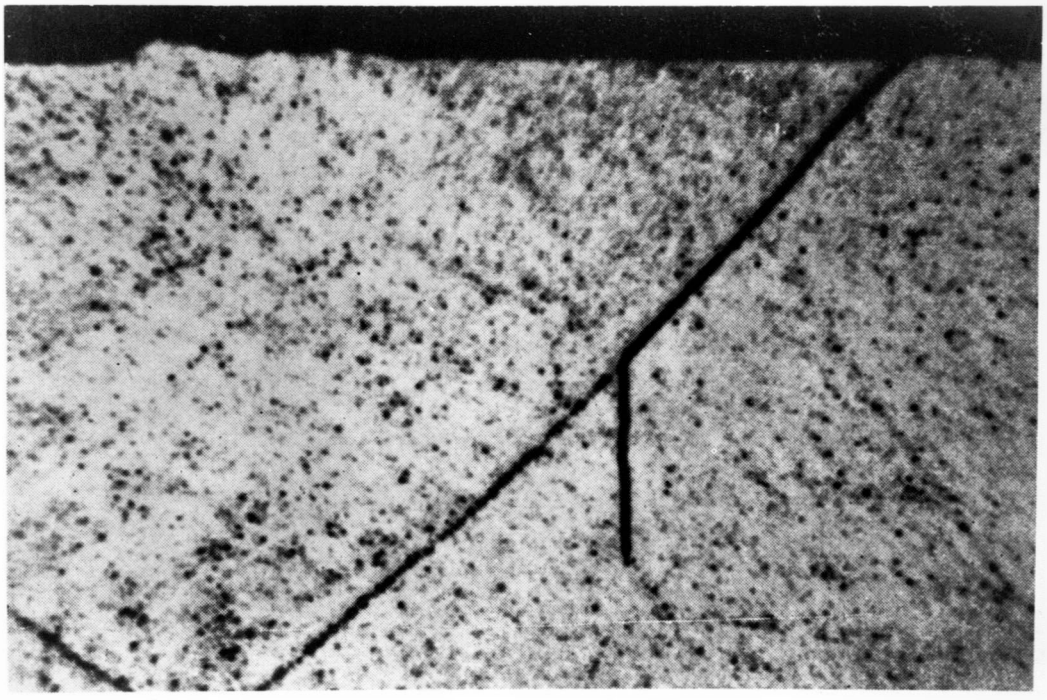


Fig. 4.02 Transition from Stage I to Stage II fatigue crack growth in a grain boundary (after Stubbington [4.04])

cracks at a triple point, but the changeover has also been reported [4.04] at random positions along the grain boundary, Fig. 4.02.

4.2 Fracture Surface Observations and Suggested Mechanisms of Stage II Growth

Forsyth and Ryder [4.05] demonstrated in a high strength aluminium alloy that striations produced during Stage II growth were directly related to the number of fatigue cycles. Observations of fracture profile revealed a hill to hill and valley to valley matching of opposing fracture surfaces. This led them to suggest a growth mechanism based on void formation ahead of the 'growing' crack accompanied by necking of the connecting ligament, Fig. 4.03.

Stubbington [4.04, 4.06] identified two types of striations in an AlZnMg alloy which exhibited different amounts of cleavage-ductile fracture depending on environment, Fig. 4.04. Those produced in air were described as ductile (Type A) because they lay on non-crystallographic plateaus and were comprised of approximately equal proportions of shear and tensile fracture; but those produced in a corrosive environment were decribed as brittle (Type B) because they exhibited an increased cleavage component of fracture associated with tensile mode separation occuring along (100) crystallographic planes.

Based on the observations of Stage II growth in an aluminium alloy Forsyth [4.07] proposed the model for striation formation shown in Fig. 4.05. In this model it was suggested that the growth mechanism consisted of two components of fracture: a relatively easy slip component where glide occurs at a relatively low stress on a flat crystallographic plane as shown in (A); and a second component where

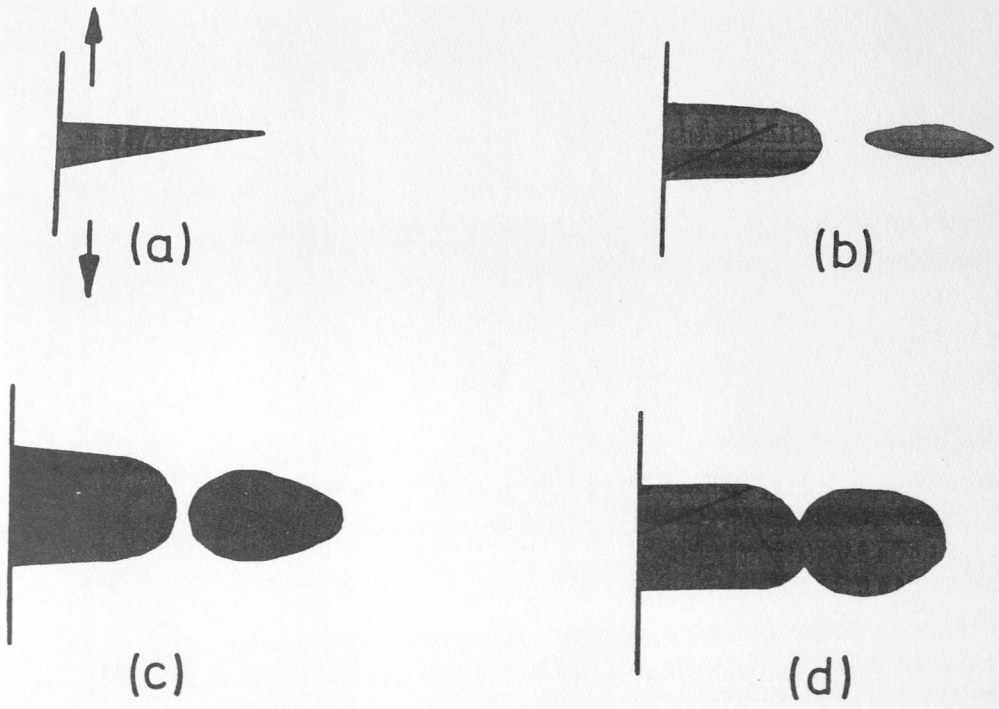


Fig. 4.03 The crack growth model proposed by Forsyth and Ryder [4.05]

(a) End of compressive half cycle.

(b) Tensile half cycle blunts the crack tip and produces a void ahead of crack in the triaxial stress region.

(c) Thinning of unfractured bridge occurs under biaxial tension.

(c) Final separation of bridge by thinning.

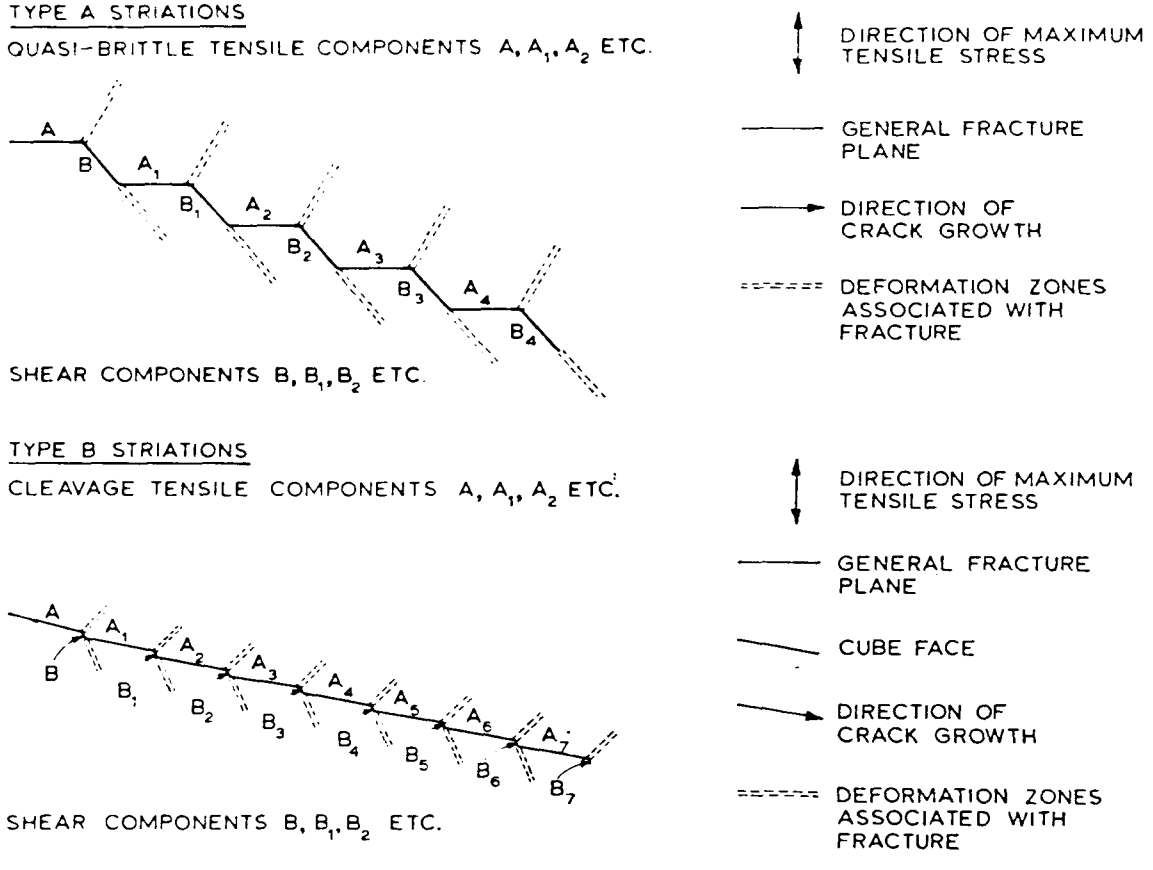


Fig. 4.04 A schematic illustration of sections taken through Type A and Type B striations observed by Stubbington [4.04].

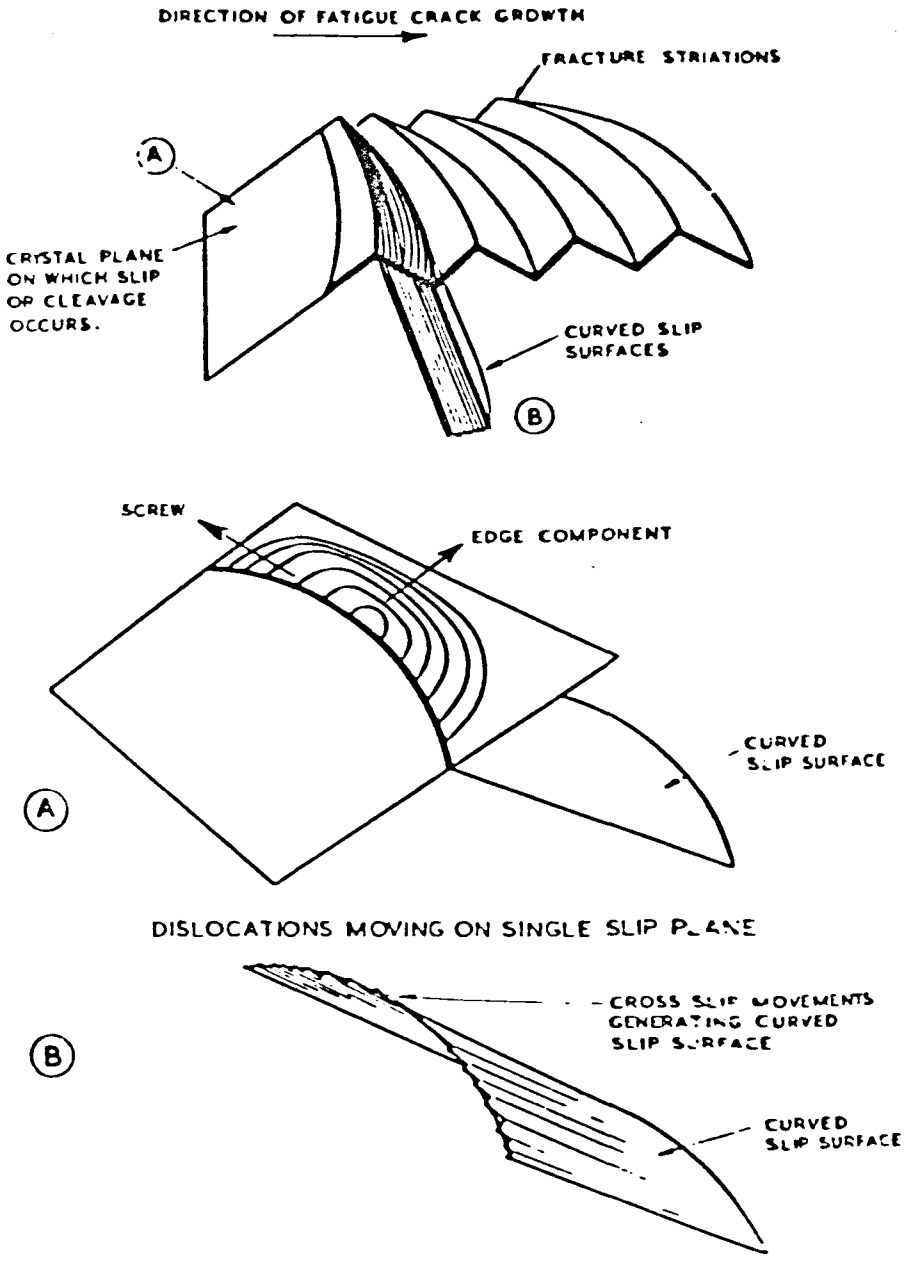


Fig. 4.05 Stage II ductile striation mechanism involving two components of slip. (After Forsyth [4.07]).

slip conforms to the curved crack front by a process of cross slip occurring on crystallographic planes as shown in (B). Forsyth then argued that the sequential action of both fracture modes resulted in the formation of curved ductile striations and a curved fracture surface as illustrated in Fig. 4.06.

Laird [4.08] proposed that the plastic blunting mechanism first presented to describe the Stage II fracture surface observations of pure aluminium and nickel subject to low cycle fatigue [4.09], also operated in ductile materials subject to compression - compression and tension - tension cycle fatigue. The operation of this mechanism, which is presented in Fig. 4.07, was described in five stages for a compression - tension cycle as follows. At the zero load position the closed crack is assumed to have a double notch at its tip, Fig. 4.07(a). As tensile load is applied the small double notch at the crack tip serves to concentrate slip zones along planes at 45 degrees to the plane of the crack whilst simultaneously maintaining a square geometry, Fig. 4.07(b). When the specimen is deformed to the maximum tensile strain, Fig. 4.07(c), the stress concentration effect of the crack is lessened, broadening of the slip zones occurs, and the crack tip blunts to a semi circular configuration. Reversing the load changes the slip direction, Fig. 4.07(d), and as the crack faces are crushed together new crack surface is created which is forced into the plane of the crack to form another notch, Fig. 4.07(e).

The versatility of this model in describing the formation of four basic types of striation, Fig. 4.08, led Laird to conclude 'The plastic blunting process of fatigue crack propagation is quite general in Stage II and probably operates in Stage I also but with differences in crack tip geometry; the mechanism may be used to explain

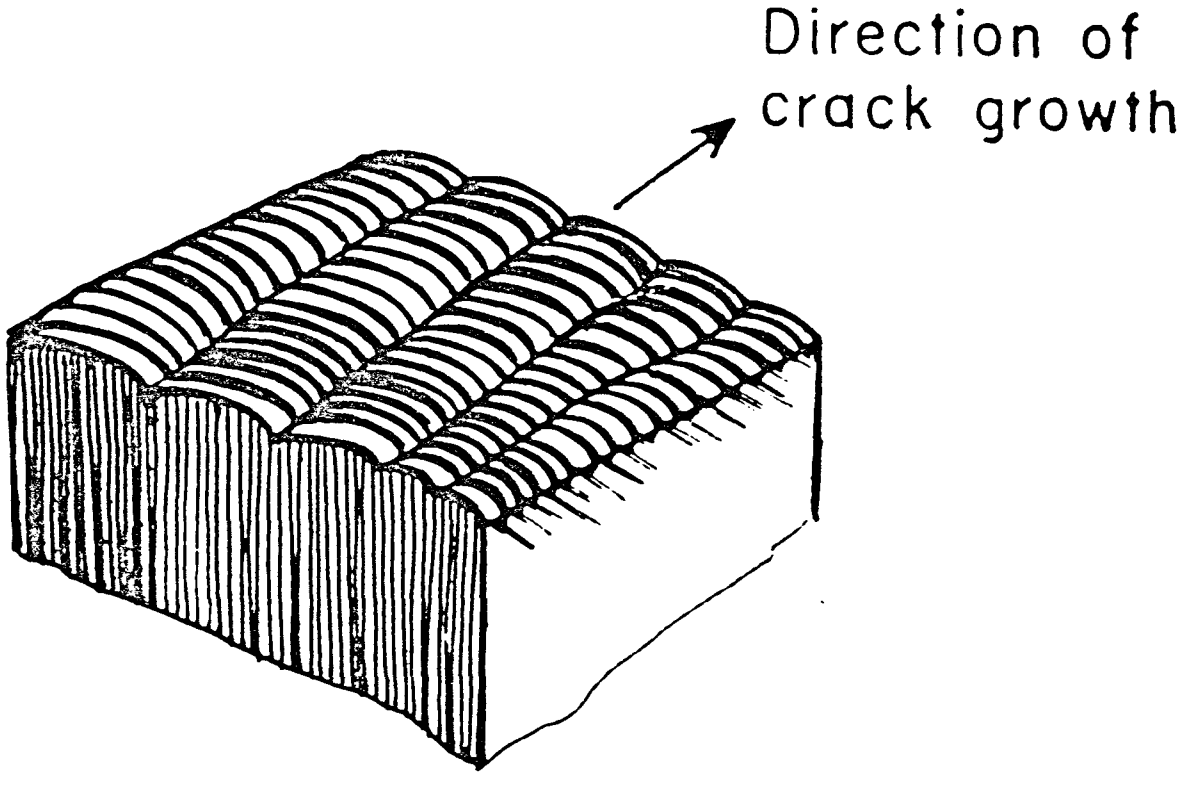


Fig. 4.06 Pictorial representation of ductile fracture striations observed by Forsyth [4.07].

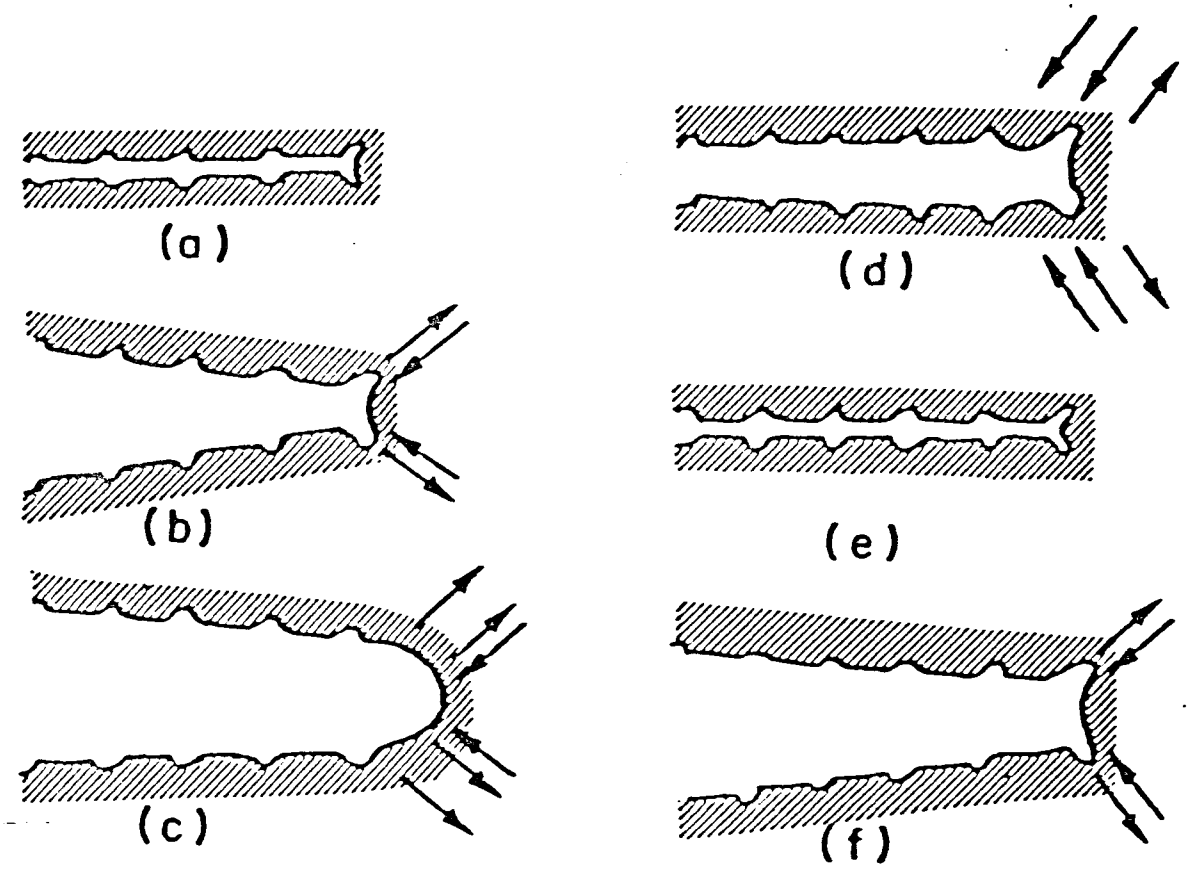


Fig. 4.07 Stage II fatigue crack propagation by plastic blunting (After Laird [4.08]).

(a) Zero load.

(b) Small tensile load.

(c) Maximum tensile load.

(d) Small compressive load.

(e) Maximum compressive load.

(f) Small tensile load.

The double arrow heads signify increased width of slip bands. The macroscopic stress axis is vertical.

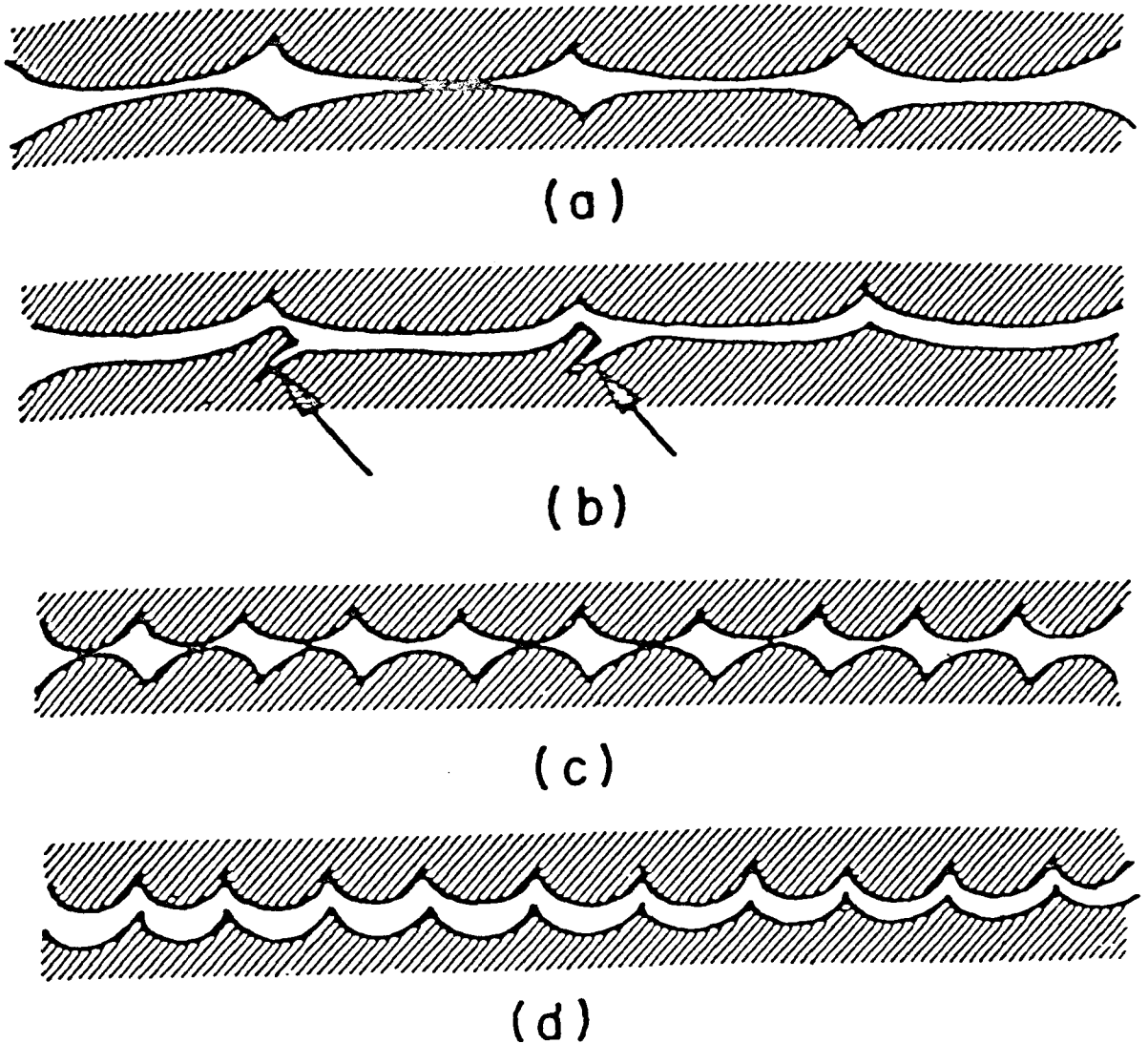


Fig. 4.08 Schematic representation of the various types of striation morphology observed on ductile fatigue fracture surfaces. (After Laird [4.08]).

the varieties of fracture surface striations and associated interstriation markings, and the differences between the two growth stages'.

The conflict whether crack extension occurs by a discrete crystallographic mechanism or by plastic blunting has been discussed by Meyn [4.10, 4.11] with respect to the fatigue of a 2024 aluminium alloy in vacuum and air. Tests in air conducted at low strain amplitudes produced very flat striations, and increasing strain amplitude resulted in a matching hill and valley fracture contour indicative of extensive plastic deformation. In vacuum the fracture surface topography was faceted and contained no striations at all. From these observation Meyn concluded that fatigue crack growth in air was dependent on environmental tensile cracking accompanied by small scale plastic blunting. No attempt was made to explain the growth mechanism operating in vacuum.

To explain the observations of Meyn, Pelloux [4.12, 4.13] proposed the alternating shear model for striation formation shown in Fig. 4.09. In this model shear is first assumed to occur along plane AC. Subsequent strain hardening restricts further flow and results in shear occurring on plane AB. Continued tension produces a repetition of this sequence on the same family of planes until the maximum load is reached. During load reversal, reversed slip in vacuum occurs and no striations are formed, but in air irreversable slip produced by oxidation effects results in a peak to peak fracture surface topography as shown in Fig. 4.10.

Tomkins and Biggs [4.14] developed the shear band decohesion model shown in Fig. 4.11 to describe the growth mechanism operating in aluminium subject to high strain fatigue. Here the application of

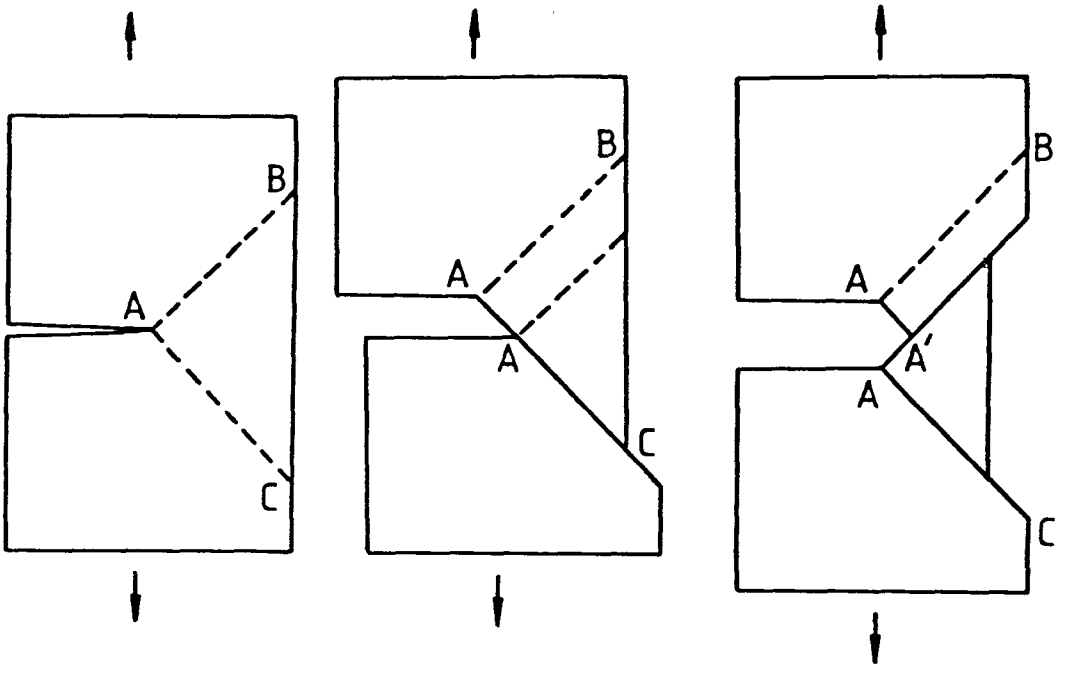


Fig. 4.09 The mechanism of crack propagation by alternating shear as suggested by Pelloux [4.12].

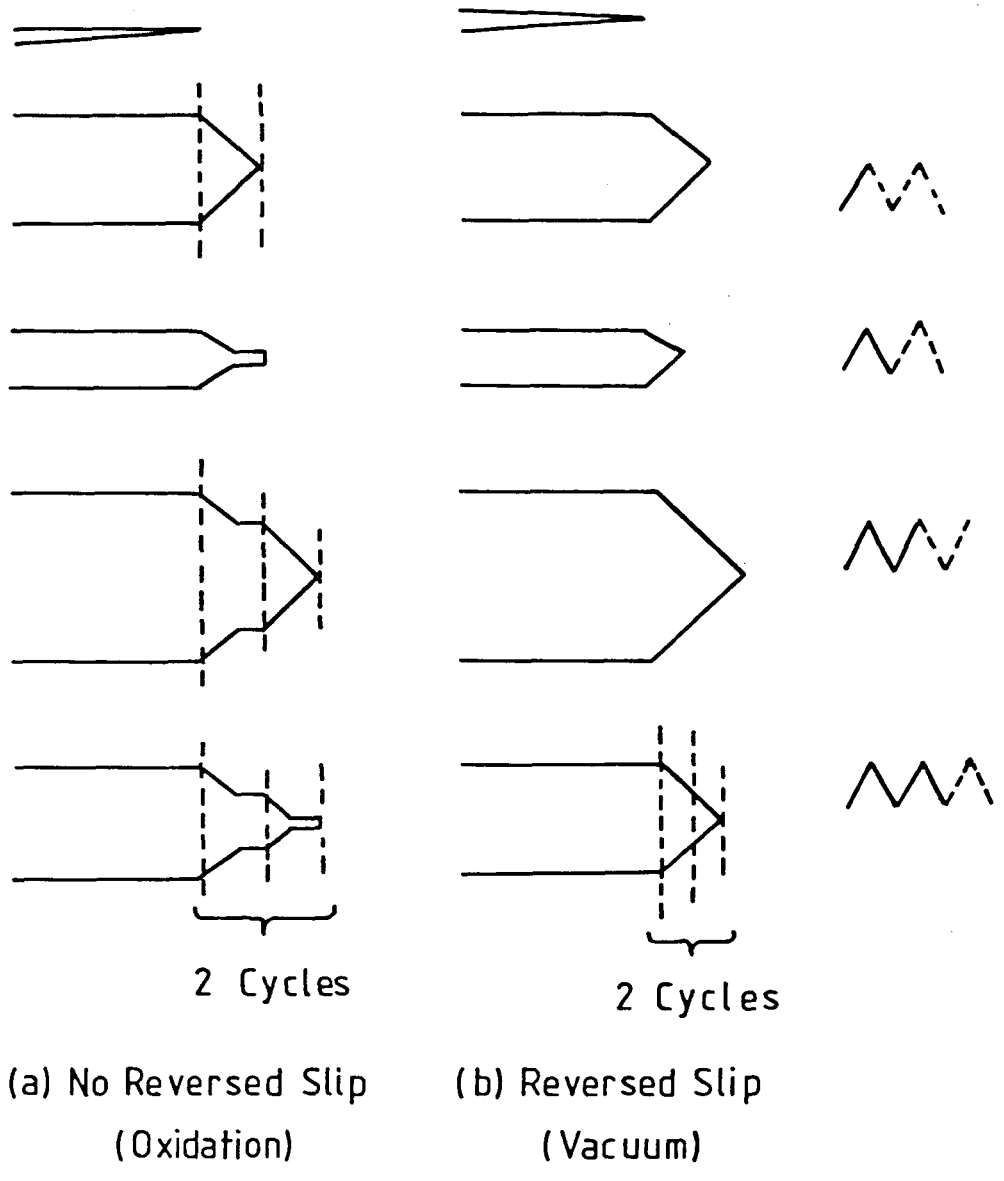


Fig. 4.10 A schematic representation of crack tip extension in vacuum and air. (After Pelloux [4.12]).

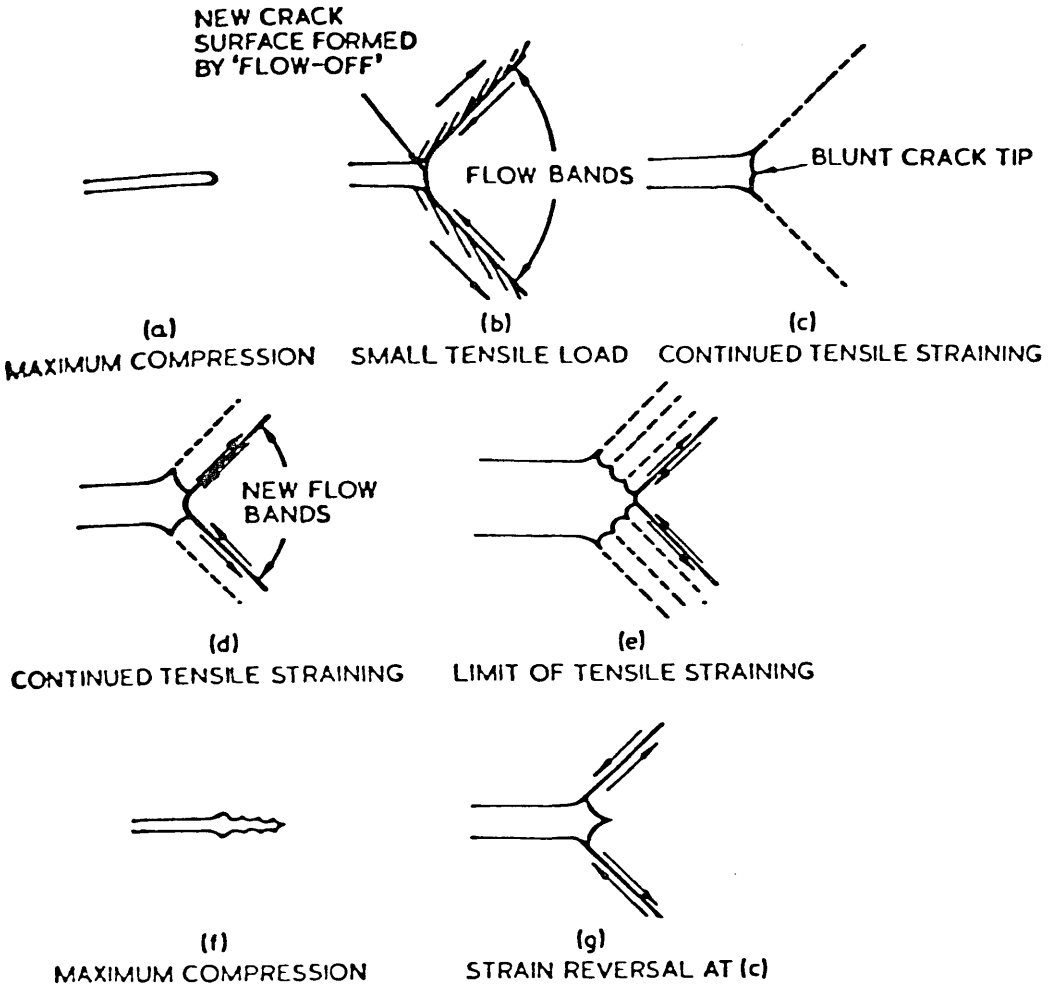


Fig. 4.11 Stage II fatigue crack propagation by a shear band decohesion mechanism. (After Tomkins and Biggs [4.14]).

a small tensile load to the crack tip initiates slip on planes inclined at 45 degrees to the overall growth direction and the creation of new surface by "flow off", Fig. 4.11 (b). Progressive strain hardening gradually restricts dislocation flow and eventually a condition of crack blunting is achieved, Fig. 4.11(c). Continued tensile loading then results in localised tensile fracture at the centre of the notch and crack extension. New slip bands are then activated, Fig. 4.11(d), and the process repeats until the maximum tensile stress is reached, Fig. 4.11(e). During the compression cycle slip occurs in the reversed direction and forces the crack surfaces together leaving it resharpened for the next cycle.

Grosskreutz and Shaw [4.15], who studied the dislocation substructure just below the fracture surface of an aluminium alloy, found that no correlation existed between dislocation substructure and striation topology. They concluded that the mechanism of striation formation was non-crystallographic but resulted from a plastic blunting process.

Similar studies conducted by Lucas et al [4.16] in copper single crystals revealed that a considerable difference in dislocation substructure existed between the matrix and the crack tip. The matrix dislocation structure consisted of tangles and bands of dislocations but as the fracture surface was approached this reverted to a fine cellular structure characteristically produced by intense plastic deformation. Observations of the interaction between crack tip and plastic zone geometry led them to suggest that the mechanism of crack propagation was not dependent on microscopic dislocation motion, but on the resulting macroscopic deformation produced at the crack tip.

Wilkins and Smith [4.17], who carried out an extensive study of the dislocation substructures associated with a growing fatigue crack in an aluminium alloy, found that Stage II crack propagation did not take place along dislocation sub-grain boundaries. From their results they concluded that mechanisms of crack propagation which involved growth along dislocation cell boundaries were unrealistic,and crack extension involved generalised plastic deformation as proposed by Laird.

4.3 References

[4.01] Forsyth, P.J.E.,
Proc. Crack Prop. Symp., 1, pp 76, College of Aeronautics, Cranfield, Beds., England, 1972.

[4.02] Gell, M., and Leverent, G.R.,
Trans. of the Met. Soc. of A.I.M.E., 1968, 242, pp 1869.

[4.03] Dunquette, D.J. and Gell, M.,
Met. Trans., 1971, 2, pp 1325.

[4.04] Stubbington, C.A.,
Metallurgica, 1963, 68, pp 109.

[4.05] Forsyth, P.J.E., and Ryder, D.A.,
Metallurgica, 1961, 63, pp 117.

[4.06] Stubbington, C.A., and Forsyth, P.J.E.,
Metallurgica, 1966, 74, pp 15.

[4.07] Forsyth, P.J.E.,
Acta. Met., 1963, 11, pp 703.

[4.08] Laird, C.,
A.S.T.M., STP 415, 1967, pp 131.

[4.09] Laird, C., and Smith, G.C.,
Phil. Mag. 1962, 7, pp 847.

[4.10] Meyn, D.A.,
Trans, A.S.M., 1968, 61, pp 52.

[4.11] Meyn, D.A.,
Trans. A.S.M., 1968, 61, pp 42.

[4.12] Pelloux, R.M.N.,
Trans., A.S.M., 1969, 62, pp 281.

[4.13] Pelloux, R.M.N.,
E.F.M., 1970, 1, pp 697.

[4.14] Tomkins, B., and Biggs, W.D.,
J. Mat. Sc., 1969, 4, pp 532.

[4.15] Grosskreutz, J.C., and Shaw, G.G.,
A.S.T.M., STP 415, 1967, pp 226.

[4.16] Lukas, P., Klesnil, M., and Shaw, G.G.,
Phil. Mag., 1969, 8, pp 799.

[4.17] Wilkins, M.A., and Smith, G.C.,
Acta Met., 1970, 18, pp 1035.

CHAPTER FIVE

FATIGUE CRACK PROPAGATION AT LOW GROWTH RATES AND THRESHOLD

5.0 Nomenclature

K_{max}	=	maximum crack tip stress intensity
K_{min}	=	minimum crack tip stress intensity
ΔK	=	stress intensity range
ΔK_T	=	threshold stress intensity range
ΔK_{TO}	=	threshold stress intensity range at R = 0
R	=	stress ratio (i.e. K_{min}/K_{max})
K_{CO}	=	stress intensity required to open crack
C	=	constant
γ	=	emprical constant
K_C	=	fracture toughness parameter
$\Delta\sigma_e$	=	fatigue limit or endurance limit
ρ	=	Neuber's effective crack tip radius
σ_{UTS}	=	ultimate tensile stress
d	=	grain size
K_f	=	material constant
ΔK_{eff}	=	effective stress intensity range
$K_{T(max)}$	=	maximum crack tip stress intensity corresponding to K_T
C.M.O.D.	=	crack mouth opening displacement
a.c.p.d.	=	alternating current potential drop
d.c.p.d.	=	direct current potential drop
C.O.D.	=	crack opening displacement
K_{IC}	=	mode I fracture toughness parameter

B = specimen thickness

SEM = scanning electron microscope

5.1 Introduction

In the past many investigators have applied linear elastic fracture mechanics theory to the phenomenon of fatigue crack propagation and have confirmed that fatigue crack growth in the range 10^{-5} to 10^{-3} mm/cycle obeys the generalised Paris "Law" of Eq. 2.19. In this regime the log da/dN versus log ΔK plot is linear and provides a certain degree of confidence in growth rate prediction. Unfortunately at high and low ΔK's this relationship breaks down producing under and over estimates of growth rate respectively. At low growth rates ΔK rapidly approaches a threshold stress intensity range below which crack growth cannot be detected. In this regime growth rates are strongly influenced by microstructure, stress conditions, stress history, environment, crack closure and crack length.

In this Chapter an attempt is made to review the influence of some of these factors on near threshold fatigue crack growth. Before doing so it must be emphasised that many of these are inter-related and inseperable.

5.2 Stress Effects on Growth Rate

5.2.1 Stress Ratio

The effect of R on near threshold fatigue crack growth of many alloys [5.01 to 5.03] is illustrated with respect to that of a pearlitic steel shown in Fig. 5.01.

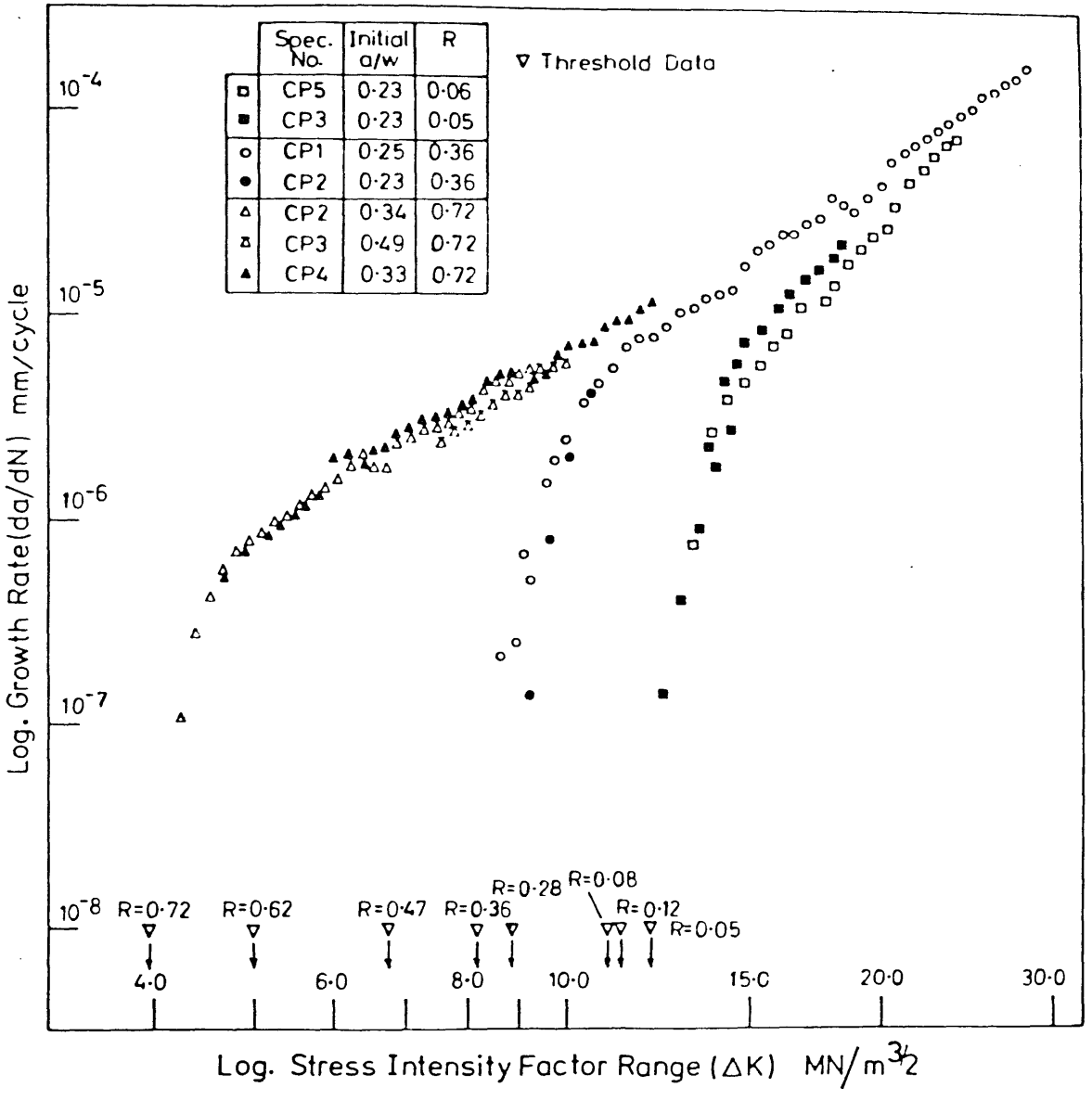


Fig. 5.01 The influence of R on the fcg curves of a medium carbon/manganese pearlitic steel tested in laboratory air at a frequency of ∿ 85 HZ.
(After Cooke and Beevers [5.10])

To account for the variation at low growth rates [5.04] Wei and McEvily proposed the relationship

$$\frac{da}{dN} = C \left[\left[\frac{2\Delta K}{1 - \frac{2R}{1-R}\frac{\Delta K}{\Delta K_C}} \right]^2 - \Delta K_T^{\,2} \right] \qquad \ldots(5.01)$$

suggesting that ΔK_T was a material constant and that R affects growth only above the threshold condition. In a latter paper [5.05] McEvily reported that this model successfully predicted the growth rate behaviour of 3 steels and an aluminium alloy at ΔK's ranging from 4 to 400 $MPam^{-\frac{1}{2}}$.

Similar studies of Klesnil and Lukas [5.06, 5.07] have shown that ΔK_T is sensitive to both R and stress history. They encorporated both effects into a single relationship of the form

$$\frac{da}{dN} = C \left[\left[\frac{\Delta K}{(1-R)^{\gamma}} \right] - \left[\frac{\Delta K_T}{(1-R)^{\gamma}} \right] \right] \qquad \ldots(5.02)$$

where ΔK_T specified the apparent threshold for a given stress history and γ is an empirical constant. These authors considered that the growth rate dependency on stress ratio at low ΔK's can be explained in terms of the compressive stresses at the crack tip. They argued that at low stress ratios the magnitude of the compressive stresses within the crack tip plasticity zone are relatively large and constituted a barrier to crack growth.

5.2.2 Stress History

Klesnil and Lukas [5.07] studied the threshold behaviour in a number of steels and emphasised the importance of stress history. A series of tests were conducted in which they evaulated the effect of:

(a) increasing K_{max} whilst keeping the stress amplitude constant; and

(b) decreasing stress amplitude and keeping K_{max} constant.

From their results they concluded that in the case of (a) K_{max} was not a sufficient parameter for the description of crack growth because subsequent growth rates were described by Eq. 5.02; but in the case of (b) the achievement of lower internal compressive stresses retarded crack growth and realistic growth rates were not attained until the crack grew into a plastic zone representative of the new stress condition.

5.3 Stress Effects on Threshold Stress Intensity Range

In fatigue situations having constant amplitude and constant positive stress ratio the stress intensity range can be expressed as

$$\Delta K = K_{max} (1 - R) \qquad \ldots(5.03)$$

This is true for all values of K_{max} provided $0 \leqslant R \leqslant 1$ and also holds for the threshold condition, i.e.

$$\Delta K_T = K_{T(max)} \ (1 - R) \qquad \ldots(5.04)$$

Now when R = 0, $K_{T(max)} = \Delta K_{TO}$, Eq. 5.04 can be rewritten to give Eq. 5.05 which implies that ΔK_T is a linear function of R.

$$\Delta K_T = \Delta K_{TO} \ (1 - R) \qquad \ldots(5.05)$$

Masounave and Bailon [5.08] have reported that Eq. 5.05 suitably described the threshold behaviour of five ferritic-pearlitic steels (with the least squares fit correlation coefficient ranging from 0.990 to 0.998). Klesnil and Lukas [5.07] however, found in three different steels that ΔK_T and R were related by a simple power law relationship of the form

$$\Delta K_T = \Delta K_{TO} \ (1 - R)^{\gamma} \qquad \ldots(5.06)$$

where γ was equal to 0.71. Interpretation of the results of similar studies in steels by other investigators [5.02, 5.09, 5.10] has produced γ values of 0.53, 0.82 and 1.00 respectively.

Wei and McEvily [5.04] proposed an expression for ΔK_T which incorporated the fracture toughness parameter K_C, i.e.

$$\Delta K_T = \frac{\Delta K_{TO} \ K_C \ (1 - R)}{(1 - R) \ K_C + R \ \Delta K_{TO}} \qquad \ldots(5.07)$$

which was subsequently reduced to

$$\Delta K_T = \Delta K_{TO} \left[1 - \frac{R \ K_{TO}}{K_C \ (1 - R)} \right] \qquad \ldots(5.08)$$

When $\Delta K_{TO}/K_C\ (1 - R) = 1$ this relationship approximates that of Klesnil and Lukas (Eq. 5.06) with $\gamma = 1$. In a latter paper [5.05] McEvily suggested that the ΔK_T dependency on R was described by

$$\Delta K_T = \Delta K_{TO} \sqrt{(1 - R)\ (1 + R)^{-1}} \qquad ...(5.09)$$

which simplifies to

$$\Delta K_T = \Delta K_{TO}\ (1 - 2R)^{0.5} \qquad ...(5.10)$$

Other investigators [5.08, 5.10] have shown that ΔK_T occurs at a constant value of K_{max} suggesting that ΔK_T is K_{max} controlled.

Davenport and Brook [5.11] reasoned that any theory of fatigue threshold must consider the parameters ΔK_{TO}, K_C, K_{max} and R. These were combined to produce the expression

$$\Delta K_T = \Delta K_{TO} \left[\frac{(K_C - K_{max})\ (1 - R)}{(K_C - \Delta K_{TO})} \right]^{\alpha} \qquad ...(5.11)$$

where α was a material constant, for a 0.15%C steel this was found to be 0.33.

Klesnil and Lukas [5.06] related stress history effects to the threshold stress intensity values of steel specimens in the "as received" and stress relieved conditions. From their studies they derived the relationship

$$\Delta K_{TE} = \Delta K_{TT} \left[\frac{\Delta K}{\Delta K_{TT}} \right]^{\alpha} \qquad ...(5.12)$$

where ΔK_{TE} is the effective stress intensity range which is dependent on stress history, and ΔK_{TT} is the true threshold intensity range.

This then led them to reason that once ΔK_{TE} has been determined for a given stress history, the true threshold stress intensity range can be determined using Eq. 5.12.

5.4 Effect of Metallurgical Variables

5.4.1 Mechanical Properties

A surprisingly large dependence of near threshold behaviour on mechanical strength has been observed in many metals and alloys in comparison to crack propagation in the medium growth rate regime. In low strength ferritic-pearlitic steels (with $\sigma_{ys} < 500$ MNm^{-2}) many [5.12, 5.13] have found that increasing material strength produces a corresponding decrease in near threshold stress intensity and a substantial increase in near threshold crack propagation rate. Similar effects have also been reported [5.14, 5.15] in high and ultra-high strength martensitic steel in which the threshold behaviour was related to the cyclic rather than monotonic yield stress.

Observations in non-ferrous alloys have revealed a somewhat different behaviour. In aluminium bronze [5.16] and Al-Zn-Mg alloys [5.17] small reductions in ΔK_T have been reported as the cyclic strength is decreased. This behaviour is opposite to that observed in steels and the magnitude of the effect is smaller. In an aluminium alloy Knott and Pickard [5.17] reported that increasing the cyclic flow stress by a factor of nearly two resulted in an increase in ΔK_T from 2.5 to 3.7 MNm$^{-3/2}$, whereas a similar increase in a tempered martensitic steel [5.14] leads to a decease in ΔK_T from 8.5 to 3.0 MNm$^{-3/2}$.

The small increase in ΔK_T with increase in flow stress in non-ferrous materials has been attributed to a decrease in the alternating plastic crack tip opening displacement [5.16, 5.17]. These authors reasoned that if near threshold crack growth is dependent on the alternating crack tip opening displacement, increasing the flow stress at the crack tip results in a reduction of crack tip plastic strain and growth rate. On the basis of this assumption materials with a high cyclic flow stress would be expected to exhibit a high ΔK_T. Ritchie [5.18] however, refutes this approach illustrating that the crack tip opening displacement predictions of crack growth produces a far too small dependency of growth rates on strength and threshold predictions in the wrong direction.

Many investigators [5.14, 5.19, 5.20] have discovered in steel that whilst increasing material strength reduces ΔK_T, an inverse effect is observed on the fatigue or endurance limit ($\Delta\sigma_e$). In an attempt to explain this inconsistency Ritchie [5.18] proposed two arguments.

(a) In the case of a body containing a small crack he equated the characteristic length constant a_o of Topper et al [5.21, 5.22] and McEvily [5.23] to Neuber's effective crack tip radius ρ and arrived at the relationship

$$\Delta K_T = \Delta\sigma_e \sqrt{\pi\rho} \qquad \ldots(5.13)$$

From the studies of Kuhn and Hardrath [5.24] ρ for steel was found to be inversely proportional to σ_{UTS}^4.

(b) In an uncracked body when R = 0, $\Delta\sigma_e$ approximates to

$$\Delta\sigma_e = \frac{2}{3} \sigma_{UTS} \qquad \ldots(5.14)$$

Thus in (a) an increase in σ_{UTS} produces a decrease in ΔK_T, but in (b) an increase in σ_{UTS} produces an increase in $\Delta\sigma_e$.

5.4.2 Grain Size

Masonnave and Bailon [5.25] studied the effect of ferrite grain size on the near threshold characteristics of a low carbon steel and arrived at a Petch Hall relationship of the form

$$\Delta K = \Delta K_0 + K_f \, d^{\frac{1}{2}} \qquad \ldots(5.15)$$

where d is the grain size, K_f is a material constant and ΔK_0 is the theoretical stress intensity range at $d^{\frac{1}{2}} = 0$ and R = 0. This was then combined with Eq. 5.05 to give Eq. 5.16 containing both grain size and R effects.

$$\Delta K_T = (1 - R) \, (\Delta K_0 + K_f \, d^{\frac{1}{2}}) \qquad \ldots(5.16)$$

Ritchie and coworkers [5.14, 5.15, 5.26, 5.27] assessed the influence of prior austenitic grain size on near threshold crack growth in an ultra high strength modified AISI 4340 alloy steel tested at R = 0.05. They found that whilst grain size had little effect on intermediate growth rates, coarsening the grain size produced a noticable reduction in growth rates at low stress intensities. In the same series of tests

the effect of grain size was evaluated on the near threshold behaviour of two high strength steels (300-M and a Fe-Cr-Co alloy) exhibiting the same monotonic yield strength but differing cyclic mechanical properties. In the 300-M steel, which undergoes cyclic work softening, coarsening of the prior austenitic grain size by an order of magnitude decreased near threshold growth rates but left ΔK_T unchanged. But in the Fe-Cr-Co alloy, which cyclically work hardens, increasing the austentic grain size produced an increase in the near threshold growth rate and a corresponding reduction in ΔK_T.

Similar trends in threshold-grain size behaviour to those reported in steel have also been observed in non-ferrous alloys [5.28].

5.4.3. Microstructure

Whilst a wealth of information exists on the effects of mean stress, specimen thickness, flow stress, toughness and environment on the growth mechanisms operating in steel at low growth rates, the role of microstructure has received less attention. Many attempts have been made to relate the microstructure of quenched and tempered steels to near threshold behaviour but only a few investigators have successfully evaluated the role of microstructure at constant yield strength.

Comparison at constant monotonic yield stress of a 300-M steel have been made [5.14, 5.15] between isothermally transformed structures containing a network of retained austenite within a lower banite-tempered martensitic matrix, and a quenched and tempered fully martensitic structure containing no martensite at all. The quenched and tempered

martensitic steel exhibited greater resistance to crack propagation in comparison to the isothermally transformed structure, but when compared at equivalent cyclic yield strength levels the isothermally transformed steel did offer marginally superior resistance to crack growth in the form of higher thresholds. Increasing tempering temperature from 100 to 650^{o}C proved beneficial in raising the threshold stress intensity factor of the tempered martensitic steel from 3.0 to 8.5 $MNm^{-3/2}$, but this was accompanied by a corresponding increase in growth rate of two orders of magnitude.

The beneficial effect of interlath retained γ on near threshold crack propagation resistance in tempered steel has been observed in a 9Ni-4Co-0.2C high strength aerospace steel tested in moist air [5.29]. Here it was suggested that the role of the austenite effectively reduced the environmental contribution to cracking (resulting from hydrogen embrittlement) by slowing down the rate of diffusion of absorbed hydrogen atoms ahead of the crack tip.

Suzuki and McEvily [5.30] illustrated the possibility of producing enhanced near threshold properties in AISI 1018 steel whilst similtaneously producing substantial increase in yield strength. By a suitable heat treatment process they were able to produce two types of duplex ferrite-martensite structures in which, (a) the martensitic α' was continuous and totally encapsulated the ferritic phase, and (b) the ferritic phase was continuous and totally encapsulated the martensitic phase. A comparison of the near threshold behaviour revealed that in the case of (a) the threshold stress intensity factor was approximately 20 $MNm^{-3/2}$ (σ_{ys} = 452 MNm^{-2}), but in the case of (b) the threshold stress intensity factor was approximately 10 $MNm^{-3/2}$ (σ_{ys} = 293 MNm^{-2}).

This trend was opposite to that expected based on material strength behaviour but no suggestions were forwarded to explain the anomoly.

Patton et al [5.31] have reviewed the fatigue behaviour of two titanium alloys, Ti-6Al-4V and Ti-6Al-2Sn-4Zr-6Mo, and found that the lowest near threshold growth rates occurred in β annealed material followed by transformed β and martensitic structures. Eylon and Bania [5.32, 5.33] argued that refining the microstructure of β titanium alloys increases crack tortuosity and arrest and leads to slower crack growth rates. Yonder et al [5.34] attributed the low growth rates in β annealed material to crack bifurcation which reduces the effective stress intensity by dispersing the strain field energy amongst the multiple crack tips.

5.5 Environmental Effects

It is commonly agreed that the atmosphere is "agressive" in comparison to an inert environment and a considerable effort has gone into determining the active species responsible for this deleterious effort. Oxygen has been consider the major embrittling species in copper and lead [5.35], while for aluminium alloys water vapour is generally the most agressive component [5.01, 5.36, 5.37]. In steel the situation is more complex, water vapour usually has the most significant effect [5.38, 5.39, 5.40], while oxygen is thought to be of secondary importance.

The reported threshold behaviour of steels [5.02] and titanium alloys [5.03, 5.41] suggests that the R effect on threshold and low growth rate behaviour detected in humid environments is diminished or totally eradicated when testing is conducted in vacuum. This is coincident with a decrease in percentage intergranular or facet

fracture when going from air to a vacuum environment suggesting that these monotonic modes of failure are enhanced by environment activity.

A model explaining stress ratio, fractographic, and environmental effects in titanium alloys and steels has been proposed by Beevers and co-workers [5.03, 5.28, 5.42]. It was proposed that the creation of intergranular or transgranular facets is a ΔK controlled process whilst their subsequent connection is K_{max} controlled. The authors then argued that either of these components may be rate controlling depending upon stress ratio. At low stress ratios where it is difficult for the K_{max} controlled process to operate, growth will be K_{max} dependent. At high mean loads the reverse will be true and growth will tend to be ΔK dependent. Environmental influences may alter the rate controlling process by affecting the efficiency of either of these components of fracture. Hence, R effects may be observed in one environment but not in another.

Bucci et al [5.43] conducted fatigue tests in a Ti-6Al-4V alloy in air and dry argon and found that increased environmental components of crack growth were associated with increased stress levels. This led to the suggestion that environmentally accelerated components of fatigue extension could be a partial reason for the observed stress ratio effects.

Ritchie and coworkers [5.44, 5.55] have evaluated the fatigue characteristics of a $2\frac{1}{4}$ Cr-1 Mo steel and reported higher fatigue thresholds in moist air in comparison to dry hydrogen at constant stress ratio. On the basis of fracture surface observations

the increase was attributed to crack closure arising from fracture surface oxide deposits present in air and absent in hydrogen. Tests conducted in dry helium concurred with the results of dry hydrogen irrespective of fracture surface morphology.

Spitzig and Wei [5.46] found in a 250 maraging steel that similar propagation rates existed in dry and humid argon and humid hydrogen, but in dry hydrogen crack propagation rate was increased by a factor of three. Later work [5.38] on a 300 grade maraging steel revealed increased growth rates in a moist environment which they attributed to a decrease in K_{IC} from 121 to 58 $MPam^{-\frac{1}{2}}$.

The specific mechanisms whereby environmental effects occur are subject to speculation and are difficult to elucidate. Originally it was suggested that an improved fatigue life in vacuum was due to a degree of rewelding at the crack tip during the compressive part of the load cycle. Alternatively some form of corrosion mechanism was envisaged to occur ahead of the crack tip which weakens the material and leads to enhanced growth rates.

Atcher [5.47] dimissed the first of these ideas on the ground that oxygen, which is readily absorbed onto the virgin metal, would only take a second to form a monolayer even at a vacuum of 10^{-6} torr. Broom and Nicholson [5.36] suggested in their aluminium alloys that a hydrogen embrittlement mechanism operated which envolved the release of hydrogen from the reaction between water vapour and the metal. They imagined that hydrogen ions diffuse ahead of the crack front and combine in microstructural voids to produce large internal stresses which weaken the material. Unfortunately, whilst this mechanism is considered to be funadementally correct, it fails under very low hydrogen pressure

conditions in ductile materials where the internal stresses are insufficient to cause cracking [5.48].

Pittinato [5.49] has shown that a hydrogen environment increases the fatigue crack growth rate of an α/β titanium alloy in the temperature range 75 to 100°F, but at -200°F there was no difference between the growth rate in hydrogen and that in helium. Based on the results of Berquist [5.50], which revealed that hydrogen readily adsorbs onto clean metal surfaces of titanium even at cryogenic temperatures where no embrittlement is observed, Pittinato concluded that his results were incompatible with an adsorption mechanism and suggested a model based on hydrogen diffusion ahead of the crack tip which was consistent with the strong temperature dependence of the embrittling mechanism. Unfortunately this mechanism, Fig. 5.02, which is based on Lairds plastic blunting model [5.51] fails to predict the observed cleavage planes.

A simple quantitative method has been employed to estimate the effect of aggressive environment in some ultra high strength steels [5.52]. The rate of fatigue crack growth is considered to be a sum of a mechanical fatigue component in an inert environment and an environmental component of crack extension due to monotonic loading in the environment in question, i.e.

$$\left(\frac{da}{dN}\right)_{total} = \left(\frac{da}{dN}\right)_{fatigue} + \left(\frac{da}{dN}\right)_{environmental} \qquad \ldots(5.17)$$

If the growth rate per cycle due to the environmental component is the integral over one cycle T of the static crack growth velocity da/dt with respect to time, then

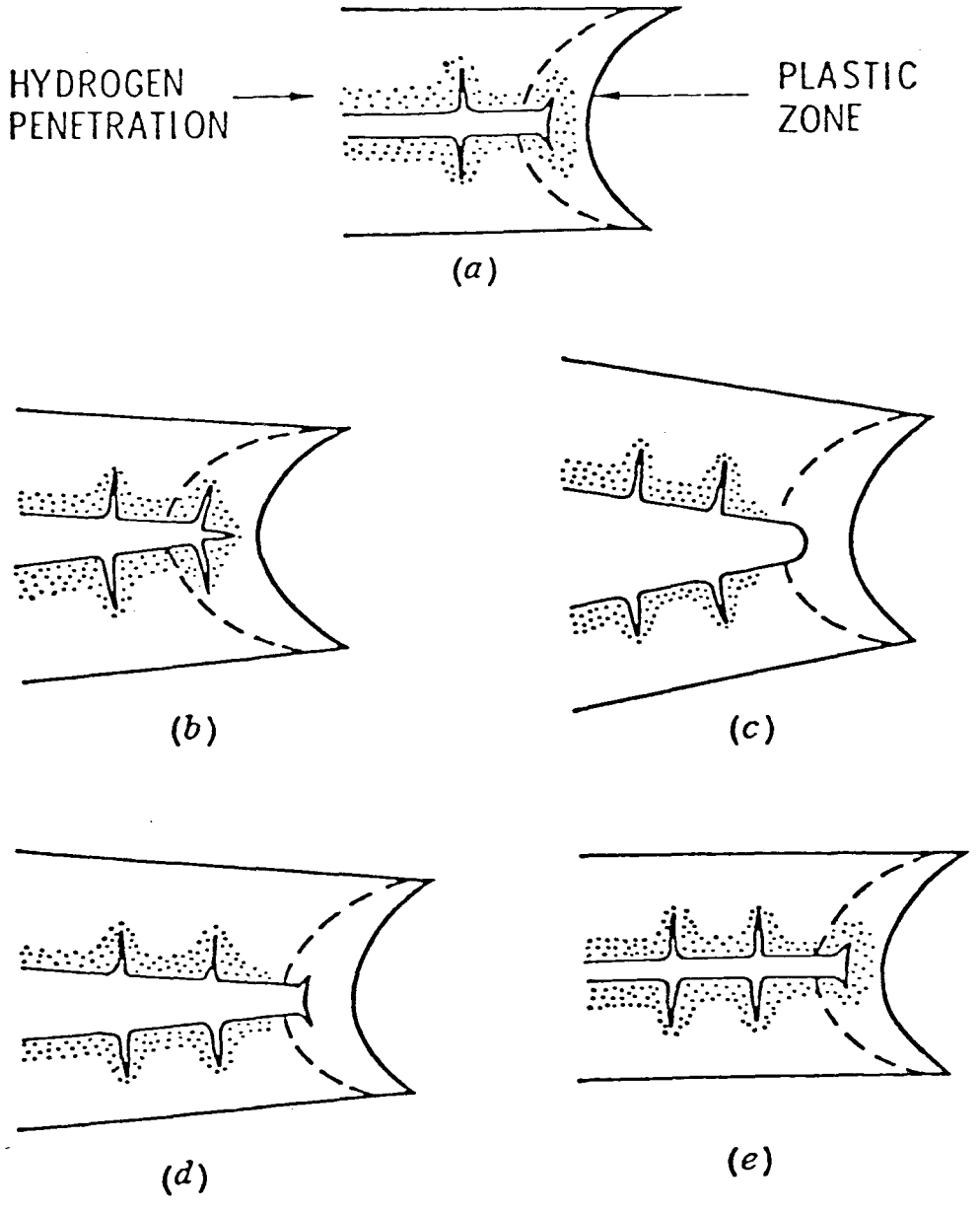


Figure 5.02 Fatigue Crack propagation by hydrogen embrittlement.

a) zero load

b) small tensile load

c) maximum tensile load

d) small compressive load

e) maximum compressive load

(After Pittinato [5.49])

$$\left(\frac{da}{dN}\right)_{environmental} = \int_T \frac{da}{dt}\, dt = \int f(k)\, dt \qquad \ldots(5.18)$$

Experimental results [5.46] have shown that the model correctly predicts the effects of test frequency and therefore it was assumed that environmental action alone was responsible for the increase growth rates associated with a decreased frequency.

5.6 Fatigue Crack Closure

Elber [5.53, 5.54] discovered using a side face strain gauge compliance technique that during tensile loading of aluminium alloys the load versus displacement response of a fatigue cracked specimen was not linear but took on the form shown in Fig. 5.03. To explain this behaviour Elber reasoned that the departure from linearity (region B-C) was the consequence of crack closure resulting from permanent tensile lattice deformation left in the wake of the propagation crack. This further led him to suggest that growth only occurred when the crack was fully open, i.e. above K open, and that the basic Paris "Law" of Eq. 2.19 should be modified by replacing the theoretical stress intensity amplitude, ΔK, by its effective magnitude ΔK_{eff} to give

$$\frac{da}{dN} = C\,(\Delta K_{eff})^m \qquad \ldots(5.19)$$

$$(\text{were } \Delta K_{eff} = K_{max} - K_{open})$$

or

$$\frac{da}{dN} = C\,(\mu\,\Delta K)^m \qquad \ldots(5.20)$$

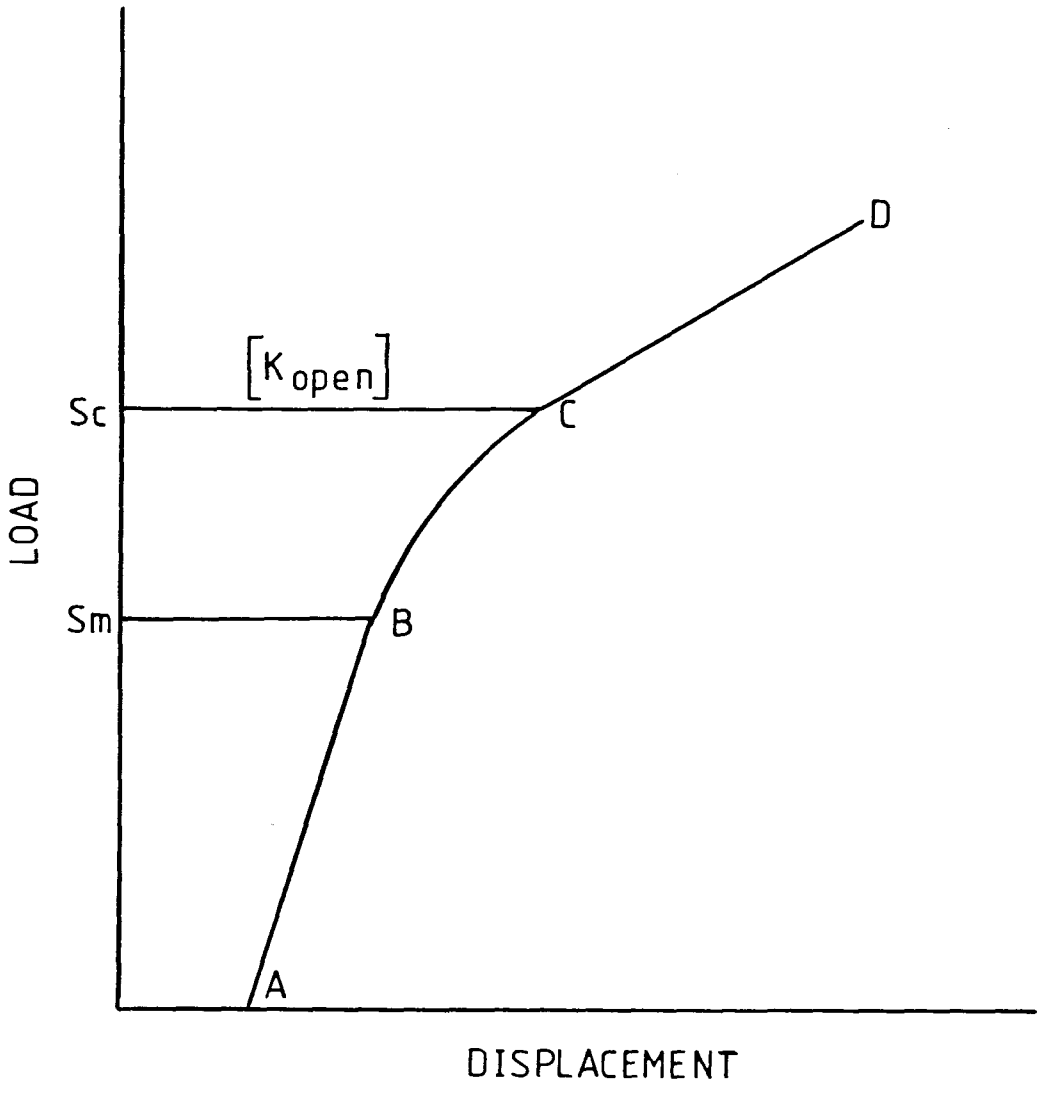


Fig. 5.03 Load-gauge displacement curve for a crack exhibiting closure.

where $$U = \frac{\sigma_{max} - S_c}{\sigma_{max} - S_m} = \frac{\Delta S_{eff}}{\Delta S} \quad \ldots(5.21)$$

For a 2024 aluminium alloy

$$U = 0.5 + 0.4R$$

when $-0.1 < R < 0.7$ $\ldots(5.22)$

Using a similar approach Roberts and Schmidt [5.55] reported for aluminium alloys 2024-T3 and 7075-T6 that U = 0.8 for R = 0 and K_{max} values ranging from 8.8 to 16.5 $MPam^{-\frac{1}{2}}$.

Shih and Wei [5.56] using a d.c.p.d. system found in a Ti-6Al-4V alloy that the onset of crack closure was a function of K_{max} as well as R. For $R \leqslant 0.3$ closure was detected and U was found to decrease with increased ΔK and K_{max}. Other studies [5.57] using the same alloy revealed that near threshold growth rates were influenced by stress ratios $\leqslant 0.9$.

Bachmann and Munz [5.58] using the same alloy found that U increased with increasing ΔK and K_{max} at constant R. Crack opening loads were determined in air and vacuum using both C.M.O.D. and d.c.p.d. techniques. They found under vacuum conditions that artificially high opening loads were recorded using the d.c.p.d. system and suggested this was attributed to the occurrance of non-oxidised non-load bearing sliding contacts in the wake of the crack tip.

To add further confusion, Katcher and Kaplan [5.59] using the same alloy reported that for $R > 0.35$, U varied with a/w but not K_{max}.

Buck and coworkers [5.60 - 5.52], who studied crack closure in a 2219 - T851 alloy using an ultrasonic technique, found when crack opening loads were based on the intersection of the initial and final apparent crack length versus load slopes, that U = 0.85 for R = 0.25 to 0.55. When crack closure was related to the point where the ultrasonic signal versus apparent crack depth became constant, U was found to increase from 0.30 to 0.62 with increasing R.

Frandsen et al [5.60] used an Elber gauge and an accoustic emission technique to monitor crack closure in 2219-T851 and 7075-T651 aluminium alloys. Good agreement existed between both techniques at stress ratios < 0.5 but at R = 0.5 the Elber gauge recorded no closure whereas the accoustic gauge did. In both alloys U was observed to increase with increasing K_{max} but remained constant at $K_{max} > 10$ MPam$^{-\frac{1}{2}}$.

Unangst et al [5.63] reported in a 2219-T851 aluminium alloy that U exhibited a dependency on K_{max}, R and specimen thickness (B). Their results revealed that U can increase, decrease or remain constant, with increasing K_{max}, and tended to increase with R and decrease with B.

Similar results were reported by Clarke et al [5.14] for a 7075-T65 alumina alloy. Crack tip opening load was found to be a function of B, R and K_{max}, but not crack length as suggested by Irving et al [5.65]. Fatigue tests conducted at constant ΔK, K_{max} and R revealed that U remained constant for crack lengths ranging from a/w = 0.10 to 0.25. U increased with R at constant K_{max} as reported by Elber, but the variation was greater than expected. For B = 6.35 and 25.4 mm U increased with K_{max}, but for B = 12.7 mm the trend was reversed.

Lindley and Richards [5.66, 5.67] used an a.c.p.d and d.c.p.d system to evaluate closure in carbon steel specimens of varied thickness. They found that crack closure did not occur during plane strain fatigue unless the minimum load was compressive or reduced below that associated with prior testing. A slight amount of closure was observed following a tensile overload but this was removed after only a small number of cycles. Metallographic sectioning of test pieces in a direction parallel to the loading axis revealed that the plane strain region was always open, but closure was evident above K_{min} in plane stress regions. These observations led to the suggestion that the effect of stress ratio in aluminium alloys and steels could not be explained in terms of crack closure.

In opposition to this view Halliday [5.68] has shown in two titanium alloys that crack closure is not purely a surface effect but results from a fracture surface mismatch mechanism as suggested by Walker and Beevers [5.69]. Side grooves machined along the plane of crack propagation resulted in a reduction in crack opening load to a level concurrent with the reduced thickness.

The work of Irving et al [5.65] on titanium alloys and EN24 steel using d.c.p.d and C.M.O.D. techniques revealed that crack closure decreased with increased R and was sensitive to crack length, loading mode and environment. Using Ti-318 a comparison of the monitoring techniques produced consistent results. In air crack closure occurred below K_{min}, but in vacuum it occurred above K_{min}. These observations led them to suggest that their results were consistent with environmental influence of crack tip deformation, i.e. in an innert environment a reduced C.O.D. leads to earlier contact of the crack faces during



the unloading cycle.

In an endeavour to explain the occurrance of the threshold level in a 2024-T3 aluminium alloy Smidt and Paris [5.70] reasoned that if the stress intensity required to open a crack is assumed constant, K_{CO} a critical portion of the stress intensity range above K_{CO} i.e. ΔK_O, will be necessary to produce crack growth. This model predicts that at low stress ratios where $K_{min} < K_{CO}$.

$$\Delta K_T = K_{max} - K_{min}$$

$$= K_{Max}(1-R)$$

Now because $K_{max} = K_{CO} + \Delta K_O$ = constant

$$\Delta K_T = (K_{CO} + \Delta K_O)\ (1-R) \qquad \ldots(5.23)$$

At higher stress ratios where $K_{min} > K_{CO}$

$$\Delta K_T = \Delta K_O \qquad \ldots(5.24)$$

Using this model Ritchie and coworkers [5.44, 5.55] have conveniently described the threshold (ΔK_T) dependency on stress ratio and environment of a $2\frac{1}{4}$ Cr - 1 Mo steel. Tests conducted in dry hydrogen, dry helium and moist air at R = 0.75 revealed consistently low thresholds (i.e. ΔK_T = 2.9 MPa $m^{-\frac{1}{2}}$) irrespective of environment. Decreasing stress ratio to 0.05 produced an increase in ΔK_T to higher values depending on environment. In dry hydrogen and dry helium threshold stress levels were approximately the same, but in moist air ΔK_T was shifted to higher values. The authors suggested that the increase in threshold stress level with decreasing R resulted from a decrease in ΔK_{eff}, and the increase in ΔK_T at constant R was attributed

in a similar manner to an increase in closure arising from fracture surface oxidation effects.

In view of the conflicting evidence that exists on the occurrance and magnitude of crack closure its influence on near threshold fatigue crack growth must be regarded as questionable. Crack closure undoubtably exists, but whether it offers a complete explanation of the threshold phenomena has yet to be established.

5.7 Threshold Hysteresis

Druce [5.71] studied the near threshold behaviour in low carbon steels fatigued in air and found that threshold hysteresis occurred during the 'load step down - threshold - increasing load' sequence, Fig. 5.04. This effect was observed to decrease with decrease in threshold stress intensity range and was found to be absent in tests carried out in vacuum.

In a vague attempt to explain this phenomena it was suggested that threshold hysteresis resulted from reduced crack tip stress efficiacy arising from:

(a) crack bifurcation by a dissolution process;

(b) crack blunting aided by the build up of corrosion products on the fracture surface wedging the crack tip open; and

(c) the presence of intergranular components of fracture.

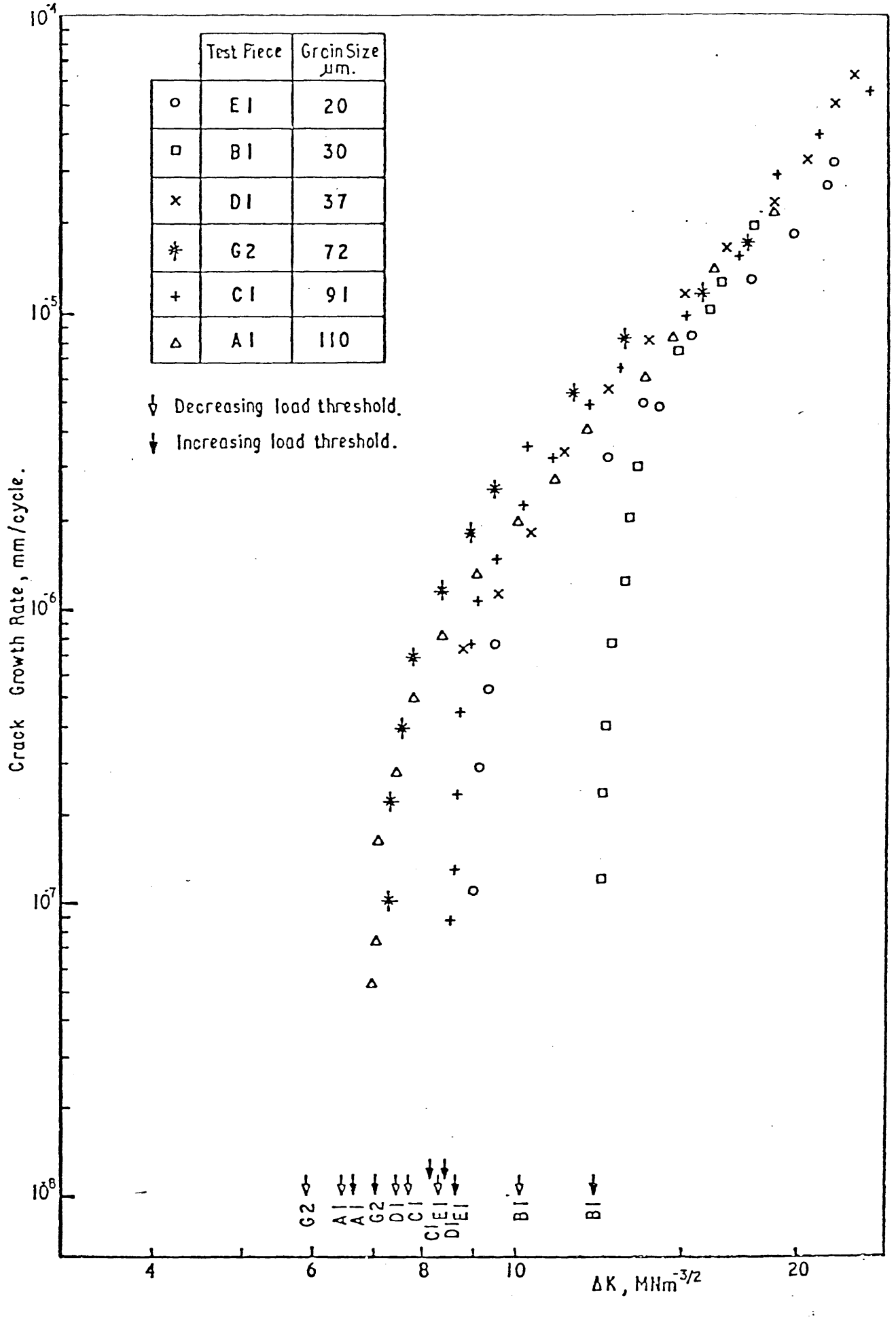


Fig. 5.04 Near threshold crack growth of steel tested in humid air illustrating threshold hysteresis effect. (After Druce [5.71])

5.8 Fracture Surface Observations

The deviation from linearity of the log da/dN versus log ΔK plot at low growth rates has been attributed to the occurrance of microstructural sensitive fatigue crack growth. This has in many cases been typified by a crystallographic mode of fracture. For instance, in quenched and tempered EN 24 steel intergranular faceting has been reported [5.09] to occur over the ΔK range 25 to 14 $MNm^{-3/2}$, but as ΔK_T is approached facet formation decreases. In 316 stainless steel transgranular facet formation was found to occur [5.72] at ΔK's ranging from 15 to 30 $MNm^{-3/2}$.

Birbeck et al [5.73] found in mild steel that the fracture mode operating at low growth rates produced some intergranular faceting whilst at high growth rates featureless striations were produced. The distinction between the two fracture modes, which were labelled Stage IIa and Stage IIb respectively, was found to occur when the ratio of the maximum plastic zone size to grain size was approximately equal to four.

Cooke and Beevers [5.42] reported similar findings to Birbeck et al in two pearlitic steels. Crack growth occurred preferentially in pearlitic colonies by a discontinuous two stage process: first microstructural damage occurred in the form of voids, interlamellar cracks and intergranular cracking ahead of the main crack; then seperation was achieved by ductile tearing of the connecting ligaments.

Lankford [5.74] studied the micromechanisms of crack

initiation and early growth in 4340 steel using a SEM and reported that initiation and growth of very short surface cracks was intermittent, becoming consistent when they had achieved a length of 50 μm. The mode of separation of Stage I and Stage II growth was predominantly transgranular with the distance between growth steps corresponding to the prior austenitic grain size. This suggested that the austenitic grain boundaries served as barriers to crack growth.

The occurrance of microstructural sensitive crack growth has been related to crack tip plasticity by Cooke et al [5.02]. These authors found in EN24 that transgranular and intergranular faceting occurred when the reversed plastic zone size approached the grain size. Ritchie and Knott [5.75] and Austen et al [5.75] have argued that a stronger correlation exists between percentage intergranular fracture and K_{max}, implying that the monotonic rather than the reversed plastic zone size is the critical factor.

Many attempts have been made to determine the transgranular facet planes using laue X-ray reflection technique and area channeling patterns in a number of alloys. Table 5.01. In most instances the trend exhibited is the same, i.e. the facet planes correspond to the close packed planes of the parent lattice.

TABLE 5.01

Crystallographic facets formed during microstructural sensitive fatigue crack growth.

Material	Reference	Environment	Facet Plane	Technique
Al-Zn-Mg	5.77	Laboratory air	{001}	Laue X-ray
Al-Zn-Mg	5.78	3% NaCl Soln.	{001}	Laue X-ray
Cu 47.6% Zn	5.79	Laboratory air	{110} ± 10°	Laue X-ray
Al 2024	5.80	Laboratory air	3° to 20° from {110}	Laue X-ray
Al 2024	5.80	Vacuum	{001} ± 5° {111}	Laue X-ray
Nickel Superalloy	5.81	Laboratory air	{111}	Laue X-ray
Ti-8Al-1Mo-1V	5.82	3½% NaCl Soln.	{0001} 15° from {0001}	Laue X-ray
Al-3% Cu	5.83	Laboratory air	{001} ± 5 - 10°	Laue X-ray
Ti-6Al-4V	5.84	Dry air	15° from {0001}	Laue X-ray
Ti-4Al-4Mo-2Sn-0.5Si	5.84	Moist air	$\{10\bar{1}\bar{1}\}$	Laue X-ray
316 Stainless steel	5.72	Laboratory air	{111}	X-ray
Ti-155	5.85	Laboratory air	{0001} ± 5%	S.A.C.P.

5.9 References

[5.01] Bradshaw, J.F., and Wheeler, C.,
App. Mat. Res., 1966, 5, pp 112.

[5.02] Cooke, R.J., Irving, P.E., Booth, G.S., and Beevers, C.J.,
E.F.M., 1975, 7, pp 65.

[5.03] Irving, P.E., and Beevers, C.J.,
Met. Sc. and Eng., 1974, 14, pp 229.

[5.04] Wei, P.E., and McEvily, A.J.,
'Fracture Mechanisms and Corrosion Fatigue',
Conf. Proc. "Corrosion Fatigue", Storrs., Conn, U.S.A.,
1971, pp 381-395: NACE.

[5.05] McEvily, A.J.,
Met. Sc., 1977, 11, pp 274.

[5.06] Klesnil, M., and Lukas, P.,
E.F.M., 1972, 4, pp 77

[5.07] Klesnil, M., and Lukas, P.,
Mat. Sc. and Eng., 1972, 9, pp 239.

[5.08] Masounave, J., and Bailon, J.P.,
Scripta Met., 1975, 9, pp 723.

[5.09] Paris, P.C., Bucci, R.J., Wessel, E.T., and Mager, T.R.,
A.S.T.M. STP 513, 1972, pp 141.

[5.10] Cooke, R.J. and Beevers C.J.,
E.F.M., 1973, 5, pp 1061.

[5.11] Davenport, R.T. and Brook, R.,
Fatigue of Engineering Mats. and Structure, 1979.
1, pp 15.

[5.12] Kitagawa, H., Nishitani, H., and Matsumoto, J.,
Proc. 3rd Int. Cong. on Fracture, 5, paper V-44/A;
1973, Dusseldorf Germany.

[5.13] Masounave, J., and Bailon, J.P.,
Proc. 2nd Int. Conf. on Mechanical Behaviour of
Materials, 1976, pp 636. A.S.M.

[5.14] Ritchie, R.O.,
J. Eng. Mat. Tech. (Trans. A.S.M.E., H), 1977, 99, pp 195.

[5.15] Ritchie, R.O.,
Met. Sc., 1977, 11, pp 368.

[5.16] Pickard, A.C., Ritchie, R.O., and Knott, J.F.,
Proc. 4th Int. Conf. on Strength of Metals and Alloys,
1976, pp 473, Nancy, France, I.N.P.L.

[5.17] Knott, J.F., and Pickard, A.C.,
Met. Sc., 1977, 11, pp 399.

[5.18] Ritchie, R.O.,
International Metals Reviews, 1979, 24, pp 205.

[5.19] Fine, M.E., and Ritchie, R.O.,
'Fatigue and Microstructure' pp 245, American Soc. for Metals.

[5.20] Benson, J.P. and Edmunds, D.V.,
Met. Sc., 1978, 12, pp 223.

[5.21] El Haddad, M.H., Topper, K.N., and Smith K.N.,
J. Eng. Material Tech. (Trans A.S.M.E., H), 1979, 101, pp 42.

[5.22] El Haddad, M.H., Topper, T.H., and Smith, K.N.,
E.F.M., 1979, 11, pp 573.

[5.23] McEvily, A.J.,
'Recent Research on Mechanical Behaviour of Solids' 1972, Tokyo, University of Tokyo Press.

[5.24] Kuhn, P., and Hardrath, C.E.,
N.A.C.E. Tech. Report. No. NACE TN2805, 1952.

[5.25] Masonnave, J., and Bailon, J.P.,
Scripta Met., 1976, 10, pp 165.

[5.26] Ritchie, R.O.,
Met. Trans., 1971, 8A, pp 1131.

[5.27] Carson, M.F., and Ritchie, R.O.,
Scripta, Met., 1977, 11, pp 1113.

[5.28] Robinson, J.L., and Beevers, J.C.,
Met. Sc. 1973, 7, pp 153.

[5.29] Ritchie, R.O., Chang, V.A., and Paton, N.E.,
J. Fat. Eng. Mats. and Structures, 1979, 1, pp 1.

[5.30] Suzuki, H., and McEvily, A.J.,
Met. Trans., 1979, 10A, pp 475.

[5.31] Paton, N.E., Williams, J.C., Chestnutt, J.C., and Thompson, A.W.,
Proc. A.G.A.R.D. Conf. on 'Alloy Design for Fatigue and Fracture Resistance', No. 185, 1975, 4-1, France, N.A.T.O.

[5.32] Bania, P.J., and Eylon, D.,
Met. Trans., 1978, 9, pp 847.

[5.33] Eylon, D., and Bania, P.J.,
Met. Trans., 1978, 9, pp 1273.

[5.34] Yonder, G.R., Cooley, C.A., and Crooker, T.W.,
2nd Int. Conf. on 'Mechanical Behaviour of Mats'.,
Boston, Mass., 1976.

[5.35] Wandsworth, N.J., and Hutchings, J.,
Phil. Mag., 1958, 3, pp 1154,

[5.36] Broom, T., and Nicholson, A.,
J. Inst. Met., 1960, 89, pp 183.

[5.37] Bradshaw F.J., and Wheeler, C.,
Int. J. Frac. Mech., 1969, 5, pp 225.

[5.38] Spitzig, W.A., and Wei, R.P.,
E.F.M., 1970, 1, pp 719.

[5.39] Shaninian, P., Watson, H.E., and Smith H.H.
J. of Mats. JMLSA, 1972, 7, pp 527.

[5.40] Van Swam, L.F., Pelloux, R.M. and Grant, N.J.,
Met. Trans. A., 1975, 6A, pp 45.

[5.41] Irving P.E., Beevers, C.J.,
Met. Trans, 1974, 5, pp 391.

[5.42] Cooke R.J., and Beevers, C.J.,
Mat. Sc., and Eng., 1974, 13, pp 201

[5.43] Bucci, R.J., Paris, P.C., Hertzberg, R.W. and Schmidt, R.A.,
and Anderson,
A.S.T.M. STP 513, 1972, pp 125.

[5.44] Suresh, S., Zamiski, G.F. and Ritchie R.O.,
A.S.M., 1981, 12A, pp 1435.

[5.45] Ritchie, R.O., Suresh, S., and Moss. C.M.,
J. of Eng. Mats. Tech., 1980, 102, pp 293.

[5.46] Spitzig, W.A., and Wei, R.P.,
Trans. A.S.M., 1967, 60, pp 279.

[5.47] Atcher, M.R.,
A.S.T.M., STP 415, 1967, pp 181.

[5.48] Bernstein, I.M.,
Mat. Sc. and Eng., 1970, 6, pp 1

[5.49] Pittinato, G.F.,
Met. Trans., 1972, 25, pp 235.

[5.50] Berquist, L.E.,
"Gauge Calibration of Extremely Low Pressures",
4th Int. Vacuum Congress, Manchester, England, 1968

[5.51] Laird, C.,
A.S.T.M. STP 415, 1967, pp 131.

[5.52] Wei, R.P. and Landes, J.D.,
Mats. Res. and Stand., 1969, 9, pp 25.

[5.53] Elber, W.,
E.F.M., 1970, 2, pp 37.

[5.54] Elber, W.,
A.S.T.M., STP 486, 1971, pp 250.

[5.55] Roberts, R. and Schmidt, R.A.,
Int. J. Frac., 1972, 8, pp 469

[5.56] Shih, T.T. and Wei, R.P.,
E.F.M., 1974, 6, pp 19.

[5.57] Fitzgerald, J., and Wei, R.P.,
J. Test and Eval., A.S.T.M., 1973

[5.58] Bachmann V. and Munz D.,
"Fatigue Testing and Design",
City Univ. Soc. Env. Eng., 1976, 2, pp 35.

[5.59] Katcher, M., and Kaplan, M.,
A.S.T.M., STP 559, 1974, pp 264

[5.60] Frandsen J.D., Inman, R.V., and Buck O.
Int. J. Frac., 1975, 11, pp 343.

[5.61] Buck, O., Ho. C.L., Marcus, H.L., and Thompson, R.B.,
A.S.T.M., STP 513, 1972, pp 280.

[5.62] Buck, O., Ho, C.L., and Marcus, H.L.,
E.F.M., 1973, 5, pp 23.

[5.63] Unangst, K.D., Shih, T.T., and Wei, R.P.
E.F.M., 1977, 9, pp 725.

[5.64] Clarke, C.K., and Cassat, G.C.,
E.F.M., 1977, 9, pp 675.

[5.65] Irving, P.E., Robinson J.L., and Beevers, C.J.,
E.F.M., 1975, 7, pp 619.

[5.66] Lindley, T.C. and Richards, C.E.,
"The influence of Crack Closure and Plastic Zone Geometry on Fatigue Crack Prop".
3rd Int. Conf. on Frac., Munich 1973.

[5.67] Lindley T.C., and Richards, C.E.,
Mat. Sc. and Eng. 1974, 14, pp 281.

[5.68] Halliday, M.,
"Advances in Frac. Research", 2, pp 253
Proc. of 5th Int. Conf. on Frac., Cannes, France, 1981,

[5.69] Walker, N., and Beevers, C.J.,
Fat. of Eng. Mats. and Structs, 1979, 1, pp 135

[5.70] Schmidt, R.A. and Paris, P.C.,
A.S.T.M., STP, 536, 1973, pp 79.

[5.71] Druce, S.G.,
Ph.D. Thesis, University of Birmingham, 1977.

[5.72] Priddle, E.K., and Walker, F.E.,
J. Mat. Sc., 1976, 11, p 386.

[5.73] Birbeck, G., Inckle, A.E., and Waldron, G.W.J.,
J. Mat. Sc., 1971, 6, pp 319.

[5.74] Lankford, J.,
E.F.M., 1977, 9, pp 617.

[5.75] Ritchie, R.O., and Knott, J.F.,
"Effect of Fracture Mechanics on Fatigue Crack Propagation", P.M.C., Conf. 'Mechanics and Mechanisms of Crack Growth', Cambridge, 1973.

[5.76] Austen, I.M., Ingle, R.M., and Walker, E.F.,
Tech. Report. PH C/6795/5/75/A, Phys. Met.,
University of Birmingham.

[5.77] Forsyth, P.J.E., Stubbington, C.A., and Clark, D.,
J. Inst. Met., 1962, 90, pp 238.

[5.78] Stubbington, C.A.,
Metallurgia, 1963, 68, pp 109.

[5.79] Williams, H.D., and Smith, G.C.,
Phil. Mag., 1966, 13, pp 835.

[5.80] Meyn, D.A.,
Trans. A.S.M., 1968, 61, pp 42.

[5.81] Gell, M., and Leverant, G.R.,
Acta Met., 1968, 16, pp 553.

[5.82] Meyn, D.A.,
Met. Trans., 1971, 2, pp 853.

[5.83] Garrett, G.G., and Knott, J.F.,
Acta. Met., 1975, 23, pp 841.

[5.84] Neal, D.E., and Blenkinsop, P.A.,
Acta. Met., 1975, 24, pp 59.

[5.85] Ward-Close, C.M.,
M.Sc. Thesis, University of Birmingham, 1976.

CHAPTER SIX

FATIGUE CRACK GROWTH AT SHORT CRACK LENGTHS

6.0 Nomenclature

ΔK_T	=	threshold stress intensity range.
$\Delta\sigma_{TH}$	=	threshold stress intensity range dependent on crack length.
ΔS	=	applied nominal stress range
l	=	measured crack length
l_o	=	effective crack length contribution
ΔK	=	stress intensity range
ω_o	=	elastic stored energy
ΔJ	=	J integral
a_o	=	crack length below which $\Delta\sigma_{TH} \neq \Delta K_T$
K	=	stress intensity factor
a	=	crack length
R	=	stress ratio
LEFM	=	linear elastic fracture mechanics
$\Delta\sigma_e$	=	fatigue limit stress

6.1 Introduction

Recently it has been reported that the near threshold fatigue crack growth behaviour in a number of alloys is crack length dependent, with 'short' cracks exhibiting higher growth rates and lower thresholds in comparison to 'long' cracks.

The purpose of this Chapter is to review the reports and theories of a number of investigators describing crack length effects on near threshold fatigue crack growth.

6.2 Experimental Observations and Theories of Short Crack Behaviour

Frost et al [6.01 - 6.03] conducted a series of endurance tests on four different alloys and determined ΔK_T of precracked notched specimens containing 'long' and 'short' cracks of length 0.500 to 5.000 mm and 0.025 to 0.250 mm respectively. A comparison of ΔK_T values revealed the same trend, Table 6.01. Lower threshold values were found in specimens containing short cracks.

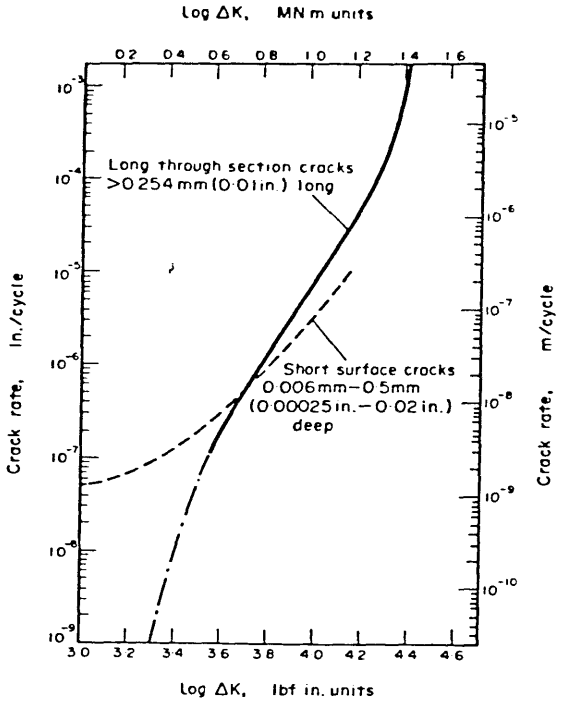
Pearson [6.04] observed the initiation and growth of very short cracks up to depths of 0.5 mm in aluminium alloys BSL 65 and DTD 5050. Comparison of near threshold behaviour with that of long through section cracks of depths > 0.25 mm revealed that the growth rate of short cracks at low ΔK's far exceeded that predicted by long cracks, Fig. 6.01. However, when crack depths exceeded 0.127 mm propagation rates were the same.

The growth of small surface cracks under uni-axial cyclic tensions has been studied by Kitagawa and Takahashi [6.05] in HT 80 low alloy steel. Cracks were grown from surface flaws introduced by spark erosion and crack shape was monitored by a combination of surface replication, heat tinting and "beach mark" treatment techniques. Thresholds were approached using a 3% stress reduction sequence until da/dN was less than 2×10^{-9} mm/cycle (this growth rate was defined as the threshold stress for fatigue crack growth $\Delta\sigma_{TH}$). At crack lengths greater than 0.5 mm ΔK_T was constant, but at shorter crack lengths $\Delta\sigma_{TH}$

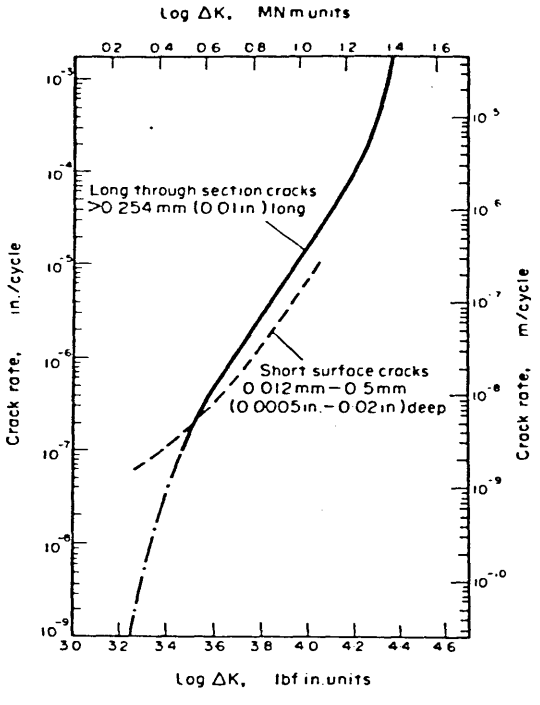
TABLE 6.01

ΔK_T dependence on Crack Length (After Frost et al [6.01 - 6.03])

Material	ΔK_T ($MNm^{-3/2}$)	
	a = 0.500 to 5.000 mm	a = 0.025 to 0.250 mm
Mild Steel	6.4	4.2
Ni-Cr low alloy steel	6.4	3.3
Copper	2.7	1.6
L65 Al alloy	2.1	1.2



Aluminium alloy BS L65. Fatigue crack propagation curves for long and short cracks.



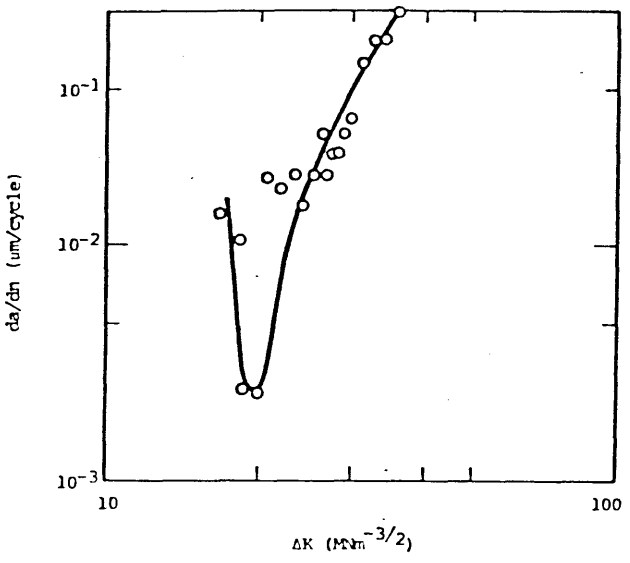
Aluminium alloy DTD 5050. Fatigue crack propagation curves for long and short cracks.

Fig. 6.01 Fatigue crack growth data of 'long' and 'short' cracks illustrating different near-threshold behaviour.
(After Pearson [6.04])

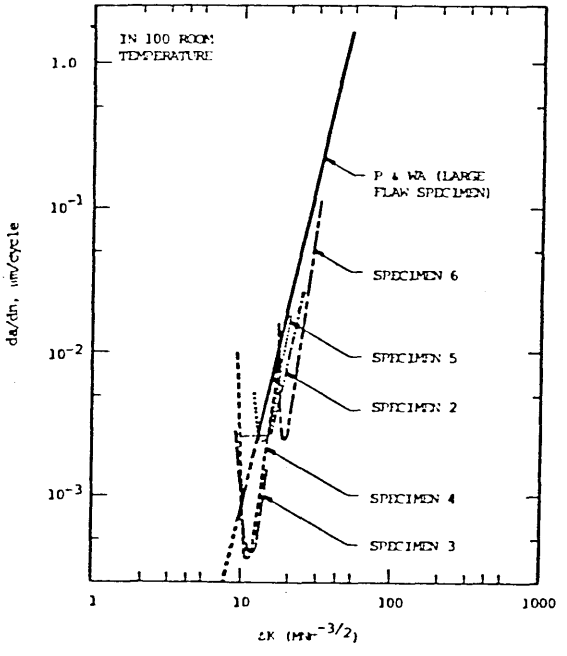
asymtotically approached the fatigue limit. Extrapolation of their results led to the conclusion that a common power law relationship between da/dN and ΔK can be applied to very small cracks of length greater than 0.1 mm.

Sheldon et al [6.06] conducted an interferometric study of deformation fields associated with the plane stress surface condition at the crack tip of a nickel base superalloy IN-100. They found that 'short' and 'long' crack deformation fields were consistent with the predictions of LEFM for crack depths $\geqslant$ 0.06 mm. It was suggested that because the crack tip interacted strongly with the grain boundaries crack advance at low stresses and short crack lengths was unlikely to correlate with the stress intensity predictions for longer crack lengths. To support this proposal it was further argued that in the case of a small flaw only a few obstacles are needed to pin the crack for a large number of stress cycles. As the crack grows, and its crack front increases, the blockages become less effective because of the increased ΔK and crack front line tension.

In a later paper Sheldon and coworkers [6.07] observed that small cracks initially grew more rapidly than predicted by LEFM. This was then followed by a period of decreasing growth rate relative to long crack growth behaviour, and further propagation resulted in growth rates approaching that of longer cracks, Fig. 6.02. It was suggested that the initial fast growth rate was a specimen geometry artifact and not a "real" effect, but the lower growth rate was a "real" effect and was directly attributed to the proportionately greater influence of grain boundary barriers at shorter crack lengths. The authors concluded that in the ΔK range of study the mechanism of crack growth was consistent irrespective of crack length, but growth



(a)



(b)

Fig. 6.02 Crack growth in a IN-100 superalloy.

(a) Crack growth rate versus stress intensity factor.

(b) Crack growth rate versus stress intensity factor of several specimens.

(After Lankford [6.07])

rates differed due to a difference in their statistical response to grain boundaries. Grain boundary retardation effects are only overcome when the cyclic plastic zone size is greater than the average grain size.

Fatigue crack growth studies in high strength steels [6.08, 6.09] have revealed similar results by Sheldon and coworkers [6.07] In every case a lower overall growth rate was exhibited by shorter crack lengths. Lankford [6.08] suggested this effect resulted from intermittent growth at crack lengths $\leqslant$ 60 μm.

Chauhan and Roberts [6.10] studied the near threshold crack propagation behaviour of a 3.4Ni-1.6Cr-0.5Mo-0.1V steam turbine rotor steel. Initially a precrack was generated at ΔK = 22 $MNm^{-3/2}$ in a SEN side grooved fatigue specimen, and then a short crack configuration was achieved by machining away the notch to leave a short remanent crack of depth 0.68 to 6.70 mm ($0.014 \leqslant a/w \leqslant 0.134$). Subsequently threshold was approached by adopting a 10% load reduction sequence as recommended by Klesnil and Lukas [6.11]. Chauhan and Roberts reported that a reduction in initial a/w to less than 0.2 led to increased near threshold crack propagation, Fig. 6.03. Threshold stress intensity was found to increase with increased crack length, Fig. 6.04, becoming asymptotic at a/w = 0.2 and ΔK_T = 6.6 $MNm^{-3/2}$. Variation in ΔK_T with respect to R for short cracks exhibited the same trend for long cracks.

El Haddad et al [6.12, 6.13] reported that the threshold behaviour of short cracks (0.001 to 1.000 in) in CSA G40.11 steel subject to fatigue at R = -1 exhibited similar trends to those of others [6.01 - 6.06], i.e. high growth rates were obtained at low ΔK's.

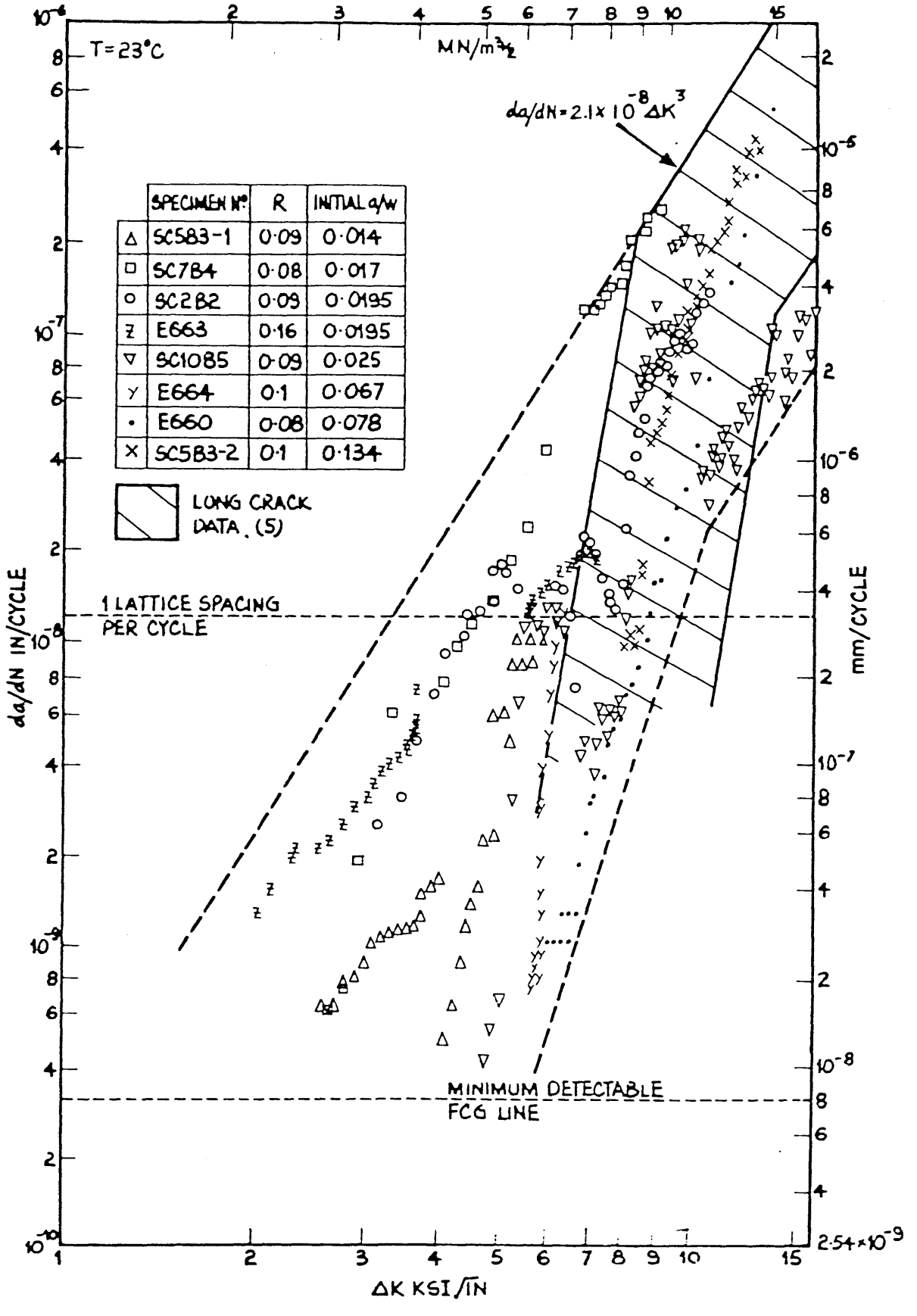


Fig. 6.03 Comparison of fcg data of 'short crack' and 'long crack' data for a 3½NiCrMoV rotor steel (After Chauhan and Roberts [6.10])

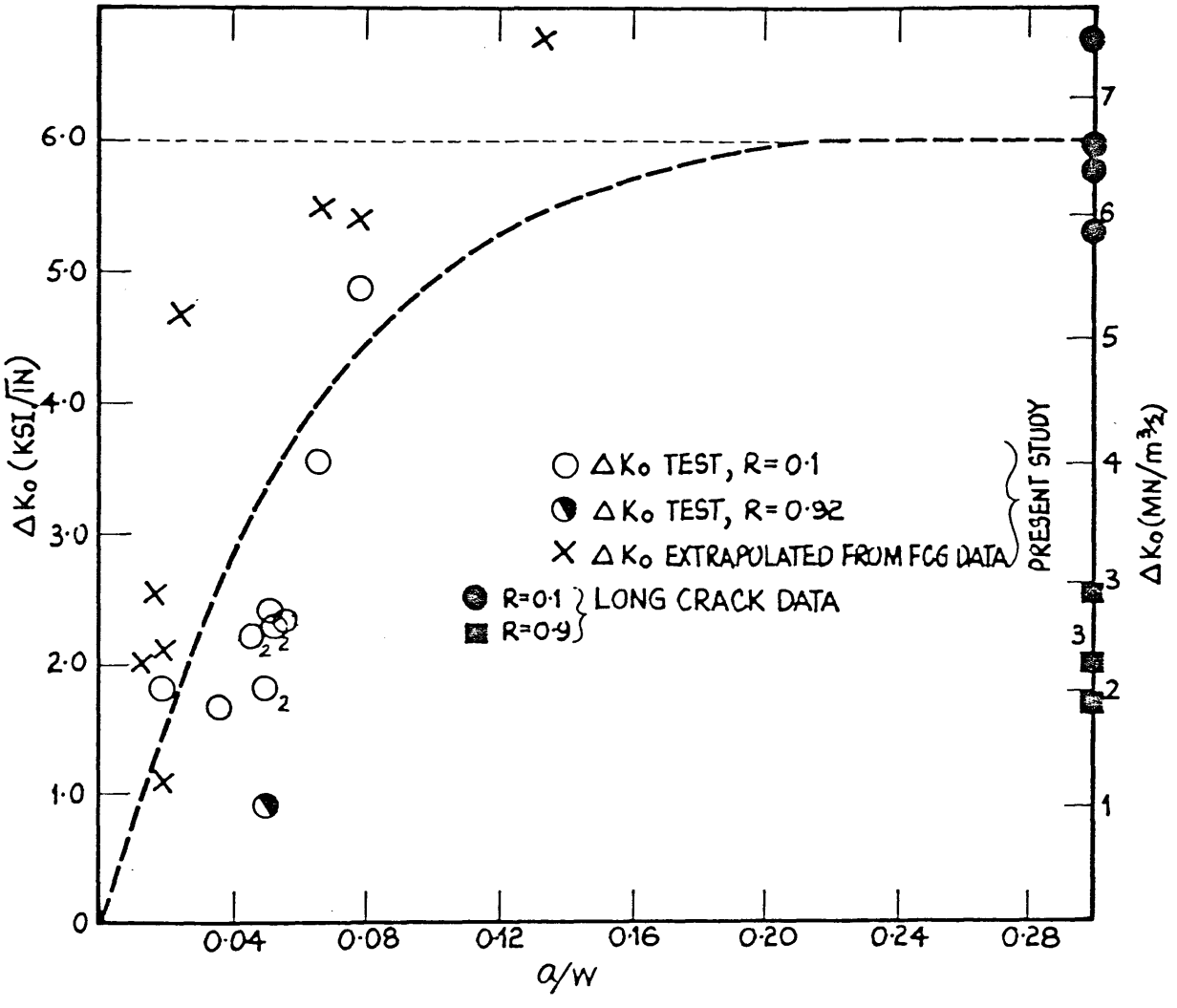


Fig. 6.04 Variation of ΔK_o with non-dimensional crack length a/w (After Chauhan and Roberts [6.10])

Note: $\Delta K_o = \Delta K_T$

In a attempt to model this behaviour, Figs. 6.05 and 6.06, they modified the long crack ΔK expression.

$$\Delta K = \Delta S \sqrt{\pi l} \qquad \ldots(6.01)$$

to give $$\Delta K = \Delta S \sqrt{\pi(l + l_o)} \qquad \ldots(6.02)$$

which contained an effective crack length contribution l_o. It was then reasoned that as $l \to 0$ the parameter l_o constituted an increasing fraction of the effective crack length until at very short crack lengths it represented the crack length at which the fatigue limit stress ($\Delta\sigma_e$) can propagate a crack into the interior of the specimen, i.e.

$$\Delta K_T = \Delta\sigma_e \sqrt{\pi l_o} \qquad \ldots(6.03)$$

At any other effective crack length $(l + l_o)$ the threshold stress range ($\Delta\sigma_T$) can be expressed as

$$\Delta\sigma_T = \frac{\Delta K_T}{\sqrt{\pi(l + l_o)}} \qquad \ldots(6.04)$$

The effective crack length concept was also encorporated in the J integral equation

$$\Delta J = \frac{\Delta K^2}{E} \qquad \ldots(6.05)$$

to give $$\Delta J = 2 \pi \omega_o (l + l_o) \qquad \ldots(6.06)$$

where ω_o is the elastic stored energy

Smith [6.14] argued that if a plot is constructed of tensile stress range at threshold versus crack length and the upper bound stress is taken as the fatigue limit, the reduction in ΔK_T at short crack lengths is predicted as shown in Fig. 6.07. He then reasoned that as the crack decreases ΔK_T must eventually equal the plain fatigue

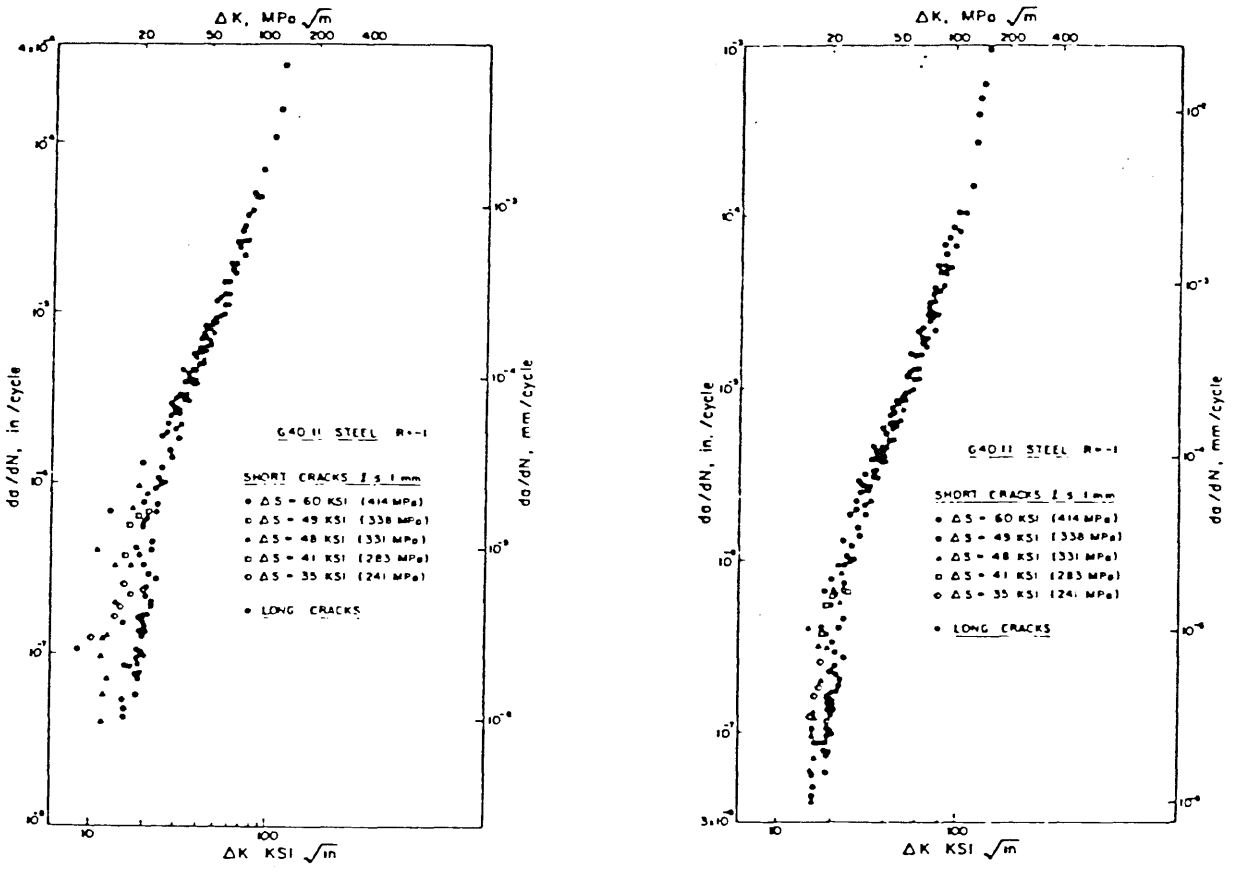


Fig. 6.05 Fatigue crack growth of G40.11 Steel (After El Haddad et al [6.12]).

(a) Near threshold behaviour of long and short cracks.

(b) Superimposition of short crack near-threshold behaviour on the long crack response using the 1_o concept.

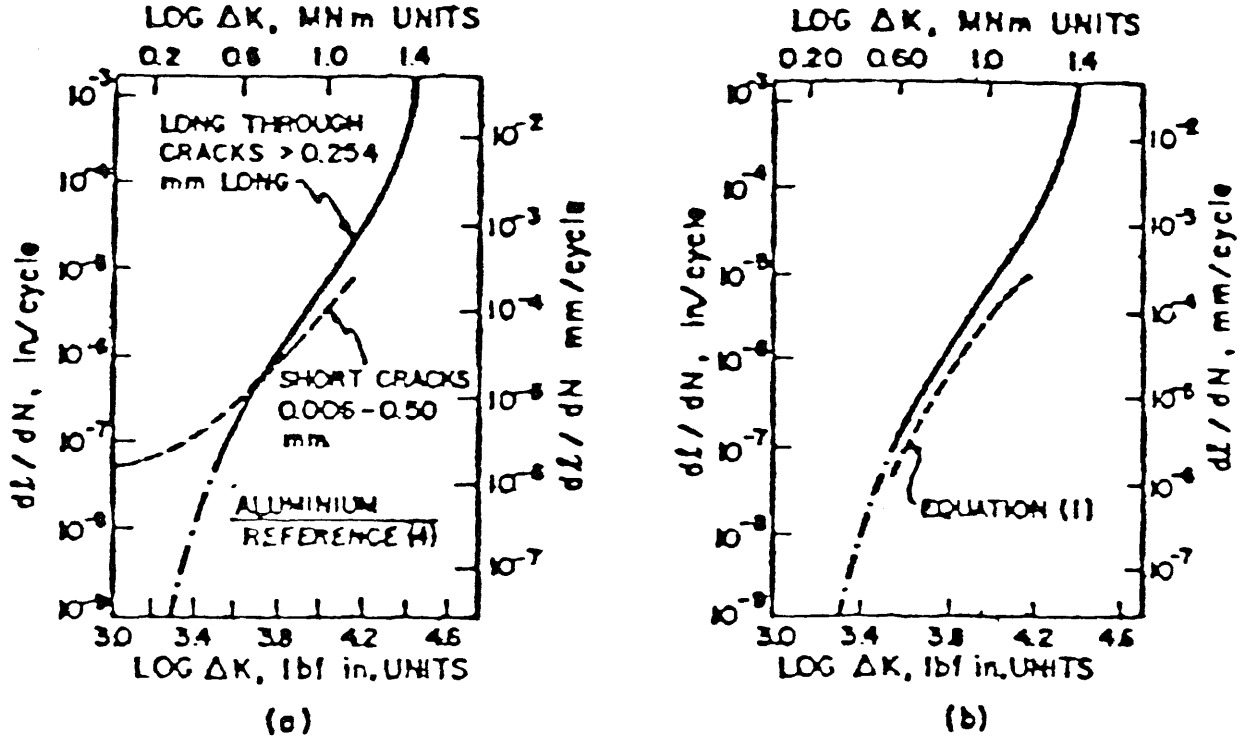


Fig. 6.06 Normalisation of Pearsons [6.04] 'long' and 'short' crack data using the 1_o concept. (After El Haddad et al [6.13])

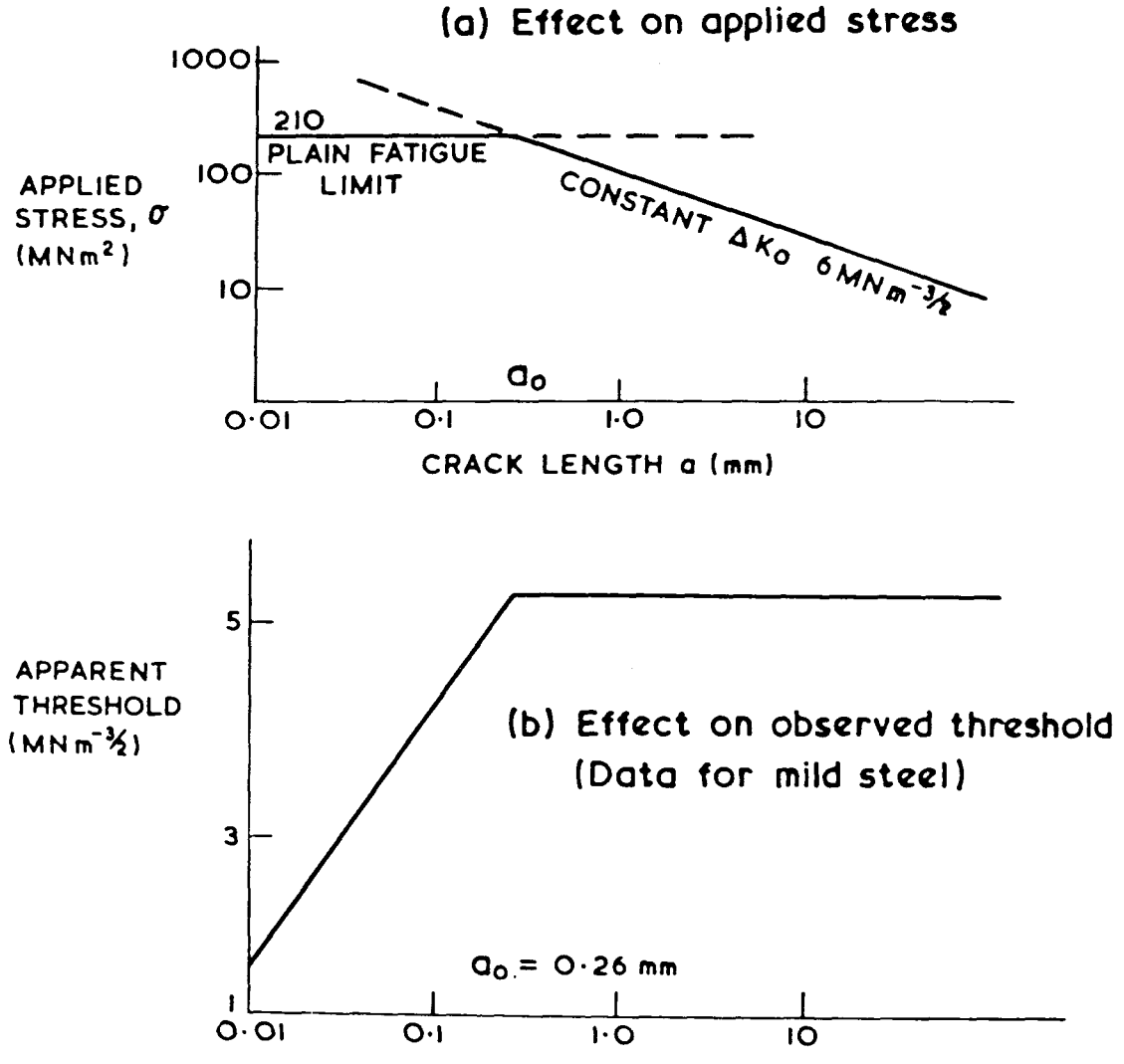


Fig. 6.07 Short cracks and the threshold stress intensity factor.

(After Smith [6.14])

limit at $a = a_o$, and at crack lengths less than a_o thresholds will experience fatigue limit control. This led to the proposal that a decrease in ΔK_T due to the fatigue limit would be expected to occur when

$$a_o \leq \frac{1}{\pi} \left[\frac{\Delta K_T}{\Delta \sigma e}\right]^2 \qquad \ldots(6.07)$$

a_o for mild steel and a Cr-Mo alloy steel was found to be 0.26 and 0.05 mm respectively.

Using the results of Kitagawa and Takahashi, Taylor and Knott [6.15] suggested there existed two other significant crack lengths (l_1 and l_2) smaller and greater than l_o, Fig. 6.08. They reasoned that at l values $\leqslant l_o$ thresholds were dominated by fatigue limit control and were insensitive to crack length; for crack lengths that lie between l_1 and l_2 fatigue thresholds were lower than predicted by LEFM; and for crack lengths $\geqslant l_2$ thresholds occur at constant ΔK_T. For a cast nickel aluminium bronze l_2 was estimated to be approximately three grain diameters. Cracks shorter than this were observed to grow fast, and cracks less than the average grain diameter grew most rapid. The authors suggested that in the latter case high growth rates resulted from the exploitation of weak microstructural features by the crack when its size was of the order of the microstructural unit.

Smith [6.14] tried to establish the minimum crack size for which continum consideration hold by proposing that the near crack tip stress field was characterised by

$$K = \sigma_a \sqrt{\pi a} \qquad \ldots(6.08)$$

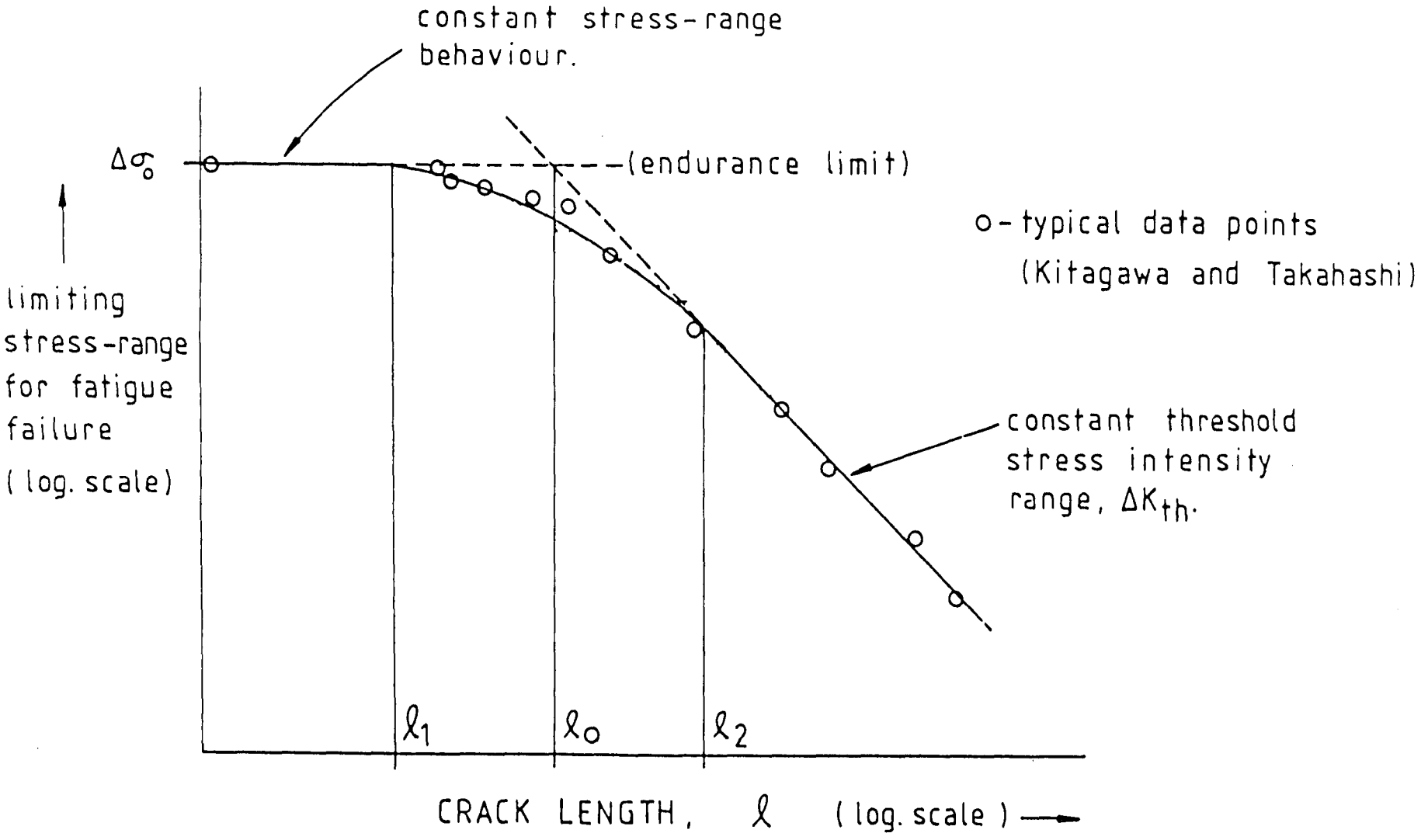
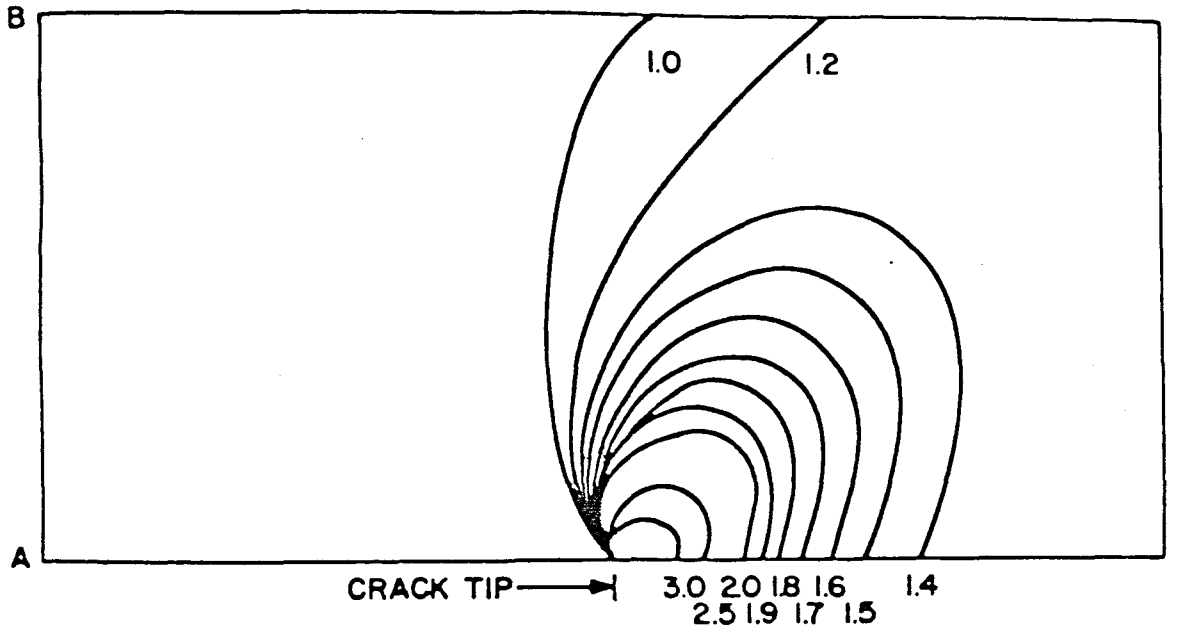


Fig. 6.08 A plot of limiting stress-range for fatigue failure versus crack length illustrating the crack lengths ℓ_0, ℓ_1, and ℓ_2 of Taylor and Knott [6.15].

and lay within a distance a/10 from the crack tip. He then argued that for "global" applications of linear elastic fracture mechanics the near crack tip field should be at least the size of the largest microstructural feature of a real alloy, i.e. the grain size. For a given diameter of 10μm a minimum crack length of 0.1 mm would be needed to satisfy this criteria. However, if the remotely applied stress represents the boundary stresses applied to a single grain and the crack length is half the grain diameter (say 5μm), the near crack tip stress field would extend a distance of 50μm, i.e. approximately 10^5 x typical lattice parameter values for metals, thereby comfortably satisfying continuum requirements.

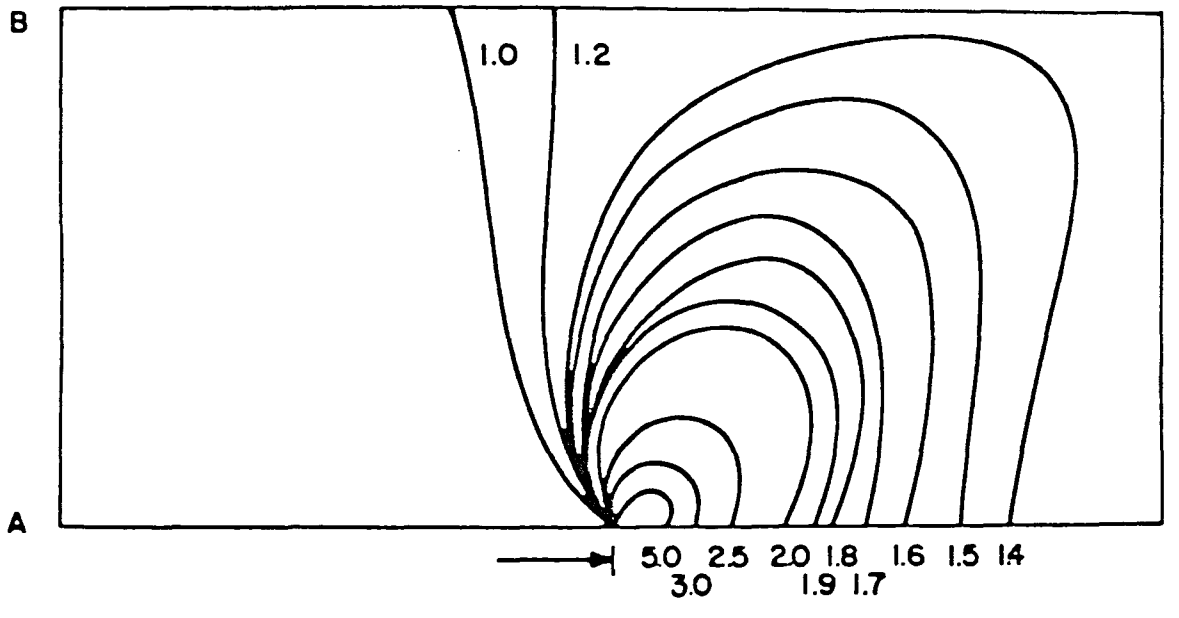
Smith further argued that in a real material where a plastic zone is formed at the crack tip the applicability of K requires that the plastic zone is limited in size compared with the near crack tip behaviour. He assumed that for K validity the crack tip plastic zone size needed to be less than ½ the near crack tip elastic field and proposed that the minimal microstructural feature associated with the crack tip zone would be a subgrain slip band of length ≅ 0.5 μm. On this assumption the minimum crack size for K to be applicable needs to be 50 X larger than the sub-grain slip band dimension, i.e. 25 μm (Smith erroneously quoted 0.25 mm [6.16]).

Talug and Reifsnider [6.17] argued that the description of crack propagation by a Paris Type relationship which is based on the singular part of the stress field at a crack tip becomes questionable for short cracks unless an artifice such as an effective crack length is introduced. They developed a singular field and full field stress solution employing a Williams Stress Function and analysed the stress



Contours of $(\sigma_{yy}/\sigma^{\circ})$ = *constant for* a/w = 0.01. K = 704 $MPa\sqrt{mm}$.

(a)



Contours of $(\sigma_{yy}/\sigma^{\circ})$ = *constant for* a/w = 0.25. K = 704 $MPa\sqrt{mm}$.

(b)

Fig. 6.09 Stress contours at a crack tip.

(a) Short crack.

(b) Long crack.

(After Talug and Reifsnider [6.17])

concentration at the tip of a small and large crack, Fig. 6.09. The general trend observed was a decrease in the size of the singular stress region with decrease in crack length. At short crack lengths the traction free edge produced a redistribution of stress along the crack axis to give a stress gradient at the crack tip greater than predicted by the singular stress field solution. This led them to suggest that any LEFM stress analysis of short cracks must incorporate the full field stress solution.

6.3 References

[6.01] Frost, N.E., Marsh, K.J., and Pook, L., 'Metal Fatigue', pp 44, Oxford Eng. Sc. Series, Claredon Press.

[6.02] Frost, N.E., Pook, L.P. and Denton, K., E.F.M., 1971, 3, pp 109.

[6.03] Frost, N.E., Proc. Inst. Mech. Engrs., 1959, 173, pp 811.

[6.04] Pearson, S., R.A.E. Tech. Report 72236, 1973

[6.05] Kitagawa H., and Takahashi, S., "Applicability of Fracture Mechanics to Very Small Cracks or Cracks in the Early Stage". Proc. Second Int. Conf. on Mech. Behav. of Mats., Boston, 1976.

[6.06] Sheldon, G.P., Cook, T.S., Jones, J.W., and Lankford, J., Fat. of Eng. Mats. and Structs., 1981, 3, pp 219.

[6.07] Lankford, J., Cook, T.S. and Sheldon, G.P., Int. J. of Frac., 1981, 17, pp 143.

[6.08] Lankford, J., E.F.M., 1977, 9, pp 617.

[6.09] Yokobori, T., Kuribayashi, H., Kawagashi, M. and Takeuchi, Rep. Res. Inst. Strength and Fract. of Mats, Tohoku Univ., 1971, 7, pp 1.

[6.10] Chauhan, P., and Roberts, B.W., The Metallurgist and Mats. Technologist, 1977, 3, pp 131.

[6.11] Klesnil, M., and Lukas, P.,
Mat. Sc. and Eng., 1972, 9, pp 239

[6.12] El Haddad, M.H., Dowling, N.E., Topper, T.H., and Smith, K.N.,
E.F.M., 1979, 11, pp 573.

[6.13] El Haddad, M.H., Topper, T.H., and Smith, K.N.,
J. Eng. Mat. Tech. (Trans ASME, H), 1979, 101, pp 42

[6.14] Smith R.A.,
Inst. J. of Frac., 1977, 13, pp 717

[6.15] Taylor, D., and Knott, J.F.,
Fat. Eng. Mats. and Structs, 1981, 4, pp 147.

[6.16] Lankford, J.,
Int. J. of Frac., 1980, 16, pp R7.

[6.17] Talug, A., and Reifsnider,
A.S.T.M., STP 637, 1977, pp 81.

CHAPTER SEVEN

FATIGUE CRACK PROPAGATION AT INTERMEDIATE GROWTH RATES

7.0 Introduction

The purpose of this Chapter is to briefly review the experimental evidence supporting the power law relationship describing crack growth, Eq. 2.19, and the effect of loading and metallurgical variables on crack propagation at intermediate growth rates.

7.1 Experimental Evidence in Support of a Power Law Relationship

From a review of the intermediate growth rate behaviour of a range of materials Johnston and Paris [7.01] concluded that the power exponent m of the Paris 'Law' was 4. This was also endorsed by the results of others [7.02 - 7.07] for a variety of materials including a polymer. In three high strength steels Crooker and Lange [7.08] found that m was equal to 2.5. Birbeck et al [7.09] quoted m values ranging from 2.5 to 2.8 for low carbon manganese steels. Miller [7.10] reported that in steel m was dependent on mechanical properties and ranged from 2.5 to 6.7. In reviewing the variation in m values Crooker and Lange [7.08] concluded that m may assume any value between 2 and 6 with higher values being characteristic of low toughness material. Yang [7.11], who applied a dimensionless analysis to the proposed crack propagation variables in a finite width specimen, determined that m was a material characteristic. For stainless steel he proposed m = 7 and aluminium m = 5.

The general conclusion drawn from these and many other studies is that a power law relationship can be used to describe fatigue crack growth in the intermediate growth regime. The exponent of this relationship is not equal to any fixed value but is variable depending on mechanical properties.

7.2 Stress Effects on Growth Rate

7.2.1 Stress Ratio

It has been reported [7.12-7.15] that in the intermediate growth rate regime there is little or no effect of stress ratio on propagation rate and fatigue crack growth is entirely determined by the alternating stress intensity factor. In cases where a stress ratio dependence has been observed it was attributed to the presence of additional brittle fracture mechanisms in the form of microcleavage [7.16], intergranular separation [7.17, 7.18] and void coalescence [7.18 - 7.20]. These modes of failure are more dependent on the K_{max} component of the stress cycle than its alternating nature and therefore predominantly occur at high stress ratios.

7.2.2 Stress History

The effect of stress history on crack growth of the intermediate growth rate regime has been evaluated by varying load amplitude [7.21 - 7.24]. Increases in ΔK led to an immediate increase in growth rate to that associated with the higher stress level, but reductions in ΔK halted crack propagation for several million cycles.

Recent studies involving detailed overload testing, which involves subjecting a specimen to a constant "baseline" cyclic load followed by one or more cycles of increased mean load or load range before returning to the "baseline" condition, have shown that an overload cycle retards crack growth during subsequent "baseline" cycles. In most cases the growth rate ultimately reached is equal to the pre-load rate, but some investigators [7.25, 7.26] have reported subsequent growth rates either side of this level. Von Euw et al [7.27] found that the application of a constant overload produced increased retardation with increased ΔK, but Jones and Wei [7.28] observed the contrary.

Early theories relating retardation effects to decrease in ΔK gravitated around the retention of residual stresses as the consequence of higher loads [7.29]. In support of this Raju et al [7.30] have shown that crack retardation following an overload can be eliminated by subjecting the overload condition to a stress relieving anneal.

Several attempts [7.31, 7.32] have been made to correlate retarded crack length to the magnitude of the overload plastic zone and subsequent steady state loading. Fracture surface examination has revealed that a "stretched zone" is associated with each single overload cycle [7.31] or the first cycle of an overload block [7.27], whose width is three to four times that of subsequent striations. Lankford and Davidson [7.25] found that retardation period was governed by the number of cycles for the crack to reach the nearest elastic/plastic interface.

In general it has been found that crack retardation resulting from an overload sequence is directly related to increase in percentage overload. However, if the overload is severe complete arrest results.

7.3 Effect of Metallurgical Variables

7.3.1 Microstructure

Many attempts have been made to determine the effects of inclusion content and morphology on fatigue failure. Observations in aluminium alloys [7.33, 7.34] have revealed that an increase in striation spacing, and hence growth rate, results from an increase in inclusion content. Pelloux [7.33] attributed the enhanced growth rate to brittle fracture of hard inclusions ahead of the crack tip aiding crack growth. Conversely, in aluminium alloys which exhibit low growth rates, McEvily [7.36] has suggested that crack growth is inhibited as the result of crack blunting caused by soft inclusions in the vicinty of the crack tip.

Barson [7.37] studied the role of microstructure in low carbon steels having ferrite-pearlite and martensitic structures. Metallographic sections and scanning electron microscopic observations revealed that crack branching occurred within the pearlite colonies. He then argued this produced a reduction in crack tip opening of the primary crack and resulted in a corresponding decrease in growth rate. Close examination of fracture surface topography revealed crack propagation preferentially occurred through ferrite grains and around pearlite colonies. This then led to the suggestion that the composite nature of the pearlite colony offered greater resistance to crack

growth than the surrounding soft ferrite matrix.

Microstructural anisotropy has been investigated in a range of steels [7.38, 7.39] and a significant effect on growth rate was noted at high stress levels. This behaviour was linked with montonic components of fracture which supplimented the striation growth mechanism.

Studies in single crystals [7.40, 7.41] have indicated that crack growth rates are sensitive to stacking fault energy and crystal orientation. A high stacking fault energy coupled with a favourable crystal orientation produced enhanced growth rates.

7.3.2 Mechanical Properties

Whilst generally it has been reported that an increase in yield strength or ultimate tensile strength produces no significant effect on crack propagation in the intermediate growth régime, Radhakrishnam and Baburamani [7.42] found in mild steel that pre-straining produced an increase in the number of cycles to initiation and a decrease in subsequent growth rate. This increase in fatigue strength was reported to vary linearly with the degree of pre-strain.

Evans et al [7.17] examined the effect of increasing fracture toughness of EN24 steel without significantly altering yield strength by removing trace elements from commercially pure specimens. A doubling of the fracture toughness resulted in improved fatigue properties by reducing the monotonic fracture modes typical of low toughness material. Ritchie and Knott [7.19] reported similar trends

in quenched and tempered steels and presented the results of a number of authors in the form of an m versus K_{IC} plot, Fig. 7.01. This was used to illustrate that a power exponent m of four was confined to materials of low fracture toughness.

7.4 Fracture Surface Observations

The appearance of striations have been commonly observed in low carbon steels [7.09, 7.43] but in high strength steels this phenomena is less common or absent [7.18, 7.44]. Miller [7.44] found in three high strength steels that fracture surface appearance could be directly related to fracture toughness. Material of low fracture toughness exhibited a fracture surface comprised of quasi-cleavage, intergranular fracture and dimpled rupture. Increasing toughness promoted striation formation as the result of enhanced crack tip opening and blunting.

Kawaski et al [7.43] applied fracture surface etching technique to study the relationship between fracture surface topography and the underlying microstructure. In a low carbon steel subject to high cycle fatigue they observed ductile striations, substriations, surface holes and occasional cleavage facets. Etching and metallographic sectioning followed by scanning electron microscopic examination revealed that fracture path was random relative to the microstructure. Crack growth occurred across the pearlite lamellae and along the ferrite-pearlite interface. Elements of cleavage fracture were shown to be associated with pearlite colonies.

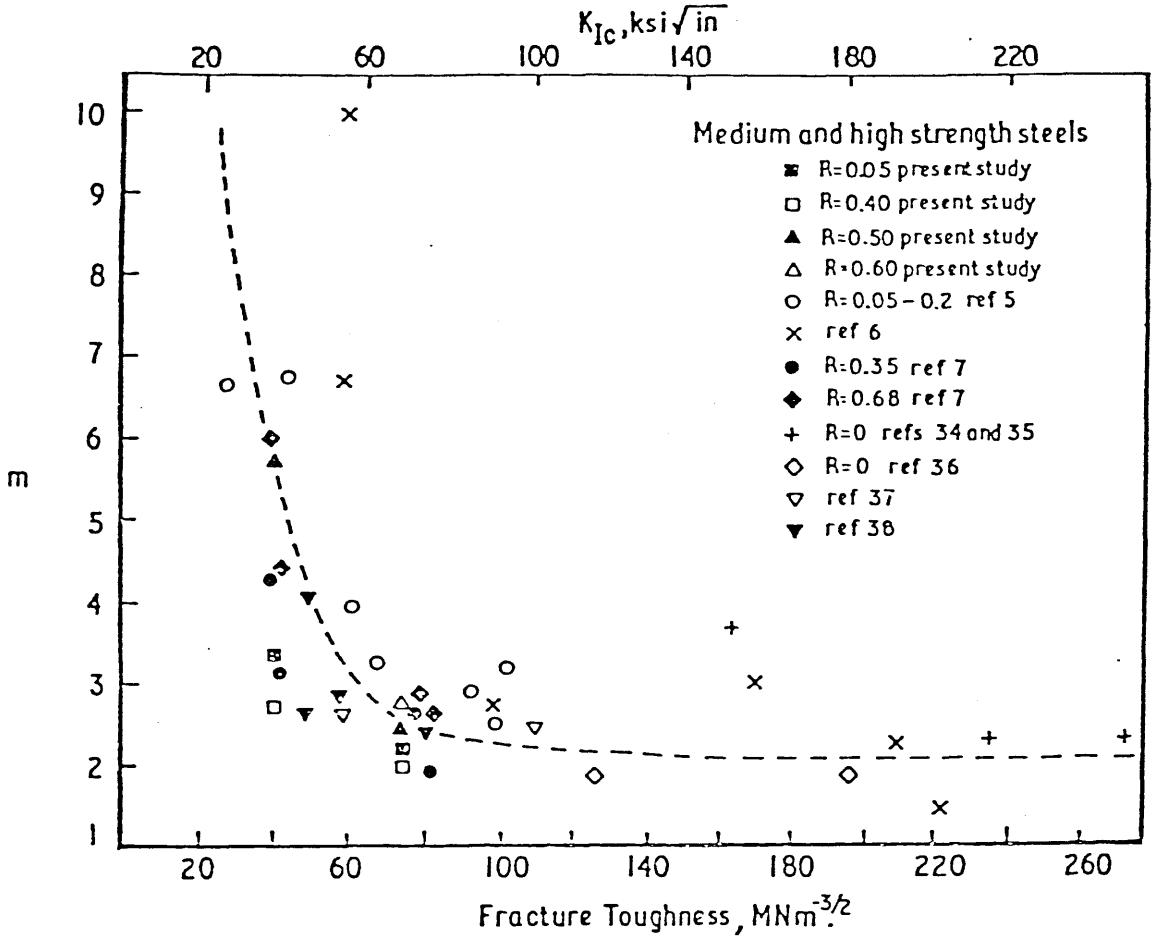


Fig. 7.01 Variation of the Paris exponent m (Eq. 2.21) with static fracture toughness K_{IC} for a number of steels.
(After Ritchie and Knott [7.19])

The effect of microstructural anisotropy due to mechanical fibreing has been studied by Heisser and Hertzberg [7.39]. By careful heat treatment of a hot rolled low alloy steel several different types of bonded structure were obtained of ferrite-pearlite and ferrite-martensite. Fracture surface observations revealed that the martensitic steels exhibited cleavage faceting and all materials showed evidence of local fracture of brittle microconstituents by a mechanism of inclusion-matrix interfacial fracture or cleavage. At low growth rates ($\cong 10^{-5}$ mm/cycle) striation spacing and macroscopic growth rates were comparable, but at high growth rates ($\cong 10^{-2}$mm/cycle) the macroscopic growth rate was much greater.

7.5 References

[7.01] Johnston, H.H., and Paris, P.C., E.F.M., 1968, 1, pp 3.

[7.02] Evans, P.R.V., Owen, N.B., and Hopkins, B.E., J.I.S.I., 1870, 208, pp 560.

[7.03] Carman, C.M., and Katlin, J.M. J. Basic Eng., 1966, 88, pp 792.

[7.04] Flewitt, P.E.J., and Heald, P.J., Int. J. Frac. Mech., 1971, 7, pp 17.

[7.05] Brothers, A.J., and Yukawa, S., J. Basic. Eng., 1967, 89, pp 19.

[7.06] Feeney, J.A., McMillan, J.C., and Wei, R.P., Met. Trans., 1970, 1, pp 1741.

[7.07] Burns, D.J., J. Basic, Eng., 1967, 89, pp 26.

[7.08] Crooker, T.W., and Lange, E.A., J. Basic Eng., 1969, 91, pp 570.

[7.09] Birbeck, G., Incle, A.E., and Waldon, G.W.J., J. Mat. Sc., 1971, 6, pp 319.

[7.10] Miller, G.A.,
Trans. A.S.M., 1968, 61, pp 442.

[7.11] Yang, G.T.,
J. Basic. Eng., 1967, 89, pp 489.

[7.12] Gough, H.J.,
J. Inst. Metals., 1932, 49, pp 17.

[7.13] Roberts, R., and Erdogan, F.,
J. Basic. Eng., 1967, 89, pp 885.

[7.14] Hudson, C.M., and Scardina, J.F.,
E.F.M., 1969, 1, pp 429.

[7.15] Forman, R.G., Kearney, V.E., and Engle, R.M.,
J. Basic Eng., 1967, 89, pp 459.

[7.16] Richards, C.E.,
Acta. Met. 1971, 19, pp 583.

[7.17] Evans, P.R.V., Owen, N.B., and Hopkins, B.E.,
E.F.M., 1971, 3, pp 463

[7.18] Spitzig, W.A., and Wei, R.P.,
Trans. A.S.M., 1967, 60, pp 279.

[7.19] Ritchie, R.O., and Knott, J.F.,
Acta. Met., 1973, 21, pp 639.

[7.20] Griffiths, J.R., Mogford, I.L., and Richards, C.E.,
C.E.G.B., Research Report, No. RD/LR 11698, 1970.

[7.21] Hudson, C.M.,
N.A.S.A. Tech Note No. D960 - 1961

[7.22] Cobly, C.M., and Fackman, P.F.,
E.F.M., 1974, 6, pp 479.

[7.23] Hertzberg, R.W.,
A.S.T.M., STP 513, 1972, pp 230.

[7.24] Jones, R.E.,
E.F.M., 1973, 5, pp 585.

[7.25] Lankford, J., and Davidson, D.L.,
Trans ASME, J. of Eng. Mats and Tech, 1976, pp 17.

[7.26] Bernard, P.J., Lindley, T.C., and Richards, C.E.,
Tech. Note. No. CERL RD/L/N104/75, 1975

[7.27] Von Euw, E.G.J., Hertzberg, R.W., and Roberts, R.,
A.S.T.M. STP 513, 1972, pp 230.

[7.28] Jonas, O., and Wei, R.P.,
Int. J. of Frac. Mech., 1971, 7, pp 116.

[7.29] Donaldson, D.J., and Anderson, W.E.,
'Proc. Cranfield Crack Prop'. Symposium,
Cranefield College of Aeronautics, 1962.

[7.30] Raju, K.N., Ningiah, V., and Rauo, B.V.S.,
Int. J. Frac. Mech., 1972, 8, pp 99.

[7.31] Mill, W.J., and Hertzberg, R.W.,
E.F.M., 1975, 7, pp 705.

[7.32] Wheeler, O.E.,
Trans, A.S.M.E., J. Basic Eng., 1972, 94, pp 181.

[7.33] Pelloux, R.M.N.,
Trans. A.S.M., 1964, 57, pp 511.

[7.34] Kershaw, J., and Lui, H.W.,
Int. J. Frac. Mech., 1971, 7, pp 269.

[7.35] Broek, D.,
'Fracture 69' Ed Pratt et al (1968) pp 754

[7.36] McEvily, A.J.,
N.A.S.A., TD328, 1962.

[7.37] Barson J.M.,
A.S.M.E., Paper No. 71-PVP-12 (1971).

[7.38] Heiser, F.A., and Mortimer, W.,
Met. Trans. 1972, 3, pp 2119.

[7.39] Heisser, F.A. and Hertzberg, R.W.,
J. Basic Eng., 1971, 93, pp 211

[7.40] Ishi, H., and Weertman, J.,
Met. Trans., 1971, 2, pp 344-1.

[7.41] Beevers, C.J., Cooke, R.J., Knott, J.F., and Ritchie, R.O.,
Met. Sc., 1975, 9, pp 119.

[7.42] Radhakrishnan, V.M., and Baburami, P.S.,
Mat. Sc. and Eng., 1975, 17, pp 283

[7.43] Kawaski, T., Yokobori, T., and Nakanishi, S.,
Rep. Inst. Strength and Fracture of Mats., Tohoku, Univ.
1969, 6, pp 25.

[7.44] Miller, G.A.,
Trans, A.S.M., 1969, 62, pp 651.

CHAPTER EIGHT

ALTERNATING CURRENT FIELD THEORY AND CRACK LENGTH MEASUREMENT

8.0 Nomenclature

RMS	=	root mean square
AC	=	alternating current
DC	=	direct current
PD	=	potential difference
ACPD	=	alternating current potential difference
V_o	=	voltage at a = 0.0
a	=	flaw depth measured in the specimen width direction.
μ_r	=	relative permeability
μ_o	=	permeability of free space
f	=	frequency
i	=	ith observation
mv	=	milli volts
K_B	=	constant
ΔV	=	voltage difference
SEN	=	single edge notch
DCPD	=	direct current potential difference.
σ	=	conductivity of metal

Note : the term flaw is used in generality to represent fatigue crack or mechanically assimulated fatigue crack depending on the context.

8.1 Introduction

The AC technique for measuring crack depths in fatigue specimens is based on the measurement of ACPD of an electric field contained within a thin surface layer of the material. Unlike the DC approach which relates DCPD to the resistance of the uncracked cross sectional area, changes in ACPD are related to an increase in current path length produced by crack growth normal to the bulk current carrying surface.

Unfortunately, in many practical fatigue situations the disturbance of the electric field within the skin cannot be easily modelled using AC field theory because reproducibility in ACPD response is susceptible to eddy current effects. Investigators have therefore been forced to develop empirical models describing the ACPD versus flaw depth response based on fatigue and fatigue analogue studies.

The purpose of this Chapter is to present the one dimensional AC field theory used by many to describe their ACPD versus flaw depth response, and to review the trends in ACPD to fatigue and fatigue analogue calibration studies.

8.2 One Dimensional Alternating Current Field Theory

When an alternating current is passed through a metal body it is restricted to a thin surface layer of depth d where

$$d = (\mu_r \mu_o \pi \sigma f)^{-\frac{1}{2}} \qquad \ldots(8.01)$$

Now if the current terminals are sufficiently far apart the electric field between them will contain a uniform potential gradient, Fig. 8.01 (a), whose potential difference along any current line will be proportional to sampling probe contact seperation A - B, i.e.

$$V_o \propto AB \qquad \ldots(8.02)$$

where V_o is a function of many factors, e.g. stress, chemical composition, mechanical properties....etc. Now provided these factors remain constant, the number of volts per mm is simply

$$\frac{V_o}{AB} \qquad \ldots(8.03)$$

Consider now the introduction of a flaw between A and B lying perpendicular to the bulk current carrying surface. This results in a change of potential gradient as shown in Fig. 8.01 (b) to give

$$Vi = V_o + \Delta V \qquad \ldots(8.04)$$

or

$$\Delta V = Vi - V_o \qquad \ldots(8.05)$$

where $Vi \propto AB + 2a$

$\Delta V \propto 2a$

Vi = new voltage

ΔV = voltage difference

If Eq. 8.05 is divided by Eq. 8.03 to give Eq. 8.06, the increase in path length 2a can be expressed in terms of measured potential difference, i.e.

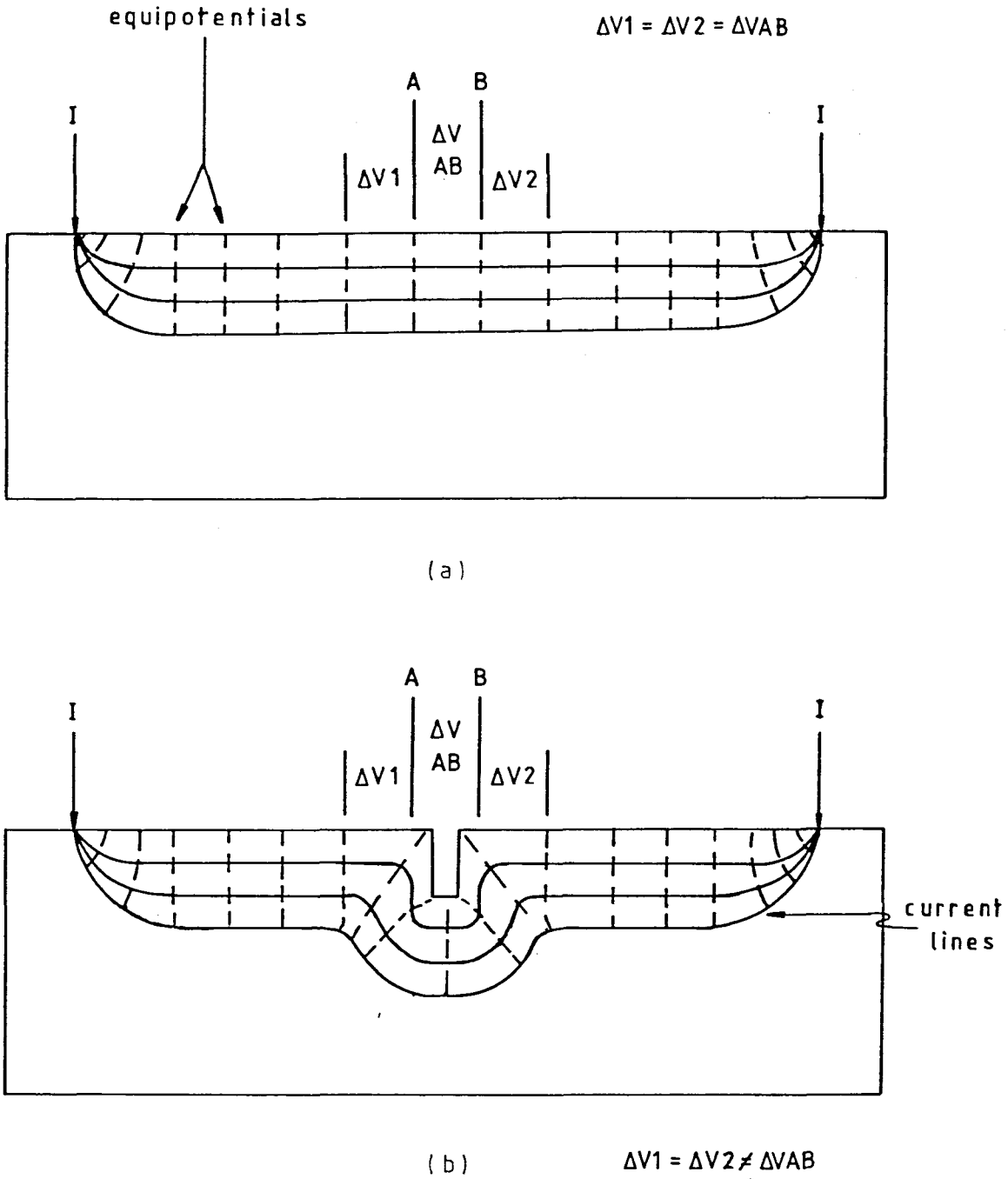


Fig. 8.01 (a) Schematic representation of the AC field distribution within the longitudinal across section of a specimen.

(b) The same specimen containing a flaw perpendicular to the bulk current carrying surface.

$$2a = \left[\frac{Vi - V_o}{V_o}\right] AB \qquad \ldots(8.06)$$

Rearranging Eq. 8.06 gives

$$Vi = V_o + \left[\frac{2a\ V_o}{AB}\right] \qquad \ldots(8.07)$$

which is a linear relationship of the form

$$Y = B\ X + C \qquad \ldots(8.08)$$

where $X = a$

$$B = \frac{2\ V_o}{AB}$$

$$C = V_o$$

8.3 Alternating Current versus Flaw Depth Calibration Studies

8.3.1 State of the Art

Gille [8.01], who reviewed the basic principles of the electric potential methods (AC and DC) in their application to non-destructive testing, implied that in the AC case the simple relationship of Eq. 8.06 cannot be used to predict fatigue crack depth because the magnetic permeability of a material is affected by many factors, e.g.

(a) stress state (this is dependent on applied load and compliance and is inhomogeneous in the regime of study);

(b) chemical composition (normal variations in composition

are due to minority alloying and trace elements, but resistance welded sensing leads can also effect localised composition);

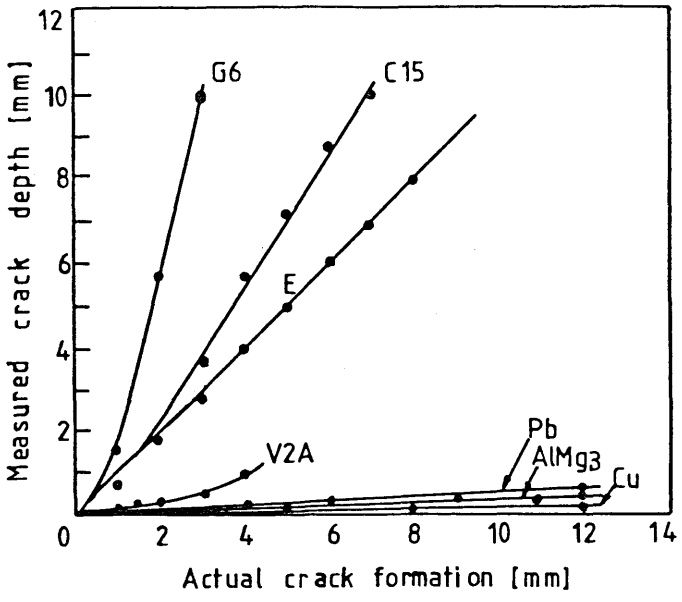
(c) microstructure (this can vary throughout the specimen as the result of mechanical working and heat-treatment); and

(d) mechanical properties (finishing treatments may induce residual stresses and workhardening of the surface layers, and the fatigue process may produce workhardened or worksoftened material at the crack tip).

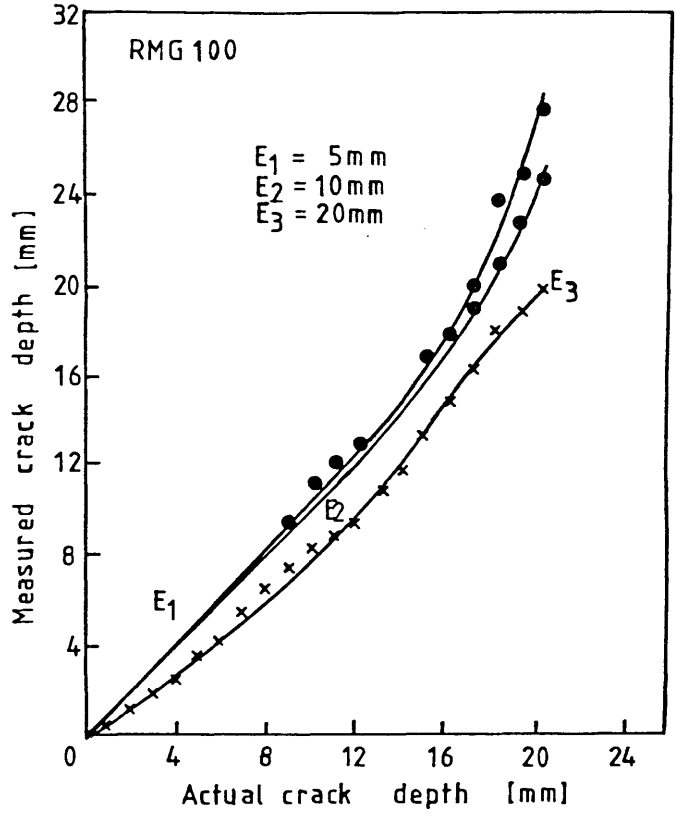
Intuitive consideration of these factors leads to the conclusion that it is highly unlikely that a linear relationship exists at all. But a number of investigators have claimed there is.

Kruse [8.02] reported that the relationship between ACPD and crack depth was dependent on material, Fig. 8.02 (a), and varied with crack depth and sensing probe position, Fig. 8.02 (b). Over short crack depths it could be assumed linear, but over larger crack depths it was more accurately described by a higher degree polynomial.

Betz [8.03] developed on ACPD multiple measuring device which was capable of determining crack depth at several adjacent locations during fatigue cracking. This sophisticated detector, which had dual sensing probes, was utilised to similtaneously measure crack depth (Vi) and the voltage across uncracked material (V_o). Saw cut simulation tests in hollow tube segments exhibited a linear relationship between ACPD and depth of cut which was dependent on



(a)



(b)

Fig. 8.02 Measured crack depth (PD) versus Actual crack depth showing:

(a) the effect of material; and

(b) the influence of probe seperation E.

(After Kruse [8.02])

tube length, Fig. 8.03 (a). Increasing tube length produced a reduction in two dimensional AC field effects and resulted in a decrease in sensitivity. A similar calibration response to the analogue studies was also observed in the fatigue of hollow tubes and solid bars as shown in Fig. 8.03 (b)-(c).

In Al 7075-T6 Birchak [8.04] studied the ACPD response to fatigue cracks and similar sized flaws introduced by EDM and saw slitting techniques. Three types of flaw were investigated in standard reference blocks and flaw profiles were measured using a scanning sensing probe. The results revealed that signals from machine flaws were approximately the same as those of fatigue cracks of corresponding size and shape,and led to the conclusion that cracks of small aspect ratio in a uniform electric field satisfied the linear relationship

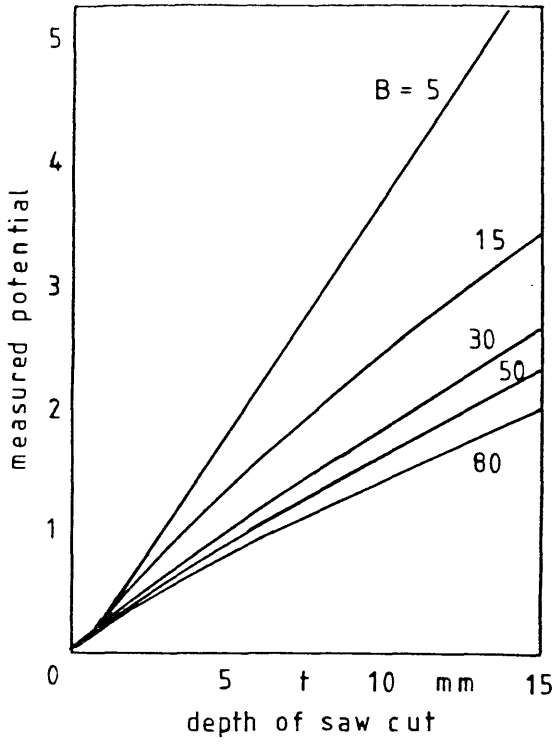
$$a \cong \frac{1}{K_B} \left[\frac{V}{V_o}\right]^{\frac{1}{2}} \qquad \ldots(8.9)$$

where K_B is a calibration constant which was found to be dependent on the type of flaw present, i.e.

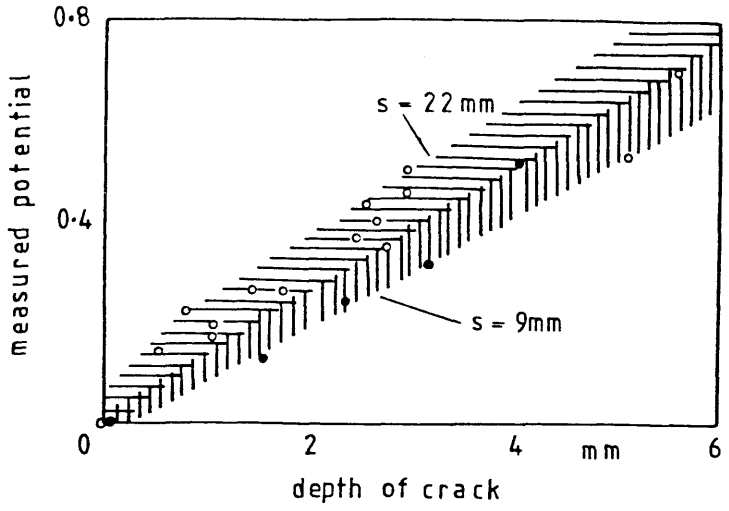
K_B (average machine flaw) = 6.8 ± 0.8 in

K_B (average fatigue crack) = 6.3 ± 0.7 in

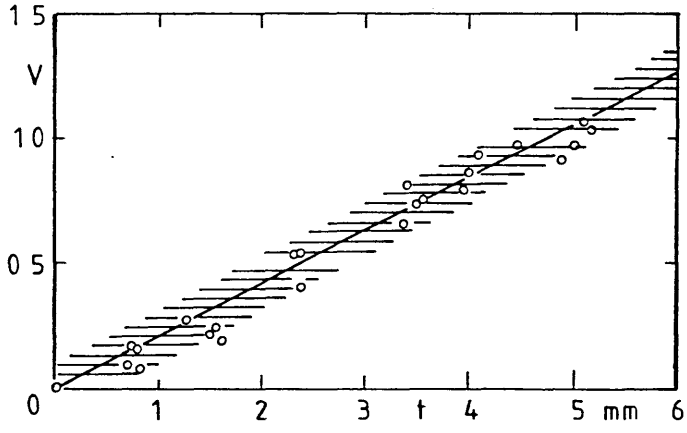
Testwell Ltd. [8.05] compared calibration data obtained from saw slit simulation tests in SEN specimens of steel and a titanium alloy with predicted values of Eq. 8.06, Fig. 8.04. On the basis of their results they suggested that the theoretical and observed potential difference versus crack depth response were comparative, and concluded that Eq. 8.06 adequately described the performance of their ACPD detector.



(a)



(b)



(c)

Fig. 8.03 ACPD calibration studies in steel.

(a) PD versus depth of saw cut in tube segments of length B

(b) PD versus depth of crack in tubes of internal radius 9 and 22 mm.

(c) Measured voltage (v) as a function of crack depth (t) in rotating bar specimens.

(After Betz [8.03])

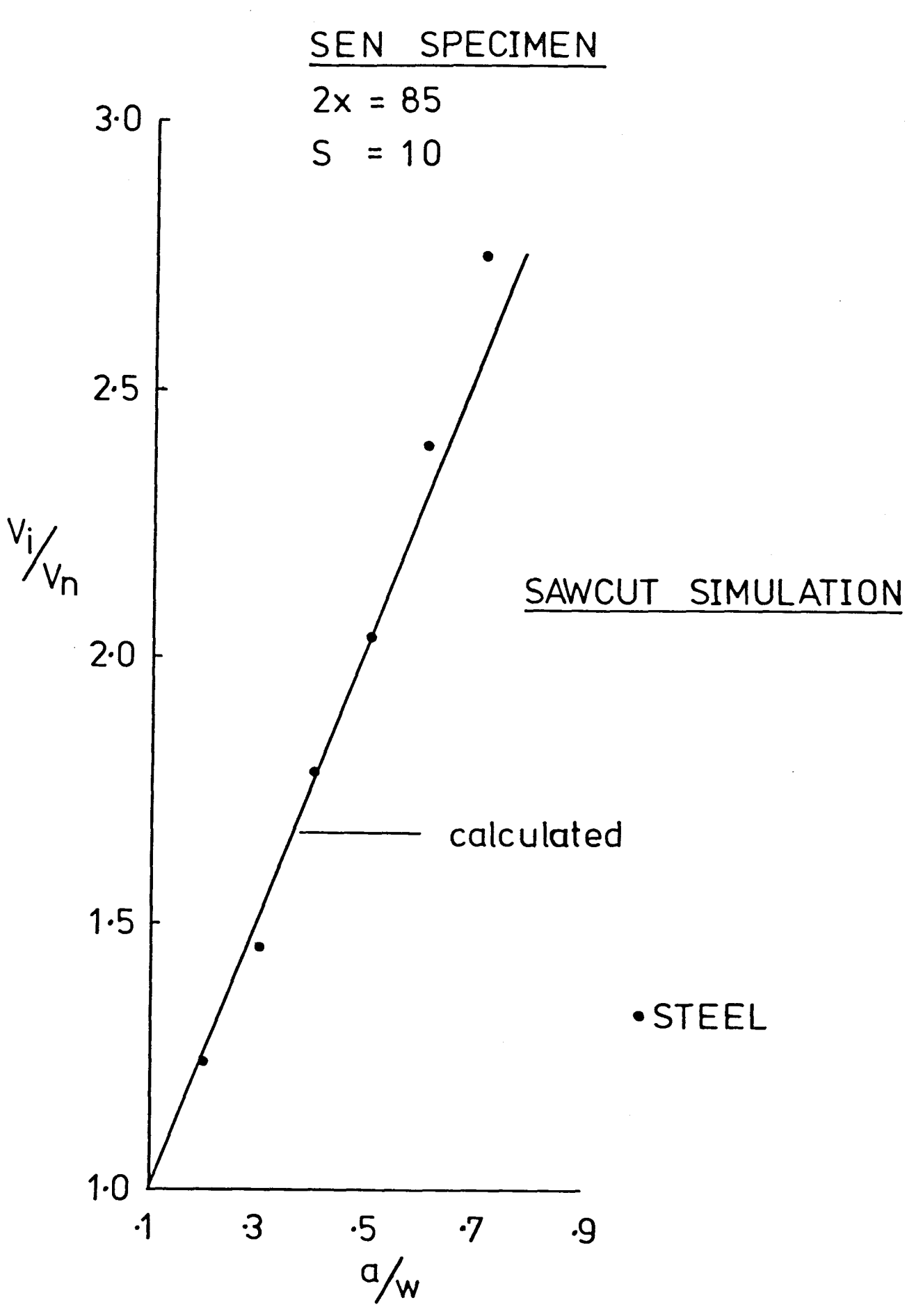


Fig. 8.04 A comparison of saw cut simulation data of SEN steel specimen with the theorectical values calculated from 1D AC field theory. (After Testwell Ltd [8.05]) Note: 1D = one dimensional

However, a word of caution must be included here, from the accuracy of their investigation this conclusion is open to considerable doubt.

Dover et al [8.06] carried out fatigue crack calibration studies in steel, aluminium and titanium alloys and found that Eq. 8.07 could be successfully used to predict the results of an AC crack microgauge detector manufactured by Unit Inspection Company. They reported that provided one dimensional AC field theory conditions were satisfied the depth of circular arc and semi elliptical cracks in members removed from fatigue conditions could be predicted to an accuracy of 10%. However, in the case of short deep cracks (of low aspect ratio) they found it necessary to use the full two dimensional AC field theory to interpret measured voltage readings. This was implemented in two steps: first crack depth was determined using Eq. 8.06, and this was then multiplied by a factor M which incorporated the 2 dimensional field solution.

Dover et al also reported that the ACPD calibration response of fatigue compact tension steel specimens exhibited excellent linearity as shown in Fig. 8.05. Unfortunately this relationship could not be modelled in terms of their two dimensional AC field theory, which led to them conclude that optical calibration was necessary.

Verpoest et al [8.07] carried out calibration tests employing an analogue technique in which they introduced thumb nail type grooves into steel rods and compared these results with similar fatigue crack studies in steel wires, Fig. 8.06. In both studies the ACPD versus crack depth relationship was non-linear and exhibited a dependency on AC frequency. Increasing frequency produced a decrease in the minimum size of crack detectable (at 40 KH_z this corresponded to 0.06 mm) and the optimum operating frequency was found to be 5 KHz (at this

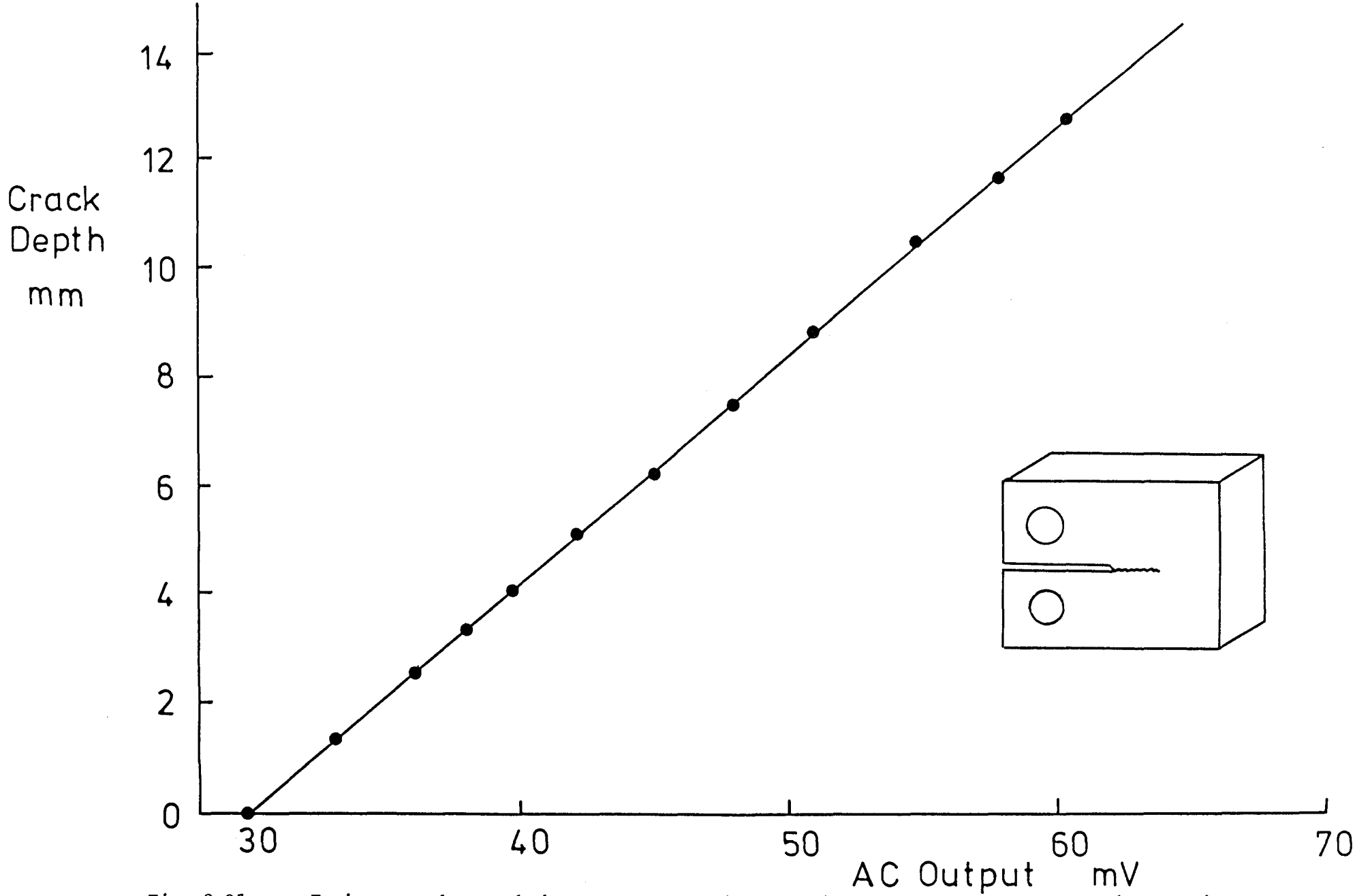
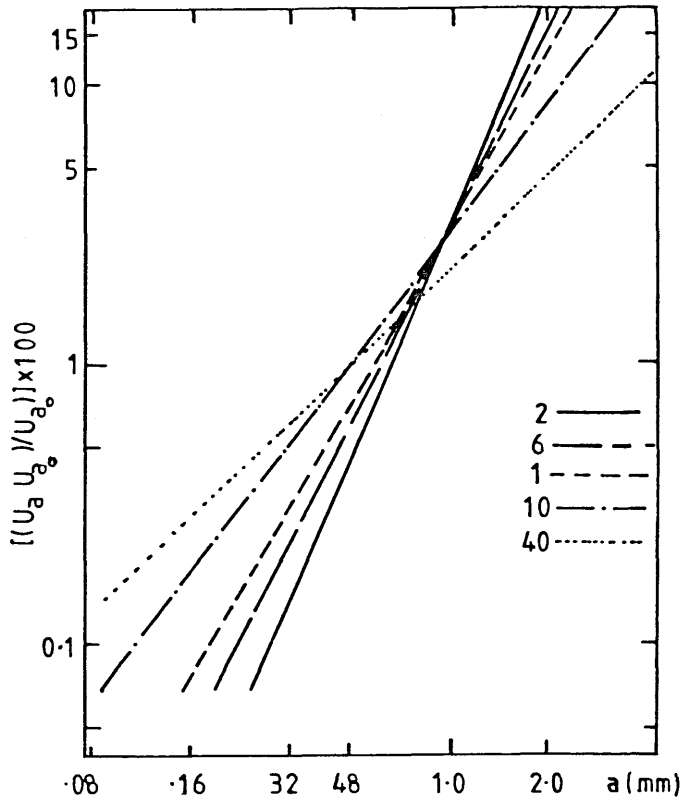
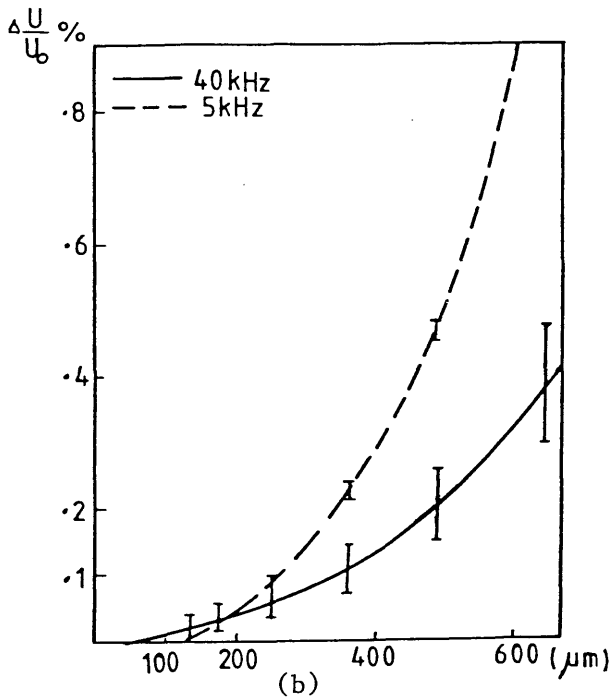


Fig. 8.05 Fatigue crack growth data recorded during a fatigue test on a Compact Tension Specimen made from steel. (After Dover et al [8.06])



(a)



(b)

Fig. 8.06 ACPD calibration studies in steel.

(a) Relative increase of ACPD due to a saw cut in steel rods.

(b) Preliminary calibration curves for steel wires.

(After Verpoest et al [8.07])

level the size of the minimum crack detectable was ≅ 0.15 mm). A direct comparison of results revealed that the calibration response of the analogue and fatigue ACPD studies were disimilar, which they attributed to a difference in flaw shape.

Wei and Brazill [8.08] studied the AC and DC calibration response of SEN steel specimens in the crack depth regime 3 mm < a < 50 mm and found that both systems satisfied a third order polynomial relationship of the form

$$a = 15.19 + 52.0\ (Z) + 26.0\ (Z)^2 - 41.4\ (Z)^3 \text{ (mm)} \quad \ldots(8.11)$$

where $Z = (V - Vr)/Vr$

V = actual potential difference corresponding to a given crack length.

Vr = reference potential difference at the crack starter notch.

The accuracy of the AC system was estimated to be better than 1% for cracks of 20 to 45 mm, and resolution was better than 0.01 mm with the instrument set to provide 20 nv resolution in electrical potential difference at an operating current of 1 amp RMS.

8.3.2 Summary of Observations

In conclusion of the existing evidence the main findings are:

(1) Provided one dimensional AC field theory conditions are satisfied Eq. 8.07 can be utilised to predict crack depth and no prior calibration is necessary [8.06].

(2) Over short crack depths a linear relationship exists between ACPD and crack depth but over larger depths this is more accurately described a higher degree polynomial [8.02].

(3) Different materials exhibit a different calibration response [8.02, 8.05].

(4) Sensitivity of crack depth measurement is increased if sensing probe seperation A-B is decreased [8.02, 8.05].

(5) AC voltages are dependent on factors affecting magnetic permeability in addition to flaw depth [8.01].

(6) Predictions of crack depth in a two dimensional AC field can only be made if one utilises an appropriate two dimensional multiplication factor in conjunction with Eq. 8.07 [8.06].

(7) Analogue techniques have been used in ACPD studies [8.03 - 8.07] but they are only valid when the machine flaw accurately describes the fatigue crack under study [8.07].

(8) The ACPD versus crack depth response in hollow tubes and solid bars is linear in the regime 0.5 mm < a < 6.0 mm [8.03].

(9) The ACPD versus crack depth response in solid bars is non-linear in the regime 0.1 mm < a < 0.6 mm [8.07].

(10) Increasing AC frequency produces an increase in sensitivity. The optimum frequency is 5 KH_Z [8.07].

(11) ACPD versus crack depth response is dependent on specimen shape [8.03].

(12) The ACPD versus crack depth relationship is satisfied by a third order polynomial, and for crack depths of 3 to 50 mm the same response was also obtained using a DC system [8.08].

8.4 References

[8.01] Gille, G.,
N.D.T., Feb 1971, pp 36.

[8.02] Kruse, J.,
Untersuchungen zur RiBtiefenmessung mit Hilfe von Potential-Sonden-und Wirbelstrom-verfahren.
Feingerätetechnik Bd. 18 (1969) S.75/78.

[8.03] Betz, U.,
Materialprufing, 1972, 14, pp 73.

[8.04] Birchak, J.R.,
Proc. 10th Symp. on N.D.E. San Antonio 1975.

[8.05] Testwell Ltd.,
Tech. Memo. 126.

[8.06] Dover, W.D., Charlesworth, F.D.W., Taylor, K.A., Collins, R., and Michael, D.H.,
"The Use of AC Field Measurements to Determine the Shape and Size of a Crack in a Metal".
University College London, London WC1, U.K.

[8.07] Verpoest, I., Aernoudt, E., De uyttere, A., and Neyrinck, M.,
"An Improved AC-Potential Drop Method for Detecting Surface Microcracks during Fatigue Tests of Unnotched Specimens".
(submitted for publication in 'Fatigue of Engineering Materials', Pergammon Press).

[8.08] Wei and Brazill,
'The Measurement of Crack Length and Shape During Fracture and Fatigue', pp 136. EMAS 1980.

CHAPTER NINE

MATERIALS

9.0 Introduction

The two stock materials selected for the investigations of Chapter 10 and 11 were British Standard EN3B and EN19 Steels. EN3B was chosen because it presented a simple ferritic-pearlitic microstructure which could be modified by heat treatment to produce two materials (EN3BN and EN3BA) containing ferrite grain sizes 10 μm and 53 μm respectively; and EN19, a 1% Cr-Mo steel exhibiting good hardenability, facilitated the production of a tempered martensitic microstructure (EN19QH).

9.1 Stock Materials and Composition

Both Stock Materials were supplied by Herringshaw Steels Ltd. Birmingham [9.01]. EN3B was received in the 'as drawn' state in rectangular bars of dimensions 32 mm x 57 mm x 7000 mm, and EN19 in hot rolled rounds of 7000 mm length and 100 mm diameter. Both contained an inhomogeneous microstructure characteristic of their primary process route and were therefore homogenised by heat treatment as described in 9.2. Their reported [9.01] chemical compositions are presented in Table 9.01.

9.2 Experimental Materials (preparation and microstructure)

9.2.1 Ferritic Steels EN3BN and EN3BA

The two ferritic steels EN3BN and EN3BA containing 10 and 53 μm ferrite grain sizes respectively were prepared by heat treating blanks of dimensions 30 mm x 55 mm x 220 mm of stock material EN3B.

TABLE 9.01

Chemical Composition

Constituent	Composition wt %	
	EN3B	EN19
C	0.180	0.360
Si	0.270	0.230
Mn	0.850	0.600
S	0.032	0.046
P	0.013	0.037
Ni	-	1.110
Cr	-	1.140
Mo	-	0.310
Fe	Remainder	

Related Specifications

EN3B: S.A.E. 1021, 1022; A.I.S.I. C102, C1022

EN19: S.A.E. 4137, 4140; A.I.S.I., 4137, 4140

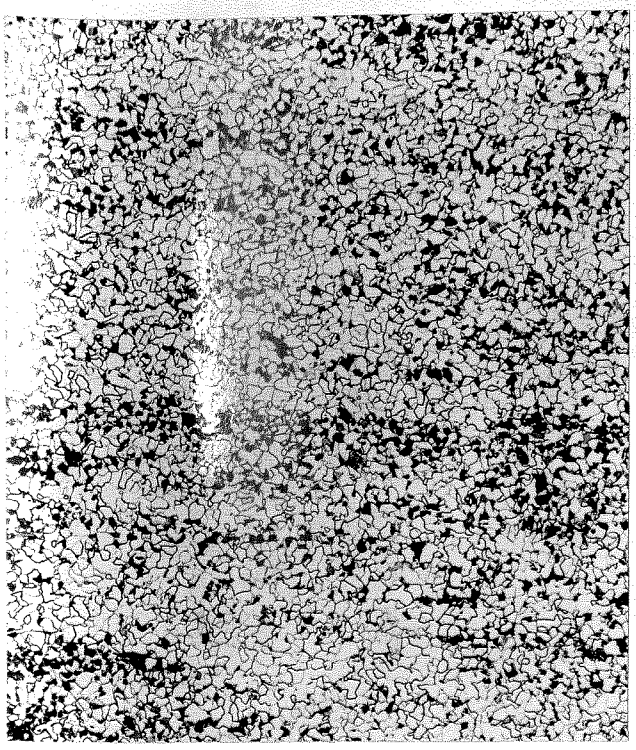
EN3BN was obtained by normalising EN3B at 900°C for 1 hour, and EN3BA by annealing EN3B at 1200°C for 5 hours [9.02].

The microstructure of EN3BN consisted of colonies of pearlite in a ferritic matrix, Fig. 9.01. Microscopic anisotropy was observed in the drawing direction in the form of ferritic banding and fibred non-metallic inclusions. Small dove grey inclusions which appear circular in the transverse direction and lenticular in the longitudinal direction were identified as Type II manganese sulphide particles characteristically found in free cutting steels [9.03].

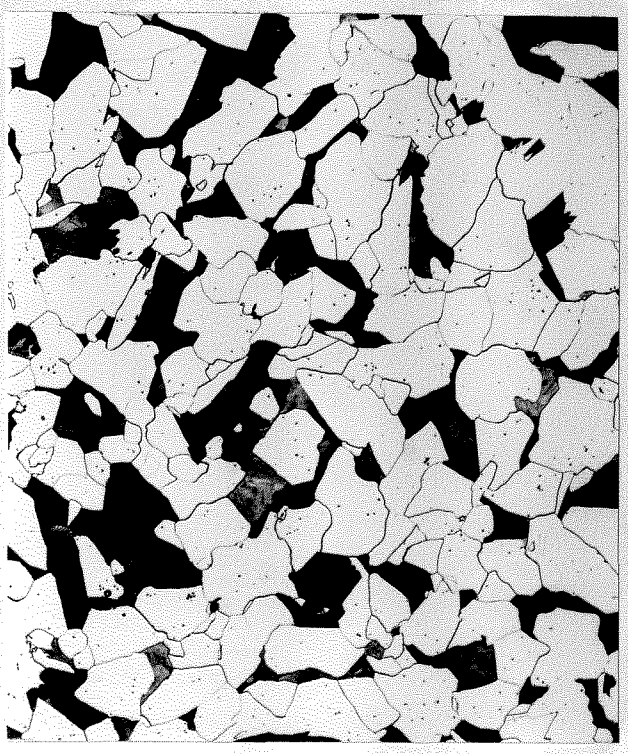
The microstructure of EN3BA was approximately five times larger than EN3BN, Fig. 9.02. In general it exhibited greater isotropy and a more equixed ferritic grain structure. Small quantities of widmanstatten ferrite were present which were characteristic of the high temperature anneal. Slow cooling through the A_{C1} did not produce any noticeable coarsening of the pearlitic lamella.

9.2.2 Tempered Martensitic Steel EN19QH

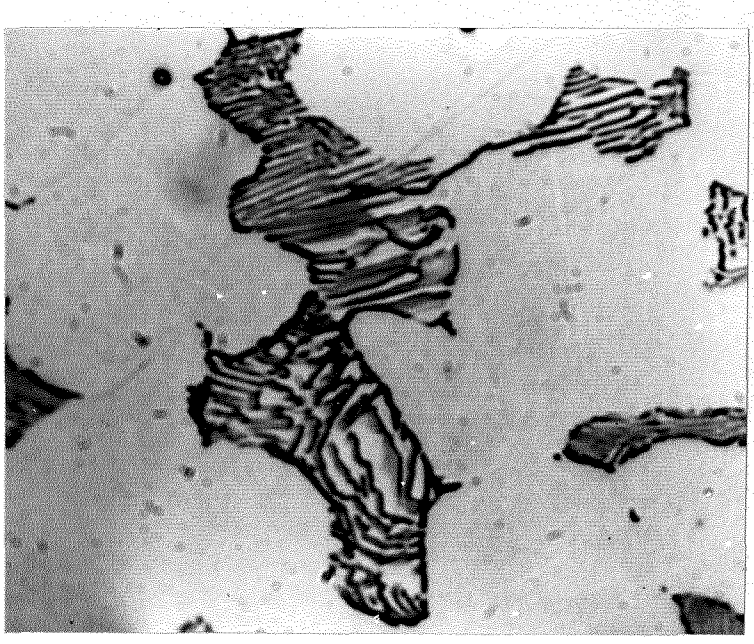
The heat treatment sequence adopted to modify the as received microstructure of EN19 was selected to produce a continuous tempered martensitic structure with optimum mechanical properties [9.02]. Blanks of dimensions 15 mm x 55 mm x 220 mm were solution treated at 860°C for 90 minutes, quenched in oil and then tempered at 550°C for 90 minutes. The resulting microstructure was almost entirely tempered martensitic, except for a small number of manganese sulphide inclusions orientated in the rolling direction, Fig. 9.03.



(a)



(b)



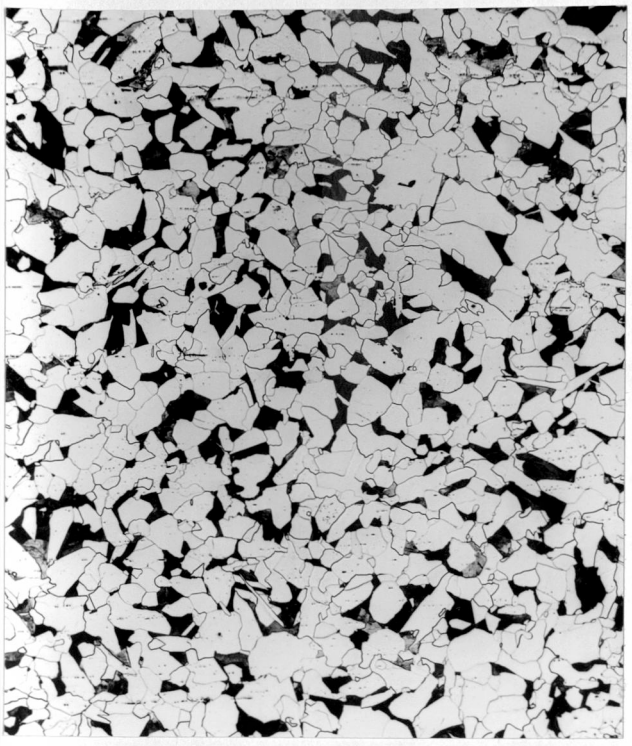
(c)

Fig. 9.01 Optical micrographs of EN3BN illustrating the ferritic-pearlitic microstructure.

(a) Longitudinal section, etched in 2% nital, x 100

(b) Transverse section, etched in 2% nital, x 200

(c) Transverse section, etched in 2% nital, x 2500



(a)



(b)



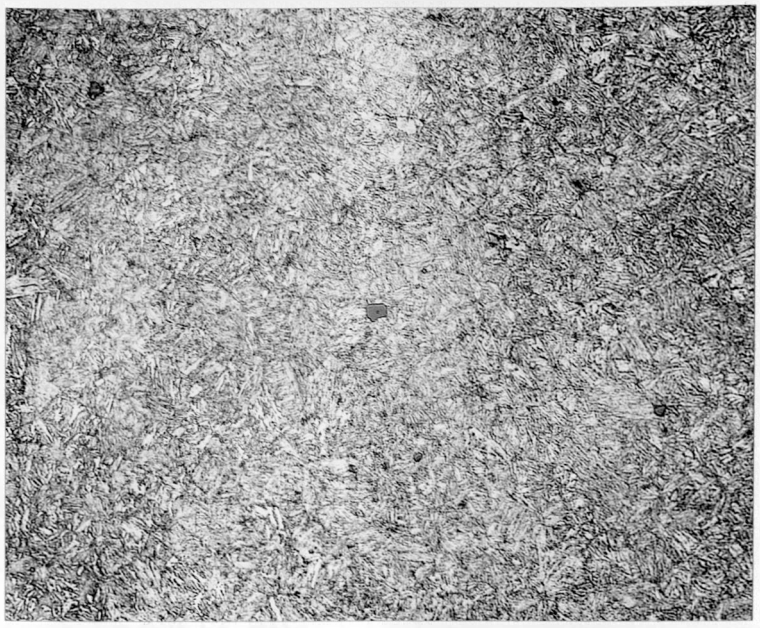
(c)

Fig. 9.02 Optical Micrographs of EN3BA illustrating the ferritic-pearlitic microstructure and the occurrence of widmanstatten ferrite

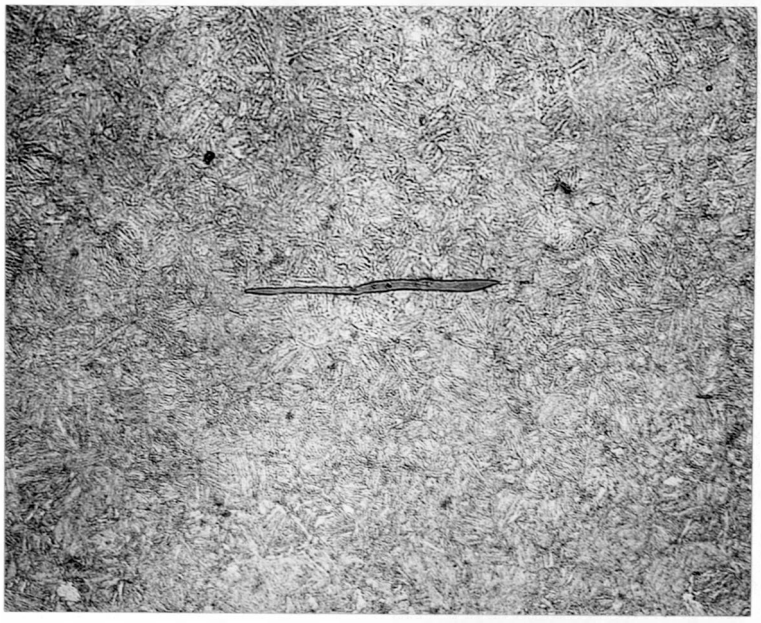
(a) Longitudinal section, etched in 2% nital, x 100

(b) Longitudinal section, etched in 2% nital, x 200

(c) Transverse section, etched in 2% nital, x 300



(a)



(b)

Fig. 9.03 Optical micrographs of EN19QH illustrating the occurrence of MnS needles in a tempered martensite matrix.

(a) Transverse section, etched in 2% nital, x 400

(b) Longitudinal section, etched in 2% nital, x 400

9.3 Quantitative Metallography

The quantities and sizes of the relevant microstructural constituents presented in Table 9.02 were based upon examination of longitudinal and transverse metallographic specimens mounted in conducting bakelite. These were wet ground using silicon carbide paper ranging from 120 to 1200 grades and finally polished using 6 μm, 3 μm and 1 μm diamond paste. In all cases a 2% nital etch was used for general examination of microstructure. To reveal the prior austenitic grain boundaries of EN19QH it was found necessary to first etch with Vilella's Reagent [9.04] and then with a saturated solution of picric acid and 'teepol' at 75°C [9.05].

Volume percent constituents, which were estimated using a Metals Research Quantimet Q.T.M., were based on average readings taken from longitudinal and transverse sections. Inclusion volume percent was determined on unetched specimens. Volume percent pearlite and ferritic and prior austenitic grain sizes were estimated optically by a mean linear intercept method [9.06] using a Ziess Ultraphot II Photomicroscope.

9.4 Mechanical Properties

The nominal tensile properties of each material were obtained from a series of tensile tests conducted on standard specimens, Fig. 9.04. A total of six specimens were machined from the centre of two bars with their tensile axis aligned in the longitudinal direction. These were mechanically polished and measured using a travelling microscope and tested on a 5,000 kg Instron Universal Testing Machine as recommended

TABLE 9.02

Microstructural Constituents and Sizes

Material	Volume % Constituent				Ferrite Grain Size (μm)	Prior Austenite Grain Size (μm)
	Ferrite	Pearlite	Tempered Martensite	Inclusion		
EN3BN	Remainder	24.2	-	0.6	10	-
EN3BA	Remainder	24.5	-	0.6	53	-
EN19QH	-	-	Remainder	0.3	-	10

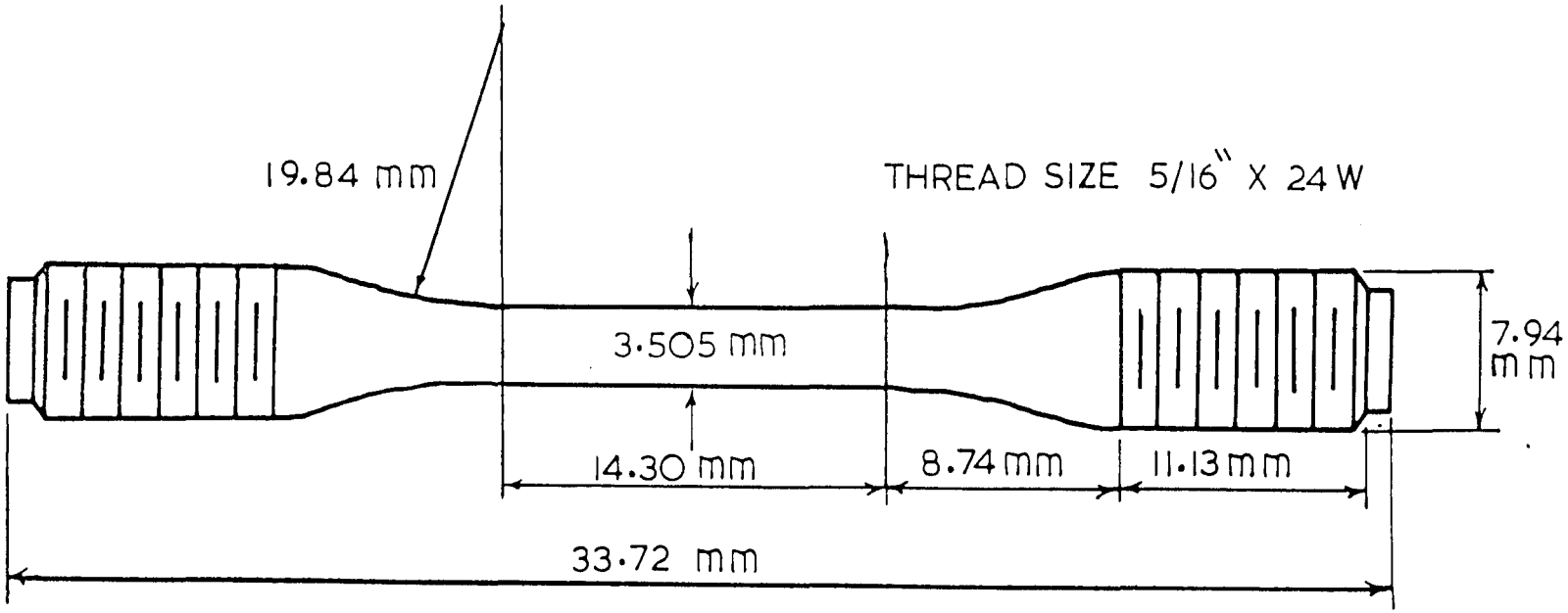


Fig. 9.04 Tensile Test Specimen

TABLE 9.03

Mechanical Properties

Material	Yield Stress (MPam)	U.T.S. (MPam)	Percentage Elongation	Reduction In Area (%)
EN3BN	460	505	20	63
EN3BA	223	436	32	68
EN19QH	1023	1121	23	60

by the American Society for Testing and Materials [9.07]. The results, which are accurate to within 5%, are presented in Table 9.03.

9.5 References

[9.01] Herringshaw Steels Ltd., Arley Road, Birmingham, B8 1BH.

[9.02] Woolman J., and Mottram, R.A., "The Mechanical and Physical Properties of the British Standard EN Steels", 1, British Iron and Steel Research Association, 1964.

[9.03] Baker, T.J. and Charles, J.A., J.I.S.I., 1972, 207, pp 680.

[9.04] Metals Handbook, A.S.M., 1972, 7.

[9.05] Ritchie, R.O. and Knott, J.F., Acta Met., 1973, 21, pp 639.

[9.06] De Hoff, R.T. and Rhimes, F.N., "Quanlitative Microscopy", McGraw-Hill, New York, 1968.

[9.07] '1972' Annual Book of ASTM Standards', Part 31, American Society for Testing and Materials, Philadelphia.

CHAPTER TEN

AN ALTERNATING CURRENT POTENTIAL DIFFERENCE CALIBRATION STUDY OF EN3BN STEEL

10.0 Nomenclature

PD	=	measured potential difference
PD_{AB}	=	potential difference contribution of the sensing probes
PD_{CD}	=	potential difference contribution due to compensation.
PD_{O}	=	theoretical PD at a = 0.00 mm
PD_{C}, PD_{OE}	=	empirical constant
PD_{n}	=	notch PD
PD_{ABE}, PD_{CDE}	=	eddy current potential difference contribution.
PD_{TED}	=	total eddy current potential difference contribution.
ACPD	=	alternating current potential difference.
AC, I	=	alternating current
a	=	flaw depth measured in the specimen width direction.
a_{n}	=	notch depth.
GD	=	groove depth.
fcg	=	fatigue crack growth
EDM	=	electric discharge machine
T	=	specimen thickness

DVM	=	digital volt meter
voltage gain	=	electrical gain imposed on measured voltage signal.
A_0, A_1, A_2	=	Chebyshev polynomial coefficients
T_0, T_1, T_2	=	constants
RMS PD	=	standard residual error expressed in terms of PD
RMS a	=	standard residual error expressed in terms of a.
mv	=	milli volts
μm	=	micro volts
SEN	=	single edge notch
VR	=	voltage ratio of empirical model.

Note: the term flaw is used in generality to represent fatigue crack or mechanically assimulated fatigue crack depending on the context.

10.1 Introduction

The major objective of this investigation was to establish the calibration response of a Testwell ACPD2 Crack Detector to crack growth in EN3BN in the a/w régime 0.01 to 0.50. To overcome the problems associated with the irregular growth of short cracks mechanical grooves were spark eroded [10.01] in plane specimens up to a/w ratios of 0.14. In the a/w régime 0.08 and 0.49 fcg calibration studies were conducted using standard SEN specimens. The effect of specimen geometry of fcg calibration response was also evaulated by varying specimen width and thickness dimensions.

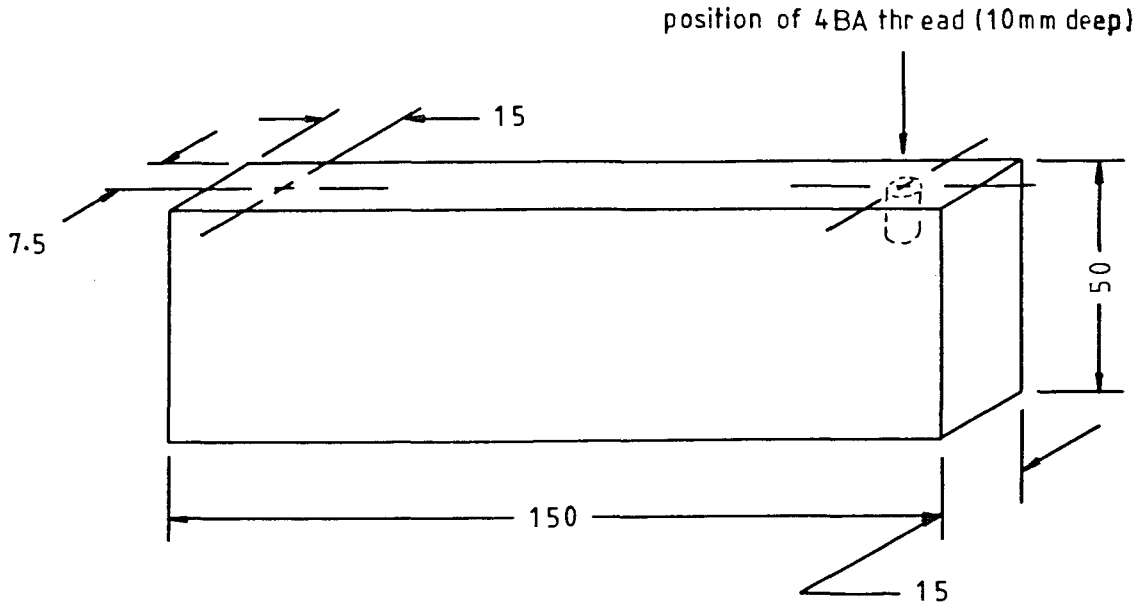
10.2 Experimental Equipment and Procedures

In the following text only a brief description is given of the experimental procedures of this investigation. Full details are to be found in Appendices A1-A4.

10.2.1 Specimen Details and Preparation

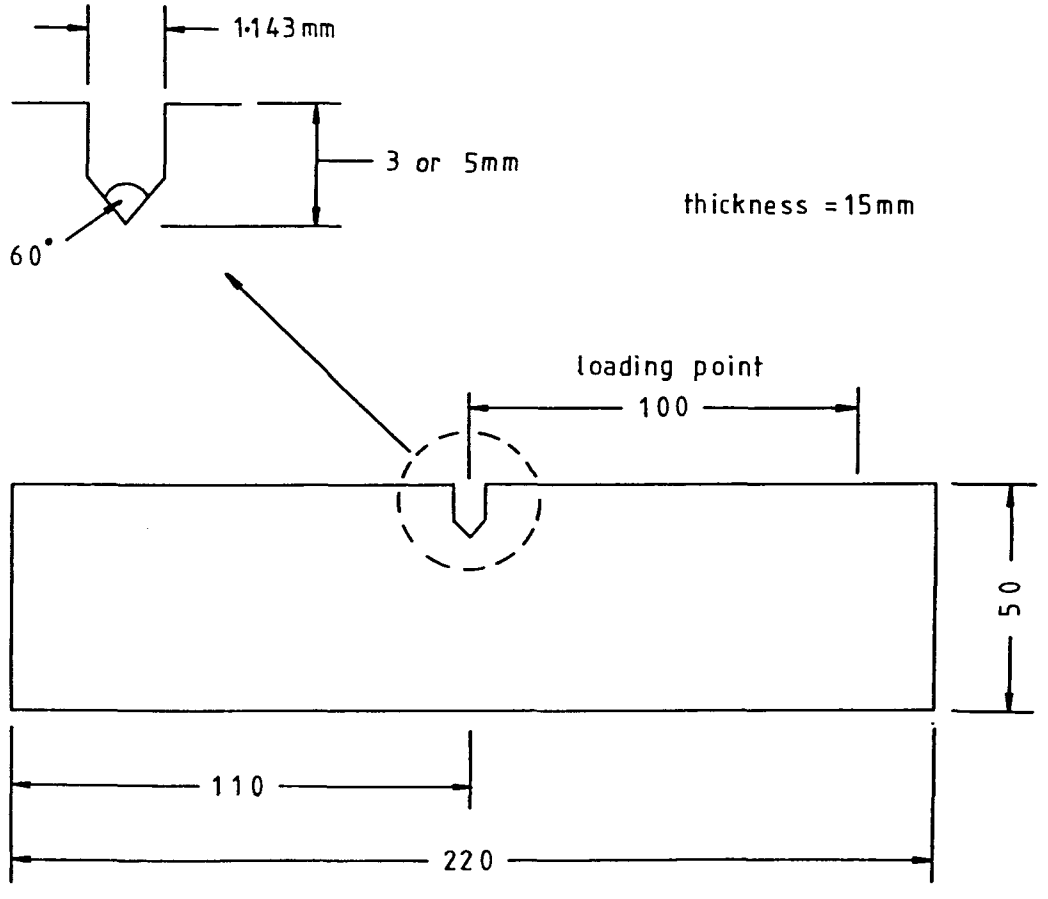
From the centre of the heat treated EN3BN blanks (Section 9.2.1) plane and SEN specimens were machined and ground to dimension shown in Fig. 10.01.

The influence of specimen width of fcg calibration response was evaluated using a precracked specimen of width $\cong$ 40 mm. This configuration was achieved by subjecting a SEN specimen to fatigue at R = 0.1 and $\Delta K \cong 20$ MPam$^{-\frac{1}{2}}$, and when a crack depth of $\cong$ 11 mm had been attained, the notch was machined away to give a final specimen of width 40 mm.



PLANE SPECIMEN

(unless otherwise stated all dimensions are in mm)



SEN SPECIMEN

Fig. 10.01 Specimen Dimensions

The effect of specimen thickness on fcg calibration response was evaluated using two SEN specimens of thickness dimensions ≅ 10 and 20 mm.

10.2.2 Potential Difference Measurement

The general arrangement and techniques of current and sensing lead attachment are described in detail in Appendix A1. In the following text only a brief description is given of PD measurement with special reference to fcg.

The Testwell ACPD2 Crack Detector employed to monitor crack depth was used in conjunction with a voltage sensing-control back off unit and chart recorder, Fig. 10.02. At the beginning of each test the detector was set at:

voltage gain	=	5×10^3
current	=	5 amps
detector internal calibration	=	5.00 volts
detector offset	=	0.00
DVM range	=	0.00 to 10.00 volts

After recording the initial starting potential the DVM output voltage was then reduced to ≅ 0.10 volt using the detector offset, and the output was fed to a chart recorder set at 1.00 volt full scale deflection. During crack growth the DVM output voltage was allowed to increase until a threshold value was exceeded set by the voltage sensing-control back off unit. This was normally ≅ 0.90 volts

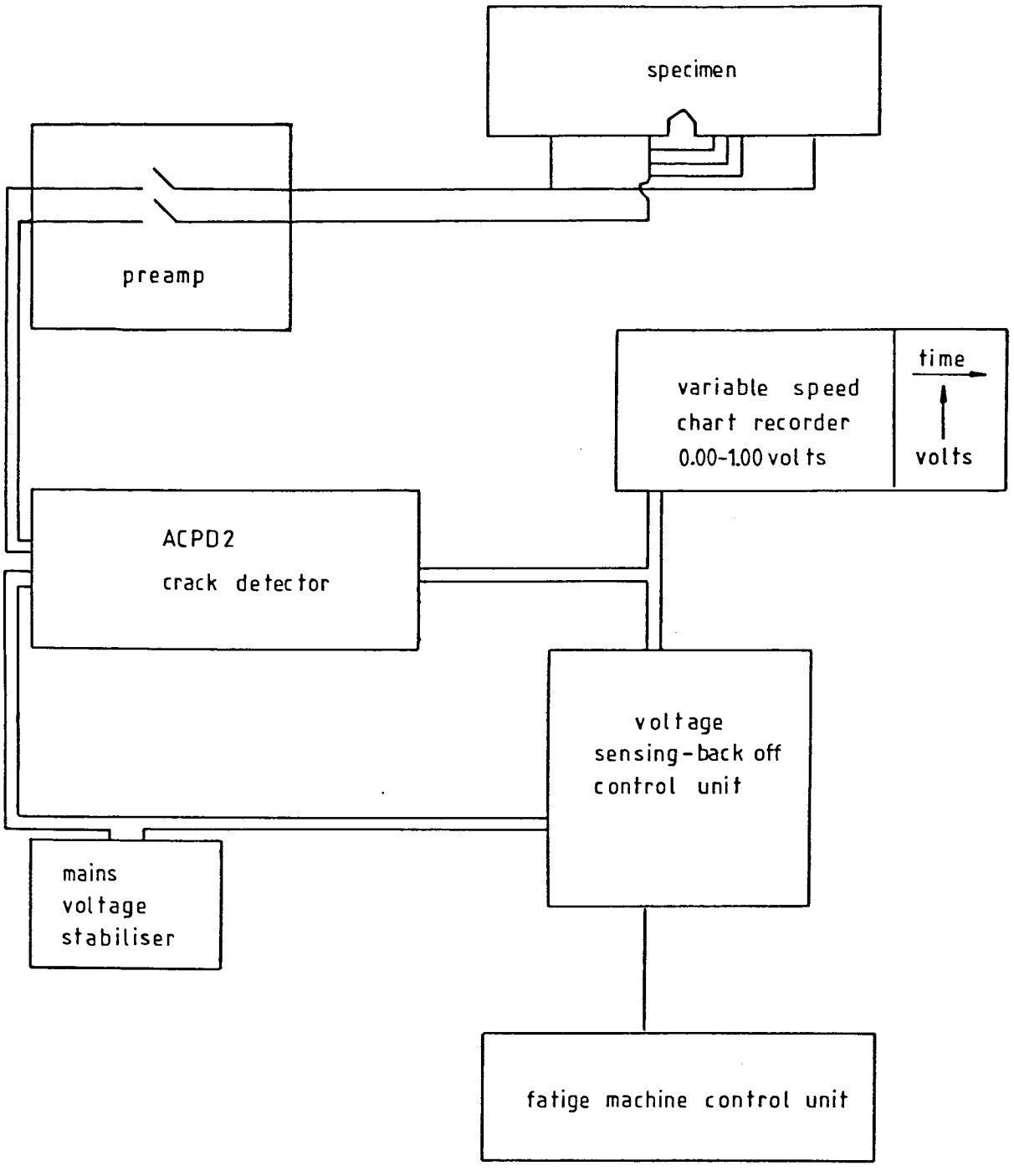


Fig. 10.02 A schematic diagram illustrating equipment arrangement.

but any threshold value could be chosen from 0.00 to 5.00 volts. On achieving this level the mains power to the Amsler was automatically switched off and the DVM output voltage to the chart recorder was then backed off to ≅ 0.10 volt using the voltage sensing-control back off unit. The process was then repeated. When a total output of ≅ 4.90 volts had been achieved the detector offset and DVM range facilities were utilized to reduce the DVM output voltage to ≅ 0.10 volt and the process was repeated.

Using this system full DVM output voltage control to the chart recorder was possible from 0.00 to 30.00 volts in increments of 0.01 volt, i.e. 0 to 6000 μv in increments of 2 μv measured across the specimen surface.

At any stage during the crack growth sequence the 'absolute' DVM output voltage could be checked by zeroing the detector offset and switching in the most suitable DVM range.

At the end of testing PD measurements were compensated (where appropriate) for changes in detector internal calibration and paraffin bath temperature as described in Appendices A2 and A3.

10.2.3 Groove Cutting using a Spark Erosion Technique

The electric discharge technique used to progressively introduce a reference flaw between sensing leads A-B, Figs 10.03 and 10.04, involved the use of a Servomet Electric Discharge Machine which is shown in Fig. 10.05. The technique consisted of submerging the specimen in a paraffin medium and then spark eroding a groove in incremental steps of 0.10 mm to any prechosen depth using a micrometer

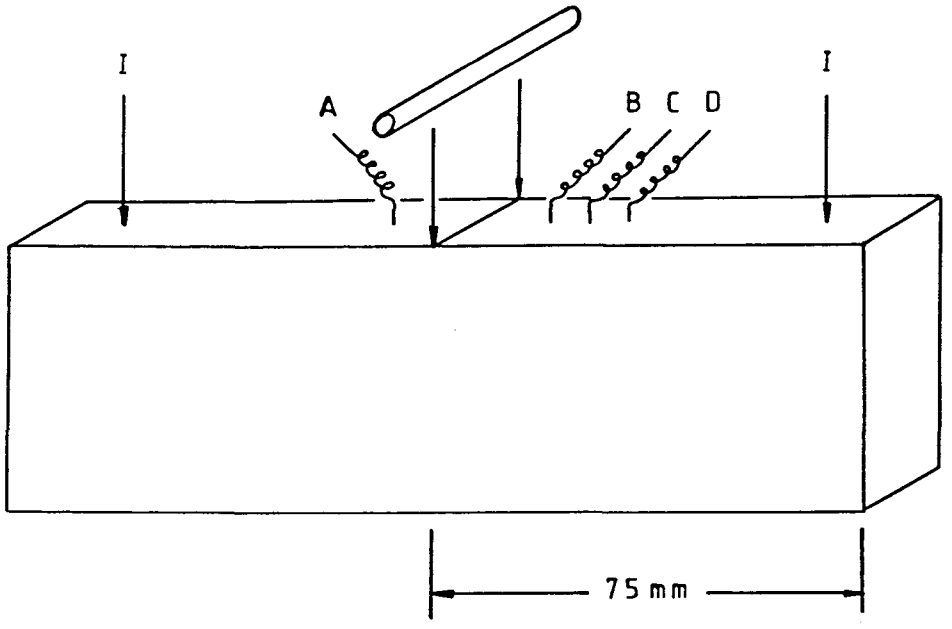


Fig. 10.03 A schematic representation of the EDM fcg-analogue test configuration illustrating cutting wire position.

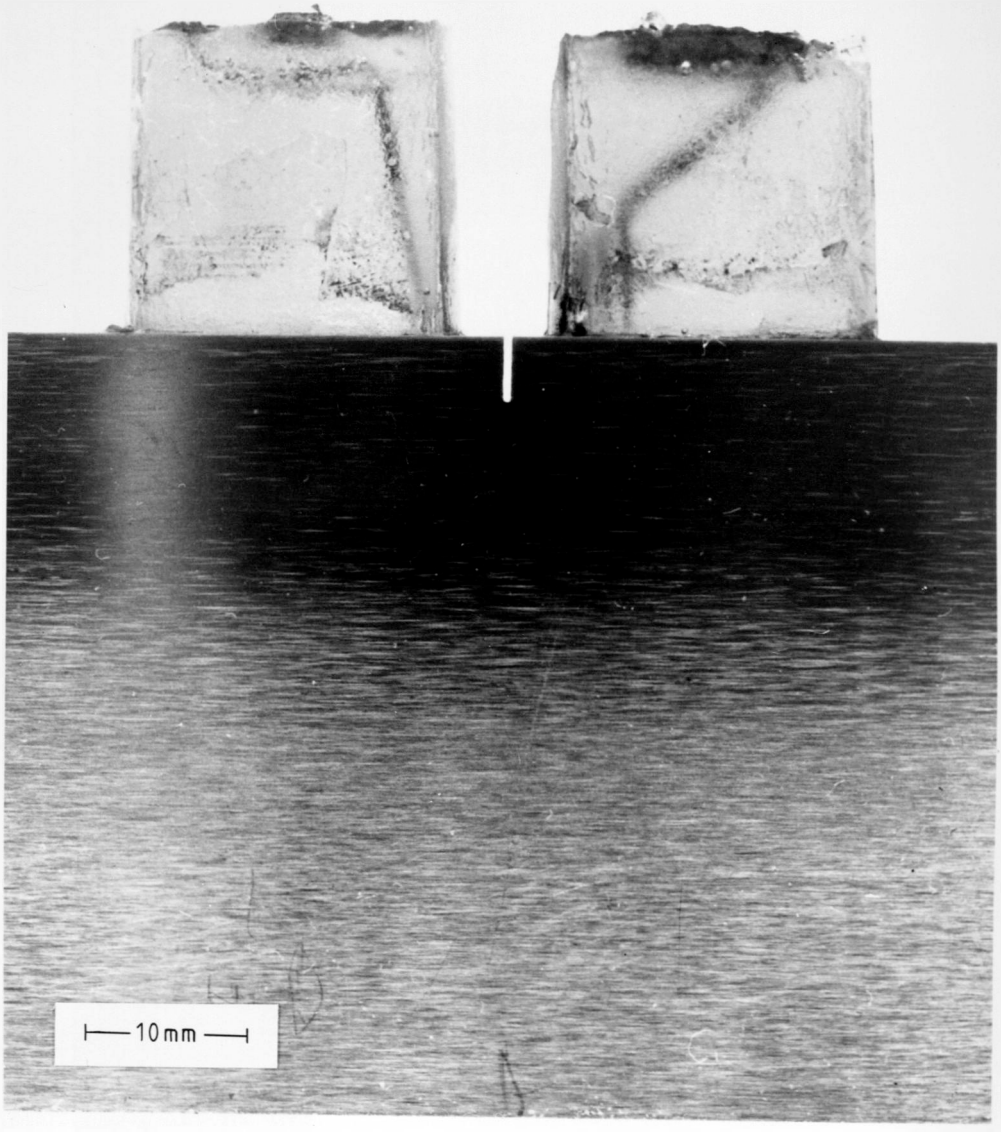


Fig. 10.04 The EDM groove in profile

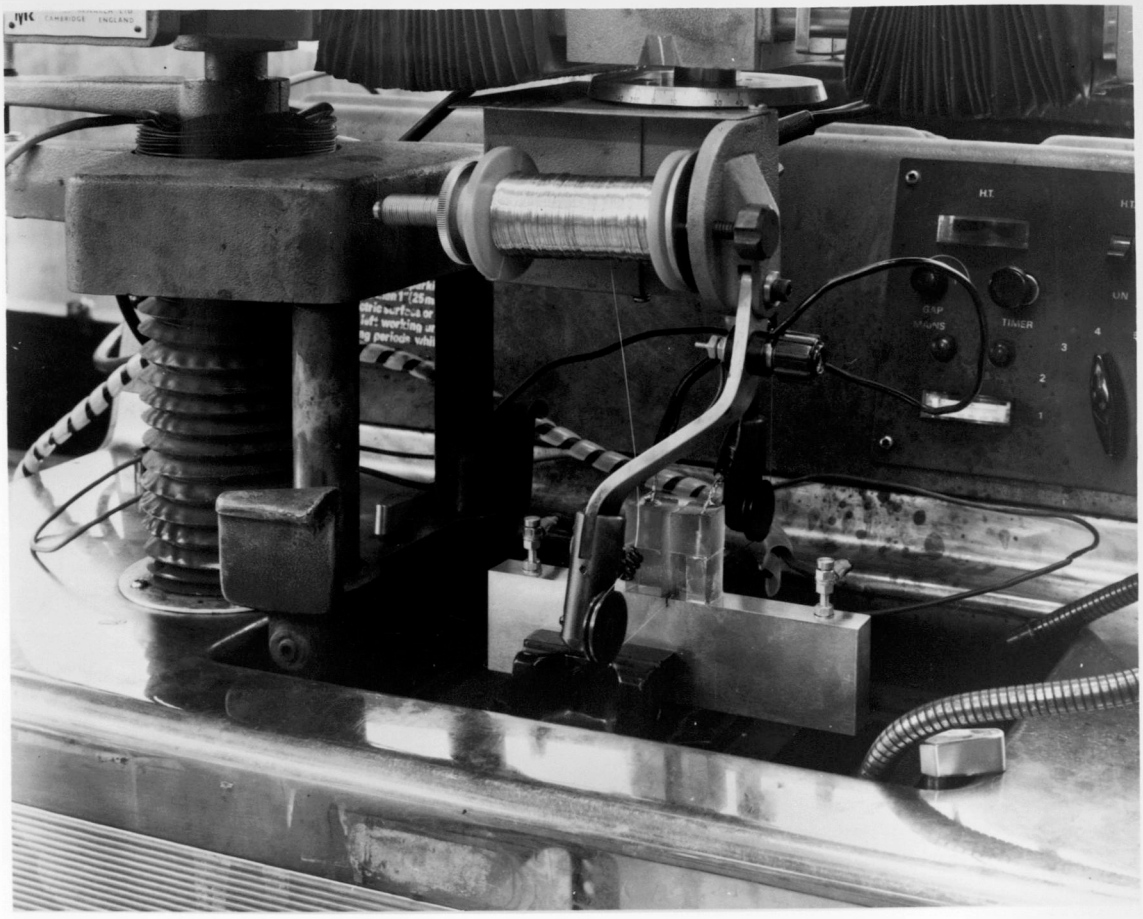


Fig. 10.05 EDM groove cutting with the whole assembly in the raised position.

controlled limit switch. After each 'cut' the spark erosion wire was then raised and the Servomet Electric Discharge Machine was turned off. The detector preamplifier was then switched on, and after 15 minutes, PD was recorded with the whole assembly in the submerged position. The preamplifier was then turned off and groove cutting was continued.

10.2.4 Fatigue Crack Growth in SEN and Precracked Specimens

Fatigue tests were conducted in laboratory air at 21 ± 1°C using an Amsler 100 KN High Frequency Vibrophone Fatigue Machine equipped with a 100 KN dynanometer operating at 135 ± 5 H_Z. A standard three point bend attachment was used at a span to width ratio of 4:1 as illustrated in Fig. 10.06.

The fatigue process involved initiating a fatigue crack from the starter notch/crack configuration and growing it in the specimen width direction to produce fracture surface wave patterns which could be related to PD, Fig. 10.07. This was achieved by subjecting the specimen to pairs of alternating stress ranges of common mean load. First a series of large stress range cycles of $R \leqslant 0.1$ and $\Delta K \cong 30$ MPam$^{-\frac{1}{2}}$ were imposed to produce the waves, and then a series of small stress range cycles of $R \geqslant 0.5$ and $\Delta K \cong 20$ MPam$^{-\frac{1}{2}}$ the wave markings.

To achieve a realistic comparison with the EDM fcg-analogue study it was necessary to grow fatigue cracks at K_{max} values ranging from 20 to 30 MPam$^{-\frac{1}{2}}$ to ensure a crack wavefront aspect ratio of < 0.07. Stress intensity factors were calculated using the compliance

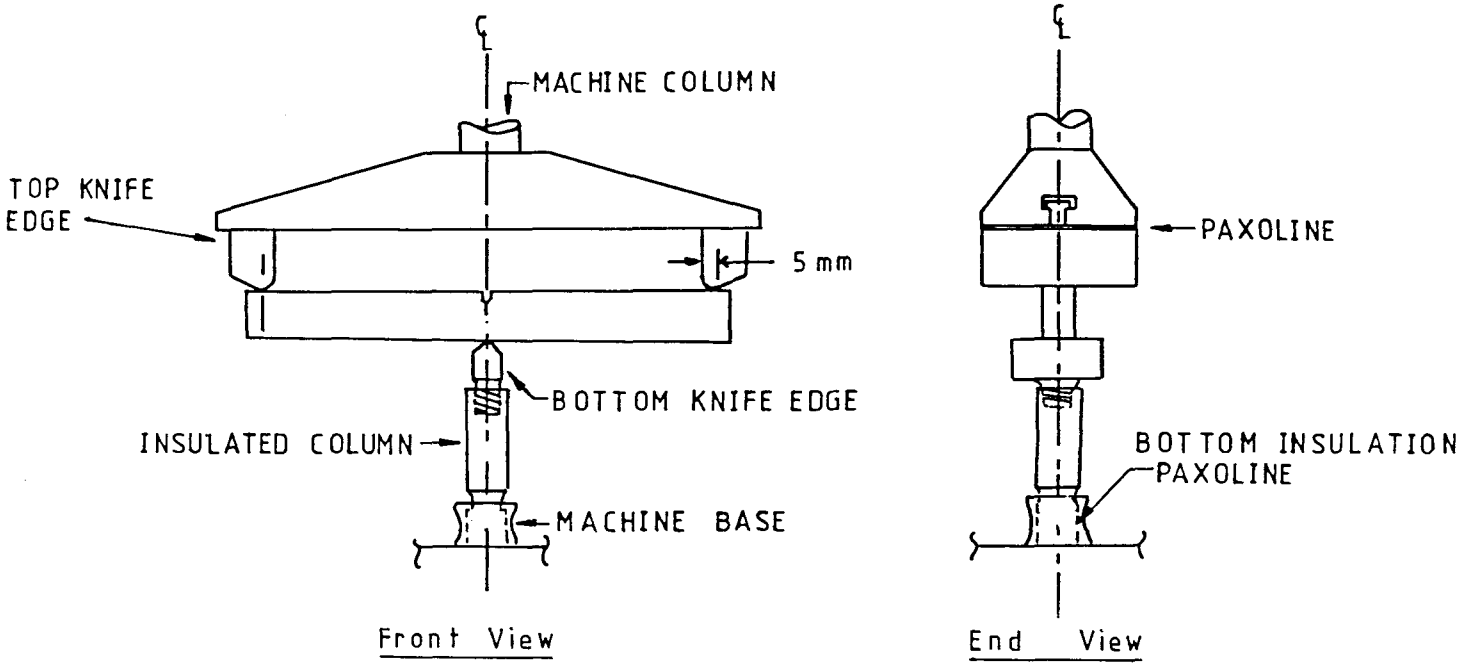


Fig. 10.06 A schematic illustration of the fatigue configuration

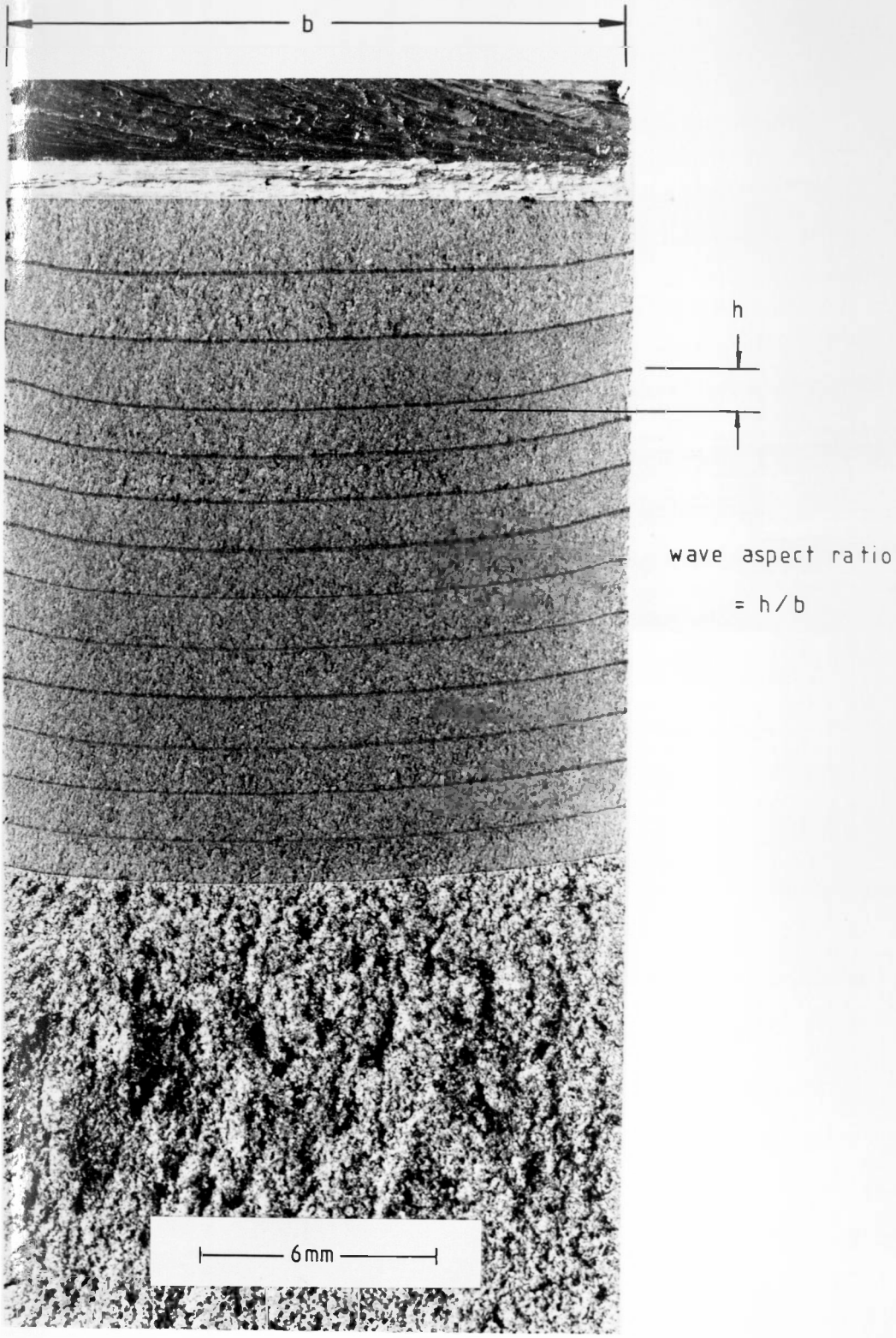


Fig. 10.07 Fracture surface wave markings on Specimen 11

functions of Tada et al [10.02].

Full details of experimental technique and crack wavefront analysis are to be found in Appendix A4.

10.3 Accuracy of Results

10.3.1 Flaw Depth

At the end of every EDM fcg-analogue test the extent of groove cutting, i.e. groove depth, was determined from a X10 profile print and was found to be within ± 0.01 mm of the predicted values indicated by the micrometer controlled limit switch of the Servomet Electric Discharge Machine. Groove depths were therefore accurate to within 3.0% at a/w = 0.01 to 1.0% at a/w = 0.13.

A pessimistic estimate of the accuracy of crack depth measurement based on the worst case of crack bowing, Fig. 10.07, revealed that crack depths were accurate to within 11.0% at a/w = 0.08 to 2.0% at a/w = 0.49. A more optimistic estimate based on the analysis of cracked area, Appendix A5, revealed that at a/w = 0.8 crack depths were underestimated by 3.0%, but at a/w = 0.49 they were overestimated by 0.3%.

10.3.2 Potential Difference Measurement

Long term stability checks (28 days) revealed that the error in PD resulting from electrical drift was minimal, i.e. ± 0.004 mv, and could be attributed to a corresponding change in

detector internal calibration.

The maximum error in PD of the EDM fcg-analogue study was found to be ± 0.006 mv. This corresponded to a maximum percentage error of ± 0.5% at a/w = 0.01. In the fcg studies this was reduced to ± 0.004 mv, which resulted in a maximum percentage error of ± 0.3% at a/w = 0.08.

10.4 Treatment of Results

The raw data of every test was corrected (where appropriate) for offset, chartcross, paraffin bath temperature and detector internal calibration using computer programme Tidy described in Appendix A6.

The relationship between PD and flaw depth was evaluated using a degree 1 linear regression analysis and a Chebyshev degree 2 polynomial curve fitting routine given in Appendices A7 and A8. In both cases error analysis was based on the assumption that flaw depth was error free, and all the remaining errors could be resolved with respect to PD, or vice versa. In this way the relative error to the appropriate model was expressed as either the standard residual error in PD (RMS PD), or the standard error in a (RMS a), depending on the choice of dependent and independent variable.

Use was also made of the Chebyshev degree 2 polynomial curvefit analysis to generate the theoretical PD at a = 0.00 mm, i.e. PD_o, which was used for data normalisation presented in the following text.

10.5 Results and Discussion

10.5.1 Introduction

The major objective of this investigation was to study the performance of a Testwell ACPD2 Crack Detector with a view to employing it to monitor the growth of fatigue cracks in the a/w regime 0.01 to 0.50. The main interest therefore, lay in evaluating the nature of the PD calibration response, and thereby, establish whether the data could be normalised with respect to a master PD/PD_o plot as suggested by Testwell Ltd [10.04].

To initially embark on a series of calibration studies involving the growth of short cracks was consider inappropriate because of the problems associated with accurately defining crack depth and shape. Instead an EDM fcg-analogue study was conducted as recommended by Birchak [10.01], and to validate and complement this, calibration data was generated for large through section cracks in the a/w regime 0.08 to 0.49.

The question of directly comparing the results of both studies was initially open to question, Mann [10.03] however, claimed there was no reason to suspect any difference in calibration response, and reported that the EDM fcg-analogue study had been successfully used to generate calibration data for titanium. When questioned on the aspect of geometrical effects, he reported that differences in specimen length and width were unlikely to affect calibration response provided that current-sensing lead configuration and specimen thickness remain constant. On the basis of these comments

and the recommendations of Birchak the entire investigation was planned.

10.5.2 EDM fcg-analogue and SEN-fcg Calibration Studies

10.5.2.1 A Comparison of Results

From a comparison of Figs. 10.08 to 10.10 the PD calibration relationship appeared to be consistent and homogeneous irrespective of a/w régime. The SEN-fcg results revealed that starting potential was a function of notch configuration, increasing with increased notch depth. This was unexpected and cast doubt on the validity of the EDM fcg-analogue calibration results. Initially it was assumed that once the electric field associated with a mechanically induced flaw has been established, i.e. when flaw depth > flaw opening [10.01], the only contribution to PD arose from increased current path length resulting from flaw 'growth'. The present evidence suggested that this simple assumption was innapplicable and sequential removal of material plays a significant role in determining the magnitude of the resulting PD.

10.5.2.2 Potential Difference versus Flaw Depth Relationship

Throughout the literature it has been reported that the ACPD calibration relationship in a wide variety of specimens is satisfied by a polynomial response ranging from degree 1 [10.04] to degree 3 [10.05]. Analysis of the present data in terms of degree 1 and 2 polynomials, Tables 10.01 and 10.02, revealed the following.

(a) Correlation coefficients of the linear regression analysis, which ranged from 0.9977 to 0.9995, indicated the relationship was linear.

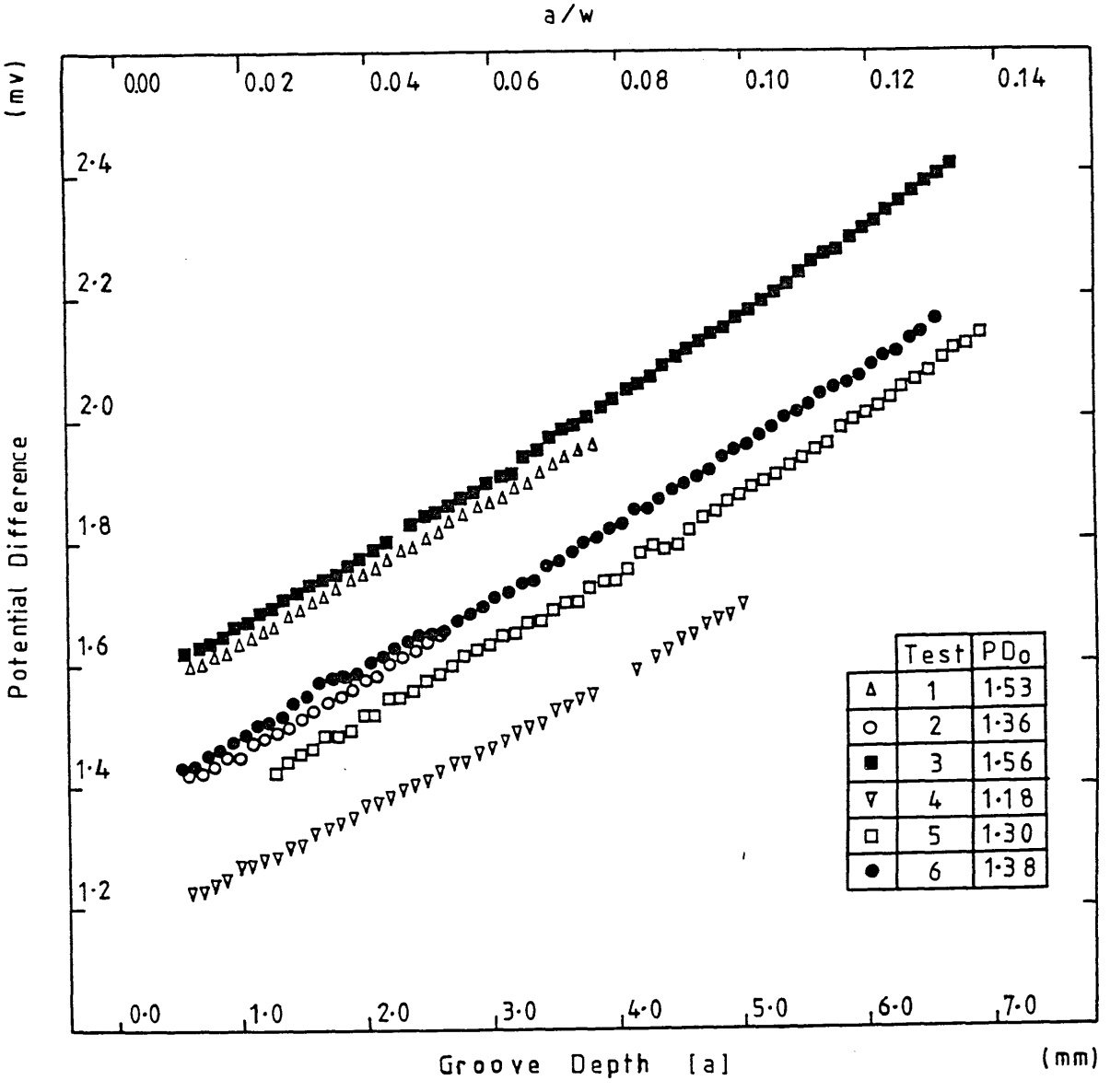


Fig. 10.08 A plot of Potential Difference versus Groove Depth of the EDM fcg-analogue study.

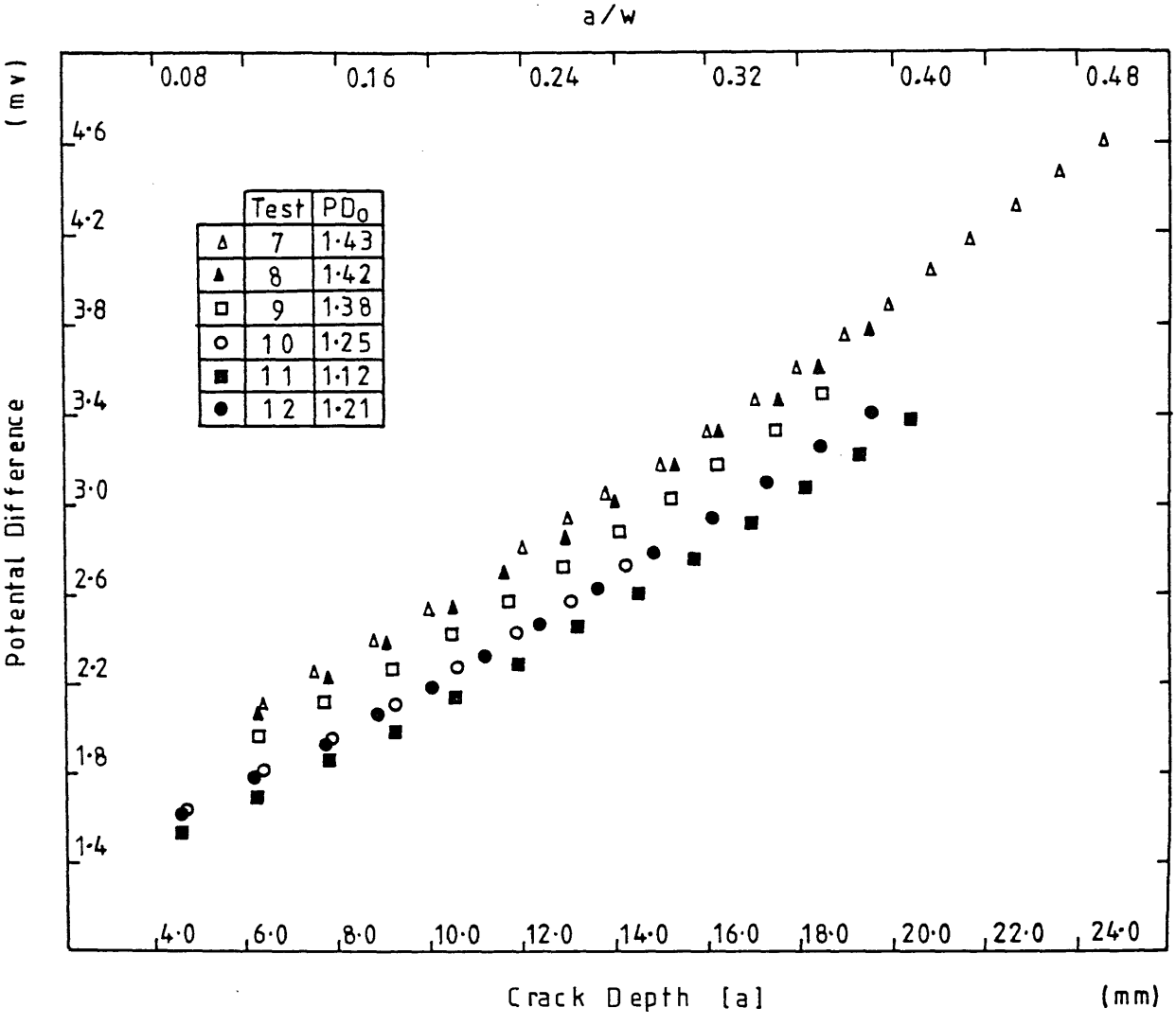


Fig. 10.09 A plot of Potential Difference versus Crack Depth of the SEN-fcg study.

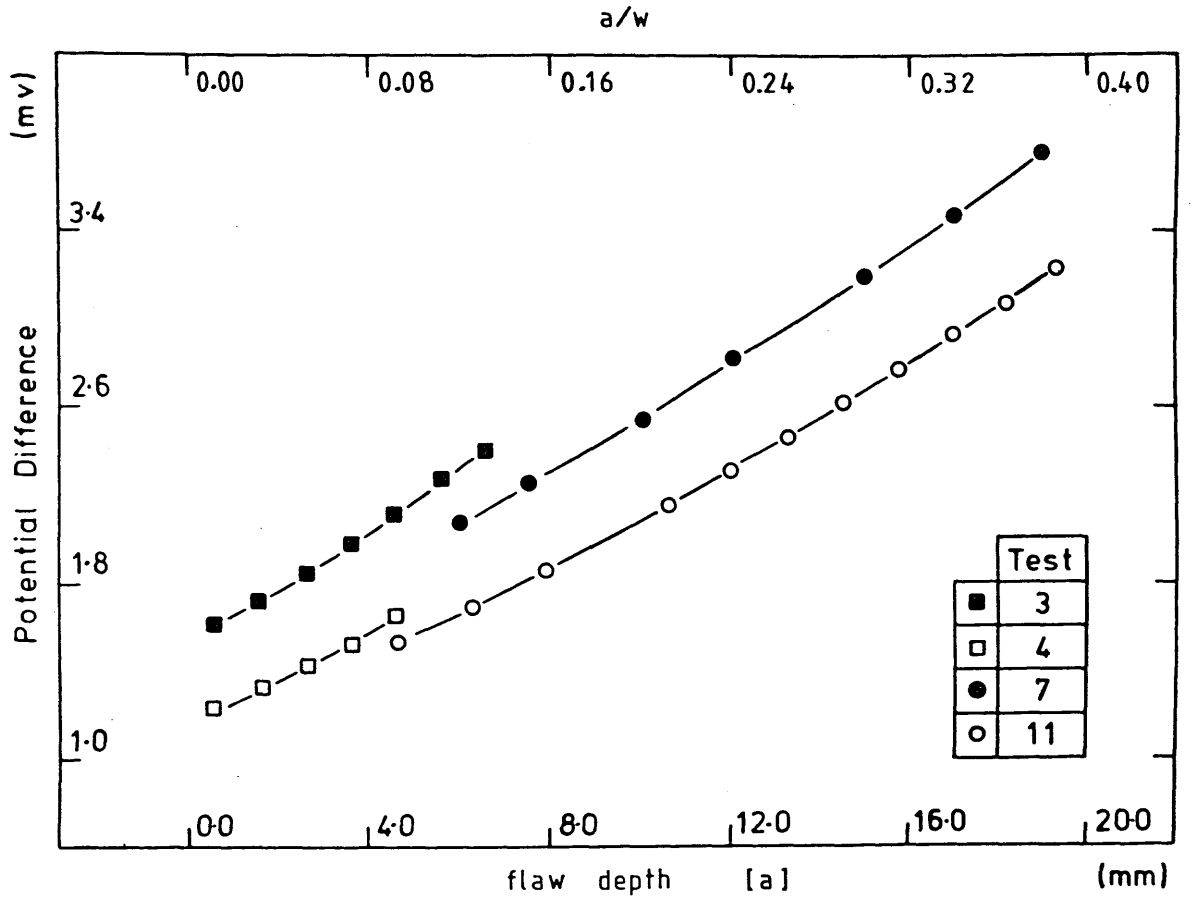


Fig. 10.10 A plot of potential difference versus flaw depth of the EDM fcg-analogue and SEN-fcg studies.

TABLE 10.01

Degree 1 Linear Regression Analysis of the EDM fcg-analogue and SEN-fcg Calibration Results

		Test	a (mm) min	a (mm) max	Correlation Coefficient	RMS PD (μv)	Regression Coefficient (mv/mm)
EDM fcg-analogue Study		1	0.59	3.78	0.9995	4	0.116
		2	0.58	2.58	0.9977	5	0.118
		3	0.57	6.67	0.9990	11	0.130
		4	0.59	4.99	0.9990	6	0.106
		5	1.08	6.88	0.9986	12	0.124
		6	0.53	6.53	0.9990	10	0.120
SEN-fcg Study	$a_n \cong 5.0$mm	7	6.38	24.58	0.9990	36	0.138
		8	6.27	19.54	0.9991	25	0.130
		9	6.30	18.50	0.9987	27	0.126
	$a_n \cong 3.0$mm	10	4.64	14.25	0.9986	22	0.114
		11	4.59	19.52	0.9986	32	0.120
		12	4.63	20.40	0.9986	33	0.118

TABLE 10.02

Chebyshev Degree 2 Polynomial Curve Fit Analysis of EDM fcg-analogue and SEN-fcg Calibration Results

		Test	a (mm) min	a (mm) max	RMS PD (μv)	Chebyshev Coefficients A_0	A_1	A_2
EDM fcg-analogue Study		1	0.59	3.78	4	3.557	0.185	0.001
		2	0.58	2.58	4	3.061	0.118	0.005
		3	0.57	6.67	4	4.000	0.398	0.016
		4	0.59	4.99	4	2.913	0.234	0.007
		5	1.08	6.88	7	3.498	0.372	0.013
		6	0.53	6.53	6	3.568	0.360	0.013
SEN-fcg Study	$a_n \cong 5.00$mm	7	6.38	24.58	8	6.628	1.247	0.050
		8	6.27	19.54	10	5.784	0.860	0.030
		9	6.30	18.50	8	5.397	0.763	0.032
	$a_n \cong 3.00$mm	10	4.64	14.25	4	4.325	0.545	0.025
		11	4.59	19.52	3	4.950	0.894	0.044
		12	4.63	20.40	3	4.828	0.925	0.043

(b) The linear regression coefficients were relatively consistent in both regimes but were slightly greater in the SEN-fcg case. (implying that $d(PD)/da = f(\Delta a)$).

(c) The RMS PD values of the linear regression analysis exhibited a substantial increase with increased sample range (suggesting a non-linear response).

(d) The RMS PD values of the degree 2 polynomial analysis exhibited similar trends to degree 1 analysis but to a lesser extent (indicating a better fit).

(e) If a comparison is made between the RMS PD values of the degree 2 analysis with those of degree 1, in every instance those of degree 2 are less. If attention is not centred on the SEN-fcg studies, degree 1 analysis produces RMS PD values which differ by an order of magnitude of + 1 in comparison to those of degree 2.

On the basis of these findings it was concluded that the relationship between potential difference and flaw depth in both regimes is adequately described by a Chebyshev degree 2 polynomial of the form

$$PD = \frac{A_0}{2} + A_1 \left[\frac{2a - a_{max} - a_{min}}{a_{max} - a_{min}}\right] + A_2 \left[2 \left[\frac{2a - a_{max} - a_{min}}{a_{max} - a_{min}}\right]^2 - 1\right] \quad \ldots(10.01)$$

where A_0, A_1 and A_2 are Chebyshev coefficients generated using a sample of range a_{min} to a_{max}.

The suitability of this model in describing the PD calibration response is clearly illustrated by the RMS a values of the reversed relationship presented in Table 10.03. The Chebyshev degree 2 polynomial model exhibited a relatively high degree of accuracy with RMS a values ranging from 0.03 to 0.07 mm.

10.5.2.3 Conventional Approach to Normalising Data

Two conventional attempts were made to rationalise the calibration data. Plots were constructed of $PD-PD_o$ and PD/PD_o, Figs. 10.11 to 10.14.

Normalisation with respect to $PD-PD_o$ revealed that in both a/w regimes $d^2(PD)/da^2$ was PD_o dependent. This dependency did not however, satisfy the requirements of the PD/PD_o normalising technique.

In an attempt to normalise the SEN-fcg data with respect to notch potential, plots were constructured of $PD-PD_n$ and PD/PD_n, Figs. 10.15 and 10.16. Chebyshev degree 2 polynomial analysis of the respective sets of data, which exhibited RMS a values of 0.13 and 0.18 mm respectively, suggested that specimens containing similar notch configurations and starting potentials were most suitably normalised by adopting the $PD-PD_o$ technique.

Intuitively this result indicated that if PD_n remains constant irrespective of notch depth, subsequent calibration data can be normalised by plotting $PD-PD_n$ with respect to $a-a_n$. Unfortunately this criteria was not satisfied in the present series of tests and the approach was therefore invalid as shown in Fig. 10.17.

TABLE 10.03

A Comparison of RMS a Values Generated using Chebyshev Degree 2 Polynomial Curve Fit Analysis

		Test	RMS a (mm)	Chebyshev Coefficients A_0	A_1	A_2
EDM fcg-analogue Studies		1	0.03	4.44	1.56	-0.01
		2	0.03	3.28	0.95	-0.04
		3	0.03	7.54	3.01	-0.12
		4	0.04	5.78	2.18	-0.07
		5	0.05	8.44	2.79	-0.11
		6	0.05	7.29	3.02	-0.10
SEN fcg	$a_n \cong 5.0$mm	7	0.06	31.61	9.07	0.36
		8	0.06	22.94	4.99	-0.18
		9	0.07	25.35	6.09	-0.26
	$a_n \cong 3.0$mm	10	0.05	19.33	4.77	-0.22
		11	0.06	24.86	7.42	-0.35
		12	0.04	25.82	7.81	-0.37

Note: data analysis is based on a = f(PD)

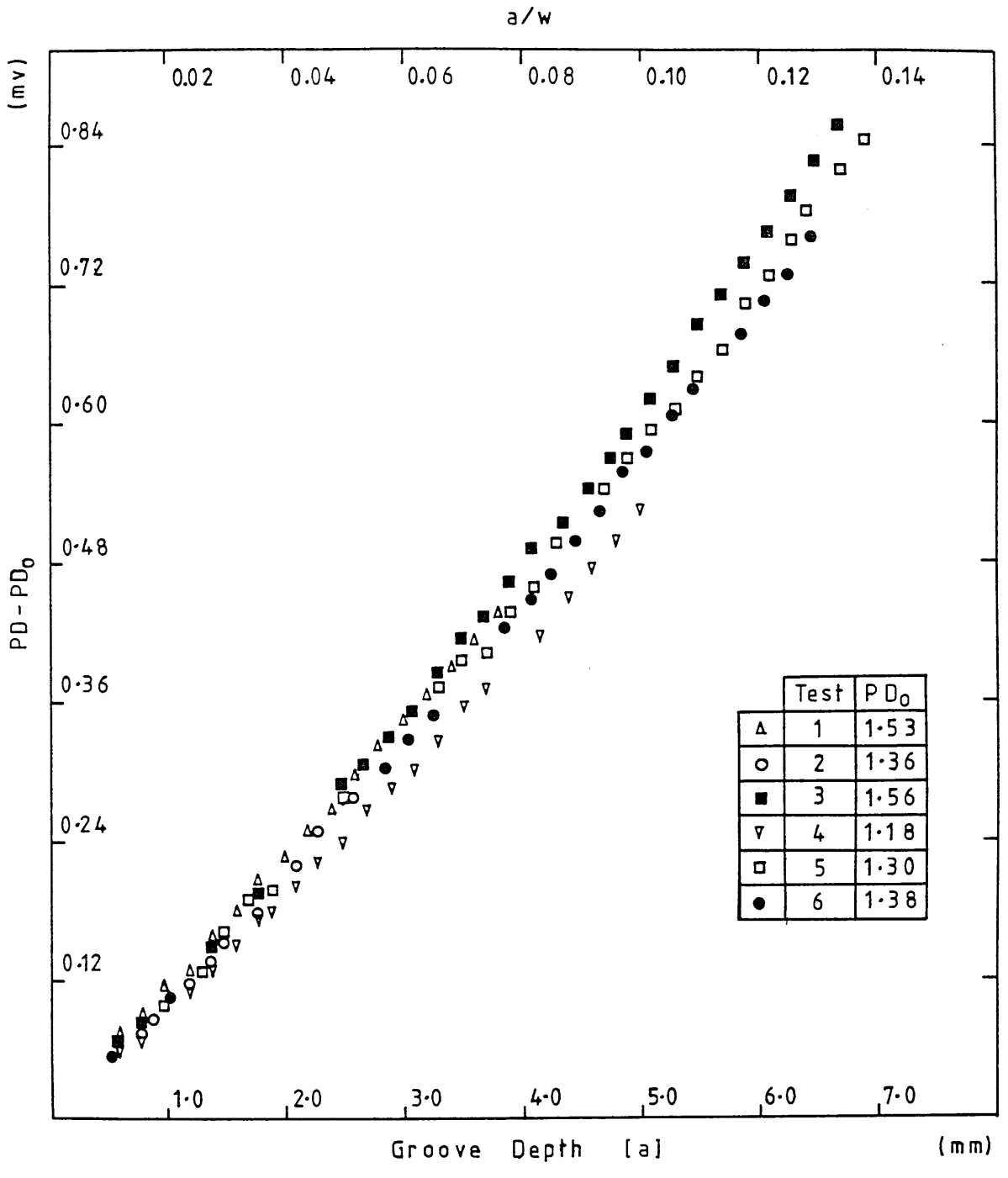


Fig. 10.11 A plot of $PD-PD_o$ versus Groove Depth of the EDM fcg-analogue study.

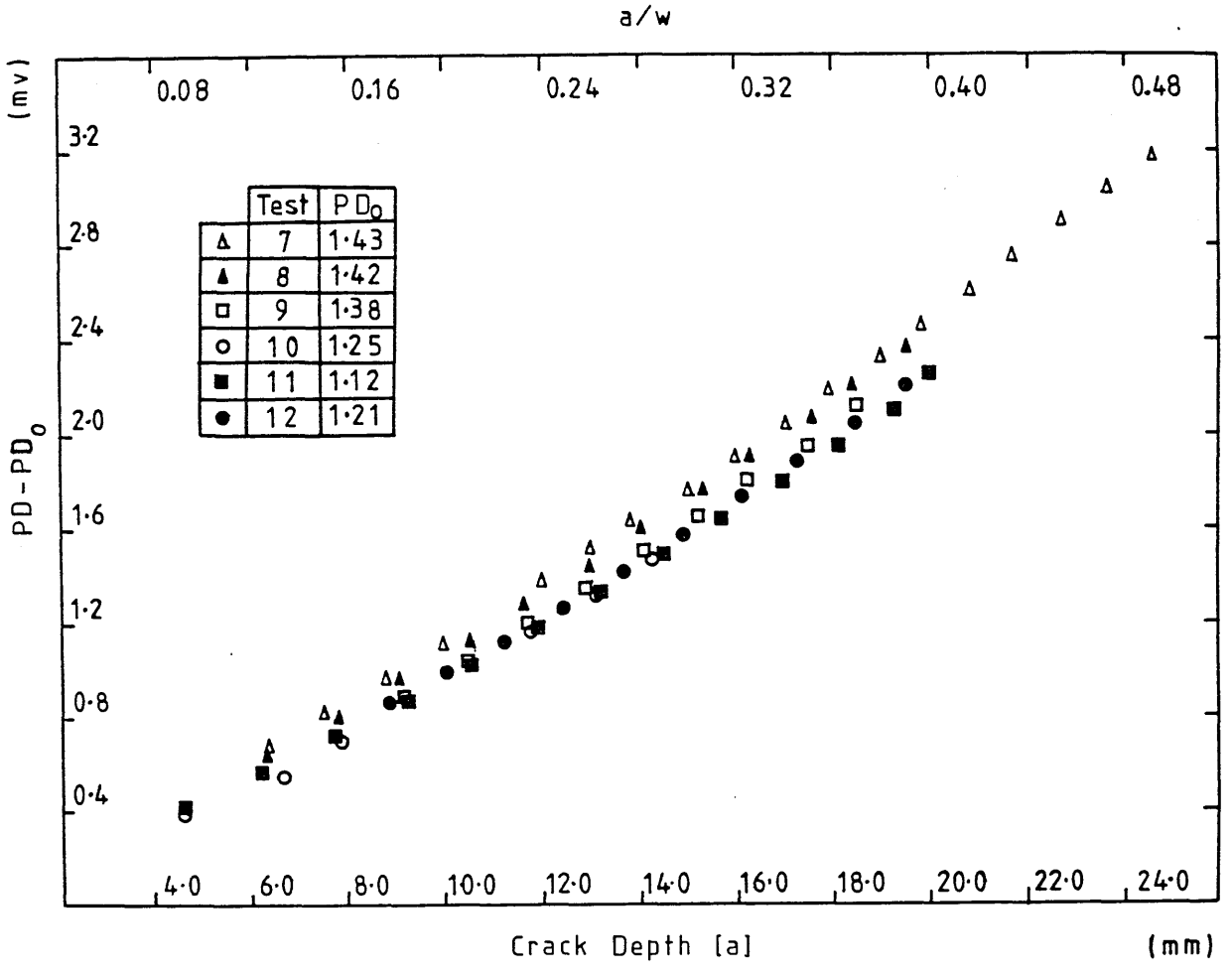


Fig. 10.12 A plot of PD-PD$_o$ versus Crack Depth of the SEN-fcg study.

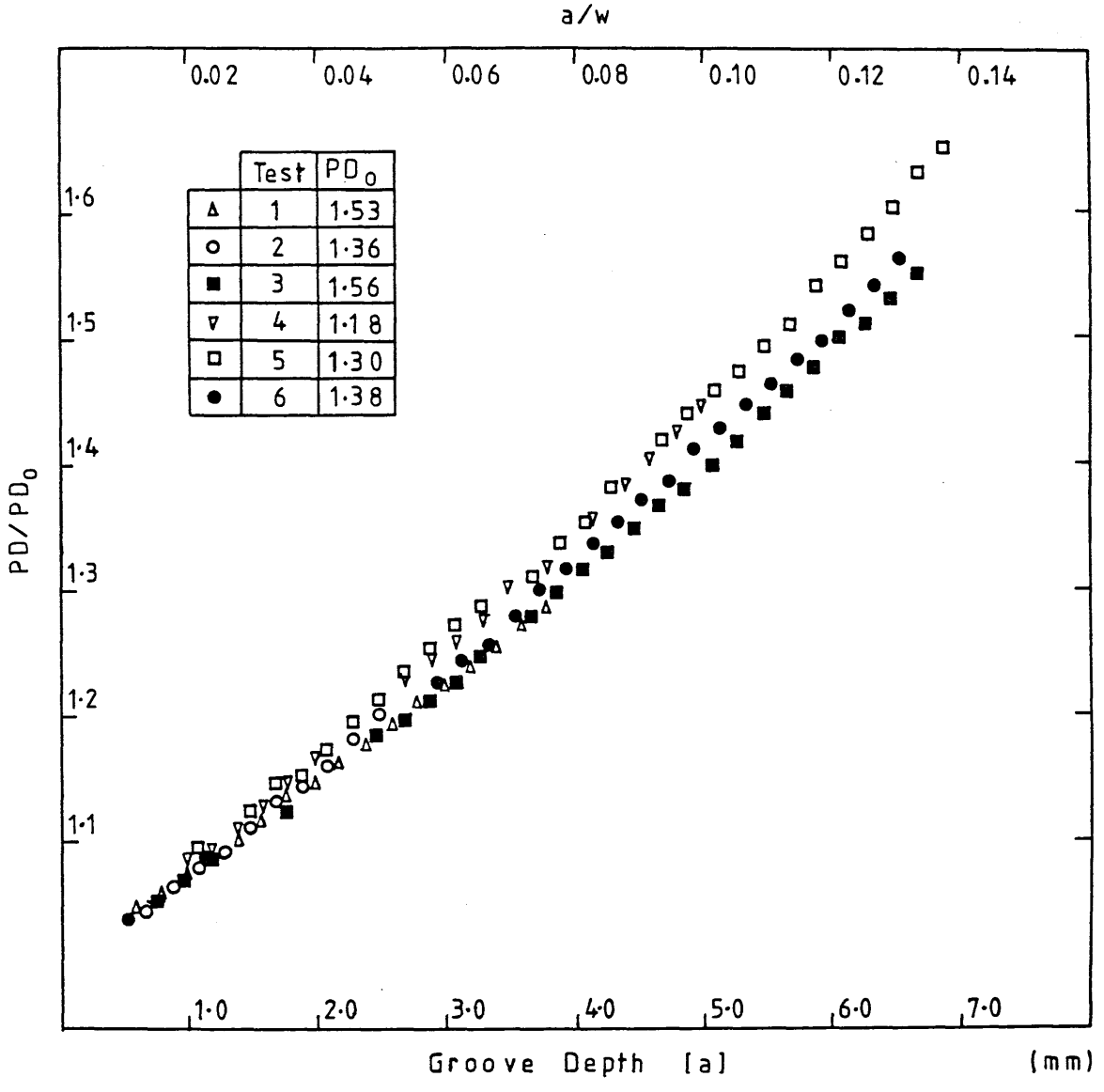


Fig. 10.13 A plot of PD/PD_o versus Groove Depth of the EDM fcg-analogue study.

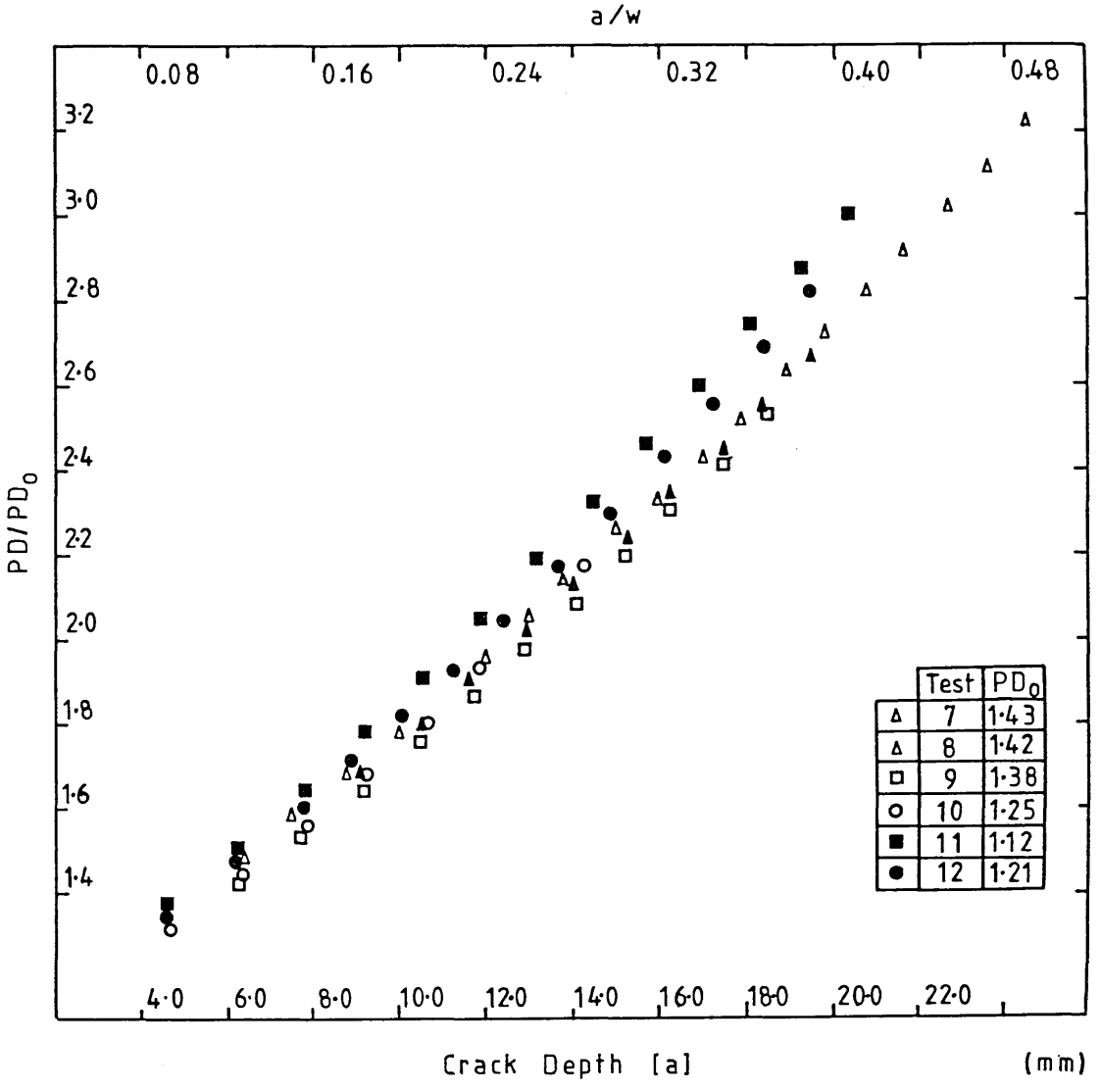
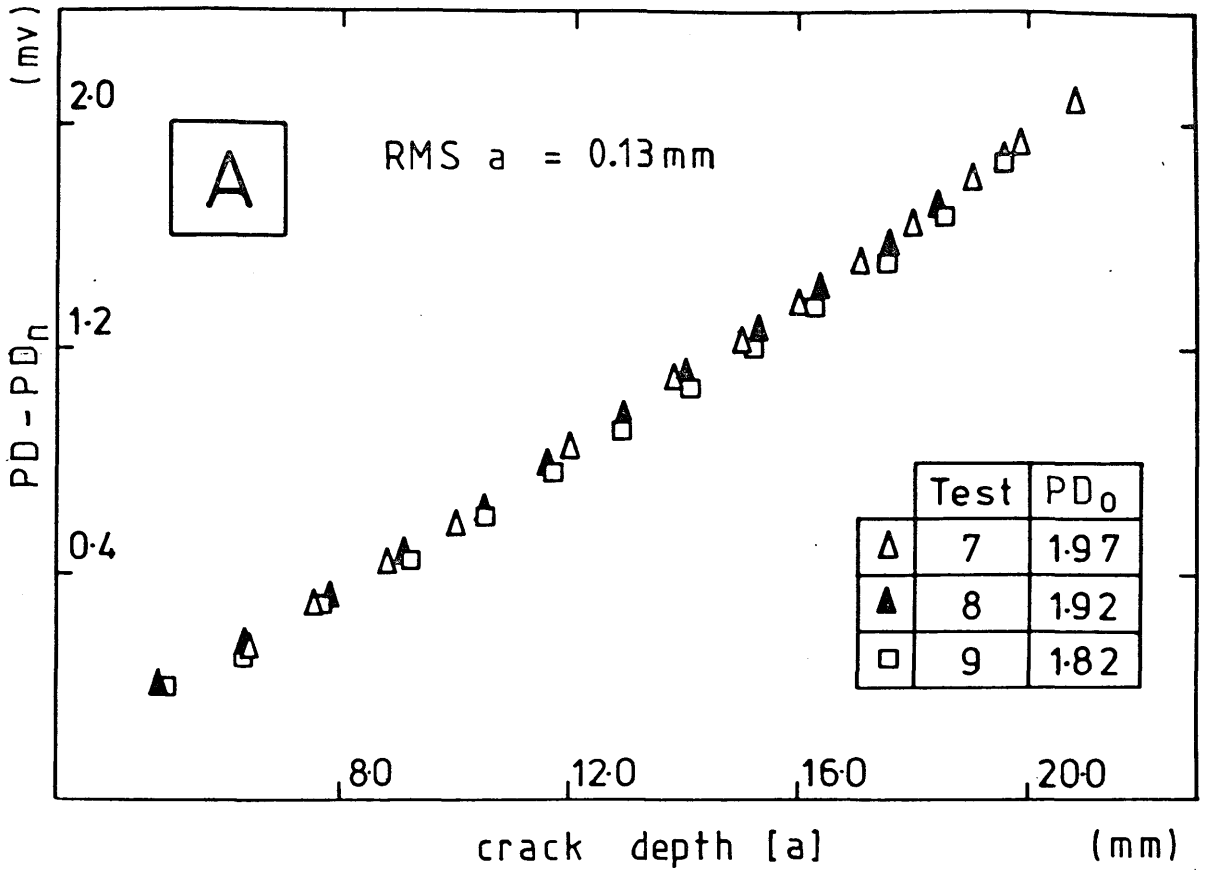


Fig. 10.14 A plot of PD/PD_o versus Crack Depth of the SEN-fcg study.



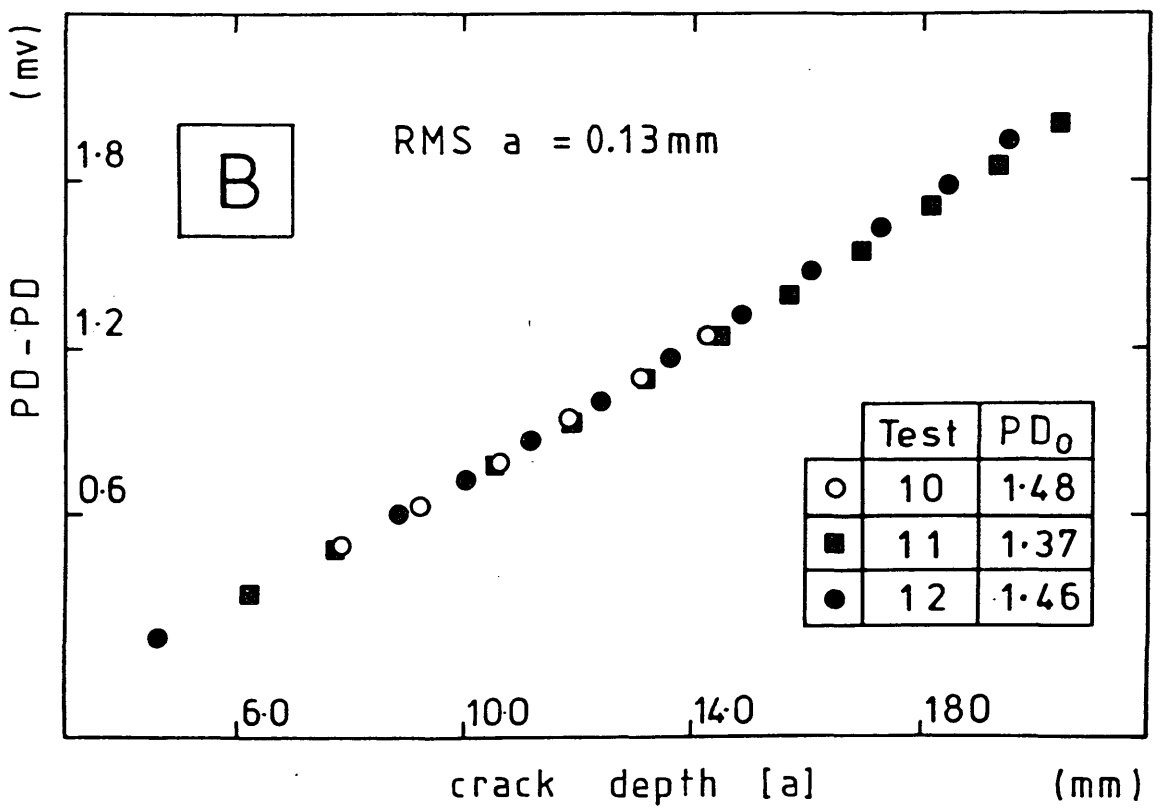
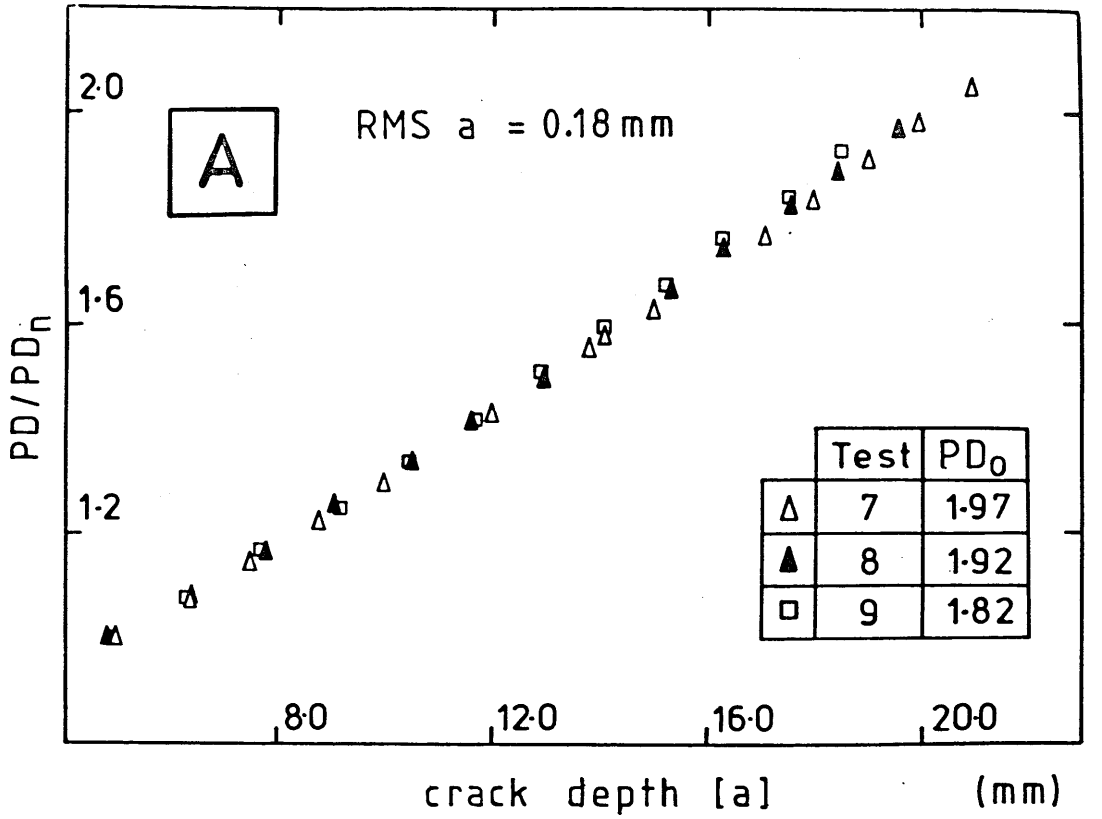


Fig. 10.15 A normalised plot of PD-PD$_n$ versus crack depth of the SEN-fcg study.

(A) Notch Depth ≅ 5 mm

(B) Notch Depth ≅ 3 mm



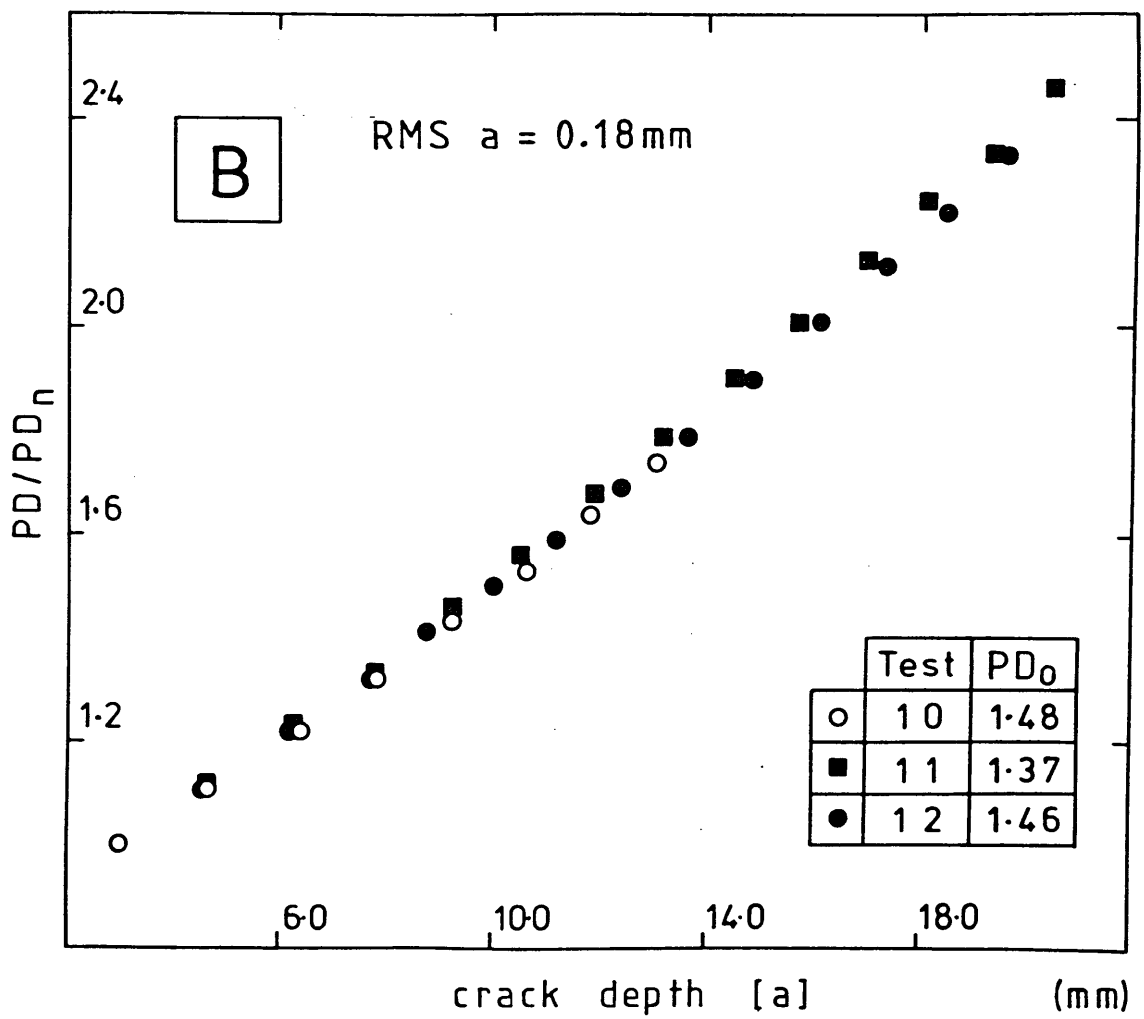


Fig. 10.16 A plot of PD/PD_n versus crack depth of the SEN-fcg study.

(A) Notch Depth ≅ 5 mm

(B) Notch Depth ≅ 3 mm

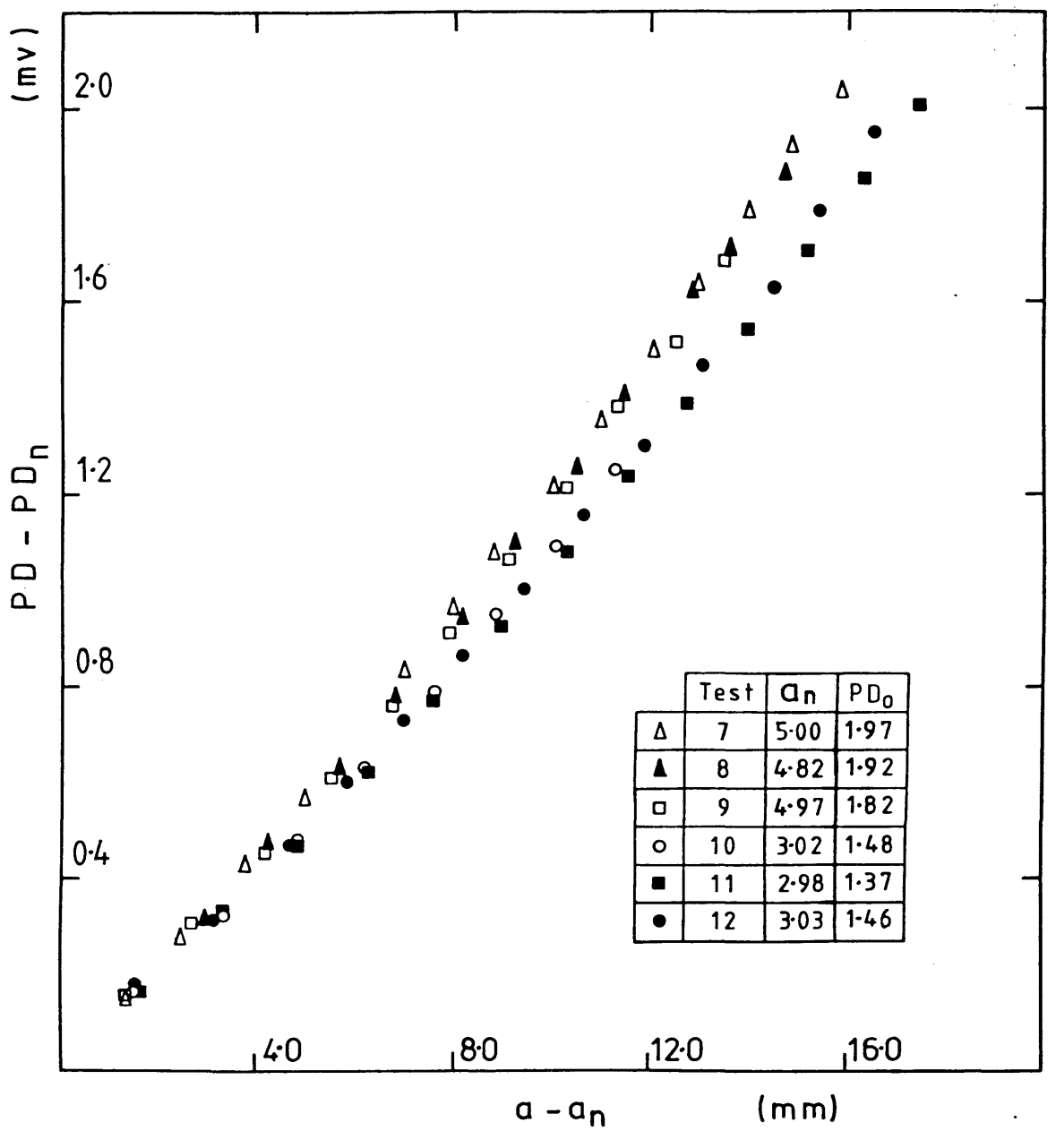


Fig. 10.17 A plot of PD-PD_n versus a-a_n of the SEN-fcg study.

10.5.3 Geometrical Effects on Calibration Response

10.5.3.1 Fatigue Crack Growth in a Plane Specimen

The relationship between PD and crack depth in the plane specimen was well behaved and compared very well with the calibration response of Test 7, Fig. 10.18. The comparison illustrated that $d^2(PD)/da^2$ was dependent on PD_o irrespective of specimen width and initial notch/starter crack geometry.

10.5.3.2 Specimen Thickness Effects

Fig. 10.19 clearly illustrated that increasing specimen thickness resulted in a decrease in $d^2(PD)/da^2$. Similar trends have also been reported by other investigators [10.06] and arise due to a decrease in AC field strength. Greater sensitivity is therefore possible in thinner specimens.

10.5.4 Empiricial Normalisation of Calibration Data

Faced with the dilema of not being able to normalise any of the calibration data and having established that $d^2(PD)/da^2$ is related to PD_o, attention was turned to the factors effecting measured potential difference (PD).

Consideration of the test configuration revealed that measured potential difference had four components:

(a) potential difference across the flaw (PD_{AB});

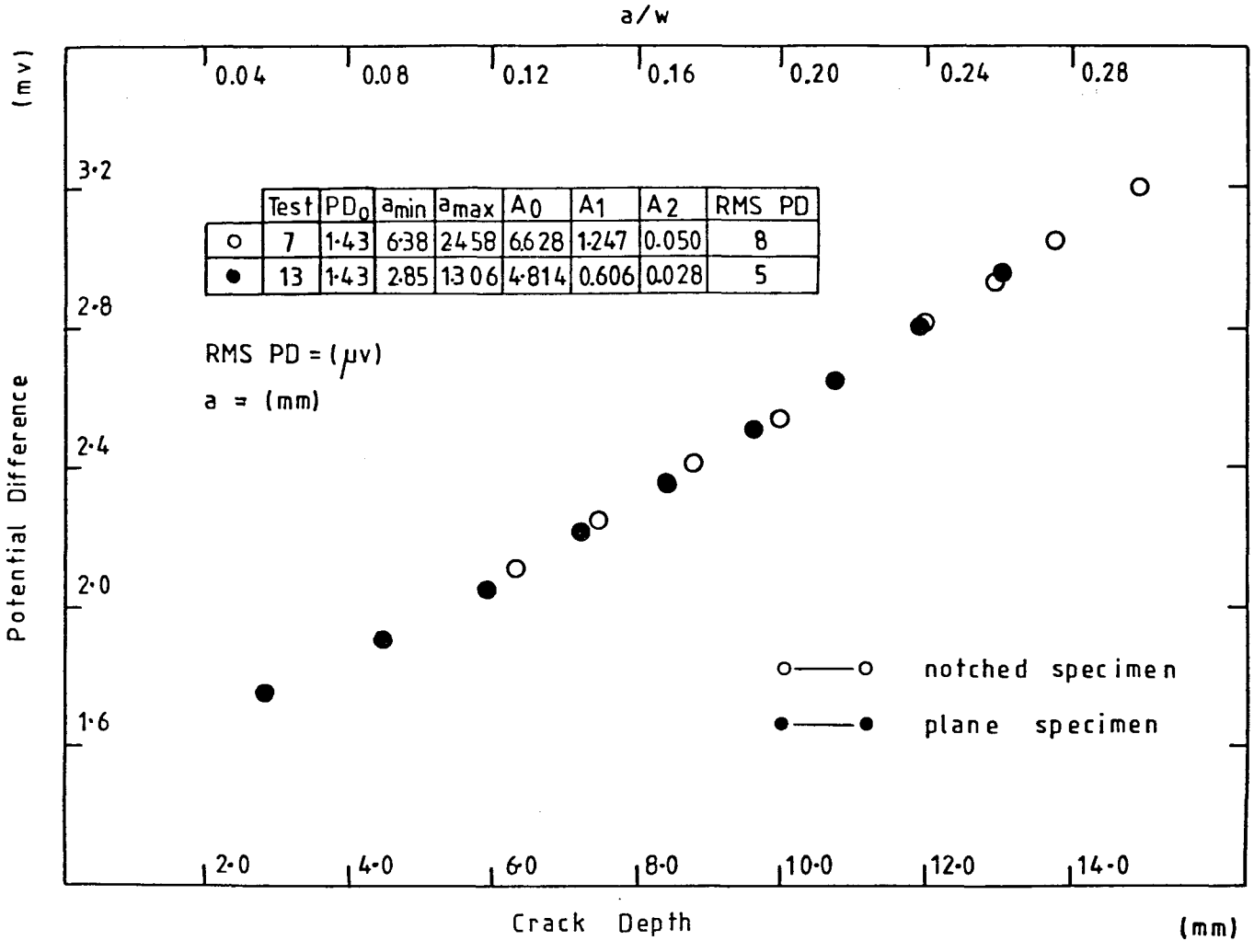
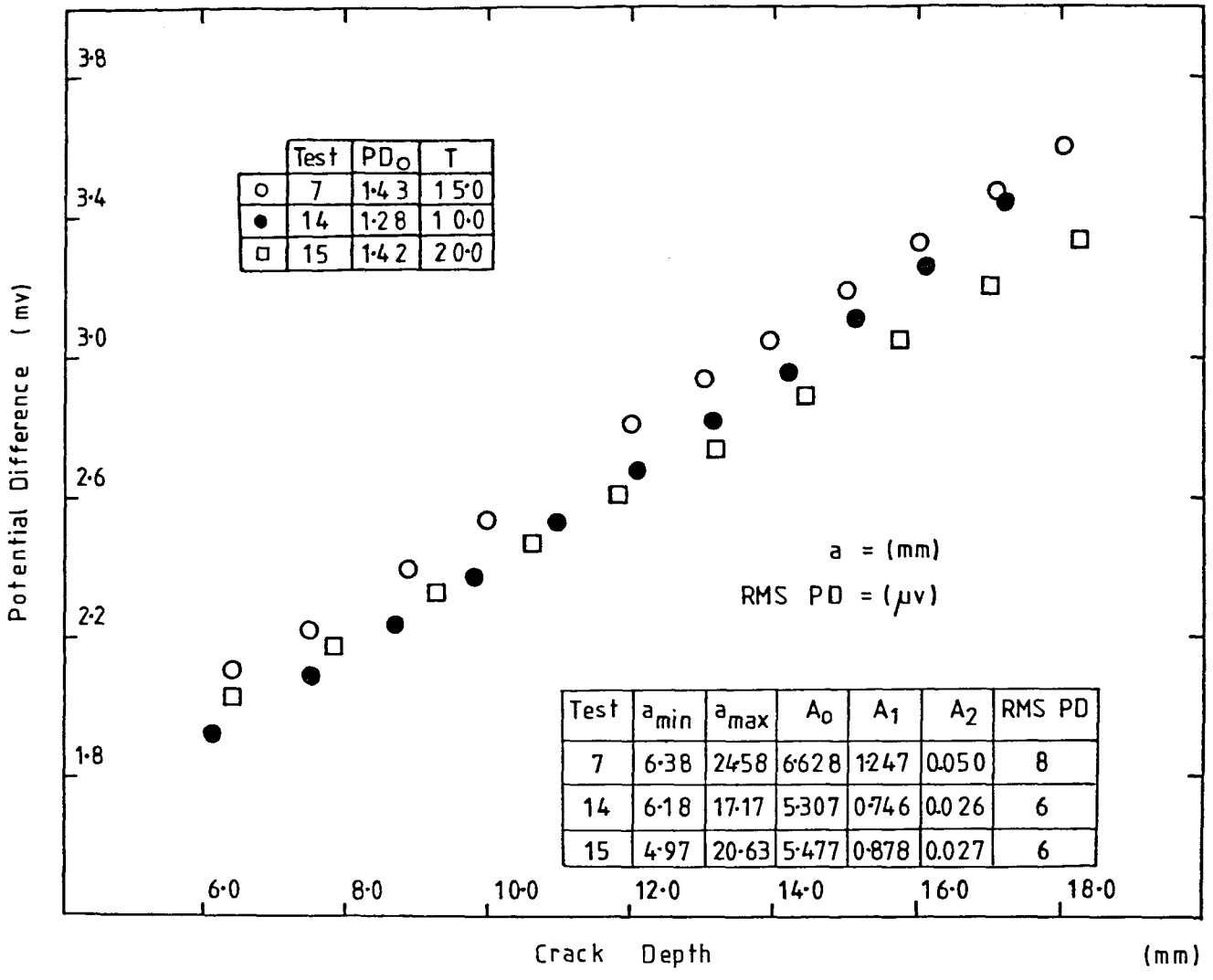


Fig. 10.18 A comparison of Potential Difference versus Crack Depth response in notched and plane specimens of width 50 and 40 mm respectively.



	Test	PD_o	T
○	7	1·43	15·0
●	14	1·28	10·0
□	15	1·42	20·0

Test	a_{min}	a_{max}	A_o	A_1	A_2	RMS PD
7	6·38	24·58	6·628	1·247	0·050	8
14	6·18	17·17	5·307	0·746	0·026	6
15	4·97	20·63	5·477	0·878	0·027	6

Fig 10.19 A plot of Potential Difference versus Crack Depth of SEN-fcg illustrating the effect of specimen thickness on calibration response.

(b) a contribution arising from eddy current effects in the sensing leads (PD_{ABE});

(c) potential difference due to compensation (PD_{CD}); and

(d) a contribution arising from eddy currents effects in the compensation leads (PD_{CDE}).

These combine to give

$$PD = PD_{AB} + PD_{ABE} - PD_{CDE} - PD_{CD} \qquad ...(10.02)$$

or $$PD = PD_{AB} - PD_{CD} + PD_{TED} \qquad ...(10.03)$$

where PD_{TED} is the total eddy current contribution.

Now because $PD_{AB} > PD_{CD} >> PD_{TED}$ the magnitude of PD is principly determined by PD_{AB}. If there is no compensation then $PD = PD_{AB}$ and $d^2(PD)/da^2 = f\ (PD_{AB})$ with the magnitude of PD_{AB} being governed by probe position, A-B seperation, flaw geometry.....etc. In a plane specimen containing no flaw if all other factors remain constant then $PD = PD_o = PD_{AB(a = 0)}$ and $d^2\ (PD)/da^2$ can be expressed directly as a function of $PD_{AB(a = 0)}$. If compensation is introduced, $d^2(PD)/da^2$ will remain a function of $PD_{AB(a = 0)}$ but will not be related to PD_o because of the $- PD_{CD}$ contribution. If PD_{CD} remains constant irrespective of calibration test, then $d^2(PD)/da^2$ will exhibit a consistent PD_o dependency. But in reality this is highly unlikely.

Unfortunately when the tests of this investigation were

conducted, PD_{AB}, PD_{CD} and PD_{TED} could not be measured. Subsequently however, Testwell Ltd have produced at our request (and are currently marketing) a modified pre-amp system facilitating an absolute measure of the three potential difference contributions.

In the light of the previous arguments and on the recommendations of Mann [10.03] it was assumed that in the present series of calibration tests $d^2(PD)/da^2$ exhibited a $PD_{AB(a = 0)}$ dependency which satisfied the voltage ratio normalising technique. To rationalise the data a univariate optimisation search technique was then developed which determined for each calibration test the empirical constants

PD_{OE} (analagous to $PD_{AB(a = 0)}$)

and PD_C (analagous to PD_{CD})

facilitating a plot of $(PD-PD_C)/PD_{OE}$ versus flaw depth to be constructed which normalised the data with respect to the Chebyshev degree 2 polynomial model describing the PD/PD_o calibration relationship of Test 7. Details are given in Appendix A9. This enabled the empirically normalised plots of Figs. 10.20 to 10.24 to be drawn.

From these plots, which exhibited RMS a values ranging from 0.11 to 0.14 mm, it was concluded that the empirical normalising technique satisfactorily normalised all calibration data irrespective of a/w régime and specimen geometry effects.

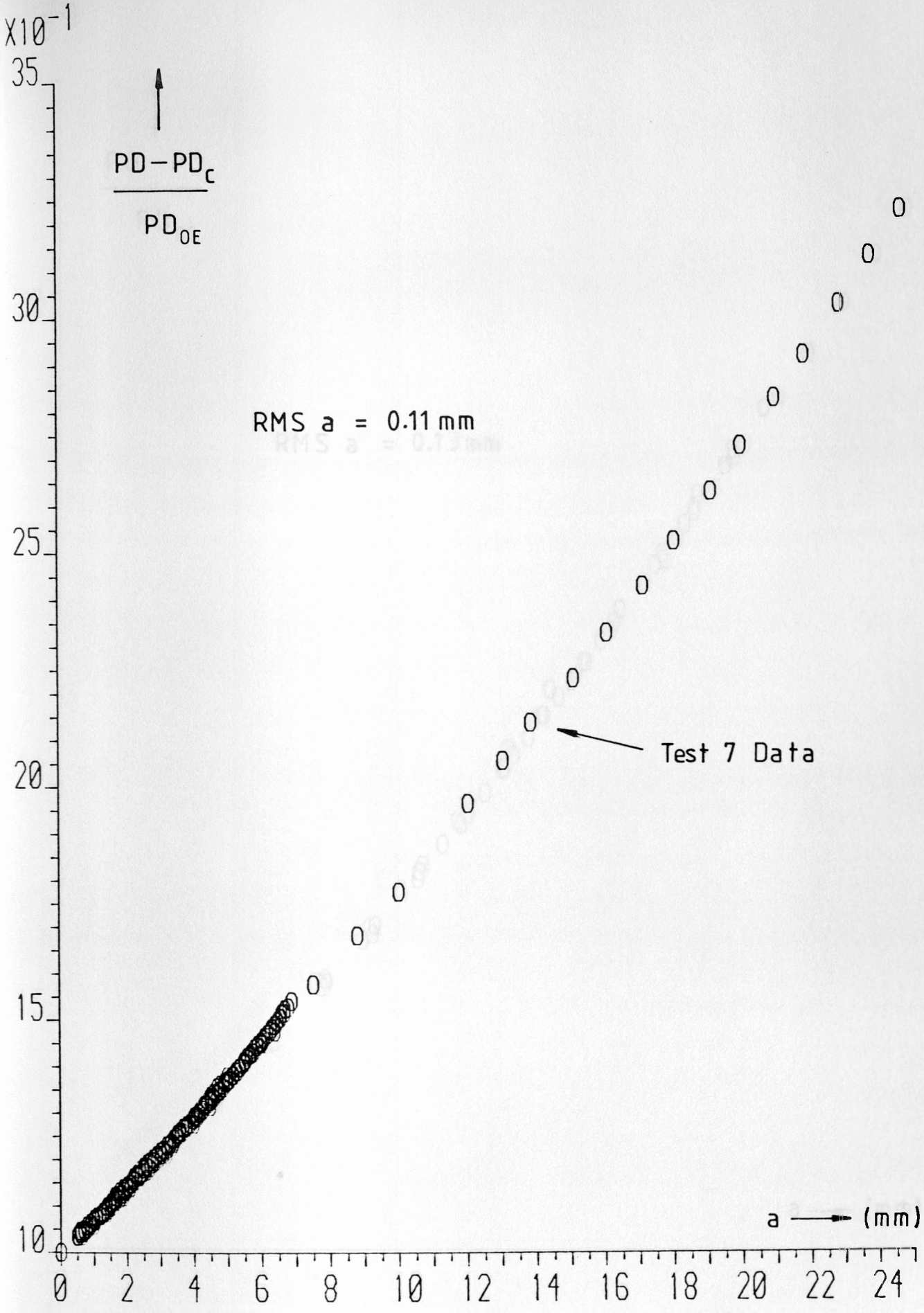


Fig. 10.20 A computer plot of Emprically Normalised Potential Difference Ratio versus Groove Depth of the EDM fcg-analogue study.

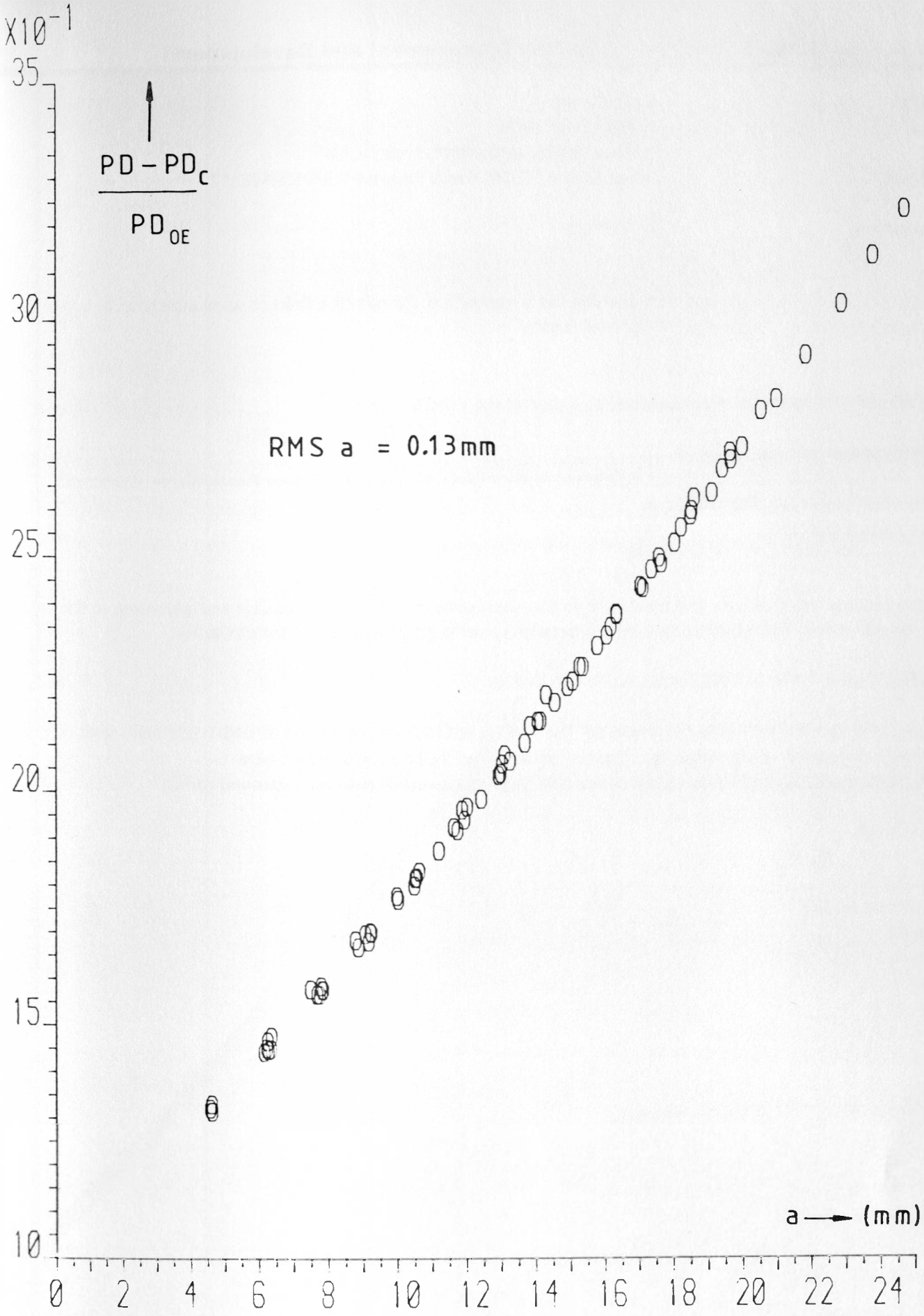


Fig. 10.21 A computer plot of Empirically Normalised Potential Difference Ratio versus Crack Depth of the SEN-fcg study.

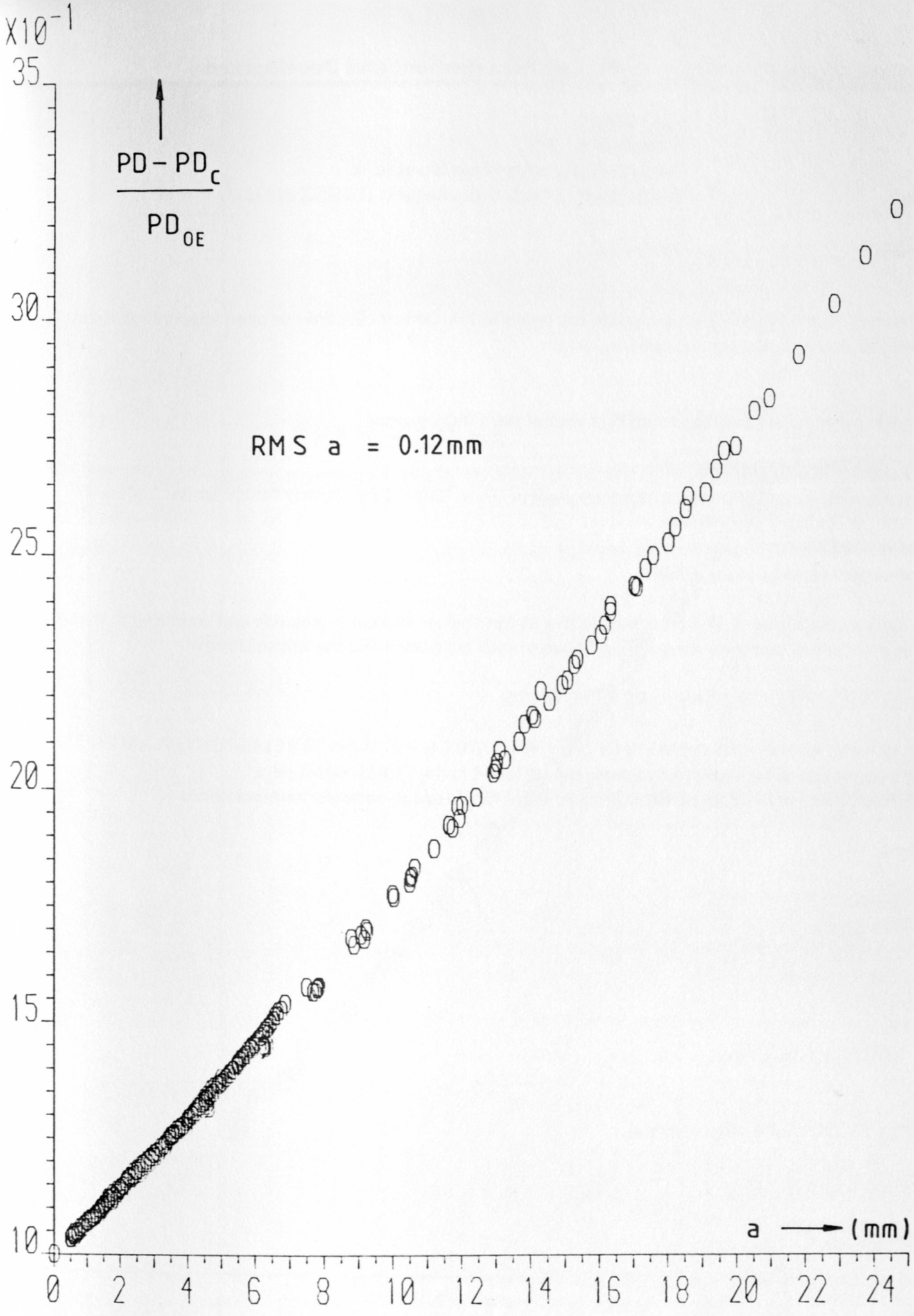


Fig. 10.22 A computer plot of Empricially Normalised Potential Difference Ratio versus Flaw Depth of the EDM fcg-analogue and SEN-fcg Tests 1 to 12

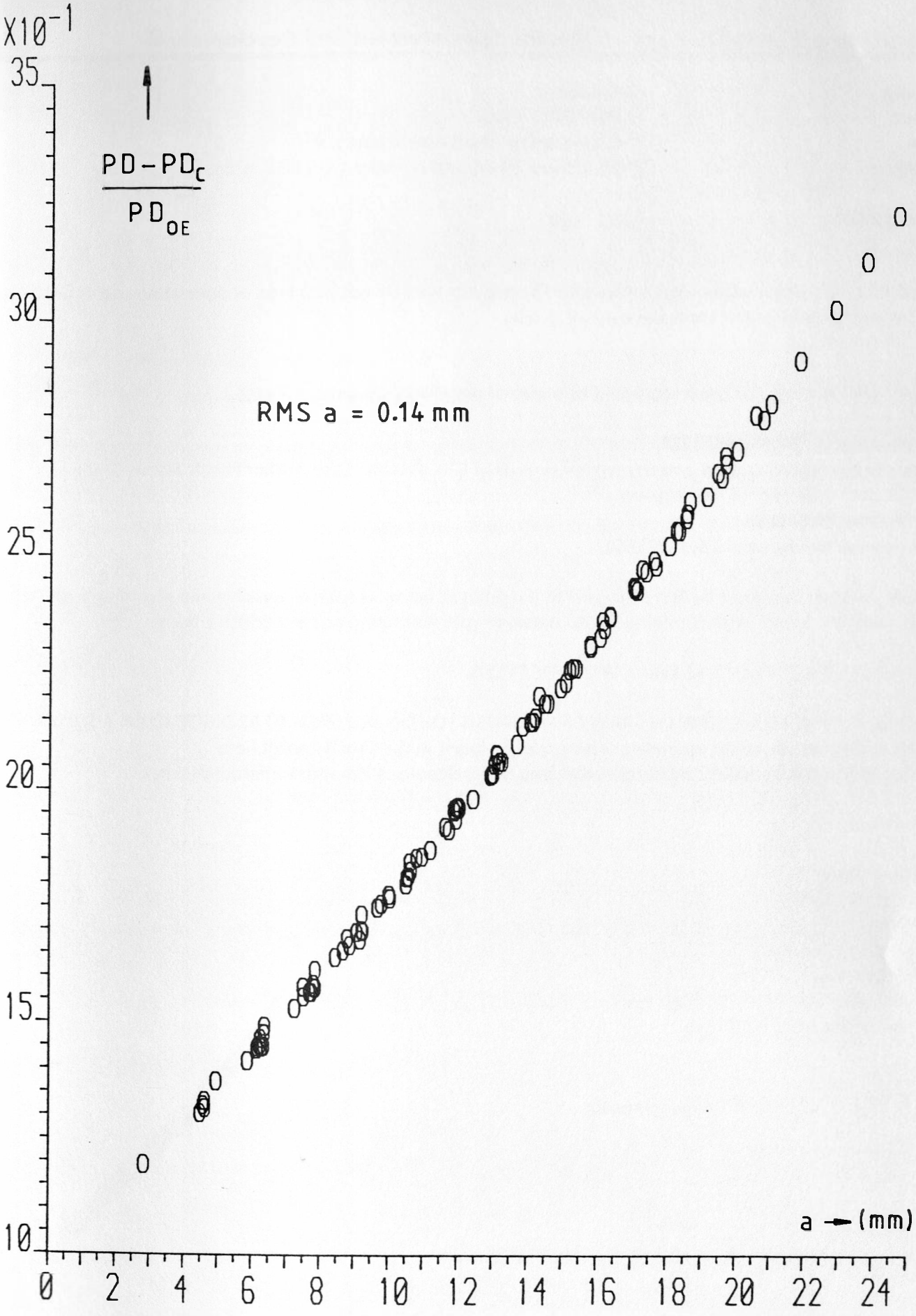


Fig. 10.23 A computor plot of Empirically Normalised Potential Difference Ratio versus Crack Depth of all avaliable fcg calibration data.

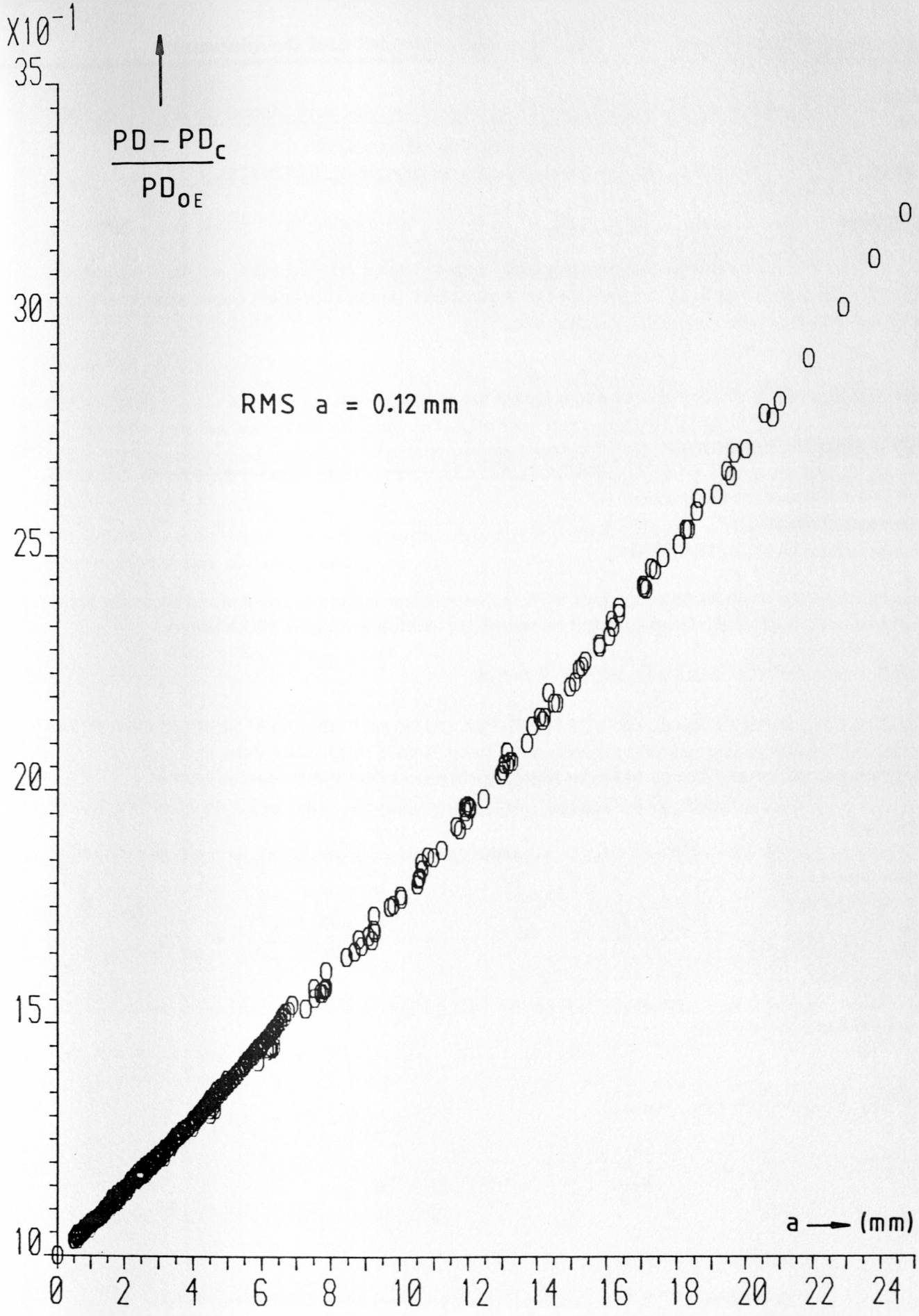


Fig. 10.24 A computer plot of Empirically Normalised Potential Difference Ratio versus Flaw Depth of all the calibration data of the present investigation.

10.5.5 Crack Depth Prediction based on Empirical Normalisation

The ability to empirically normalise all calibration data prompted a series of calculations designed to illustrate that the technique can be applied to crack depth prediction based on only two pairs of data points.

The approach assumes that the ACPD calibration response of EN3BN can be related to the calibration voltage ratio model of Test 7 through the empirical constants PD_C and PD_{OE}. If this is true then at sample points $a_1 PD_1$ and $a_2 PD_2$ the sample data can be equated to the calibration model, i.e.

$$(PD_1 - PD_C)/PD_{OE} = VR_1 \qquad \ldots(10.04)$$

and

$$(PD_2 - PD_C)/PD_{OE} = VR_2 \qquad \ldots(10.05)$$

where VR_1 and VR_2 are the calibration model values at a_1 and a_2. Subtracting Eq. 10.05 from Eq. 10.04 gives

$$PD_{OE} = \frac{PD_1 - PD_2}{VR_1 - VR_2} \qquad \ldots(10.06)$$

PD_C is then obtained by rearranging Eq. 10.04 to given Eq. 10.07 and then substituting Eq. 10.06 into Eq. 10.07 to give Eq. 10.08.

$$PD_C = PD_1 - VR_1 . D_{OE} \qquad \ldots(10.07)$$

$$PD_C = PD_1 - VR_1 \cdot \frac{PD_1 - PD_2}{VR_1 - VR_2} \qquad \ldots(10.08)$$

Thus from only two pairs of data points and a knowledge of the calibration model PD_C and PD_{OE} can be determined and the ratio

$(PD-PD_C)/PD_{OE}$ can be calculated for any value of PD. Crack depths can then be computed directly from the calibration model.

The application of this technique and accuracy of crack depth prediction is illustrated with respect to Tests 8, 12 and 14 presented in Tables 10.04 to 10.06. From these results it can be seen that predicted crack depths were underestimated to within 2.7%. This observation suggested that the calibration response of Test 7 exhibits greater linearity in comparison to any of the other tests, and may not be the most suitable choice as the model relationship.

10.5.6 Sensitivity and Resolution

Throughout this investigation it was apparent that the sensitivity of the Testwell ACPD2 Crack Detector was determined by many factors including starting potential, specimen geometry and notch depth. If, however, it is assumed that the PD calibration relationship is described by the Chebyshev degree 2 polynomial relationship of Test 7, then in the a/w régime 0.08 to 0.49 (4.00 mm $\leqslant$ a $\leqslant$ 24.58 mm) sensitivity increases from 0.100 to 0.157 mv/mm.

When used in a continuous mode the crack detector was capable of detecting changes in PD of 0.002 ± 0.001 mv. Based on the above figures this corresponded to a change in crack depth of 0.02 ± 0.01 mm at a/w = 0.08 to 0.01 ± 0.01 mm at a/w = 0.49.

10.5.7 Concluding Remarks

The results of this investigation indicated that the Testwell

TABLE 10.04

Crack Depth Prediction Based on Empirical Normalisation

CALIBRATION TEST 8					
a (mm)	PD (mv)	$\frac{PD-PD_C}{PD_{OE}}$	Model Predicted a Values (mm)	Residual (mm)	Accuracy of Crack Depth Prediction (% error)
6.27	2.068	1.471	-	-	-
7.81	2.232	1.588	7.70	-0.11	-1.4
9.08	2.387	1.698	9.01	-0.07	-0.8
10.52	2.552	1.815	10.33	-0.19	-1.8
11.62	2.703	1.922	11.58	-0.04	-0.3
12.96	2.862	2.037	12.79	-0.17	-1.3
14.01	3.016	2.144	14.00	0.00	0.0
15.30	3.176	2.258	15.22	-0.08	-0.5
16.26	3.328	2.365	16.32	+0.06	+0.4
17.56	3.479	2.473	17.43	-0.13	-0.7
18.40	3.619	2.572	18.41	+0.01	+0.1
19.54	3.782	2.688	-	-	-

a_1 = 6.27 mm	a_2 = 19.54 mm
PD_1 = 2.068 mv	PD_2 = 3.782 mv
VR_1 = 1.471	VR_2 = 2.687

PD_{OE} = 1.409 mv

PD_C = -0.005 mv

TABLE 10.05

Crack Depth Predictions based on Empirical Normalisation

CALIBRATION TEST 12					
a (mm)	PD (mv)	$\frac{PD-PD_C}{PD_{OE}}$	Model Predicted a Values (mm)	Residual (mm)	Accuracy of Crack Depth Prediction (% error)
4.63	1.538	1.342	-	-	-
6.25	1.689	1.480	6.13	-0.12	-1.9
7.83	1.846	1.581	7.62	-0.21	-2.7
9.26	1.998	1.699	9.10	-0.16	-1.7
10.56	2.146	1.815	10.36	-0.20	-1.9
11.92	2.300	1.934	11.72	-0.20	-1.7
13.22	2.456	2.056	13.03	-0.19	-1.4
14.50	2.612	2.177	14.38	-0.12	-0.8
15.71	2.762	2.294	15.60	-0.11	-0.7
16.96	2.919	2.416	16.84	-0.12	-0.7
18.13	3.074	2.536	18.06	-0.07	-0.4
19.30	3.228	2.656	19.24	-0.06	-0.3
20.40	3.382	2.776	-	-	-

$a_1 = 4.63$ $\quad a_2 = 20.40$

$PD_1 = 1.538$ $\quad PD_2 = 3.382$

$VR_1 = 1.342$ $\quad VR_2 = 2.776$

$PD_{OE} = 1.286$

$PD_C = 0.1874$

TABLE 10.06

Crack Depth Prediction based on Empirical Normalisation

CALIBRATION TEST 14					
a (mm)	PD (mv)	$\frac{PD-PD_C}{PD_{OE}}$	Model Predicted a Values (mm)	Residual (mm)	Accuracy of Crack Depth Prediction (% error)
6.18	1.933	1.464	-	-	-
7.52	2.091	1.568	7.46	-0.06	-0.8
8.68	2.236	1.664	8.61	-0.07	-0.8
9.79	2.382	1.760	9.73	-0.06	-0.6
10.95	2.530	1.858	10.86	-0.09	-0.8
12.02	2.681	1.957	11.97	-0.05	-0.4
13.10	2.818	2.048	12.97	-0.13	-1.0
14.15	9.965	2.144	14.01	-0.14	-1.0
15.12	3.113	2.242	15.04	-0.08	-0.5
16.05	3.264	2.341	16.07	+0.02	+0.1
17.17	3.425	2.448	-	-	-

a_1 = 6.18 mm
PD_1 = 1.933 mv
VR_1 = 1.464

a_2 = 17.17 mm
PD_2 = 3.425 mv
VR_2 = 2.448

PD_{OE} = 1.517 mv
PD_C = -0.288 mv

ACPD2 Crack Detector can be successfully employed to continuously monitor fatigue crack growth in 3 point bend SEN specimens at crack depths ranging from 4.00 to 24.58 mm. Unfortunately because starting potential is dependent on lead arrangement and specimen geometry, limitations are imposed on the application of any standard normalising technique. To overcome this problem an empirical normalising technique has been developed which effectively normalises all PD calibration data irrespective of a/w régime. The accuracy of crack depth prediction based on empirical normalisation was good, but further work is necessary to increase this further.

10.6 Conclusions

(1) The Testwell ACPD2 Crack Detector can be successfully employed to measure flaw depths in EN3BN ranging from 0.50 mm to 24.58 mm.

(2) It is doubtful that the EDM fcg-analogue study accurately assumlates fatigue crack growth when applied to ACPD calibration response.

(3) Sensitivity and resolution varied with starting potential. An increase in starting potential produced a corresponding increase in $d^2(PD)/da^2$.

(4) Resolution, based on fatigue crack growth, was found to be $\geqq$ 0.02 ± 0.01 mm in the a/w régime 0.08 to 0.49.

(5) Increasing specimen thickness produced a decrease in sensitivity, but decreasing specimen width had no effect.

(6) The PD calibration relationship can be described as linear over small flaw depths but considerable loss in accuracy is incurred as the range is increased.

(7) The calibration data of specimens containing similar notch configurations and starting potentials were suitably normalised by adoping a $PD-PD_0$ approach.

(8) An empirical normalising technique developed to normalise all calibration data irrespective of specimen geometry and starting potential was successful in normalising all calibration data with respect to an empirical model

based on Test 7.

(9) Crack depth prediction based on empirical normalisation is possible in the case of EN3BN provided two pairs of calibration data points are known. When applied to a sample of the present calibration data, 30 crack depths were predicted to within an accuracy of 2.7%.

10.7 Recommendations for Further Work

(1) Using the present fatigue crack growth calibration data and Computer Programme Gandalf presented in Appendix A9, determine the most appropriate calibration model for empirical normalisation.

(2) Sensitivity of the Testwell ACPD2 system is dependent on sensing probe position. Evaluate optimum sensing probe position.

(3) Determine calibration response using the modified Testwell pre-amp system and relate this to PD_{AB} and PD_{CD}.

(4) Determine whether empirical normalisation can be extended to other materials.

10.8 References

[10.01] Birchak, J.R.,
Proc. 10th Symp. on N.D.E. San Antonio 1973.

[10.02] Tada, H., Paris, P., and Irwin, G.,
'The Stress Analysis of Cracks Handbook'
Del Research Corporation, Hellertown, Pennsylvania,
1973, pp 216.

[10.03] Private communication with D. Mann of Testwell Ltd.,

[10.04] Testwell Ltd.,
Tech. Memo, 126.

[10.05] Wei, and Brazill,
'The measurement of crack length and shape during
fracture and fatigue', pp 190, EMAS 1980.

[10.06] Betz, U.,
Materialprufing, 1972, 14, pp 73.

CHAPTER ELEVEN

FATIGUE CRACK GROWTH IN STEEL

11.0 Nomenclature

fcg	=	fatigue crack growth
SEN	=	single edge notch
ΔK	=	applied stress intensity range
a	=	crack length measured in the specimen width direction
w	=	specimen width
P	=	load
P_{open}	=	crack tip opening load
ΔK_{eff}	=	effective stress intensity range ($K_{max}-K_{open}$)
$\Delta K_{eff.Ti}$	=	effective stress intensity range corresponding to ΔK_{Ti}
K_{max}	=	maximum crack tip stress intensity
K_{min}	=	minimum crack tip stress intensity
K_{open}	=	crack tip opening stress intensity
ACPD	=	alternating current potential difference
ΔK_{Ti}	=	load shedding fcg threshold stress intensity range
ΔK_{To}	=	post threshold fcg threshold stress intensity range
R	=	stress ratio (K_{min}/K_{max})
RMS a	=	standard residual error expressed in terms of a
ΔK_T	=	threshold stress intensity range
COD	=	crack opening displacement
COD_{min}	=	minimum crack opening displacement

11.1 Introduction

The aim of the research of this investigation was to study the near threshold fatigue behaviour of materials EN19QH, EN3BN and EN3BA. Effects of crack length, stress ratio and microstructure on threshold stress intensity range were related to crack tip opening behaviour, and a special crack closure study of threshold testing was conducted to illustrate the closure response to fatigue testing at low growth rates.

These objectives were achieved by subjecting precracked fatigue specimens to fatigue using an Amsler Vibrophore Fatigue Machine. Crack lengths were measured using the ACPD system described in Chapter 10, and crack tip opening loads were determined using an Elber side face strain gauge technique.

All results were subject to traditional linear elastic fracture mechanics and a semi quantitative analysis of crack tip opening load behaviour was used to explain near threshold trends.

11.2 Experimental Techniques

11.2.1 Fatigue Testing

11.2.1.1 Introduction

Fatigue crack growth studies were conducted using a solid state 20 KN Amsler Vibrophone Fatigue Machine equipped with a 20 KN dynometer operating between 140 ± 5 Hz. All specimens were tested in air at 21 ±1°C in three point bend using a specially designed jig

set to a span to width ratio of 4:1, Fig. 11.01. Stress intensity factors for this testing mode were calculated using the compliance functions given by Tada et al [11.01].

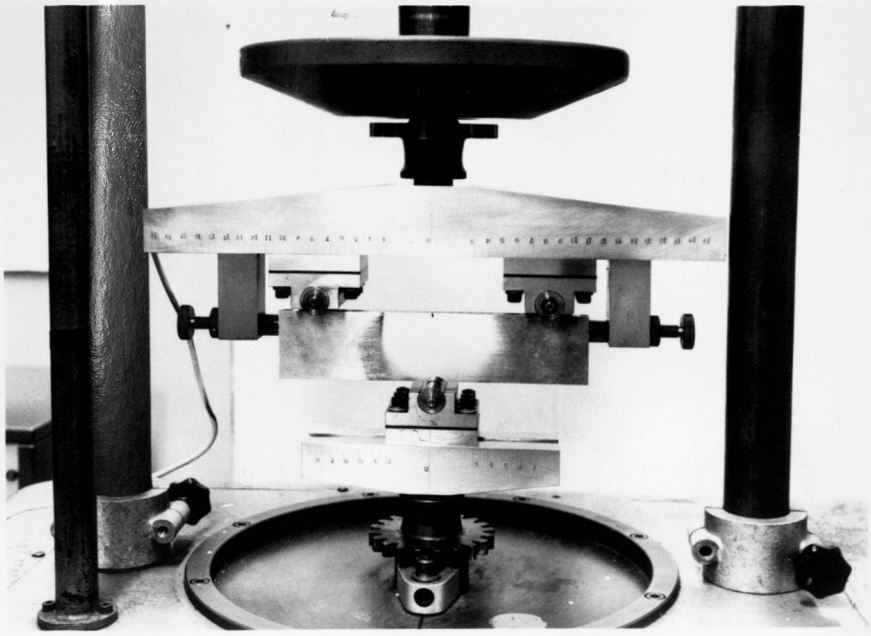
11.2.1.2 Specimen Details and Precracking

From the centre of each heat treatment blank (Section 9.2) a standard SEN fatigue specimen was machined, ground and polished to dimensions shown in Fig. 11.02(a). This was then precracked by fatigue at R = 0.1 and ΔK = 20.0 $MPam^{\frac{1}{2}}$, and subject to a 10% load reduction sequence until ΔK = 10.0 $MPam^{\frac{1}{2}}$. During each load reduction stage crack growth was allowed to exceed twice the plain strain maximum plastic zone size of the previous maximum load given by Eq. 2.07. On achieving an average surface crack length of 8.0 to 11.0 mm the precrack was then progressively machined away to leave a short remenant through section crack of approximately 1mm in length. Final dimensions were then ground and polished to 10 mm x 40 mm x 220 mm, Fig. 11.02 (b).

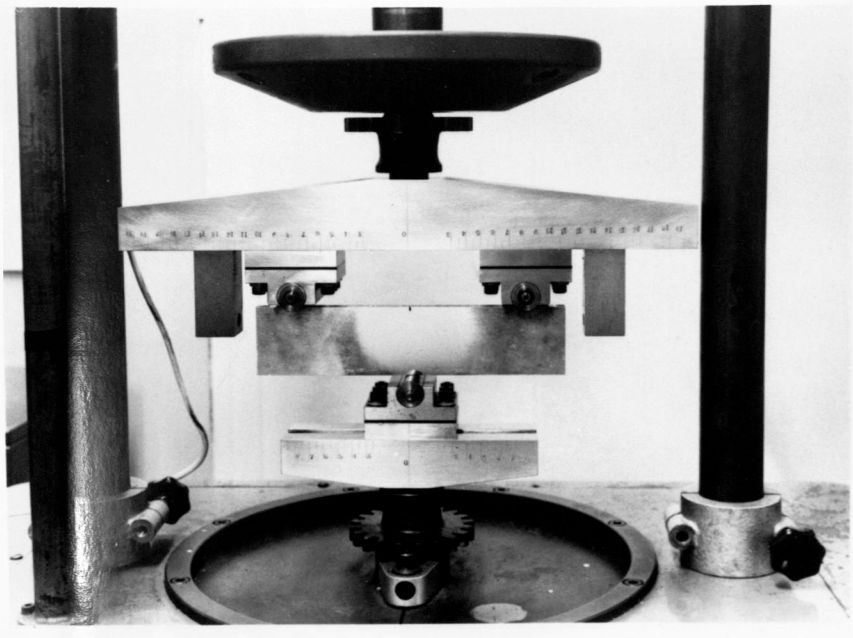
11.2.1.3 Fatigue Crack Growth and Threshold Testing

The procedure adopted for threshold testing was based on the recommendation of ASTM [11.02]. To achieve the proposed objectives this was punctuated by three levels of crack tip opening load measurement more fully described in Section 11.3. Only the basic procedure relating to load versus fcg is given below.

The problem of initiating a fatigue crack from the starter crack configuration and achieving the threshold growth condition presented no real difficulties. Crack initiation was conducted by



(a)



(b)

Fig. 11.01 Two photographs showing :

(a) specimen alignment; and

(b) fatigue configuration

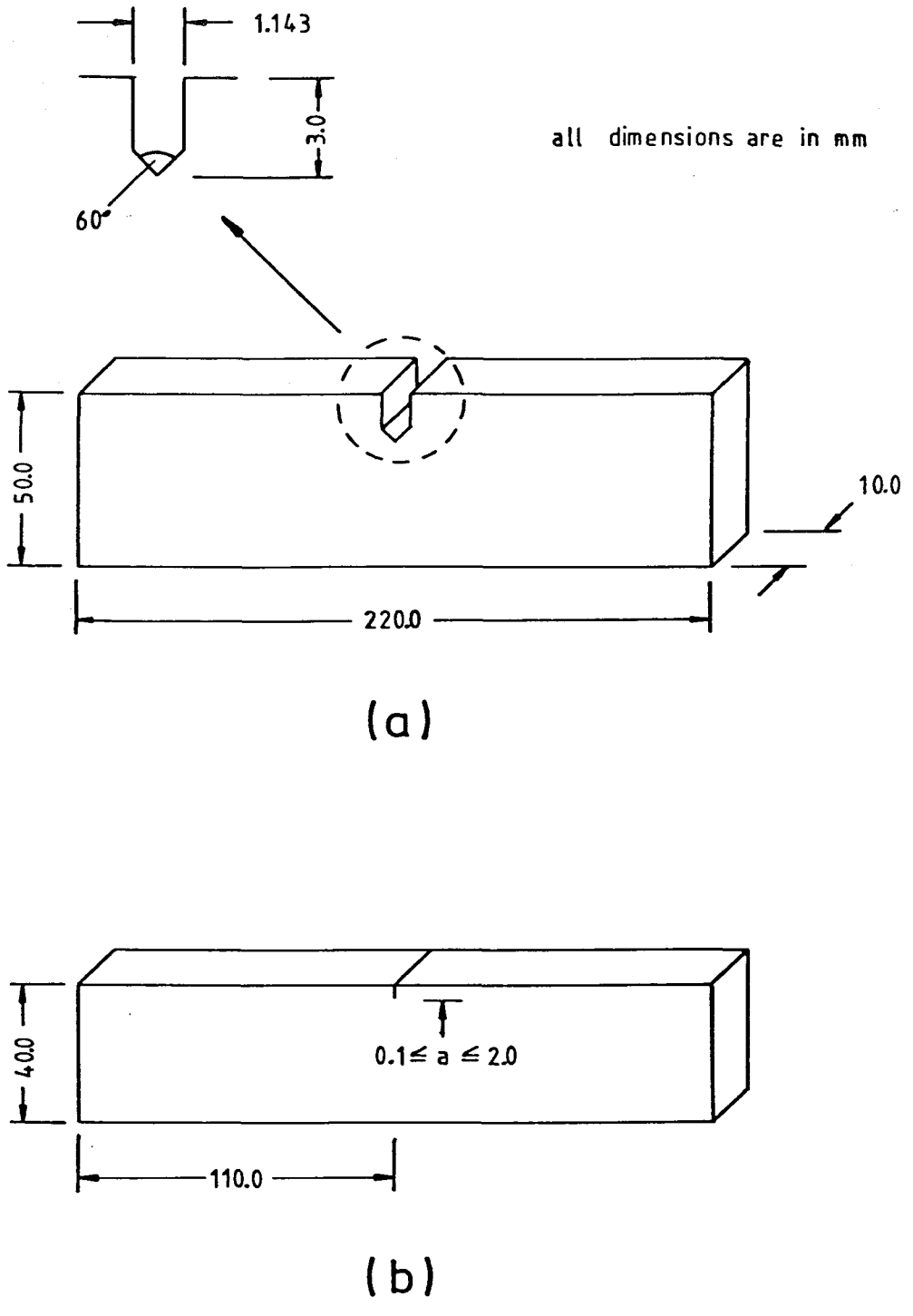


Fig. 11.02 Specimen dimensions

(a) SEN configuration

(b) Precracked configuration

increasing load range (at constant R) until a crack growth rate of $\geqslant 1 \times 10^{-6}$ mm/cycle was achieved. Growth was then allowed to continue under constant load conditions (constant load fcg).

At a prechosen crack length the threshold step down sequence (load shedding fcg) was initiated by adopting the 10% load reduction procedure described in Section 11.2.1.2. On achieving a growth rate of approximately 10^{-6} mm/cycle further load shedding decrements were reduced to 0.2 to 0.5 ΔK and growth was allowed to continue until a reduced load level produced no further growth during 10^{7} cycles. This condition was defined as the decreasing load fcg threshold, ΔK_{Ti}, and corresponded to a growth rate of 10^{-9} mm/cycle.

On attaining ΔK_{Ti} the process was reversed and growth was monitored over 10^{6} cycles. If no growth occurred during this period, or some initial crack growth had ceased, the load range was increased. Eventually, at some increased load range, rapid crack propagation occurred and was allowed to proceed under constant load conditions (post threshold fcg). The post threshold fcg threshold stress intensity range (ΔK_{To}) was defined by a no measurable growth condition corresponding to 10^{-8} mm/cycle.

11.2.2 Crack Length Measurement and Accuracy

The ACPD system described in Chapter 10 was employed to accurately and conveniently monitor crack growth. This was incorporated into the testing program as discussed in Section 10.2.2. and used at a voltage gain of 10^{4}. Use of the higher gain was made possible by a modification of the existing circuitry. This imparted no detrimental effects in detector response, but increased stability and lowered noise.

Excessive fracture surface oxidation made it impractical to relate ACPD to specific crack wavefronts and empirically normalise as described in Section 10.5.4. ACPD was therefore related to average surface crack length measured optically to an accuracy of ± 0.02 mm using a travelling vernier microscope. A total of at least eight pairs of data points collected throughout each test were then subject to a Chebyshev degree 2 polynomial curvefit as described in Appendix A8. Crack lengths corresponding to specific voltages were then generated accordingly.

This approach produced consistent calibration data for all three materials, Figs. 11.03 and 11.04, enabling crack lengths to be computed to within ± 0.15 mm, Table 11.01. Maximum resolution was dependent on crack length and approached the level of electrical drift, i.e. ± 0.005 mm.

Errors in crack length arising from crack bowing were difficult to quantify without precise fracture surface markings. However, from X10 enlarged fracture surface prints it was estimated that average surface crack length was an underestimate of maximum crack length by 5% at $a/w = 0.09$ to 1% at $a/w = 0.68$.

Standard error analysis [11.03] of the errors associated with crack length determination produced an increase in the above estimates to 9% at $a/w = 0.09$ and 2% at $a/w = 0.68$.

11.2.3 Evaluation of Growth Rate Results

The raw data from each test took the form of a number of potential versus cycle traces. These were analysed to give pairs of potential difference readings corresponding to a specific number of stress cycles.

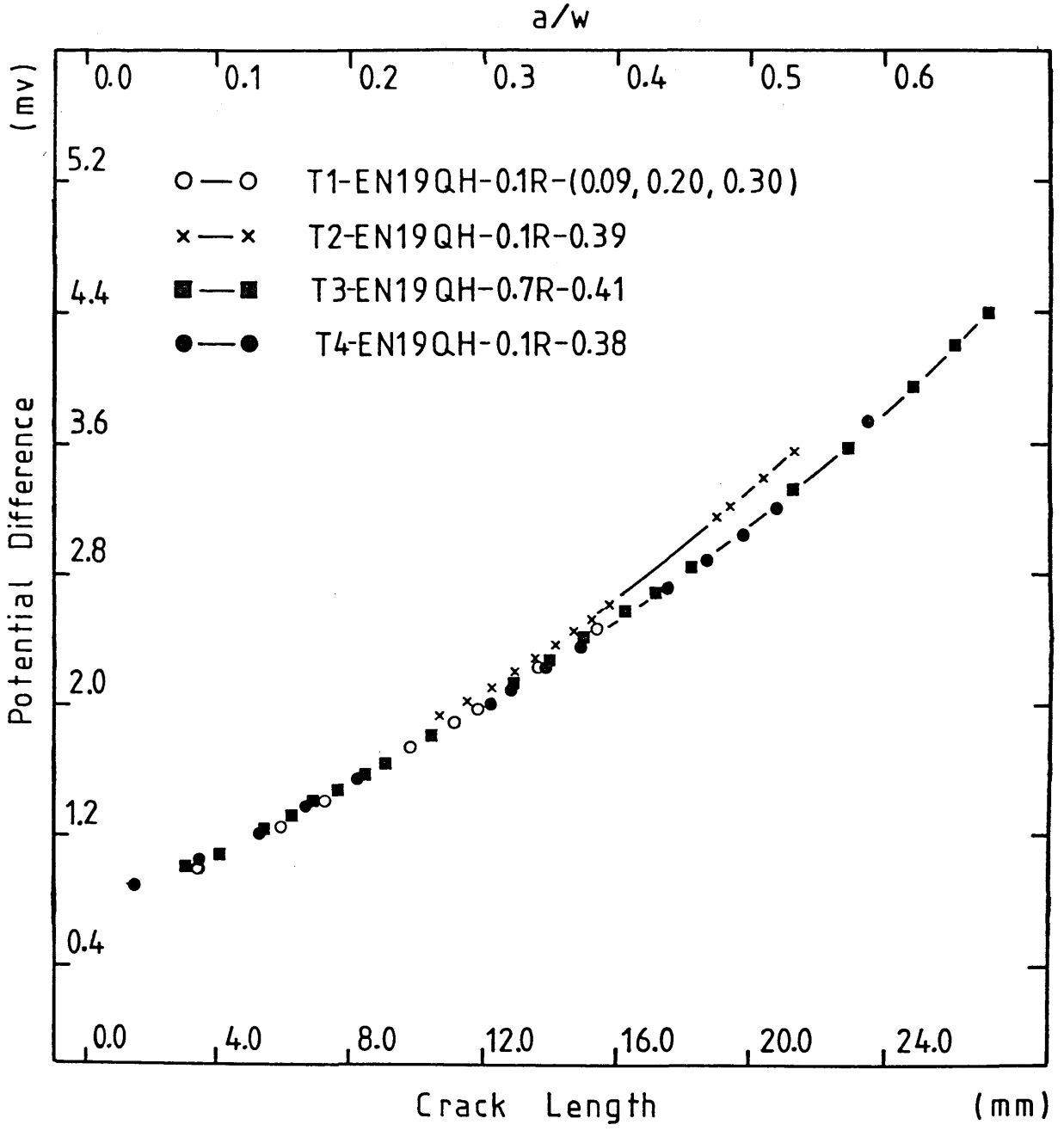


Fig. 11.03 Potential Difference versus Crack Length of EN19QH

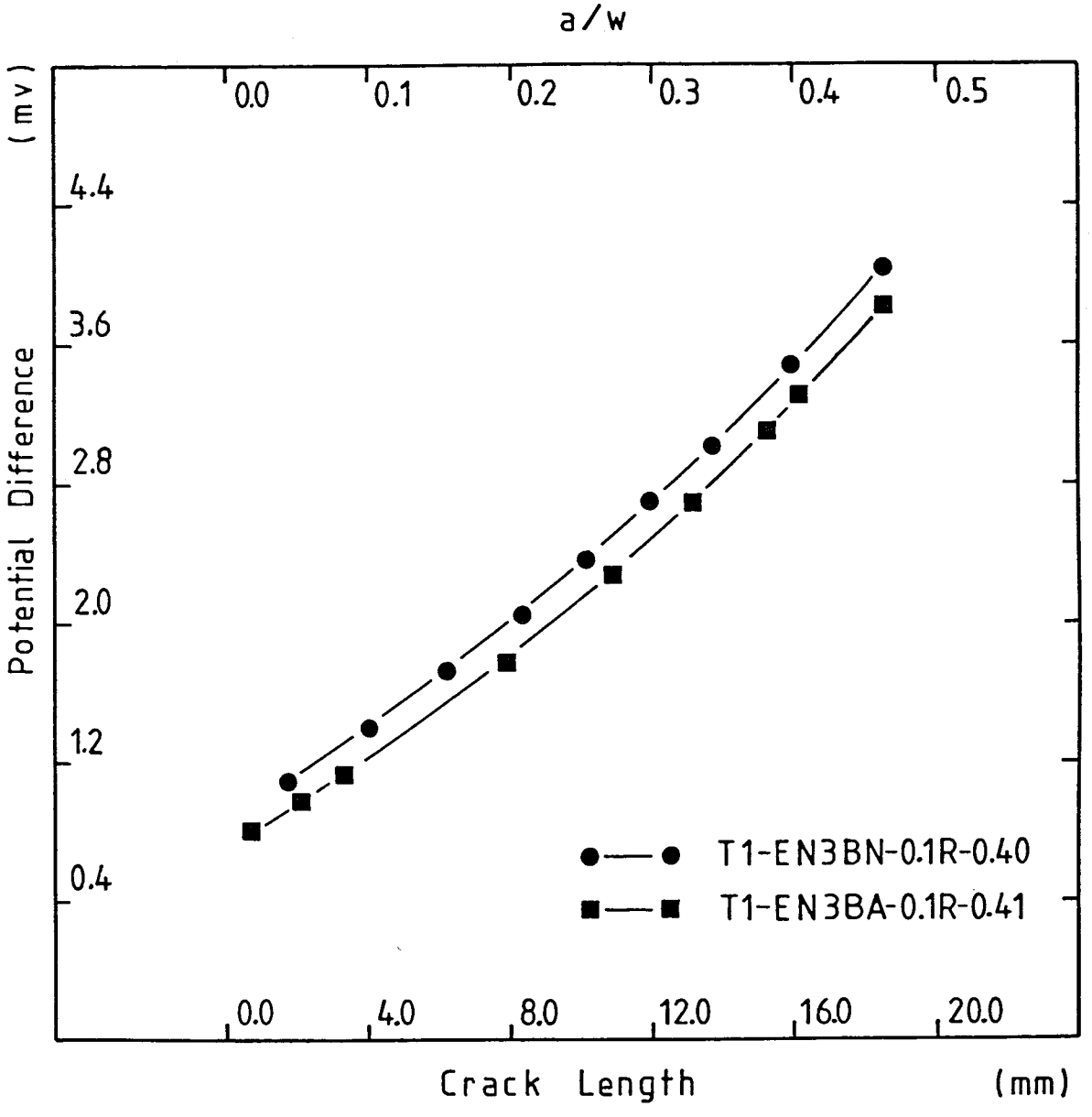


Fig. 11.04 Potential Difference versus Crack Length of EN3BN and EN3BA

TABLE 11.01

Chebyshev Degree 2 Polynomial Curve Fit Analysis describing the Fatigue Crack Growth ACPD Calibration Results.

Material	Test	Accuracy RMS a (mm)	Maximum Resolution (mm)	
			a/w = 0.1	a.w = 0.6
EN19QH	T1-EN19QH-0.1R-(0.09, 0.20, 0.30)	0.08	0.009	0.007
	T2-EN19QH-0.1R-0.38	0.07	-	0.006
	T3-EN19QH-0.7R-0.41	0.05	0.008	0.007
	T4-EN19QH-0.1R-0.38	0.15	0.010	0.007
EN3BN	T1-EN3BN-0.1R-0.40	0.05	0.007	0.004
EN3BA	T1-EN3BA-0.1R-0.41	0.08	0.007	0.004

From the appropriate Chebyshev degree 2 polynomial formula describing the ACPD versus crack length calibration response, crack lengths were computed and stress intensity factors corresponding to specific growth rates were generated as described in Appendix A10.

11.2.4 Accuracy of Growth Rate Results

The major sources of error in ΔK arose mainly from the measurement of crack length. From the conservative estimate of Section 11.2.2 accuracy of crack length was found to range from 9% at $a/w = 0.09$ to 2% at $a/w = 0.68$. Errors in compliance function induced through crack length were minimal, ranging from 1% at $a/w = 0.09$ to 2% at $a/w = 0.68$.

Errors resulting from applied loads were small. Maximum and minimum load levels were maintained using a 20 KN dynanometer to an accuracy of ± 10 N. All growth rates were conducted using at least 10% of the full scale load range, which meant that the accuracy in load maintanance was within 0.5%. During fatigue testing at $R = 0.1$ and $R = 0.7$ the maximum error in load amplitude ranged from 1 to 2% respectively.

Accounting for all the above errors the overall accuracy in ΔK was estimated to vary from 3% to 10% depending on crack length and load amplitude.

The error involved in growth rate determination was estimated along similar lines. Here again the major dominating factor was the uncertainty in crack length. By adopting a pessimistic approach and combining the error in crack length determined at $a/w = 0.09$ with a 1% maximum error in cycles counting, the maximum error in da/dn for $0.09 \leqslant a/w \leqslant 0.68$ was less than 10%.

11.2.5 Crack Closure Measurement

11.2.5.1 Measurement of Crack Tip Opening Load

In an attempt to analyse growth rate data from a ΔK_{eff} viewpoint crack tip opening loads were determined using a side face strain gauge change in compliance technique [11.04]. This involved attaching a 120 ohm strain gauge across the crack tip (the latter being held in three point bend at an applied load of 100N) which was incorporated into the quarter bridge arrangement of a Vishay/Ellis-2A Digital Strain Gauge Indicator, Fig. 11.05. After allowing 24 hours for the adhesive to set the gauge was balanced, and the specimen was sequentially loaded in three point bend to the maximum fatigue load. Readings of microstrain generated at 50 N intervals were then related to applied load, Fig. 11.06, and an estimate of crack tip opening load was computed to an accuracy of 5%, Fig. 11.07.

11.2.5.2 Treatment of Results (determination of K_{open})

Initially a plot of P_{open} versus a/w was constructed and a best fit curve was drawn through the available data. From this response values of P_{open} corresponding to specific growth rates were computed and used to determine respective values of K_{open}. ΔK_{eff} was then calculated using the formula

$$\Delta K_{eff} = K_{max} - K_{open} \qquad \ldots(11.01)$$

This approach was adopted for the following reasons:

(a) crack tip opening loads determined at specific crack lengths could not be accurately related to an average growth rate occurring over that crack length;

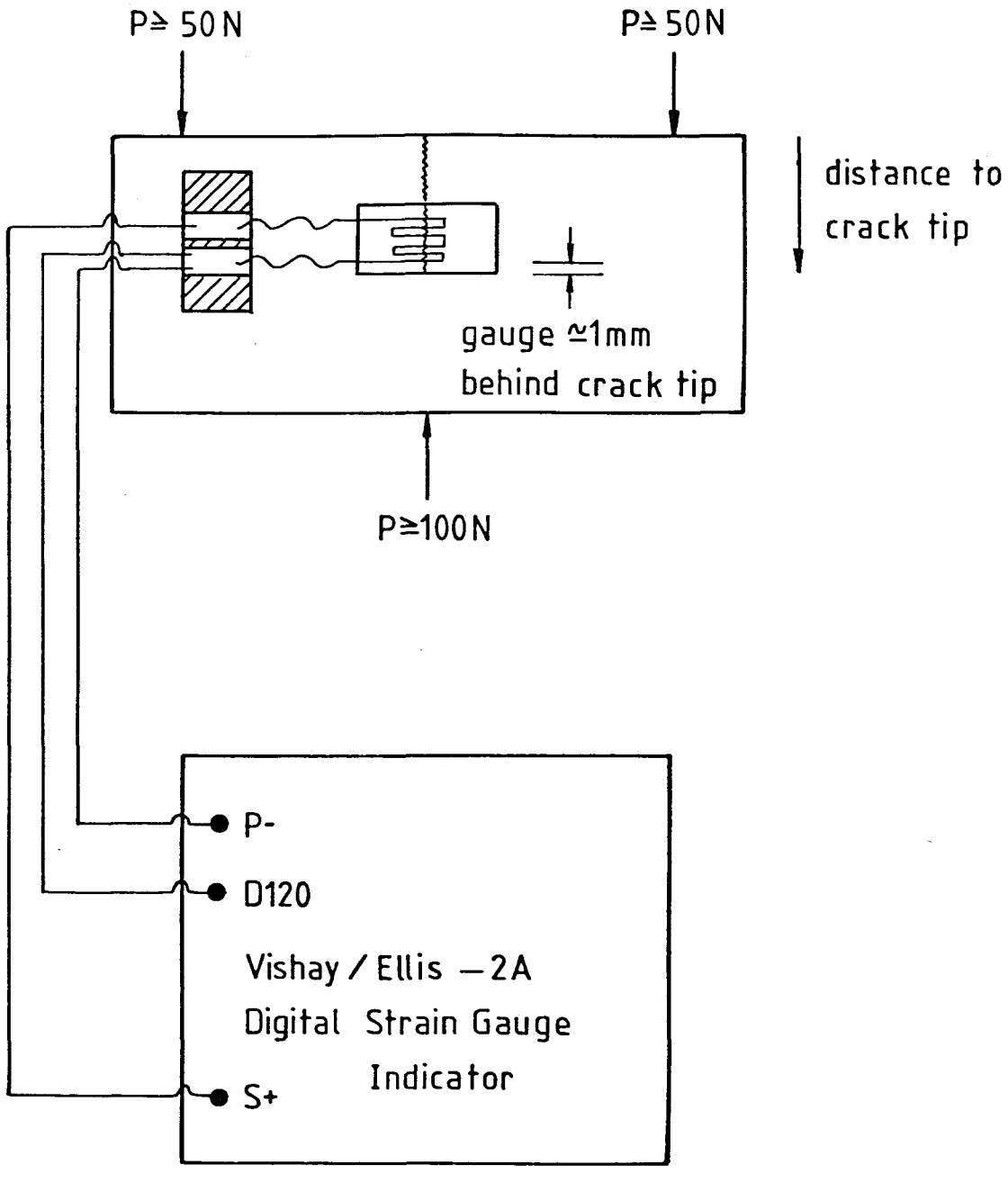


Fig. 11.05 Strain gauge arrangement

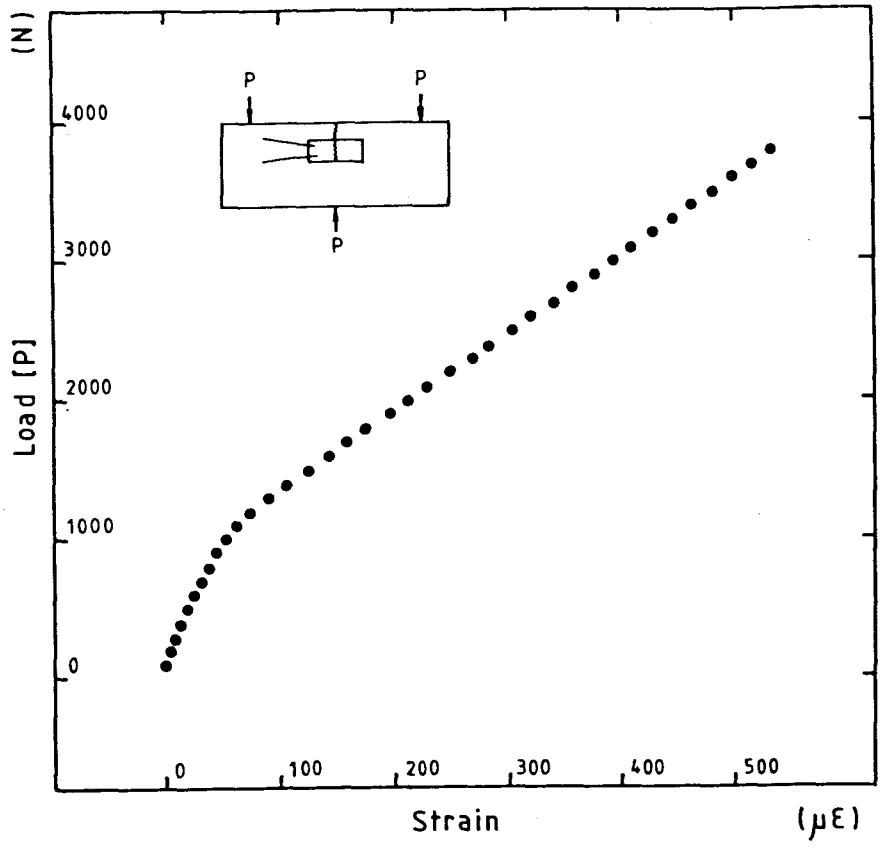
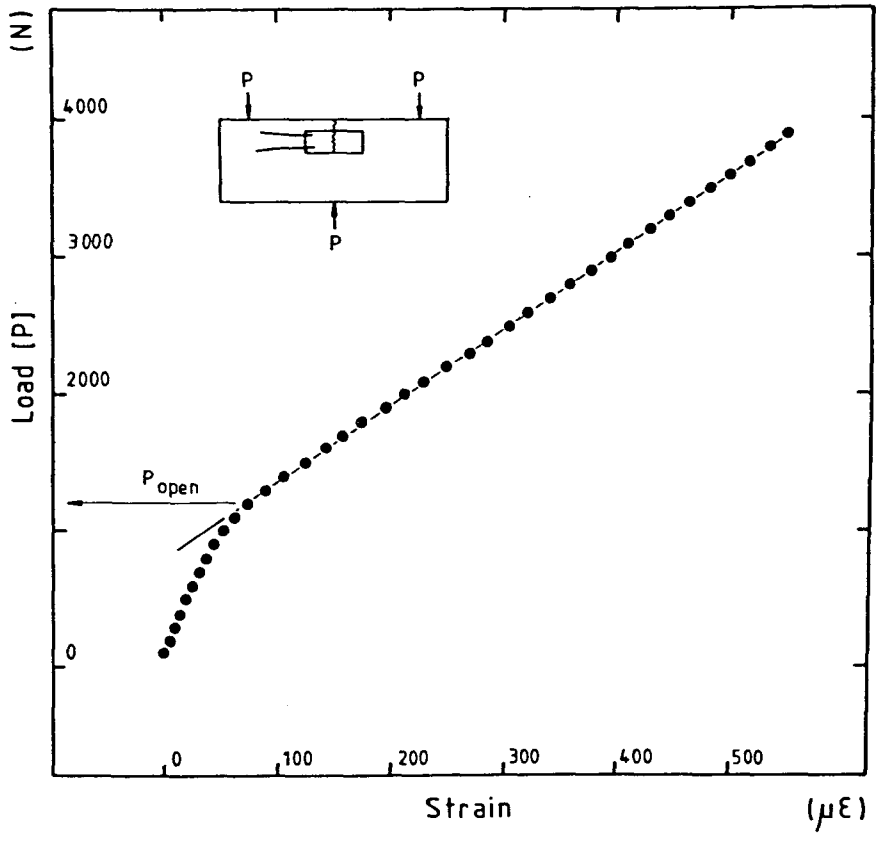


Fig. 11.06 Typical load versus strain gauge response.



Type. 11.07 Determination of P_{open}

(b) during constant fcg growth rates immediately proceeding the determination of P_{open} were in many instances momentarily reduced; and

(c) this method offered the irresitable advantage of smoothing out the errors in P_{open} whilst still providing a representative trend in closure response.

Accuracy of the predicted values of ΔK_{eff} was obviously of major concern. In the worst possible threshold case this was estimated to be 13%. A general conservative estimate of the error in ΔK_{eff} was therefore increased to 20%.

11.2.6 Crack Profile Replication and Examination

During each test surface crack profiles were examined indirectly through replication at a number of static loads. This was achieved by moistening a small piece of cellulose acetate sheet approximately 2 mm thick with acetone and then pressing it onto the test piece over the crack length. After the surface of the cellulose sheet had hardened, which took approximately 10 minutes, it was removed and the negative crack profile replica was examined optically using a Zeiss Ultraphot II Photomicroscope. For closer examination in the scanning electron microscope the replicated surface was sputter coated with a thin layer of gold approximately 4 nm thick. Copper was then electroplated onto the back to provide support and a positive replica was obtained by carefully removing the acetate sheet.

All specimens were then mounted on a micrometer controlled stage and examined using a Philips SEM 500 at a tilt angle of 0^{o}.

11.2.7 Fractography

Fractographic studies of broken test pieces were conducted using either a Cambridge Stereoscan 600 or a ISI 100A Scanning Electron Microscope. All specimens were mounted on a micrometer controlled stage which allowed crack lengths to be located to within ± 0.05 mm. Each centre section was then examined at 1mm intervals using a test angle of 45^{o}.

11.3 Experimental Program

To achieve the desired objectives outlined in Section 11.1 A series of eight threshold tests were conducted in materials EN19QH, EN3BN and EN3BA, Table 11.02. Fatigue testing was conducted as detailed in Section 11.21 and crack closure was monitored at one of the following levels.

Low (L). Crack tip opening loads were determined after ΔK_{Ti} had been achieved and at the end of increased load fcg. Overall process time was 11 days (9 fcg days plus 2 dormant days).

Medium (M). Crack tip opening loads were determined on the attainment of ΔK_{Ti} and throughout the increased load fcg sequence. Total process time was 16 days (11 fcg days plus 5 dormant days).

High (H). Crack tip opening loads were determined at regular intervals throughout the entire test. Total process time was 35 days (15 fcg days plus 20 dormant days).

TABLE 11.02

Details of Experimental Program

Material	Major Objectives		Other Objectives	Test/Specimen	R	Threshold a/w	Closure Level
EN19QH	study R effect on threshold	study a/w effect on threshold	crack closure study	T1-EN19QH-0.1R-(0.09, 0.20, 0.30) — T1-EN19QH-0.1R-0.09	0.1	0.09	M
				T1-EN19QH-0.1R-(0.09, 0.20, 0.30) — T1-EN19QH-0.1R-0.20		0.20	L
				T1-EN19QH-0.1R-(0.09, 0.20, 0.30) — T1-EN19QH-0.1R-0.30		0.30	L
			crack closure study	T2-EN19-0.1R-0.39		0.39	M
				T3-EN19-0.7R-0.41	0.7	0.41	L
	special crack closure study			T4-EN19-0.1R-0.38	0.1	0.38	H
EN3BN	determine microstructural effect on threshold		crack closure study	T1-EN3BN-0.1R-0.40		0.40	M
EN3BA			special crack closure study	T1-EN3BA-0.1R-0.41		0.41	H

NOTE: L, M, H represent crack tip opening loads determined — at threshold and the end of post threshold crack growth; at threshold and during post threshold crack growth; throughout the entire test

11.4 Results

11.4.1 Fatigue of Quenched and Hardened Martensitic Steel EN19QH

11.4.1.1 Crack Length Effects on Near Threshold Fatigue Crack Growth (R = 0.1)

11.4.1.1a Growth Rate Results

The fcg response to threshold testing conducted at threshold a/w ratios 0.09, 0.20, 0.30 and 0.39 displayed similar trends, Figs. 11.08 to 11.11. Near threshold crack growth exhibited threshold hysteresis and during the initial stages of post threshold fcg a rapid return to intermediate growth rates occurred over small increases of ΔK.

Near threshold fcg of tests conducted at threshold a/w ratios 0.20 and 0.30 differed slightly from those at 0.09 and 0.39. During the load shedding threshold approach sequence fcg was irregular and initial post threshold crack growth was rapidly terminated at higher ΔK's.

Combining all the results in a single plot, Fig. 11.12, illustrated that near threshold fcg subscribed a threshold hysteresis envelope ranging from ΔK = 5.8 to 9.1 $MPam^{-\frac{1}{2}}$ at $da/dn \leqslant 10^{-8}$ mm/cycle.

The effect of crack length on threshold stress intensity ranges ΔK_{Ti} and ΔK_{To} was minimal and lay within the limits of accuracy of experimental technique. Both sets of data were contained within scatter bands ranging from 5.8 to 6.7 $MPam^{\frac{1}{2}}$ and 8.1 to 9.1 $MPam^{-\frac{1}{2}}$ respectively with a minimum and maximum seperation of 2.0 to 2.7 $MPam^{-\frac{1}{2}}$, Fig. 11.13.

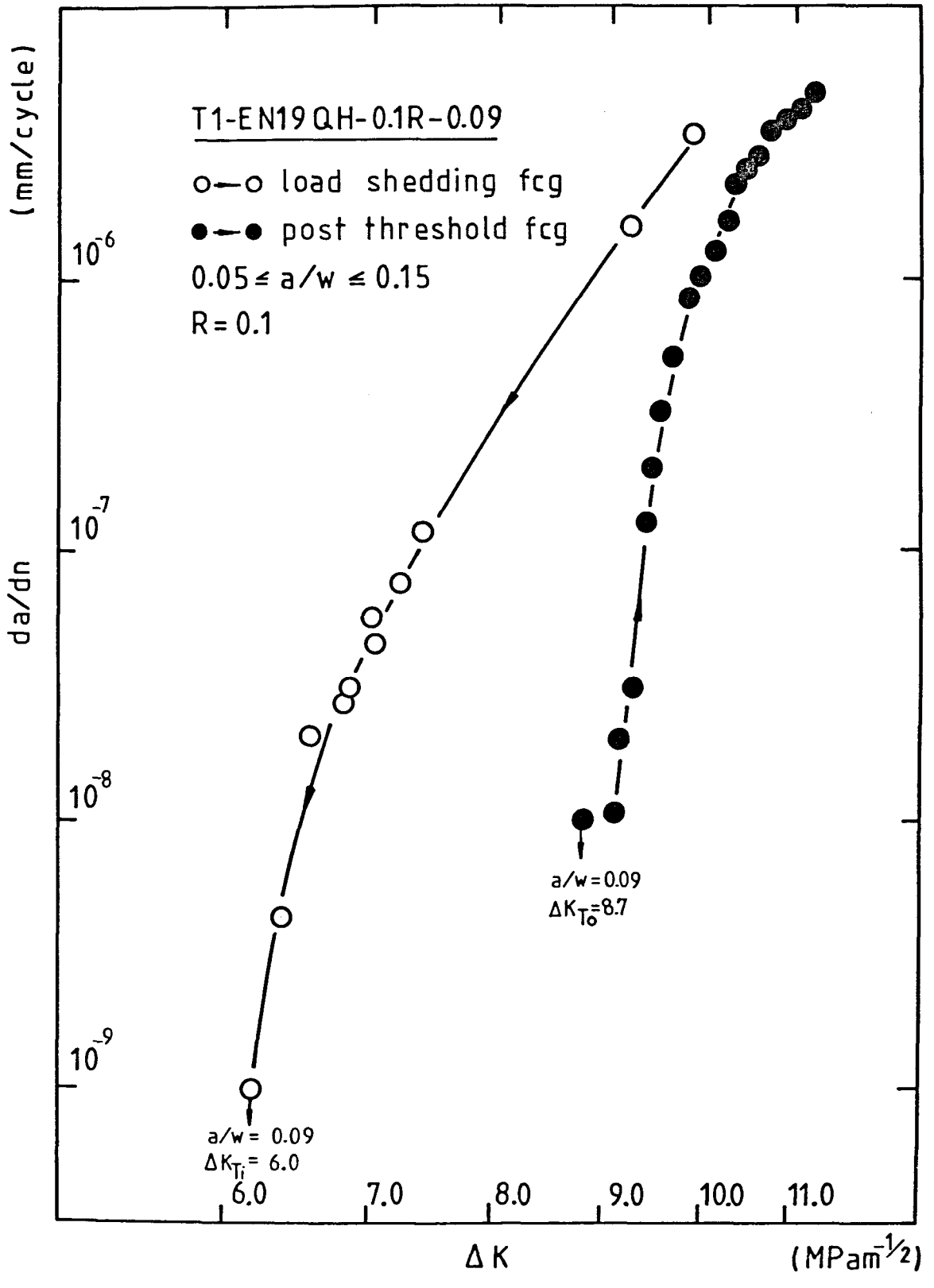


Fig. 11.08 A double logarithm plot of da/dn versus ΔK of EN19QH exhibiting threshold hysteresis. (threshold a/w = 0.09)

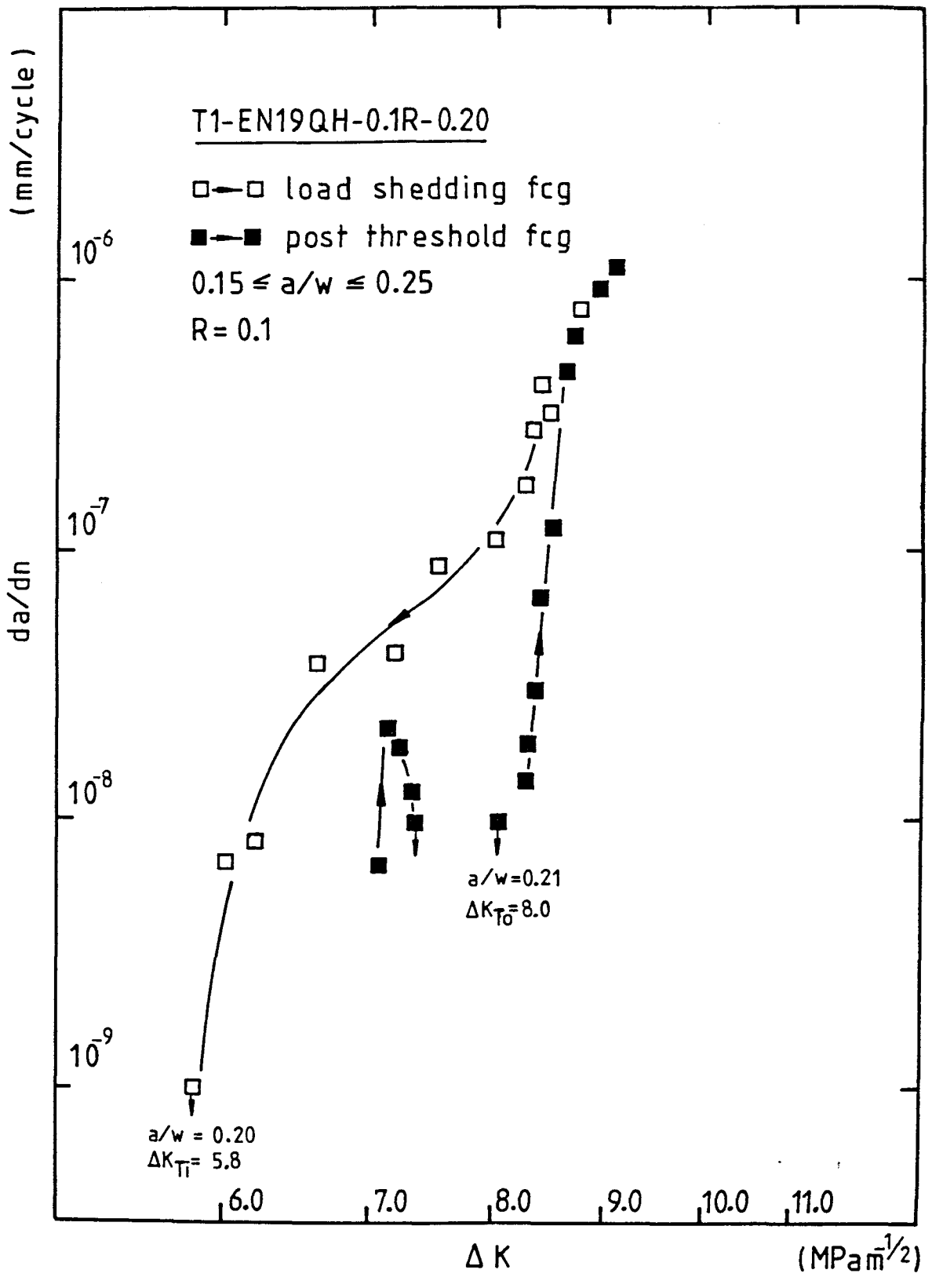


Fig. 11.09 A double logarithm plot of da/dn versus ΔK of EN19QH exhibiting threshold hysteresis. (threshold a/w = 0.20)

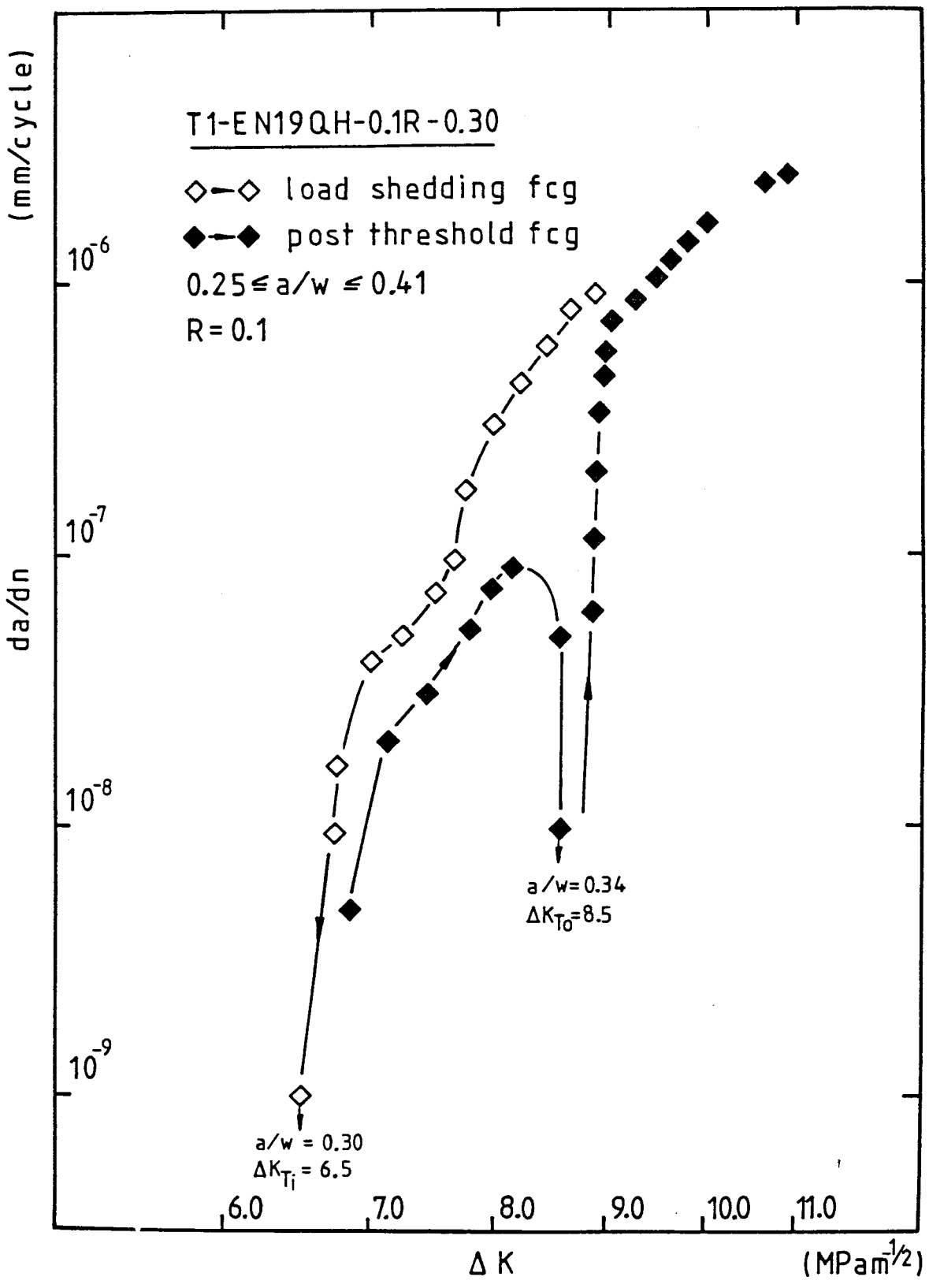


Fig. 11.10 A double logarithm plot of da/dn versus ΔK of EN19QH exhibiting threshold hysteresis. (threshold a/w = 0.30)

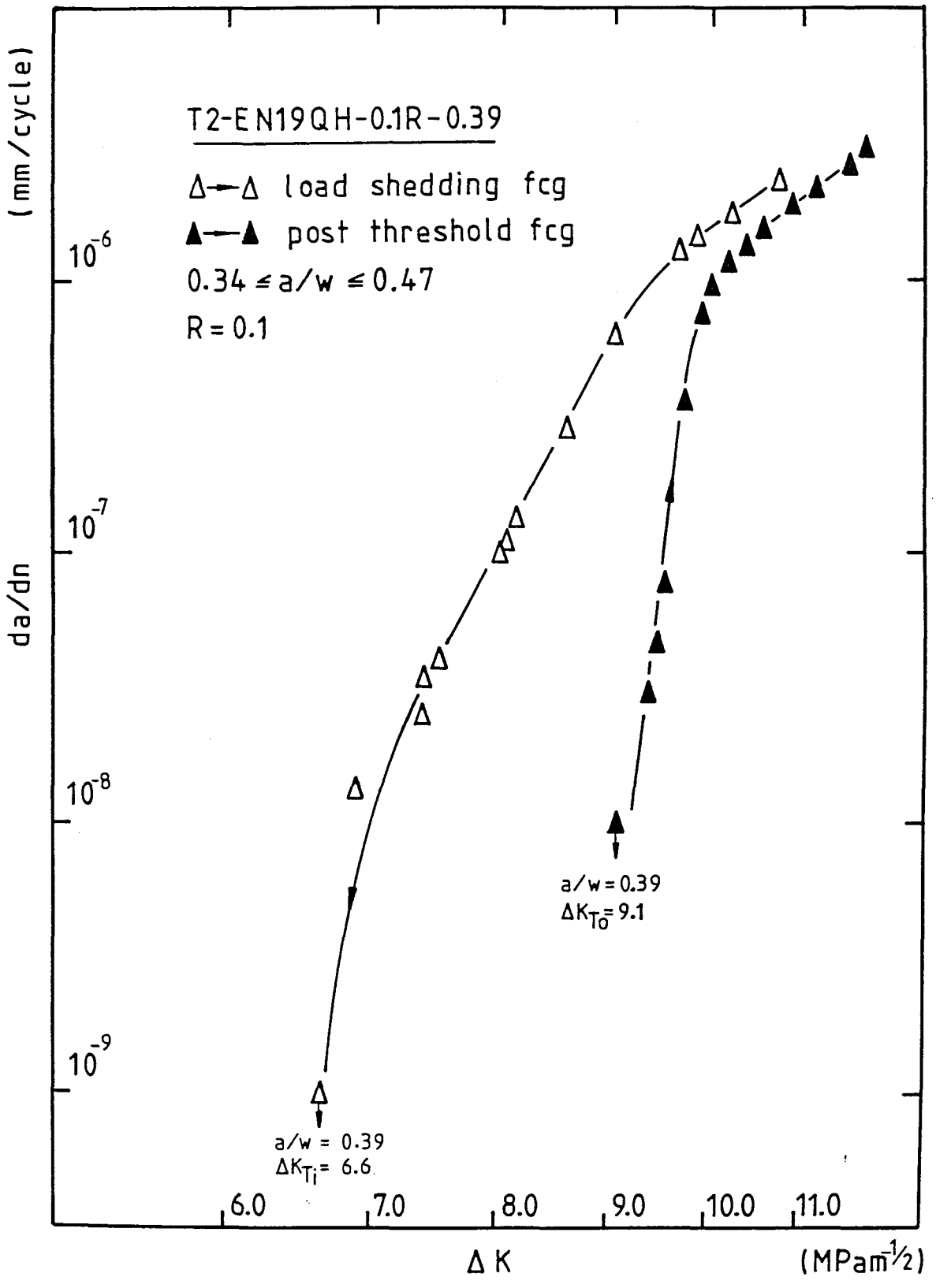


Fig. 11.11 A double logarithm plot of da/dn versus ΔK of EN19QH exhibiting threshold hysteresis. (threshold a/w = 0.39)

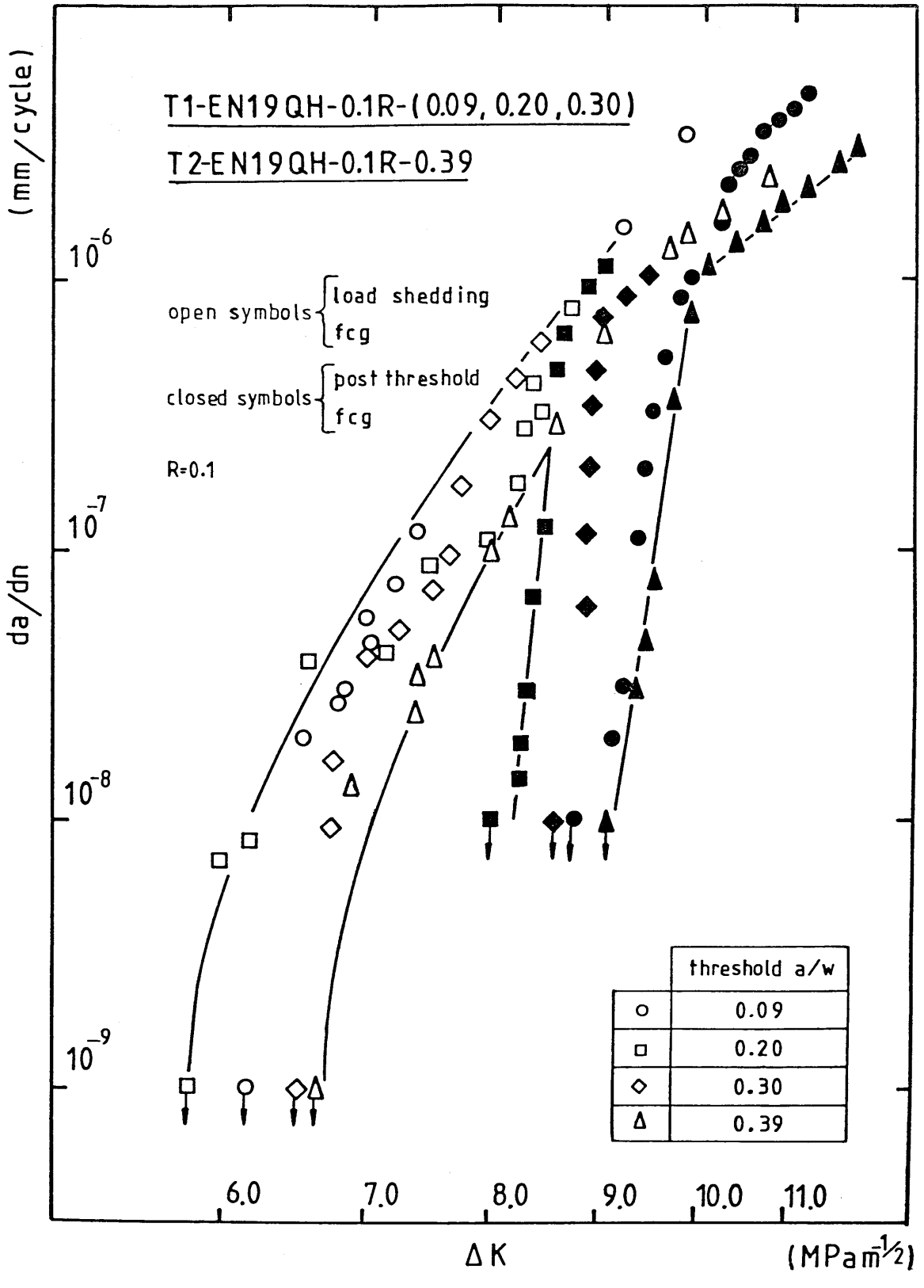


Fig. 11.12 A double logarithm plot of da/dn versus ΔK summarising the near threshold growth behaviour of EN19QH.

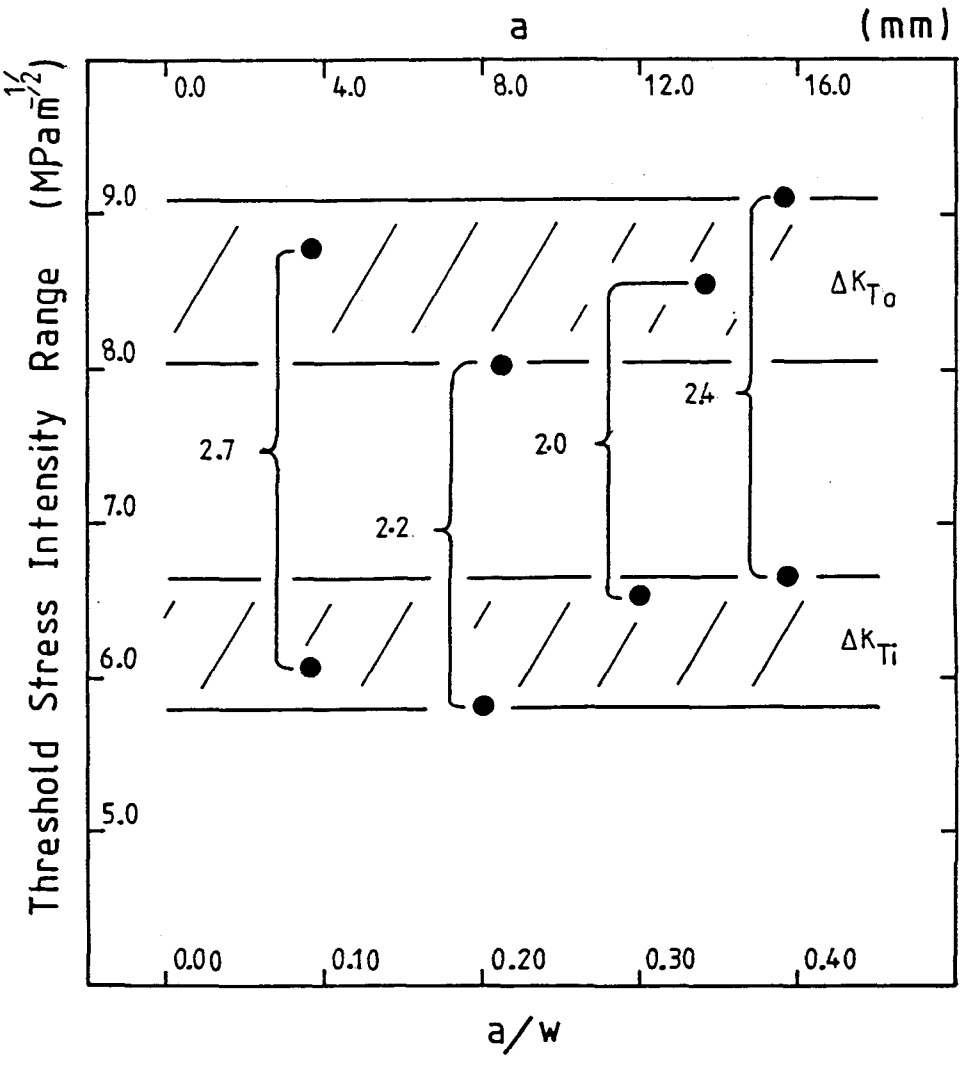


Fig. 11.13 A plot of Threshold Stress Intensity Range (ΔK_{Ti} and ΔK_{To}) versus a/w of EN19QH determined at a/w ratios 0.09, 0.20, 0.30 and 0.39.

R = 0.1.

11.4.1.1b Crack Tip Opening Loads, Stress Intensities and ΔK_{eff} Analysis of Results

The crack tip opening load response to threshold testing of T1-EN19QH-0.1R- (0.09, 0.20, 0.30) expressed as a function of a/w exhibited a general decrease in crack tip opening load with increased crack length, Fig. 11.14. For positions A, B and C which mark the end of post threshold crack growth, and D, E and F of the threshold condition ΔK_{Ti}, K_{open} was consistent and constant irrespective of a/w regime, Fig. 11.15(a). A plot of ΔK versus K_{open} also revealed there existed a correlation between the two variables as shown in Fig. 11.15(b).

Crack tip opening load response to threshold crack arrest and post threshold fcg of fatigue studies conducted at threshold a/w ratios 0.09 and 0.39 disclosed that associated with threshold hysteresis was an increase and decay in crack tip opening load, Figs. 11.16 and 11.17. Analysis of this behaviour in terms of crack tip stress intensities revealed a similar trend in K_{open}, Figs. 11.18 and 11.19. ΔK_{eff} analysis of growth rates, Figs. 11.20 and 11.21, illustrated that post threshold fcg was suitably aligned with that of $\Delta K_{eff.Ti}$.

Presentation of all avaliable ΔK_{eff} growth data produced the normalised plot of Fig. 11.22.

11.4.1.2 Stress Ratio Effect on Near Threshold Fatigue Crack Growth (R = 0.7)

11.4.1.2a Growth Rate Results

The fatigue response of material EN19QH tested at R = 0.7 did

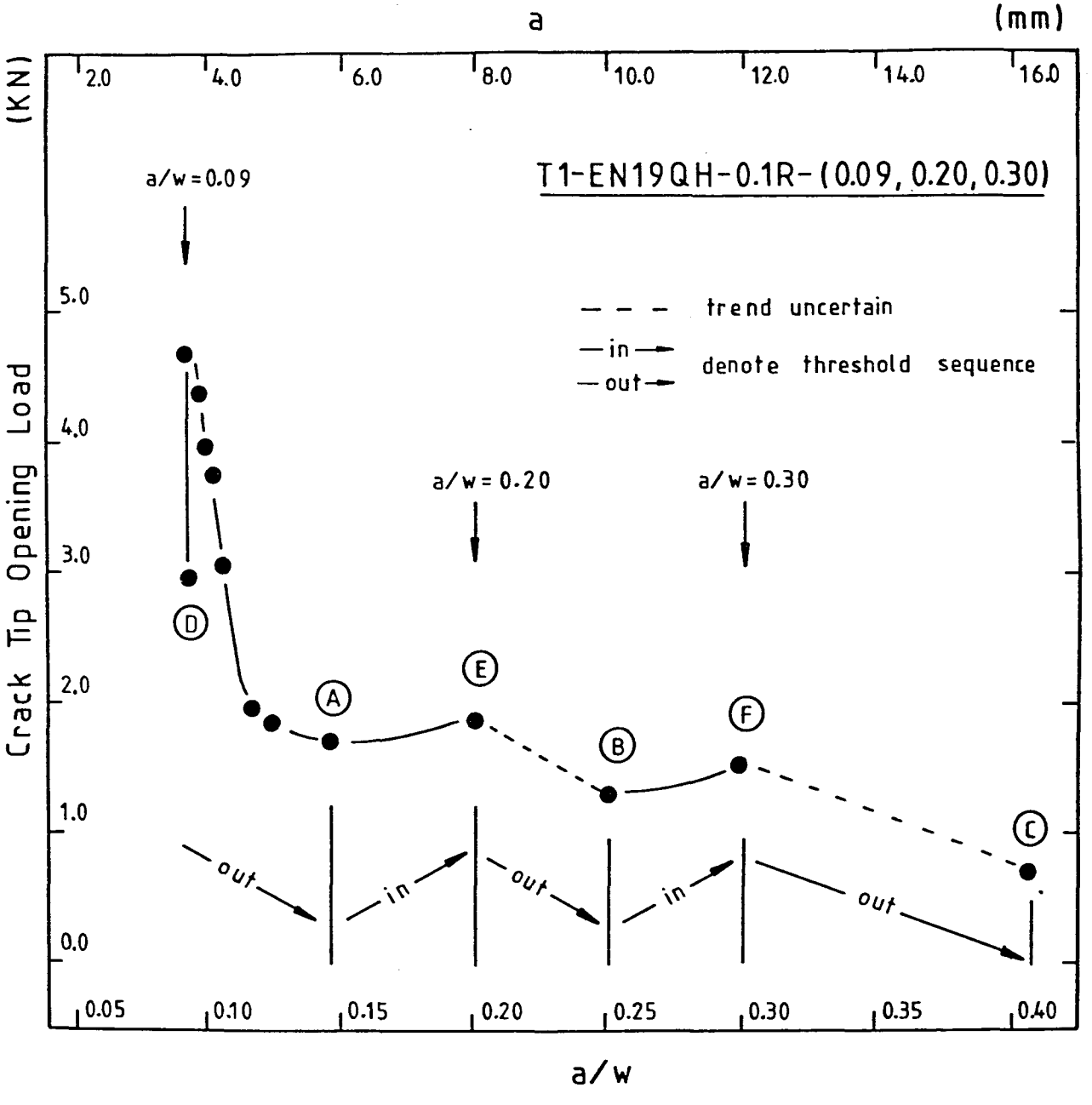


Fig. 11.14 A plot of Crack Tip Opening Load versus a/w of T1-EN19QH-0.1R-(0.09, 0.20, 0.30).

Positions A, B and C indicate the end of post threshold fcg, and D, E and F the ΔK_{Ti} threshold positions.

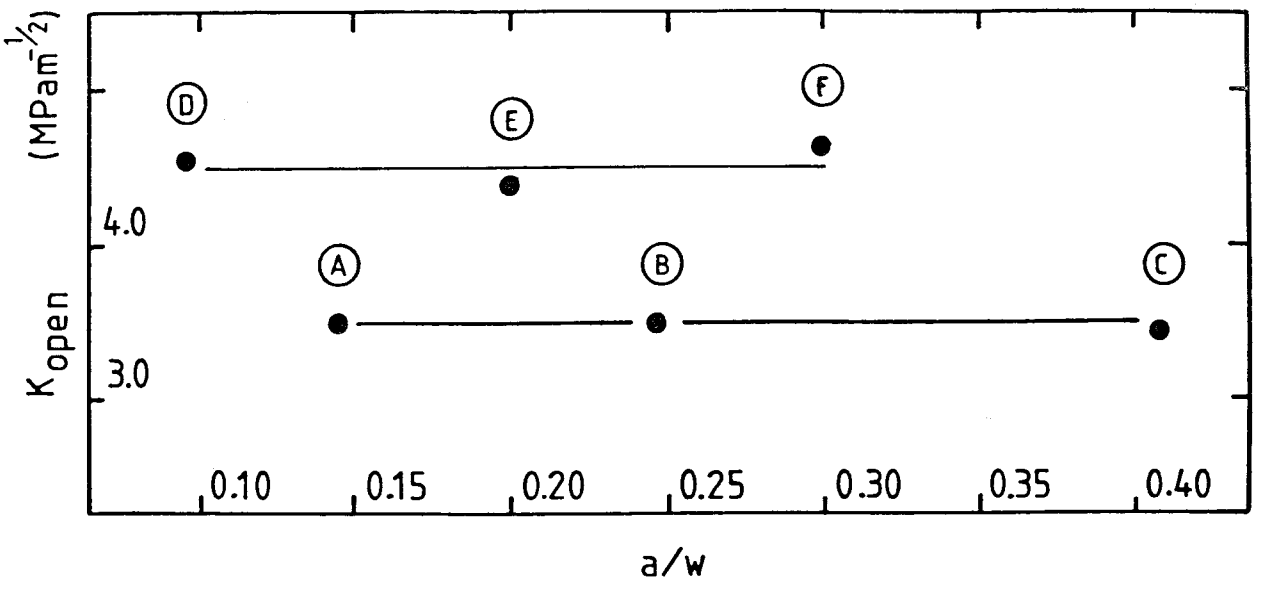


Fig. 11.15 (a) A plot of K_{open} versus a/w illustrating the magnitude of K_{open} determined at fatigue position A to F of Fig. 11.14

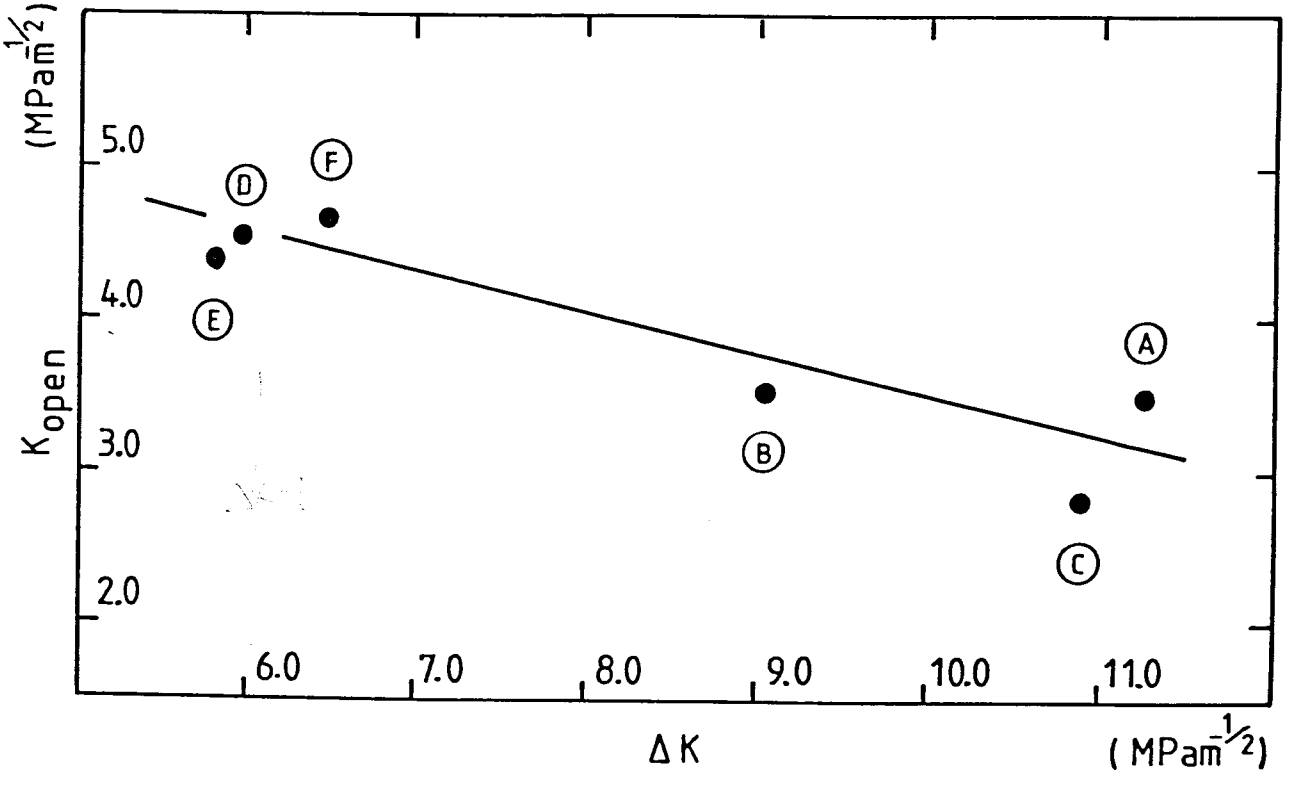


Fig. 11.15 (b) A plot of K_{open} versus ΔK illustrating the K_{open} response to ΔK at positions A to F of Fig. 11.14.

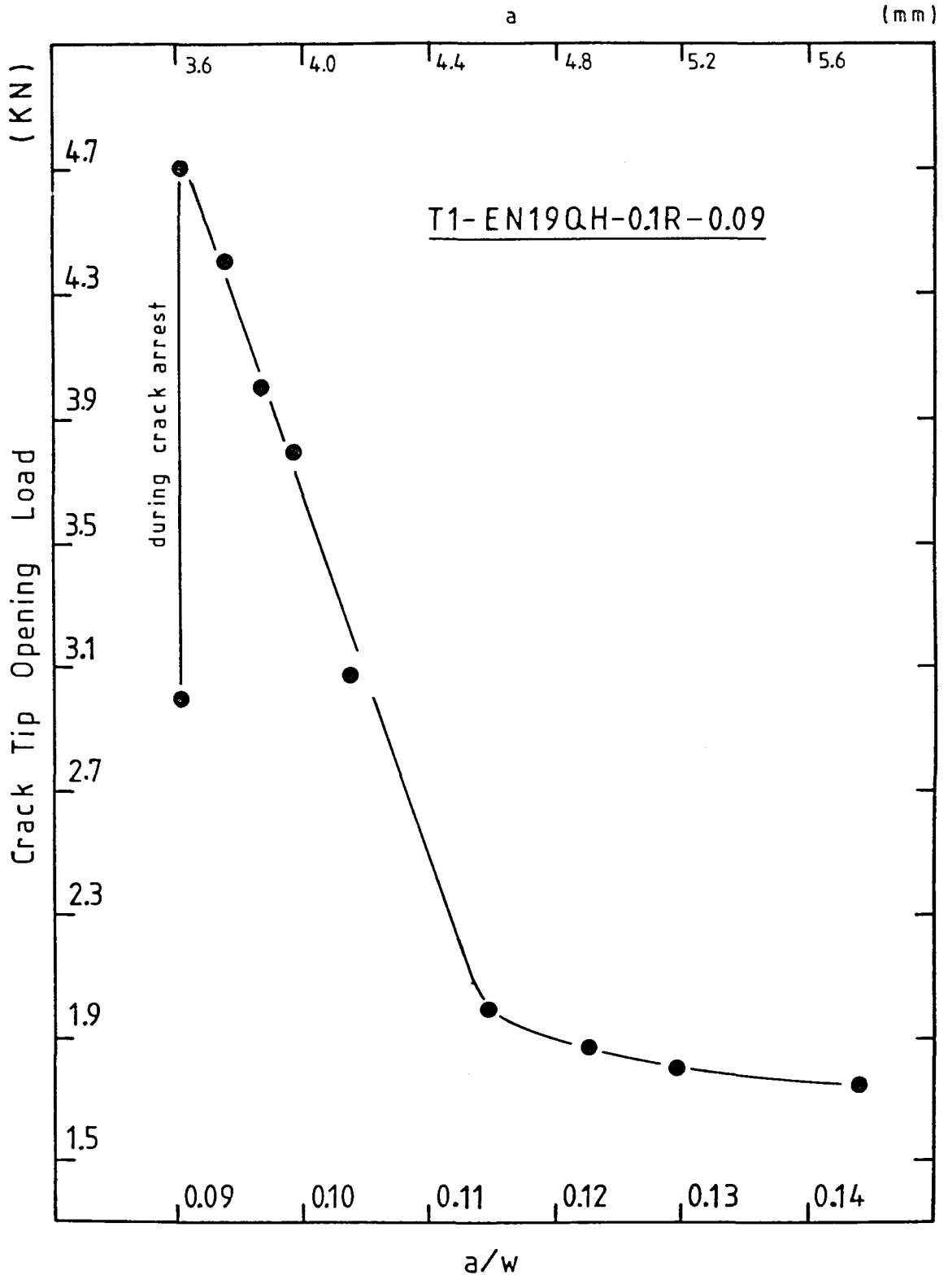


Fig. 11.16 A plot of Crack Tip Opening Load versus a/w of EN19QH illustrating the increase and decay of crack tip opening load associated with threshold hysteresis. (threshold a/w = 0.09)

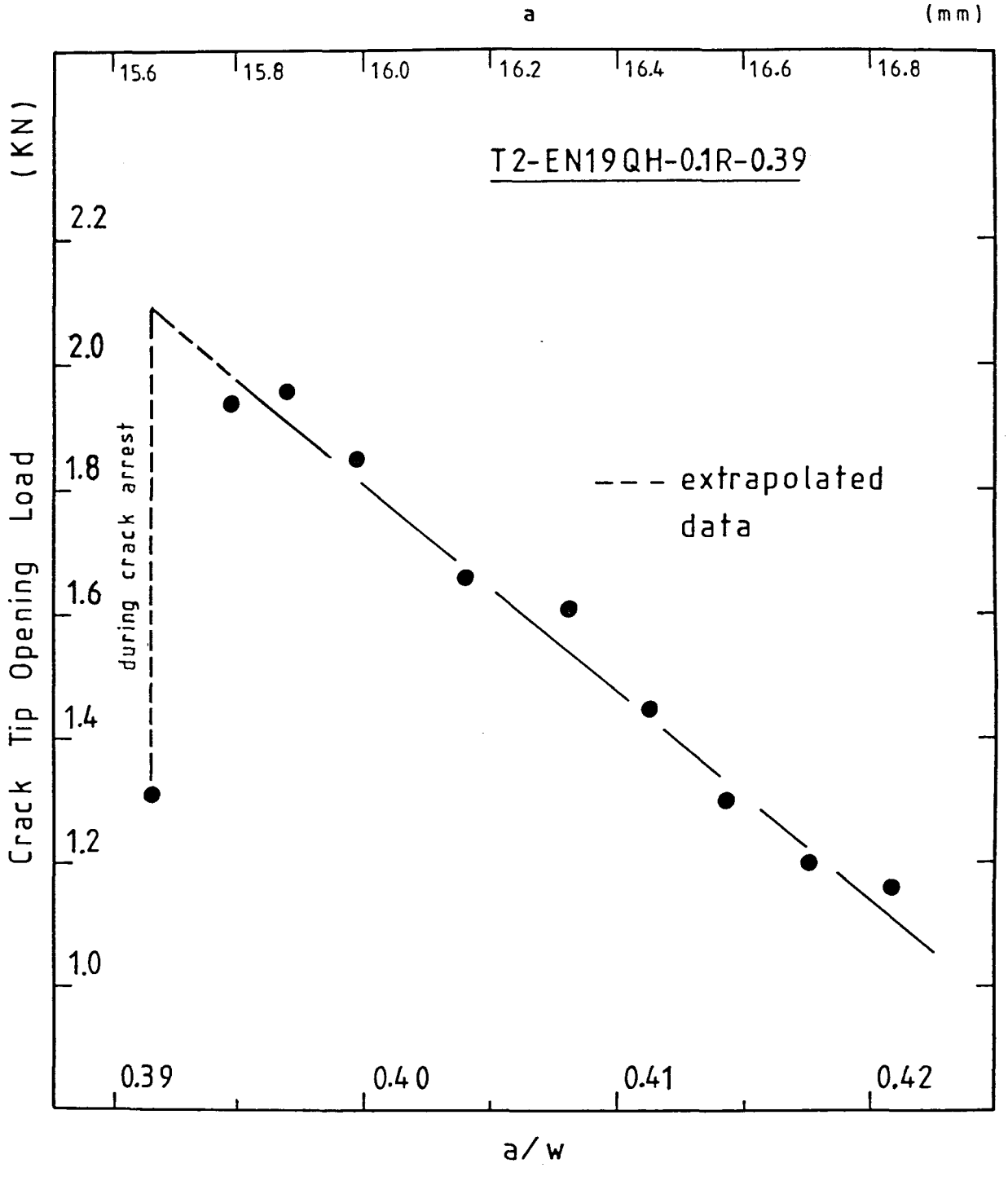


Fig. 11.17 A plot of Crack Tip Opening Load versus a/w of EN19QH illustrating the increase and decay of crack tip opening load associated with threshold hysteresis (threshold a/w = 0.39)

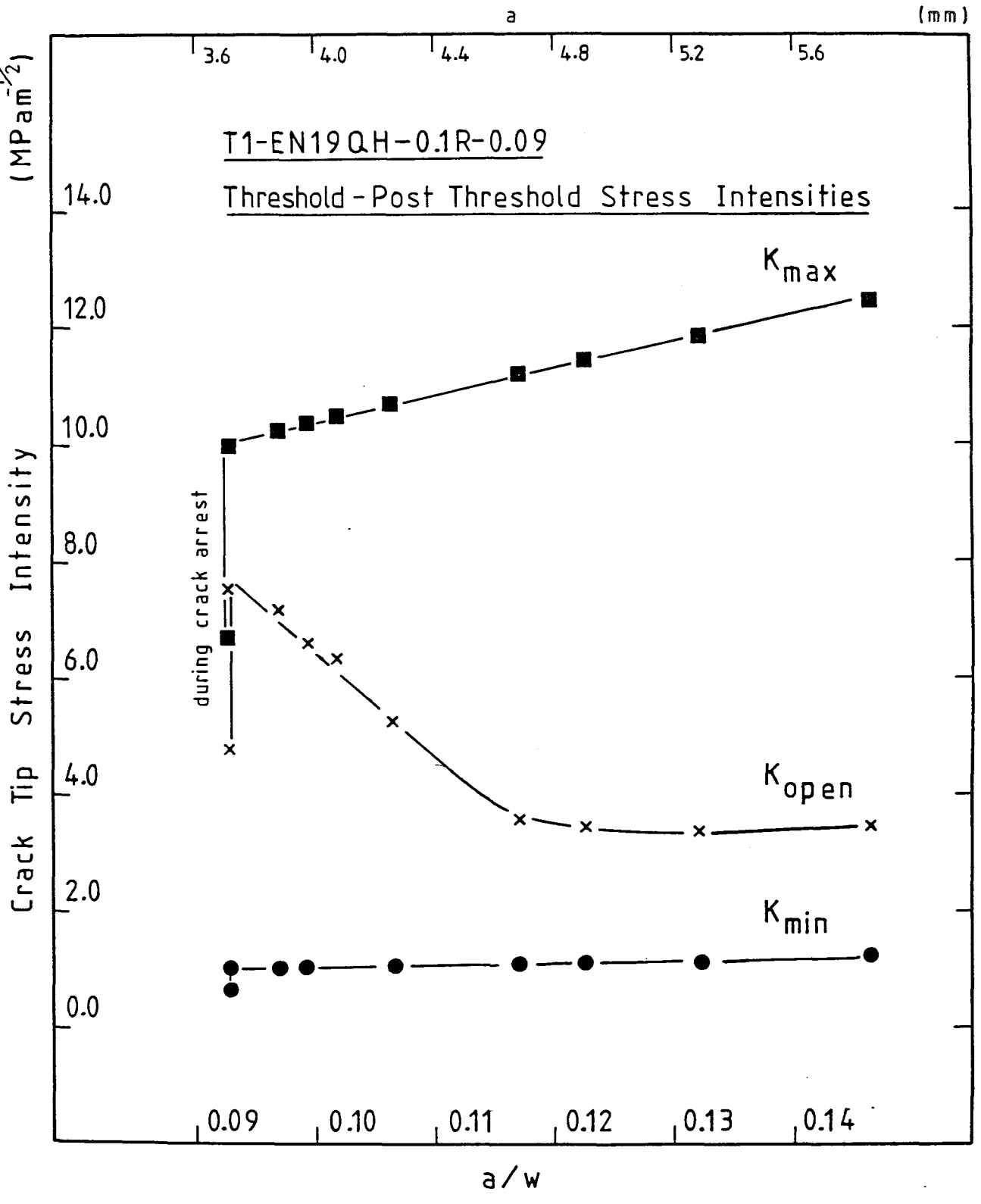


Fig. 11.18 A plot of Crack Tip Stress Intensity versus a/w of EN19QH illustrating the increase and decay of K_{open} associated with threshold hysteresis.
(threshold a/w = 0.09)

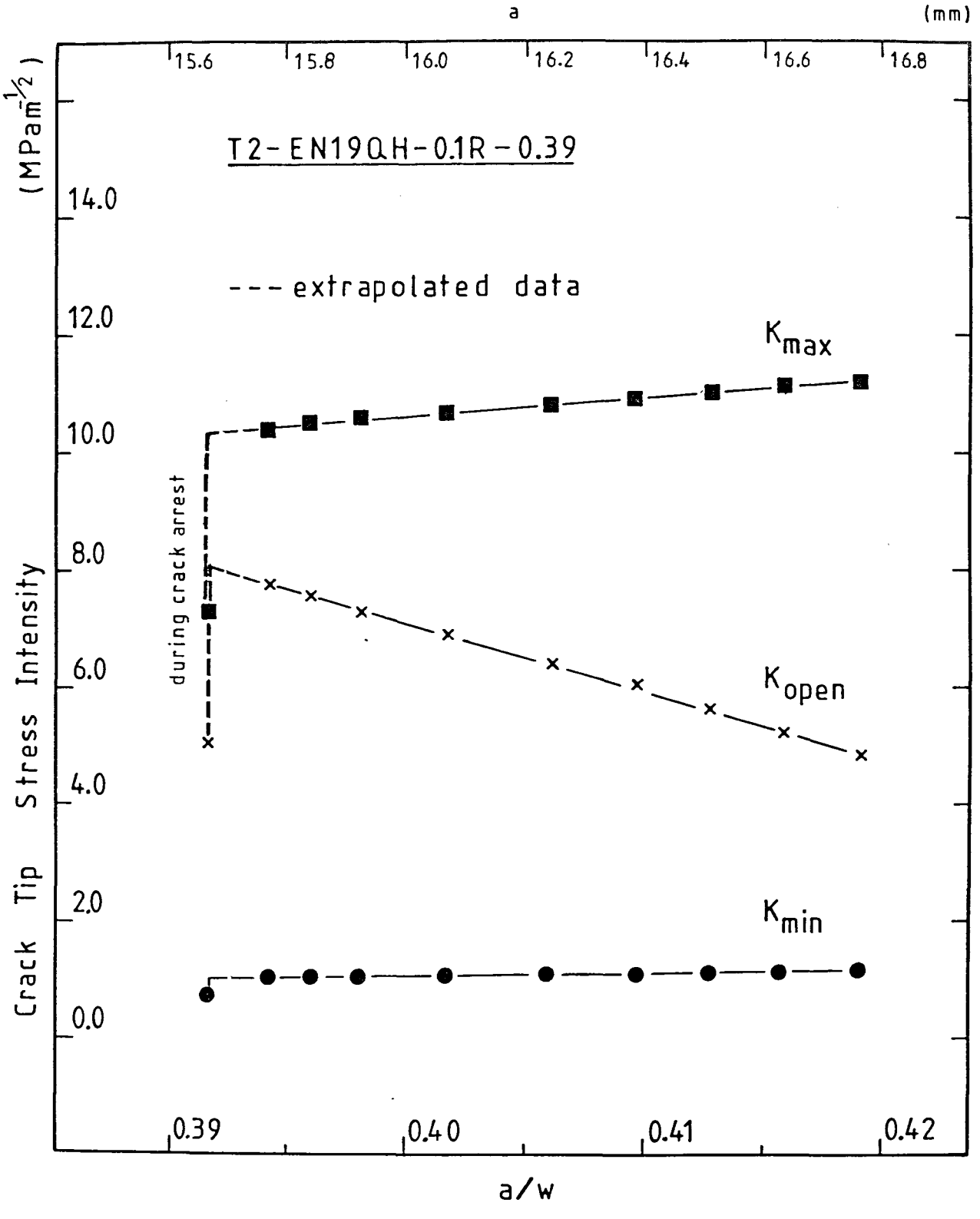


Fig. 11.19 A plot of Crack Tip Stress Intensity versus a/w of EN19QH illustrating the increase and decay of K_{open} during threshold hysteresis.
(threshold a/w = 0.39)

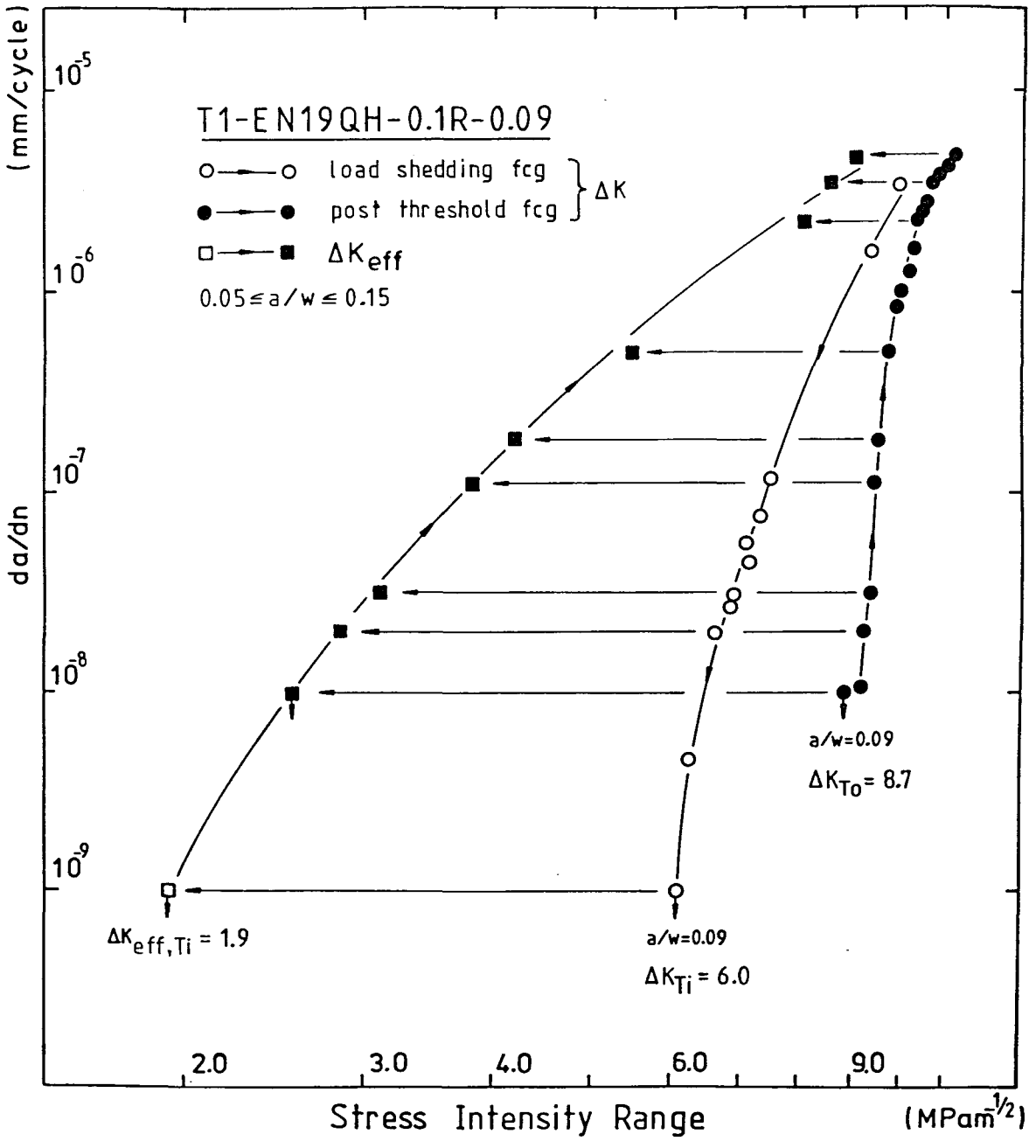


Fig. 11.20 A double logarithm plot of da/dn versus Stress Intensity Range of EN19QH which includes the ΔK_{eff} growth rate response of ΔK_{Ti} and post threshold fcg.
(threshold a/w = 0.09)

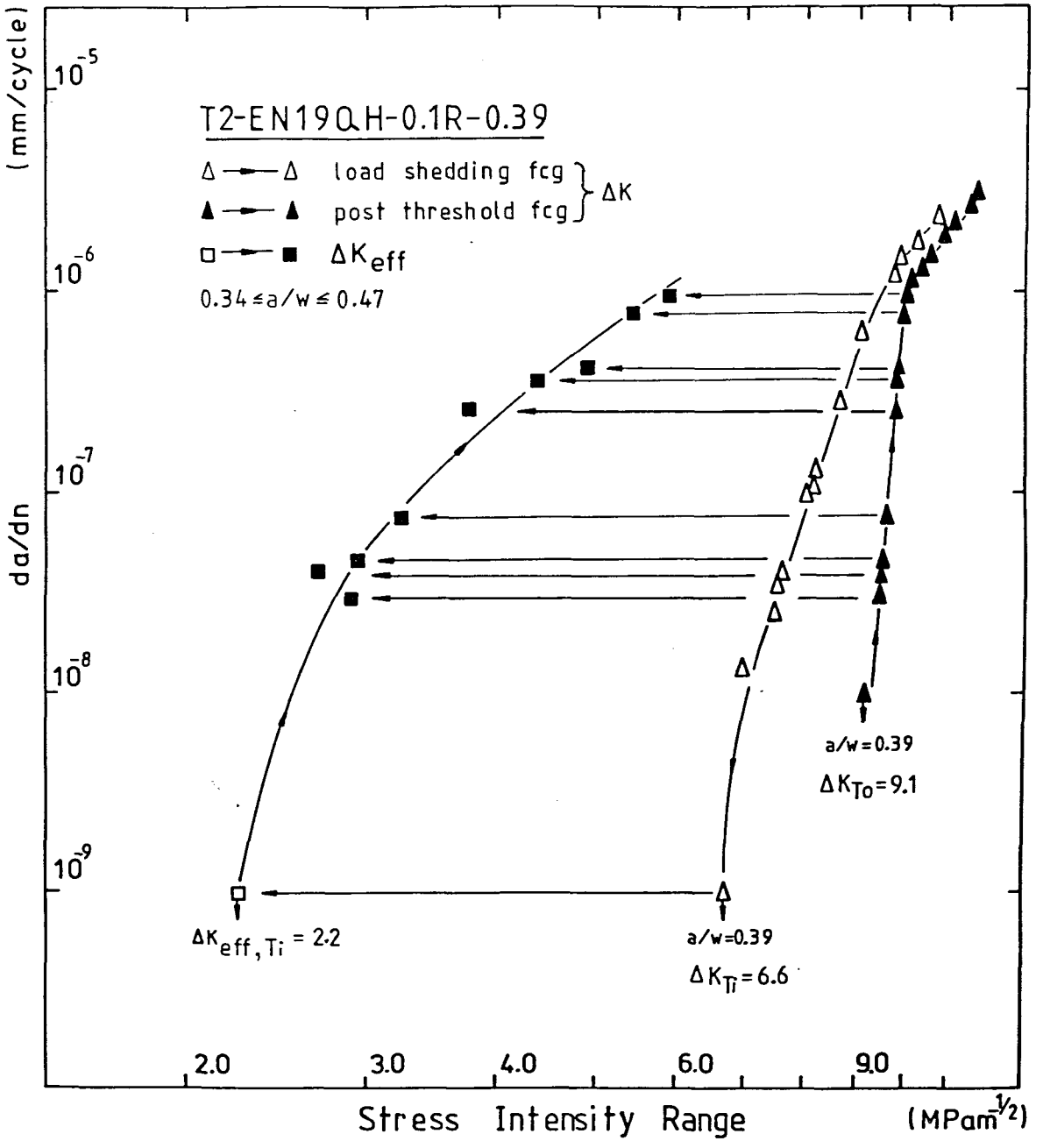


Fig. 11.21 A double logarithm plot of da/dn versus Stress Intensity Range of EN19QH which includes the ΔK_{eff} growth rate response of ΔK_{Ti} and post threshold fcg (threshold a/w = 0.39)

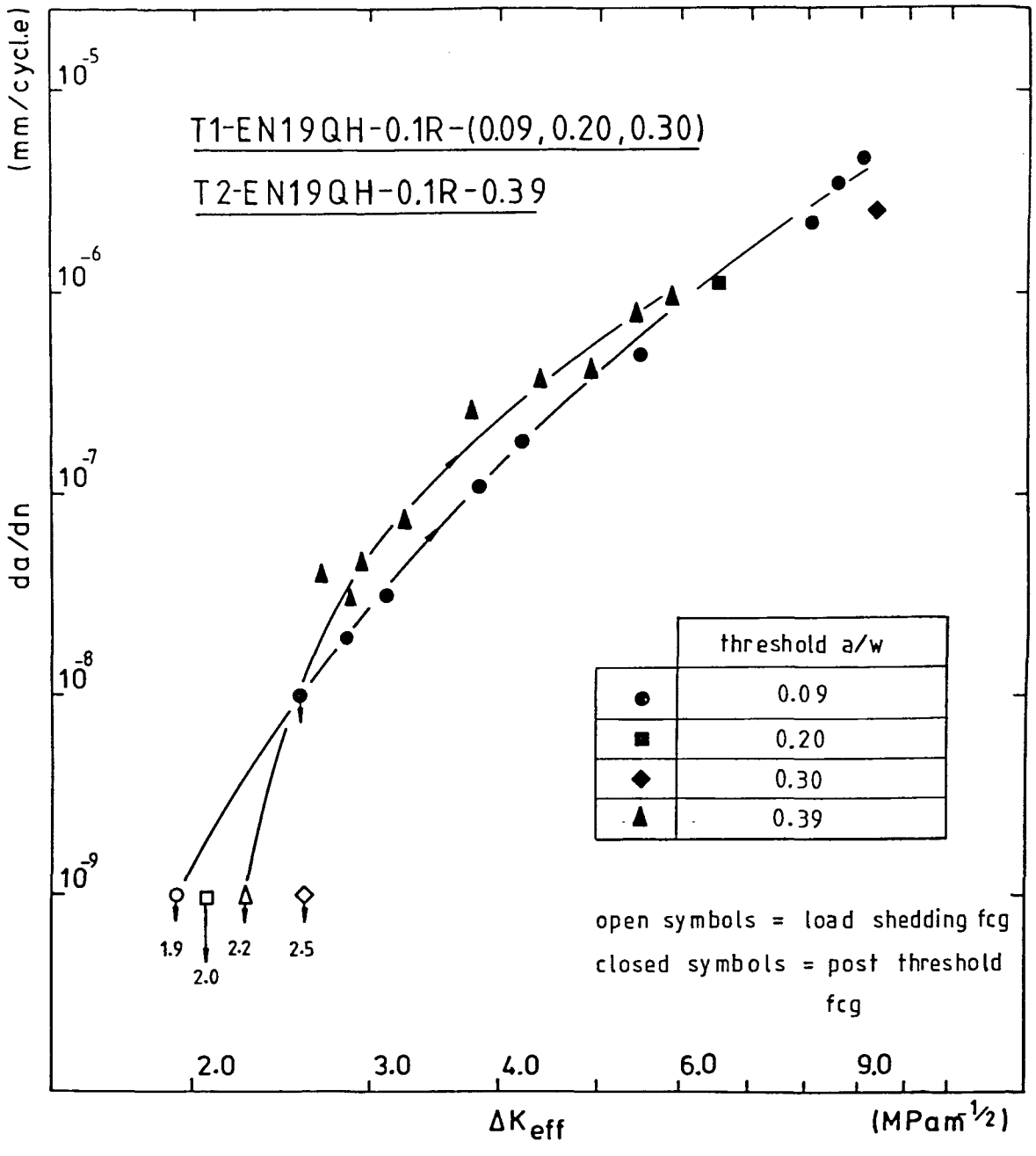


Fig. 11.22 A double logarithm plot of da/dn versus ΔK_{eff} of EN19QH constituting the data gathered at four different threshold a/w ratios.

not exhibit threshold hysteresis, Fig. 11.23. Irreversibile fcg existed with lower growth rates occurring at longer crack lengths. This trend was also confirmed by an additional test subject to constant load amplitude fcg as shown in Fig. 11.24.

11.4.1.2b Threshold and Post Threshold Crack Tip Stress Intensities

Analysis of threshold and post threshold crack tip stress intensities, Fig. 11.25, revealed that at threshold K_{open} and K_{min} were coincedential, but during post threshold fcg crack propagation was closure free, i.e. $K_{max} < K_{min} < K_{open}$. During the initial stages of post threshold crack growth a decrease in K_{open} suggested that crack closure at threshold was artificially high, but it then increased slightly with increase ΔK.

11.4.1.3 A Comparison of Stress Ratio Effects on Near Threshold Fatigue Crack Growth

Increasing stress ratio from 0.1 to 0.7 produced an increase in growth rate and a reduction in threshold as shown in Fig. 11.26.

A ΔK_{eff} comparison of results revealed that near threshold crack growth could be normalised irrespective of R as shown in Fig. 11.27.

11.4.1.4 A Closure Study of Threshold Testing

11.4.1.4a Growth Rate Results

The fatigue response to prolonged threshold testing exhibited

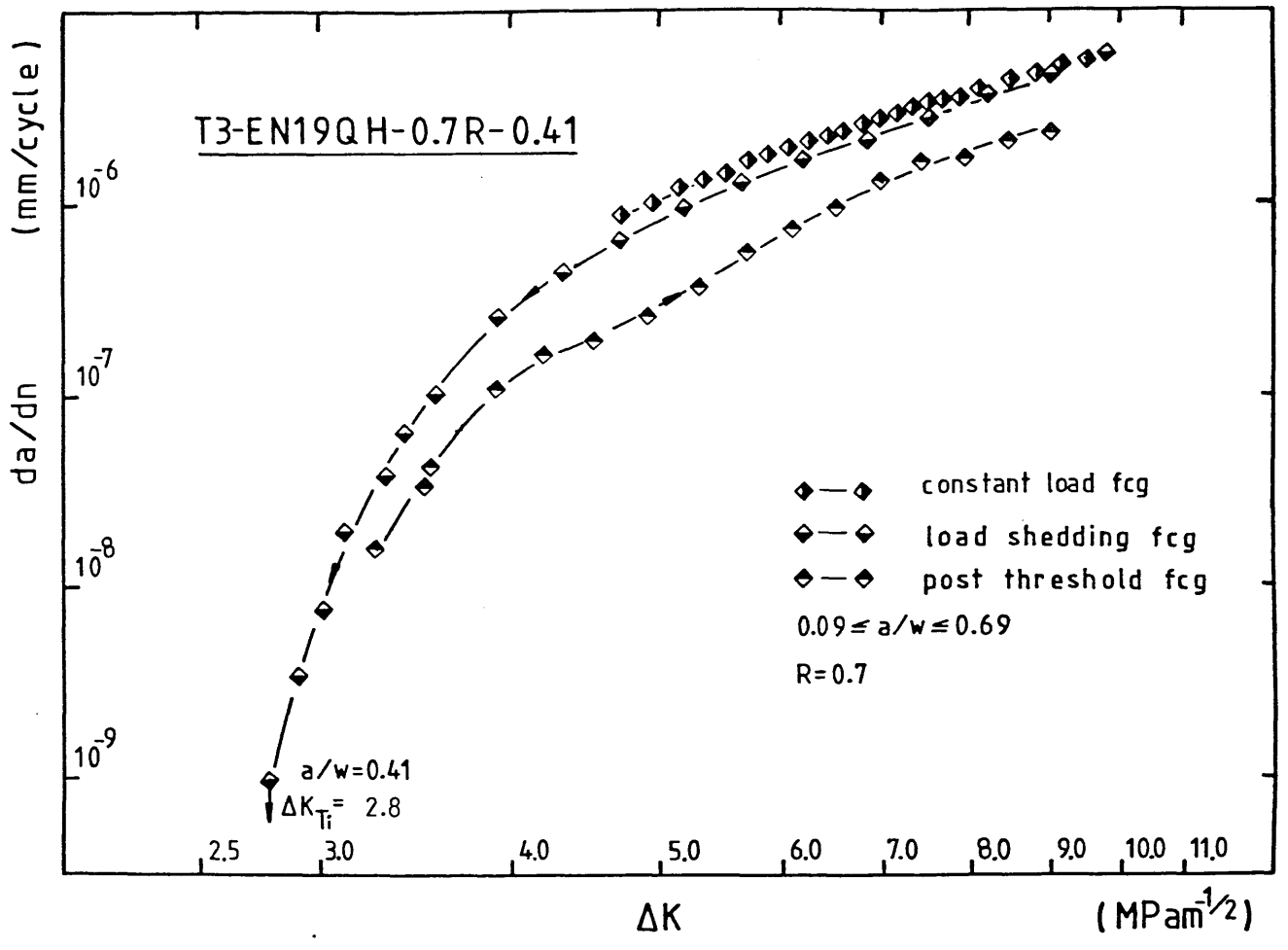


Fig. 11.23 A double logarithm plot of da/dn versus ΔK of EN19QH tested at R = 0.7

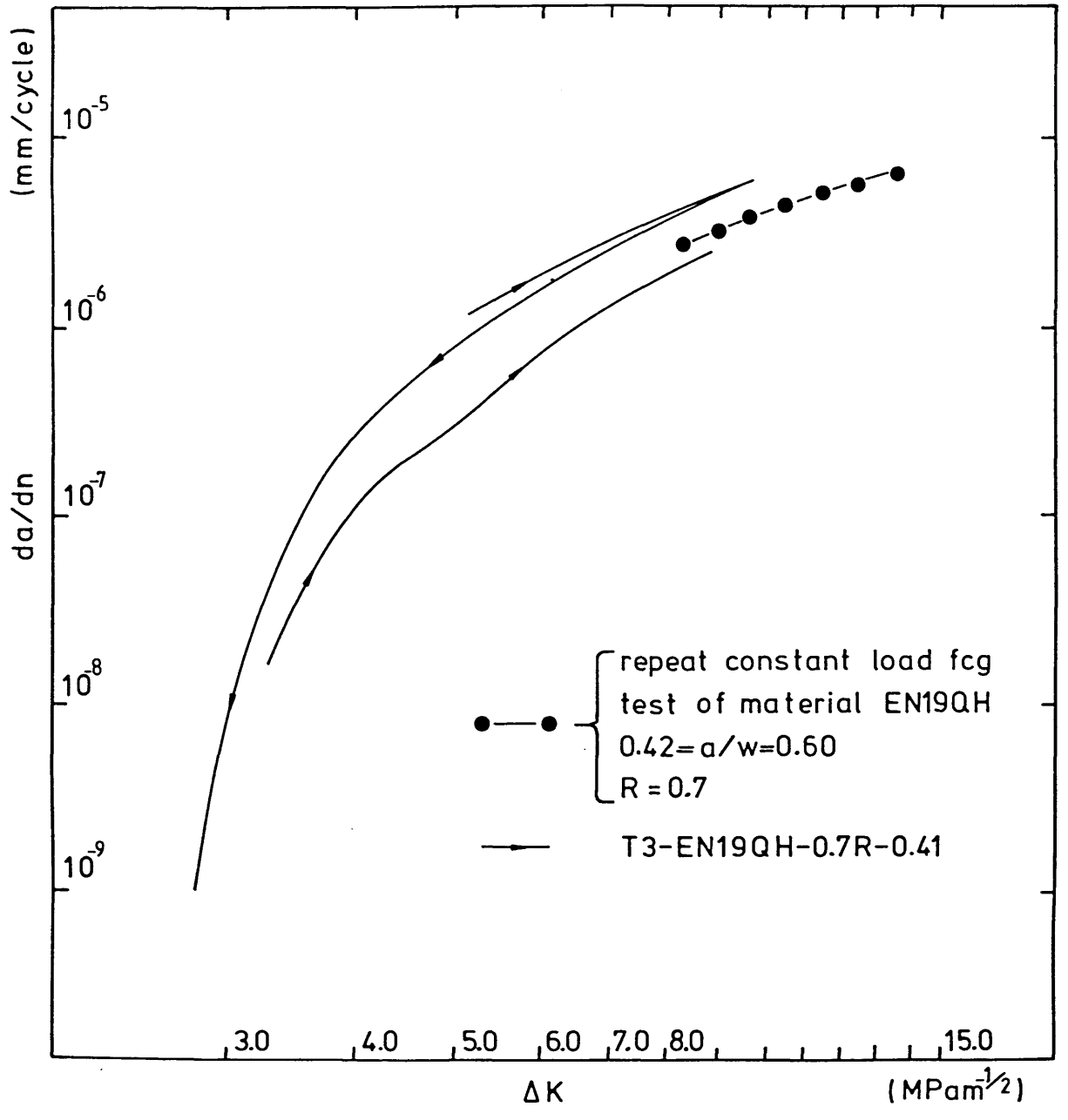


Fig. 11.24 A double logarithm plot of da/dn versus ΔK of EN19QH tested at R = 0.7 illustrating the growth rate dependency on crack length.

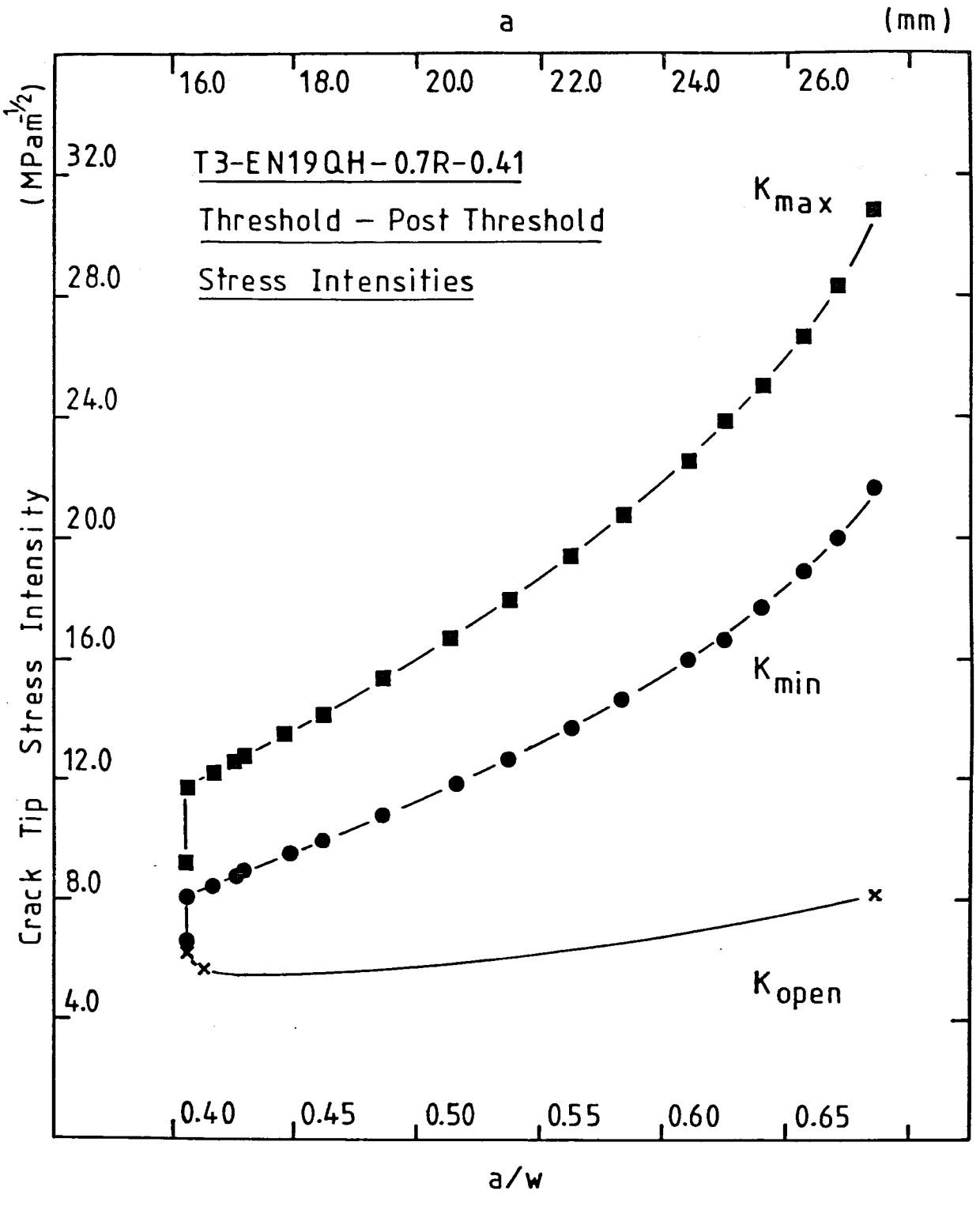


Fig. 11.25 A plot of Crack Tip Stress Intensity versus a/w of EN19QH tested at R = 0.7 illustrating threshold and post threshold crack tip stress response.

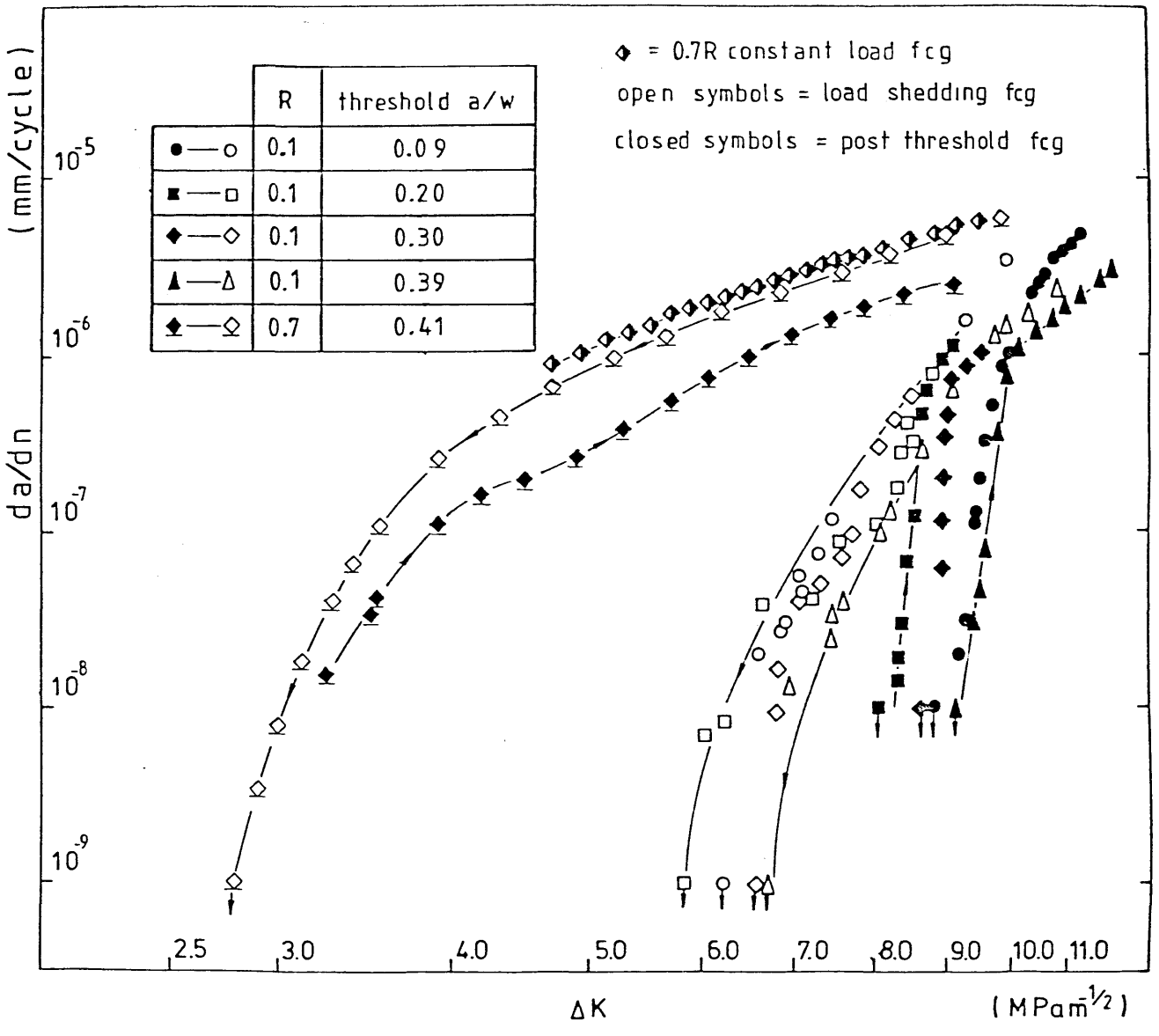


Fig. 11.26 A double logarithm plot of da/dn versus ΔK of EN19QH illustrating stress ratio effects on near threshold fcg.

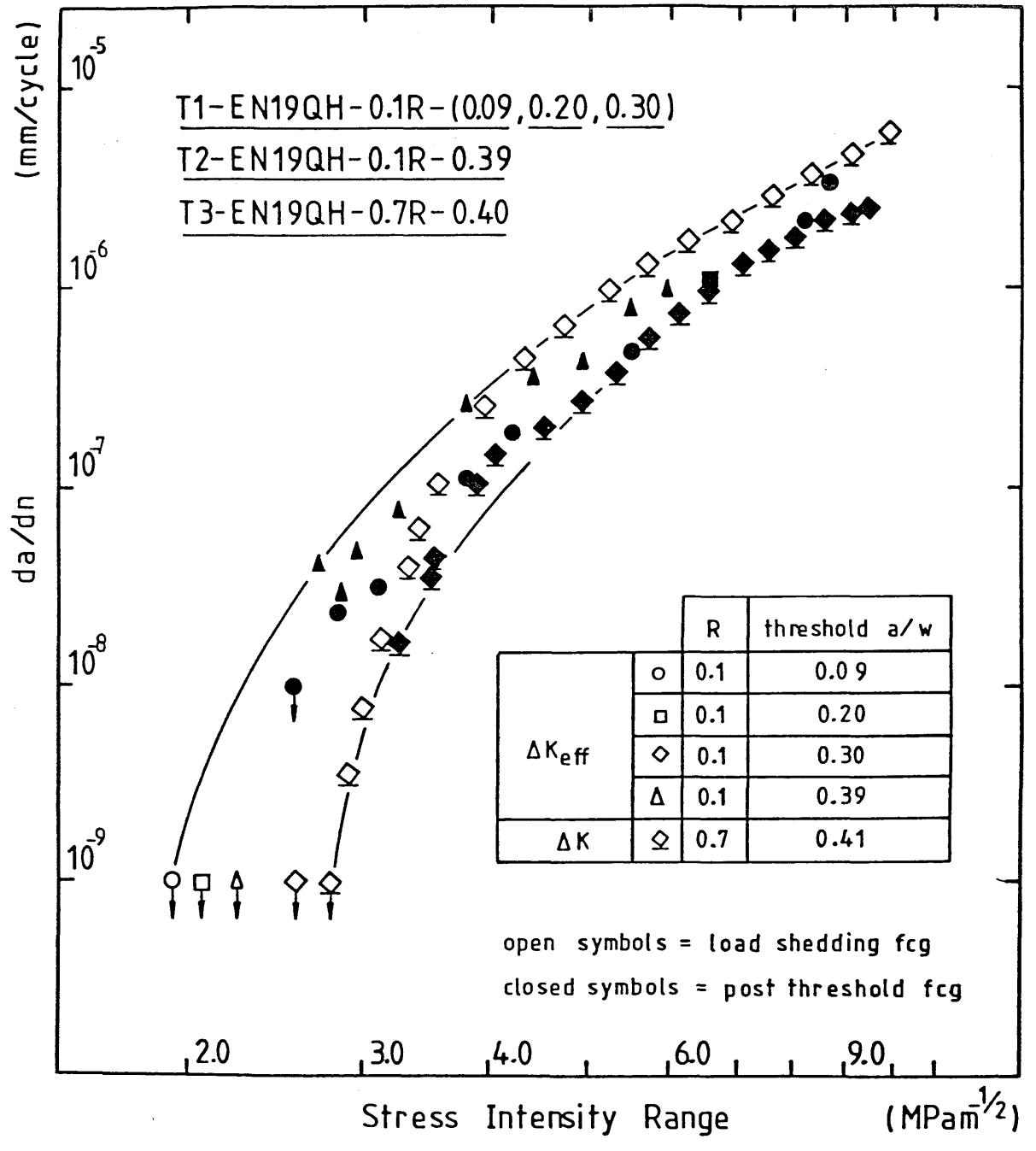


Fig. 11.27 A normalised plot of da/dn versus Stress Intensity Range of EN19QH.

Note: at R = 0.7, $\Delta K_{eff} = \Delta K$; constant load fcg has been omitted for simplicity, this omission does not distract from the general trend.

threshold hysteresis and irreversible growth rate behaviour, Fig. 11.28 Throughout the load shedding threshold approach sequence lower growth rates were recorded in comparison to constant load fcg, with threshold eventually being achieved by self crack arrest at $\Delta K_{Ti} = 8.4$ MPam$^{-\frac{1}{2}}$. Increasing the load range produced a small amount of post threshold crack growth, but this was rapidly terminated by self crack arrest. Eventually, at $\Delta K = 10.1$ MPam$^{-\frac{1}{2}}$, a rapid return to intermediate growth rates marked the onset of final post threshold fcg.

11.4.1.4b Crack Tip Opening Loads, Stress Intensities and ΔK_{eff} Analysis of Results

From the plot of P_{open} versus a/w, Fig. 11.29, crack tip opening loads corresponding to specific growth rates were computed and used to determine related values of K_{open}. This data was then combined with K_{min} and K_{max} and plotted with respect to a/w to give Fig. 11.30. This plot revealed the following trends:

(a) $K_{min} < K_{open} < K_{max}$ irrespective of a/w;

(b) during constant load fcg K_{min} and K_{max} increased with a/w but K_{open} decreased;

(c) during load shedding an increase in K_{open} corresponded to a decrease in K_{max} but at growth rates $\leq 10^{-7}$ mm/cycles K_{open} increased rapidly;

(d) threshold hysteresis was accompanied by an increase in K_{open}; and

(e) during the initial stages of post threshold crack growth

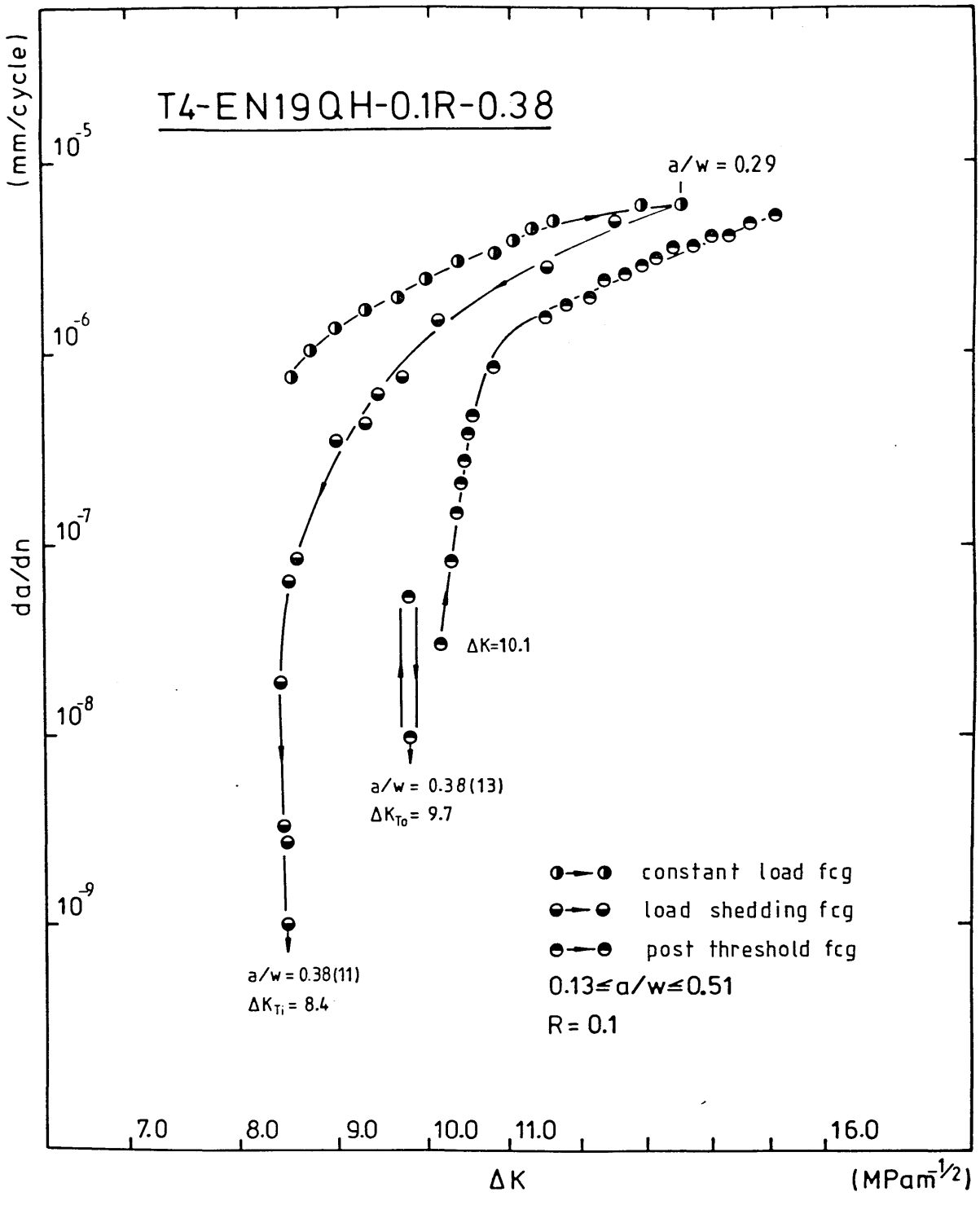


Fig. 11.28 A double logarithm plot of da/dn versus ΔK of EN19QH subject to prolonged threshold testing.

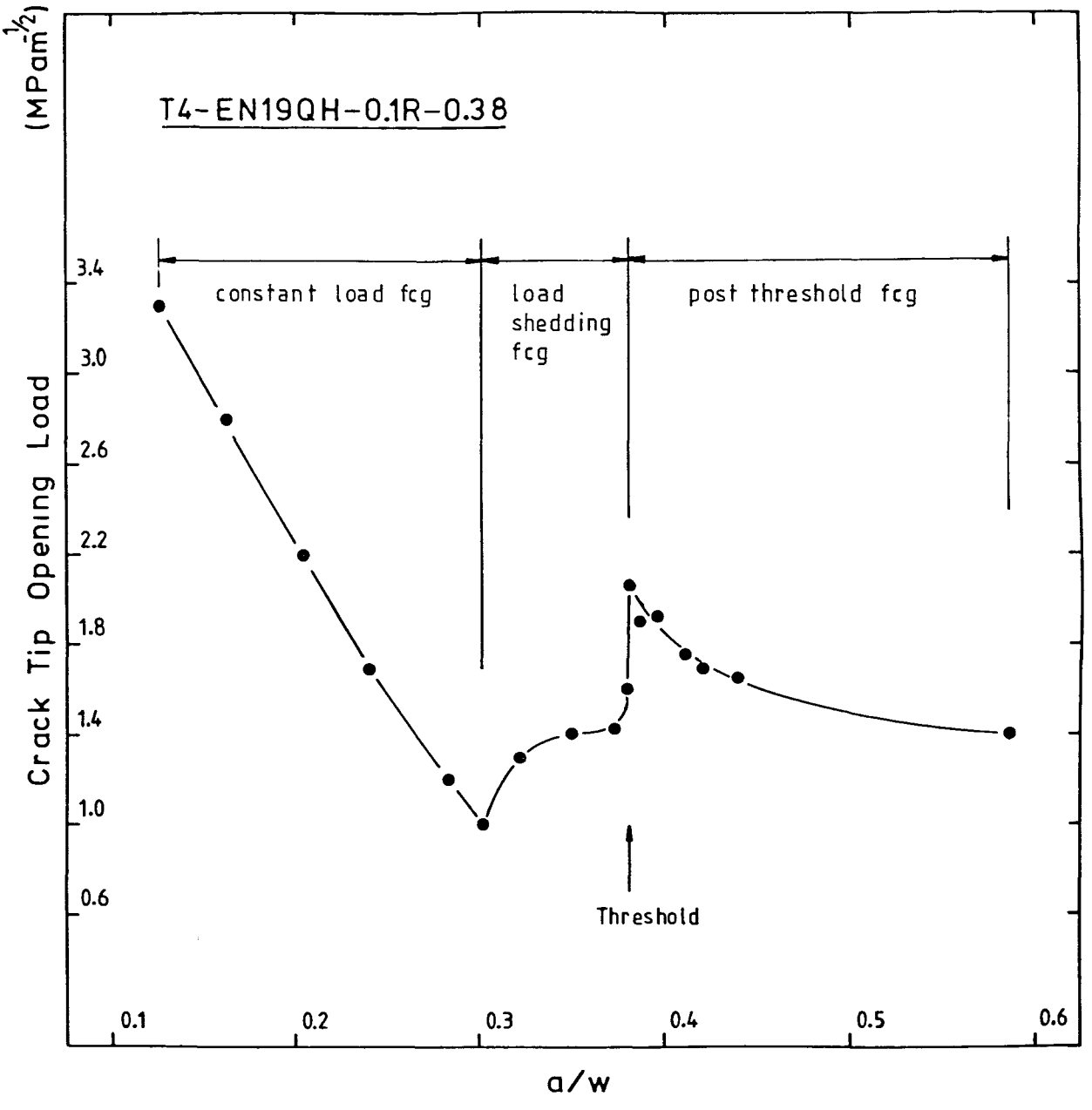


Fig. 11.29 A plot of Crack Tip Opening Load versus a/w of EN19QH subject to prolonged threshold testing.

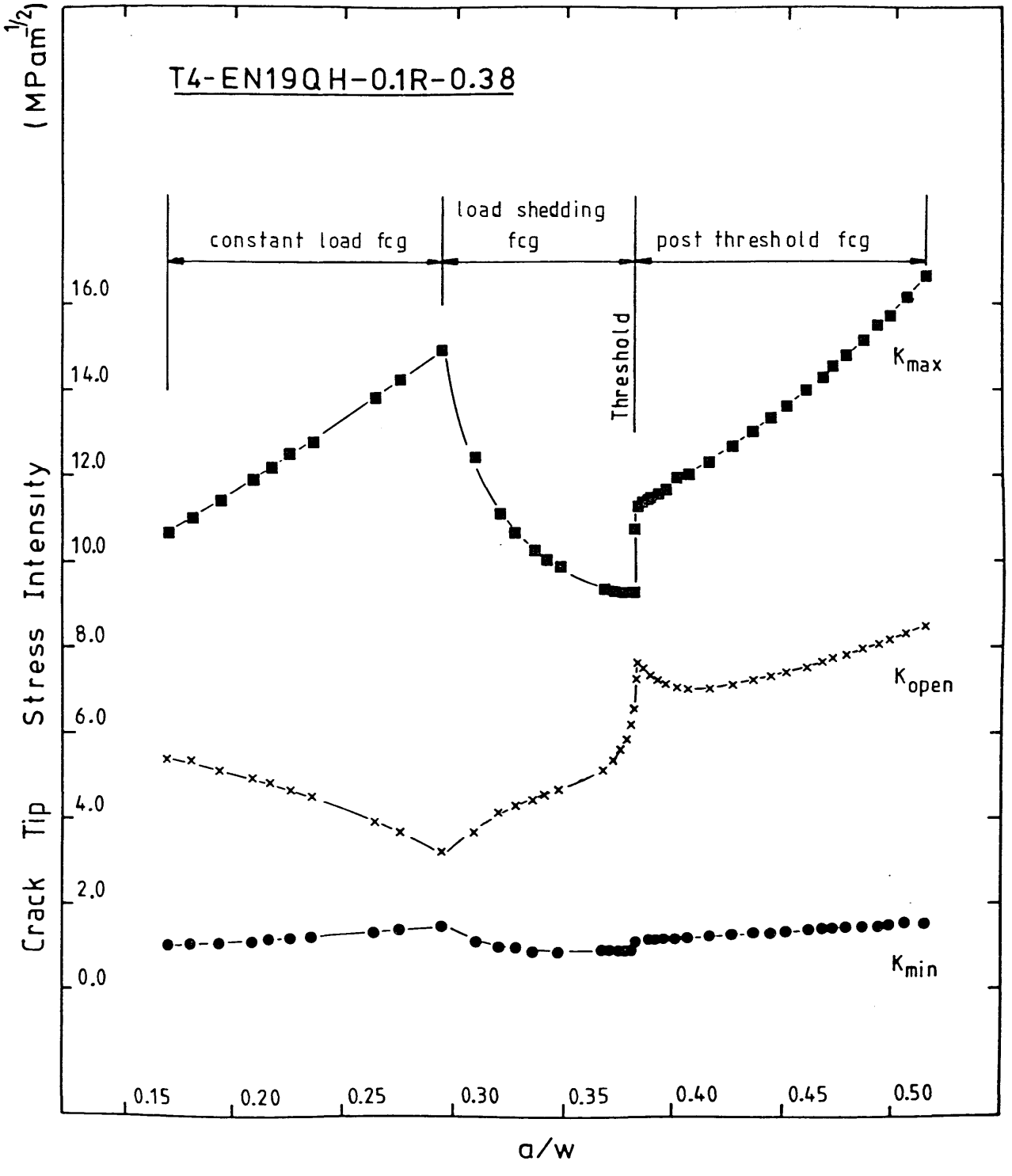


Fig. 11.30 A plot of Crack Tip Stress Intensity versus a/w of EN19QH illustrating the K_{open} trend.

K_{open} decreased rapidly to a minimum before increasing gradually with increased ΔK.

ΔK_{eff} analysis of the fatigue data illustrated that the closure free growth response subscribed a hysteresis envelope, Fig. 11.31. When compared with the closure free crack growth plot of T3-EN19QH-0.7R-0.41 both sets of data were suitably normalised as shown in Fig. 11.32.

11.4.1.5 Fractography

11.4.1.5a Macroscopic Fracture Surface Appearance

Macroscopic examination of all fracture surfaces, Fig. 11.33, revealed two types of fracture surface oxidation. A highly localised black surface oxide was present which was thought to be Fe_3O_4 [11.05], and a lighter corrosion product existed in definite bands which was thought to be Fe_2O_3 [11.06]. The latter, which resulted from fretting oxidation [11.07], was particularly dense in low growth rate regions and in the low load ratio specimens. Macroscopic measurements of a X10 print of Specimen T2-EN19QH-0.1R-0.39, Fig. 11.34, revealed that fretting oxidation occurred during load shedding at growth rates approximating 10^{-6} mm/cycle.

11.4.1.5b Microscopic Fracture Surface Appearance

A comprehensive SEM microscopic examination of fracture surface morphology, which was made difficult by the presence of corrosion products in the near threshold regions, was restricted to Specimens T4-EN19QH-0.1R-0.38 and T3-EN19QH-0.7R-0.41 of stress ratio 0.1 and 0.7 respectively.

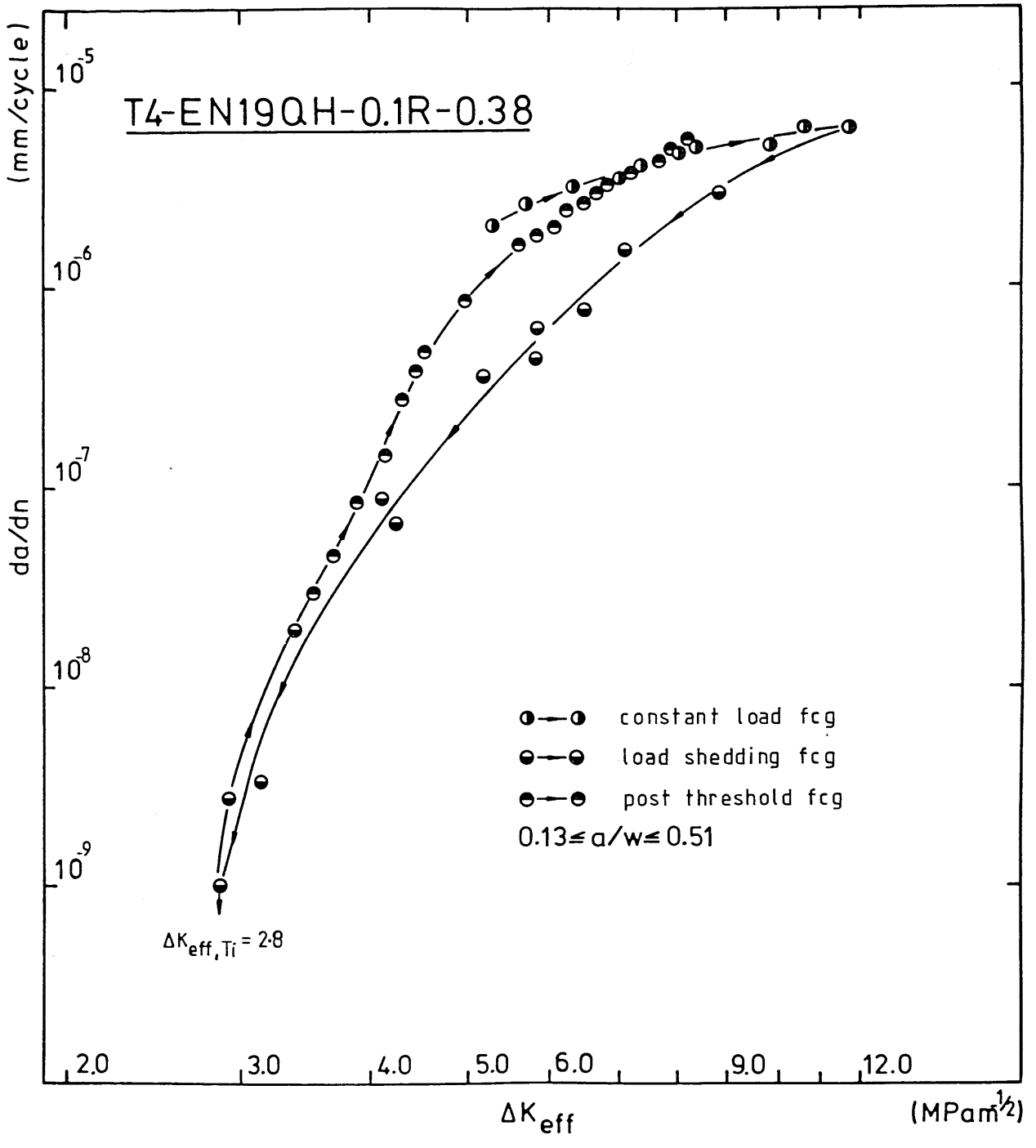


Fig. 11.31 A double logarithm plot of da/dn versus ΔK_{eff} of EN19QH subject to prolonged threshold testing at R = 0.1

(threshold a/w = 0.38)

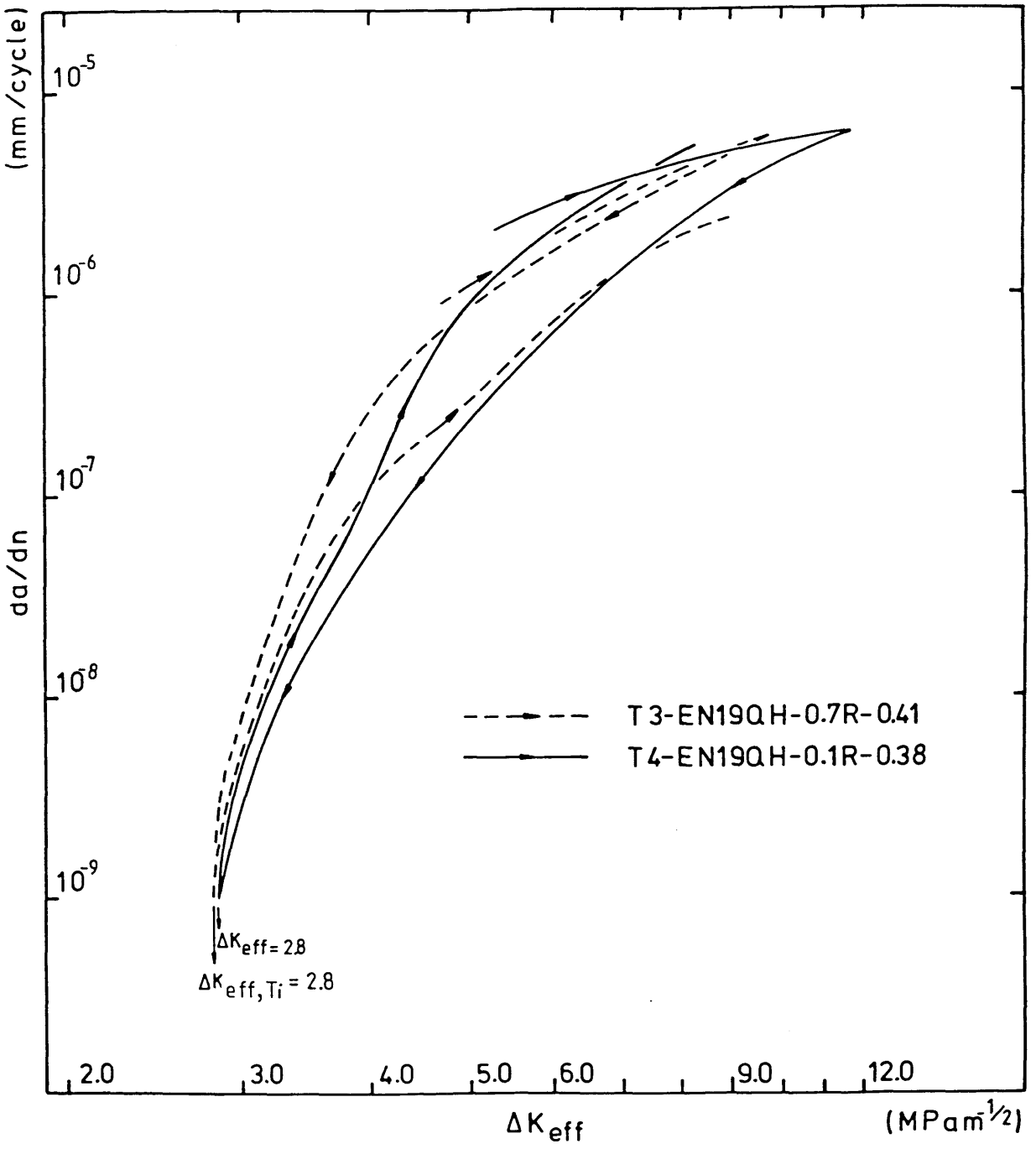


Fig. 11.32 A double logarithm plot of da/dn versus ΔK_{eff} of EN19QH tested at R = 0.1 and 0.7

Note: at R = 0.7, $\Delta K_{eff} = \Delta K$

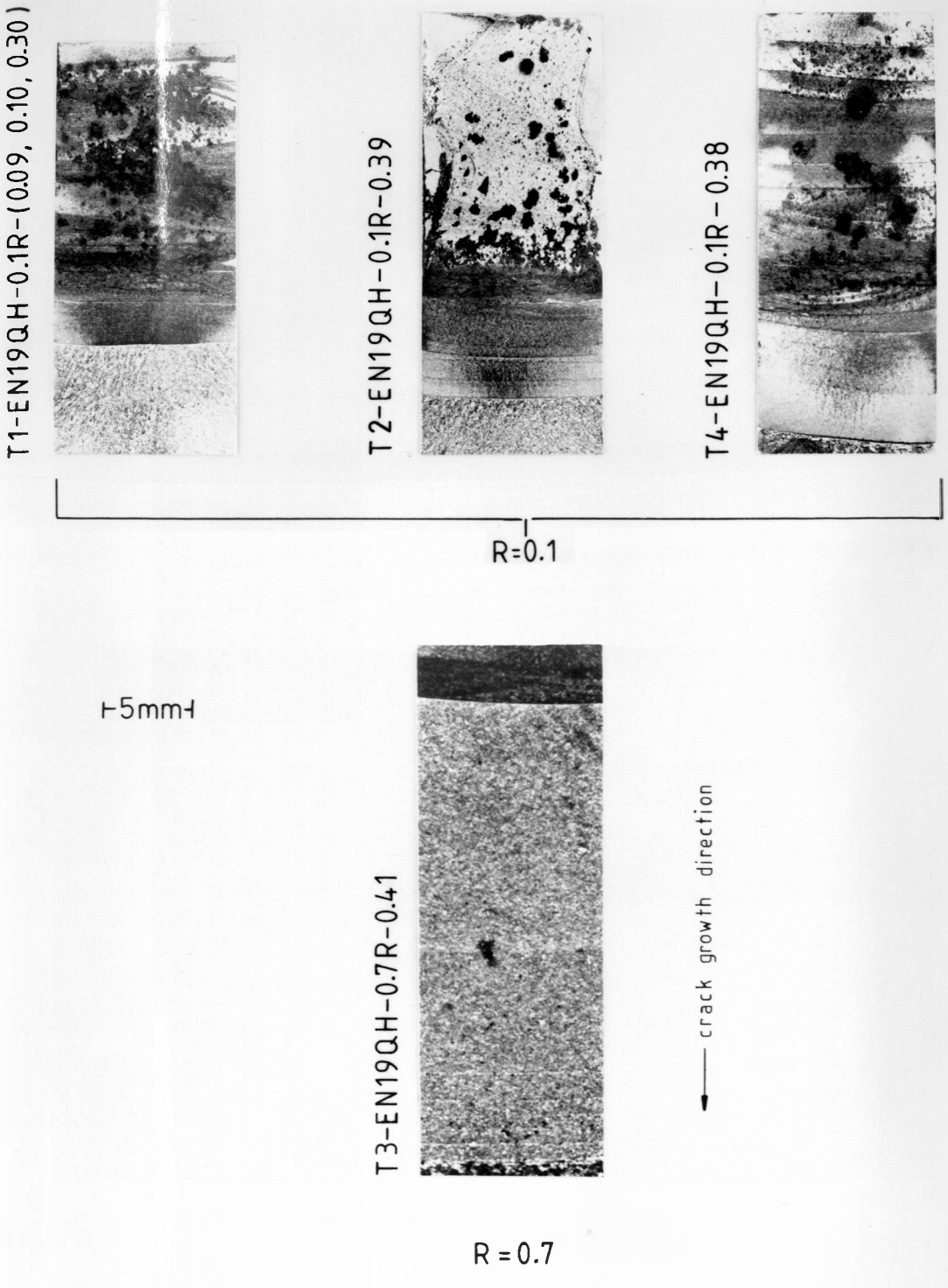


Fig. 11.33 Macroscopic fracture surface appearance of the tempered martensitic steel specimens

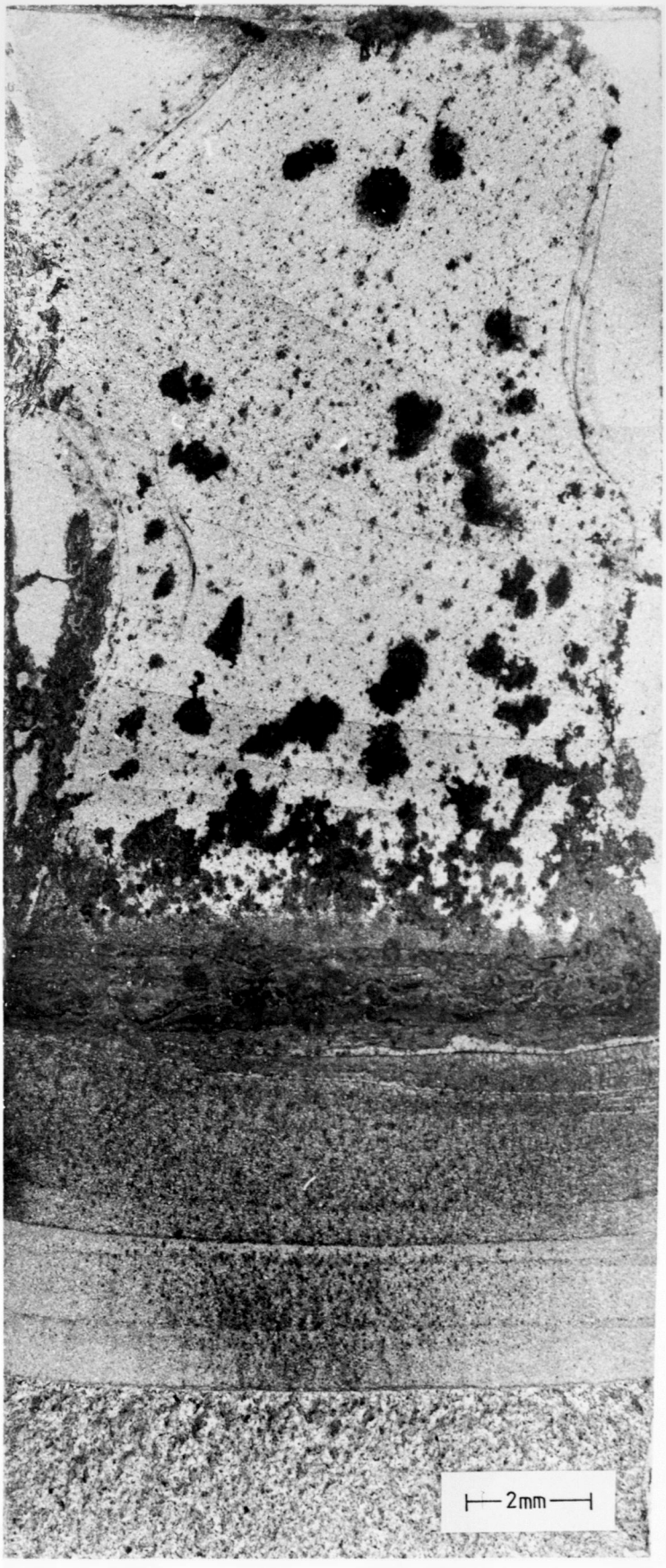


Fig. 11.34 An enlarged view showing the fracture surface appearance of specimen T2-EN19QH-01R-039

With reference to Fig. 11.35 typical fracture surface micrographs of Specimen T4-EN19QH-0.1R-0.38 are presented in Fig. 11.36(a)-(f). From this series it can be seen that crack propagation at low growth rates resulted mainly from transgranular ductile fracture, Fig. 11.36(a)(c)(e), but at higher growth rates intergranular seperation also occurred, Fig. 11.36(b)(f).

A similar series of SEM fracture surface micrographs of Specimen T3-EN19QH-0.7R-0.41, which are indexed with respect to Fig. 11.37 and appear in Fig. 11.38, exhibited the same trend. At low growth rates crack propagation occurred by a process of amorphous transgranular ductile fracture, Fig. 11.38(a)(c)(d)(f), but at higher growth rates this was succeeded by transgranular ductile seperation containing elements of intergranular faceting, Fig. 11.38(b). In the threshold region a dense oxide layer characteristically produced by fretting oxidation was present, Fig. 11.38(d). Close examination revealed this layer to be flaked, but no spalling was observed, Fig. 11.38(e).

Secondary cracking lying perdendicular to the macroscopic growth direction was observed in both specimens at random intervals across the fracture surface. In some instances this was particularly severe as illustrated in Fig. 11.39.

11.4.1.6 Crack Profile Appearance

A crack profile replica of Specimen T4-EN19QH-0.1R-0.38 produced at threshold clearly illustrated the occurance of excessive fretting oxidation at growth rates $\leqslant 3.6 \times 10^{-7}$ mm/cycle, Fig. 11.40.
At the end of the threshold testing crack profile replicas also revealed

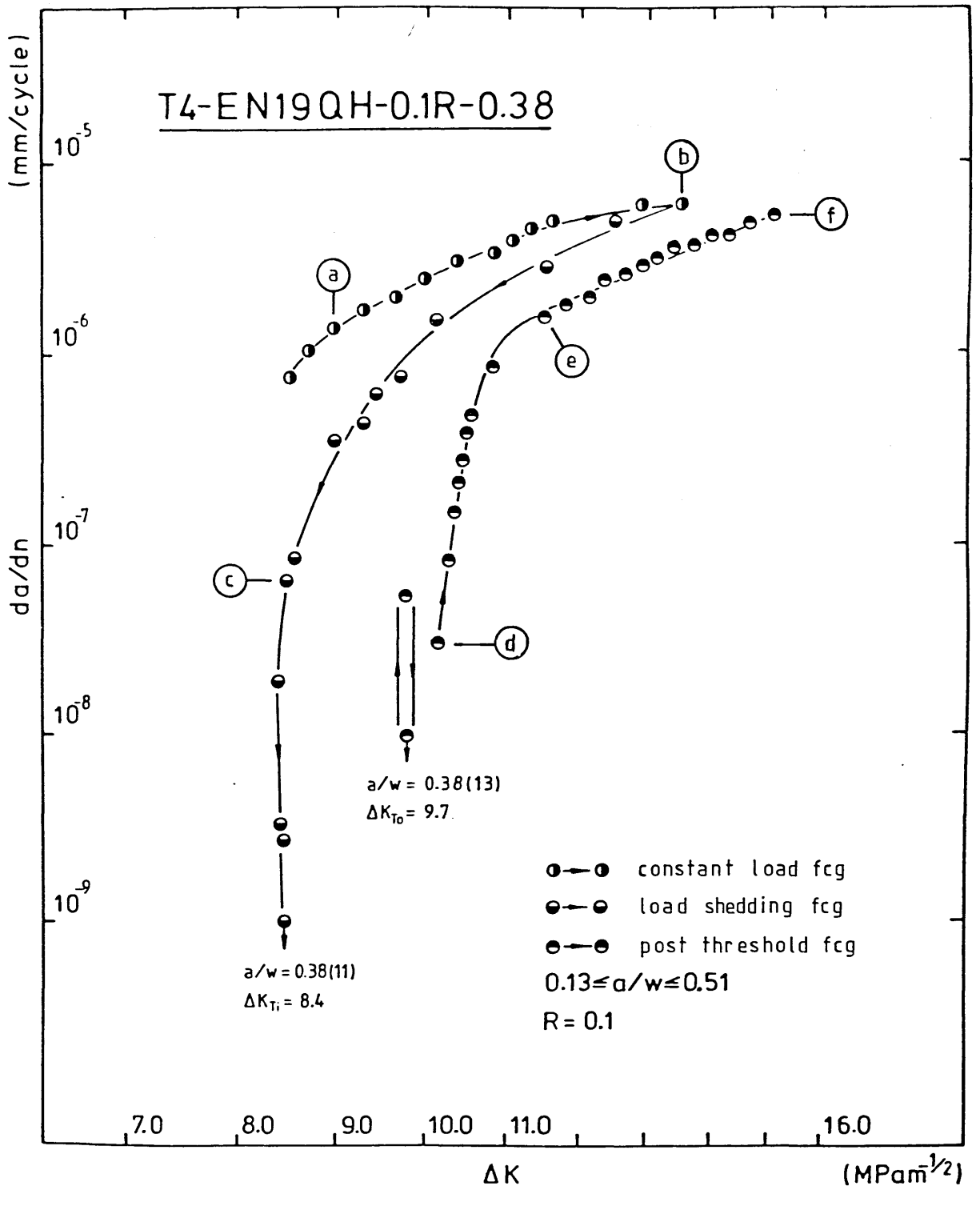
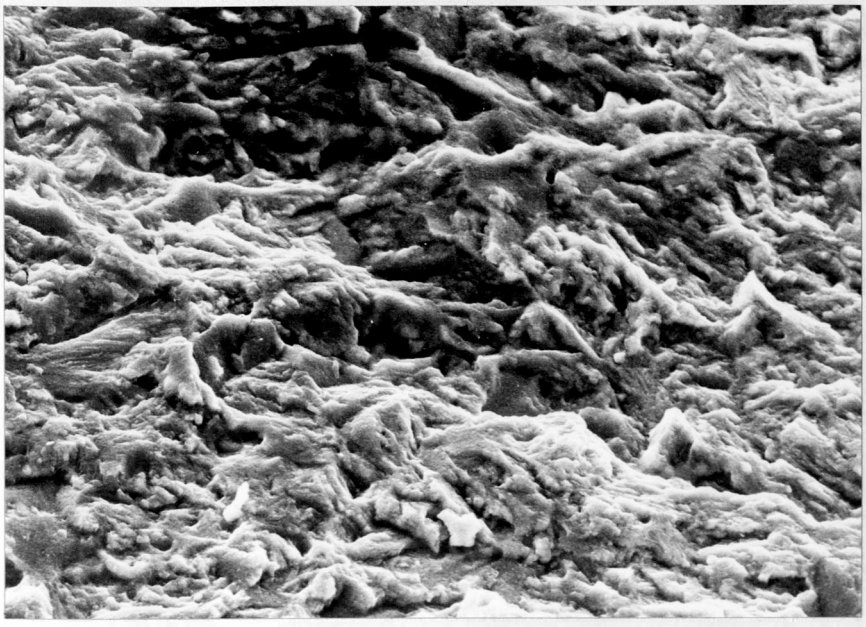
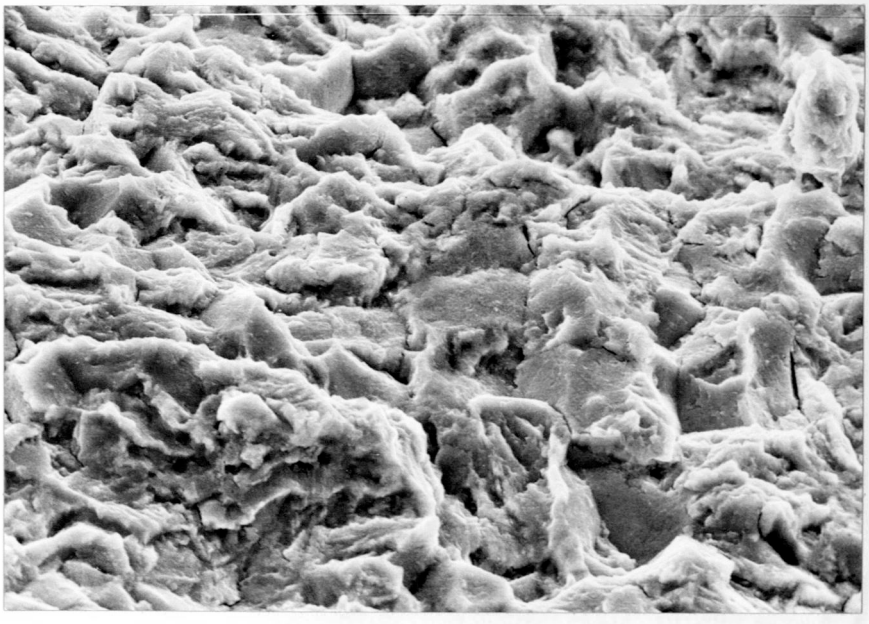


Fig. 11.35 A double logarithm plot of da/dn versus ΔK of EN19QH indicating the SEM micrograph positions of Fig. 11.36.

Crack growth direction ⟶



(a)



(b)

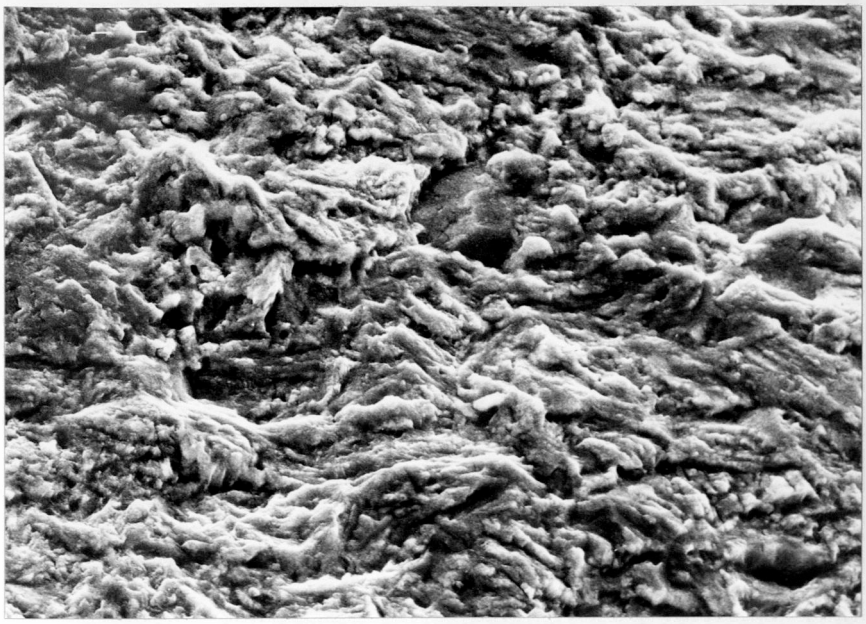
Fig. 11.36 SEM micrographs of Specimen T4-EN19QH-0.1R-0.38 illustrating the change of fracture mode during constant load fcg.

(a) $\Delta K = 8.9\ MPam^{-\frac{1}{2}}$, $da/dn = 1.4 \times 10^{-6}$ mm/cycle, $a/w = 0.15$.

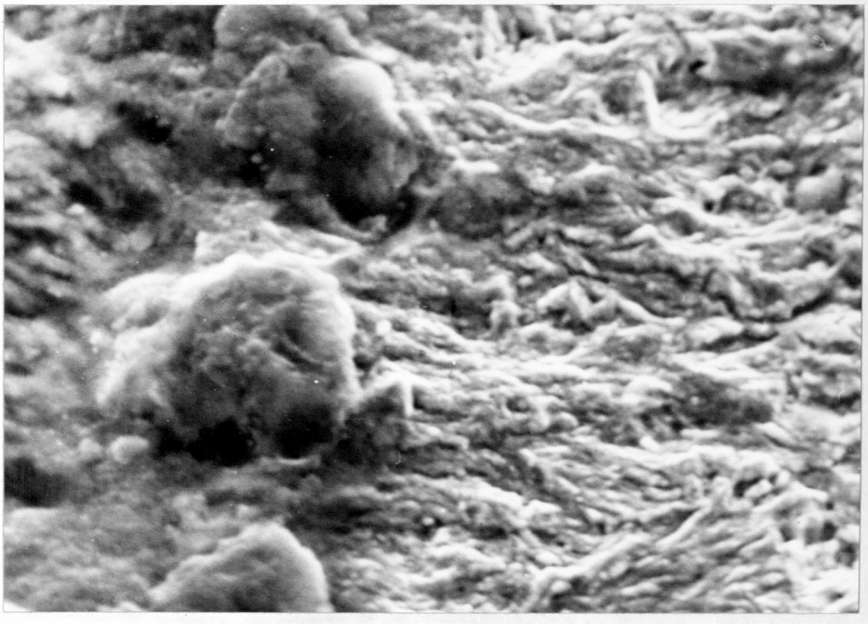
(b) $\Delta K = 13.5\ MPam^{-\frac{1}{2}}$, $da/dn = 6.0 \times 10^{-6}$ mm/cycle, $a/w = 0.29$.

magnification = x 1400

Crack growth direction ⟶



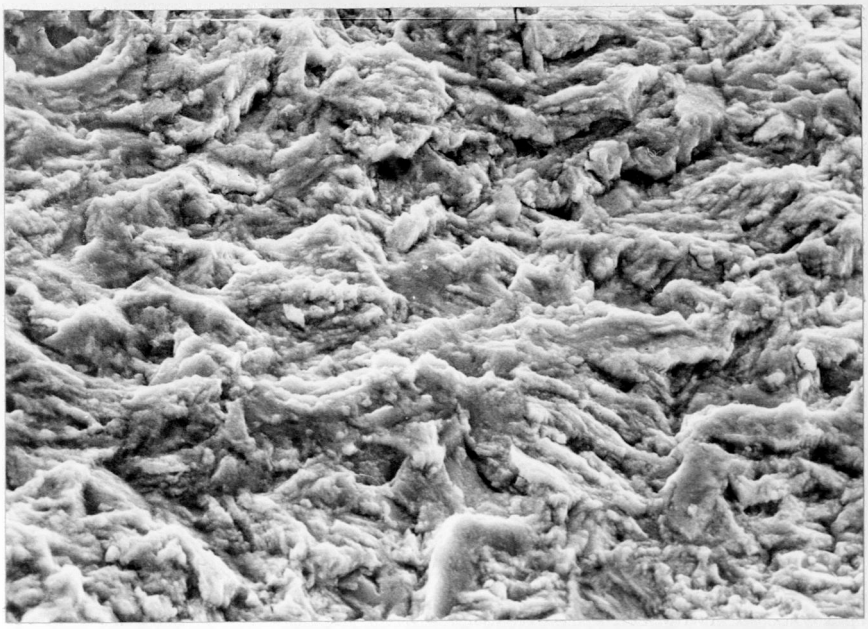
(c)



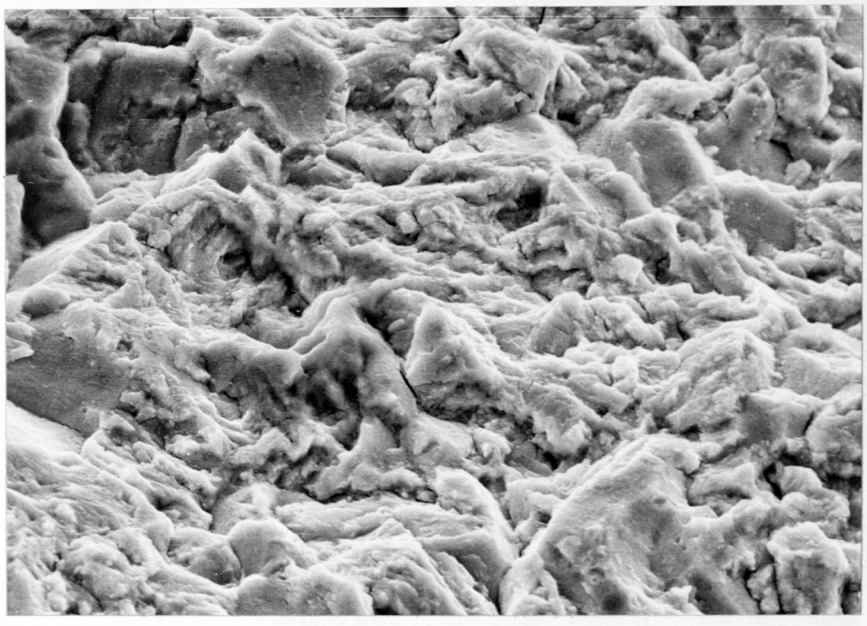
(d)

Fig. 11.36 SEM micrographs of Specimen T4-EN19QH-0.1R-0.38 illustrating fracture surface morphology:
(c) just before threshold, ΔK = 8.3 MPam$^{-\frac{1}{2}}$, da/dn = 8.8 x 10^{-8} mm/cycle, a/w = 0.37, magnification = 1400; and
(d) at the threshold-post threshold interface
ΔK = 10.1 MPam$^{-\frac{1}{2}}$, da/dn = 3.0 x 10^{-8}, a/w = 0.38.
magnification = x 2000.

Crack growth direction ⟶



(e)



(f)

Fig. 11.36 SEM micrographs of Specimen T4-EN19QH-0.1R-0.38 illustrating the fracture surface morphology during post threshold fcg.

(e) ΔK = 11.4 MPam$^{-\frac{1}{2}}$, da/dn = 1.6 x 10^{-6} mm/cycle, a/w = 0.62

(f) ΔK = 15.0 MPam$^{-\frac{1}{2}}$, da/dn = 5.3 x 10^{-6} mm/cycle, a/w = 0.51

magnification = x 1400

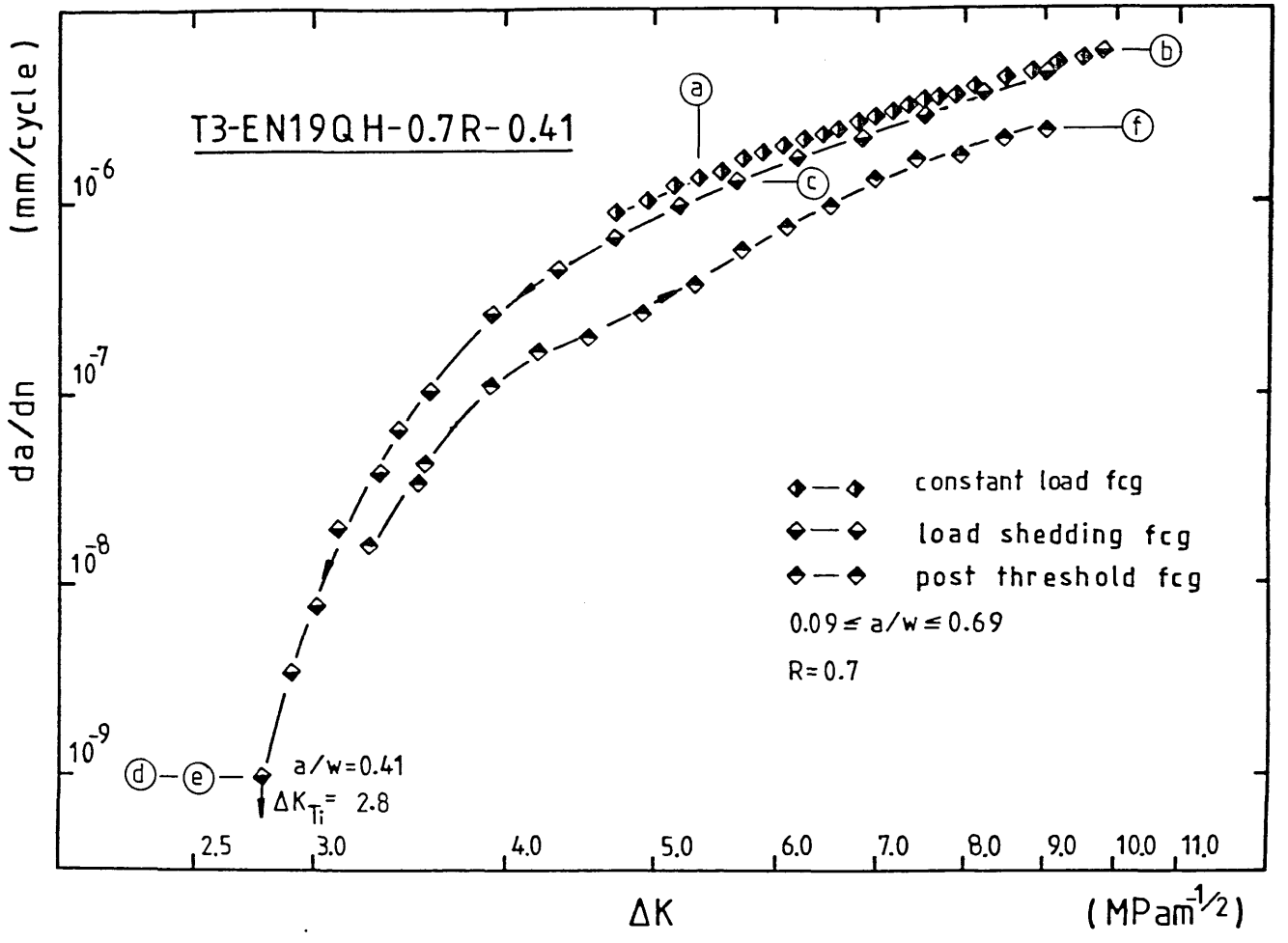
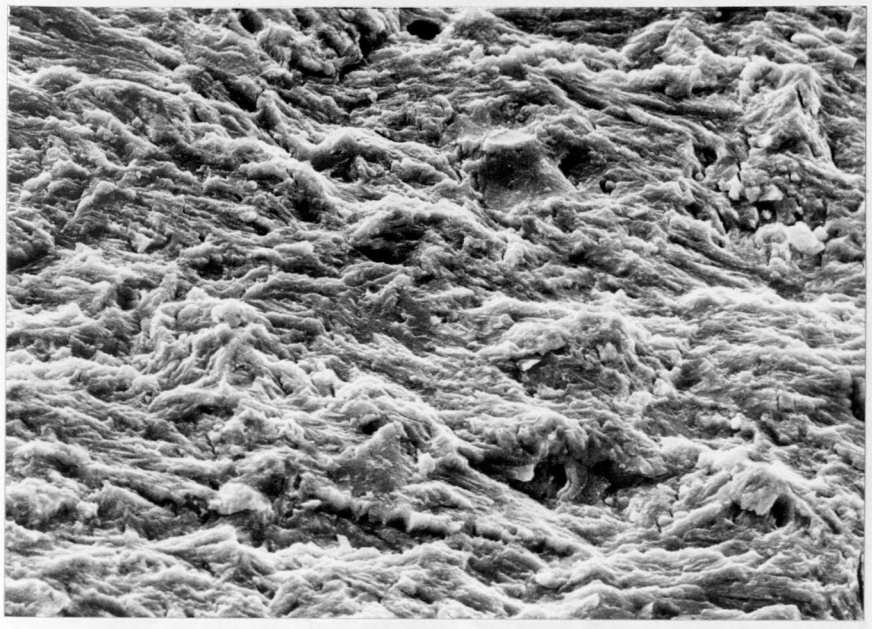
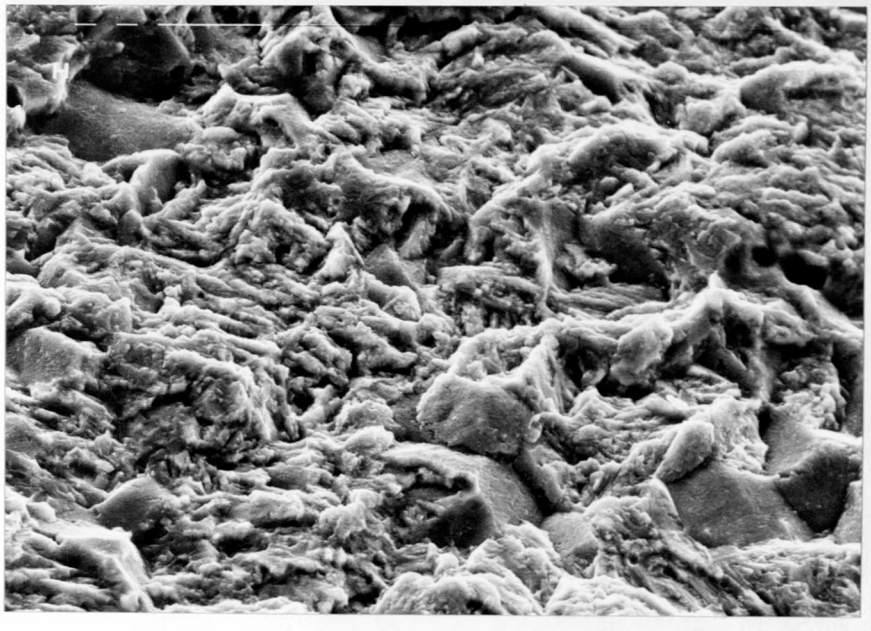


Fig. 11.37 A double logarithm plot of da/dn versus ΔK of EN19QH illustrating the SEM micrograph positions of Fig. 11.38.

Crack growth direction ⟶



(a)



(b)

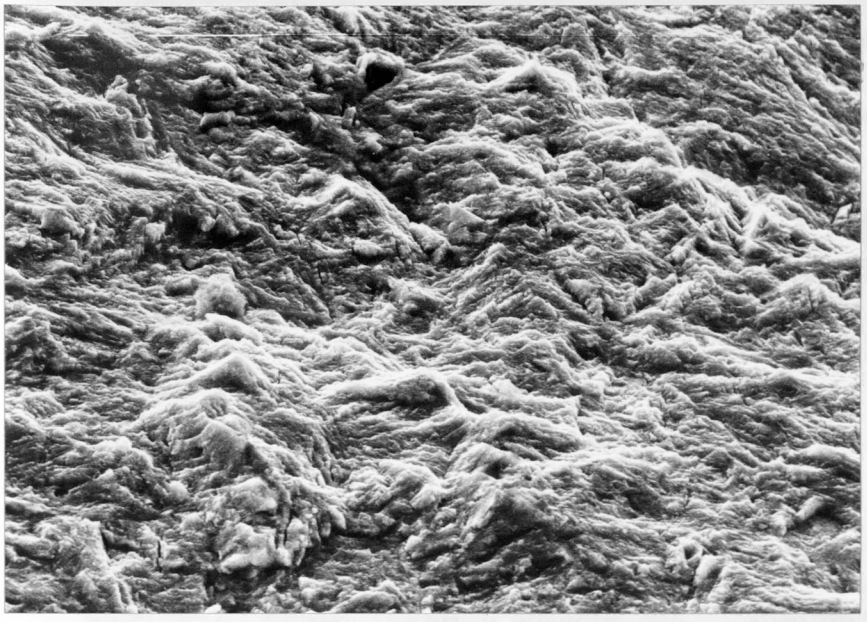
Fig. 11.38 SEM micrographs of Specimen T3-EN19QH-0.7R-0.41 illustrating the change of fracture mode during constant load fcg

(a) ΔK = 5.3 $MPam^{-\frac{1}{2}}$, da/dn = 1.4 x 10^{-6} mm/cycle, a/w = 0.12

(b) ΔK = 9.7 $MPam^{-\frac{1}{2}}$, da/dn = 6.0 x 10^{-6} mm/cycle, a/w = 0.32

magnification = x 1400

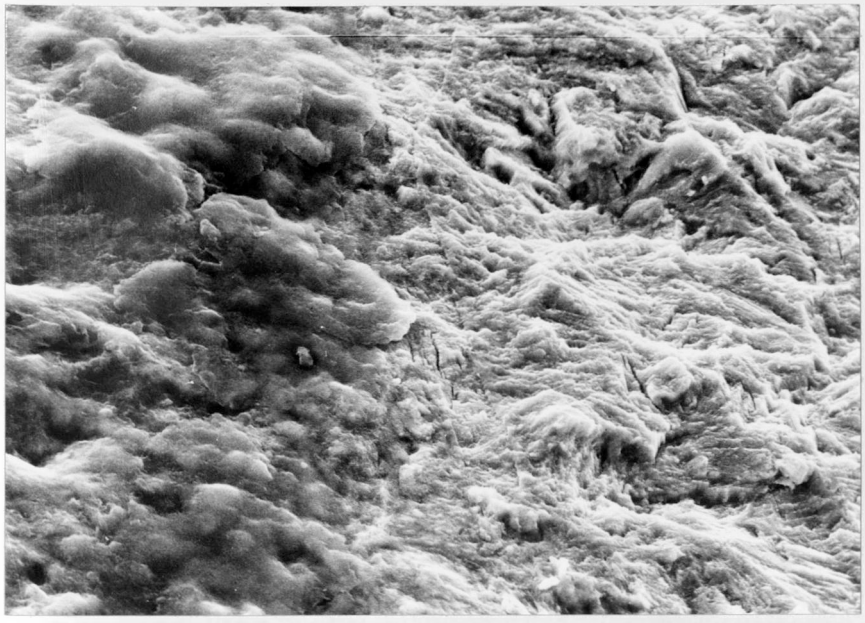
Crack growth direction ⟶



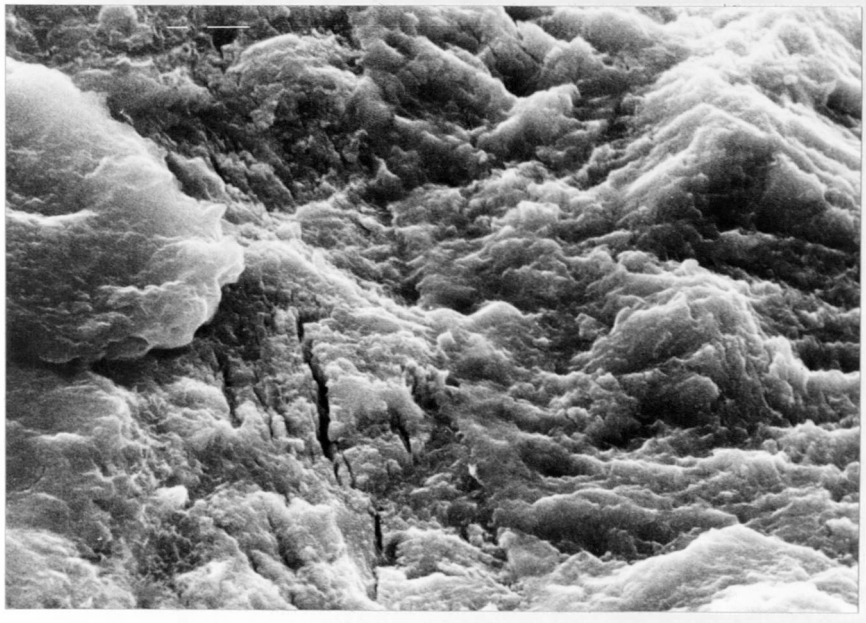
(c)

Fig. 11.38 An SEM micrograph of Specimen T3-EN19QH-0.7R-0.41 illustrating the occurrance of amorphous ductile fracture during the threshold load shedding approach sequence. $\Delta K = 5.6\ MPam^{-\frac{1}{2}}$, $da/dn = 1.3 \times 10^{-6}$ mm/cycle, $a/w = 0.36$, magnification = x 1400

Crack growth direction ⟶



(d)



(e)

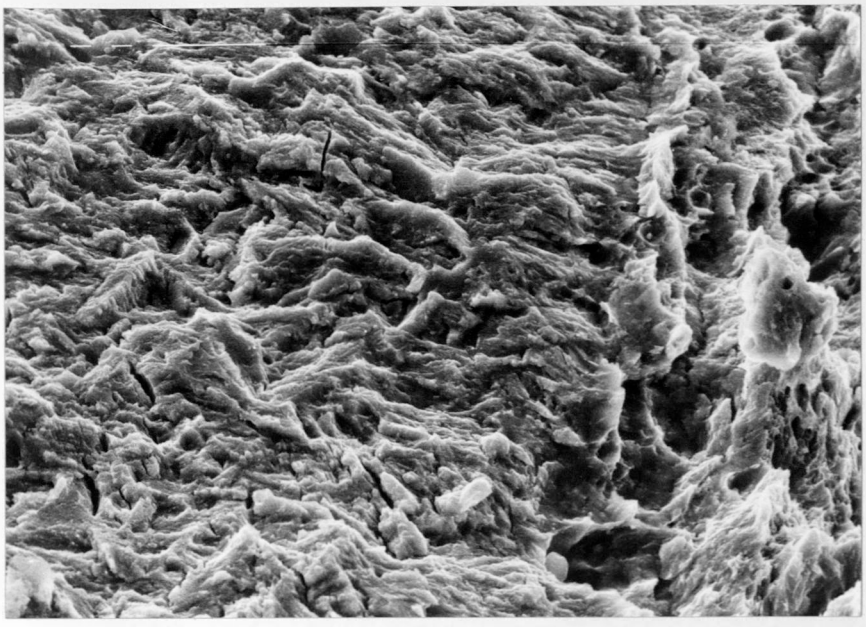
Fig. 11.38 SEM micrographs of Specimen T3-EN19QH-0.7R-0.41 illustrating the occurrance of oxide debris, secondary cracking and transgranular dutile fracture at the threshold-post threshold interface.

(d) magnification = x 1400

(e) magnification = x 5000

ΔK = 3.6 MPam$^{-\frac{1}{2}}$, da/dn = 1.0 x 10^{-9} mm/cycle, a/w = 0.41

Crack growth direction ⟶



(f)

Fig. 11.38 An SEM micrograph of Specimen T3-EN19QH-0.7R-0.41 illustrating the occurrance of amorphous transgranular ductile fracture during post threshold fcg (i.e., at the fast fracture interface).
ΔK = 8.9 MPam$^{-\frac{1}{2}}$, da/dn = 2.4 x 10^{-6} mm/cycle, a/w = 0.69
magnification = x 1400

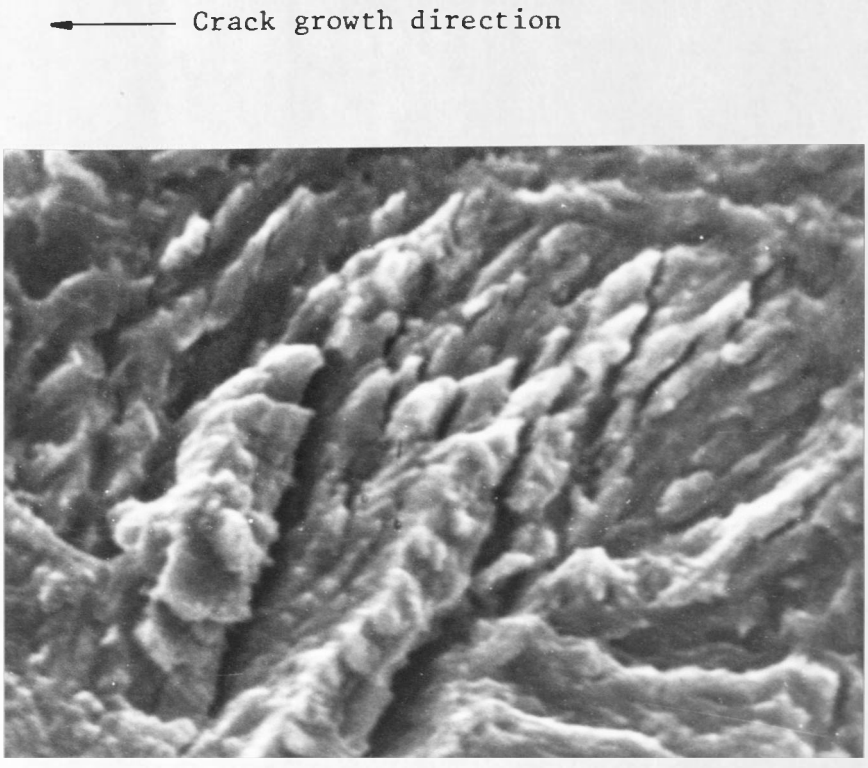


Fig. 11.39 An SEM micrograph of Specimen T3-EN19QH-0.7R-0.41 illustrating the severity of secondary cracking during post threshold fcg.
$\Delta K = 3.5$ MPam$^{-\frac{1}{2}}$, $da/dn = 3.8 \times 10^{-7}$ mm/cycle,
$a/w = 0.48$, magnification = x 5000

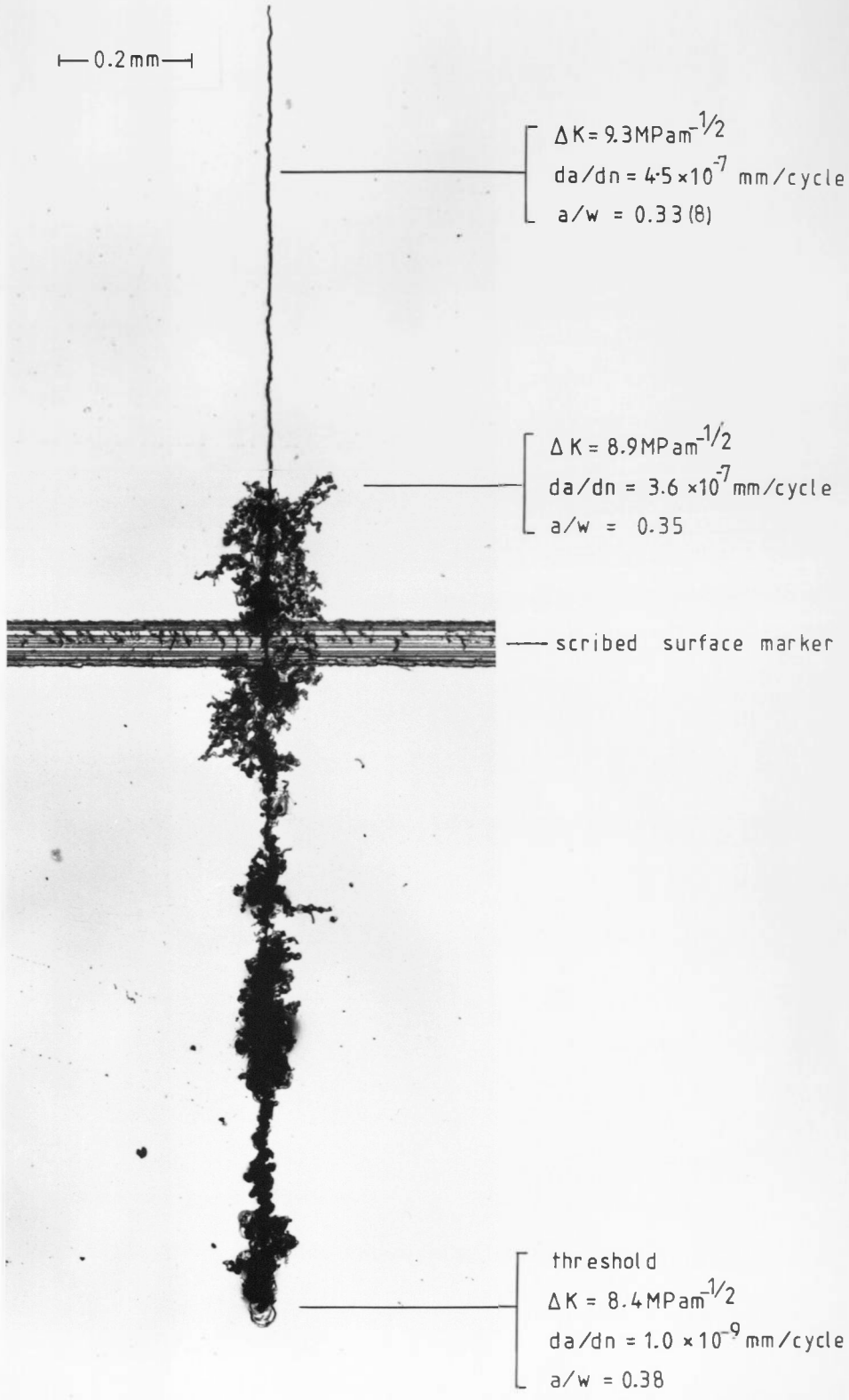


Fig. 11.40 A negative crack profile replica of specimen T4-EN19QH-0.1R-0.38 illustrating the extent of oxide extrusion as threshold is approached. $K_{applied} = K_{max} = 9.4 MPam^{-1/2}$

that the fretting oxide layer had spalled, as shown in Figs. 11.41 and 11.42.

Unlike Specimen T4-EN19QH-0.1R-0.38 the crack profile replica of Specimen T3-EN19QH-0.7R-0.41 at threshold did not exhibit excessive fretting oxide debris, Fig. 11.43. Enlargement of a small area beyond the crack tip confirmed that the crack was closed at minimum load, suggesting that either $K_{open} = K_{min}$ or $K_{open} < K_{min}$.

11.4.2 Fatigue of Ferritic Steels EN3BN and EN3BA

11.4.2.1 Near Threshold Fatigue Crack Growth

11.4.2.1a Growth Rate Results

The fatigue behaviour of materials EN3BN and EN3BA subject to threshold testing at R = 0.1 exhibited similar trends, Figs. 11.45 and 11.46. A rapid fall in growth rate to the threshold level occurred during the load shedding threshold approach sequence, threshold hysteresis was present, and during the initial stages of post threshold crack growth a rapid increase in growth rate occurred over a small increase in ΔK.

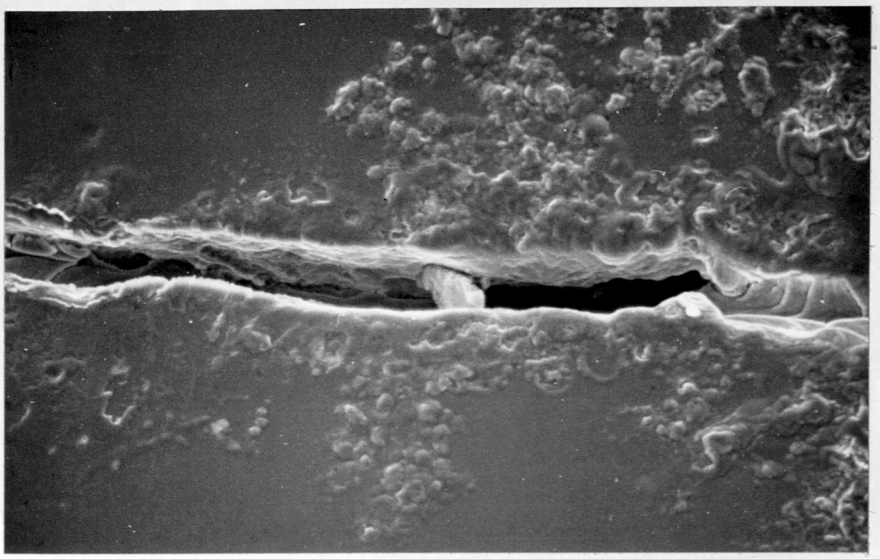
A comparison of both growth rate plots, Fig. 11.47, illustrated that during constant load fcg growth rates were coincidental and conformed to a linear response of the form

$$\text{Log } da/dn = m \log \Delta K + C \qquad \ldots(11.02)$$

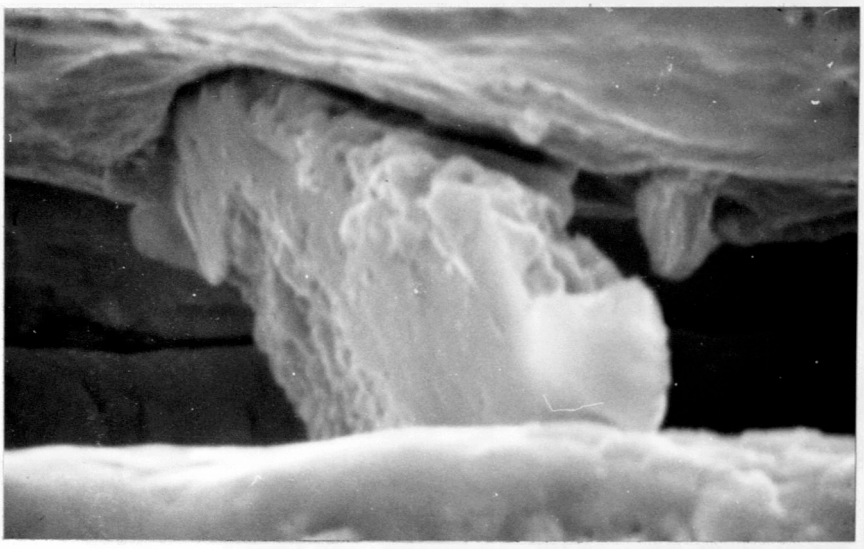
Using standard linear regression analysis (Appendix A7) m was found to be 2.7.

Increasing ferrite grain size from 10 to 53 μm produced a small increase in ΔK_{Ti} from 9.9 to 11.2 $MPam^{-\frac{1}{2}}$ and a similar shift in post threshold growth rates to higher ΔK's.

← Crack growth direction



(a)



(b)

Fig. 11.41 Positive crack profile replicas of Specimen T4-EN19QH-0.1R-0.38 produced at the end of threshold testing which illustrate oxide spalling in the wake of the crack tip.

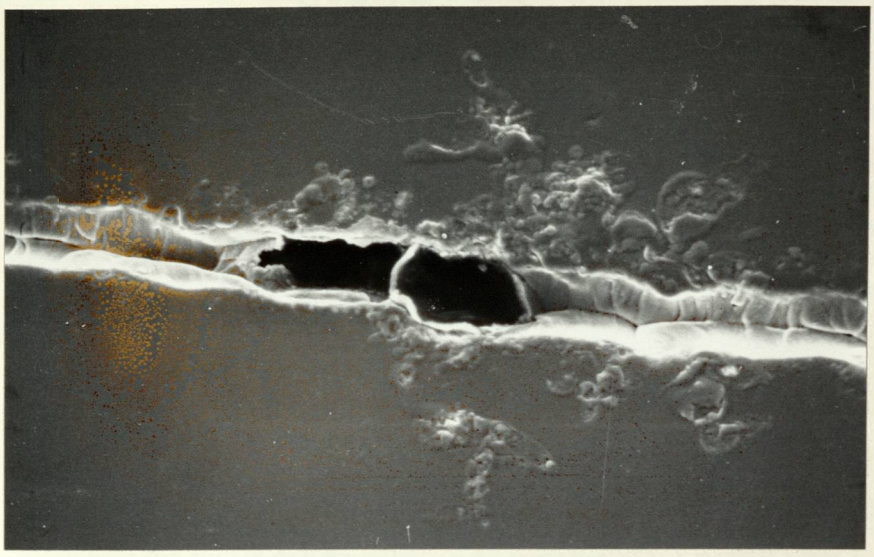
(a) magnification = x 640, a/w = 0.37

(b) magnification = x 5000, a/w = 0.37

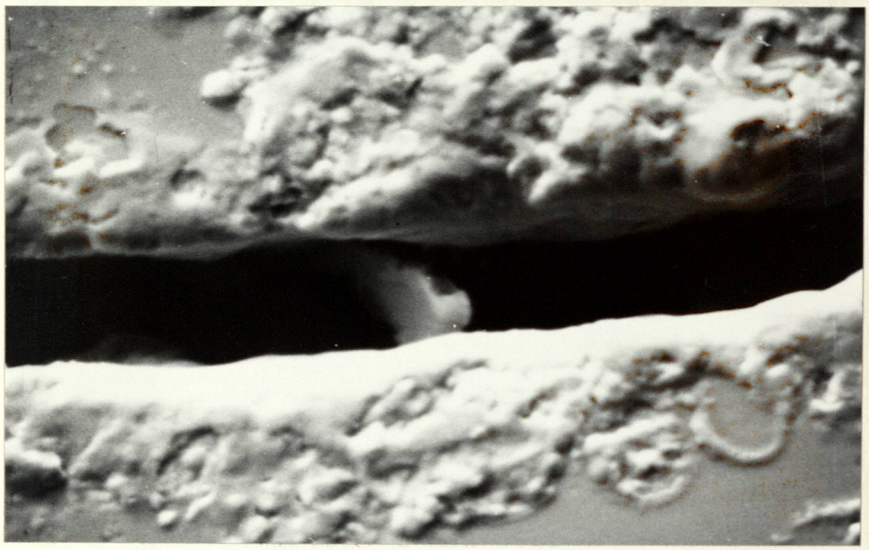
$K_{applied} = K_{min} = 1.6\ MPam^{-\frac{1}{2}}$

(crack tip a/w = 0.51)

Crack growth direction



(a)



(b)

Fig. 11.42 Positive crack profile replicas of Specimen T4-EN19QH-0.1R-0.38 produced at the end of threshold testing. Further examples of oxide flaking in the wake of the crack tip.

(a) a/w = 0.35 (b) a/w = 0.39

$K_{applied} = K_{min} = 1.6\ MPam^{-\frac{1}{2}}$

(a) ×640 (b) ×1250

(crack tip a/w = 0.51)

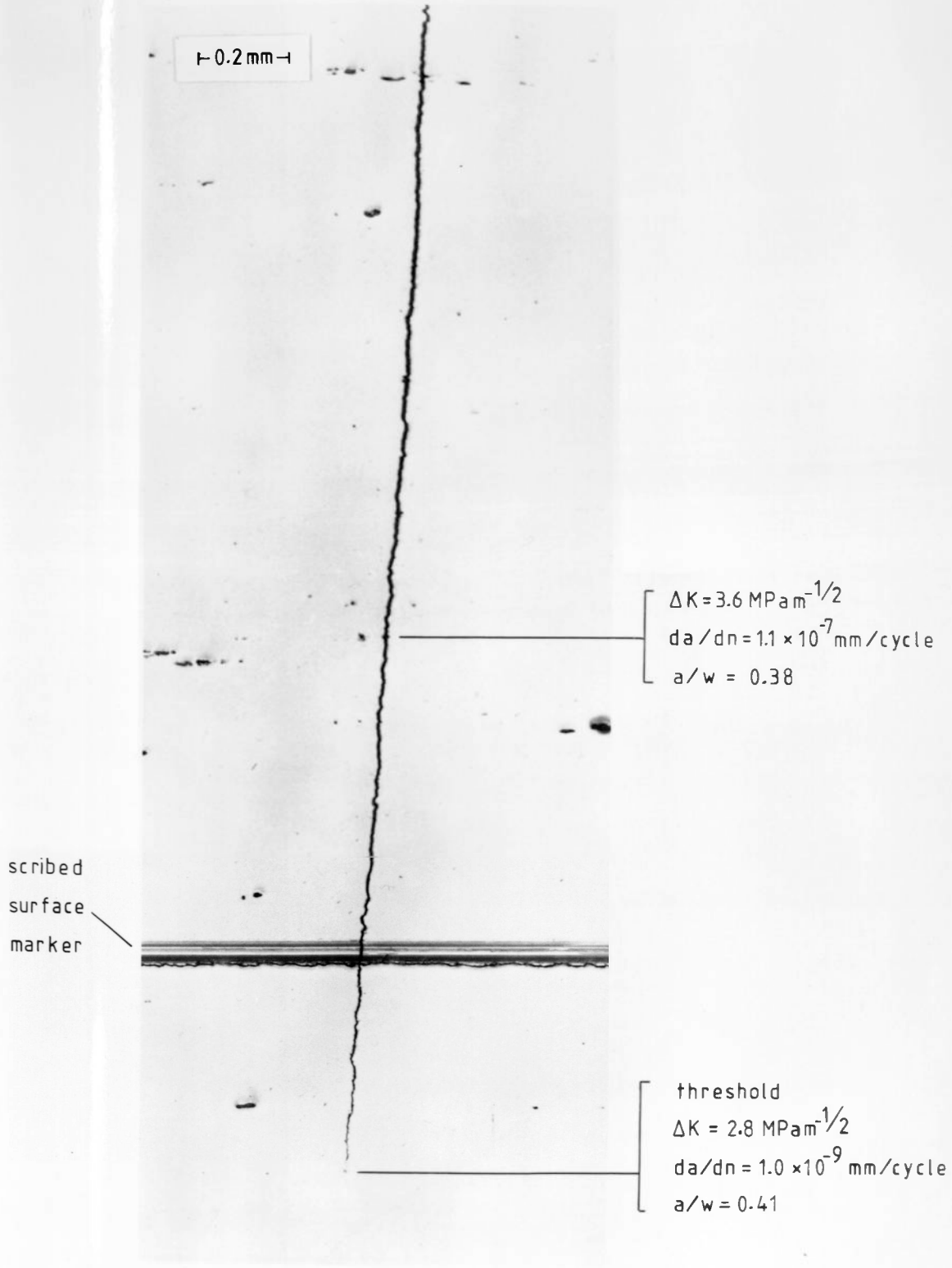
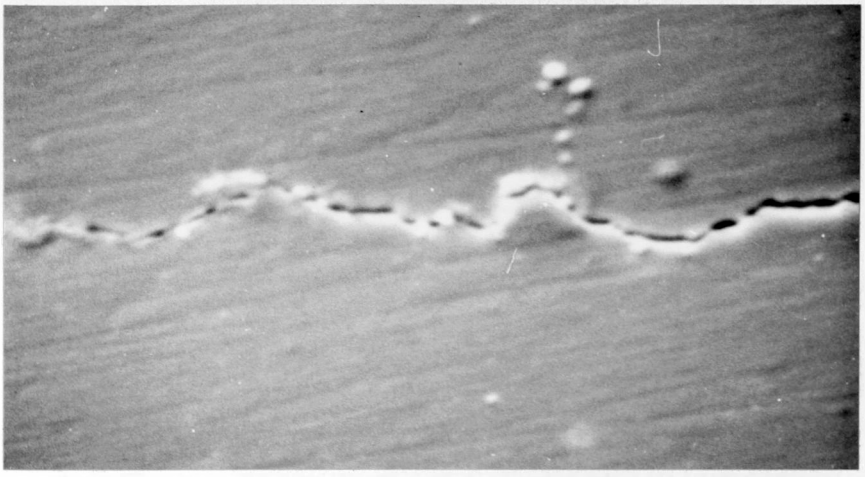


Fig. 11.43 A negative crack profile replica of specimen T3-EN19QH-0.7R-0.41 illustrating the clean appearance of the crack tip as threshold is approached.

$K_{applied} = K_{max} = 9.2$ MPam$^{-1/2}$

Crack growth direction



(a)



(b)

Fig. 11.44 Positive crack profile replicas of Specimen T3-EN19QH-0.7R-0.41 produced at threshold

(a) $K_{applied} = K_{max} = 9.2\ MPam^{-\frac{1}{2}}$, $a/w = 0.40(5)$

(b) $K_{applied} = K_{min} = 6.1\ MPam^{-\frac{1}{2}}$, $a/w = 0.40(5)$

magnification = x 2500

(crack tip $a/w = 0.41$)

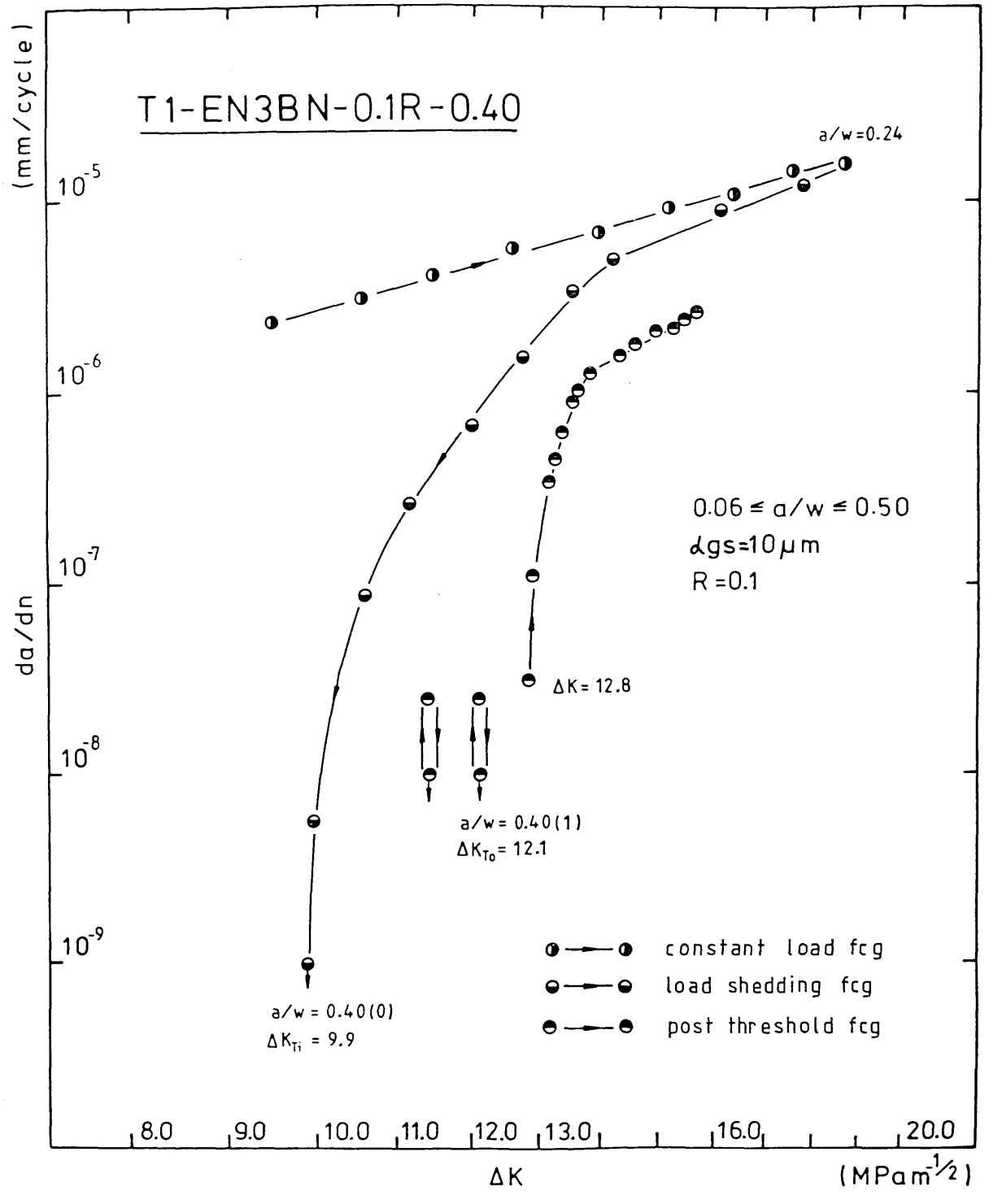


Fig. 11.45 A double logarithm plot of da/dn versus ΔK of EN3BN exhibiting threshold hysteresis and irreversible growth behaviour.

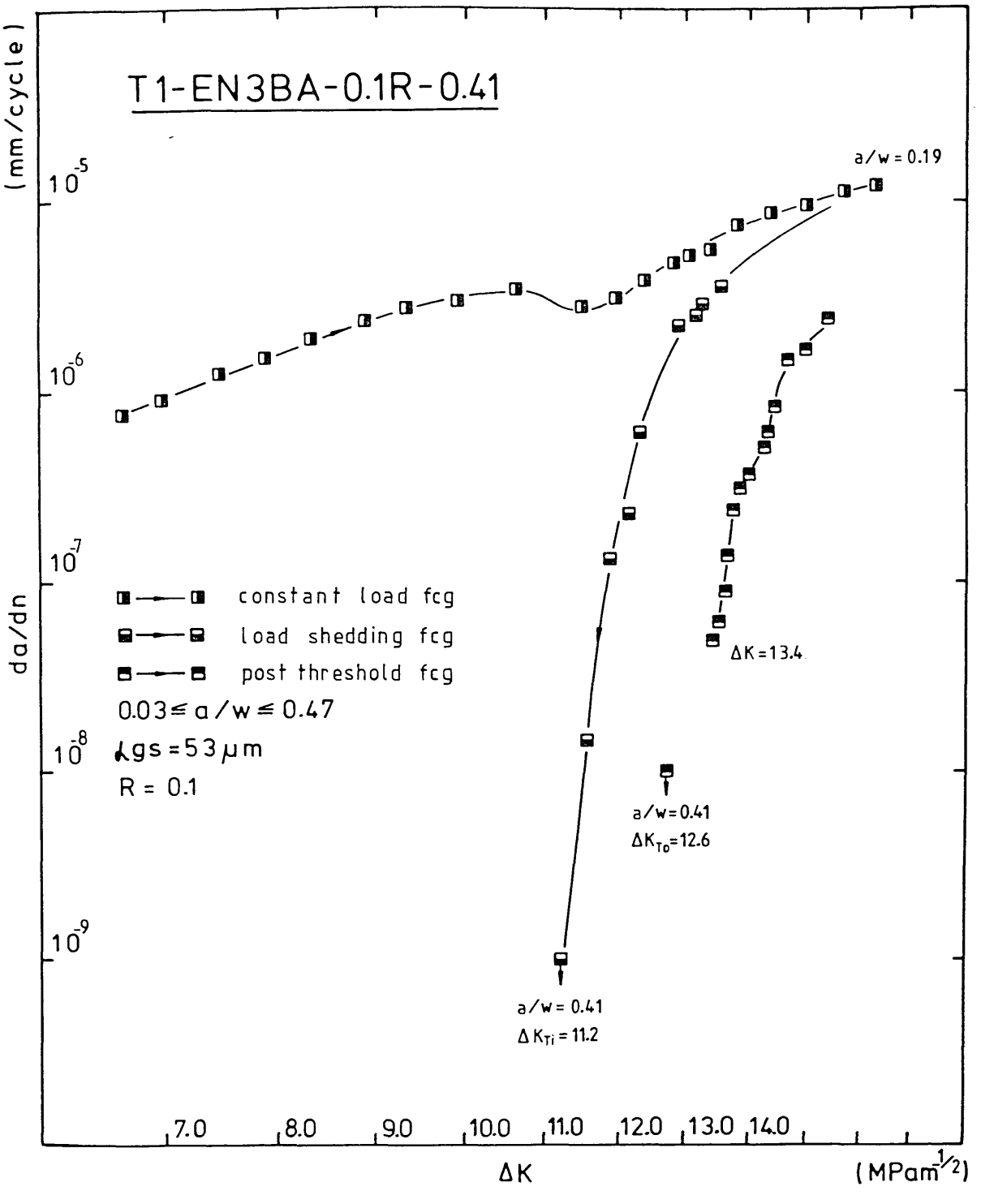


Fig. 11.46 A double logarithm plot of da/dn versus ΔK of EN3BA exhibiting threshold hysteresis and irreversible growth behaviour.

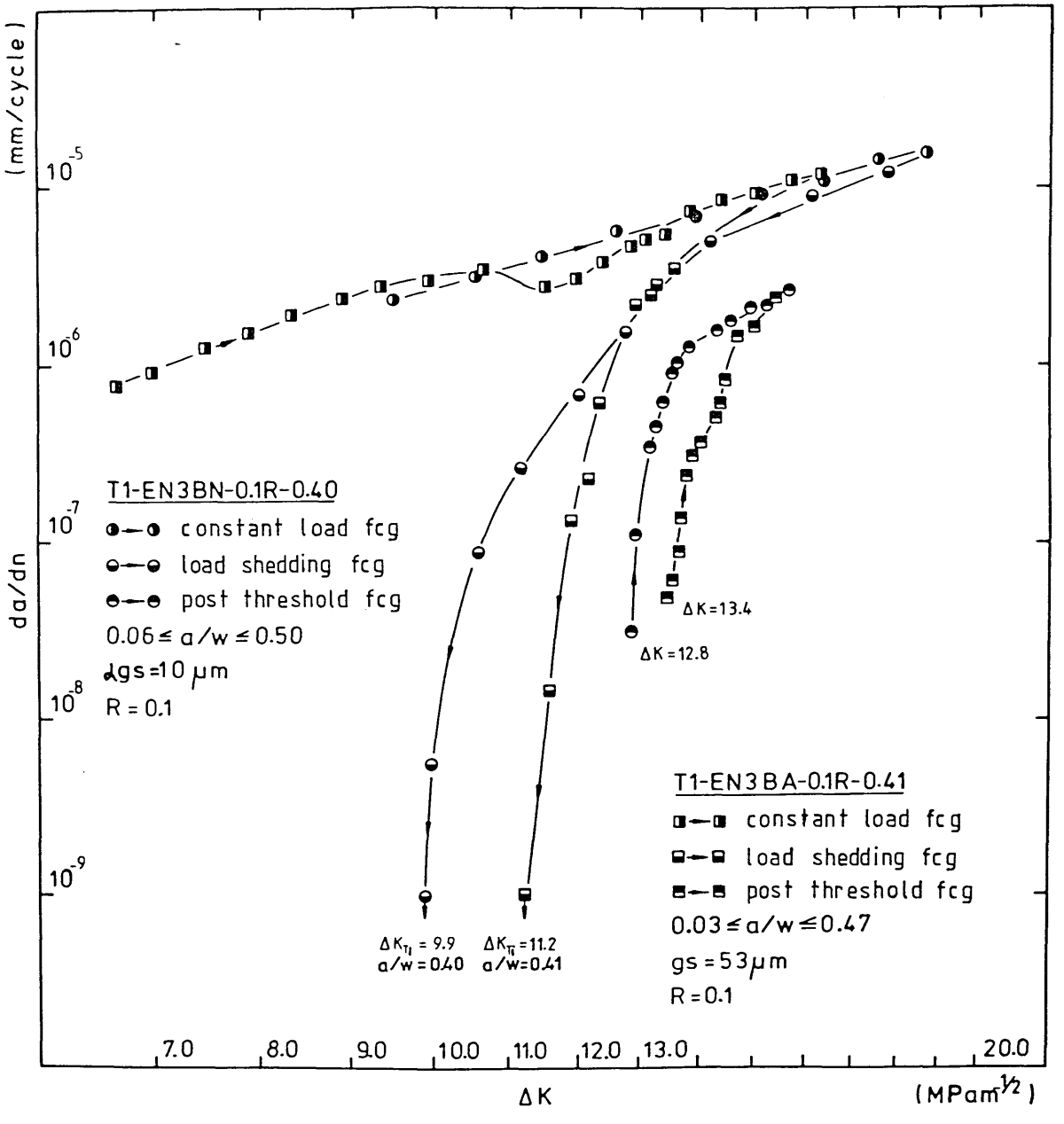


Fig. 11.47 A growth rate comparison of materials EN3BN and EN3BA

11.4.2.1b Crack Tip Opening Loads, Stress Intensities and ΔK_{eff} Analysis of Results

EN3BN The crack tip opening load response of EN3BN determined at threshold and throughout post threshold fcg revealed that temporary threshold crack arrest and subsequent crack growth was associated with an increase and decay in crack closure, Fig. 11.48. When analysed in terms of K_{open} it was evident that during threshold crack arrest a sequential increase in K_{max} induced or was accompanied by a related increase in K_{open}, Fig. 11.49. This increase then decayed rapidly during the initial stages of post threshold fcg.

ΔK_{eff} analysis of the data, Fig. 11.50, revealed that whilst post threshold growth rates were suitably aligned with $\Delta K_{eff.Ti}$ it failed to merge with the ΔK growth rate response of constant load fcg.

EN3BA Although crack tip opening load behaviour was monitored at a high level, during the initial stages of constant load fcg a well defined change in the load versus strain response did not exist, Fig. 11.51. Reliable closure data was only available towards the latter stages of constant load fcg and throughout the remaining fatigue sequence, Fig. 11.52. From this response P_{open} was computed corresponding to specific growth rates and used to determine related values of K_{open}. The data was then combined with K_{min} and K_{max} and plotted with respect to a/w to give Fig. 11.53.

This plot illustrated that throughout threshold testing similar trends in crack closure existed as reported for EN19QH i.e.

(a) $K_{min} \leqslant K_{open} \leqslant K_{max}$;

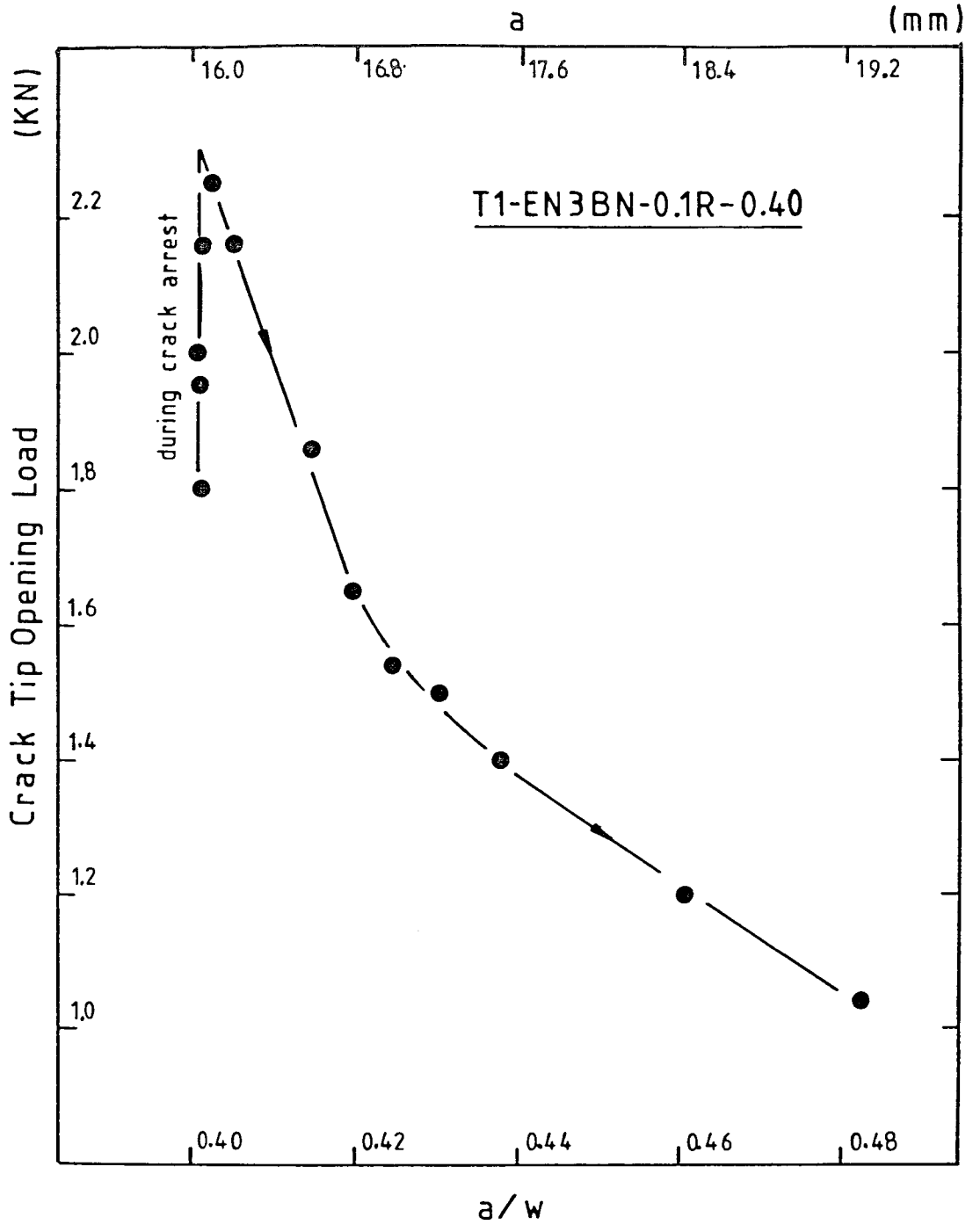


Fig. 11.48 A plot of Crack Tip Opening Load versus a/w of EN3BN illustrating the increase and decay of crack tip opening load associated with threshold hysteresis
(threshold a/w = 0.40)

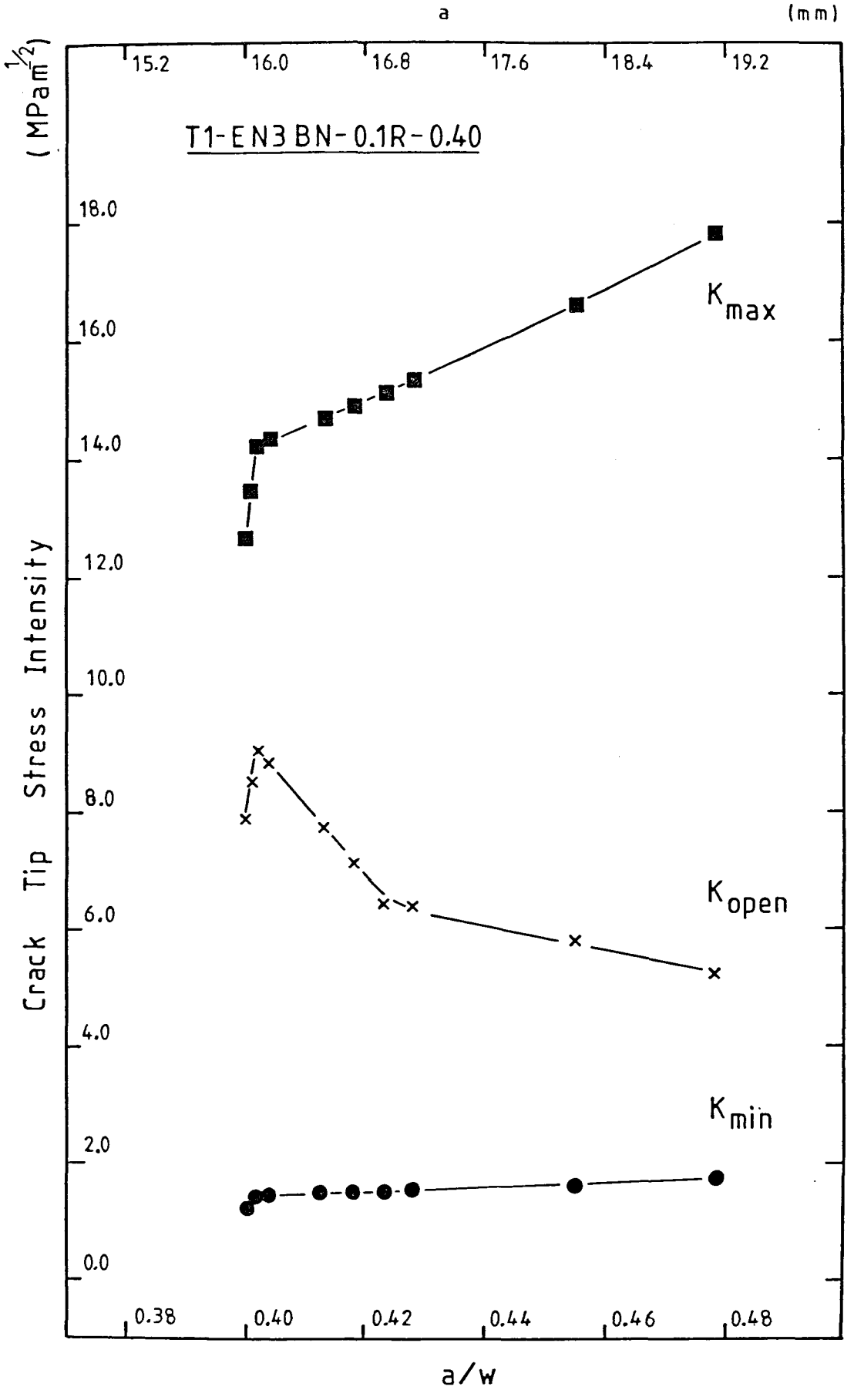


Fig. 11.49 A plot of Crack Tip Stress Intensity versus a/w of EN3BN illustrating the increase and decay of K_{open} associated with threshold hysteresis (threshold a/w = 0.40)

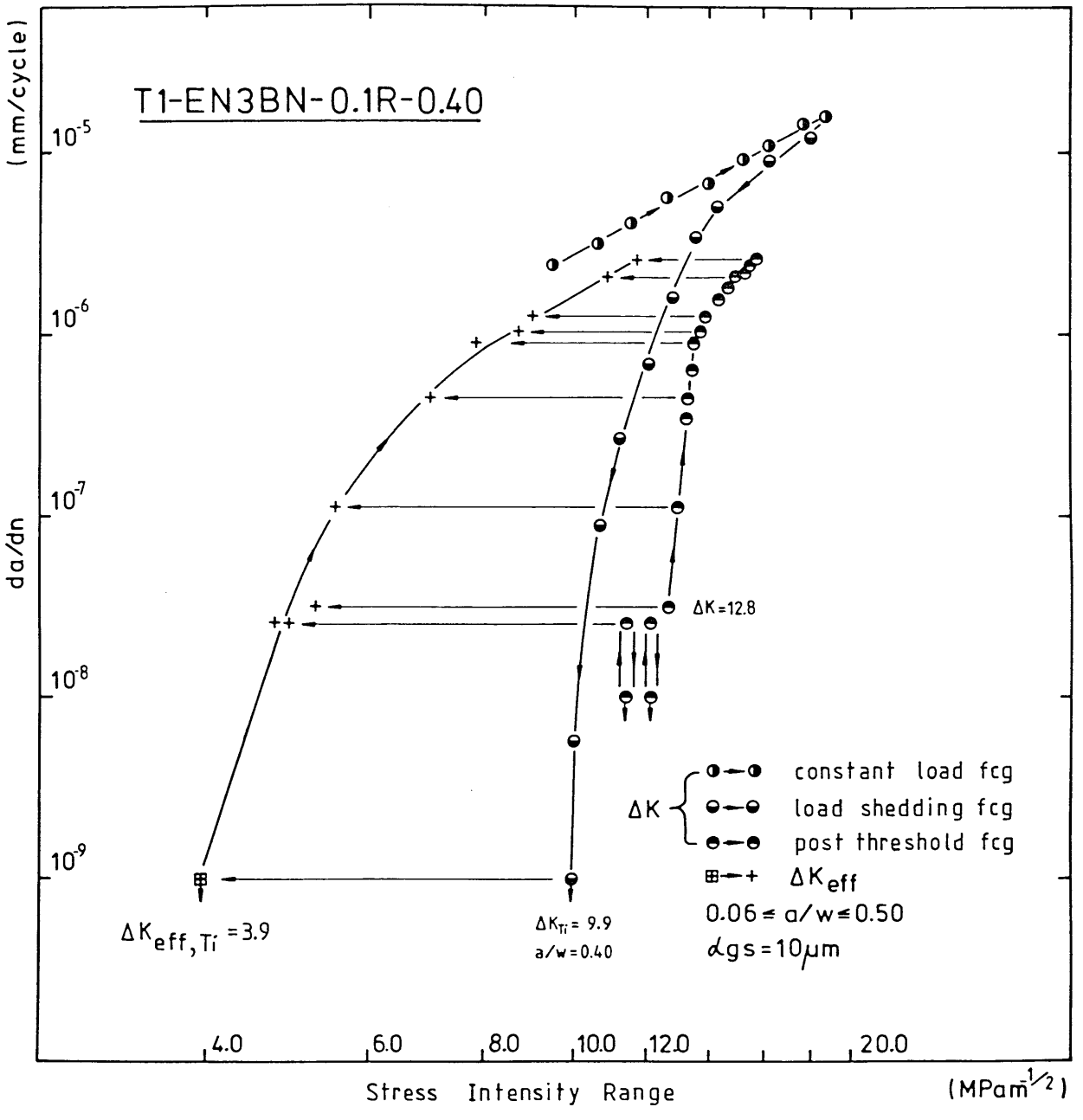
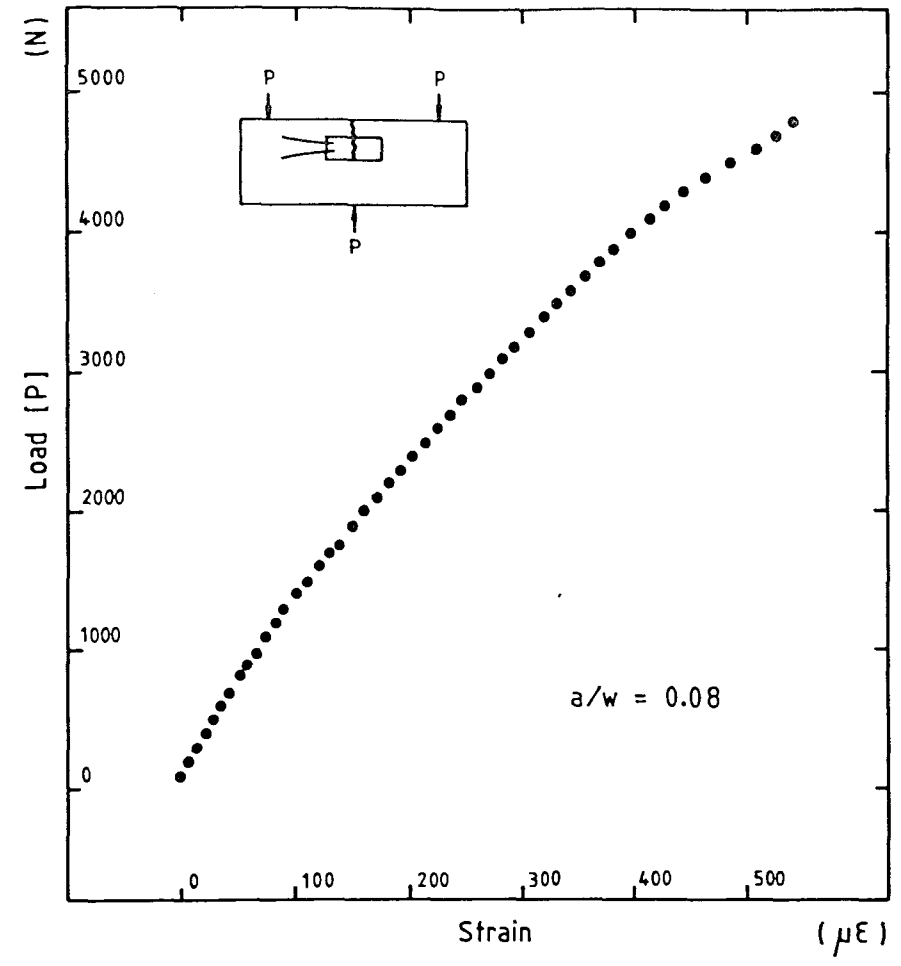


Fig. 11.50 A double logarithm plot of da/dn versus Stress Intensity Range of EN3BN which includes the ΔK_{eff} growth rate response of ΔK_{Ti} and post threshold fcg.



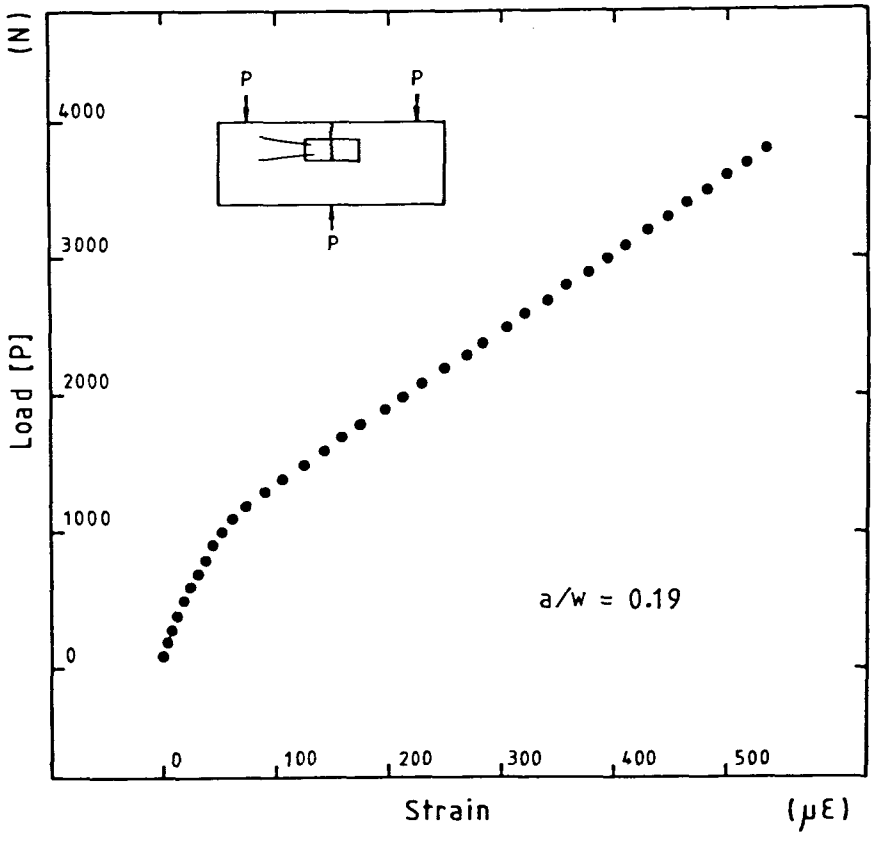


Fig. 11.51 Load versus Strain response of EN3BA sampled at a/w ratios 0.08 and 0.19 respectively.

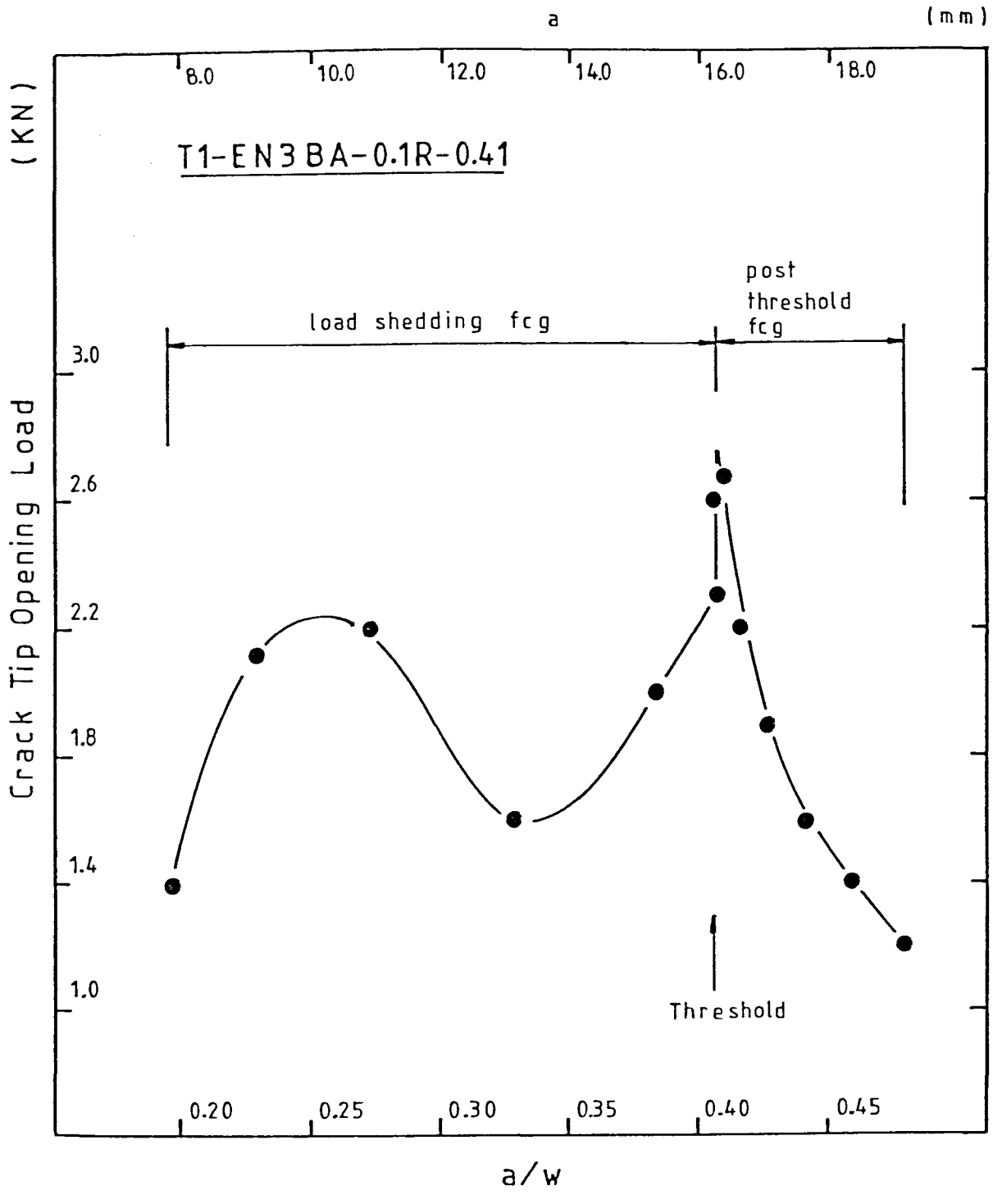


Fig. 11.52 A plot of Crack Tip Opening Load versus a/w of EN3BA

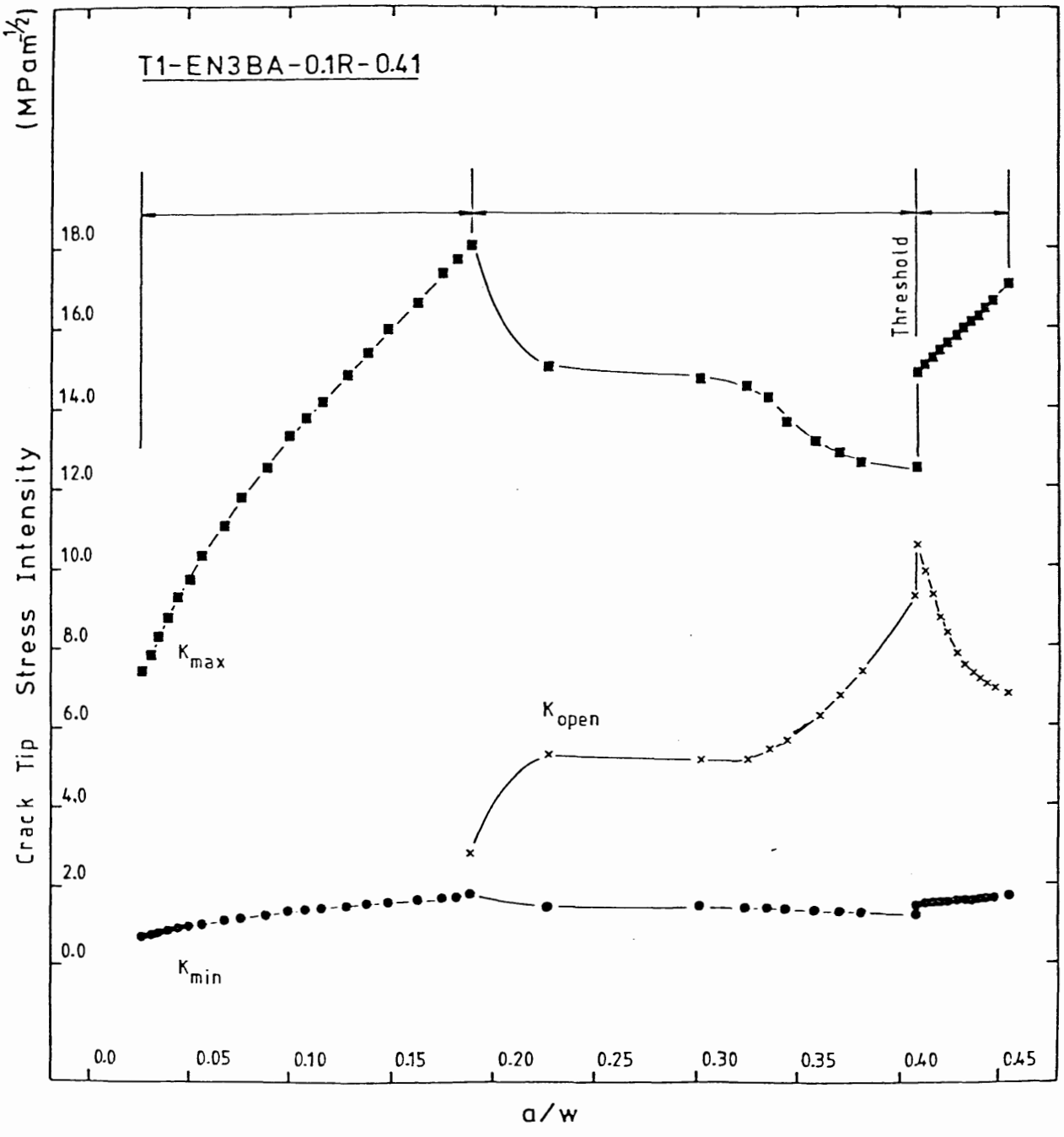


Fig. 11.53 A plot of Crack Tip Stress Intensity versus a/w of EN3BA illustrating K_{open} trend.

(b) during load shedding an initial increase in K_{open} corresponded to a decrease in K_{max};

(c) as threshold was approached K_{open} increased rapdily;

(d) threshold hysteresis was accompanied by an increase in K_{open}; and

(e) during post threshold fcg K_{open} decayed rapidly over a very small increase in a/w.

ΔK_{eff} analysis of growth rates corresponding to load shedding and post threshold fcg, Figs. 11.54-11.56, revealed the following:

(a) the ΔK_{eff} growth rate response of the threshold load shedding approach sequence merged with the ΔK growth response of constant load fcg;

(b) the ΔK_{eff} growth rate data of post threshold fcg was continuous in the near threshold regime with that of the load shedding threshold approach sequence; and

(c) the ΔK_{eff} growth rate response was irreversible tending to lower growth rates at longer crack lengths.

This latter trend was also exhibited by EN19QH tested at R = 0.7 (Fig. 11.23).

EN3BN, EN3BA A ΔK_{eff} comparison of growth behaviour in both materials, Fig. 11.57, illustrated that marginal differences existed in 'normalised' fatigue crack growth. At low growth rates this was maximised at the threshold level where both $\Delta K_{eff.Ti}$ values were contained in overlapping error bands.

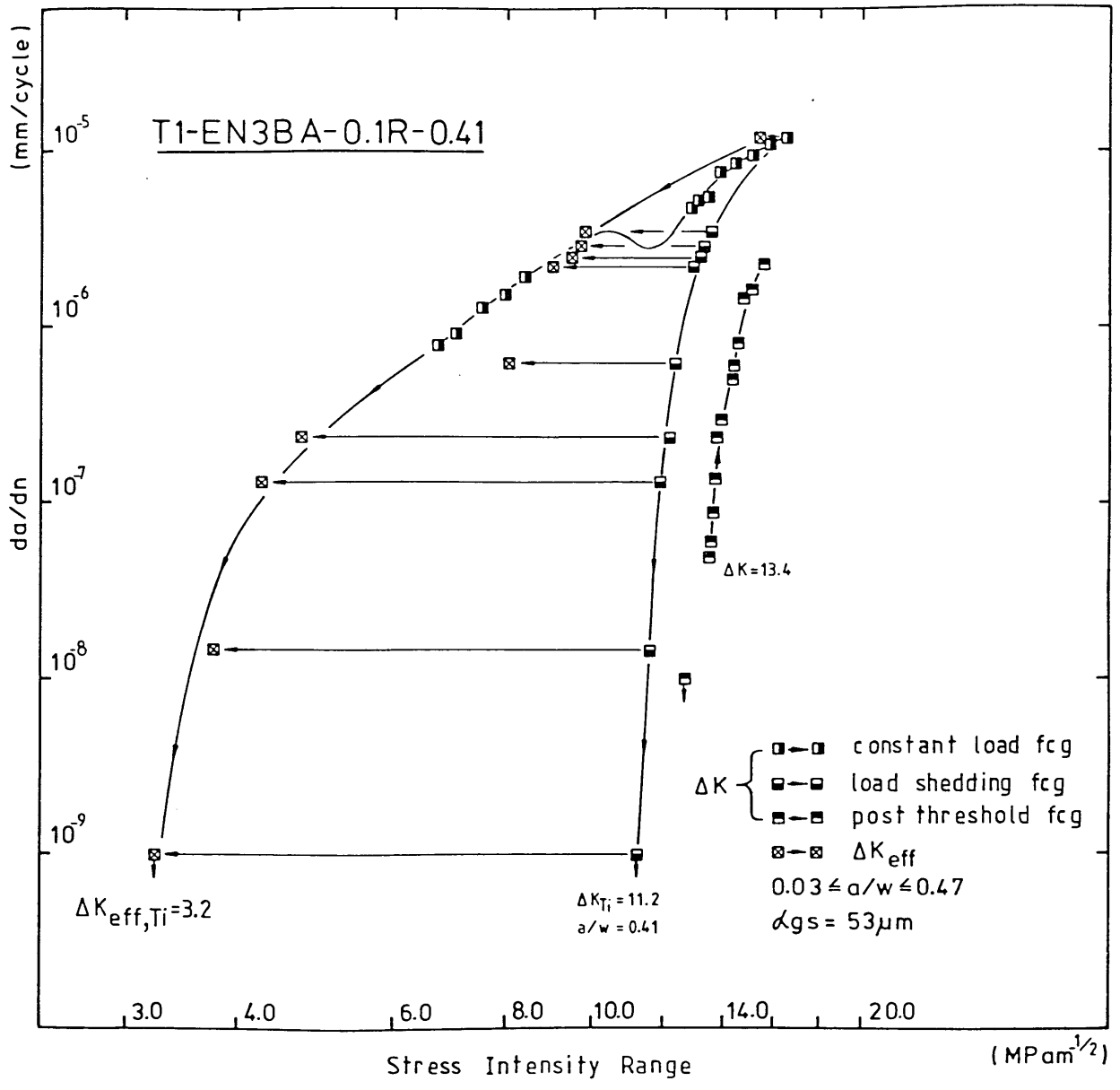


Fig. 11.54 A double logarithm plot of da/dn versus Stress Intensity Range of EN3BA which includes the ΔK_{eff} growth rate response of load shedding fcg.

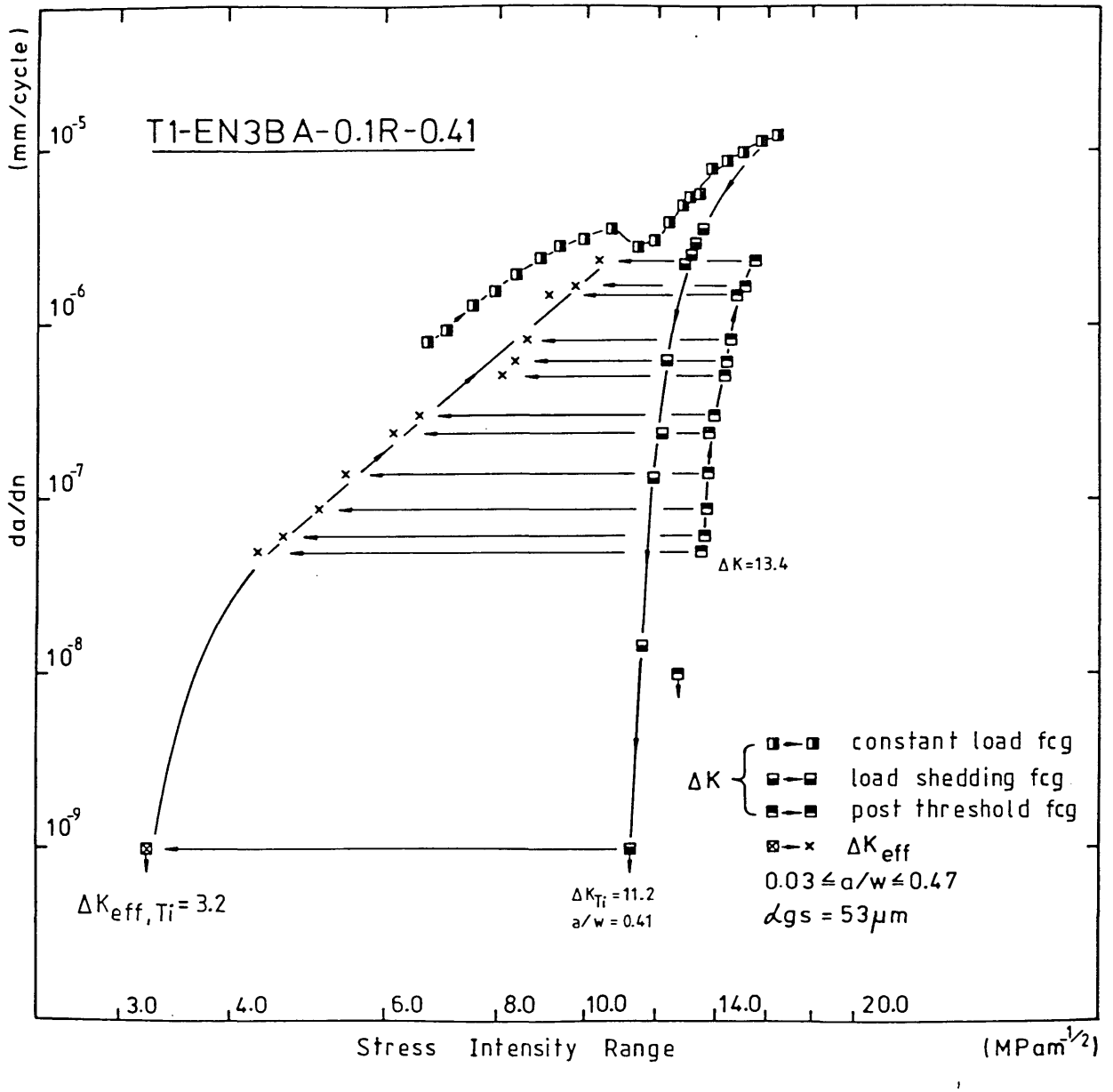


Fig. 11.55 A double logarithm plot of da/dn versus Stress Intensity Range of EN3BA which includes the ΔK_{eff} growth rate response of ΔK_{Ti} and post threshold fcg.

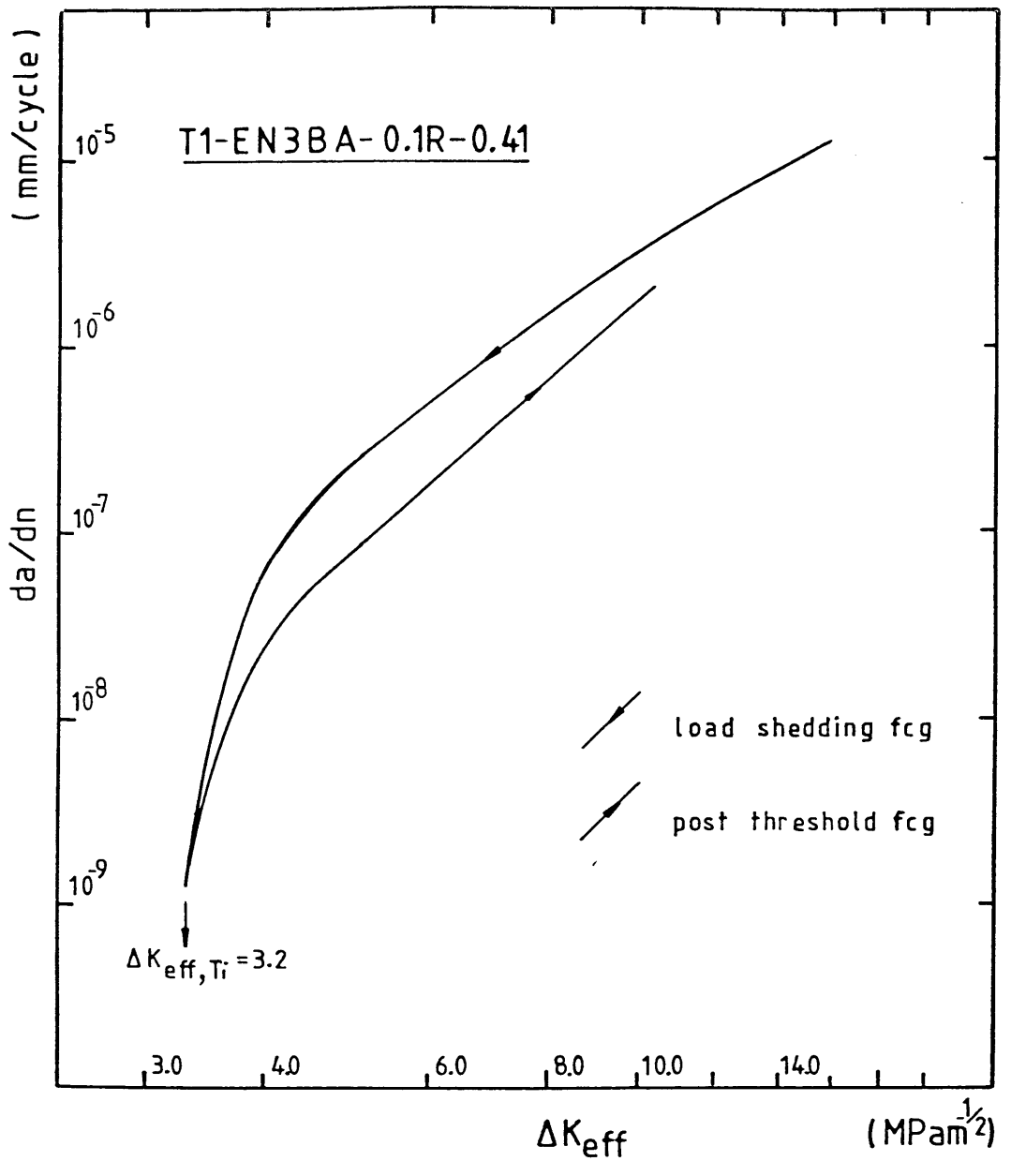


Fig. 11.56 A double logarithm plot of da/dn versus ΔK_{eff} of EN3BA exhibiting irreversible growth behaviour.

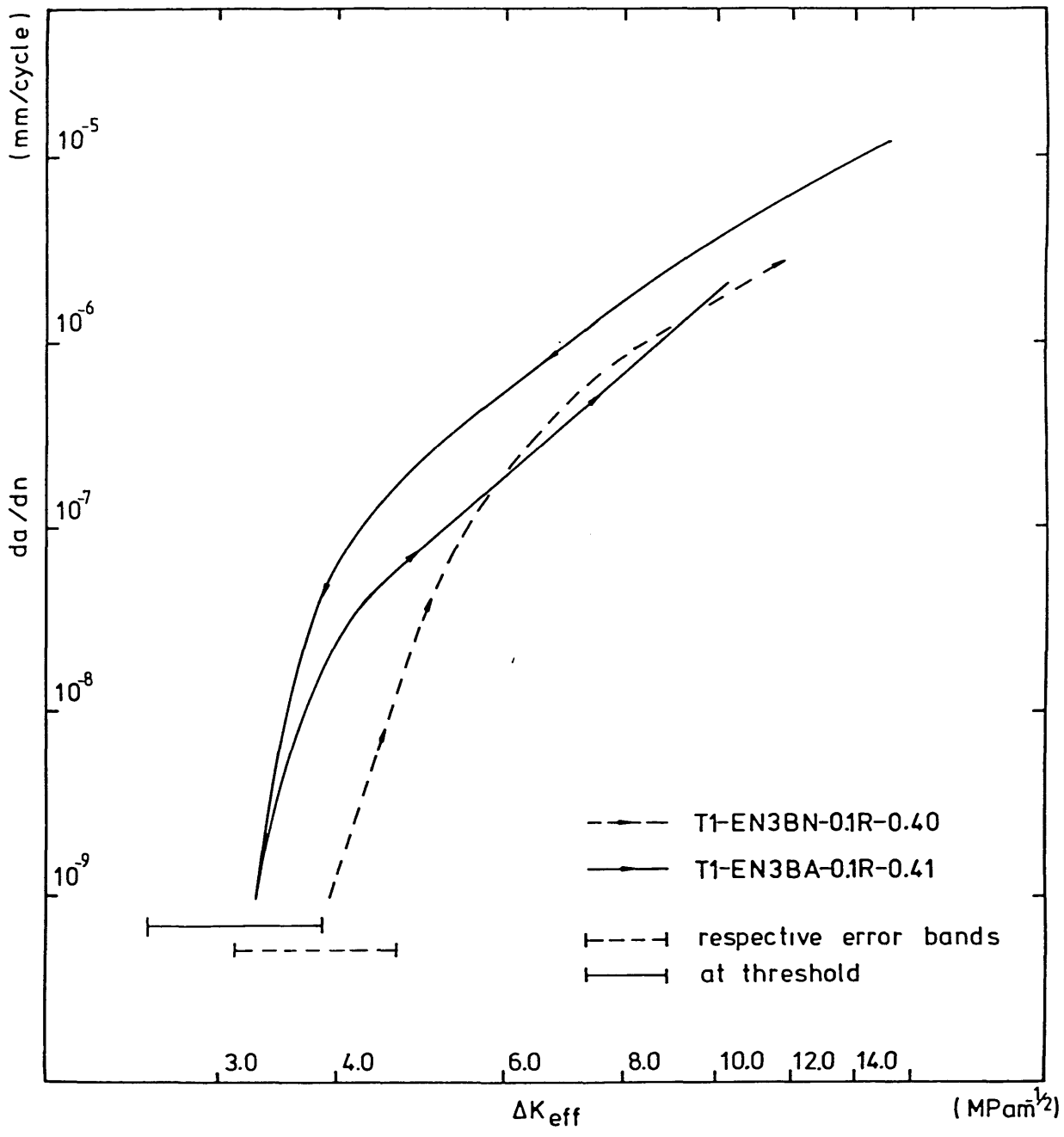


Fig. 11.57 A double logarithm plot of da/dn versus ΔK_{eff} of materials EN3BN and EN3BA

11.4.2.2 Fractography

11.4.2.2a Macroscopic Fracture Surface Appearance

The macroscopic fracture surface appearance of Specimens T1-EN3BN-0.1R-0.40 and T2-EN3BA-0.1R-0.41 are presented in Fig. 11.58. Similar features were observed on the fracture surface of EN3BN as for EN19QH tested at R = 0.1, i.e. a highly localised black surface oxide product was present and a lighter corrosion product was visible in low growth rate regions. In the case of EN3BA the irregular fracture surface made it difficult to distinguish the occurance and type of oxide present. However, close examination using an optical microscope revealed the presence of similar corrosion products as for EN3BN.

11.4.2.2b Microscopic Fracture Surface Appearance

EN3BN SEM micrographs representing the fracture surface appearance in material EN3BN, which are indexed with respect to Fig. 11.59 and appear in Fig. 11.60, revealed that crack propagation during constant load and post threshold fcg occurred by a process of transgranular ductile fracture accompanied by small amounts of intergranular faceting. The amount of intergranular faceting decreased with decreasing growth rate and was found to be a minimum within the threshold region, Fig. 11.60(a)-(c). During the process of load shedding the occurance of fretting oxidation corrosion products at growth rates $\leqslant 10^{-6}$ mm/cycle made it impossible to decide on fracture trend, Fig. 11.60(e)(f).

EN3BA SEM fracture surface micrographs of EN3BA, which are indexed with respect to Fig. 11.61 and appear in Fig. 11.62, illustrated that crack propagation during constant load and post threshold fcg resulted from either a single or mixed mode fracture mechanism. At low growth rates crack propagation occurred by a transgranular

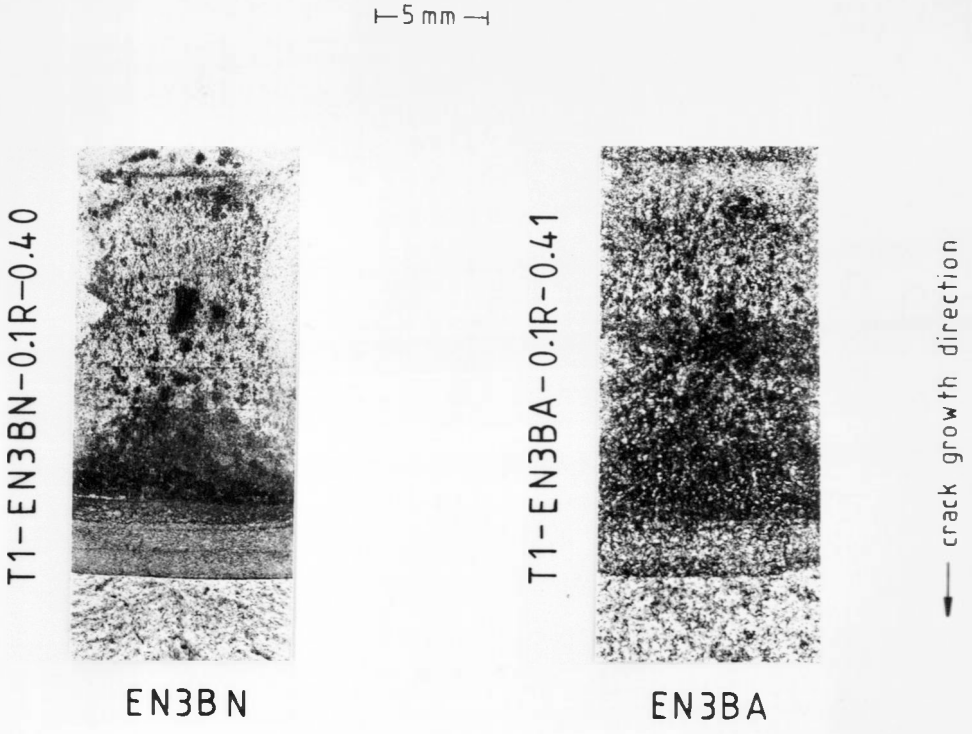


Fig. 11.58 Macroscopic fracture surface appearance of materials EN3BN and EN3BA subject to fatigue at R=0.1

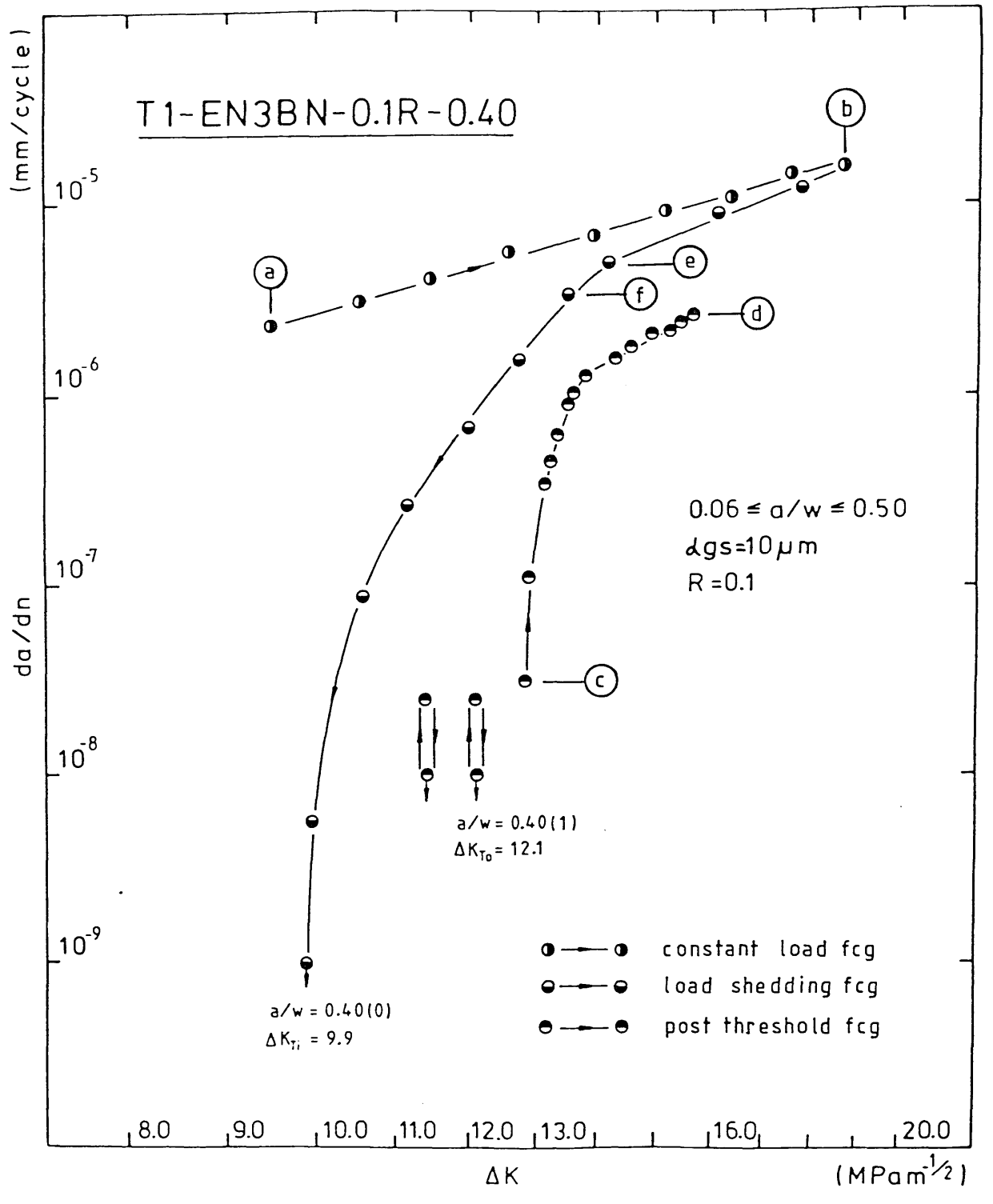
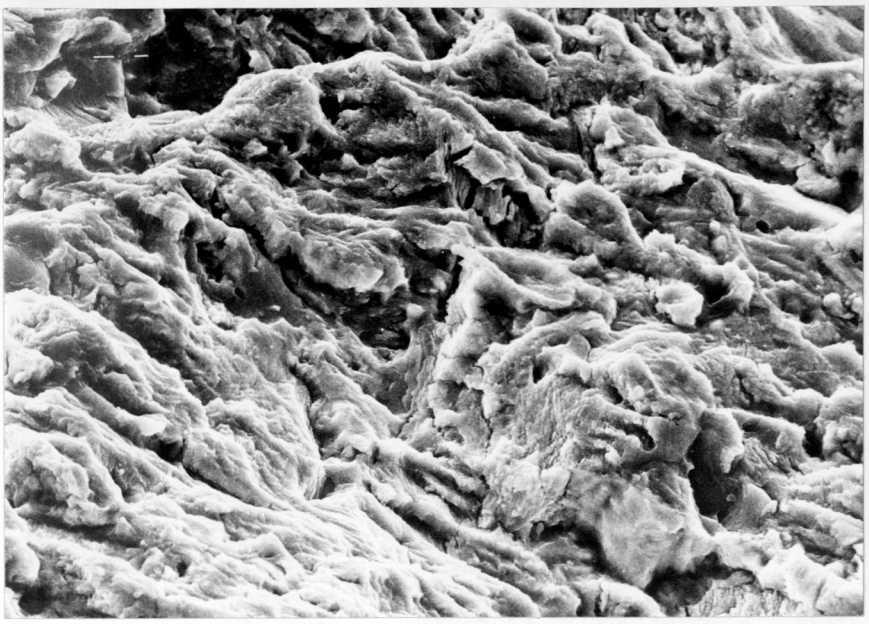
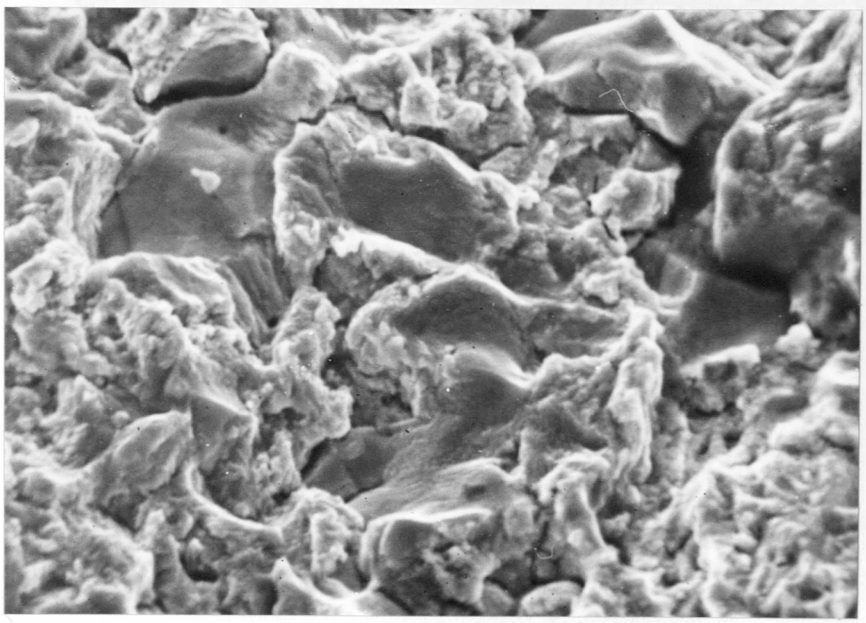


Fig. 11.59 A double logarithm plot of da/dn versus ΔK of EN3BN indicating the SEM micrograph positions of Fig. 11.60.

Crack growth direction ⟶



(a)



(b)

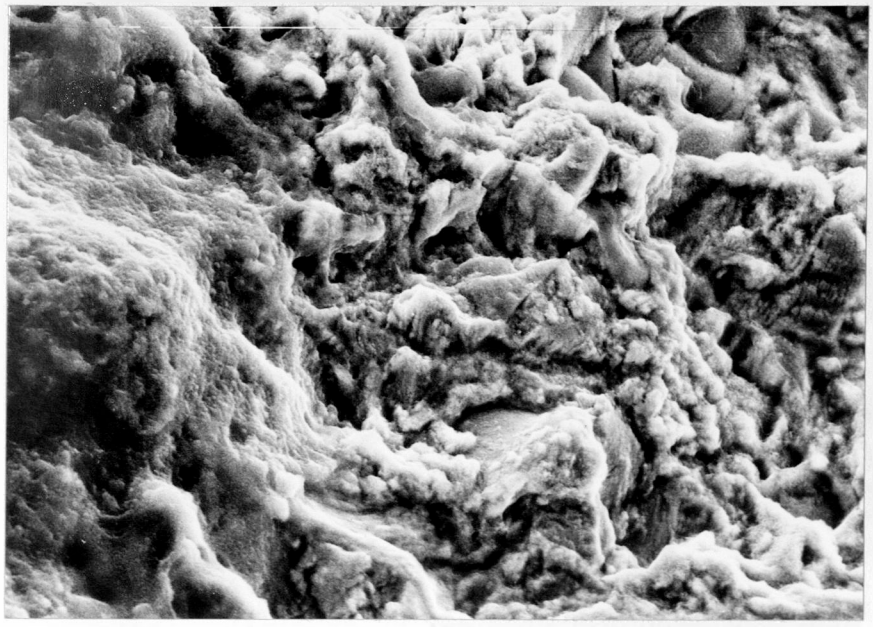
Fig. 11.60 SEM micrographs of Specimen T1-EN3BN-0.1R-0.40 illustrating the change of fracture mode during constant load fcg.

(a) ΔK = 9.5 $MPam^{-\frac{1}{2}}$, da/dn = 2.4 x 10^{-6} mm/cycle, a/w = 0.06

(b) ΔK = 18.8 $MPam^{-\frac{1}{2}}$, da/dn = 1.6 x 10^{-5} mm/cycle, a/w = 0.24

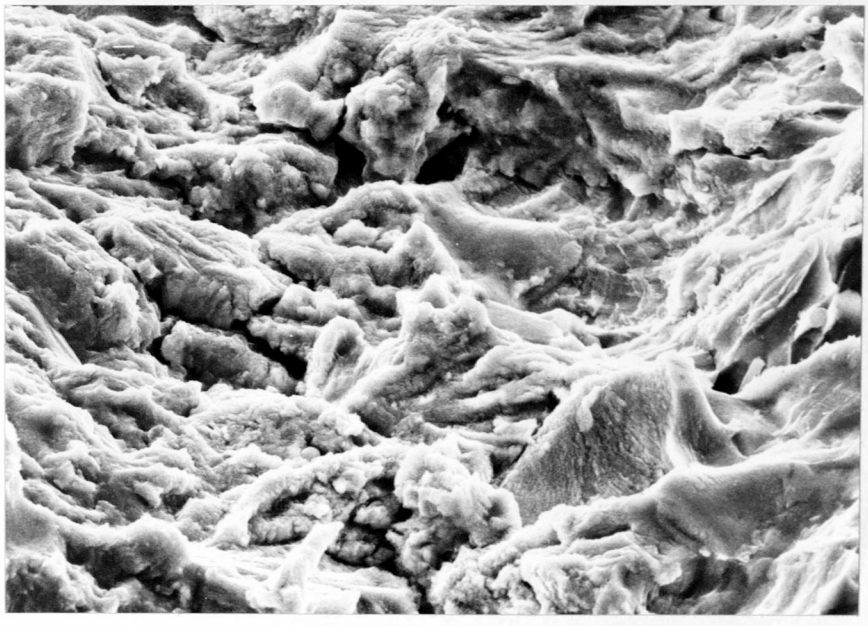
magnification = x 1400

Crack growth direction ⟶



threshold interface

(c)



(d)

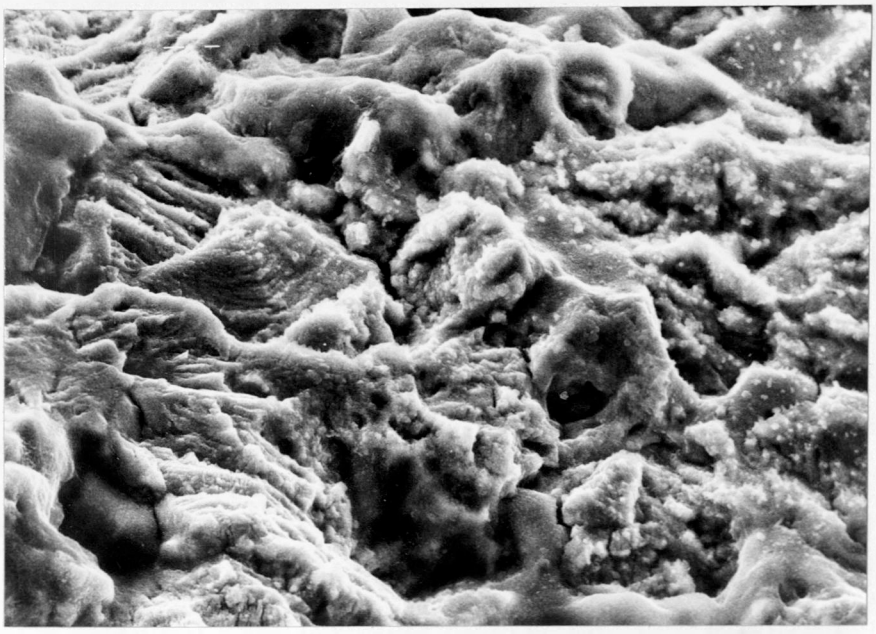
Fig. 11.60 SEM micrographs of Specimen T1-EN3BN-0.1R-0.40 which illustrate the ductile fracture mode operating during:

(c) the initial stages of post thresholds fcg, ΔK = 12.8 MPam$^{-\frac{1}{2}}$ da/dn = 3.2 x 10^{-8} mm/cycle, a/w = 0.40; and

(d) the latter stages of post threshold fcg, ΔK = 15.7 MPam$^{-\frac{1}{2}}$, da/dn = 2.6 x 10^{-6} mm/cycle, a/w = 0.50.

magnification = x 1400

Crack growth direction ⟶



(e)



(f)

Fig 11.60 SEM micrographs of Specimen T1-EN3BA-0.1R-0.40 illustrating:

(e) surface battering at a growth rate just above the knee of the log ΔK versus log da/dn plot, ΔK = 14.2 $MPam^{-\frac{1}{2}}$, da/dn = 5.0 x 10^{-6} mm/cycle, a/w = 0.31; and

(f) the occurrance of excessive amounts of oxide debris at a growth rate just below the knee of the log ΔK versus log da/dn plot. ΔK = 13.5 $MPam^{-\frac{1}{2}}$, da/dn = 3.5 x 10^{-6} mm/cycle, a/w = 0.34.

magnification = x 1400

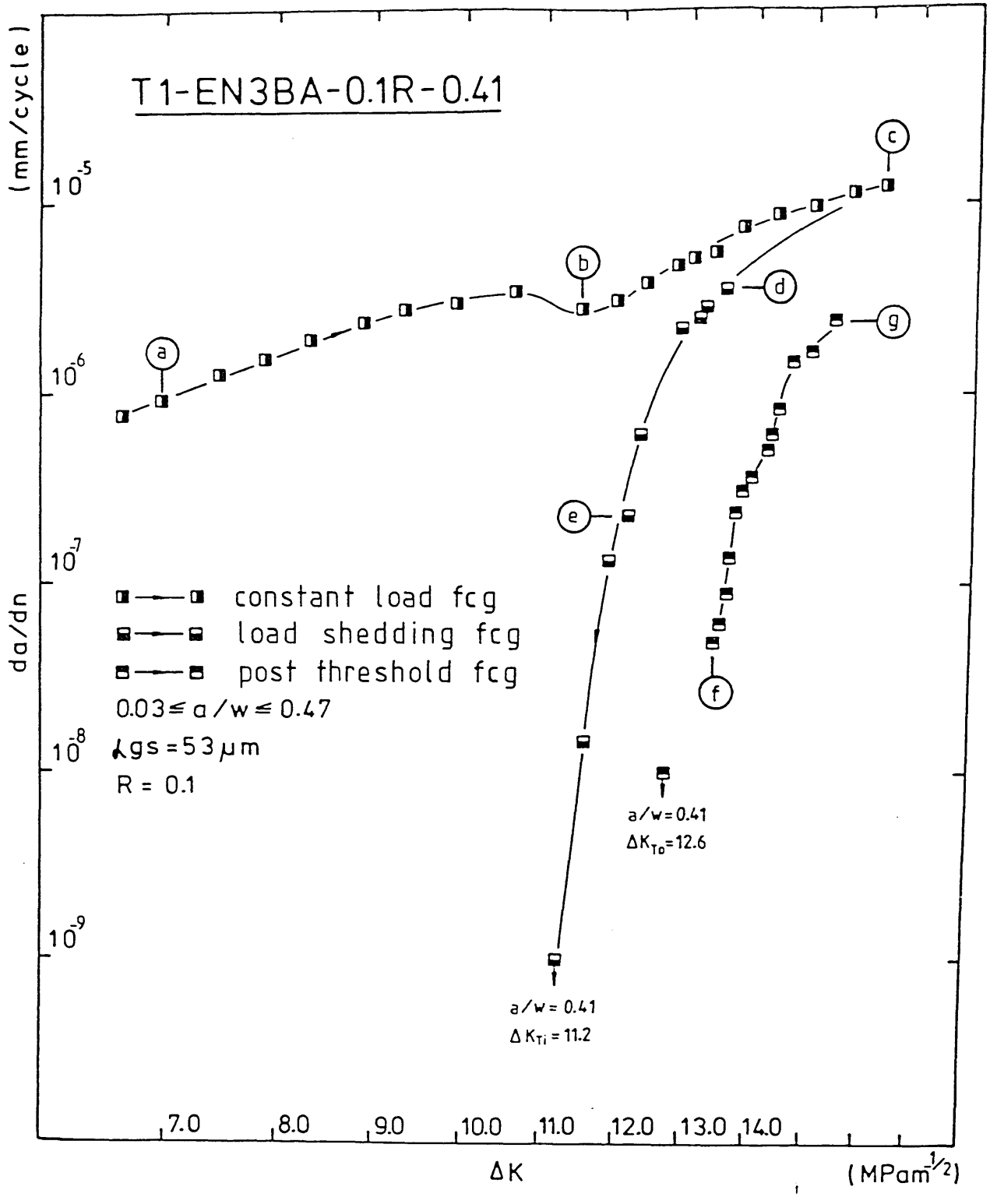


Fig. 11.61 A double logarithm plot of da/dn versus ΔK of EN3BN illustrating the SEM micrograph positions of Fig. 11.62.

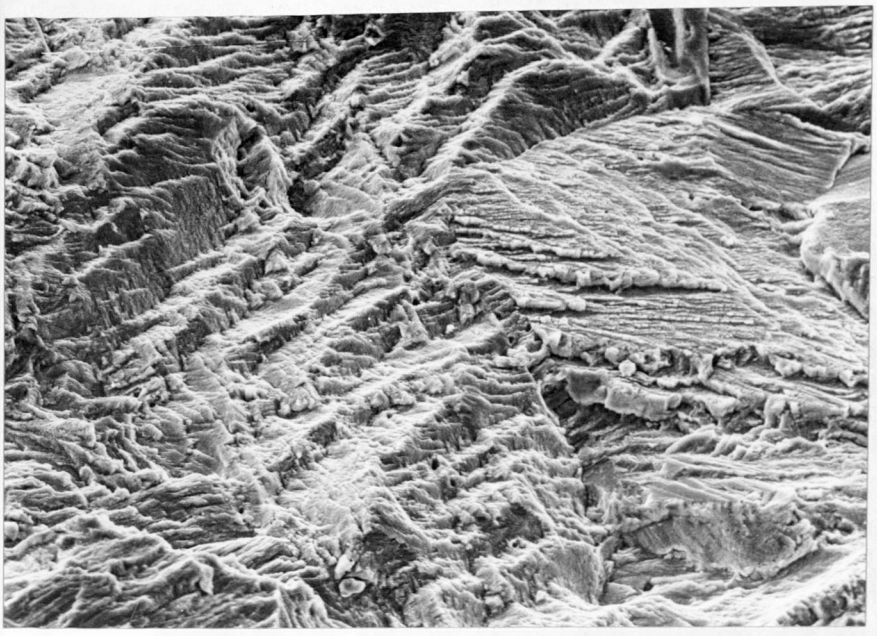


Fig. 11.62(a)

$\Delta K = 6.9\ MPam^{-\frac{1}{2}}$

$da/dn = 9.4 \times 10^{-7}$ mm/cycle

$a/w = 0.03$

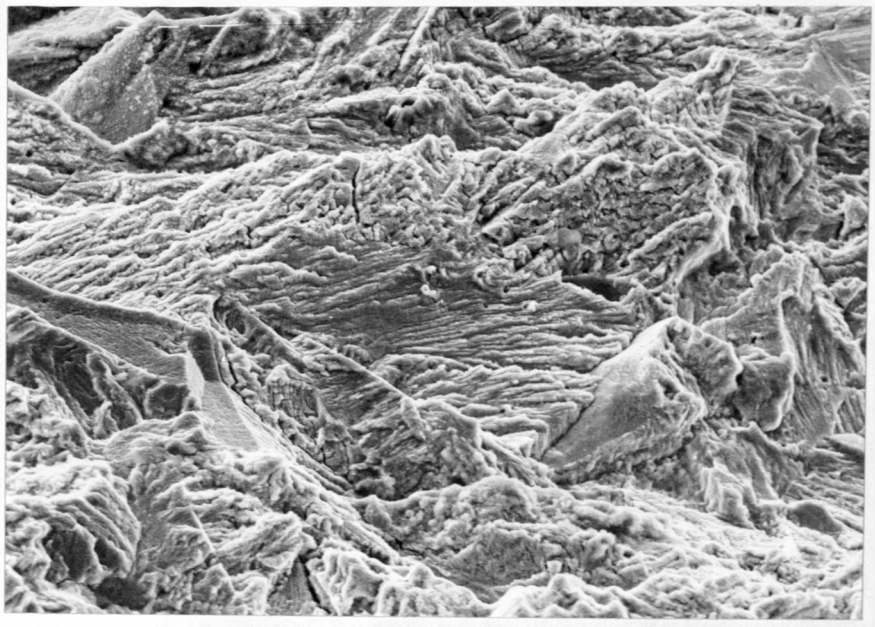


Fig. 11.62(b)

$\Delta K = 11.4\ MPam^{-\frac{1}{2}}$

$da/dn = 2.8 \times 10^{-6}$ mm/cycle

$a/w = 0.09$

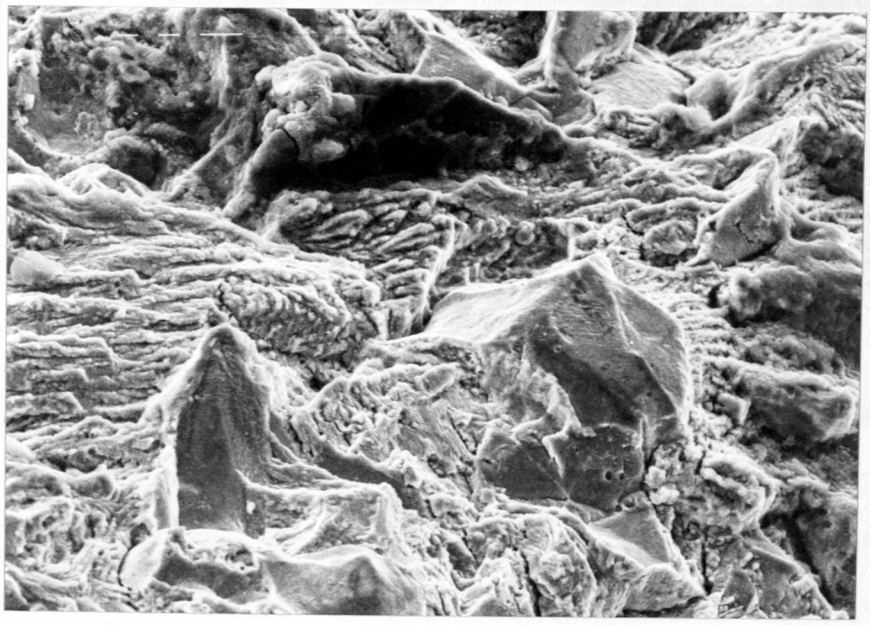


Fig. 11.62(c)

$\Delta K = 15.0\ MPam^{-\frac{1}{2}}$

$da/dn = 9.6 \times 10^{-6}$ mm/cycle

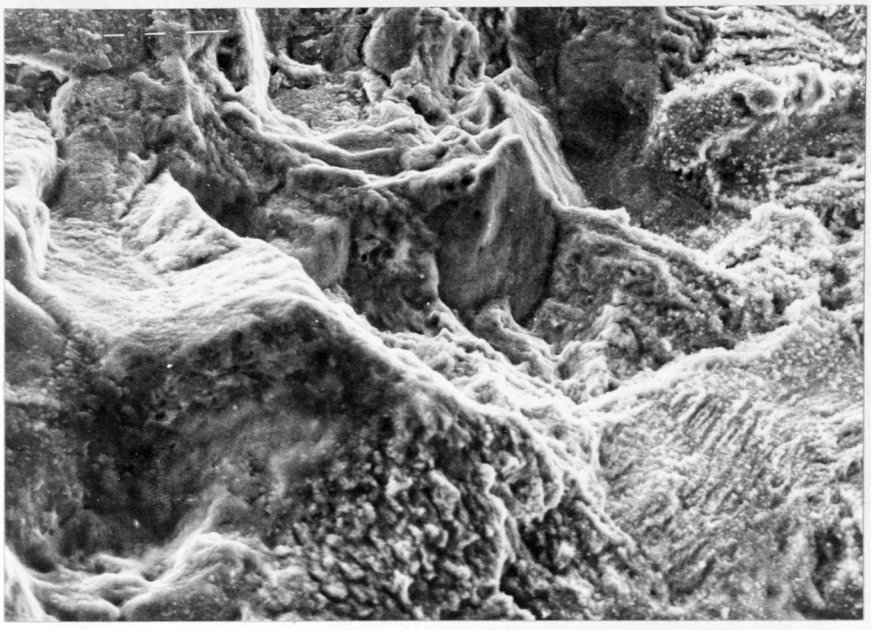
$a/w = 0.17$

Fig. 11.62 SEM micrographs of Specimen T1-EN3BA-0.1R-0.41 illustrating the change of fracture mode during constant load fcg.

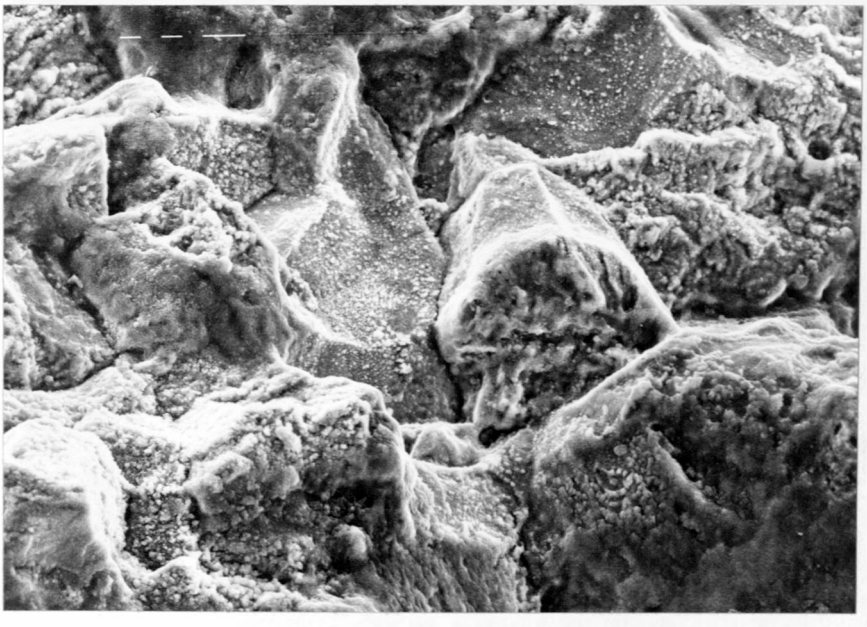
magnification = X 1400

crack growth direction ⟶

crack growth direction ⟶

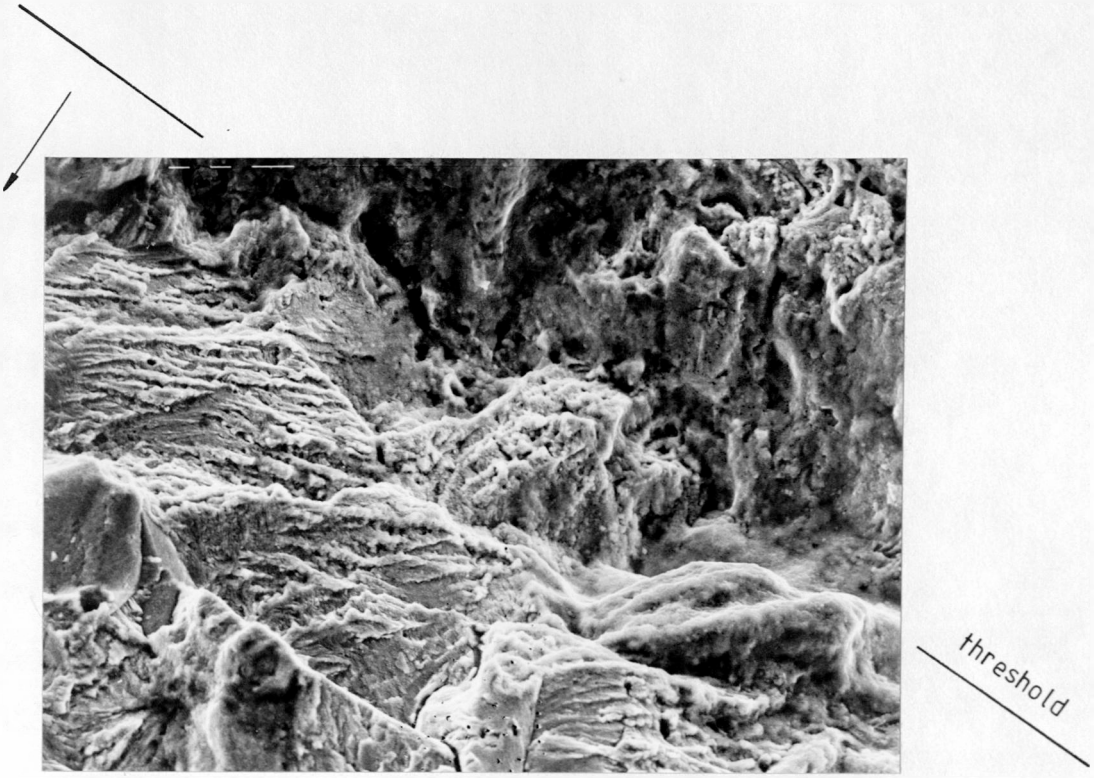


(d)

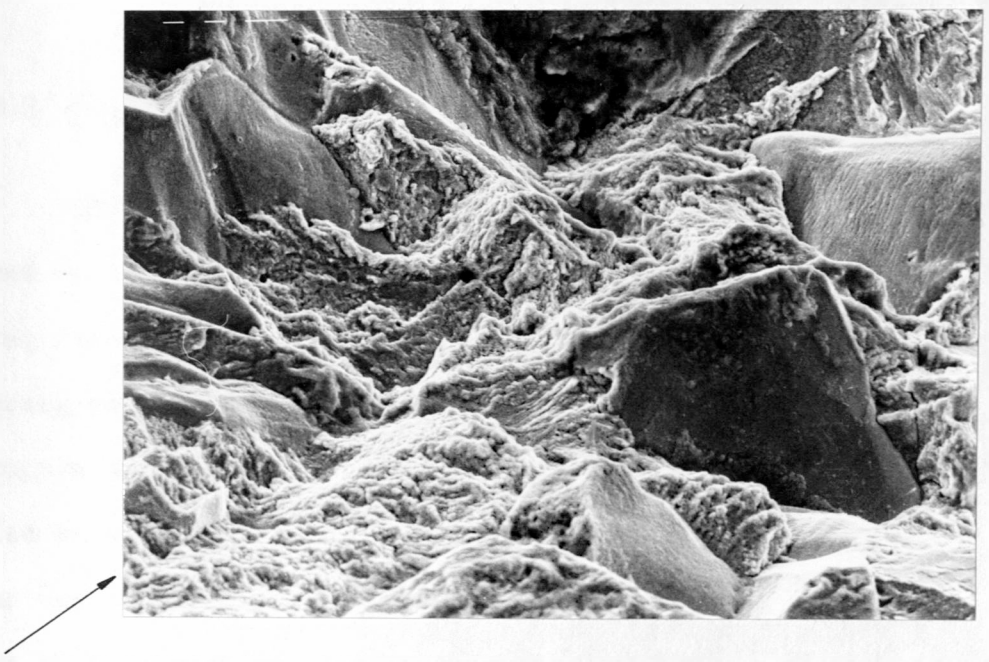


(e)

Fig. 11.62 SEM micrographs of Specimen T1-EN3BA-0.1R-0.41 illustrating fracture surface morphology as threshold is approached. (d) Oxide debris and fracture surface battering, ΔK = 13.5 MPam$^{-\frac{1}{2}}$, da/dn = 3.5 x 10^{-6} mm/cycle, a/w = 0.22. (e) Intergranular fracture, ΔK = 12.1 MPam$^{-\frac{1}{2}}$, da/dn = 1.1 x 10^{-7} mm/cycle, a/w = 0.36. magnification = x 1400.



(f)



(g)

Fig. 11.62 SEM micrographs of Specimen T1-EN3BA-0.1R-0.41 illustrating:

(f) post threshold crack growth, ΔK = 13.4 $MPam^{-\frac{1}{2}}$, $da/dn = 5.0 \times 10^{-8}$ mm/cycle, a/w = 0.41; and

(g) the occurance of transgranular striation and intergranular seperation during the latter stages of post threshold fcg, ΔK = 15.9 $MPam^{-\frac{1}{2}}$, $da/dn = 1.9 \times 10^{-6}$ mm/cycle, a/w = 0.47

magnification = x 1400

(arrows denote crack growth direction)

striation mechanisms, Fig. 11.62(a)(f), but at higher growth rates this was succeeded by a mixed mode fracture containing elements of transgranular striation and intergranular fracture, Fig. 11.62(b)(c)(g). The change in fracture mode was gradual and could not be simply related to reversed or maximum plane strain plastic zone size [11.45, 11.46].

During the load shedding threshold approach sequence fracture surface battering and excessive oxide deposits made it difficult to decide the fracture trend, Fig. 11.62(d). However, at growth rates $\leqslant 2 \times 10^{-7}$ mm/cycle small isolated areas of intergranular fracture were present contained within a matrix whose morphology was typified by ductile transgranular separation, Fig. 11.62(e).

11.4.2.3 Crack Profile Appearance

EN3BN A crack profile replica of Specimen T1-EN3BN-0.1R-0.40 produced at threshold clearly illustrated the occurrance of excessive fretting oxidation at growth rates $\leqslant 2.7 \times 10^{-7}$ mm/cycle, Fig. 11.63. SEM micrographs of the same replica revealed that during constant load fcg crack propagation at short crack lengths and low growth rates was typified by a hill and valley topography, Fig. 11.64(a). At longer crack lengths and higher growth rates this was replaced by a irregular crack profile characteristics of transgranular/intergranular cracking, Fig. 11.64(b). During the load shedding threshold approach sequence the fracture trend was uncertain because battering of the fracture surface acted to destroy and conceal the crack profile, Fig. 11.64(c).

SEM examination of positive crack profile replicas produced at the end of fatigue testing revealed the presence of

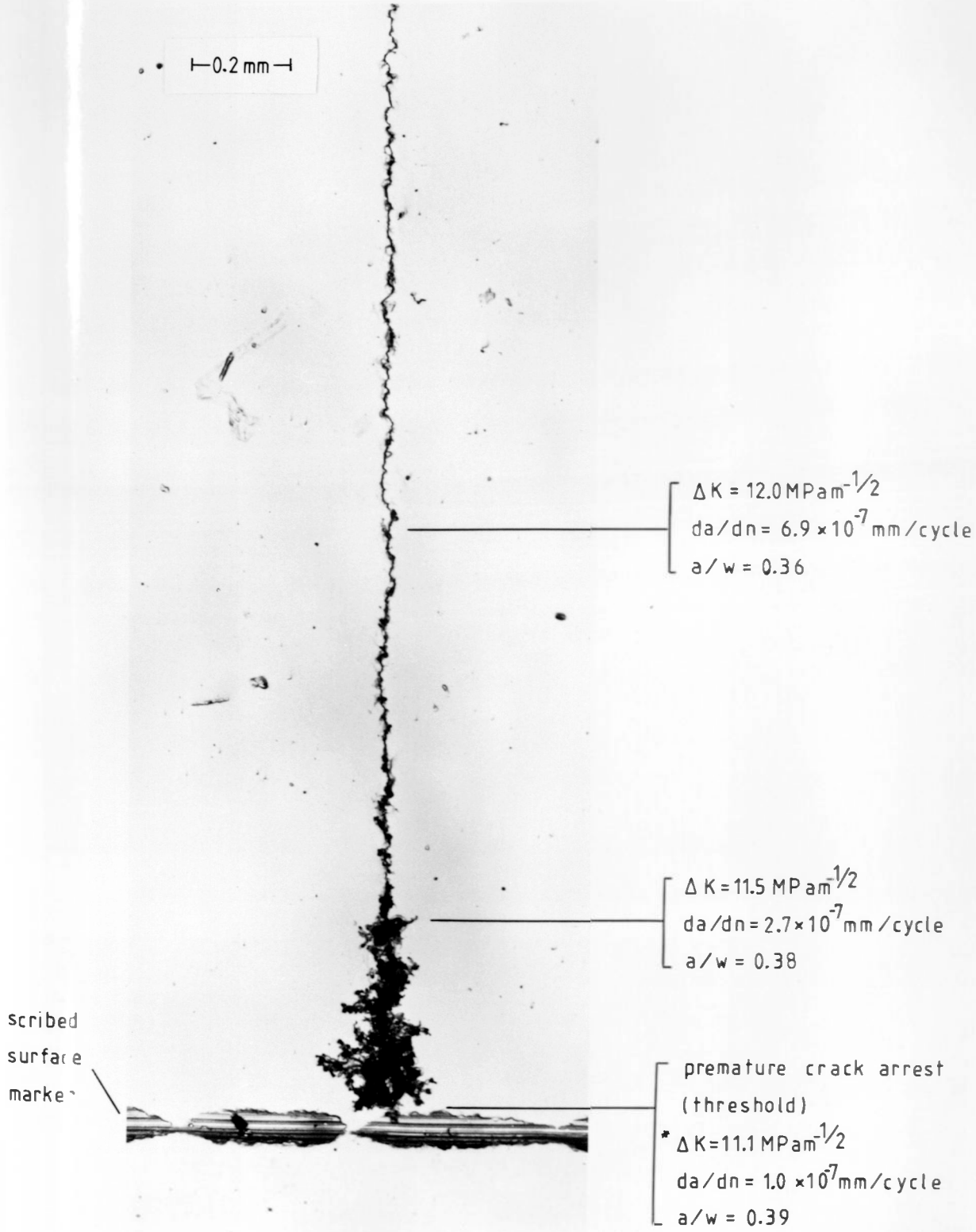
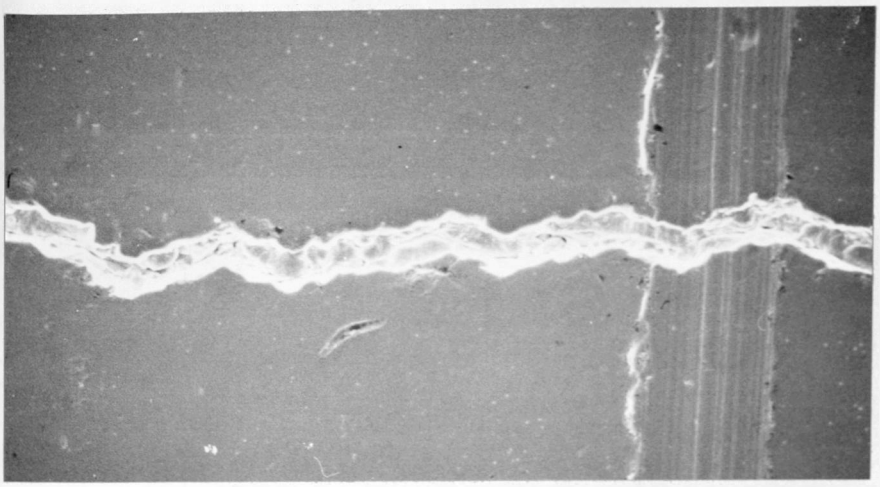


Fig. 11.63 A negative crack profile replica of specimen T1-EN3BN-0.1R-0.40 illustrating the extent of oxide extrusion as threshold is approached. $K_{applied} = K_{min} = 1.2 MPam^{-1/2}$

*ΔK expressed for this crack length

Crack growth direction

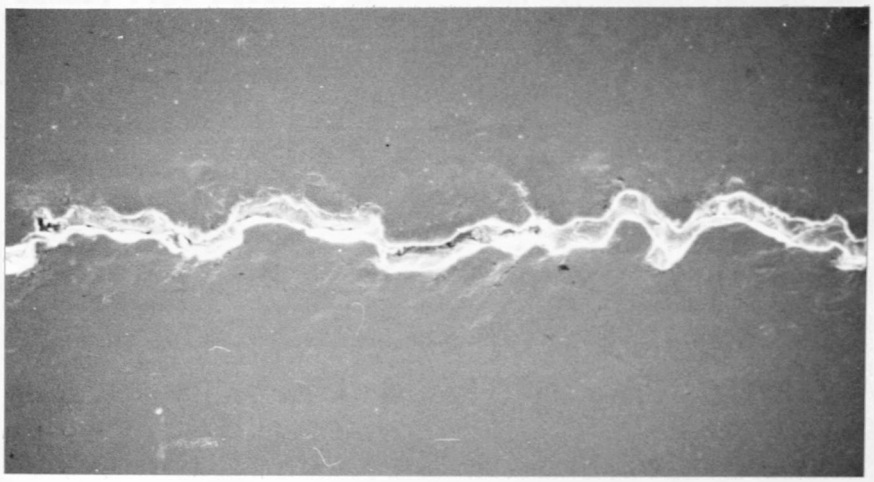


$\Delta K = 12.0\ MPam^{-\frac{1}{2}}$

$da/dn = 4.9 \times 10^{-6}$ mm/cycle

$a/w = 0.10$

(a)

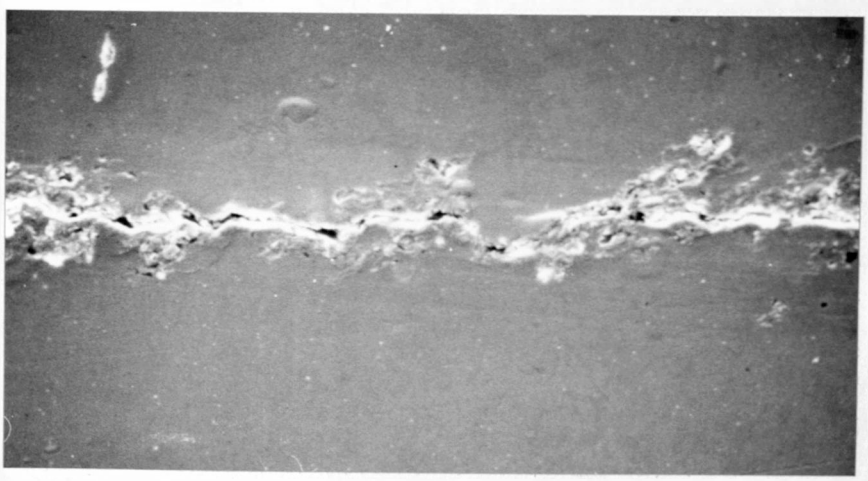


$\Delta K = 17.6\ MPam^{-\frac{1}{2}}$

$da/dn = 1.4 \times 10^{-5}$ mm/cycle

$a/w = 0.21$

(b)



$\Delta K = 12.0\ MPam^{-\frac{1}{2}}$

$da/dn = 1.6 \times 10^{-7}$ mm/cycle

$a/w = 0.38$

(c)

Fig. 11.64 Positive crack profile replicas of Specimen T1-EN3BN-0.1R-0.40 produced at threshold illustrating:

(a) a hill and valley topography;

(b) transgranular-intergranular cracking; and

(c) a battered irregular fracture surface and fretting oxidation debris. $K_{applied} = K_{min} = 1.1\ MPam^{-\frac{1}{2}}$, magnification = x 320

oxide debris in the crack mouth in vicinity of the threshold region, Fig. 11.65.

EN3BA The appearance of the crack profile of Specimen T1-EN3BA-0.1R-0.41 produced at threshold was disimilar to Specimen T1-EN3BN-0.1R-0.40, Fig. 11.66. Oxide debris was present but only barely discernable on the specimen side face. Fracture surface morphology changed from flat to irregular to flat-irregular as threshold was approached, Fig. 11.67. Final threshold crack arrest was associated with both intergranular and transgranular components of fracture, Fig. 11.68.

At the end of fatigue testing no oxide flakes were observed in the crack mouth.

11.5 Discussion

11.5.1 Introduction

The purpose of this discussion is to relate near threshold fcg in materials EN19QH, EN3BN and EN3BA to crack length, microstructure and stress ratio effects. Where appropriate these effects are also described in terms of crack closure and tentative closure arguments are presented to describe closure trends.

For convenience the discussion is subdivided into six major sections:-

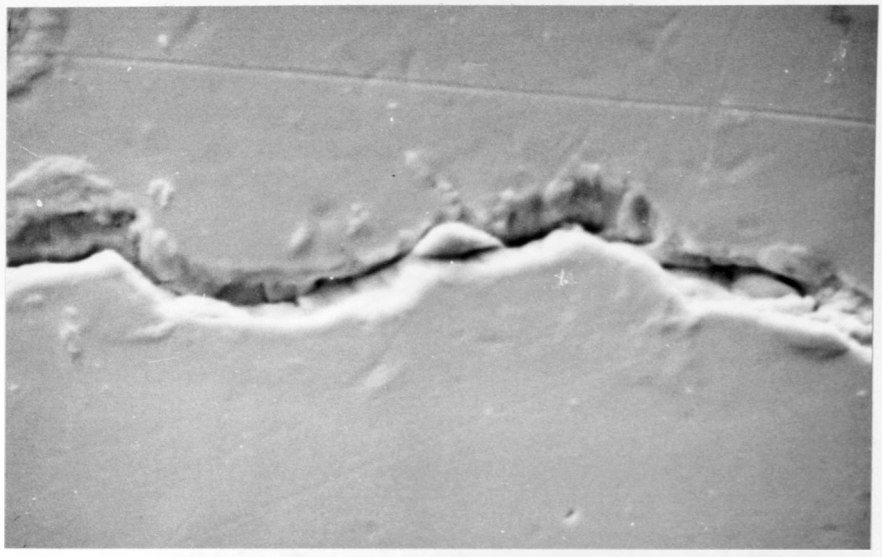
11.5.2 Threshold Fatigue Crack Growth, its Measurement and Crack Closure.

11.5.3 Near Threshold Fatigue Crack Growth in EN19QH.

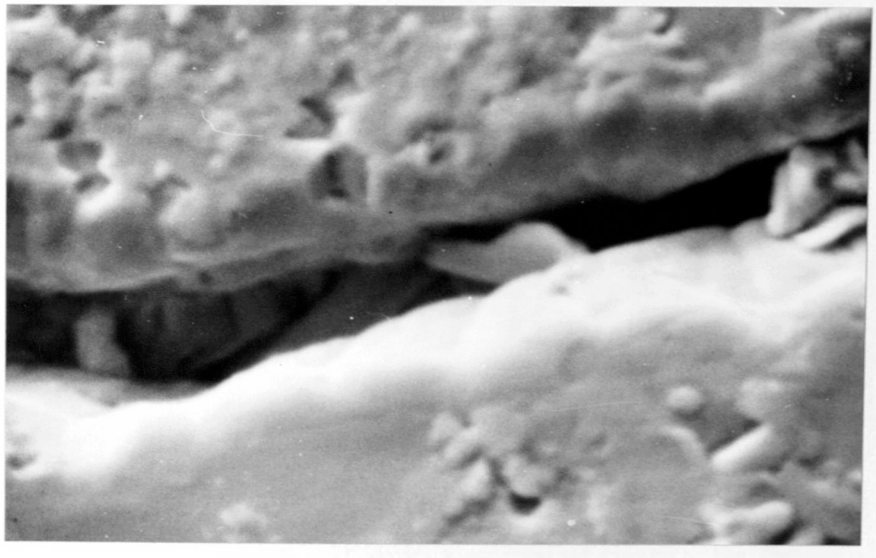
11.5.3.1 Crack length Effect on Threshold.

11.5.3.2 A Crack Closure Explanation of Stress Ratio

Crack growth direction



(a)



(b)

Fig. 11.65 Positive crack profile replicas of Specimen T1-EN3BN-0.1R-0.40 produced at the end of threshold testing illustrating the occurrance of oxide debris in the wake of the crack tip.

(a) a/w = 0.41, magnification = x 1250

(b) a/w = 0.36, magnification = x 2500

$K_{applied} = K_{min} = 1.9\ MPam^{-\frac{1}{2}}$

(crack tip a/w = 0.50)

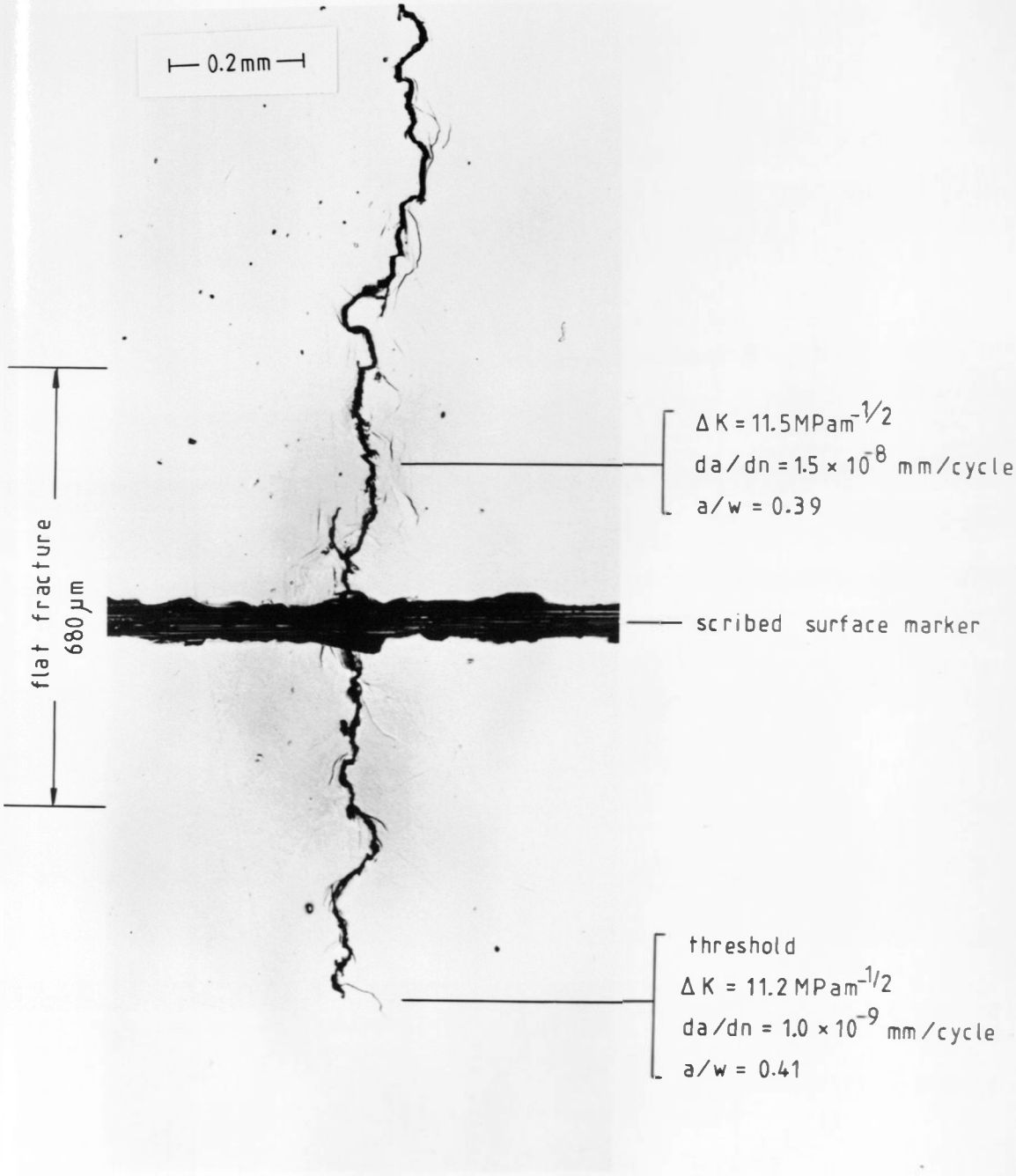
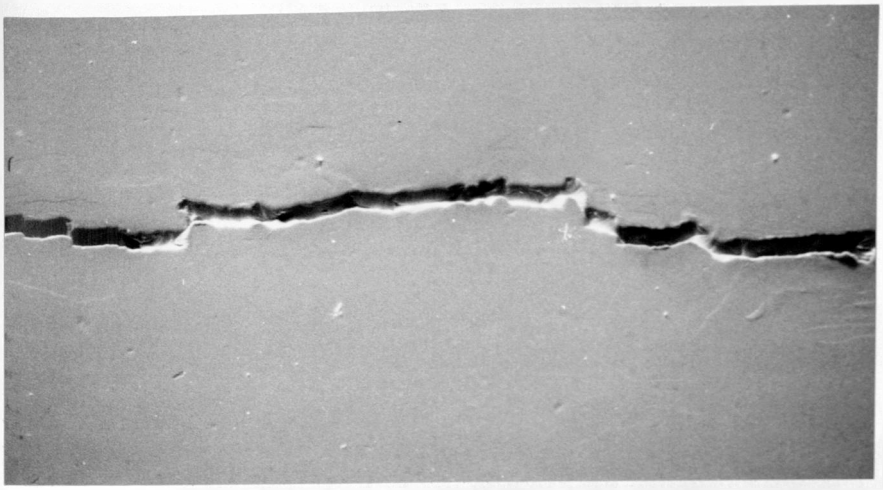


Fig. 11.66 A negative crack profile replica of specimen T1-EN3BA-0.1R-0.41 illustrating the relatively clean appearance of the crack tip as threshold is approached.

$$K_{applied} = K_{max} = 12.4 MPam^{-1/2}$$

Crack growth direction

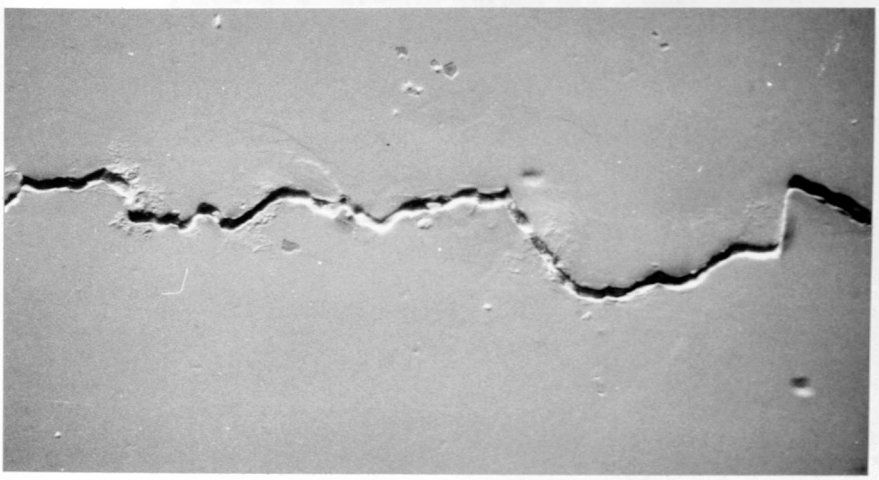


$\Delta K = 10.6\ MPam^{-\frac{1}{2}}$

$da/dn = 3.5 \times 10^{-6}$ mm/cycle

$a/w = 0.08$

(a)

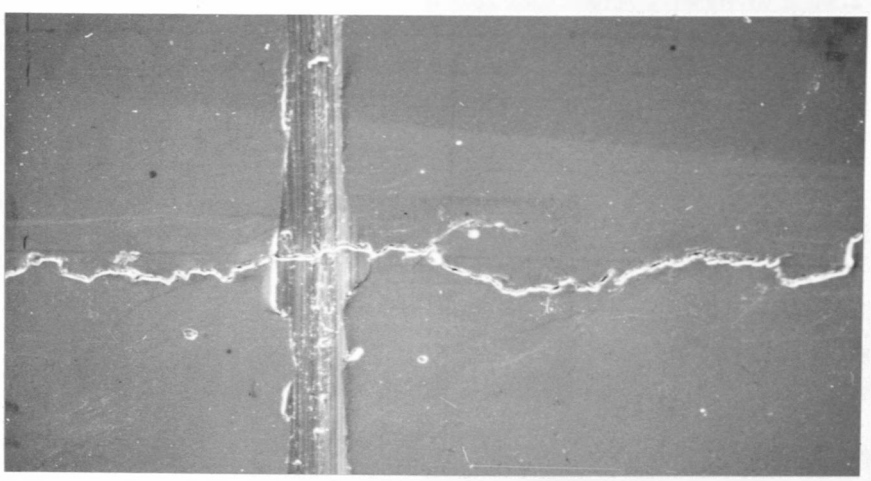


$\Delta K = 15.0\ MPam^{-\frac{1}{2}}$

$da/dn = 9.6 \times 10^{-6}$ mm/cycle

$a/w = 0.16$

(b)



$\Delta K = 11.3\ MPam^{-\frac{1}{2}}$

$da/dn = 5.0 \times 10^{-9}$ mm/cycle

$a/w = 0.40$

(c)

Fig. 11.67 Positive crack replicas of T1-EN3BA-0.1R-0.41 produced at threshold illustrating:

(a) a relatively flat fracture profile;

(b) an irregular fracture profile; and

(c) a flat-irregular fracture profile.

$K_{applied} = K_{max} = 12.4\ MPam^{-\frac{1}{2}}$, magnification = x 160

← Crack growth direction

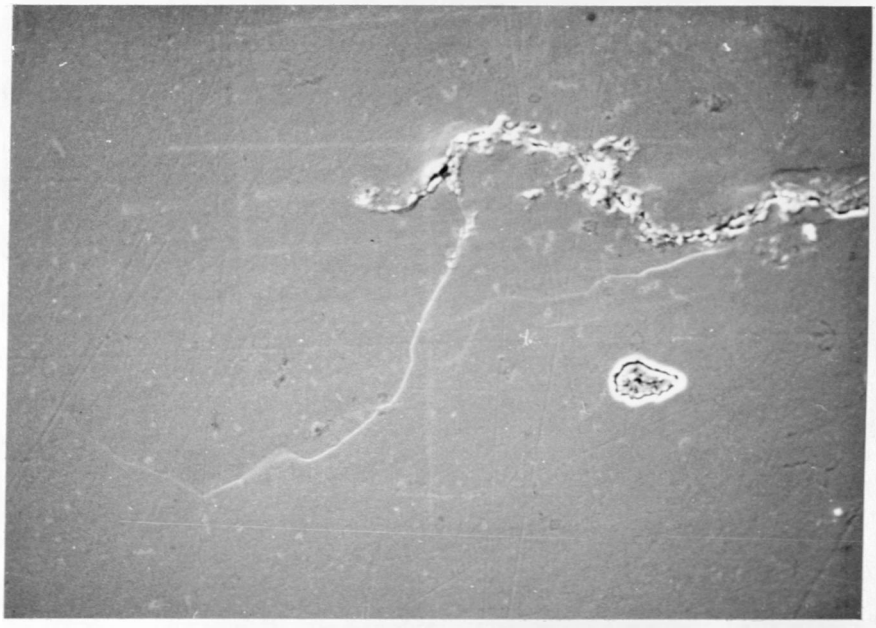


Fig. 11.68 A postive crack profile replica of Specimen T1-EN3BA-0.1R-0.41 illustrating that threshold crack arrest was associated with both intergranular and transgranular components of fracture ΔK = 11.2 $MPam^{-\frac{1}{2}}$, da/dn = 1.0 x 10^{-9} mm/cycle, a/w = 0.41, $K_{applied} = K_{max}$ = 12.4 $MPam^{-\frac{1}{2}}$, magnification = x 640.

Effects on Threshold.

11.5.3.3 Crack Closure and Threshold Testing.

11.5.4 Near Threshold Fatigue Crack Growth and Crack Closure in Materials EN3BN and EN3BA.

11.5.5 The Phenomena of Threshold Hysteresis.

11.5.6 Fretting Fatigue and Oxide Induced Crack Closure

11.5.7 Concluding Remarks.

To avoid unnecessary repetition the phenomena of threshold hysteresis which was present in all tests conducted at R = 0.1 is discussed in Section 11.5.5.

11.5.2 Threshold Fatigue Crack Growth, its Measurement and Crack Closure

Throughout the history of fracture mechanics a large amount of published data has confirmed that at low ΔK's fcg decreases rapidly to a threshold level, ΔK_T, at which minimal or no measurable crack growth occurs. This limit, which ranges from 2×10^{-9} to 8×10^{-9} mm/cycle [11.08, 11.09], is normally defined by the extent of technological interest and is determined by the sensitivity of the crack monitoring system and the maximum amount of experimental effort.

The general practice of achieving low growth rates is to adopt a sequential crack growth load reduction sequence which avoids stress history effects on subsequent crack growth and eventually terminates on the attainment of the threshold growth condition [11.10, 11.11]. The load shedding sequence is then reversed and crack growth is allowed to return to high growth rates under constant load conditions. In cases where reversing the last load decrement produces instantaneous crack growth, ΔK_T is unique and is normally defined by the last reduced load

level. But when temporary crack arrest occurs, or post threshold growth stops [11.11, 11.13, 11.14], the threshold growth condition is satisfied by a ΔK range with near threshold fcg exhibiting a hysteresis behaviour.

In the past investigators who have reported temporary crack arrest have conveniently ignored the ireversibility in near threshold fcg and have related ΔK_T to the threshold growth condition measured just prior to the immediate return to high growth rates. In the present investigation however, the threshold hysteresis phenomena was defined by two levels of no measurable crack growth. During the load shedding threshold approach sequence ΔK_T was defined by a growth rate of 10^{-9} mm/cycle, but during load reversal this was increased to 10^{-8} mm/cycle. In accordance with this practice threshold stress intensity range ΔK_{Ti} and ΔK_{To} corresponded to growth rates of 10^{-9} and 10^{-8} mm/cycle respectively.

The occurrance of the threshold growth condition has in recent years been attributed to many factors and is now being described in terms of crack closure. In its origianl form plasticity induced closure [11.15] has proved extremely effective in explaining many aspects of fatigue crack propagation under plane stress conditions. Under conditions of plane strain, however, where this mechanism only plays a minor role, other microscopic closure mechanisms have been suggested based on the role of crack flank corrosion products [11.06, 11.17, 11.18] and fracture surface roughness [11.19, 11.20, 11.21].

Ritchie et al [11.06, 11.17] suggested that the former effect results from the build up of corrosion products near the crack tip by a process of fretting oxidation. Oxide debris formed in this manner then results in an increase in crack closure by promoting earlier contact of the fracture surfaces during the crack closing sequence.

Surface roughness induced crack closure, first reported by Walker and Beevers [11.19] and subsequently modelled by McEvilly and others [11.20, 11.23, 11.24], relies on the size and the scale of the fracture surface roughness being comparible with crack tip opening displacements and mode II displacements of the crack tip. The mechanism relies on the production of point contacts in the wake of the crack tip by a process of in-plane shear which wedge the crack open. The mechanism is specially favoured in materials which exhibit Stage I growth [11.24] when the 'maximum plastic zone size' is less than the grain size.

The major problem encountered in describing fcg with respect to crack closure stems from the semi quantitative nature of crack closure measurement. Those [11.25-11.30] who have employed surface measurement techniques or have established fatigue under plane stress conditions have obtained consistent results with those of Elber. But many [11.31-11.33] who have ensured plane strain conditions and have used potential drop closure evaluation techniques failed to detect closure at positive loads unless testing was conducted in vacuum.

Interpretation of fcg in terms of crack closure had been, and still is, a major problem. In Elber's original study, as adopted here, growth rate analysis was based on a ΔK_{eff} model defined by

$$\Delta K_{eff} = K_{max} - K_{open} \qquad \ldots(11.02)$$

with K_{open} being derived from P_{open}, Fig. 11.69(a). Shaw and LeMay [11.34] however, suggested that

$$\Delta K_{eff} = K_{max} - K_{cl} \qquad \ldots(11.03)$$

which is based on the crack closure stress intensity K_{cl} evaluated

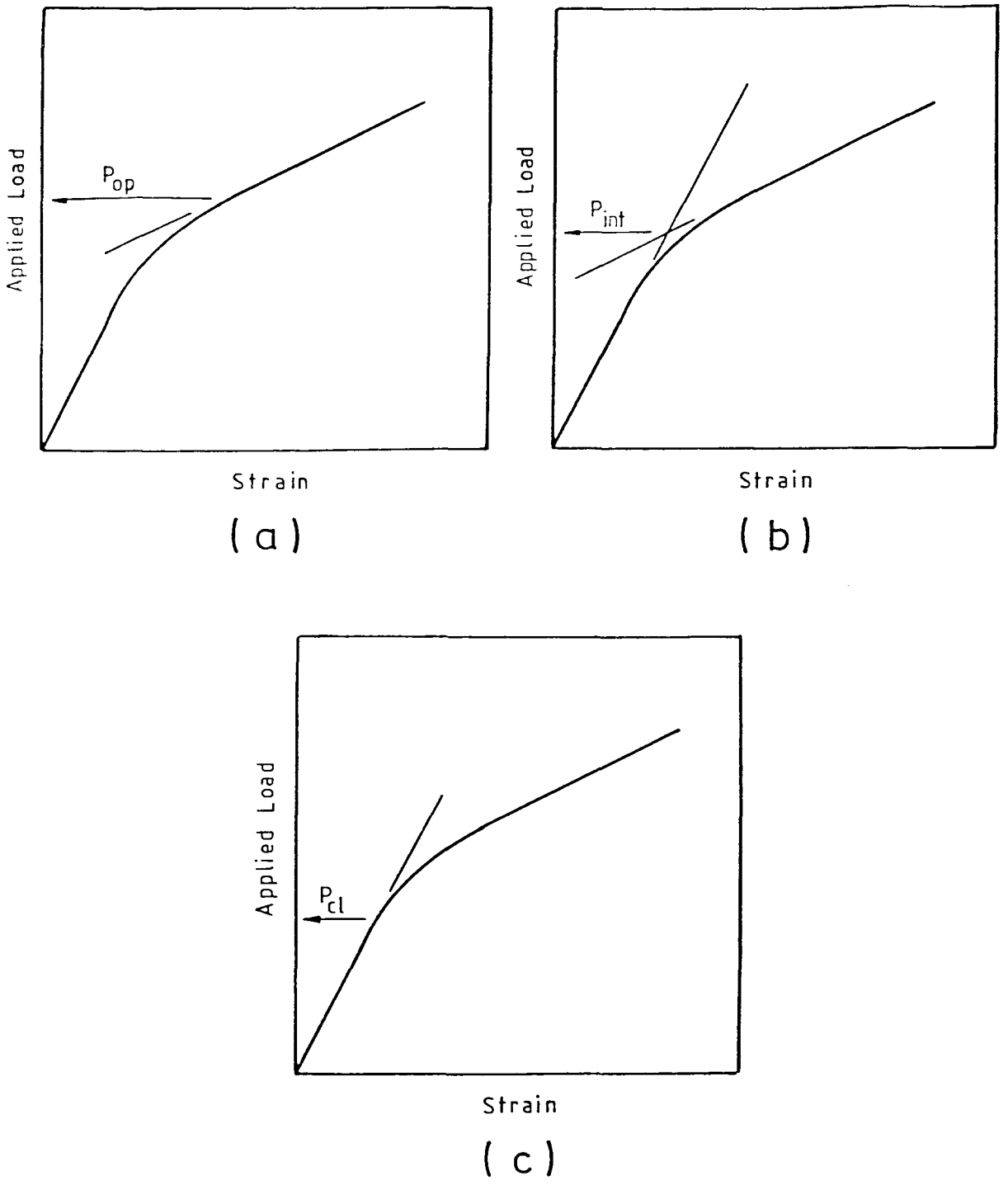


Fig. 11.69 Typical crack tip compliance behaviour measured using a side face strain gauge technique illustrating:

(a) crack tip opening load;

(b) intermediate crack tip closure load; and

(c) crack tip closure load.

using P_{cl}, Fig. 11.69(c). Others [11.35, 11.36] have compromised by suggesting that

$$\Delta K_{eff} = K_{max} - K_{int} \qquad \ldots(11.04)$$

and have used P_{int} to determine K_{int}, Fig. 11.69(b).

The general conclusion to be drawn from all crack closure studies of the past 20 years is that crack closure is a complicated phenomena that exists. Unfortunately its occurrance is difficult to quantify and comments regarding its interpretation must be tempered with the knowledge that crack closure analysis is based on data generated using semi quantitative techniques.

11.5.3 Near Threshold Fatigue Crack Growth in EN19QH

11.5.3.1 Crack Length Effect on Threshold

Since as far back as 1959 a scant series of reports have suggested there exists a crack length effect on threshold stress intensity range. Many [11.37, 11.38] have argued that this dependency occurs below a critical crack length, a_o, and in the limit as $(a \leqslant a_o) \rightarrow 0$, $\Delta K_T \rightarrow$ plane fatigue limit. Frost et al [11.40] have reported that a_o is material dependent, and Chauhan and Roberts [11.09] found this ranged from 1.0 to 9.6 mm ($0.02 \leqslant a/w \leqslant 0.20$) in a 3½%Ni steel.

In the present series of fatigue tests conducted at R = 0.1 there existed no significant crack length effect on threshold fcg at threshold a/w ratios 0.09, 0.20, 0.30 and 0.39, Fig. 11.12. During threshold testing temporary threshold crack arrest occurred as reported by Druce [11.12], but ΔK_{Ti} and ΔK_{To} were reproducible irrespective of a/w regime, Fig. 11.13.

ΔK_{eff} analysis of threshold crack growth revealed that $\Delta K_{eff.Ti}$ was substantially lower than ΔK_{Ti}, i.e. transposed from 5.6-6.7 to 1.9-2.8 $MPam^{-\frac{1}{2}}$. This observation is in agreement with the reports of others [11.17] who have argued that the threshold dependency on stress ratio is determined by crack closure.

The general increase in K_{open} with decreasing ΔK indicated that crack closure was more dominant in the near threshold regime. Reproducibility of closure trend irrespective of a/w suggested that consistent closure dominated thresholds were possible provided a standard test sequence was adopted, Fig. 11.15.

11.5.3.2 A Crack Closure Explanation of Stress Ratio Effects on Threshold

The effect of stress ratio on ΔK_{Ti} was found to be consistent with that reported for similar alloys by other investigators, Table 11.03. Increasing R from 0.1 to 0.7 produced well sustained growth rates down to low ΔK's, and a ΔK_{eff} comparison of growth rates revealed that stress ratio effects on near threshold fcg could be normalised by adopting a ΔK_{eff} approach, Fig. 11.27. This suggested that near threshold fcg was dependent on the critical portion of the stress intensity range which was closure free [11.15], and the threshold growth condition was achieved at an effective stress intensity range of 2.3 ± 0.5 $MPam^{-\frac{1}{2}}$.

From the limited amount of data it was not possible to say with any degree of certainty whether the threshold growth condition occurred at a critical value of $\Delta K_{eff.Ti}$ irrespective of stress ratio as suggested by Schmidt and Paris [11.04] and Ritchie et al [11.17].

TABLE 11.03

Fatigue Threshold Data Reported For Low Alloy Steel

(Determined in Air)

Material	σ_{ys} MPa	R	ΔK_T $MPam^{-\frac{1}{2}}$	Reference
EN24	1275	0.13	5.2	11.14
ASTM 542	500	0.05	7.7	11.06
	500	0.75	3.2	
	769	0.05	7.1	
	769	0.75	2.8	
Low Alloy Steel	680	0.00	6.6	11.44
	680	0.33	5.1	
Austenitic Stainless Steel (18/8)	665	0.00	6.0	11.44
	665	0.33	5.9	
Maraging Steel	2010	0.70	2.7	11.44

Closure free fcg measured at R = 0.7 did suggest there existed a $\Delta K_{eff.Ti}$ dependency on crack length. Fig. 11.23. This was tentatively confirmed by tests conducted at R = 0.1, Fig. 11.70, and led to the guarded conclusion that ΔK_{eff} normalisation of threshold fcg in this alloy is only possible at constant crack length.

At present no valid reason can be forwarded to explain why there should exist a growth rate dependency on crack length at constant ΔK, except to suggest that a change in specimen compliance induced by increased crack length may have resulted in greater crack tip opening and a corresponding reduction in crack tip stress intensity.

In the past researchers who have endeavoured to describe their fcg with respect to effective stress intensity range have differed in their interpretation of crack closure by choosing the most suitable 'closure load' which achieves the desired effect. On the evidence of this investigation it is tentatively suggested that the choice is dependent on crack length. If $\Delta K_{eff.Ti}$ is assumed constant, at short crack lengths P_{cl} would be most appropriate, at intermediate crack lengths P_{int} and at long crack lengths P_{open}.

11.5.3.3 Crack Closure and Threshold Testing

The extensive study of crack closure versus threshold testing was aimed at presenting a detailed explanation of the threshold phenomena in terms of crack closure. To achieve the desired objectives it was necessary to employ a prolonged fatigue sequence which was punctuated by dormant periods of crack growth. This practice differs from that adopted for evaluating crack length effects on threshold and therefore the results are not directly comparible.

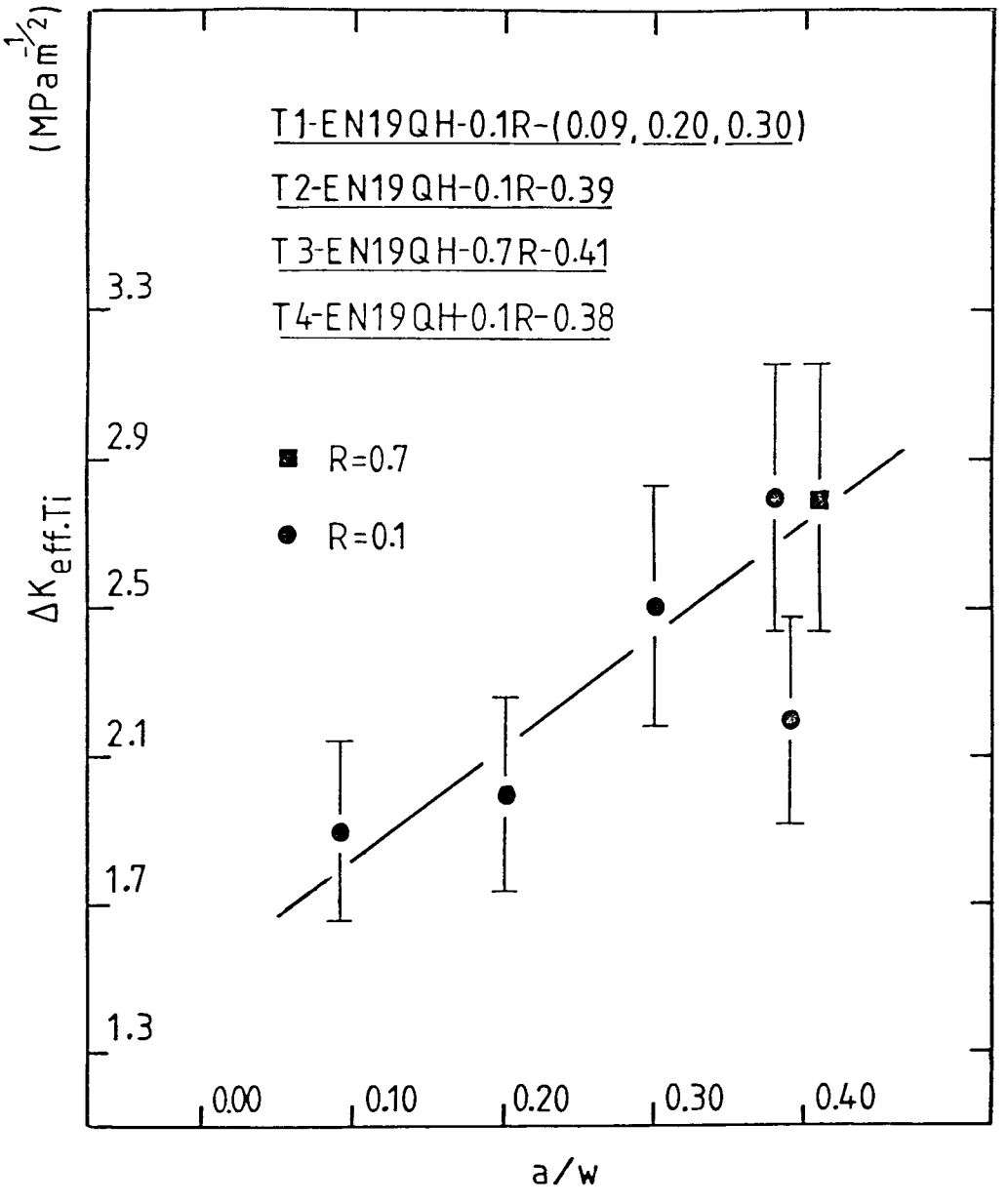


Fig. 11.70 Variation of $\Delta K_{eff.Ti}$ expressed as a function of a/w.

In order to present a clear explanation of event and associated closure argument the following discussion is subdivided into sections related to fcg sequence. All closure arguments are based on the assumption that EN19QH exhibits an intrinsic closure level which is characteristic of the material at intermediate growth rates. The magnitude of this can be attributed to a combination of factors, e.g. fracture surface roughness, and specimen compliance.

Constant Load Fatigue Crack Growth

During constant load fcg a decrease in K_{open} with increased ΔK occurred as reported by Frandsen et al [11.43], Fig. 11.30. No valid explanation for this trend existed except to suggest the following.

(a) A change in fracture surface morphology to one favouring a more planar topography would be necessary to induce a decrease in K_{open} with increased ΔK by a surface roughness mechanism. In this material fractographic evidence suggested the reverse trend, Fig. 11.36. At low ΔK's crack propagation occurred by ductile transgranular fracture containing elements of transgranular faceting, and at higher ΔK's this was replaced by ductile transgranular separation containing elements of intergranular cracking.

(b) Change in loading mode. A decrease in K_{open} with increased ΔK could have been achieved by a change in loading mode to one favouring predominantly mode II stress displacements of the crack tip. If it is assummed that a change in stress mode displacement of the crack tip occurs as suggested by Ritchie [11.24], mode II displacements would be expected when $K_{max} \leqslant 10\ MPam^{-\frac{1}{2}}$. During constant load fcg this condition was never achieved.

(c) Fretting fatigue. A decrease in K_{open} with increased ΔK could be accommodated if the total closure level includes a component arising from fretting fatigue. For instance, if it is assumed that closure originates primarily from intrinsic effects such that

$$K_{min} < K_{open(int)} < K_{max} \qquad ...(11.05)$$

and that $K_{open(int)}$ remains constant irrespective of ΔK [11.30]. At low ΔK's, where growth rates are relatively low and a large proportion of fatigue time is spent in crack closure, significant fretting oxidation occurs which results in

$$K_{open(total)} = K_{open(int)} + K_{open(oxide)} \qquad ...(11.06)$$

At higher ΔK's however, where a shorter period of time is spent in crack closure, the fretting closure component is reduced and the total closure level approaches the intrinsic value.

The suggestion that K_{open} was artificially high as the consequence of initial starter crack configuration was rejected on the grounds that sufficient crack growth had occurred ($\cong$ 5.5 mm) before crack tip opening loads were monitored. Increasing specimen compliance achieved by increased crack length may have contributed to a reduction in K_{open}, but this was considered insignificant.

Load Shedding Fatigue Crack Growth

During the initial stages of load shedding an increase in K_{open} occurred with decreasing ΔK but as threshold was approached a rapid increase in K_{open} occurred at almost constant ΔK. The occurrance of specimen side face corrosion products, Fig. 11.40, at growth rates $\leqslant 10^{-7}$ mm/cycle suggested that the increase was related to the presence

of excessive oxide debris [11.06, 11.17]; and the achievement of threshold at constant $\Delta K_{eff.Ti}$ led to the conclusion that ΔK_{Ti} was closure dominated. This does not infer that ΔK_{Ti} was solely determined by oxide induced crack closure. At near threshold growth rates where fretting oxidation contributed significantly to crack closure, Fig. 11.71, its contribution only approximated to 2 $MPam^{-\frac{1}{2}}$, Fig. 11.30. Compared with the intrinsic contribution of 5 $MPam^{-\frac{1}{2}}$, oxide induced crack closure was of secondary importance. Undoubtably the oxide closure contribution was greater than in T2-EN19QH-0.1R-0.39 and accounts for the increase in ΔK_{Ti} from 6.6 to 8.4 $MPam^{-\frac{1}{2}}$.

Threshold and Post Threshold Fatigue Crack Growth

During the latter stages of load shedding the rapid increase in K_{open} at low growth rates resulted in self crack arrest at ΔK_{Ti} = 8.4 $MPam^{-\frac{1}{2}}$ ($\Delta K_{eff.Ti}$ = 2.8 $MPam^{-\frac{1}{2}}$). Reversing the load sequence failed to produce any significant crack growth, but an increase in K_{open} occurred which was maximised just prior to post threshold fcg.

During the initial stages of post threshold crack growth K_{open} decayed rapidly over short increases in crack length. Associated with the decay was a rapid increase in growth rate which was promoted by a rapid increase in effective stress intensity range. ΔK_{eff} analysis of growth rates, Fig. 11.32, revealed that post threshold crack growth was closure related, and suggested that threshold hysteresis was closure dominated.

During post threshold fcg the decay of K_{open} to the intrinsic level associated with constant load fcg did not occur. Instead K_{open} remained high and increased slightly with increase ΔK. The reason for this behaviour was uncertain. Spalling of the oxide layer within the

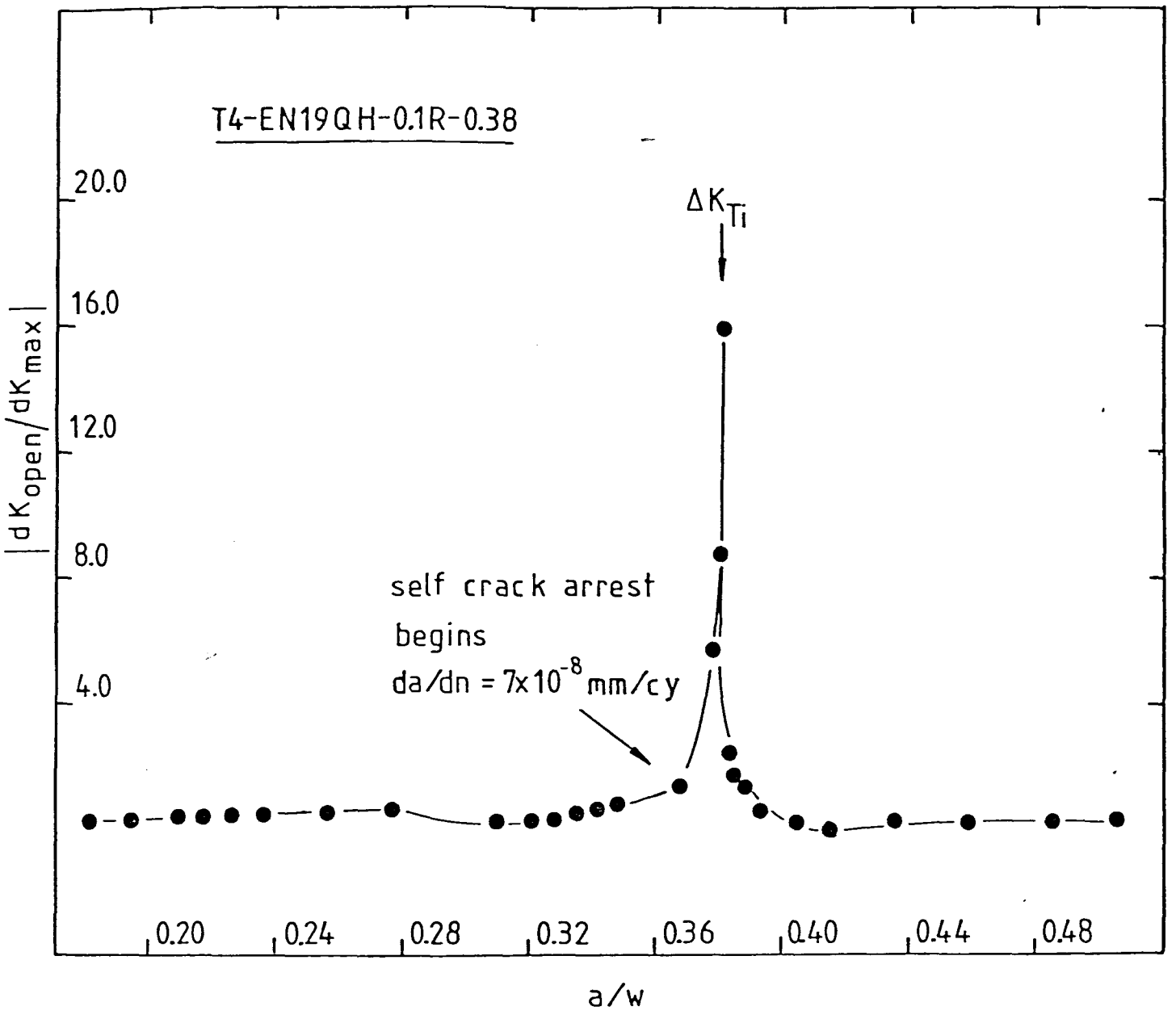


Fig. 11.71 A plot of $|dK_{open}/dK_{max}|$ versus a/w illustrating the build up in closure as threshold is approached.

threshold region was apparent, Fig. 11.41, but its effect on crack closure was considered insignificant. ΔK_{eff} analysis of growth rates revealed that within the latter stages of post threshold fcg high growth rates were recorded in comparison to fcg at R = 0.7, Fig. 11.32. This evidence led to the conclusion that during the latter stages of post threshold fcg closure loads were in error and systematically high.

11.5.4 Near Threshold Fatigue Crack Growth and Crack Closure in EN3BN and EN3BA

Near threshold fcg of EN3BN and EN3BA exhibited a very different behaviour in comparison to EN19QH. Threshold crack growth was achieved at higher $\Delta K's$ which also supported high growth rates at shorter crack lengths, Fig. 11.47. This ambiguity could not be attributed to starter crack configuration or stress history. Sufficient evidence did exist, however, to suggest that the difference in growth behaviour was related to crack closure.

In the following discussion an attempt to describe this anomoly is made based on the assumption that near threshold fcg in ferritic steels is ΔK_{eff} controlled and conforms to a $\Delta K_{eff.Ti}$ = constant model. Justification for this approach was based on a comparison of the present $\Delta K_{eff.Ti}$ threshold levels of EN3BN and EN3BA with those of Priddle and Jerram [11.47] in an almost identical alloy tested at stress ratios ranging from 0.70 to 0.91, Table 11.04.

Constant Load Fatigue Crack Growth

During constant load fcg both materials exhibited a growth rate response which was similar and characteristic of the intermediate

TABLE 11.04

A Comparison of Threshold Stress Intensity Ranges of Ferritic Steels (determined in air)

Material	R	$\Delta K_{eff.Ti}$ $MPam^{-\frac{1}{2}}$	ΔK_T $MPam^{-\frac{1}{2}}$	Reference
EN3BN	0.10	3.9	-	Present
EN3BA	0.10	3.2	-	Present
EN3A	0.70	-	3.2	11.47
	0.81	-	3.6	
	0.91	-	3.6	

growth rate regime, Fig. 11.47. This was confirmed by a Paris Law exponent m of 2.7 which compared with the results of others, Fig. 7.01.

Crack closure measurements during the fatigue of EN3BA confirmed that during the initial stages of constant load fcg crack closure was significantly low (or immeasurable) and increased slightly (or became measurable) at longer crack lengths. Evidence to support this observation was also provided by a comparison of constant load fcg rates with the ΔK_{eff} growth rates of load shedding and post threshold fcg, Figs. 11.54, 11.55. This comparison suggested that during the initial stages of constant load fcg the intrinsic closure level was insignificantly low, but towards the end it increased slightly.

Fracture mode observations of EN3BA, which changed from transgranular seperation to transgranular separation containing elements of intergranular fracture, suggested that the increase in crack closure towards the end of constant load fcg originated from surface roughness effects. In oposition to this proposal, superimposition of growth rates irrespective of α_{gs} suggested that any increase in crack closure resulting from microstructural crack growth was relatively insignificant.

Load Shedding Fatigue Crack Growth

The K_{open} response to load shedding of EN3BA, Fig. 11.53, exhibited a similar trend to EN19QH, Fig. 11.30. Initial reductions in ΔK were accompanied by related increases in K_{open}, but as the threshold growth condition was approached K_{open} increased rapidly (see also Fig. 11.72.) SEM micrographs of positive crack profile replicas and general fractographic examination of both materials suggested that the increase may have resulted from two competing mechanisms.

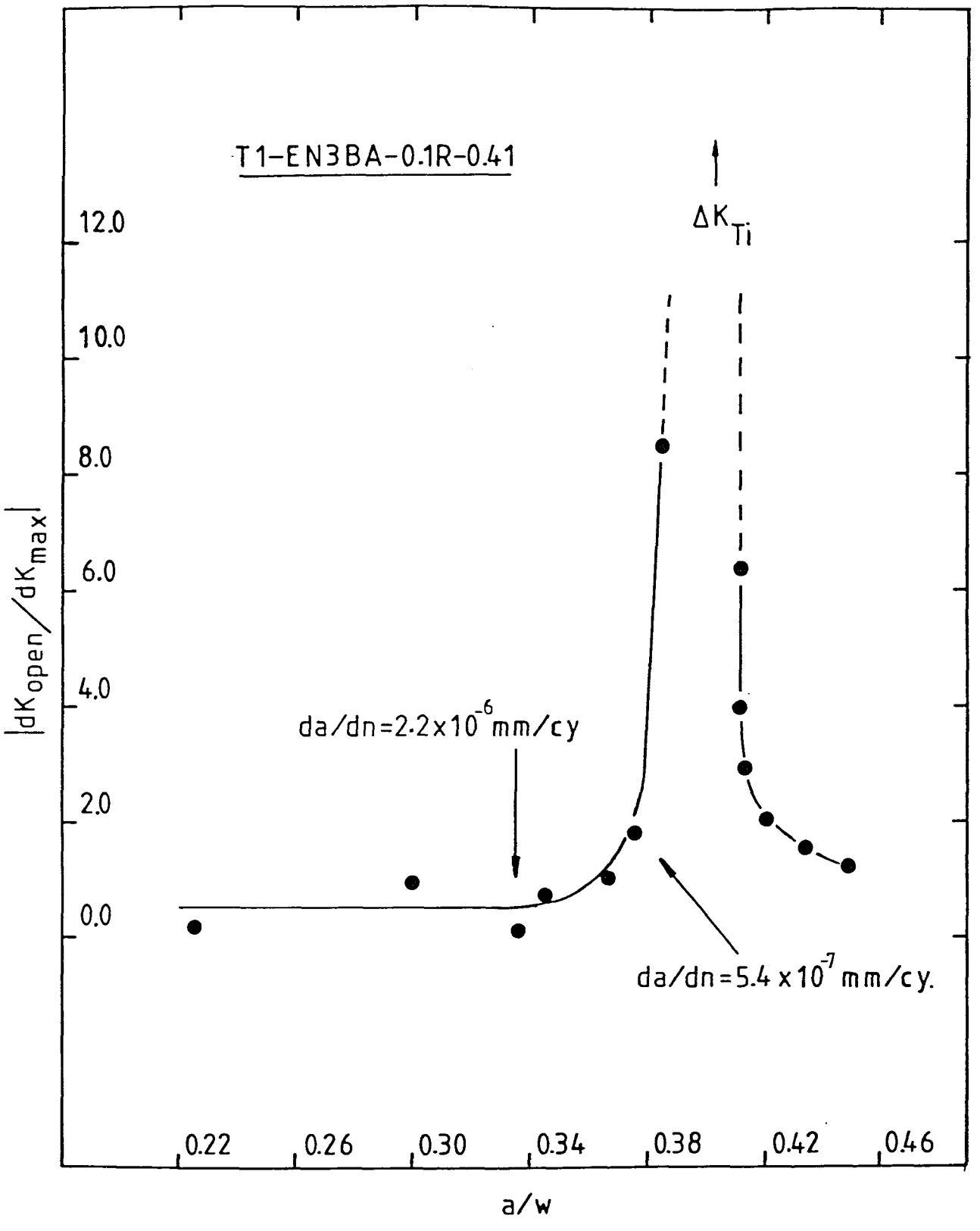


Fig. 11.72 A plot of $|dK_{open}/dK_{max}|$ versus a/w illustrating the build up in closure as threshold is approached.

(a) During load shedding oxide deposits were present on the fracture surface at growth rates $\leqslant 5 \times 10^{-6}$ mm/cycle which were absent of shorter and longer crack lengths subject to constant load amplitude fcg, Figs. 11.60(a)(d)(f) and 11.61(a)(d)(g). This led to the conclusion that during load shedding the production of fretting oxidation debris contributed significantly to crack closure as proposed by Ritchie [11.17].

(b) At low growth rates environmentally induced components of intergraunular cracking were present which suggested that the increase in crack closure resulted from surface roughness effects, Fig. 11.62(e).

Alternatively if crack closure is governed by microstructural crack growth and the initial load reduction sequence is insufficient to establish a closure level characteristic of the new stress conditions, a rapid fall in growth rate will be experienced. The situation will be further exacerbated by the onset of fretting fatigue and consequently low growth rates will be achieved at high ΔK's. If this argument applies then serious implications are evident. In materials exhibiting stress-microstructural crack growth the attainment of threshold by a conventional load shedding approach sequence will be dependent on initial fracture surface morphology. At low ΔK's, where fracture surface morphology is relatively planar, crack closure will be low and threshold will be achieved at low ΔK's. At higher ΔK's however, where intergranular components of fracture are present and fracture surface morphology is more irregular, a high level of crack closure will result in higher thresholds.

Unfortunately in the present investigation the closure contributions arising from fracture surface morphology and fretting oxidation could not be quantified. However, negative crack profile replicas clearly illustrated that the extent of fretting oxidation

was dependent on microstructure, Fig. 11.36 and 11.66. Decreasing microstructural scale produced a visible increase in oxide debris which may have been significant in retaining a high ΔK_{Ti}; whereas increasing microstructural scale resulted in a high ΔK_{Ti} as the direct consequence of significant surface roughness closure effects.

Threshold and Post Threshold Fatigue Crack Growth

The threshold levels (ΔK_{Ti}) of EN3BN and EN3BA which ranged from 9.9 to 11.2 $MPam^{-\frac{1}{2}}$ respectively were greater than expected in comparison to the results of others, Table 11.05. The difference was probably due to the occurrance of excessive amounts of oxide debris coupled with microstructural and environmentally induced crack growth resulting from the protracted load shedding threshold approach sequence.

Temporary threshold crack arrest and post threshold crack growth in both materials was associated with an increase and decrease in K_{open} as reported for EN19QH. No reason existed to suggest that the occurance of threshold hysteresis differed from EN19QH, and therefore no further discussion on this subject is included here.

11.5.5 Threshold Hysteresis

From the limited data of this investigation it is not possible to present a rational mechanism describing the phenomena of temporary crack arrest constituting the threshold hysteresis phenomena. Instead a tentative proposal is forwarded based on crack closure in an attempt to describe the hysteresis effect.

TABLE 11.05

Fatigue Threshold Data reported for Steel (determined in air)

Material	σ_{ys} MPam	R	ΔK_T $MPam^{-\frac{1}{2}}$	Reference
EN3A	-	0.09	8.1	11.47
A533-B1 Steel	518	0.10 0.70	8.0 3.1	11.13
EN1A	190	0.12	11.4	11.14
Mild Steel	430	0.13 0.75	6.6 3.8	11.44

In the present studies threshold hysteresis occurred in all materials subject to fatigue at R = 0.1 but was absent at R = 0.7. The presence of corrosion products at low growth rates, which was significant at R = 0.1 and insignificant at R = 0.7, suggested that the phenomena was dependent on oxide debris. The view that temporary threshold crack arrest is an environmental effect is also supported by Druce [11.12] who found in ferritic steels that the phenomena was present when fatigue was conducted in air but absent in vacuum.

From a closure viewpoint therefore, it is argued that temporary threshold crack arrest results from an increase in crack closure maintaining the condition $\Delta K_{eff} < \Delta K_{eff.Ti}$. This situation is initially developed during prolonged cycling at ΔK_{Ti} by the production of excessive fretting oxidation. Increasing the load range fails to satisfy the growth requirement, and further cycling generates more oxide debris maintaining the precedence. Eventually, when $\Delta K_{eff} > K_{eff.Ti}$, a rapid return to intermediate growth rates occurrs over insignificant increases in ΔK.

Evidence in support of this proposal is provided by the following observations at R = 0.1.

(a) The ΔK required to establish uninterupted post threshold fcg approached that of the load shedding sequence which corresponded to a growth rate of $\cong 10^{-6}$ mm/cycle, i.e. the onset of visible fretting oxidation.

(b) Significant fretting oxidation occurred at growth rates $\leqslant 10^{-7}$ mm/cycle.

(c) In several instances where post threshold fcg occurred at growth rates $< 10^{-7}$ mm/cycle crack growth was rapidly terminated by

self crack arrest.

(d) Post threshold fcg was adequately normalised by adopting a ΔK_{eff} analysis of growth rates.

Collectively these observations suggested that temporary threshold crack arrest was induced at growth rates $< 10^{-7}$ mm/cycle as the result of significant oxide induced crack closure; and a return to intermediate growth rates was determined by a critical value of ΔK which ensured growth rates in excess of that required to produce significant fretting oxidation.

Before concluding this section it is interesting to reflect the fatigue results of EN19QH with those of a bainitic steel reported by Suresh et al [11.06]. Suresh, who conducted threshold tests on a 2¼Cr-Mo bainitic steel in dry hydrogen and moist air, reported the influence of environment and stress ratio on near threshold fcg as shown in Fig. 11.73. At high stress ratios (0.75) threshold stress intensity levels (ΔK_o) were identical irrespective of environment, but at low stress ratios (0.05) a significant difference in ΔK_o existed which could not be attributed to fracture surface morphology. The difference in ΔK_o measured at R = 0.05 in hydrogen and air (i.e. $\delta\Delta K = 2.5$ MPam$^{-\frac{1}{2}}$) was attributed to oxide induced crack closure, but no explanation was presented to describe the stress ratio effect on ΔK_o tested in hydrogen.

In view of Suresh's results it is tentatively suggested that during the fatigue of specimens T1-EN19QH-0.1R-(0.09, 0.20, 0.3)_ and T2-EN19QH-0.1R-0.39 the adopted load shedding threshold approach sequence minimised fretting oxidation and resulted in a threshold stress level (ΔK_{Ti}) which was dominated almost entirely by the intrinic closure level (analogous to Suresh's hydrogen results at R = 0.05).

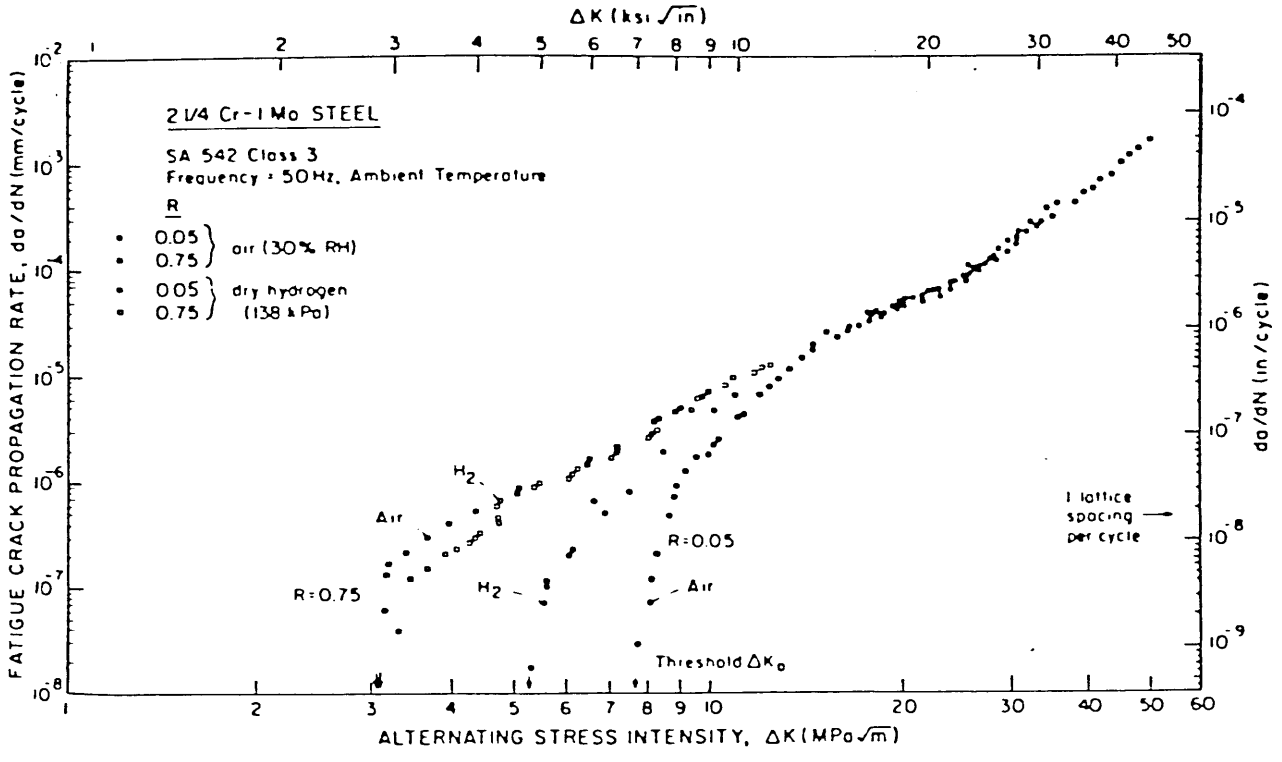


Figure 11.73 Fatigue crack propagation in a bainitic steel.

(After Suresh et al [11.06])

Fatigue cycling at threshold then resulted in an increase in crack closure through fretting oxidation effects, and an eventual return to intermediate growth rates was achieved at higher $\Delta K'$s (analogous to Suresh's air results at R = 0.05).

11.5.6 Fretting Fatigue and Oxide Induced Crack Closure

The phenomena of oxide induced crack closure first introduced by Ritchie et al [11.06, 11.17] has received little attention upto the present time. As a consequence only the original vague suggestion exists and no further evidence has been forwarded to support this proposal. Ritchie et al's closure mechanism involves the thickening of naturally formed oxide scale by a process of fretting fatigue at near threshold growth rates. This is achieved by 'smashing' together of cracked fracture surfaces made possible by plasticity induced crack closure. Oxide debris formed in this manner is then compacted and wedges the crack open causing an increase in closure level. The absence of this mechanism at high stress ratios is attributed to a reduction in plasticity induced crack closure.

The view held by the present author is similar to Ritchie's with the exception that crack closure at intermediate growth rates arises principly from surface roughness and other intrinsic effects. The results of EN19QH clearly confirmed that an increase in crack closure at low growth rates was related to the occurrance of fracture surface oxide debris. During load shedding fcg at R = 0.1 where $K_{min} < K_{open}$, substantial oxide debris was observed at growth rates $\leqslant 10^{-6}$ mm/cycle; but at R = 0.7 where $K_{min} \geqslant K_{open}$, oxidation debris was insignificant down to growth rates of 10^{-9} mm/cycle. The absence of oxide debris during post threshold fcg suggested that thickening

of naturally formed oxide deposits to give a visible oxide film was time dependent and relied heavily on 'smashing' together of both fracture surfaces.

In the light of these observations it is suggested that at low stress ratios and high growth rates, where $K_{min} < K_{open}$, fracture surface oxidation of steel occurrs by the formation of ferric oxide [11.05]. Now assuming the build up of corrosion product satisfies a logarithmic law as in the case of Fe, Fig. 11.74(a), the volume of oxide formed will be greater than the volume of the metal destroyed and a protective layer is formed of constant thickness. If crack growth is sufficiently rapid to ensure that by the time the oxide layer is formed the minimum crack opening displacement is greater than the combined oxide thickness, i.e.

$$\frac{d}{dt}\,(\text{oxide thickness}) < 2\,\frac{d}{dt}\,(COD_{min}) \qquad \ldots(11.07)$$

the oxide layer will remain intact and will not contribute to crack closure. But if ΔK is reduced such that

$$\text{oxide thickness} > 2\ COD_{min} \qquad \ldots(11.08)$$

or

$$\frac{d}{dt}\,(\text{oxide thickness}) > \frac{d}{dt}\,(COD_{min}) \qquad \ldots(11.09)$$

compressive forces acting on the oxide layer from apposing fracture surfaces will result in oxide fragmentation and further surface oxidation. Continued cycling then leads to an increase in oxide weight, Fig. 11.74(b), and compaction of the oxide debris wedging the crack open. Continued reduction in ΔK exacerbates the situation further by bringing into contact fracture surface remote from the crack tip, and a reduced COD and growth rate leads to excessive amounts of oxide debris, Fig. 11.74(c).

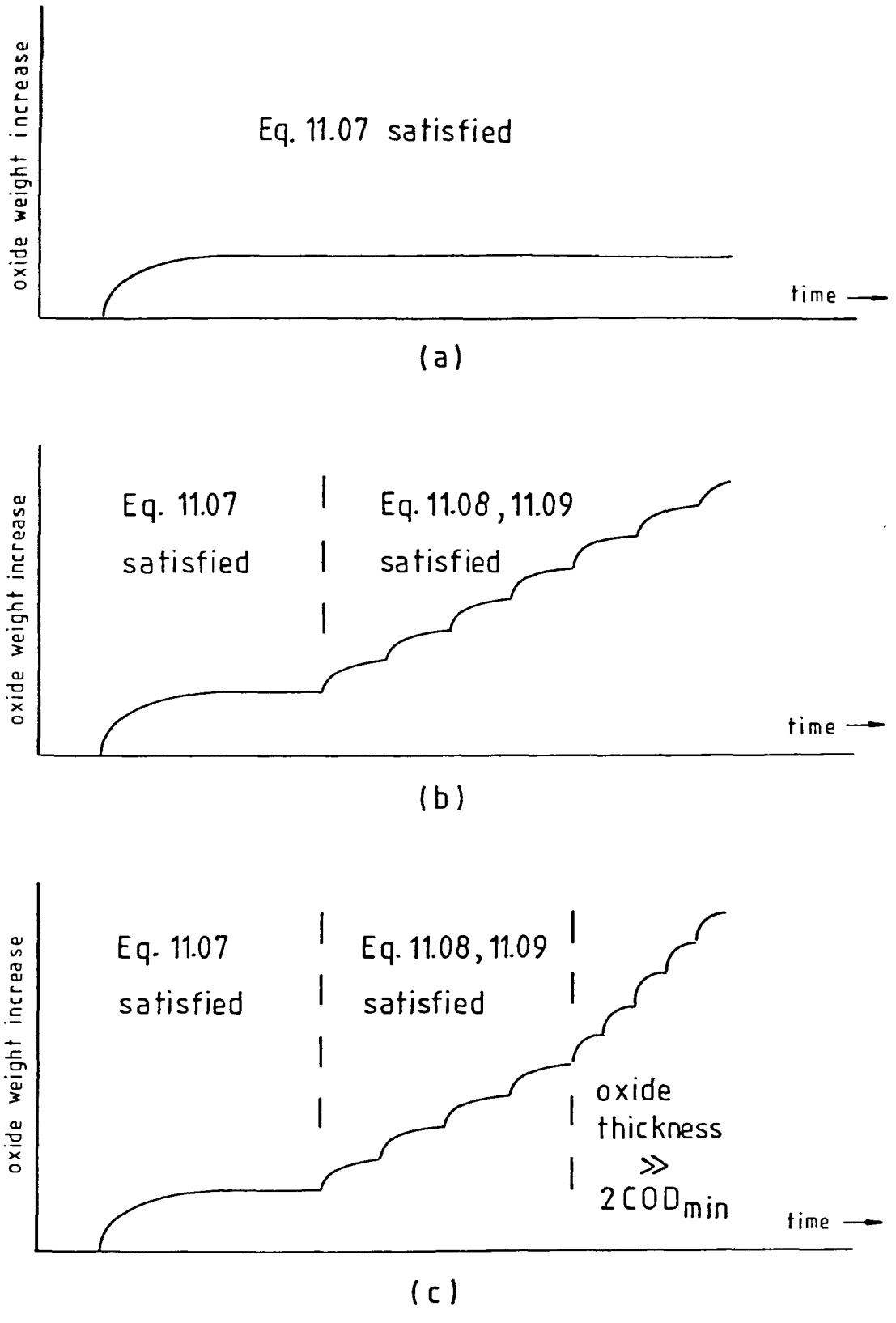


Fig. 11.74(a)-(c) Oxide thickening by fretting fatigue.

The extent of oxidation debris will be determined by a number of factors including fracture surface morphology, stress range, closure level, growth rates and COD. If all factors remain constant but fracture surface roughness is increased, the onset of fretting oxidation will be expected at high growth rates and high ΔK's. Conversely if fracture surface roughness is decreased the onset of fretting oxidation will be expected at low growth rates and low ΔK's. Thus increasing grain size may have a doubled effect on crack closure by increasing the surface roughness missmatch component and initiating the oxide mechanism at higher growth rates. In coarser grained material the extent of fretting oxidation may not be as prevelent as in finer grained material at lower growth rates, but the enhanced closure level at high growth rates may prove determental in attaining the most pessimistic threshold stress level.

11.5.7 Concluding Remarks

The results of this investigation confirmed that fatigue thresholds in steel are influenced by crack closure.

In EN19QH threshold stress levels were ΔK_{eff} controlled and exhibited a growth rate dependence on stress ratio through crack closure effects. The magnitude of ΔK_{Ti} was principly governed by intrinsic closure level, but a closure component arising from fretting oxidation was significant during prolonged threshold testing.

In EN3BN and EN3BA thresholds determined R = 0.1 were strongly influence by significant crack closure arising from microstructural

crack growth and fretting oxidation effects.

The extent and occurrence of fretting oxidation was determined by fatigue sequence, intrinsic closure level, stress ratio and growth rate. Its presence was ensured if $K_{min} < K_{open}$, but considerable thickening of the oxide layer was time dependent. Increasing environmental effects by prolonging process time did not signficantly increase the critical growth rate associated with the occurrence of visible fretting oxidation. It did however, significantly increase the extent of fretting oxidation at growth rates $\leqslant 10^{-7}$ mm/cycle.

Collectively the results suggested that a unique threshold stress intensity range characteristic of a material can only be obtained from closure free fatigue data. This can be obtained directly by choosing a suitable stress ratio which ensures that $K_{min} < K_{open}$, or indirectly through closure measurement.

Finally, the validity of threshold fcg data of steel determined in air or moist environments must always be questioned from a closure viewpoint.

11.6 Conclusions

EN19QH

(1) Fatigue thresholds and near threshold growth rates determined at R = 0.1 are influenced by crack closure arising from intrinsic and fretting oxidation effects.

(2) The high intrinsic closure level in this material ensured a stress ratio effect on near threshold growth behaviour.

(3) Provided a standard threshold test sequence is adopted and environmental conditions remain constant, reproducible closure dominated thresholds are possible.

(4) The phenomena of threshold hysteresis was associated with an increase in crack closure.

(5) Near threshold crack growth could be adequately normalised irrespective of stress ratio by employing a ΔK_{eff} analysis of growth rates.

(6) Fatigue threshold tests conducted at R = 0.1 in the regime $0.09 \leqslant a/w \leqslant 0.39$ exhibited no threshold dependency on crack length.

EN3BA and EN3BN (R = 0.1)

(1) The intrinsic closure level in both materials was insignificantly low at low ΔK's.

(2) During threshold testing a significant increase in crack closure in both materials resulted from microstructural crack growth and fretting oxidation.

(3) Fatigue thresholds and near threshold crack growth were closure dominated.

(4) The phenomena of threshold hysteresis exhibited by both materials was associated with an increase in crack closure.

General

(1) To minimise environmentally induced components of closure fatigue threshold testing in air should be conducted in the minimum time possible.

(2) The side face strain gauge technique employed to measure crack closure produced consistent and reliable closure results.

(3) In the steels of this investigation intrinsic crack closure level could not simply be related to fracture surface roughness effects.

(4) To avoid threshold hysteresis in steel it is essential to choose a threshold growth condition which is not dominated by fretting oxidation closure effects. The present series of fatigue tests suggest a limiting growth rate of 10^{-7} mm/cycle measured over 10^{5} stress cycles.

11.7 Recommendations for Further Work

This investigation has revealed that in steel fatigue thresholds are strongly influenced by stress conditions and crack closure. In the future it will therefore be necessary to evaluate the influence of fatigue sequence on threshold stress intensity range. In particularly, the ultimate objective must be to arrive at a load shedding sequence which minimises environmentally induced

crack closure effects whilst producing the most pessimistic fatigue threshold. Initial studies must be conducted at low stress ratios, i.e. 0.05, where fretting oxidation effects are most predominant. The optimum load shedding profile should be classified in terms of d^2K_{max}/d^2a, thereby facilitating its applicability to fatigue threshold testing conducted at high stress ratios.

Having established the optimum load shedding fatigue sequence it would then be of interest to determine the minimum threshold growth condition free from fretting oxidation closure effects.

11.8 References

[11.01] Tada, H., Paris, P., and Irwin, G.,
'The Stress Analysis of Cracks Handbook'
Del Research Corporation, Hellertown,
Pennsylvania, 1973, pp 216.

[11.02] American Society for Testing and Materials
"Proposed Method of Test For Constant Amplitude Fatigue Crack Growth Rates Below 10^{-8} mm/cycle", a Working Document
A.S.T.M. Philadelphia, 1977.

[11.03] Barry, B.A.,
'Errors in Practical Measurement in Science, Engineering and Technology'. John Wiley and Sons, Inc., New York.

[11.04] Schmidt, R.A. and Paris, P.C.,
A.S.T.M. STP 536, 1973, pp. 79.

[11.05] Chilton, J.P.,
'Principles of Metallic Corrosion'
The Chemical Society, London, 1973.

[11.06] Suresh, S., Zaminski, G.F., and Ritchie, R.O.,
American Soc. for Metals, Met. Trans. A., 1981.
12A, pp 1435.

[11.07] Benoit, D., Namdar-Tixier, R., and Tixier, R.,
Mater. Sci. Eng., 1981, 45, pp 1.

[11.08] Hicks, M.,
Ph.D. Thesis, University of Birmingham, 1980

[11.09] Chauhan, P., and Roberts, B.W.,
The Metallurgist and Mat's Technologist, 1977,
3, pp 131.

[11.10] Klesnil, M., and Lukas, P.,
Mat. Sci. Eng. 1972, 9, pp 231.

[11.11] Klesnil, M., and Lukas, P.,
E.F.M., 1972, 4, pp 77.

[11.12] Druce, S.G.,
Ph.D. Thesis, University of Birmingham, 1977

[11.13] Paris, P.C., Bucci, R.J., Wessel, E.T., Clark, W.G. and Mager, T.R.,
A.S.T.M., STP 513, 1872, pp 141.

[11.14] Cooke, R.J.,
Ph.D. Thesis, University of Birmingham, 1970.

[11.15] Elber, W.,
E.F.M., 1970, 2, pp 37.

[11.16] Elber, W.,
A.S.T.M., STP 486, 1971, pp 230.

[11.17] Ritchie, R.O., Suresh, S., and Moss.
J. Eng. Mat. Tech., Trans, ASME Series M, 1980, 102, pp 233.

[11.18] Stewart, A.T.,
E.F.M., 1980, 13, pp 463.

[11.19] Walker, N., and Beevers, C.J.,
Fat. Eng. Mat. Struct., 1979, 1, pp 135.

[11.20] Minakawa, K., and McEvily, A.J.,
Scripta Met., 1981, 15, pp 633.

[11.21] Mayes, I.C. and Baker, T.J.,
Fat. Eng. Mat. Tech., 1981, 4, pp 79.

[11.22] Davidson, D.L.,
Fat. Eng. Mat. Tech., 1981, 3, pp 229.

[11.23] Ritchie, R.O.,
In Fatigue Thresholds, Proceedings 1st Intl. Conf.,
Stockholm, J. Bäcklund, A. Bloom, and C.J. Beevers,
eds, EMAS Publ. Ltd., Warley, U.K., 1981.

[11.24] Ritchie, R.O., and Suresh, S.,
American Soc for Metals, Met. Trans A., 1982, 13A
pp 937.

[11.25] Adams, N.J.I.,
E.F.M., 1972, 4, pp 543.

[11.26] Roberts, R., and Smidt, R.A.,
Int. J. of Frac., 1972, 8, pp 469.

[11.27] Sharpe, W.N., and Grandt, A.F.,
AFML-TR-74-203, 1975.

[11.28] Sharpe, W.N., Corbly, D.M., and Grandt, A.F.,
AFML-TR-75-57, 1975.

[11.29] Katcher, M., and Kaplan, M.,
A.S.T.M. STP 559, 1974, pp 264

[11.30] Bachmann, V., and Mundz, D.,
Int. J. of Frac. 1975, 11, pp 713.

[11.31] Lindley, T.C. and Richards, C.E.,
"The Influence of Crack Closure and Plastic Zone
Geometry on Fatigue Crack Propagation",
3rd Int. Conf. on Fracture, Munich, 1973.

[11.32] Irving, P.E., Robinson, J.L., and Beevers, C.J.
E.F.M., 1975, 7, pp 619.

[11.33] Lindley, T.C., and Richards, C.E.,
Mats. Sc. and Eng., 1974, 14, pp 281.

[11.34] Shaw, W.J.D. and LeMay, I.,
A.S.T.M. STP, 677, 1979, pp 233.

[11.35] Buck, O., Frandsen, J.D., Ho, C.L., Marcus, H.L.,
'The Effect of Gaseous Environments on Crack Tip
Closure', Presented at the Third Int. Conf. on the
Strength of Metals and Alloys, Cambridge, England, 1973.

[11.36] Buck, O., Frandsen, J.D., and Marcus, H.L.,
E.F.M., 1975, pp 161, 7.

[11.37] Kitagawa, H., and Takahashi, S.,
'Applicability of Fracture Mechanics to Very, Small Cracks
or Cracks in the Early Stage',
Proc. 2nd Int. Conf. on Mech. Behaviour of Mats.,
Boston, 1976.

[11.38] Smith, R.A.,
Int. J. Frac., 1977, 13, pp 717.

[11.39] Lankford, J.,
Int. J. of Frac., 1980, 16, pp R7.

[11.40] Frost, N.E., Marsh, K.J., and Pook, L.,
'Metal Fatigue', pp 44, Oxford Eng. Sc., Series,
Clareden Press.

[11.41] Frost, N.E., Pook, L.P., and Denton, K.,
E.F.M., 1971, 3, pp 109.

[11.42] Frost, N.E.,
Proc. Inst. Mech. Engrs., 1959, 173, pp 811.

[11.43] Frandsen, J.D., Inman, R.V., and Buck, O.,
Inst. J. of Frac., 1975, 11, pp 345.

[11.44] Pook, L.P.,
J. Strain, Analy., 1975, 10, pp 242.

[11.45] Cooke, R.J., Irving, P.E., Booth, G.S., and Beevers, C.J.,
E.F.M., 1975, pp 65.

[11.46] Ritchie, R.O., and Knott, J.F.,
'Effects of Fracture Mechanics' on Fatigue Crack Propagation, P.M.C., Conf. 'Mechanics and Mechanisms of Crack Growth', Cambridge, 1973.

[11.47] Priddle, E.K., and Jerram, K.,
C.E.G.B. Report No. RD/B/N2143, 1972.

[11.48] Pickard, A.C., Ritchie, R.O., and Knott, J.F.,
Proc. 4th Int. Conf. on 'Strength of Metals and Alloys', 1976, pp 473, Nancy France, I.N.P.L.

[11.49] Knott, J.F. and Pickard, A.C.,
Met. Sc., 1977, 11, pp 399.

[11.50] Austen, I.M., Ph.D. Thesis, Sheffield University, 1973.

APPENDIX A1

CURRENT AND SENSING LEAD ARRANGEMENT

A1.0 Nomenclature

PD	=	potential difference
PD_T	=	total potential difference
PD_{AB}	=	potential difference measured across the flaw.
PD_{CD}	=	potential difference measured across a plane area of the specimen.
Voltage Gain	=	electrical gain imposed on the measured voltage signal.

A1.1 Introduction

The techniques of current and sensing lead attachment detailed in this Appendices are based on the recommendations of Testwell Ltd. [A1.01, A1.02]. Whilst every effort was made to adhere to these recommendations considerable deviations were necessary to ensure a high degree of stability.

A1.2 Current Lead Arrangement and Connection

Plane Specimens Both current leads were positioned 60 mm either side of the flaw and were connected to the specimen by a crimp tag - brass nut and bolt arrangement as shown in Figs. A1.01, A1.02.

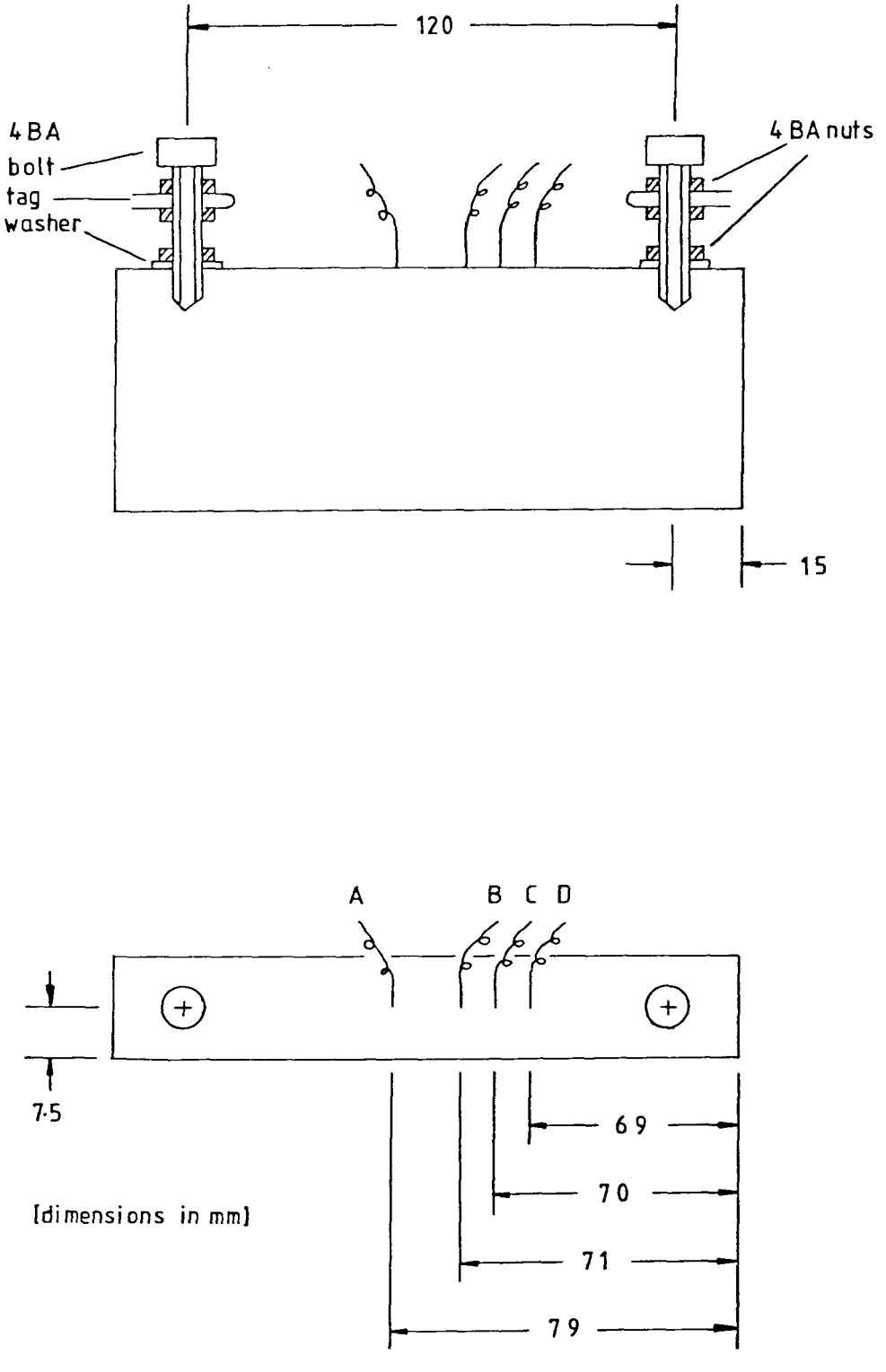


Fig. A1.01 Plane Specimen current and sensing lead arrangement.

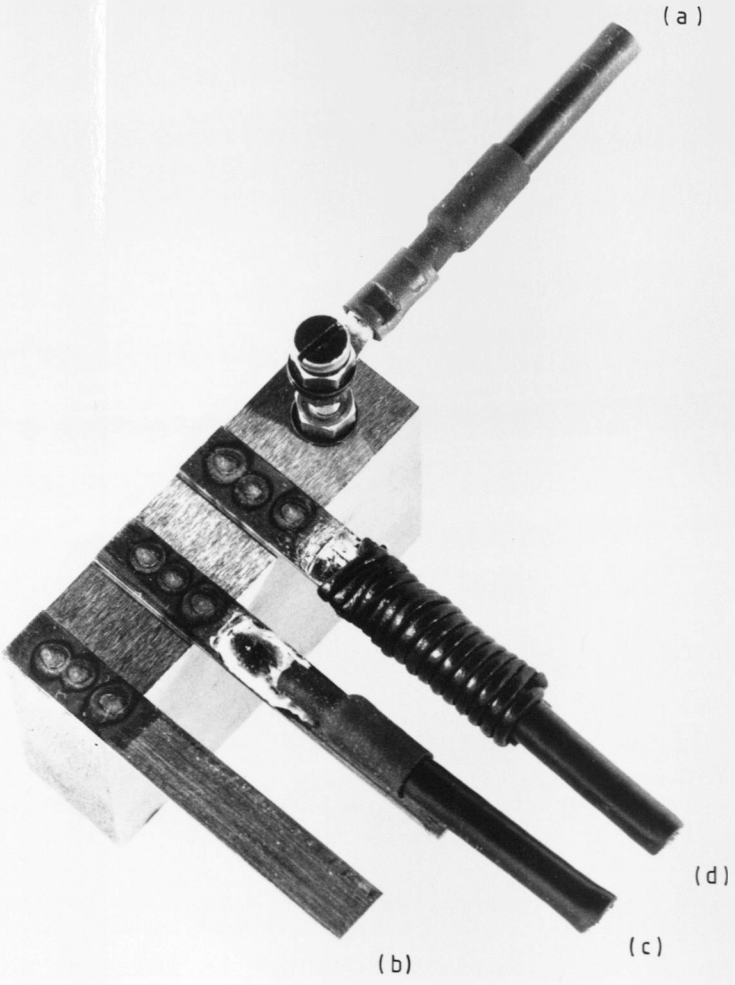


Fig. A1.02 Current Lead attachment

(a) Plane Specimen

(b), (c), (d) — SEN Specimen

SEN Specimens Both current leads were positioned 60 mm either side of the flaw and were connected to the specimen via a spot welded mild steel tag as shown in Figs. A1.02, A1.03. The tag ensured an even current distribution across the specimen surface and gave rigid support to the unshielded current lead. The connection was made as follows:

(a) first each tag was attached to the surface by three spot welds using a resistance spot welder delivering 100 amps at 520 volts, Fig. A1.02(b);

(b) then the internal copper lead was soldered to the tag, Fig. A1.02 (c); and finally

(c) the whole joint was bound with lacing tape to secure the lead in position, Fig. A1.02(d).

It is important to ensure that the current lead contact is secure, any random movement of the unshielded lead will produce vast fluctuations in PD, but movement of the shielded section has no effect.

A1.3 Sensing Lead Arrangement and Connection to Plane and SEN Specimens

Sensing leads were connected to each specimen via four 31 SWG insulated copper wires as shown in Fig. A1.04. In this arrangement leads A-B sense PD across the flaw and C-D across a plane area (C-D compensate for changes in PD arising from fluctuations in current and specimen resistivity).

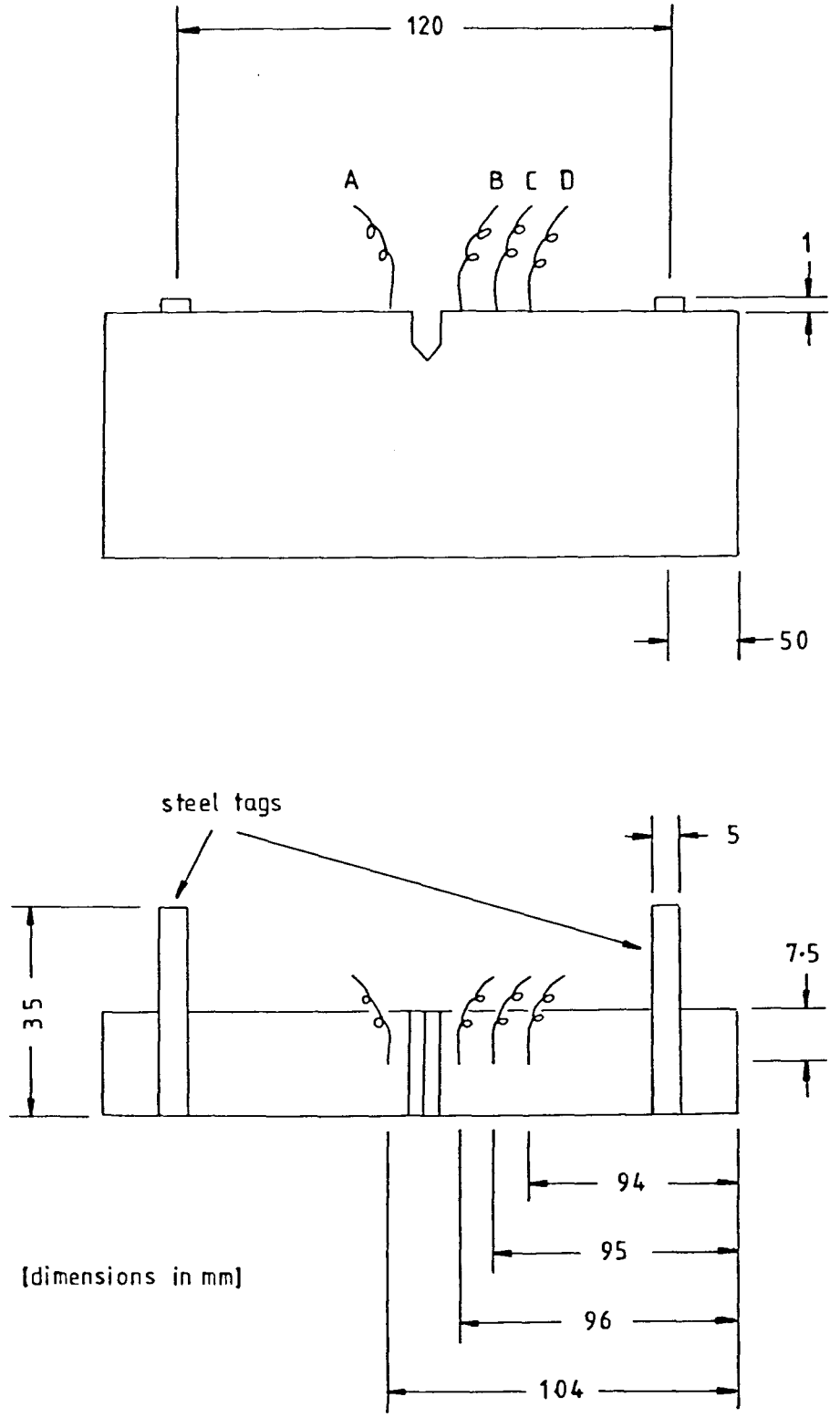


Fig. A1.03 SEN Specimen current and sensing lead arrangement.

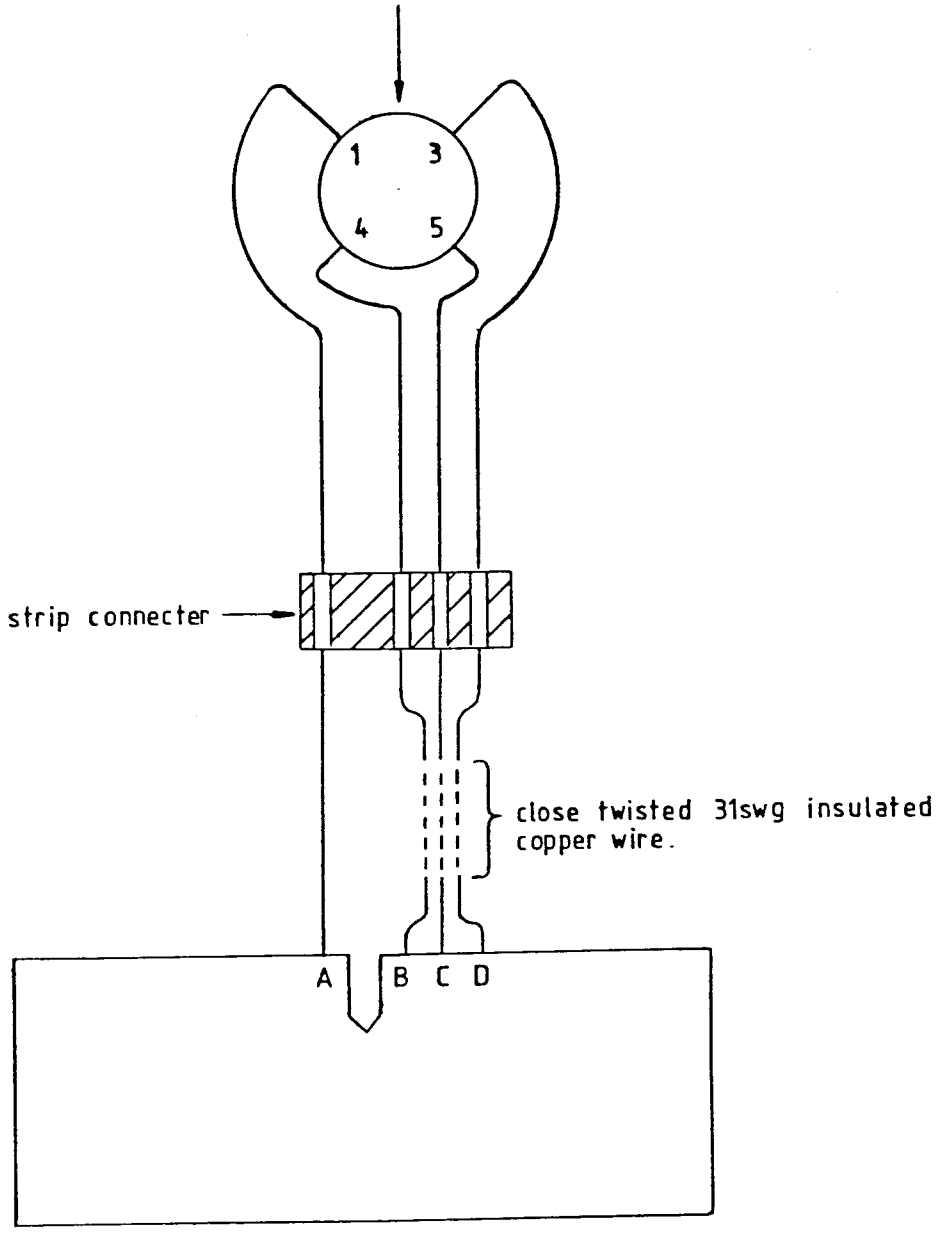


Fig. A1.04 A schematic diagram illustrating sensing and compensation wire arrangement.

Ignoring eddy current contributions the total potential difference PD_T is given by

$$PD_T = (PD_{AB} - PD_{CD}) \cdot \text{Voltage Gain} \qquad \ldots(A1.01)$$

Initially it was recommended [A1.01] that C and D should coincide with B, but subsequent reports [A1.02] have claimed that consistency in PD measurement is increased if C and D are seperated.

Positions B, C and D were arbitarily set as 1 mm intervals, and distance A-B, 8 mm. The connection was made as follows:

(a) first the copper contact leads were capacitance discharge welded to the surface as shown in Fig. A1.05 (a);

(b) then the welds were protected by encasing them in Metset Polyester Resin as illustrated in Fig. A1.05 (b);

(c) wires B, C and D were then closely wound, encased in Metset Resin, and soldered to a connecting strip, Fig. A1.05 (c); and finally

(d) the sensing leads from the pre-amplifier were soldered to the connecting strip and encased in Metset Resin as shown in Fig. A1.05 (d).

It is important to secure the unshielded sections of the sensing leads. Failure to do so results in catastrophic fluctuations in PD. Leads B, C and D must be closely wound, if not the detector becomes insensitive to flaw growth. Tests have revealed that it is detremental to position pre-amplifier leads along the bulk current carrying surface, doing so produces a large decrease

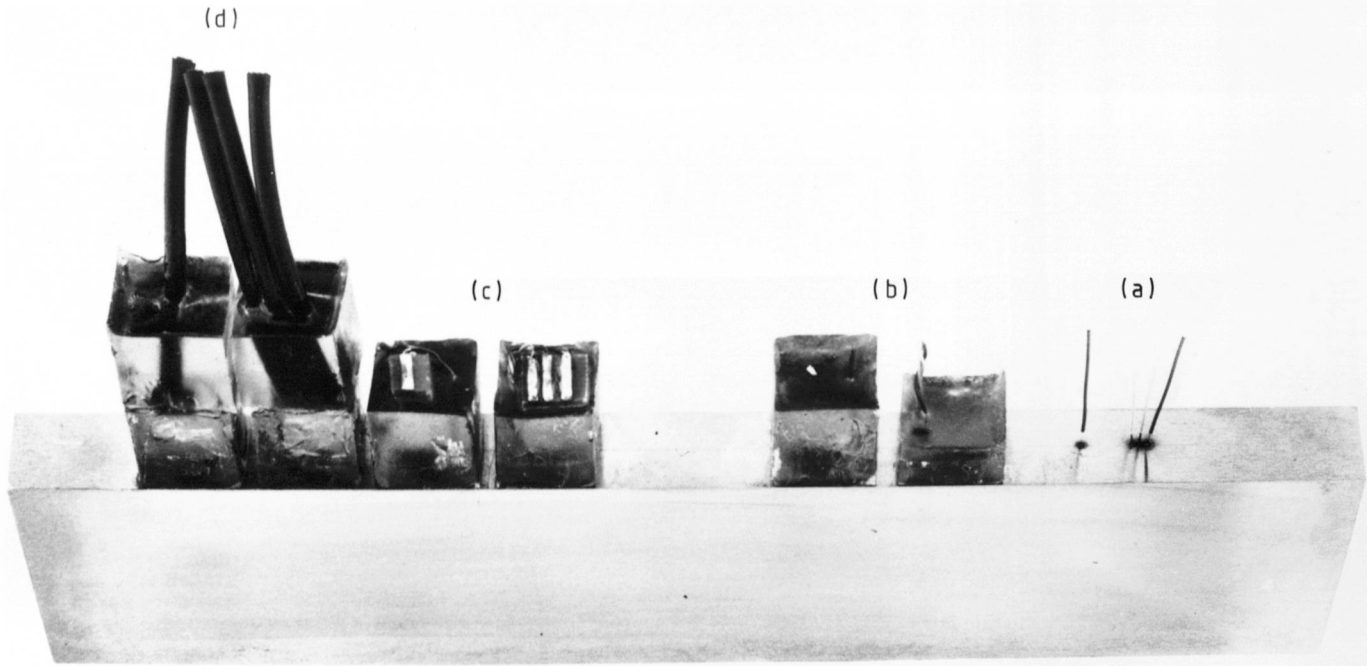


Fig A1·05 Steps (a) to (d) illustrate the sequence of sensing lead attachment.

in voltage and renders the equipment insensitive to flaw growth. All sensing leads must therefore initially lie perpendicular to the bulk current carrying surface.

A1.4 References

[A1.01] Testwell Ltd.,
Tech. Memo. 126.

[A1.02] Private Communication with D. Mann of Testwell Ltd.

APPENDIX A2

ALTERNATING CURRENT POTENTIAL DIFFERENCE VERSUS DETECTOR INTERNAL CALIBRATION

A2.0 Introduction

It was only necessary to check the potential difference response to detector internal calibration at the end of each experiment because long term stability tests had revealed it remained consistent irrespective of room temperature and mains voltage.

A2.1 Experimental Procedure

Initially the detector was set at:

Current = 5 amps

Voltage Gain = 5×10^3

Voltage Display = 5.00 volts (using voltage offset)

Potential difference readings were then recorded at regular 0.5 volt increments of detector internal calibration from 4.0 to 5.5 volts. The sequence was then reversed.

A2.2 Treatment of Data

A plot of potential difference versus detector internal calibration was constructed, Fig. A2.01, and the data was subject

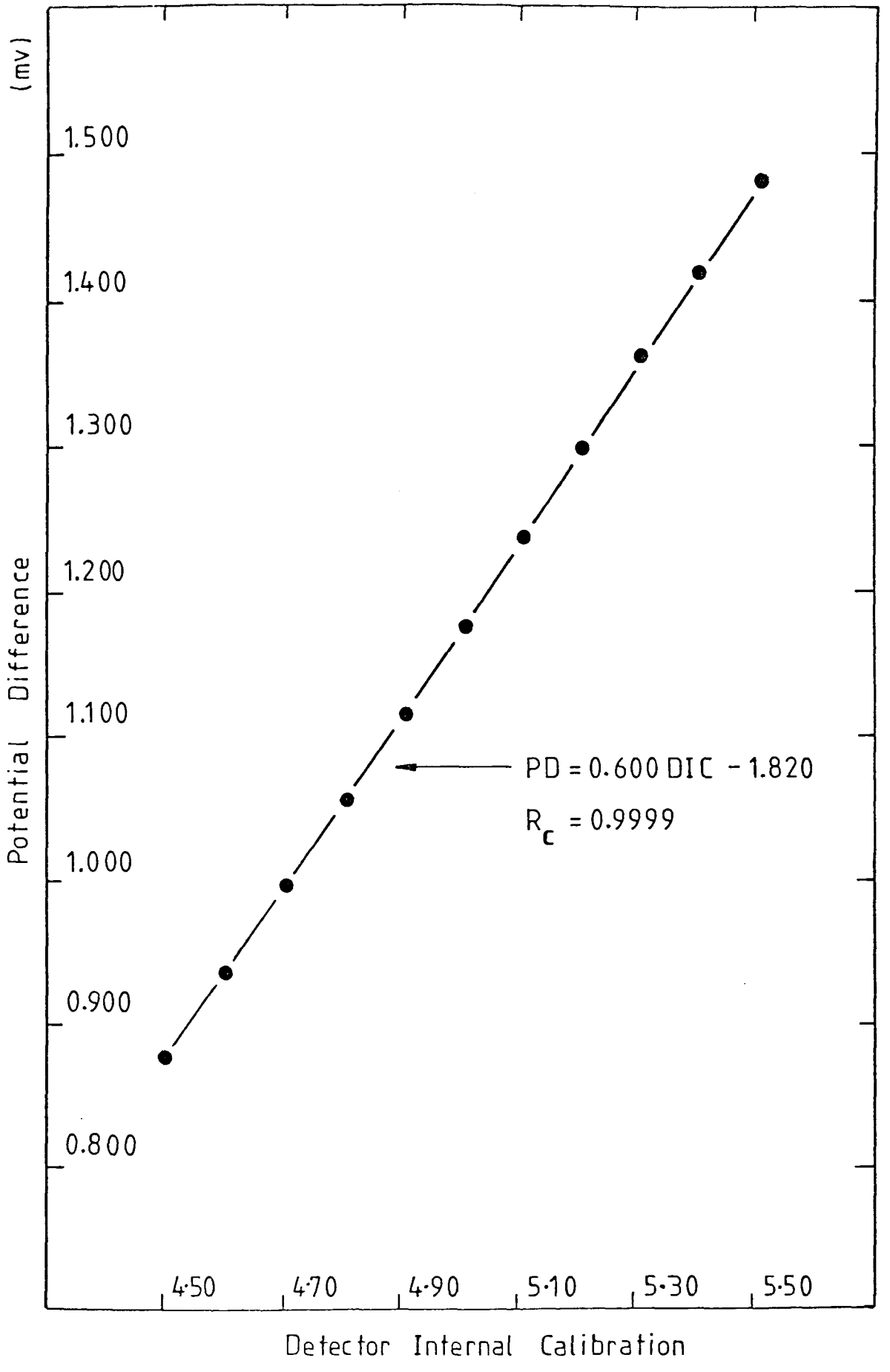


Fig. A2.01 A plot of Potential Difference versus Detector Internal Calibration (DIC).

to linear regression analysis as described in Appendix A7. Potential difference correction factors were then generated accordingly, Table A2.01.

TABLE A2.01

Typical Detector Internal Calibration - Potential Difference Correction Factors

Detector Internal Calibration (volts)	Potential Difference Correction Factors (μv)
5.05	- 30
5.04	- 24
5.03	- 18
5.02	- 12
5.01	- 6
5.00	0
4.99	+ 6
4.98	+ 12
4.97	+ 18
4.96	+ 24
4.95	+ 30

Note: potential difference correction factors are normalised with respect to a detector internal calibration of 5.00 volts.

APPENDIX A3

ALTERNATING CURRENT POTENTIAL DIFFERENCE VERSUS PARAFFIN BATH TEMPERATURE

A3.0 Experimental Procedure

The relationship between alternating current potential difference and paraffin bath temperature of the EDM calibration study was determined by monitoring the response of potential difference to changes in bath temperature during a heat-up and cool-down cycle from 10 to 45^{o}C. This was carried out over a period of approximately 5 hours during which a uniform bath temperature was maintained by continuously circulating the paraffin around the components.

A3.1 Potential Difference versus Paraffin Bath Temperature

All Tests exhibited a linear relationship as shown in Fig. A3.01. The data was subject to traditional linear regression analysis as described in Appendix A7 and potential difference correction factors arising from fluctuations in paraffin bath temperature were generated accordingly, Table A3.01.

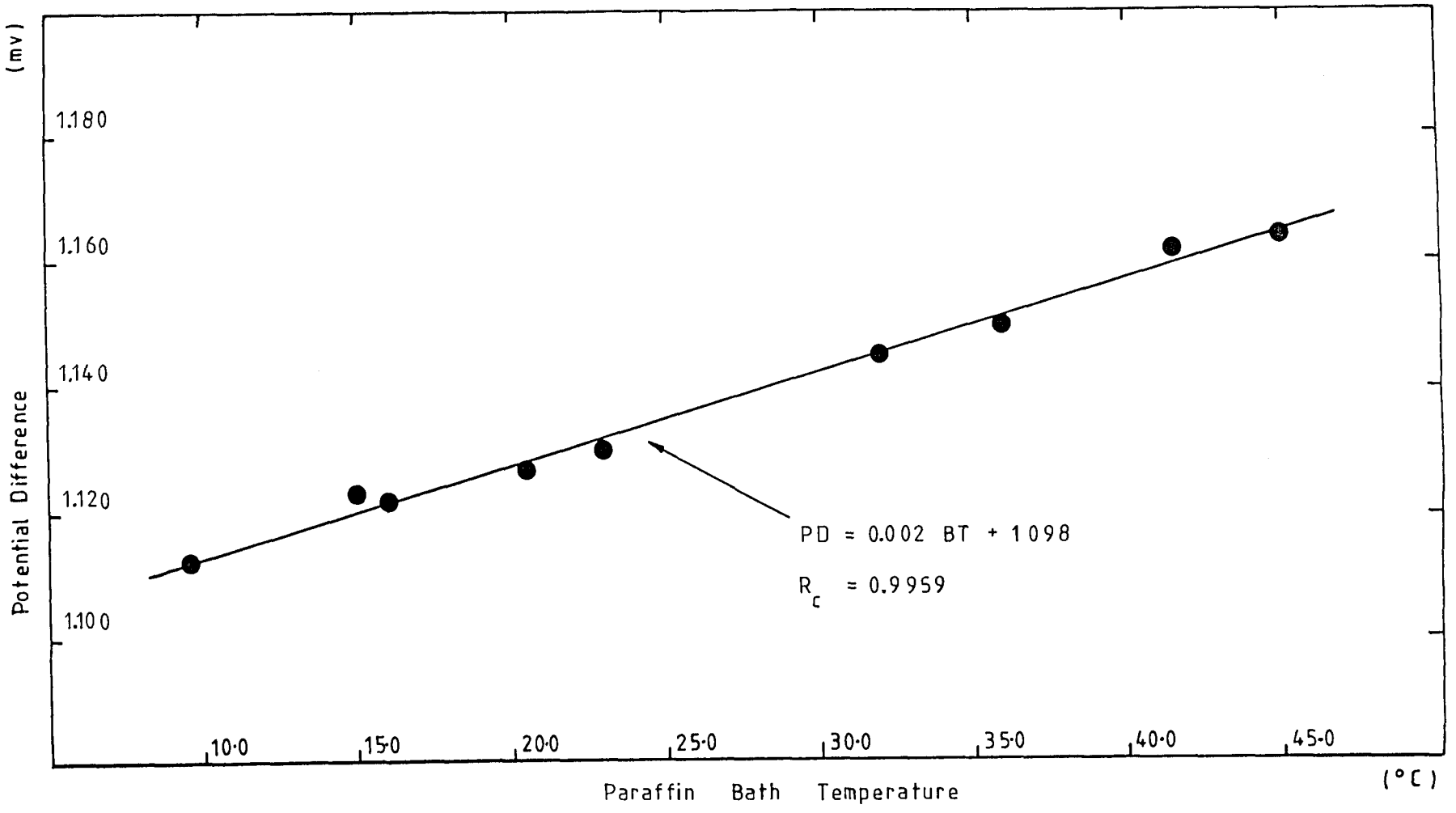


Fig. A3.01 A plot of Potential Difference versus Paraffin Bath Temperature (BT)

TABLE A3.01

Typical Paraffin Bath Temperature - Potential Difference Correction Factors

Bath Temp ^{o}C	Potential Difference Correction Factors (μv)
18	- 22
19	- 15
20	- 7
21	0
22	+ 7
23	+ 15
24	+ 22

Note: potential difference correction factors are normalised with respect to $21^{o}C$

APPENDIX A4

FATIGUE CRACK GROWTH AND FRACTURE SURFACE WAVE PATTERN ANALYSIS

A4.0 Nomenclature

a	=	characteristic measurement of crack depth in the specimen width direction
a_{ci}	=	characteristic measurement of crack depth of the ith observation in the specimen width direction.
R	=	stress ratio (K_{min}/K_{max})
K	=	stress intensity factor
PD_i	=	potential difference of the ith observation
K_{max}	=	maximum stress intensity
ACPD	=	alternating current potential difference
PD	=	potential difference.

A4.1 Introduction

The purpose of the fatigue crack growth studies was to relate measurements of crack length (a_{ci}) to potential difference (PD_i). This was achieved by periodically varying R to produce visible fracture surface wave markings.

Three techniques were tried with varying degrees of success and the most appropriate was employed in the fatigue crack growth ACPD calibration study.

A4.2 Techniques of Fracture Surface Crack Wavefront Marking

A4.2.1 Alternating Stress Ratio at Constant K_{max}. (Technique 1)

This consisted of producing light and dark wave patterns representative of fatigue crack growth by alternating R at regular intervals from 0.1 to 0.3 but keeping K_{max} constant ($\cong$ 30 $MPam^{-\frac{1}{2}}$). The major problem encountered was obtaining the true value of PD_i for a_{ci}. Inaccuracies were introduced as the direct consequence of cycling the mean load between two stress ranges, and a large degree of uncertainty was attached to the change in mean strain and specimen compliance on PD.

A4.2.2 Overload Marking (Technique 2)

This involved a sequential process in which the crack was first grown for 0.2 mv at R = 0.1 and $K_{max} \cong 30.0$ $MPam^{\frac{1}{2}}$ and then subject to a brief overload of $K_{max} \cong 40.0$ $MPam^{-\frac{1}{2}}$ and $R < 0.1$. The problems negotiated were: (a) the wave markings produced by the overload were indistinct; (b) it took considerable time to grow out of the overload condition; and (c) the mean load had to be sufficiently high to encorporate an overload cycle.

A4.2.3 Alternating Stress Ratio at Constant Mean Load (Technique 3)

This involved growing a fatigue crack for set increments of 0.16 and 0.08 mv by respectively imposed large and small stress range cycle fatigue of common mean load. The large stress range

(with $K_{max} \cong 30$ MPam$^{-\frac{1}{2}}$ and $R \leqslant 0.1$) ensured a plane crack wavefront and high growth rate, whilst the small stress range (with $K_{max} \leqslant 20.0$ MPam$^{-\frac{1}{2}}$ and $R \geqslant 0.5$) produced low growth rates with some fretting fatigue. As a calibration technique this was deemed best for two reasons: (a) relatively good demarkation lines were produced on the fracture surface; and (b) the process was easily controlled.

A4.3 Production of Fracture Surface Wave Patterns

During the fatigue crack growth studies Technique 3 was employed to produce fatigue crack wave patterns on the fracture surface as follows.

(a) Initiation was carried out by subjecting each specimen to large stress range fatigue of $K_{max} \cong 30$ MPam$^{-\frac{1}{2}}$ and $R \leqslant 0.1$, and a crack was grown to length a_{c1} which corresponded to a voltage increase of 0.16 mv.

(b) With the crack in the a_{c1} position the voltage reading PD_1 was noted.

(c) Subsequently small stress range fatigue of $R \geqslant 0.5$ and $K_{max} \leqslant 20.0$ MPam$^{-\frac{1}{2}}$ was imposed and crack growth was allowed to proceed a short distance corresponding to a voltage increase of 0.08 mv.

(d) Large stress range fatigue was now imposed until a further increment of crack growth corresponding to 0.16 mv had been achieved.

(e) With the crack now in the a_{c2} position the voltage PD_2 was noted.

(f) Steps 3 - 5 were repeated and the respective stress ratios were adjusted to give consistent growth rates.

A4.4 PD-Wave Pattern Analysis

On the completion of the fatigue process each specimen was cooled to $-196^{o}C$ in liquid nitrogen and fractured in 3 point bend to reveal the fracture surface. Direct optical analysis of the wave patterns using a vernier travelling microscope presented a major problem, because demarkation boundaries could not be accurately distinguished. To alleviate this problem each fracture surface was photographed using oblique lighting and a X10 magnified print was produced. From this print a_{ci} was determined which corresponded to an average value of crack depth measured at 5 equidistant positions across the fracture surface, Fig. A4.01.

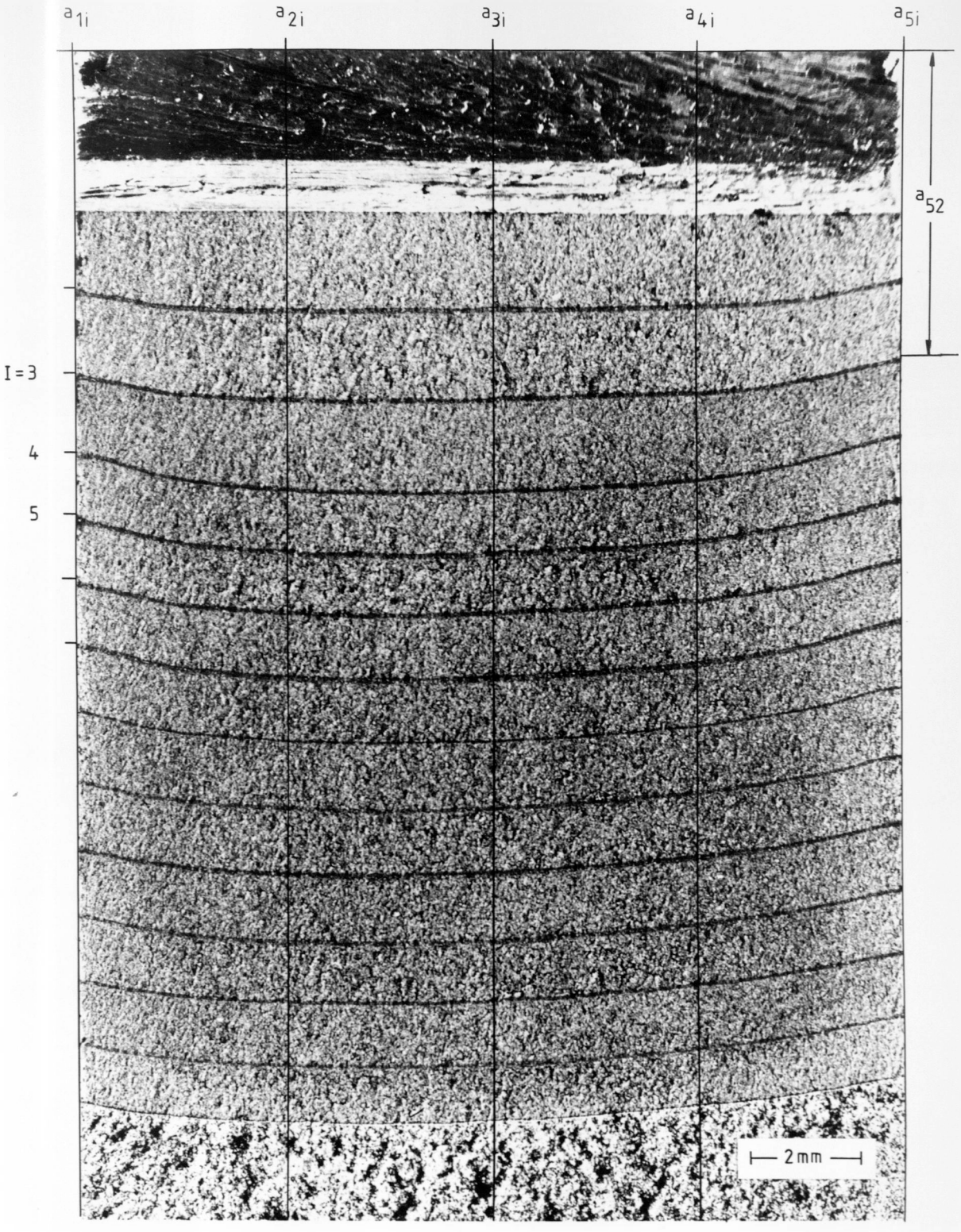


Fig. A4.01 Fatigue fracture surface wave pattern analysis

APPENDIX A5

CRACK LENGTH ERROR ANALYSIS BASED ON CRACKED AREA

A5.0 Nomenclature

a_{ci}	=	characteristic measurement of crack depth of the ith observation
TCA	=	theoretical cracked area
ACA	=	actual cracked area
R	=	radius
B	=	specimen breadth
PECA	=	percentage error in cracked area
i	=	ith observation.

A5.1 Introduction

In the past the standard practice has been to relate crack waveshape to a characteristic measurement of crack depth (a_{ci}), which is normally defined as the average of several linear measurements taken at adjacent reference positions across the fracture surface [5.01, 5.02]. Obviously this average value does not fully describe crack shape, and introduces errors in any calibration response based on a change in cracked area.

Detailed in this Appendices is an approach to estimating the errors in a_{ci} based on an approximation to actual cracked area.

A5.2 Determination of Theorectical Cracked Area Representative of a_{ci}

In the fcg studies crack depth and shape was characterised by a linear measurement (a_{ci}) which corresponded to a rectangular cracked area of dimension a_{ci} in the growth direction where

$$TCA_i = a_{ci} B \qquad \ldots(A5.01)$$

A5.3 Determination of Actual Cracked Area

If it is assumed that crack growth is well behaved and $a_{1i} \cong a_{5i}$, actual cracked area is given by the sum of the areas X and Y of Fig. A5.01. Area Y is simply

$$Y_i = \frac{(a_{1i} + a_{5i})}{2} B \qquad \ldots(A5.02)$$

Now assuming that the crack wavefront forms a circular arc of radius R_i where

$$R_i = \frac{B^2 + 4H_i^2}{8H_i} \qquad \ldots(A5.03)$$

and

$$H_i = a_{ci} - \frac{a_{1i} + a_{5i}}{2} \qquad \ldots(A5.04)$$

area X is given by

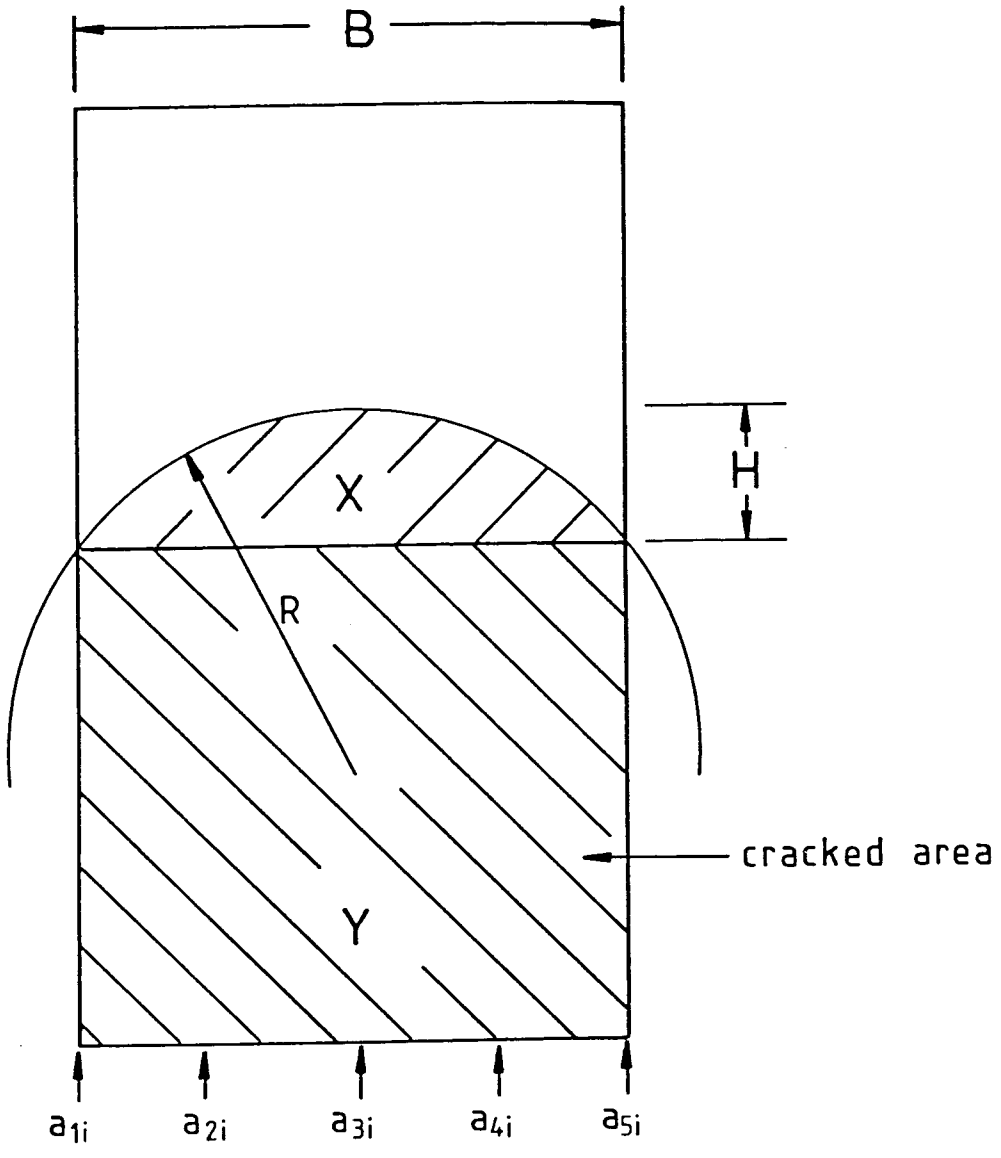


Fig. A5.01 Schematic representation of cracked configuration.

$$X = \frac{R_i^2}{2}\left[\frac{2\,(\mathrm{Sin}^{-1}\,B/2R_i)\pi}{180} - \mathrm{Sin}\,(2(\mathrm{Sin}^{-1}\,B/2R_i))\right] \qquad \ldots(A5.05)$$

Combining Eq A5.02 and Eq. A5.05 gives the actual cracked area

$$ACA_i = \frac{a_{1i} + a_{5i}}{2} B + \frac{R_i^2}{2}\left[\frac{2(\mathrm{Sin}^{-1}\,B/2R_i)\pi}{180} - \mathrm{Sin}\,(2(\mathrm{Sin}^{-1}\,B/2R_i))\right] \qquad \ldots(A5.06)$$

A5.4 Determination of Percentage Error in Cracked Area

The difference between TCA and ACA corresponds to

$$D_i = ACA_i - TCA_i \qquad \ldots(A5.07)$$

and $PECA_i$ is simply given by

$$PECA_i = \frac{100D_i}{ACA_i} \qquad \ldots(A5.08)$$

Thus when a_{ci} is representative of the actual cracked area PECA = 0. A negative value of Eq. A5.08 denotes an underestimate of a_{ci} and a positive value, an overestimate.

A5.5 Determination of Percentage Error in Crack Depth

Provided specimen thickness remains constant percentage error in crack depth is simply PECA.

A5.6 References

[A5.01] "The measurement of crack length and shape during fatigue", EMAS, 1980, U.K.

[A5.02] British Standards Institute, BS5447:1977, "Methods of test for Plane Strain Fracture Toughness (K_{IC}) of Metallic Materials".

APPENDIX A6

COMPUTOR PROGRAMME TIDY

A6.0 Introduction

Computer Programme Tidy, whose flow chart appears in Fig. A6.01, was developed to correct potential difference readings of the ACPD calibration studies of Chapter 10 for chart cross, paraffin bath temperature and detector internal calibration.

A6.1 Specific Details

The effect of paraffin bath temperature on potential difference was normalised with respect to 21^{o}C (Appendix A3). Corrections to potential difference arising from detector internal calibration drift was based on a detector internal calibration of 5.00 volts (Appendix A2)

A6.2 Running the Programme

The programme, which is presented in Fig. A6.02, was designed to correct a series of potential difference readings arranged in batches of 4 chart crosses. Data was supplied in standard form, Fig. A6.03, and results were generated as shown in Fig. A6.04.

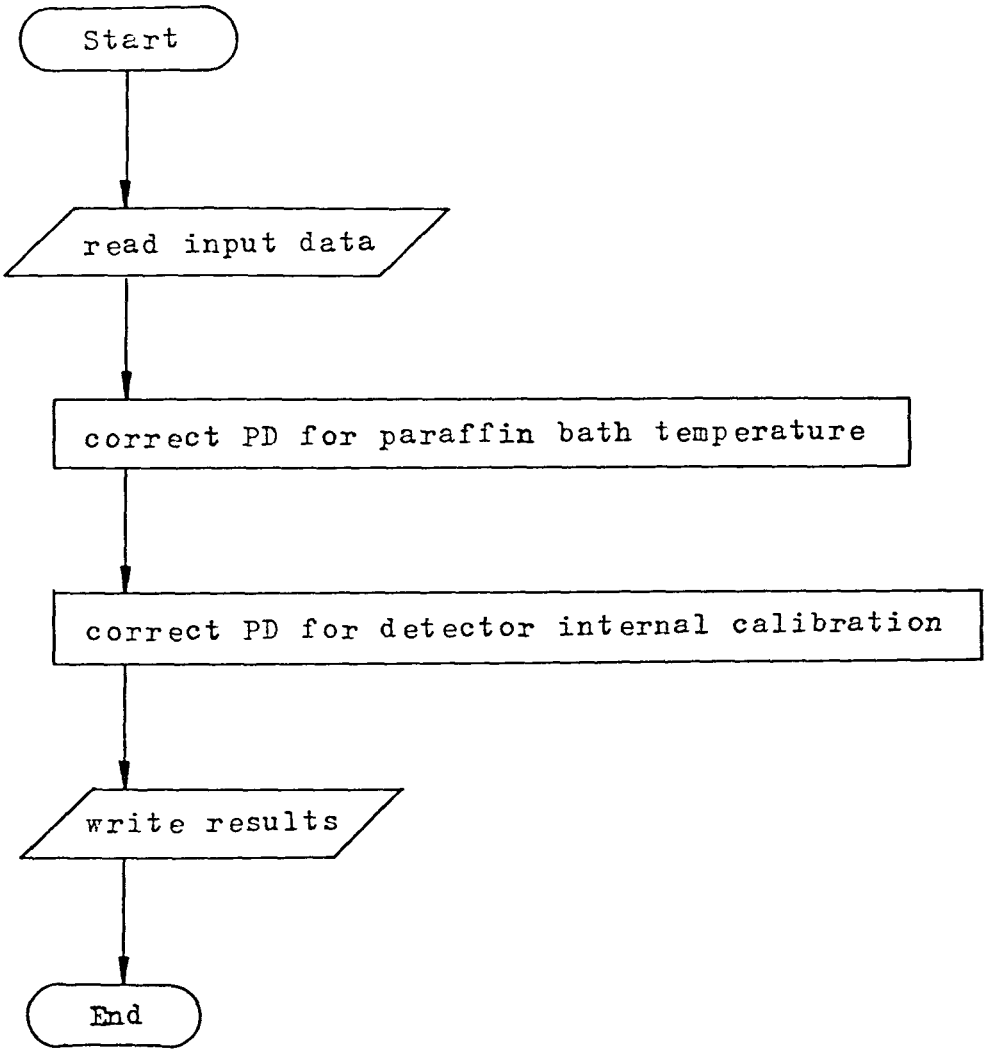


Fig. A6.01 Flowchart of Computor Programme Tidy

```
*FORTRAN
      DIMENSION X(99), Y(99),YY(99),XX(99),A(99),CAL(99), CALX(99),CC(99
     *),CK(99),PD(99),DPD(99),TITLE(80),J(99),CBTEMP(99),KTP(99),KT(99),
     * KBTEMP(99), N(99),TP(99), POCB(99),TL(99),BTEMP(99)
1     FORMAT(4F10.0)
C
 4    FORMAT(I2)
 5    FORMAT(1H ,7HOFF1 = ,F10.4,10X,7HOFF2 = ,F10.4,10X,
     *7HOFF3 = ,F10.4,10X,7HOFF4 = ,F10.4)
 6    FORMAT(1H ,4HX = , F6.3,10X,5HXX = , F6.3,10X,4HY = , F6.3,10X,
     *5HYY = ,F6.3//)
 7    FORMAT(4F10.0,4I2)
 8    FORMAT(1H ,5HJ1 = ,I2,10X,5HJ2 = ,I2,10X,5HJ3 = ,I3,10X,5HJ4 = ,I3
     *)
 9    FORMAT(1H ,3X,63H***********************************************
     ***************)
 122  FORMAT(1H ,3X,F7.4,13X,F7.4)
14    FORMAT(1H1,12HINPUT DATA :///1H ,10HDEPTH (MM),
     *11X,2HPD,11X,11HCALIBRATION,11X,11HBATH TEMP C)
 15   FORMAT(1H //1H ,9HRESULTS ://)
 16   FORMAT(1H0)
18    FORMAT(1H ,11HDATA POINTS,11X,
     *              10HDEPTH (MM),11X,6HPD+OFF,12X,10HPD+OFF+CAL,9X,
     *10HTRUE DEPTH,11X,16HPD+OFF+CAL+BTEMP/)
 19   FORMAT(1H ,23HNUMBER OF DATA POINTS =,I2)
203   FORMAT(F10.0)
204   FORMAT(1H ,15HGROOVE DEPTH = ,F7.4,4H(MM))
206   FORMAT(1H ,38HNORMALISED DEPTH ZERO POSITION = 0.5MM/)
207   FORMAT(1H ,1X, 15HNORM DEPTH (MM),6X,10HPD+OFF+CAL/)
 208  FORMAT(1H //////)
422   FORMAT(1H ,4X, 16X,
     *              F6.3,13X,F6.3,15X,F6.3,13X,F6.3,17X,F6.3)
423    FORMAT(1H ,F7.3,15X,F7.3,16X,F7.3,13X,F7.3/)
1700  FORMAT(1H0,1X,10HDEPTH (MM),11X,7HPD (MV)//)
 100  FORMAT(2F10.0)
200   FORMAT(1H ,F8.3,14X,F8.3)
300   FORMAT(1H ,10X,26HREGGRESION COEFFICIENT =  ,F20.4 )
400   FORMAT(1H1,12HINPUT DATA :///1H ,1X,10HDEPTH (MM),11X,8HPD (DVM)/)
500   FORMAT(1H ///////1H ,9HRESULTS :///)
60    FORMAT(1H0,10X,18HY INTERCEPT (C) = ,F20.4 )
700   FORMAT(1H0,10X,28HCORRELATION COEFFICIENT R = ,F20.4 )
900   FORMAT(1H0,10X,3HY =,F10.7,10X,3HX =,F10.7)
1000  FORMAT(1F10.0)
1100  FORMAT(1H ///////)
1200  FORMAT(1H ///)
1201  FORMAT(1H ,13HV0 AT 0.3MM =,F10.7)
1202  FORMAT(1H0,13HTRUE DEPTH MM,7X,11HV/V0 AT 0.5/)
1203  FORMAT(1H ,13HLEAST SQUARES)
1204  FORMAT(1H ,15HNORMALISED DATA//)
1205  FORMAT(1H0,4HV0 =,F10.4///)
1206  FORMAT(1H0,13HTRUE DEPTH MM,7X,14HDELTA V AT 0.5/)
1207  FORMAT(80A1)
1208  FORMAT(1H1,80A1,1H ///)
1210  FORMAT(1H ,12H0.001DCAL = ,F10.4)
600    FORMAT(1H ,7HRESULTS/1H ,5HDEPTH,12X,2HPD)                    ...cont
```

Fig A6.02 Computor Programme Tidy

```
      LM = 0
      M=0
      L=1
      READ(1,1207)TITLE
      READ(1,7)OFF1,OFF2,OFF3,OFF4,J1,J2,J3,J4
      READ(1,203)GD
      READ(1,203) DCAL
      WRITE(2,1208)TITLE
      WRITE(2,14)
      DO 10 I=1,J1
      READ(1,1)X(I), Y(I), CK(I),BTEMP(I)
      IF(X(I).EQ.-10.)GOTO 107
      M=M+1
      N(I)=M
      YY(I)=Y(I)+OFF1
      XX(I) = X(I)-X(1)
 10   CONTINUE
      JJ1=J1+1
      DO 11 I=JJ1,J2
      READ(1,1)X(I), Y(I), CK(I),BTEMP(I)
      IF(X(I).EQ.-10.)GOTO 107
      M=M+1
      N(I)=M
      YY(I)=Y(I)+OFF2
      XX(I) = X(I)-X(1)
 11   CONTINUE
      JJ2=J2+1
      DO 12 I=JJ2,J3
      READ(1,1)X(I), Y(I), CK(I),BTEMP(I)
      IF(X(I).EQ.-10.)GOTO 107
      M=M+1
      N(I)=M
      YY(I)=Y(I)+OFF3
      XX(I) = X(I)-X(1)
 12   CONTINUE
      JJ3=J3+1
      DO 13 I=JJ3,J4
      READ(1,1)X(I), Y(I), CK(I),BTEMP(I)
      IF(X(I).EQ.-10.)GOTO 107
      M=M+1
      N(I)=M
      YY(I)=Y(I)+OFF4
      XX(I) = X(I)-X(1)
 13   CONTINUE
 107  CONTINUE
      DO 311 I=1,M
      CBTEMP(I)=0.
      J(I)=5000-(INT(CK(I)))
      J(I)=J(I)/5
      CC(I) = YY(I) + FLOAT(J(I))* DCAL
      IF(BTEMP(I).EQ.0.)  BTEMP(I)=21.
      BTEMP(I) = BTEMP(I)*10.
      KBTEMP(I) = INT(BTEMP(I))
      KT(I) = 210 - KBTEMP(I)
      TP(I) = FLOAT(KT(I))* 0.0074
       POCB(I) = CC(I) + TP(I)/10.
      BTEMP(I) = BTEMP(I)/10.
311   CONTINUE
      ZEROG=XX(M)-GD
 17   CONTINUE
      DO 98 I=1,M
      IF(L.EQ.2) GOTO 96
      WRITE(2,423)  X(I), Y(I), CK(I), BTEMP(I)
      GOTO 97
96    A(I)=XX(I)-ZEROG
      WRITE(2,422)  XX(I), YY(I), CC(I), A(I), POCB(I)
```

...cont

```
 97     CONTINUE
        IF(I.EQ.J1)WRITE(2,9)
        IF(I.EQ.J2)WRITE(2,9)
        IF(I.EQ.J3)WRITE(2,9)
        IF(I.EQ.J4)WRITE(2,9)
 98     CONTINUE
        IF(L.EQ.2) GOTO 599
        WRITE(2,16)
        WRITE(2,5)OFF1, OFF2,OFF3, OFF4
        WRITE(2,8)J1,J2,J3,J4
        WRITE(2,204)GD
        WRITE(2,1210) DCAL
        WRITE(2,19)M
        WRITE (2,15)
        WRITE(2,18)
        L=L+1
        GOTO17
599     CONTINUE
        WRITE(2,600)
        WRITE(2,200)((X(I),POCB(I)),I=1,L)
1066    STOP
        END
        FINISH
```

```
        TITLE
0.00    0.90    1.80    2.70    2 3 1 2
3.50
0.001
0.003
0.00    0.000   5.00    21.0
1.00    0.700   5.00    21.0
1.50    0.150   5.00    22.0
2.00    0.500   5.00    22.0
2.50    0.850   5.00    22.0
3.00    0.300   5.05    21.0
4.00    0.100   5.10    22.0
4.50    0.450   5.00    22.0
-10.0
```

Fig. A6.03 Tidy Data

TITLE

INPUT DATA:

OFF1 = 0.00 OFF2 = 0.90 OFF3 = 1.80 OFF4 = 2.70

J1 = 2 J2 = 3 J3 = 1 J4 = 2

GROOVE DEPTH = 3.50

0.01 DCAL = 0.001

1 DEGREE C BATH TEMP = 0.003

DEPTH	PD	CALIB	BATH TEMP
0.00	0.000	5.00	21.0
1.00	0.700	5.00	21.0
1.50	0.150	5.00	22.0
2.00	0.500	5.00	22.0
2.50	0.850	5.00	22.0
3.00	0.300	5.05	21.0
4.00	0.100	5.10	22.0
4.50	0.450	5.00	22.0

RESULTS:

DEPTH	PD
0.00	0.000
1.00	0.700
1.50	1.053
2.00	1.403
2.50	1.753
3.00	2.105
4.00	2.813
4.50	3.153

Fig. A6.04 Tidy Results

APPENDIX A7

ANALYSIS OF LINEAR REGRESSION, CORRELATION AND STANDARD RESIDUAL ERROR

A7.0 Nomenclature

i	=	ith observation
xi	=	independent variable
yi	=	dependent variable
$\bar{x}$	=	arithmetic mean of x population
$\bar{y}$	=	arithmetic mean of y population
$\hat{y}$	=	predicted model value of yi
n	=	total number of data points
e	=	error term in yi
RMS, σ_e	=	standard residual error
q	=	number of free parameters
R_c	=	correlation coefficient
b	=	regression coefficient
c	=	y intercept at x = 0.00

A7.1 Regression Analysis

A relationship in y which is linearly dependent on x of the form $y = f(x) + e$, where e is an error term in y, can be subject to regression analysis by the least square technique [A7.01]. This is based on finding the parameter b of the relationship

$$\hat{y} = b.x + (\bar{y} - b.\bar{x}) \qquad \ldots(A7.01)$$

where $\bar{x} = \frac{\Sigma\, xi}{n}$

$$\bar{y} = \frac{\Sigma\, yi}{n}$$

$$b = \frac{\Sigma(xi - \bar{x})\, yi}{\Sigma(xi - \bar{x})^2}$$

$$c = (\bar{y} - b.x)$$

which minimises the sum of the squares of the errors, i.e.

$$\sum_{i=1}^{n} e = \min$$

where $e = \hat{y}i - yi$ (assuming no errors in x).

A7.2 Correlation Coefficient

A relative measure of the fit is provided by the correlation coefficient R_c of $\hat{y}i$ and yi, where

$$R_c = \frac{\sum_{i=1}^{n} (xi - \bar{x})(yi - \bar{y}i)}{\sqrt{\left[\sum_{i=1}^{n} (x - \bar{x})^2\right]\left[\sum_{i=1}^{n} (\hat{y} - \bar{y})^2\right]}} \qquad \ldots(A7.02)$$

Its value always lies between -1 and +1. A value of R_c equal to -1 indicates a perfect linear relationship between the sample points x and y, with the values of y decreasing as x increases. A value of R_c equal to +1 also indicates a perfect linear relationship between the sample values, but one in which the values of y increase as x increase. If there is no linear relationship R will tend to zero. As R_c increases from 0 to +1 (or decreases from 0 to -1) the linear relationship between the sample values of x and y becomes more pronounced.

A7.3 Standard Residual Error [A7.02]

The standard residual error is an absolute measured of the model to the data and is given by

$$\sigma_e = \sqrt{\frac{1}{n - q} \sum_{i=1}^{n} (\hat{y}i - yi)^2} \qquad \ldots(A7.03)$$

A zero standard error implies 100% correlation (R = 1) (a perfect fit).

A7.4 Determination of b, c, R_c and σ_e

Statistical values relating to degree 1 linear regression analysis were determined using Computer Programme Leastsquare whose

flowchart, main programme, input data and results are presented in Figs. A7.01 and A7.02.

A7.5 References

[A7.01] Hayslett, H.T., Murphy, P.,
'Statistics Made Simple' W.H. Allen London.

[A7.02] Hyvarrinen, L.,
'Mathematical Modelling for Industrial Processes,
No. 19' Springer - Berlag Berlin.

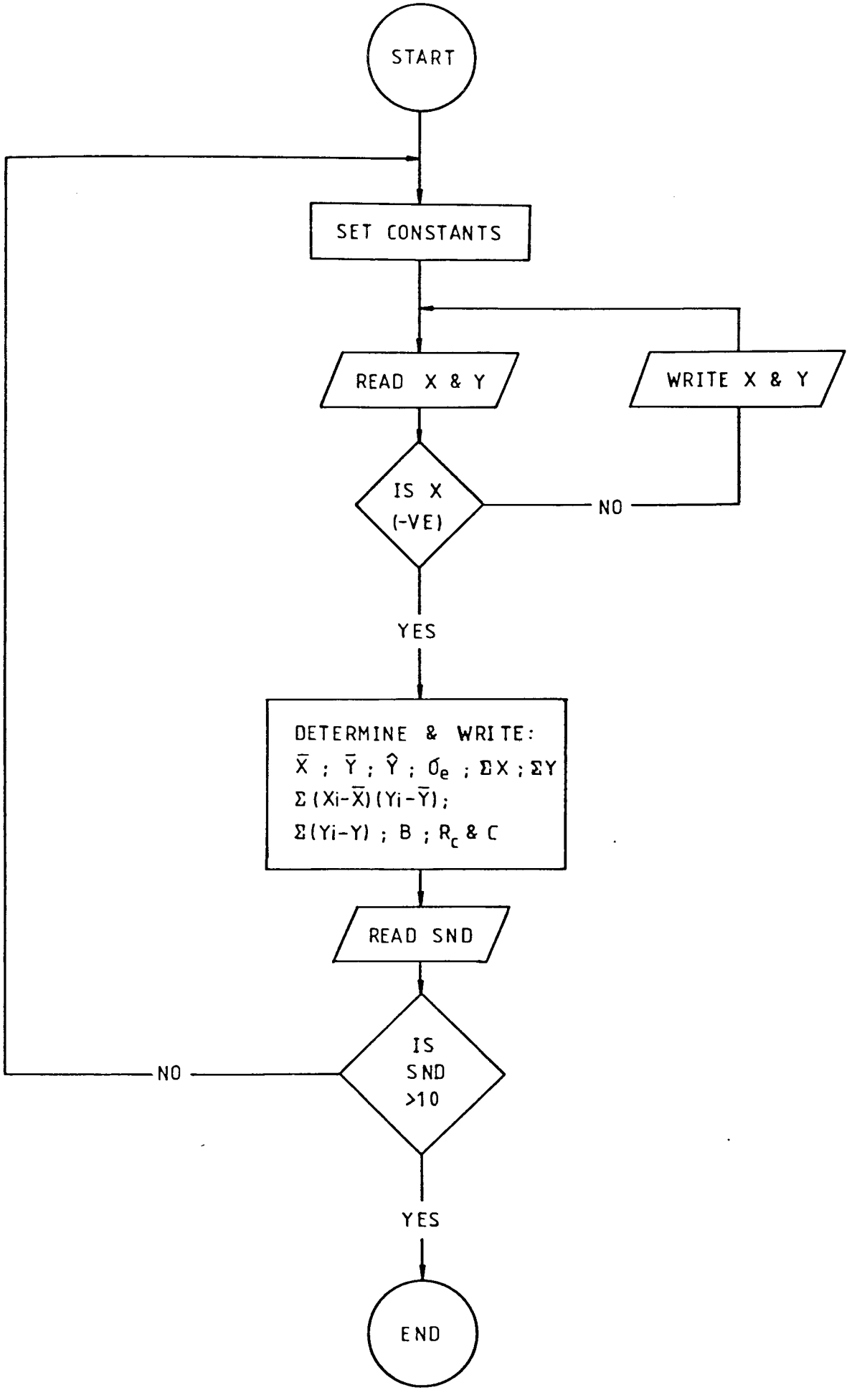


Fig. A7.01 Flowchart of Computer Programme Leastsquare

```
PROG FORTRAN,*CR0 LSQD,*LP0 LSQR
      PROGRAM(LEON)
      INPUT 1 = CR0
      OUTPUT 2 = LP0
      END
      MASTERMAIN
C
C*****************************************************************************
C
C     PROGRAMME LEASTSQUARE
C
C*****************************************************************************
C
      DIMENSION X(99), Y(99), RESID(99), YHAT(99)
 1    FORMAT(2F10.0)
 2    FORMAT(1H ,F10.7,10X,F10.7)
 3    FORMAT(1H ,10X,26HREGGRESION COEFFICIENT =  ,F20.4)
 4    FORMAT(1H1,12HINPUT DATA :///1H ,1X,10HDEPTH (MM),11X,2HPD)
 5    FORMAT(1H //1H ,9HRESULTS :)
 6    FORMAT(1H0,10X,18HY INTERCEPT (C) = ,F20.4)
 7    FORMAT(1H0,10X,28HCORRELATION COEFFICIENT R = ,F20.4)


 11   FORMAT(1H ///////)
 12   FORMAT(1H ///)
 13   FORMAT(1H ,15HNORMALISED DATA////1H ,1X,10HDEPTH (MM),11X,7HPD (MV
     *)/)
 14   FORMAT(1F10.0)
 15   FORMAT(1H ///1H ,27HCORRECTED FOR ZERO AND GAIN//)
 17   FORMAT(1H0,1X,10HDEPTH (MM),11X,7HPD (MV)//)
 18   FORMAT(1H ,7X,1HX,13X,1HY,13X,4HYHAT,10X,5HRESID/)
 19   FORMAT(1H ,F10.4,5X,F10.4,5X,F10.4,5X,F10.4)
 20   FORMAT(1H0,5HRMS =,F10.4)
110   CONTINUE
      WRITE(2,4)
      A=0.0
      SUMY = 0.
      K=0
      SUMX = 0.
      ZZZ=0.
      QQQ=0.
      I = 1
      SXS = 0.
      SRB=0.
      SQRB=0.
      SRT=0.
 103  READ(1,1)X(I),Y(I)
      IF(X(I))101,100,100
 100  WRITE(2,2)X(I),Y(I)
      I=I+1
      GOTO 103
 101  CONTINUE
      J=I-1
      DO 111 L=1,J
      SUMY=SUMY+Y(L)
      SUMX=SUMX+X(L)
 111  CONTINUE
 106  CONTINUE
      XBAR=SUMX/FLOAT(J)
```

Fig. A7.02 Computer Programme Leastsquare, Data and Results

```
      YBAR=SUMY/FLOAT(J)
      DO 104 I=1,J
      Z=(X(I)-XBAR)*Y(I)
      ZZZ=Z+ZZZ
      Q=(X(I)-XBAR)**2
      QQQ=Q+QQQ
      XMXBAR=X(I)-XBAR
      YMYBAR=Y(I)-YBAR
      RT=XMXBAR*YMYBAR
      SRT=SRT+RT
      QRB=(Y(I)-YBAR)**2
      SQRB=SQRB+QRB
  104 CONTINUE
      B=ZZZ/QQQ
      R=SRT/(SQRT(QQQ*SQRB))
      C=YBAR-B*XBAR
      DO 105 I=1,J
      YHAT(I)=B*X(I)+C
      RESID(I)=YHAT(I)-Y(I)
      AB=(RESID(I))**2
      A=A+AB
  105 CONTINUE
      RMS=SQRT(A/((FLOAT (J))-2.))
      WRITE(2,11)
      WRITE(2,5)
      WRITE (2,3)B
      WRITE(2,7)R
      WRITE(2,6)C
      WRITE(2,12)
      WRITE(2,18)
      WRITE(2,19)((X(I),Y(I),YHAT(I),RESID(I)), I=1,J)
      WRITE(2,20) RMS
      READ(1,14)SND
      IF(SND.GT.10.)STOP
      GOTO 110
      END
      FINISH

6.38        2.110
7.51        2.254
8.80        2.404
10.00       2.538
12.00       2.808
13.00       2.930
13.79       3.054
15.01       3.188
15.98       3.330
-10.0
12.0
```

INPUT DATA :

DEPTH (MM)	PD
6.3800000	2.1100000
7.5100000	2.2540000
8.8000000	2.4040000
10.0000000	2.5380000
12.0000000	2.8080000
13.0000000	2.9300000
13.7900000	3.0540000
15.0100000	3.1880000
15.9800000	3.3300000

RESULTS :

REGGRESION COEFFICIENT = 0.1268
CORRELATION COEFFICIENT R = 0.9996
Y INTERCEPT (C) = 1.2918

X	Y	YHAT	RESID
6.3800	2.1100	2.1006	-0.0094
7.5100	2.2540	2.2438	-0.0102
8.8000	2.4040	2.4073	0.0033
10.0000	2.5380	2.5595	0.0215
12.0000	2.8080	2.8130	0.0050
13.0000	2.9300	2.9398	0.0098
13.7900	3.0540	3.0399	-0.0141
15.0100	3.1880	3.1946	0.0066

RMS = 0.0130

APPENDIX A8

CURVE FITTING

A8.0 Nomenclature

PD,V	=	measured potential difference
PD_0, V_0	=	theoretical potential difference determined at ARG = 0.00
a, ARG	=	flaw depth measured in the specimen width direction.
A_0, A_1, A_2	=	Chebyshev Coefficients
T_0, T_1, T_2	=	constants
K	=	polynomial degree
ACPD	=	alternating current potential difference

A8.1 Introduction

The curvefit routine used to describe the ACPD calibration relationship was based on a least squares Chebyshev polynomial analysis. This was chosen because it was readily available as a subroutine in the Birmingham University Nag Library and could be readily accessed using an ICL 1906A computer.

A8.2 Approach

The approach to describing the ACPD versus flaw depth relationship envolved generating standard residual error values corresponding to Chebyshev polynomials ranging from degree 0 to 10 using Computer Programme Curvefit whose flowchart, main programme, data

and results appear in Figs. A8.01 and A8.02. The optimum degree (i.e. K = 2) was then chosen which produced no further substantial decrease in standard residual error, Fig. A8.03, and the programme was rerun to generate values of PD_0, $PD-PD_0$ and PD/PD_0.

A8.3 Chebyshev Polynomials [A8.01. A8.02]

A set of data in X and Y whose argument lies within the range $-1 \leqslant X \leqslant 1$ and forms a polynomial relationship can be expressed as a Chebyshev Polynomial of the form

$$Y = \frac{A_0}{2} \cdot T_0 + A_1.T_1 + A_2T_2 \ldots\ldots\ldots A_I\ T_I \qquad \ldots(A8.01)$$

where A_0, A_1, A_2,.....etc are Chebyshev polynomial coefficients and T_0, T_1, T_2,.....etc are constant.

For polynomials upto degree 6 the coefficients T are

$$T_0 = 1$$
$$T_1 = X$$
$$T_2 = 2\ X^2 - 1$$
$$T_3 = 4\ X^3 - 3X$$
$$T_4 = 8\ X^4 - 8X^2 + 1$$
$$T_5 = 16\ X^5 - 20X^3 + 5X$$
$$T_6 = 32\ X^6 - 48X^4 + 18X^2 - 1$$

Data whose argument lies outside the range $-1 \leqslant X \leqslant +1$ can be transposed into this domain by employing the dummy argument Z where

$$Z = \frac{2X - (X_{max} + X_{min})}{(X_{max} - X_{min})} \qquad \ldots(A8.02)$$

A8.4 References

[A8.01] 'NAG Fortran Library Manual' (Mark 5) Chapter E02 'Curve and Surface Fitting', Numerical Algorithmic Group Oxford, 1977.

[A8.02] Chenshaw, C.W., 'Chebyshev series for Mathematical Functions' NPL Maths Tables, 5, MMSO, London, 1962.

PART 1

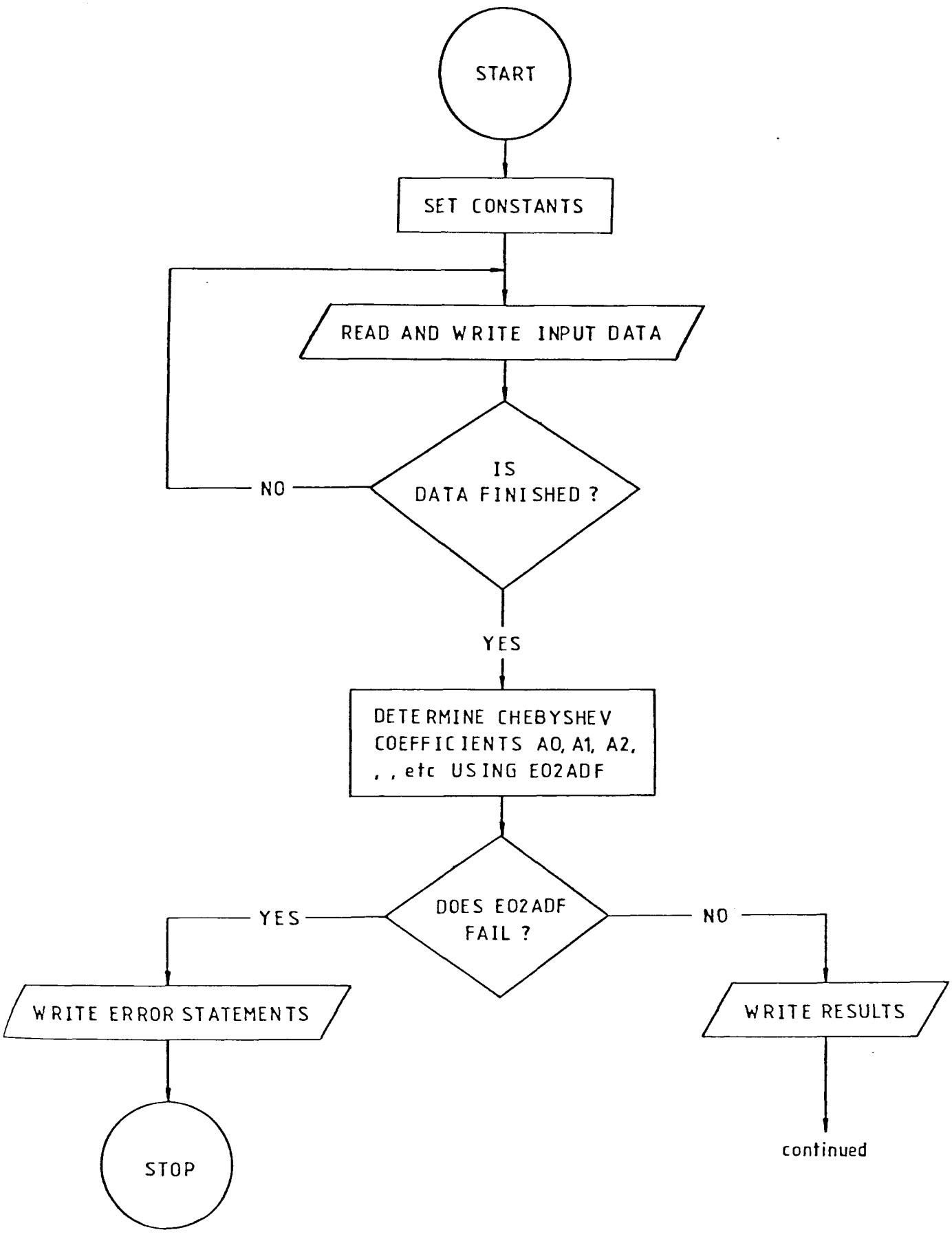
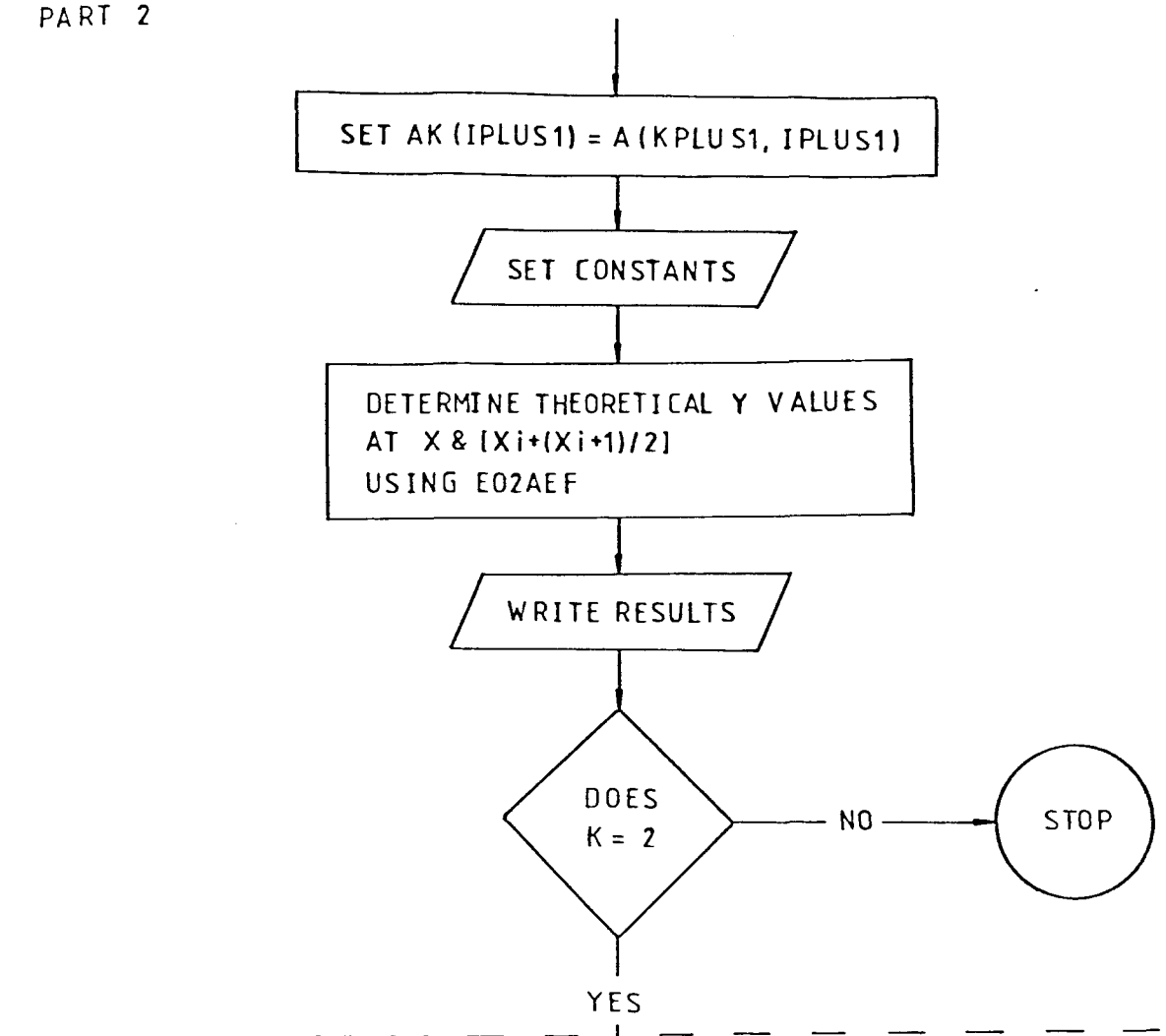
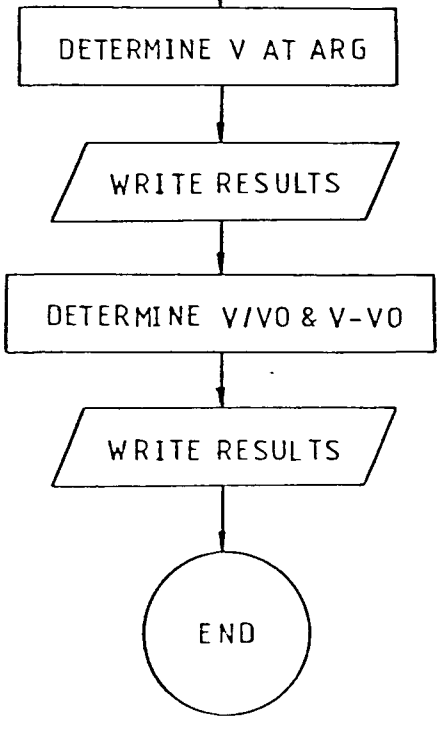


Fig. A8.01 Flowchart of Computer Programme Curvefit.

PART 2


SET AK(IPLUS1) = A(KPLUS1, IPLUS1)
SET CONSTANTS
DETERMINE THEORETICAL Y VALUES
AT X & [Xi+(Xi+1)/2]
USING E02AEF
WRITE RESULTS
DOES
K = 2
NO
STOP
YES

PART 3


DETERMINE V AT ARG
WRITE RESULTS
DETERMINE V/V0 & V-V0
WRITE RESULTS
END

```
PROG FORTRAN,*CR0 P14,*LP0 DATALL,LIB NAGF
      PROGRAM(L EON)
      OUTPU T 2 = LP0
      INPUT 1 = CR0
      END
      MASTERMAIN
C
C*************************************************************
C
C     PROGRAM CURVEFIT
C
C*************************************************************
C
      INTEGER R, R2
      DIMENSION X(100),Y(100), W(200), WORK1(3,200), WORK2(2,100)
     *,A(100,100), S(100),B(100,100)
     *,AK(100)
      LOGICAL MIDPT
99900 FORMAT(2F10.0)
99901 FORMAT(1H ,F9.3,7X,F10.3,10X,F10.3)
99902 FORMAT(1H1,12HINPUT DATA :///1H ,1X,10HDEPTH (MM),12X,2HPD,1
     *5X,8HWEIGHT W/)
99903 FORMAT(1H //1H ,9HRESULTS :///)
99904 FORMAT(1H ,F20.10)
99905 FORMAT(1H //)
99906 FORMAT(1H ,4HA0 =,F10.4,5X,4HA1 =,F10.6,5X,4HA2 =,F10.6///)
99907 FORMAT(1H , 7X,1HX,8X,1HY,8X,4HV/V0,6X,4HV-V0//)
99908 FORMAT(1H ,4F10.4)
99909 FORMAT(1H ,4HV0 =,F10.4//)
99910 FORMAT(1H ,5HARG =,F10.4//)
99978 FORMAT(/37 H NROWS FAILS TO EXCEED MAXIMUM DEGREE)
99979 FORMAT(/27H TOO FEW DISTINCT VALUES OF, 17H THE INDEPENDENT ,
     *8HVARIABLE)
99980 FORMAT(/41H VALUES OF INDEPENDENT VARIABLE ALL EQUAL)
99981 FORMAT(031H VALUES OF INDEPENDENT VARIABLE, 13H NOT INCREASI,
     *16HNG MONOTONICALLY)
99982 FORMAT(/20H NON-POSITIVE WEIGHT)
99983 FORMAT(1H , I3, E20.5, 26H ARGUMENT OUTSIDE RANGE 83)
99984 FORMAT(5 H      , E20.5, 26H ARGUMENT OUTSIDE RANGE 84)
99985 FORMAT (5H      ,2E20.5)
99986 FORMAT(/49H POLYNOMIAL APPROXIMATION AND RESIDUALS FOR DEGRE,
     *1HE, I4//24H    R    ABSCISSA       ,
     *19H      APPROXIMATION ,
     *16H         RESIDUAL/)
99987 FORMAT(/18H R.M.S. RESIDUAL =,E20.5)
99988 FORMAT(1H ,I3,E20.5)
99989 FORMAT(/7H DEGREE,I4//26H  J  CHEBYSHEV COEFF A(J) /)
99991 FORMAT(1H , I3, 3E20.5)
99994 FORMAT(40H  POLYNOMIAL FIT TO ARBITARY DATA POINTS/6H -----,34H---
     *---------- ----------//25H NUMBER OF DATA POINTS = ,I4/
     *18H MAXIMUM DEGREE = ,I4)
99997 FORMAT (I2)
99977 FORMAT(//23H   J        ORDY.   COEF/)
      L=1
      IFAIL=1
      NROWS=100
      JK=1
      WRITE(2,99902)
      READ(1,99997)M                                          ...cont.
```

Fig. A8.02 Computor Programme Curvefit, Data and Results

```
      READ(1,99997)K
      READ(1,99900)ARG
101   CONTINUE
      W(L)=1.
      READ(1,99900)X(L),Y(L)
      WRITE(2,99901)X(L),Y(L),W(L)
      IF(L.EQ.M) GOTO103
102   L=L+1
      GOTO 101
103   KPLUS1=K+1
      IFAIL=1
      CALL E02ADF(M,KPLUS1,NROWS,X,Y,W,WORK1,WORK2,A,S,IFAIL)
      IF(IFAIL.EQ.0) GOTO 300
      GOTO (320, 340, 360, 380, 400),IFAIL
320   WRITE (2,99982)
      GOTO 6000
340   WRITE(2,99981)
      GOTO  6000
360   WRITE (2,99980)
      GOTO 6000
380   WRITE(2,99979)
      GOTO  6000
400   WRITE(2,99978)
      GOTO 6 000
300   WRITE(2,99903)
      WRITE(2,99994)M,K
      DO 108 IPLUS1=1,KPLUS1
      I=IPLUS1-1
      WRITE(2,99989)I
      WRITE(2,99988)(JPLUS1,A(IPLUS1,JPLUS1),JPLUS1=1,IPLUS1)
      WRITE(2,99987)S(IPLUS1)
108   CONTINU E
      DO 110 IPLUS1 = 1,KPLUS1
      AK(IPLUS1) = A(KPLUS1,IPLUS1)
110   CONT INUE
      MIDPT = .FALSE.
      M2 = 2*M-1
      R=0
      X1=X(1)
      XM=X(M)
      D=XM-X1
      SUM=XM+X1
      WRITE (2,99986)K
      DO 280 R2=1,M2
      IF(.NOT.MIDPT) GOTO 220
      XARG = 0.5*(X(R)+X(R+1))
      XCAPR = ((XARG-X1)-(XM-XARG))/D
      IFAIL=1
      CALL E02AEF(KPLUS1, AK, XCAPR, FIT, IFAIL)
      IF(IFAIL.NE.0) GOTO 200
      WRITE (2,99985) XARG,FIT
      GOTO  260
200   WRITE(2,99984)XARG
      GOTO260
220   R=R+1
      XCAPR= ((X(R)-X1)-(XM-X(R)))/D
      IFAIL=1
      CALL E02AEF(KPLUS1, AK, XCAPR, FIT, IFAIL)
      IF(IFAIL.NE.0)GOTO240
      RES= FIT-Y(R)
      WRITE(2,99991) R, X(R), FIT, RES
      GOTO 260
240   WRITE(2,99983)R,X(R)
260   MIDPT = .NOT.MIDPT
280   CONTINU E                                          ...cont.
```

```
      IF(K.EQ.2) GOTO 5001
      GOTO 6000
5001  Z=(2.0*ARG/D)-(SUM/D)
      A0=A(3,1)
      A1=A(3,2)
      A2=A(3,3)
      V=A0/2.0+A1*Z+A2*((2.0*(Z**2))-1.0)
      WRITE(2,99905)
      WRITE(2,99906)A0,A1,A2
      WRITE(2,99909)V
      WRITE(2,99910)ARG
      WRITE(2,99907)
      DO 4001 I=1,M
      PD=Y(I)/V
      Q=Y(I)-V
      WRITE(2,99908) X(I),Y(I),PD,Q
4001  CONTINUE
6000  STOP
      END
      FINISH
```

```
 9
 2
0.00
6.38        2.110
7.51        2.254
8.80        2.404
10.00       2.538
12.00       2.808
13.00       2.930
13.79       3.054
15.01       3.188
15.98       3.330
```

INPUT DATA :

DEPTH (MM)	PD	WEIGHT W
6.380	2.110	1.000
7.510	2.254	1.000
8.800	2.404	1.000
10.000	2.538	1.000
12.000	2.808	1.000
13.000	2.930	1.000
13.790	3.054	1.000
15.010	3.188	1.000
15.980	3.330	1.000

RESULTS :

POLYNOMIAL FIT TO ARBITARY DATA POINTS

NUMBER OF DATA POINTS = 9

MAXIMUM DEGREE = 2

DEGREE 0

J	CHEBYSHEV COEFF A(J)
1	0.5 4702E 01

R.M.S. RESIDUAL = 0.42935E 00

...cont.

DEGREE 1

J	CHEBYSHEV COEFF A(J)
1	0.54181E 01
2	0.60849E 00

R.M.S. RESIDUAL = 0.12995E-01

DEGREE 2

J	CHEBYSHEV COEFF A(J)
1	0.54205E 01
2	0.60863E 00
3	0.10543E-01

R.M.S. RESIDUAL = 0.10589E-01

POLYNOMIAL APPROXIMATION AND RESIDUALS FOR DEGREE 2

R	ABSCISSA	APPROXIMATION	RESIDUAL
1	0.63800E 01	0.21121E 01	0.21359E-02
	0.69450E 01	0.21791E 01	
2	0.75100E 01	0.22467E 01	-0.73406E-02
	0.81550E 01	0.23245E 01	
3	0.88000E 01	0.24031E 01	-0.91259E-03
	0.94000E 01	0.24769E 01	
4	0.10000E 02	0.25513E 01	0.13336E-01
	0.11000E 02	0.26769E 01	
5	0.12000E 02	0.28043E 01	-0.37250E-02
	0.12500E 02	0.28687E 01	
6	0.13000E 02	0.29335E 01	0.34898E-02
	0.13395E 02	0.29850E 01	
7	0.13790E 02	0.30369E 01	-0.17136E-01
	0.14400E 02	0.31175E 01	
8	0.15010E 02	0.31987E 01	0.10748E-01
	0.15495E 02	0.32639E 01	
9	0.15980E 02	0.33294E 01	-0.59586E-03

A0 = 5.4205 A1 = 0.608634 A2 = 0.010543

V0 = 1.3965

ARG = 0.0000

X	Y	V/V0	V-V0
6.3800	2.1100	1.5110	0.7135
7.5100	2.2540	1.6141	0.8575
8.8000	2.4040	1.7215	1.0075
10.0000	2.5380	1.8174	1.1415
12.0000	2.8080	2.0108	1.4115
13.0000	2.9300	2.0982	1.5335
13.7900	3.0540	2.1870	1.6575
15.0100	3.1880	2.2829	1.7915
15.9800	3.3300	2.3846	1.9335

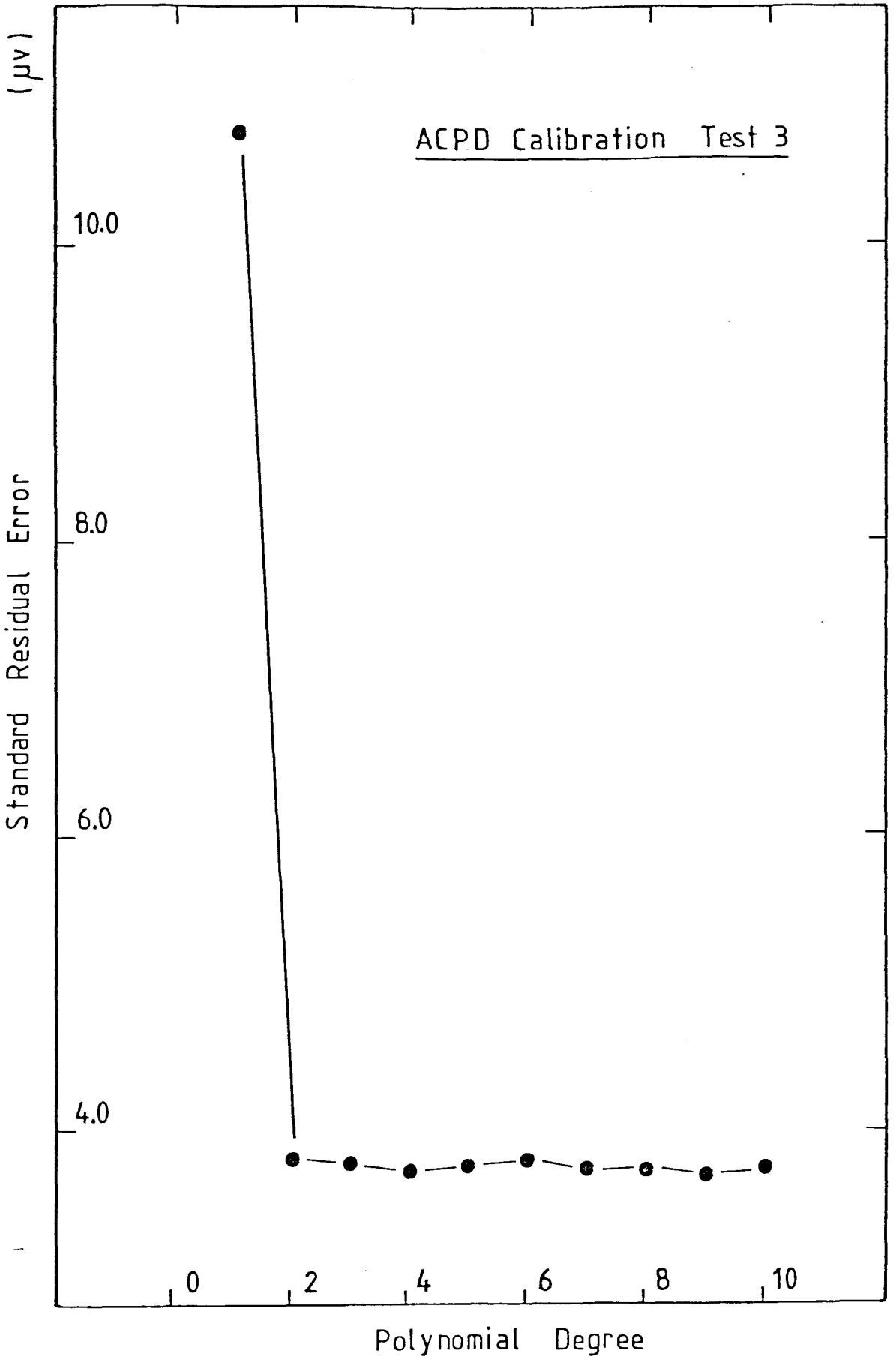


Fig. A8.03 Commonly observed trend in Standard Residual Error versus Polynomial Degree.

APPENDIX A9

AN EMPIRICAL NORMALISING TECHNIQUE

A9.0 Nomenclature

PD	=	measured potential difference
PD_S	=	potential difference contribution due to compensation, probe position and eddy currents.
PD_o	=	measured potential difference determined at a = 0.00 mm.
PD_C, PD_{OE}	=	empirical constants
a	=	flaw depth measured in the specimen width direction
RMS PD	=	standard residual error expressed in terms of PD
RMS a	=	standard residual error expressed in terms of a
VR	=	voltage ratio (PD/PD_0) of Calibration Test 7
ACPD	=	alternating current potential difference.

A9.1 Introduction

The empirical normalising technique detailed in this Appendices was developed to rationalise the ACPD calibration study of Chapter 10. Only a brief description is included here, the technique is contained in Computer Programme Gandalf whose flow chart, main programme, data and results appear in Figs. A9.01 and A9.02.

A9.2 Basic Concept

The ACPD calibration results revealed that $d^2PD/da^2 = f(PD_0)$. Now assuming that $PD_{absolute}$ can be normalised with respect to a master voltage ratio plot, measured PD cannot be normalised by this technique because

$$PD_{absolute} = PD \pm PD_S \qquad \ldots(A9.01)$$

where PD_S is a function of many factors including current and sensing lead position, compensation and eddy current effects. The problem of normalising the data revoles around adjusting the magnitude of PD by an amount PD_S to satsify the conditions of the voltage ratio normalising technique. However, because the $PD_{absolute}/PD_0$ absolute calibration relationship is unknown, PD_S is also unknown. But if the voltage ratio normalising technique is applicable empirical normalisation can be conducted with respect to the $PD_{absolute}$ voltage ratio calibration response containing a systematic error in $PD_{absolute}$ of either $\pm PD_S$, by adjusting the magnitude of measured PD by an amount PD_C.

A9.3 Empirical Normalisation (Using Computer Programme Gandalf)

This consituted normalising the data of each calibration test to the Chebyshev degree 2 polynomial model relationship describing the PD/PD_0 calibration response of Test 7 as follows.

(a) First both sets of raw data were subject to Chebyshev degree 2 polynomial analysis and PD_0 was determined in each case.

(b) Model VR values of Test 7 were then generated at crack lengths of the comparitive test.

(c) A Davies, Swann and Campey [A9.01] univariate search was then adopted which sequentially increased and decreased the magnitude of PD of the comparitive test by an amount PD_C (where -6.000 mv $< PD_C <$ + 6.000 mv).

(d) At every new increase/decrease in PD_C, PD_{OE} was determined (i.e., $PD_{OE} = PD_O - PD_C$) and data points $(PD - PD_C)/PD_{OE}$ were subject to a RMS PD analysis based on the model VR relationship.

(e) When a minimum value of RMS PD had been bracketed the RMS PD versus PD_C relationship was subject to a degree 2 polynomial curvefit which was differentiated to obtain the optimum value of PD_C.

(f) The empirically normalised data was then subject to an RMS a analysis based on the model VR relationship.

A9.4 References

[A9.01] Box, M.J. Davies, D., and Swann, W.H., "Non-linear Optimisation Techniques", ICI Monograph No.5 Pub. Oliver and Boyd.

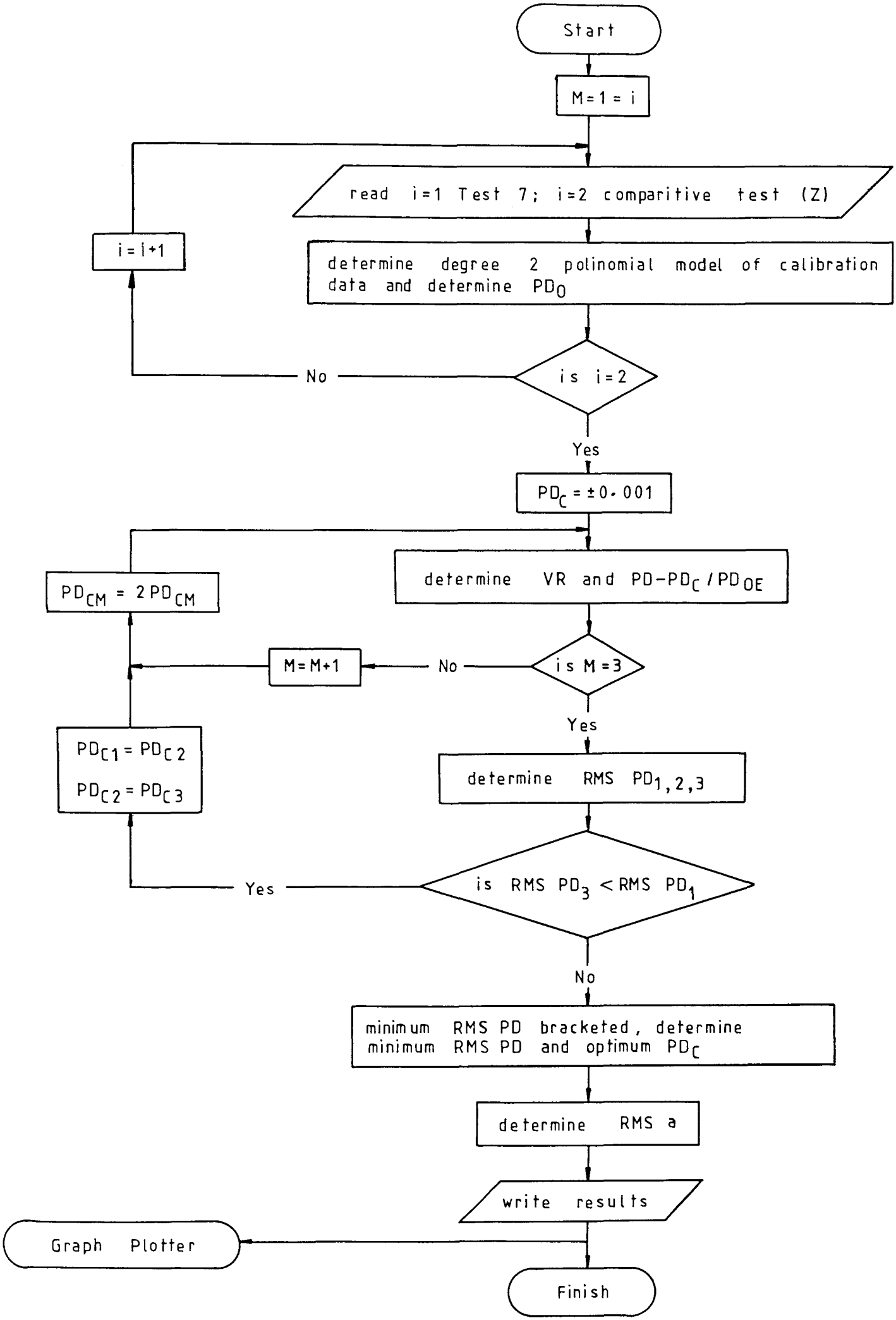


Fig. A9.01 Flowchart of Computor Programme Gandalf

```
PROG FORTRAN,*CR0 DES,*LP0 DDES,LIB NAGF,LIMIT 9000,TIME 5MINS,-
LIB GINOGRAF+GINO-F,*FW7 G3,EXIT 1X
      PROGRAM(LEON)
      OUTPUT 2,6 = LP0
      INPUT 1 = CR0
      END
      MASTERMAIN
C
C*************************************************************
C
C     PROGRAM GANDALF
C
C*************************************************************
C
      INTEGER R, R2
      DIMENSION X(1000),Y(1000), W(1000),WORK1(3,1000), WORK2(2,1000)
     *,A(10,1000), S(1000),B(10,1000)
     *,AK(1000)
     *,V0(1000),YMA(2,1000),XMA(2,1000),YRM(2,1000),T1(1000),T2(1000)
     *,T3(1000),T4(1000),E1(1000),E2(1000),E3(1000),E4(1000),AR1(1000),
     *AR2(1000)
     *,AR3(1000),AR4(1000),XX(1000),MOM(1000)
     *,AY(2,1000),RY(1000),YY(1000)
     ,,AX(2,1000),AMAX(1000),AMAY(1000)
     *,SMIT(1000),RAMAY(1000),V0T(1000),MOMT(1000)
      LOGICAL MIDPT
99900 FORMAT(2F10.0)
99901 FORMAT(1H ,F7.2,10X,F10.2,10X,F10.2)
99902 FORMAT(1H1,12HINPUT DATA :///1H ,1X,10HDEPTH (MM),11X,8HPD (DVM),1
     *1X,8HWEIGHT W/)
99903 FORMAT(1H ///////1H ,9HRESULTS :///)
99904 FORMAT(1H ,F20.10)
99905 FORMAT(1H //)
99906 FORMAT(1H ,4HA0 =,F10.4,5X,4HA1 =,F10.6,5X,4HA2 =,F10.6///)
99907 FORMAT(1H ,7X,1HX,8X,1HY,8X,4HV/V0,6X,4HV-V0//)
99908 FORMAT(1H ,4F10.4)
99909 FORMAT(1H ,4HV0 =,F10.4//)
99910 FORMAT(1H ,5HARG =,F10.4//)
99911 FORMAT(1H ,6HV0E1 =,F10.4,6HV0E2 =,F10.4,6HV0E3 =,
     *F10.4,6HV0E4 =,F10.4//)
99912 FORMAT(1H ,4HSM =,F10.4///)
99913 FORMAT(1H ,6HRMS1 =,F10.4,6HRMS2 =,F10.4,6HRMS3 =,F10.4,
     *6HRMS4 =,F10.4//)
99978 FORMAT(/37H NROWS FAILS TO EXCEED MAXIMUM DEGREE)
99979 FORMAT(/27H TOO FEW DISTINCT VALUES OF, 17H THE INDEPENDENT ,
     *8HVARIABLE)
99980 FORMAT(/41H VALUES OF INDEPENDENT VARIABLE ALL EQUAL)
99981 FORMAT(031H VALUES OF INDEPENDENT VARIABLE, 13H NOT INCREASI,
     *16HNG MONOTONICALLY)
99982 FORMAT(/20H NON-POSITIVE WEIGHT)
99983 FORMAT(1H , I3, E20.5, 26H ARGUMENT OUTSIDE RANGE 83)
99984 FORMAT(5H      , E20.5, 26H ARGUMENT OUTSIDE RANGE 84)
99985 FORMAT(5H      ,2E20.5)
99986 FORMAT(/49H POLYNOMIAL APPROXIMATION AND RESIDUALS FOR DEGRE,
     *1HE, I4//24H     R     ABSCISSA        ,
     *19H      APPROXIMATION ,
     *16H         RESIDUAL/)                                    ...con
```

Fig A9.02 Computor Programme Gandalf, Data and Results

```
99987 FORMAT(/18H R.M.S. RESIDUAL =,E20.5)
99988 FORMAT(1H ,I3,E20.5)
99989 FORMAT(/7H DEGREE,I4//26H  J  CHEBYSHEV COEFF A(J) /)
99991 FORMAT(1H , I3, 3E20.5)
99994 FORMAT(40H  POLYNOMIAL FIT TO ARBITARY DATA POINTS/6H -----,34H---
     *--------------------------------//25H NUMBER OF DATA POINTS = ,I4//
     *18H MAXIMUM DEGREE = ,I4)
99997 FORMAT (I2)
99977 FORMAT(//23H    J          ORDY.   COEF/)
801   FORMAT(1H ,F10.4,10X,F10.4)
802   FORMAT(1H ,5X,1HA,16X,1HV,16X,5HV/V0T//)
803   FORMAT(1H ,50(1H*))
804   FORMAT(1H ,50(1H-))
8050  FORMAT(1H ,I5)
      NQ=0
      READ(1,99997)MS
      KAK=0
      IL=1
      LAP=0
      KAG=0
      INO=-1
1086  CONTINUE
      MT=1
      LA=0
      KC=0
      MCT=0
1     L=1
      IT=-1
      KAG=KAG+1
      I=0
      NON=0
      IFAIL=1
      NROWS=10
      JK=1
      WRITE(2,99902)
      READ(1,99997)M
      MCT=MCT+M
      READ(1,99997)K
      READ(1,99900)ARG
      MOM(MT)=M
101   CONTINUE
      W(L)=1.
      READ(1,99900)X(L),Y(L)
      WRITE(2,99901)X(L),Y(L),W(L)
      AX(MT,L)=X(L)
      AY(MT,L)=Y(L)
      IF(L.EQ.M) GOTO1030
102   L=L+1
      GOTO 101
1030  IF(INO) 5140,5140,103
103   CONTINUE
      KAK=KAK+1
1031  CONTINUE
      I=I+1
      NON=NON+1
      AMAX(IL)=X(I)
      AMAY(IL)=Y(I)
      MOMT(KAK)=MOM(MT)
      IT=+1
      IL=IL+1
      IF(NON.EQ.MOM(MT))GOTO 5141
      GOTO 1031
5140  CONTINUE
      LAP=LAP+1
      IF(LAP.EQ.1)GOTO 103
5141  KPLUS1=K+1
```

...cont

```
      IFAIL=1
      CALL E02ADF(M,KPLUS1,NROWS,X,Y,W,WORK1,WORK2,A,S,IFAIL)
      IF(IFAIL.EQ.0) GOTO 300
      GOTO(320, 340, 360, 380, 400),IFAIL
320   WRITE(2,99932)
      GOTO 6000
340   WRITE(2,99981)
      GOTO 6000
360   WRITE(2,99980)
      GOTO 6000
380   WRITE(2,99979)
      GOTO 6000
400   WRITE(2,99978)
      GOTO 6000
300   WRITE(2,99903)
      WRITE(2,99994)M,K
      DO 108 IPLUS1=1,KPLUS1
      I=IPLUS1-1
      WRITE(2,99989)I
      WRITE(2,99988)(JPLUS1,A(IPLUS1,JPLUS1),JPLUS1=1,IPLUS1)
      WRITE(2,99987)S(IPLUS1)
108   CONTINUE
      DO 110 IPLUS1 = 1,KPLUS1
      AK(IPLUS1) = A(KPLUS1,IPLUS1)
110   CONTINUE
      MIDPT = .FALSE.
      M2 = 2*M-1
      R=0
      X1=X(1)
      XM=X(M)
      D=XM-X1
      SUM=XM+X1
      WRITE(2,99986)K
      DO 280 R2=1,M2
      IF(.NOT.MIDPT) GOTO 220
      XARG = 0.5*(X(R)+X(R+1))
      XCAPR = ((XARG-X1)-(XM-XARG))/D
      IFAIL=1
      CALL E02AEF(KPLUS1, AK, XCAPR, FIT, IFAIL)
      IF(IFAIL.NE.0) GOTO 200
      WRITE(2,99985) XARG,FIT
      GOTO 260
200   WRITE(2,99984)XARG
      GOTO260
220   R=R+1
      XCAPR=((X(R)-X1)-(XM-X(R)))/D
      IFAIL=1
      CALL E02AEF(KPLUS1, AK, XCAPR, FIT, IFAIL)
      IF(IFAIL.NE.0)GOTO240
      RES=FIT-Y(R)
      WRITE(2,99991) R, X(R), FIT, RES
      GOTO 260
240   WRITE(2,99983)R,X(R)
260   MIDPT = .NOT.MIDPT
280   CONTINUE
      IF(K.EQ.2) GOTO 5001
      GOTO 6000
 5001 MN=1
      LA=LA+1
      A0=A(3,1)
      A1=A(3,2)
      A2=A(3,3)
      WRITE(2,99906)A0,A1,A2
      Z=-(SUM/D)
      V0(LA)=A0/2.0+A1*Z+A2*((2.0*(Z**2 )-1.0)
      DO 4001 N=1,M                                          ...cont
```

```
      YRM(LA,N)=Y(N)/V0(LA)
      T1(N)=AY(2,N)
4001  CONTINUE
      IF(IT)261,261,262
262   V0T(KAK)=V0(2)
      V0T(1)=V0(1)
261   CONTINUE
      MT=MT+1
      INO=INO*(-1)
      IF(LA.EQ.2)GOTO 5020
      GOTO1
5020  CONTINUE
      STEP2=0.001
 502  CONTINUE
      V0E1=V0(2)
 503  V0E2=V0E1-STEP2
      STEP3=STEP2*2.0
      V0E3=V0E2-STEP3
      DO 4042 I=1,M
      T2(I)=AY(2,I)-(V0(2)-V0E2)
      T3(I)=AY(2,I)-(V0(2)-V0E3)
4042  CONTINUE
      N=MOM(2)
      DO 4061 I=1,N
      E1(I)=T1(I)/V0E1
      E2(I)=T2(I)/V0E2
      E3(I)=T3(I)/V0E3
4061  CONTINUE
      KM=MOM(1)+MOM(2)
      K=2
      KPLUS1=K+1
      IFAIL=1
      DO 514 I=1,KM
      W(I)=0.9
514   CONTINUE
      N=MOM(1)
      DO 626 I=1,N
      W(I)=1.0
626   CONTINUE
      CALL ORDER(AX,YRM,E1,MOM,XX,YY,W)
      CALL CHEBY(KM,KPLUS1,NROWS,XX,YY,W,WORK1,WORK2,A,S,IFAIL,K)
      RMS1=S(3)
      CALL ORDER(AX,YRM,E2,MOM,XX,YY,W)
      CALL CHEBY(KM,KPLUS1,NROWS,XX,YY,W,WORK1,WORK2,A,S,IFAIL,K)
      RMS2=S(3)
      CALL ORDER(AX,YRM,E3,MOM,XX,YY,W)
      CALL CHEBY(KM,KPLUS1,NROWS,XX,YY,W,WORK1,WORK2,A,S,IFAIL,K)
      RMS3=S(3)
      IF(RMS2.GT.RMS3) GOTO 412
      IF(MN.GT.1)GOTO 501
      STEP2=-0.001
      MN=MN+1
      GOTO 503
 412  STEP2=STEP3
      N=MOM(2)
      V0E1=V0E2
      MN=MN+1
      DO 413 I=1,N
      T1(I)=T2(I)
 413  CONTINUE
      GOTO 503
 501  CONTINUE
      WRITE (2,99911)V0E1,V0E2,V0E3
      STEP=STEP3/2.0
      V0E4=V0E3+STEP
      N=MOM(2)
```

...cont

```
      DO 513 I=1,N
      T4(I)=T3(I)+STEP
      E4(I)=T4(I)/V0E4
513   CONTINUE
      CALL ORDER(AX,YRM,E4,MOM,XX,YY,W)
      CALL CHEBY(KM,KPLUS1,NROWS,XX,YY,W,WORK1,WORK2,A,S,IFAIL,K)
      RMS4=S(3)
      WRITE(2,99904)RMS4
      WRITE(2,99904)V0E4
      WRITE(2,99913) RMS1,RMS2,RMS3,RMS4
      IF(RMS1.LT.RMS3) GOTO 510
      V0E1=V0E2
      RMS1=RMS2
      V0E2=V0E4
      RMS2=RMS4
      GOTO 511
510   V0E3=V0E4
      RMS3=RMS4
      WRITE(2,99911)V0E1,V0E2,V0E3
511   CONTINUE
      IF(V0E1.LT.V0E3) GOTO 512
      AX1=V0E1
      AX3=V0E3
      V0E1=AX3
      F1=RMS3
      F2=RMS2
      F3=RMS1
      V0E3=AX1
512   CONTINUE
      F1=RMS1
      F2=RMS2
      F3=RMS3
      WRITE(2,99911)F1,F2,F3
      WRITE(2,99911)V0E1,V0E2,V0E3
      STEPP=STEP**2
      STEPP=SQRT(STEPP)
      SM=(STEPP*(F2-F1))/(2.0*(F1-2.0*F2+F3))
      SMIN=V0E2+SM
      WRITE(2,99904)STEPP
      WRITE(2,99912)SMIN
      WRITE(2,99904)V0(1)
      WRITE(2,99904)V0(2)
      IF(KC.EQ.3)GOTO 5234
      KC=KC+1
      STEP2=-0.0001
      GOTO 503
5234  CONTINUE
      IF(KAG.EQ.MS) GOTO 5134
      SMIT(KAK)=SMIN
      GOTO 1086
5134  CONTINUE
      SMIT(KAK)=SMIN
      DO 5390 IJ=1,KAK
      SMIT(1)=V0(1)
      V0T(1)=V0(1)
      WRITE(2,99997)IJ
      WRITE(2,99904)V0T(IJ)
      WRITE(2,99904)SMIT(IJ)
      N=MOMT(IJ)
      DO 5389 IK=1,N
      NQ=NQ+1
      RAMAY(NQ)=(AMAY(NQ)-(V0T(IJ)-SMIT(IJ)))/(SMIT(IJ))
5389  CONTINUE
5390  CONTINUE
      WRITE(2,802)
      DO 5391 I=1,NQ                                          ...con
```

```
      WRITE(2,99901)AMAX(I),AMAY(I),RAMAY(I)
      WRITE(2,804)
      W(I)=1.0
5391  CONTINUE
      CALL ORD(AMAX,RAMAY,NQ,X,Y)
      KM=NQ
      WRITE(2,99997)KM
      WRITE(2,8050)NQ
      K=2
      KPLUS1=K+1
      NROWS=10
      IFAIL=1
      CALL CHEBY(KM,KPLUS1,NROWS,X,Y,W,WORK1,WORK2,A,S,IFAIL,K)
      WRITE(2,99904)S(3)
      WRITE(2,99901)((X(I),Y(I),W(I)),I=1,NQ)
      C=0.001
5133  CONTINUE
      CALL ORD(RAMAY,AMAX,NQ,X,Y)
      CALL CHEBY(KM,KPLUS1,NROWS,X,Y,W,WORK1,WORK2,A,S,IFAIL,K)
      WRITE(2,99904)S(3)
      WRITE(2,99901)((X(I),Y(I),W(I)),I=1,NQ)
      DO 6060 I=1,NQ
      X(I)=AMAX(I)
      Y(I)=RAMAY(I)
6060  CONTINUE
      NSYM=7
      NSPACE=0
      NPTS=NQ
      NINTY=5
      XMIN=0.3
      XMAX=25.0
      YMIN=1.0
      YMAX=3.5
      NINTX=25
      YOR=20.0
      XOR=20.0
      AXLEN=160.0
      AYLEN=220.0
      CALL CC1036N
      CALL DEVPAP(330.0,260.0,ITT)
      CALL AXIPOS(1,XOR,YOR,AXLEN,1)
      CALL AXIPOS(1,XOR,YOR,AYLEN,2)
      CALL AXISCA(2,NINTX,XMIN,XMAX,1)
      CALL AXISCA(2,NINTY,YMIN,YMAX,2)
      CALL PENSEL(1,0,25,3)
      CALL AXIDRA(2,1,1)
      CALL AXIDRA(-2,-1,2)
      CALL GRASYM(X,Y,NPTS,NSYM,NSPACE)
      CALL PICCLE
      CALL DEVEND
6000  STOP
      END
      SUBROUTINE ORDER(AX,AY,E,KM,X,Y,W)
      DIMENSION AX(2,1000),AY(2,1000),E(1000),KM(1000),ZZ(1000)
     *,ZZZ(1000),X(1000),Y(1000),W(1000),W1(1000)
22    FORMAT(1H ,F10.4,5X,F10.4,5X,F10.4)
      NM=KM(2)
      N=KM(1)
      NTOP=KM(1)+KM(2)
      DO 44 I=1,NTOP
      W(I)=0.1
44    CONTINUE
      DO 45 I=1,N
      W(I)=1.0
45    CONTINUE
      DO 111 I=1,N
```

...cont

```
      X(I)=AX(1,I)
      Y(I)=AY(1,I)
  111 CONTINUE
      N=N+1
      K=1
      DO 202 I=N,NTOP
      X(I)=AX(2,K)
      Y(I)=E(K)
      K=K+1
  202 CONTINUE
      K=1
  203 ZZ(K)=200.0
      DO 1012 I=1,NTOP
      IF(X(I).LT.ZZ(K)) GOTO 101
      GOTO 1011
  101 CONTINUE
      L=I
      ZZ(K)=X(I)
      ZZZ(K)=Y(I)
      W1(K)=W(I)
 1011 CONTINUE
 1012 CONTINUE
      X(L)=2000.0
      IF(K.EQ.NTOP)GOTO 204
      K=K+1
      GOTO 203
  204 DO 20 I=1,NTOP
      X(I)=ZZ(I)
      Y(I)=ZZZ(I)
      W(I)=W1(I)
   20 CONTINUE
      N=KM(2)
      I=0
  301 CONTINUE
      I=I+1
      IF(I.GT.NTOP)GOTO302
      IF(X(I).GT.AX(2,N))GOTO303
      IF(X(I).LT.AX(2,1))GOTO303
      W(I)=1.0
      GOTO301
  303 CONTINUE
      W(I)=0.001
      GOTO301
  302 CONTINUE
      RETURN
      END
      SUBROUTINE CHEBY(M,KPLUS1,NROWS,X,Y,W,WORK1,WORK2,
     *A,S,IFAIL,K)
      DIMENSION  X(1000),Y(1000),W(1000),WORK1(3,1000),WORK2(2,1000)
     *,AK(1000),A(10,1000),S(1000)
99978 FORMAT(/37H NROWS FAILS TO EXCEED MAXIMUM DEGREE)
99979 FORMAT(/27H TOO FEW DISTINCT VALUES OF, 17H THE INDEPENDENT ,
     *8HVARIABLE)
99980 FORMAT(/41H VALUES OF INDEPENDENT VARIABLE ALL EQUAL)
99981 FORMAT(031H VALUES OF INDEPENDENT VARIABLE, 13H NOT INCREASI,
     *16HNG MONOTONICALLY)
99982 FORMAT(/20H NON-POSITIVE WEIGHT)
99983 FORMAT(1H , I3, E20.5, 26H ARGUMENT OUTSIDE RANGE 83)
99984 FORMAT(5H      , E20.5, 26H ARGUMENT OUTSIDE RANGE 84)
99985 FORMAT(5H      ,2E20.5)
99986 FORMAT(/49H POLYNOMIAL APPROXIMATION AND RESIDUALS FOR DEGRE,
     *1HE, I4//24H     R     ABSCISSA        ,
     *19H      APPROXIMATION ,
     *16H          RESIDUAL/)
99987 FORMAT(/18H R.M.S. RESIDUAL =, E20.5)
99988 FORMAT(1H ,I3,E20.5)
```

...cont

```
99989 FORMAT(/7H DEGREE,I4//26H  J  CHEBYSHEV COEFF A(J) /)
99991 FORMAT(1H , I3, 3E20.5)
99994 FORMAT(40H  POLYNOMIAL FIT TO ARBITARY DATA POINTS/6H -----,34H---
     *--------------------------------//25H NUMBER OF DATA POINTS = ,I4//
     *18H MAXIMUM DEGREE = ,I4)
99997 FORMAT (I2)
      IFAIL=1
      CALL E02ADF(M,KPLUS1,NROWS,X,Y,W,WORK1,WORK2,A,S,IFAIL)
      DO 1600 IPLUS1=1,KPLUS1
      I=IPLUS1-1
 1600  CONTINUE
      DO 1800 IPLUS1 = 1,KPLUS1
      AK(IPLUS1) = A(KPLUS1,IPLUS1)
1800   CONTINUE
      RETURN
      END
      SUBROUTINE ORD(AX,AY,NQ,X,Y)
      DIMENSION AX(1000),AY(1000),KM(1000),ZZ(1000),ZZZ(1000)
     *,X(1000),Y(1000)
22    FORMAT(1H ,F10.4,5X,F10.4)
      DO 111 I=1,NQ
      X(I)=AX(I)
      Y(I)=AY(I)
111   CONTINUE
      K=1
203   ZZ(K)=200.0
      DO 1012 I=1,NQ
      IF(X(I).LT.ZZ(K)) GOTO 101
      GOTO 1011
101   CONTINUE
      L=I
      ZZ(K)=X(I)
      ZZZ(K)=Y(I)
1011  CONTINUE
 1012 CONTINUE
      X(L)=2000.0
      IF(K.EQ.NQ)GOTO 204
      K=K+1
      GOTO 203
204   DO 20 I=1,NQ
      X(I)=ZZ(I)
      Y(I)=ZZZ(I)
20    CONTINUE
      RETURN
      END
      FINISH
1X
GINODRAW G3
EJ
```

```
 2
 9
 2
0.00
6.38          2.110
7.51          2.254
8.80          2.404
10.00         2.538
12.00         2.808
13.00         2.930
13.79         3.054
15.01         3.188
15.98         3.330
13
 2
0.00
4.59          1.625
6.17          1.781
7.76          1.939
8.88          2.069
10.03         2.199
11.19         2.333
12.40         2.474
13.64         2.626
14.87         2.780
16.10         2.942
17.28         3.097
18.43         3.237
19.52         3.414
```

INPUT DATA :

DEPTH (MM)	PD (DVM)	WEIGHT W
6.38	2.11	1.00
7.51	2.25	1.00
8.80	2.40	1.00
10.00	2.54	1.00
12.00	2.81	1.00
13.00	2.93	1.00
13.79	3.05	1.00
15.01	3.19	1.00
15.98	3.33	1.00

RESULTS :

POLYNOMIAL FIT TO ARBITARY DATA POINTS

NUMBER OF DATA POINTS = 9

MAXIMUM DEGREE = 2

...cont

DEGREE 0

J CHEBYSHEV COEFF A(J)

1 0.54702E 01

R.M.S. RESIDUAL = 0.42935E 00

DEGREE 1

J CHEBYSHEV COEFF A(J)

1 0.54181E 01
2 0.60849E 00

R.M.S. RESIDUAL = 0.12995E-01

DEGREE 2

J CHEBYSHEV COEFF A(J)

1 0.54205E 01
2 0.60863E 00
3 0.10543E-01

R.M.S. RESIDUAL = 0.10589E-01

POLYNOMIAL APPROXIMATION AND RESIDUALS FOR DEGREE 2

R	ABSCISSA	APPROXIMATION	RESIDUAL
1	0.63800E 01	0.21121E 01	0.21359E-02
	0.69450E 01	0.21791E 01	
2	0.75100E 01	0.22467E 01	-0.73406E-02
	0.81550E 01	0.23245E 01	
3	0.88000E 01	0.24031E 01	-0.91259E-03
	0.94000E 01	0.24769E 01	
4	0.10000E 02	0.25513E 01	0.13336E-01
	0.11000E 02	0.26769E 01	
5	0.12000E 02	0.28043E 01	-0.37250E-02
	0.12500E 02	0.28687E 01	
6	0.13000E 02	0.29335E 01	0.34898E-02
	0.13395E 02	0.29850E 01	
7	0.13790E 02	0.30369E 01	-0.17136E-01
	0.14400E 02	0.31175E 01	
8	0.15010E 02	0.31987E 01	0.10748E-01
	0.15495E 02	0.32639E 01	
9	0.15980E 02	0.33294E 01	-0.59586E-03

A0 = 5.4205 A1 = 0.608634 A2 = 0.010543

INPUT DATA :

DEPTH (MM)	PD (DVM)	WEIGHT W
4.59	1.62	1.00
6.17	1.78	1.00
7.76	1.94	1.00
8.88	2.07	1.00
10.03	2.20	1.00
11.19	2.33	1.00
12.40	2.47	1.00
13.64	2.63	1.00
14.87	2.78	1.00
16.10	2.94	1.00
17.28	3.10	1.00
18.43	3.24	1.00
19.52	3.41	1.00

...cont

RESULTS :

POLYNOMIAL FIT TO ARBITARY DATA POINTS

NUMBER OF DATA POINTS = 13

MAXIMUM DEGREE = 2

DEGREE 0

J	CHEBYSHEV COEFF A(J)
1	0.50025E 01

R.M.S. RESIDUAL = 0.57205E 00

DEGREE 1

J	CHEBYSHEV COEFF A(J)
1	0.49261E 01
2	0.89409E 00

R.M.S. RESIDUAL = 0.31038E-01

DEGREE 2

J	CHEBYSHEV COEFF A(J)
1	0.49461E 01
2	0.89079E 00
3	0.40620E-01

R.M.S. RESIDUAL = 0.64651E 02

POLYNOMIAL APPROXIMATION AND RESIDUALS FOR DEGREE 2

R	ABSCISSA	APPROXIMATION	RESIDUAL
1	0.45900E 01	0.16229E 01	-0.21347E-02
	0.53800E 01	0.17009E 01	
2	0.61700E 01	0.17807E 01	-0.34408E-03
	0.69650E 01	0.18628E 01	
3	0.77600E 01	0.19468E 01	0.77931E-02
	0.83200E 01	0.20071E 01	
4	0.88800E 01	0.20682E 01	-0.75465E-03
	0.94550E 01	0.21320E 01	
5	0.10030E 02	0.21968E 01	-0.22436E-02
	0.10610E 02	0.22630E 01	
6	0.11190E 02	0.23303E 01	-0.27086E-02
	0.11795E 02	0.24015E 01	
7	0.12400E 02	0.24738E 01	-0.23724E-03
	0.13020E 02	0.25489E 01	
8	0.13640E 02	0.26252E 01	-0.77985E-03
	0.14255E 02	0.27020E 01	
9	0.14870E 02	0.27799E 01	-0.11487E-03
	0.15485E 02	0.28589E 01	
10	0.16100E 02	0.29390E 01	-0.30388E-02
	0.16690E 02	0.30168E 01	
11	0.17280E 02	0.30957E 01	-0.12835E-02
	0.17855E 02	0.31736E 01	
12	0.18430E 02	0.32524E 01	0.15393E-01
	0.18975E 02	0.33280E 01	
13	0.19520E 02	0.34045E 01	-0.95460E-02

... cont

A0 = 4.9461 A1 = 0.890794 A2 = 0.040620

VRO = 1.3964

PDOE = 1.2219

A	PD	(PD-PDC)/PDOE
6.38	2.11	1.51
7.51	2.25	1.61
8.80	2.40	1.72
10.00	2.54	1.82
12.00	2.81	2.01
13.00	2.93	2.10
13.79	3.05	2.19
15.01	3.19	2.28
15.98	3.33	2.38
4.59	1.62	1.34
6.17	1.78	1.47
7.76	1.94	1.60
8.88	2.07	1.71
10.03	2.20	1.81
11.19	2.33	1.92
12.40	2.47	2.04
13.64	2.63	2.16
14.87	2.78	2.29
16.10	2.94	2.42
17.28	3.10	2.55
18.43	3.24	2.66
19.52	3.41	2.81

RMS PD = 0.011
RMS A = 0.116

APPENDIX A10

DETERMINATION OF COMPLIANCE FUNCTION, STRESS INTENSITY AND GROWTH RATE

A10.0 Introduction

Computor Programme Deltak(whose flowchart, main programme, data and results are presented in Figs. A10.01 and A10.02) was used to generate values of Log (da/dN) versus LogΔK as outlined by Cooke [A10.01].

A10.1 Compliance

The compliance function (Y) for three point bend mode I fatigue testing was used as recommended by Irwin and Tada [A10.02] and is presented in Eq. 10.01.

$$Y = 1.090 - 1.735\ (a/w) + 8.20\ (a/w)^2 - 14.18\ (a/w)^3 + 14.57\ (a/w)^4 \quad \ldots(10.01)$$

This was claimed to an accuracy of 0.2% for $a/w < 0.60$.

A10.2 Stress Intensity K

Stress intensity was determined using the relationship

$$K = \frac{3PS}{2BW^2} \sqrt{\pi a}\ Y \quad \ldots(10.02)$$

where P = load

B = specimen thickness

S = 3 point bend span

W = specimen width

A10.3 Growth Rate Determination

Consider a set of crack length (a) versus cycles (N) data which corresponds to two consecutive crack lengths a_I and a_{II} and stress intensity ranges ΔK_I and ΔK_{II} as shown below

a_I	N_I	ΔK_I
a_1	N_1	ΔK_1
a_{II}	N_{II}	ΔK_{II}

Crack growth rate at a_1 was expressed as

$$(da/dN)_1 = \frac{a_{II} - a_I}{N_{II} - N_I} \qquad \ldots(10.03)$$

This was related to ΔK_1 where

$$\Delta K_1 = K_{max\ 1} - K_{min\ 1} \qquad \ldots(10.04)$$

A10.4 References

[A10.01] Cooke R.J.
M.Sc. Thesis, University of Birmingham, 1973

[A10.02] Tada, H., Paris, and Irwin, G.,
'The Stress Analysis of Cracks Handbook', DEL Research Corporation, Hellertown, Pennsylvaia, 1973, pp 2.16.

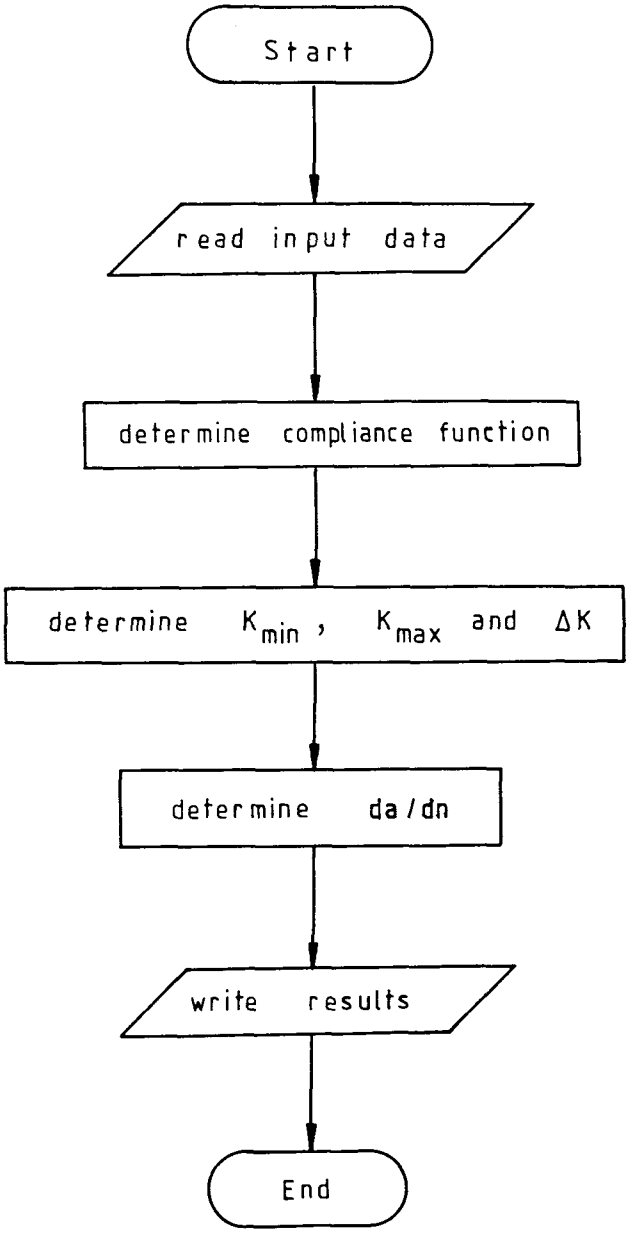


Fig. A10.01 Flowchart of Computor Programme Deltak

```
*FORTRAN
C      ************************************************************
C
C                      PROGRAMME DELTAK
C
C      ************************************************************
C
       DIMENSION A(200),          RATIO(200), Y(200), PL(200)
      *, STRESS(200), SK(200),PKN(200)
      #,AAV(200),BD(200),DN(200),DADN(200),GDADN(200),BE(200),DA(200)
1      FORMAT(1H ,7X,1HA//)
2      FORMAT(1H ,F10.4,6X,F10.3,6X,F10.4,6X,F10.5)
3      FORMAT(1H //)
  4    FORMAT(1H ,10X,7HLOAD  N,19X,8HSTRESS X,22X,1HK)
5      FORMAT(1H ,F15.1,5X,F15.1,5X,F15.1)
6      FORMAT(3F10.0)
7      FORMAT(1H0,3HA =,F10.5)
8      FORMAT(1H ,10HINPUT DATA//)
  9    FORMAT(1H ,16HSPECIMEN WIDTH =,F6.3,1HM,5X,11HTHICKNESS =,F6.3,
      *1HM,5X,8HSPAN X =,F6.3,1HM//)
10     FORMAT(1H ,7HRESULTS//)
11     FORMAT(F10.0)
12     FORMAT(1H ,8HDELTAK =,F10.4,10X,7HDLOGK =,F10.4,10X,
      #5HAAV =,F10.4//)
13     FORMAT(1H ,9HR RATIO =,F7.2)
14     FORMAT(1H ,70H**********************************************************
      ********************/)
15     FORMAT(1H ,14HCOMPLIANCE Y =,F10.4///)
16     FORMAT(1H ,4HDA =,F10.4,5X,4HDN =,F10.1,5X,11HLOG DA/DN =,F10.4)
 17     FORMAT(2F10.4)
19     FORMAT(1H ,28HREVERSED PLASTIC ZONE SIZE =,E12.4//)
20      FORMAT(1H ,9HA START =,F7.3,4X,10HA FINISH =,F7.3)
       KL=1
       L=2
       N=1
       PT=0.
       K=1
       PI=3.142
       READ(1,6)W,B,X
       READ(1,6)YS
       WRITE(2,8)
       WRITE(2,9)W,B,X
       WRITE(2,3)
       WRITE(2,10)
220    CONTINUE
       READ(1,17) A(N),BE(N)
       BD(N)=A(N)
       IF(A(N)) 2000,200,200
200    N=N+1
       GOTO 220
2000   CONTINUE
       WRITE(2,1)
       N=N-1
       J=N-1
       JA=2
       JB=1                                                    ...cont
```

Fig. A10.02 Computor Programme Deltak, Data and Results

```
      NJ=N
      DO 103 I=1,NJ
      AAV(I)=(A(I)+BE(I))/2.0
      AAV(I)=AAV(I)/1000.0
      DA(I)=BE(I)-A(I)
      A(I)=AAV(I)
103   CONTINUE
      DO 100 I=1,N
      RATIO(I) = A(I)/W
      P=RATIO(I)
      R = SQRT(P)
      Y(I)=1.09-1.735*P+8.2*(P**2)-14.18*(P**3)+14.57*(P**4)
      WRITE (2,17) BD(I),BE(I)
100   CONTINUE
      J=N+1
       WRITE(2,3)
       WRITE(2,14)
      N=N*2
      READ(1,11)((PL(I)),I=1,N)
      READ(1,11)((DN(I)),I=1,NJ)
      DO 1010 I=1,N
      PKN(I)=PL(I)
      PL(I)=PL(I)/9.81
1010  CONTINUE
300   DO 102 I=KL,L
      S=X
      STRESS(I)=(6.*PL(I)*S)/(B*4.*(W**2))
      STRESS(I)=STRESS(I)*9.81*0.000001
      Z=PI*AAV(K)
      Z=SQRT(Z)
      SK(I)=STRESS(I)*Z*Y(K)
  102 CONTINUE
      DELTK=SK(L)-SK(KL)
      AS=DELTK**2
      DELTK=SQRT(AS)
      DLOGK=ALOG10(DELTK)
      AAV(K)=(AAV(K)*1000.)
      IF (SK(L).GT.SK(KL)) GOTO 104
      AB=SK(KL)
      AC=SK(L)
      GOTO 105
104   AC=SK(KL)
      AB=SK(L)
105   R=AC/AB
      DO 221 I=1,NJ
      DADN(I)=DA(I)/(DN(I)*1.0)
      GDADN(I)=ALOG10(DADN(I))
221   CONTINUE
      WPZ=(1.0/(3.0*3.142))*((DELTK/(2.0*YS))**2)
       WRITE(2,20)BD(K),BE(K)
      WRITE(2,12)DELTK,DLOGK,AAV(K)
      WRITE(2,16)DA(K),DN(K),GDADN(K)
      WRITE(2,4)
      WRITE(2,5)((PKN(I)   , STRESS(I), SK(I)), I=KL,L)
      WRITE(2,14)
      KL=L+1
      L=L+2
      K=K+1
      IF(K.LT.J) GOTO300
      STOP
      END
      FINISH
```

...cont

```
0.04        0.10        0.160
1023.0
13.820      13.854
-2.0
280.0
2800.0
870000.0
```

RESULTS:

SPECIMEN WIDTH = 0.040M THICKNESS = 0.01M SPAN X = 0.160M

A START = 13.820 A FINISH = 13.854 AAV = 13.838

DELTAK = 8.613 DLOGK = 0.935

DA = 0.032 DN = 870000.0 LOG DA/DN = -7.434

LOAD N	STRESS X	K
280.0	4.200	0.957
2800.0	42.000	9.569

Q.E.D.